The avian flu menace—and how to fight it pp. 24 & 28

Young scientists envision the future of scientific societies p. 30

Neuroprosthetic control of baroreflex wins BII & *Science* Prize p. 46

Science

$15
7 APRIL 2023
science.org
AAAS

FATTY ACID RECEPTOR

Recognition of double bonds leads to biased signaling

p. 53

EDITORIAL

Share all SARS-CoV-2 data immediately

When the first cases of human infection with severe acute respiratory syndrome coronavirus 2 (SARS-CoV-2) were reported from Wuhan, China, in December 2019, there was quick agreement across scientific and health communities that understanding the facts about its emergence would help prevent future outbreaks. Never could I have imagined the degree of politicization that would cloud this quest. Over the past 39 months, while reported deaths from COVID-19 increased to nearly 7 million worldwide, science on the virus's origins has gotten smaller while the politics surrounding this question has grown ever bigger. Last month, the World Health Organization (WHO) learned that scientists in China possessed data on viral samples from Wuhan that had been gathered in January 2020, which should have been shared immediately—not 3 years later—with the global research community. The lack of data disclosure is simply inexcusable. The longer it takes to understand the origins of the pandemic, the harder it becomes to answer the question, and the more unsafe the world becomes.

> "...failure to share information only fuels politicization of origins tracing..."

To be clear, the work to find the origins of SARS-CoV-2 is not finished and contrary to some reports, WHO has not abandoned plans to pursue this question. When WHO established the Scientific Advisory Group for the study of the Origins of Novel Pathogens (SAGO) in 2021, the goal was for this international group of scientific experts to advise the agency on emerging and reemerging pathogens and, specifically, to study the origins of SARS-CoV-2. On 12 March of this year, WHO immediately convened SAGO to evaluate the latest findings from researchers at the Chinese Center for Disease Control and Prevention (China CDC) and from a group of international researchers who accessed these data, which appeared briefly on GISAID (Global Initiative on Sharing Avian Influenza Data), an open access repository for information (including genomic data) about influenza viruses and SARS-CoV-2. Two days later, WHO convened a meeting between SAGO, the China CDC scientists, and the international researchers.

As SAGO then stated on 18 March, the newly released data provide an important clue in understanding the amplification role that the Wuhan market played at the start of the COVID-19 pandemic. Analysis by the researchers who accessed the GISAID data indicates that animals were at the Huanan Seafood Market and suggests that some of those animals could have been an intermediate host. However, the data do not show that animals at the market were infected with SARS-CoV-2, or that people were infected from exposure to infected animals at that market. Still needed are studies that trace and test those animals to their source and serologic studies of the workers in live animal markets in Wuhan or in the source farms. Without such investigations, we cannot fully understand the factors that led to the start of this pandemic.

Every new piece of data could potentially move the world closer to stopping another pandemic—perhaps a worse one—in the future. The failure to share information only fuels politicization of origins tracing and keeps all hypotheses viable. Unfortunately, the WHO-China joint study of the origins of SARS-CoV-2 in Wuhan, published in March 2021, was heavily criticized for the lack of unfettered access to raw data on early COVID-19 cases in China. We still don't have this access.

Since its inception, SAGO has met frequently to issue recommendations for SARS-CoV-2 origins and mpox, and draft a Global Framework that defines studies into the origins of pathogens with epidemic and pandemic potential. Later this year, it will publish this framework as well as a status report on knowledge about SARS-CoV-2 origins.

China has advanced technical capabilities and I therefore believe that more data exist that have yet to be shared—on the wild and farmed animal trade; the testing of humans and animals in Wuhan and across China; the operations of labs in Wuhan working on coronaviruses; the earliest potential cases; and more. Lab audit data exist and have not been shared, for example.

WHO continues to call on China and all countries to share any data on the origins of SARS-CoV-2, immediately. The world needs to move away from the politics of blame and, instead, exploit all diplomatic and scientific approaches so that the global scientific community can do what it does best—collaborate, focus on this health crisis, and find evidence-based solutions to thwart future pandemics.

Time is running out.

–Maria D. Van Kerkhove

PHOTO: CHRISTOPHER WILLIAM BLACK

Maria D. Van Kerkhove is the COVID-19 Technical Lead and the Emerging Diseases and Zoonoses Lead in the Department of Epidemic and Pandemic Preparedness and Prevention, Health Emergencies Programme, World Health Organization, Geneva, Switzerland. vankerkhovem@who.int

10.1126/science.adi0490

EDITORIAL

Strengthening the scientific record

H. Holden Thorp
is Editor-in-Chief of the *Science* journals.
hthorp@aaas.org; @hholdenthorp

Valda Vinson
is Executive Editor of the *Science* journals.
vvinson@aaas.org

Jake Yeston
is Editor of Research at *Science*.
jyeston@aaas.org

Science is a social process. Discoveries—even by supposed "lone" geniuses—do not become knowledge until the findings are shared with the scientific community, to be vetted, challenged, and expanded on. Since the birth of the digital age, this discourse has become much more apparent, as communication outlets such as social media, blogs, and websites such as PubPeer and Retraction Watch allow the scientific community to discuss new findings. Further, the availability of greater amounts of data that support findings allows peers to redo key analyses to confirm or report discrepancies. This week, *Science* is announcing two changes—one to accelerate the conversation about papers and another to ease deposition of supporting data—that will facilitate the evaluation of research findings across the wide scientific enterprise.

> **"...*Science* is announcing two changes...that will facilitate the evaluation of research findings..."**

For years, the *Science* family of journals has offered Technical Comments as a mechanism for the scientific community to critique the core conclusions or methodology of research that we publish. The author is given a chance to respond, and both the comment and response are peer-reviewed. This time-consuming process was well suited to a pre–digital age. However, online platforms that support rapid and efficient post-publication discussions are a better fit. Therefore, we are discontinuing the Technical Comments and Technical Response article types and will instead use eLetters as a forum to host comments. eLetters are submitted on our website, directly on the relevant article page, and can be posted quickly. Moreover, comments will remain directly associated with the paper on the website. We hope this change will facilitate timely and helpful scientific conversations on published research papers.

Notably, eLetters are not a platform for correcting the scientific record. Errors that affect scientific accuracy may be addressed through our existing process of posting a corrected version of the paper along with an Erratum that can be cited. Cases of large-scale error or misconduct may lead to a retraction. Anyone with concerns regarding the integrity of a paper published in a *Science* journal should contact Science_data@aaas.org. Matters will be investigated according to guidelines from the Committee on Publication Ethics. When possible, concerns about a given paper are handled by the journal editor responsible for the original paper—these individuals are extremely knowledgeable about every paper they publish. The exception is *Science Advances*, which has a designated Research Integrity Officer to handle these issues because of the large number of papers that the journal publishes.

In keeping with our commitment to reproducibility and FAIR (findable, accessible, interoperable, reusable) data principles, we require all data underlying the results in published papers to be publicly and immediately available. An analysis of *Science* papers published in 2020 found that nearly three-quarters used external public repositories. Questions about complying with our data access requirements arise mainly in regard to datasets that lack a corresponding field-specific repository. We are now partnering with Dryad, a nonprofit open data repository, to address this issue and simplify the process overall. Authors will have the option of depositing data at Dryad directly from the submission site of any *Science* family journal when they upload their paper. To ensure that this service is available to all authors, *Science* journals will cover the cost of publishing data at Dryad that is associated with accepted papers. During peer review of a *Science* journal manuscript, data deposited at Dryad will be seamlessly and privately available to editors and reviewers. Authors will also have the opportunity to provide links to other data repositories. We hope that simplifying data deposition will strengthen the reproducibility of work published in *Science* journals.

Ensuring the accuracy of the scientific record is a community process. Researchers, journals, reviewers, image sleuths, and readers all contribute to making sure that the literature is accurate. However, each element of the ecosystem is imperfect. Researchers make inadvertent, and sometimes deliberate, errors. Reviewers don't always examine every detail. Journals make judgment calls that are not always correct. But collectively, and with the engagement of a wide community that has access to underlying data, a vetted and validated record is possible.

–H. Holden Thorp, Valda Vinson, Jake Yeston

Published online 30 March 2023; 10.1126/science.adi0333

> “Whole lines of thought get dropped when Black women walk away from physics and aren’t there to advocate for their contributions.”
>
> **Physicist Chanda Prescod-Weinstein**, in *Physics Today*, about a new bibliography, Cite Black Women+ in Physics and Astronomy. It highlights more than 4000 papers by U.S. Black women authors.

Check for updates

IN BRIEF

Edited by **Jeffrey Brainard**

Workers prepare to disinfect a Wuhan market in 2020 after researchers took samples for genetic analysis.

COVID-19

Chinese team posts key DNA from market

After intense pressure and criticism from many scientists, Chinese researchers last week released a trove of new genetic data that may offer fresh clues about the origin of the COVID-19 pandemic. Some scientists say the new evidence gives more credibility to the thesis that SARS-CoV-2 could have jumped into humans from raccoon dogs or other mammals illegally sold at a Wuhan market. Researchers mainly affiliated with the Chinese Center for Disease Control and Prevention collected 923 samples in or near the market in early 2020 and analyzed the genetic sequences in them. In a preprint posted 13 months ago, they said the abundance of human DNA in samples that contained SARS-CoV-2 “highly suggests” that people brought the coronavirus to the market. The preprint did not mention that some samples positive for the virus also contained genetic evidence that mammals susceptible to SARS-CoV-2 were present. Last week, the team updated the preprint to acknowledge the genetic evidence of the mammals. But the revised manuscript says the samples don’t resolve whether infected animals, humans, or even contaminated food introduced the virus to the market, where the first cluster of COVID-19 cases surfaced in December 2019. Chinese authorities shuttered the market on 1 January 2020.

Australia enacts emissions curbs

CLIMATE | Following through on a campaign promise, Australia’s Labor government last week enacted the nation’s first major climate law in a decade. The new law requires some 200 major industrial facilities to reduce greenhouse emissions by roughly 5% per year, to support the country’s Paris agreement commitment to cut emissions 43% by 2030 compared with 2005 levels. Climate activists welcomed the law, saying it will aid international efforts to curb global warming. But they fear it will allow Australia to continue to be one the world’s largest exporters of fossil fuels, primarily coal. A key bloc of Green Party lawmakers had pushed for the measure to bar new coal mines and oil and gas fields, but ultimately dropped that demand.

Benin metal traced to Germany

ARCHAEOLOGY | Germany’s Rhineland region was the source of the brass used to make many of the famous artworks called the Benin Bronzes, created in the West African kingdom of Benin, a study has found. Some museums, including several in Germany, have begun to return the bronzes to Nigeria, where they were looted by British soldiers in the late 19th century. Previous studies indicated the lead isotope signature in the Benin Bronzes was consistent across hundreds of works made from the 16th

A Benin Bronze representing a king was among 21 repatriated by Germany to Nigeria in December 2022.

PHOTOS: (LEFT TO RIGHT) AN YUAN/CHINA NEWS SERVICE/GETTY IM

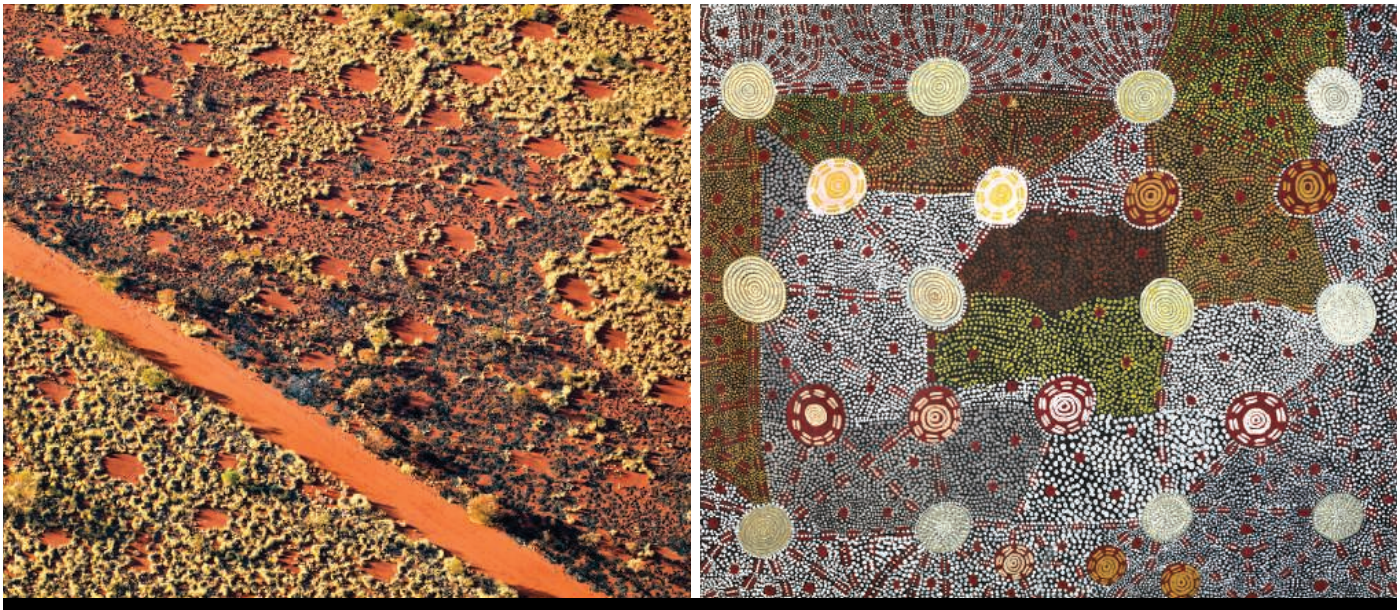

ECOLOGY

Aboriginal knowledge links Australia's 'fairy circles' to termites

Researchers say Aboriginal people in Western Australia provided insights that may help settle a debate about the origin of mysterious small patches of barren earth known as "fairy circles." Some ecologists think the patches, found in arid grasslands in Australia and Namibia, result from plants competing for water and nutrients. A study in this week's issue of *Nature Ecology & Evolution* argues this explanation ignores an alternative backed by thousands of years of Aboriginal knowledge, depicted in paintings and stories: The circles stem in part from underground nests of flying harvester termites. Aboriginal people have gathered them for food and other uses. Dozens of Aboriginal elders and experts, listed as co-authors on the new paper, shared this traditional knowledge with partners at Australian research institutions. The scientists confirmed it by digging trenches in the patches, known locally in Western Australia as *linyji*, which revealed extensive termite tunnels. The authors say the results offer a lesson for scientists who ignore the traditional knowledge of Indigenous people.

Patches in Australia created partly by termites are seen in an aerial photograph (left) and a 1976 painting (right) by Aboriginal artist Kaapa Tjampitjinpa.

century onward, indicating a common source. Now, a team has found a matching signal in a subset of the brass rings called "manillas" that served as currency for trade between Europe, Africa, and North America from the 15th to the 19th centuries. The researchers found that the isotope signature found in the bronzes matches that of the brass in manillas that were made in the Rhineland and used by Portuguese traders—and not, as previously assumed, manillas made in Britain or Flanders. The consistent signature suggests the artisans who crafted the sculptures and plaques were selective about the metal they used, say authors of the study, published this week in *PLOS ONE*.

Outsize black hole revealed

ASTRONOMY | Researchers have used gravitational lensing—the bending of light by mass—to detect an otherwise invisible black hole that is among the largest ever found. Supermassive black holes sit at the heart of most galaxies, but astronomers had only been able to detect active ones—those that consume gas and dust, which glow as they approach the hole. A team reported a way to find inactive ones last week in *Monthly Notices of the Royal Astronomical Society*. They derived the method using images from the Hubble Space Telescope showing that the galaxy Abell 1201 bends light from more distant objects. The team used supercomputer simulations in which they assumed Abell 1201 contains a central black hole. They simulated different masses of the black hole to see which bent light in a way similar to the Hubble images. The best statistical fit was one with a gigantic black hole, weighing nearly 33 billion Suns, close to a theoretical limit.

Scientists call for AI pause

COMPUTER SCIENCE | Academic and industry scientists have flocked to sign an open letter calling for a pause in the development of cutting-edge artificial intelligence (AI) applications until safeguards are installed. The signatories worry, for example, about the automated spread of misinformation and elimination of jobs. The letter was posted last week by the nonprofit Future of Life Institute; signatories include Yoshua Bengio, a Turing Prize winner at the University of Montreal, and Apple co-founder Steve Wozniak. The letter says the moratorium should apply only to "unpredictable black-box models" more powerful than GPT-4, the AI tool unveiled in March by OpenAI, a Microsoft subsidiary, that produces humanlike responses to questions. Tech companies are racing to develop such tools with little regard for economic and political consequences, the letter says. In recent months, several of the largest firms have laid off employees in "AI ethics" working to counteract potential harms. Other scientists say the letter is alarmist and overly pessimistic.

PHOTOS: F. WALSH *ET AL., NAT. ECOL. EVOL.*, 10.1038/S41559-023-01994-1 (2023)

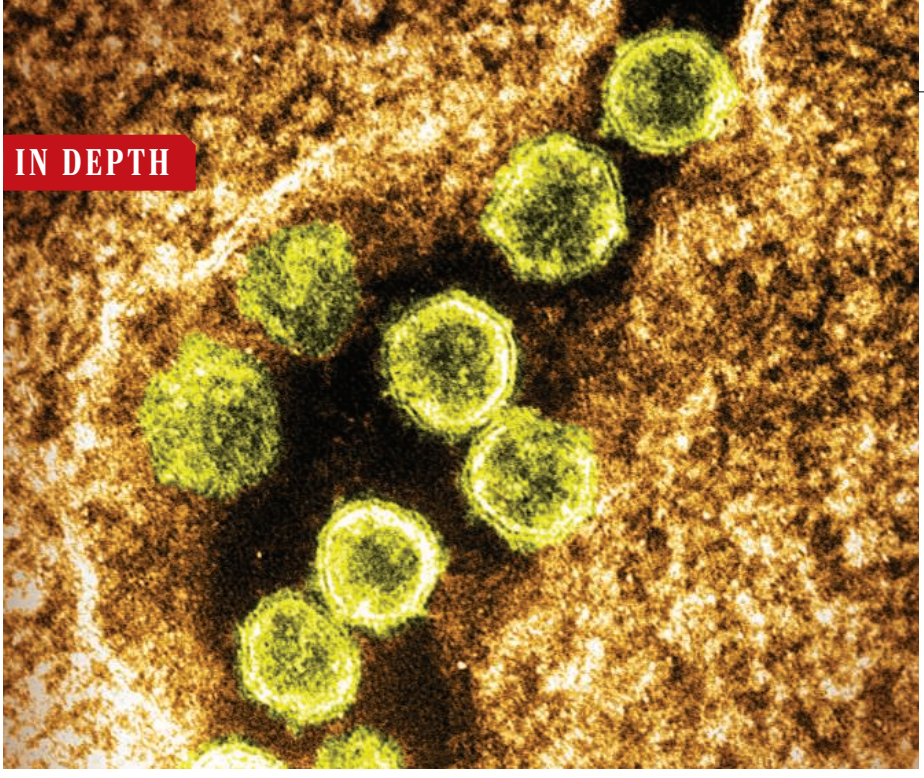

The first genome of the pandemic coronavirus, sh
here in infected cells, touched off a vaccine race.

Check for updates

VIROLOGY

Dispute simmers over who first shared SARS-CoV-2's genome

Scientists suggest that GISAID, a prominent database of virus sequences, is rewriting pandemic history

By **Martin Enserink**

GISAID, a widely used database where scientists deposit influenza and SARS-CoV-2 genomes, doubled down last month on a claim that has puzzled and infuriated some virologists for 3 years. In a statement about a set of controversial sequences from a Wuhan market that hint at the origin of the COVID-19 pandemic, GISAID emphasized it was the first place to publicly share SARS-CoV-2 genomes, on 10 January 2020.

That claim flies in the face of countless contemporaneous news and social media accounts, the memories of many researchers contacted by *Science*, and non-GISAID records. All indicate the first SARS-CoV-2 sequence was publicly shared through virological.org, an online forum, early on 11 January in Europe. It was submitted by Edward Holmes, an evolutionary biologist and virologist at the University of Sydney. Holmes received the sequence from Zhang Yong-Zhen, a virologist at Fudan University. GISAID, various sources suggest, didn't actually make its first genomes of the new coronavirus public until 12 January 2020.

"I am very surprised" at GISAID's claims, Zhang wrote in an email to *Science*. "I could not understand why some people attempted to rewrite the history."

Ben Branda, GISAID's vice president and in-house counsel, stood by its chronology in an email to *Science*. The notion that the Zhang genome came first is "inaccurate," he wrote, and based on "misinformation."

The debate is about more than scientific glory, says Scripps Research evolutionary biologist Kristian Andersen, who calls GISAID's version of events "deeply problematic." He says it could undermine trust in the database, which stores data from thousands of contributors in 215 nations and territories and has played a key role in charting the evolution of SARS-CoV-2.

Holmes says he would gladly credit GISAID if it was indeed first. "It's not an ego thing," he says. "But I have seen absolutely no evidence of their claim."

The release of the first SARS-CoV-2 genome was the subject of an intense tussle in China, where several laboratories had sequenced the virus by early January 2020. Zhang's lab, which had long collaborated with Holmes, received a sample from a COVID-19 patient on 3 January and had a sequence ready on 5 January. That day, Zhang uploaded it to GenBank, a public database run by the U.S. National Institutes of Health (NIH), but did not make it immediately visible to others. (China had reportedly banned researchers there from making the sequence public.) Zhang, Holmes, and colleagues also sent a paper on the new virus to *Nature* on 7 January.

On 8 January, *The Wall Street Journal* became the first media outlet to report that the outbreak in Wuhan was caused by a new coronavirus and that Chinese researchers had sequenced it, but the article didn't identify which scientists. Worried by the delay in sharing the viral genome, seen as key to developing diagnostics, vaccines, and drugs, Holmes had a "series of frantic calls" with Jeremy Farrar, head of the Wellcome Trust, on 9 January, as Farrar wrote in his book *Spike: The Virus vs. The People—the Inside Story*. The two decided Holmes would ask Zhang to go public with the sequence while Farrar would urge George Gao, head of the Chinese Center for Disease Control and Prevention (China CDC), to do the same with genomes they believed the agency had.

Zhang gave Holmes approval to make the sequence public on 11 January. Holmes says he then called virologist Andrew Rambaut of the University of Edinburgh, who runs virological.org. Rambaut posted the sequence at 1:05 a.m. Greenwich Mean Time (GMT) on 11 January. Three minutes later, Holmes announced the posting in a tweet.

The release was hailed as a milestone. "Potentially really important moment in global public health," Farrar tweeted. The same day, vaccine developers began plotting how to use the sequence.

But GISAID, now home to more than 15 million SARS-CoV-2 genomes, has a different version. Branda says China CDC submitted three genomes to GISAID at 11:29 p.m. GMT on 9 January 2020, the morning of 10 January in Beijing. The first two genomes were released just over an hour later, he says, or more than 24 hours before Zhang's sequence went up on virological.org. Records of the two genomes on GISAID's database list 10 January as the date of submission, but don't say when they went public.

GISAID also immediately announced the news on its website, Branda says. A search on the Wayback Machine, which records web pages, shows GISAID had a short story titled "China releases genetic sequence of newly discovered coronavirus from Wuhan" up by 13 January, but the archive did not capture GISAID's site on 10–12 January.

IMAGE: NIAID/SCIENCE SOURCE

If GISAID did make an announcement on 10 January, it appears to have gone completely unnoticed by the scientific community, the media, and services that follow disease outbreaks closely, such as ProMED and FluTrackers. "It makes no sense at all" that not a single scientist spoke or tweeted about the release of SARS-CoV-2's genome if it occurred on 10 January, Andersen says. "The internet has memories," Zhang adds.

GISAID's timeline is also at odds with official timelines released by the World Health Organization (WHO) and China. WHO received the first China CDC genomes at 6:10 p.m. GMT on 11 January, an agency spokesperson says. At 9:23 p.m. GMT—early on the morning of 12 January in Beijing—the agency reported the arrival of the sequences in a tweet. (For unclear reasons, WHO had not acknowledged the Zhang genome on virological.org.) WHO also tweeted that Chinese officials had submitted sequences to the GISAID platform, and said: "We expect them to be made publicly available as soon as possible." China's timeline, released by state news agency Xinhua in April 2020, also says the release occurred on 12 January.

Virologist Jason McLellan of the University of Texas, Austin, clearly recalls the release on virological.org as the moment the race to produce a SARS-CoV-2 vaccine began. "I don't know anybody who got the first sequence from GISAID," he says, adding that it's "very unlikely" that GISAID's timeline is correct. When a colleague first told him about it, "It sort of shocked me," McLellan says.

GISAID's Branda says the Xinhua and WHO timelines are inaccurate. To support that assertion, he shared WhatsApp messages between GISAID and WHO officials. But they appear to show only that on 10 January GISAID shared with WHO the position of the novel virus in the coronavirus family tree, based on a gene called *orf1b*, and not when the genome was posted. (WHO did not comment on the messages.)

Branda also referenced four scientific papers that cite GISAID as the source of the first genomes, including a landmark article in *The New England Journal of Medicine* (*NEJM*) in December 2020 on the COVID-19 vaccine produced by BioNTech and Pfizer. Its authors wrote that vaccine development began on 10 January 2020, "when the SARS-CoV-2 genetic sequence was … disseminated globally" on GISAID. (The authors of the *NEJM* paper referred questions from *Science* about this citation to Pfizer, which said it is looking into the issue.)

Gao has supported GISAID's chronology, saying in the 2021 CNN documentary *Race to the Vaccine* that "on the morning of January 10th, we published the sequences for the whole world to see." He did not respond to questions from *Science* but sent references to three of the four papers.

GISAID has argued for its timeline on multiple fronts. A March 2022 profile of Holmes in *The New York Times* originally reported that he and Zhang were the first to make SARS-CoV-2 genomes public, but the story was changed 6 days later to align with GISAID's version of events. A *New York Times* spokesperson says the change was made after GISAID contacted the paper.

Andersen says GISAID is also pressuring scientists to support its chronology. After he and his co-authors gave GISAID a chance to review a manuscript that credited virological.org with posting the first genome, he says GISAID officials insisted that the reference be replaced with one supporting their timeline. The team refused, he says, but agreed to cite the *NEJM* paper.

Even after Andersen and his colleagues published their paper, he says, GISAID officials kept asking them to remove the virological.org reference. "They're basically asking you to participate in their revisionist history," he says. "I'm not willing to do that." ■

A conflict over chronology

This screenshot shows entries for the first two SARS-CoV-2 genomes placed in the GISAID database. But some virologists dispute GISAID's claim to have been the first to publicly share the sequences.

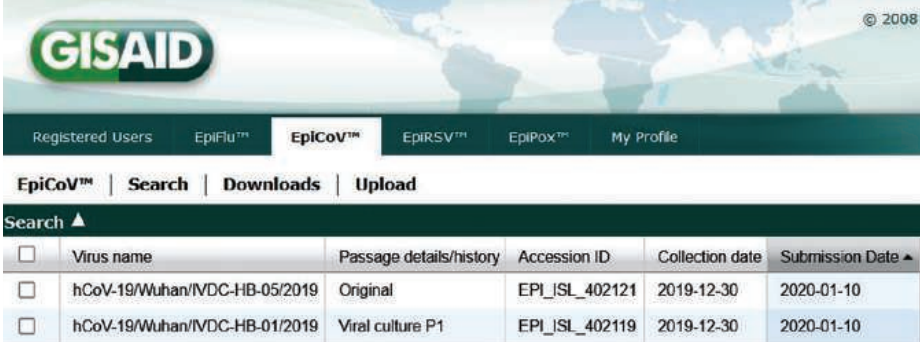

PLANETARY SCIENCE

Magnets wipe memories from meteorites

Researchers sound alarm over damage caused by popular meteorite-hunting technique

By **Zack Savitsky**

In 2011, nomads roaming the western Sahara encountered precious time capsules from Mars: coal-black chunks of a meteorite, strewn across the dunes. "Black Beauty," as the parent body came to be known, captivated scientists and collectors because it contained crystals that formed on Mars more than 4.4 billion years ago, making it older than any native rock on Earth. Jérôme Gattacceca, a paleomagnetist at the European Centre for Research and Teaching in Environmental Geosciences, hoped it might harbor a secret message, imprinted by the now-defunct martian magnetic field—which is thought to have helped the planet sustain an atmosphere, water, and possibly even life.

But when Gattacceca obtained a piece of Black Beauty and tried to decode its magnetic inscription, he found its memory had been wiped—*Men in Black* style—and replaced by a stronger signal. He instantly knew the culprit. Somewhere along its journey from Moroccan desert to street dealers to laboratory, the rock had been touched by strong hand magnets, a widely used technique for identifying meteorites. "It's a pity that, just by using magnets, we've been destroying this scientific information that was stored there for 4 billion years," Gattacceca says.

In a new study, Foteini Vervelidou, a planetary scientist at the Massachusetts Institute of Technology (MIT), and her colleagues have documented the destructive power of the hand magnets, which are often made from rare-earth metals such as neodymium and are typically about 10,000 times stronger than Earth's magnetic field. When brought within a few centimeters of a rock, the researchers found, the magnets overwrite vestigial fields contained in iron-based minerals such as magnetite and reset them to the higher strength and orientation of the

If GISAID did make an announcement on 10 January, it appears to have gone completely unnoticed by the scientific community, the media, and services that follow disease outbreaks closely, such as ProMED and FluTrackers. "It makes no sense at all" that not a single scientist spoke or tweeted about the release of SARS-CoV-2's genome if it occurred on 10 January, Andersen says. "The internet has memories," Zhang adds.

GISAID's timeline is also at odds with official timelines released by the World Health Organization (WHO) and China. WHO received the first China CDC genomes at 6:10 p.m. GMT on 11 January, an agency spokesperson says. At 9:23 p.m. GMT—early on the morning of 12 January in Beijing—the agency reported the arrival of the sequences in a tweet. (For unclear reasons, WHO had not acknowledged the Zhang genome on virological.org.) WHO also tweeted that Chinese officials had submitted sequences to the GISAID platform, and said: "We expect them to be made publicly available as soon as possible." China's timeline, released by state news agency Xinhua in April 2020, also says the release occurred on 12 January.

Virologist Jason McLellan of the University of Texas, Austin, clearly recalls the release on virological.org as the moment the race to produce a SARS-CoV-2 vaccine began. "I don't know anybody who got the first sequence from GISAID," he says, adding that it's "very unlikely" that GISAID's timeline is correct. When a colleague first told him about it, "It sort of shocked me," McLellan says.

GISAID's Branda says the Xinhua and WHO timelines are inaccurate. To support that assertion, he shared WhatsApp messages between GISAID and WHO officials. But they appear to show only that on 10 January GISAID shared with WHO the position of the novel virus in the coronavirus family tree, based on a gene called *orf1b*, and not when the genome was posted. (WHO did not comment on the messages.)

Branda also referenced four scientific papers that cite GISAID as the source of the first genomes, including a landmark article in *The New England Journal of Medicine* (*NEJM*) in December 2020 on the COVID-19 vaccine produced by BioNTech and Pfizer. Its authors wrote that vaccine development began on 10 January 2020, "when the SARS-CoV-2 genetic sequence was … disseminated globally" on GISAID. (The authors of the *NEJM* paper referred questions from *Science* about this citation to Pfizer, which said it is looking into the issue.)

Gao has supported GISAID's chronology, saying in the 2021 CNN documentary *Race to the Vaccine* that "on the morning of January 10th, we published the sequences for the whole world to see." He did not respond to questions from *Science* but sent references to three of the four papers.

GISAID has argued for its timeline on multiple fronts. A March 2022 profile of Holmes in *The New York Times* originally reported that he and Zhang were the first to make SARS-CoV-2 genomes public, but the story was changed 6 days later to align with GISAID's version of events. A *New York Times* spokesperson says the change was made after GISAID contacted the paper.

Andersen says GISAID is also pressuring scientists to support its chronology. After he and his co-authors gave GISAID a chance to review a manuscript that credited virological.org with posting the first genome, he says GISAID officials insisted that the reference be replaced with one supporting their timeline. The team refused, he says, but agreed to cite the *NEJM* paper.

Even after Andersen and his colleagues published their paper, he says, GISAID officials kept asking them to remove the virological.org reference. "They're basically asking you to participate in their revisionist history," he says. "I'm not willing to do that." ■

A conflict over chronology

This screenshot shows entries for the first two SARS-CoV-2 genomes placed in the GISAID database. But some virologists dispute GISAID's claim to have been the first to publicly share the sequences.

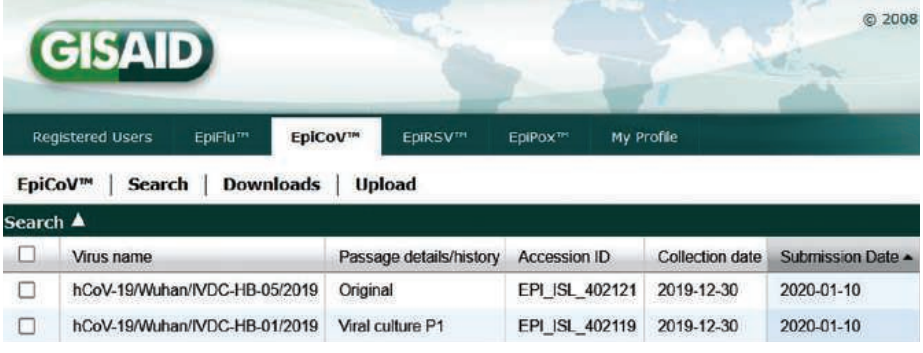

PLANETARY SCIENCE

Magnets wipe memories from meteorites

Researchers sound alarm over damage caused by popular meteorite-hunting technique

By **Zack Savitsky**

In 2011, nomads roaming the western Sahara encountered precious time capsules from Mars: coal-black chunks of a meteorite, strewn across the dunes. "Black Beauty," as the parent body came to be known, captivated scientists and collectors because it contained crystals that formed on Mars more than 4.4 billion years ago, making it older than any native rock on Earth. Jérôme Gattacceca, a paleomagnetist at the European Centre for Research and Teaching in Environmental Geosciences, hoped it might harbor a secret message, imprinted by the now-defunct martian magnetic field—which is thought to have helped the planet sustain an atmosphere, water, and possibly even life.

But when Gattacceca obtained a piece of Black Beauty and tried to decode its magnetic inscription, he found its memory had been wiped—*Men in Black* style—and replaced by a stronger signal. He instantly knew the culprit. Somewhere along its journey from Moroccan desert to street dealers to laboratory, the rock had been touched by strong hand magnets, a widely used technique for identifying meteorites. "It's a pity that, just by using magnets, we've been destroying this scientific information that was stored there for 4 billion years," Gattacceca says.

In a new study, Foteini Vervelidou, a planetary scientist at the Massachusetts Institute of Technology (MIT), and her colleagues have documented the destructive power of the hand magnets, which are often made from rare-earth metals such as neodymium and are typically about 10,000 times stronger than Earth's magnetic field. When brought within a few centimeters of a rock, the researchers found, the magnets overwrite vestigial fields contained in iron-based minerals such as magnetite and reset them to the higher strength and orientation of the

Researchers in the Atacama desert use a susceptibility meter to identify a meteorite without contaminating it.

magnet. In an instant, a unique view into the heart of distant rocky bodies can be erased. Black Beauty, for example, is the only known meteorite old enough to "remember" Mars's magnetic field before it started to disappear about 4 billion years ago.

Vervelidou hopes that raising awareness will help convince hunters, collectors, and researchers to give up a technique that's still promoted by the U.S. Geological Survey, universities, and popular meteorite hunting TV shows. "It's like having this unique piece [of information] destroyed," Vervelidou says. "Why would you buy an amazing painting and then throw some sauce on it?"

Hand magnets are effective for distinguishing ordinary chondrites, an abundant kind of meteorite that is often loaded with metals, from many Earth rocks. But their diagnostic abilities have limits. Some common iron-rich Earth rocks, such as basalt, can also attract magnets, whereas the meteorites that come from Mars or the Moon often don't. Most of the iron on those larger bodies is in their core, not their crust, where meteorites originate. "The irony is that the [meteorites] that don't stick to magnets are actually the most valuable of all," says Ben Weiss, a study co-author and MIT planetary scientist.

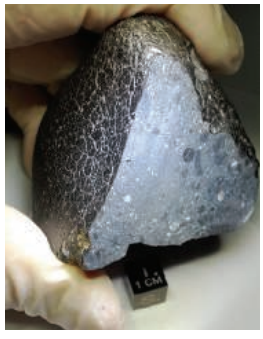

The magnetic memory of Black Beauty, a meteorite from Mars, was destroyed by magnets.

The problem is not new. Two decades ago, Weiss was studying rare meteorite samples to see whether some asteroids were ever big enough to have a dynamo—a churning molten core that generates magnetic fields. He saw spectacularly high magnetizations in each of the samples only to realize, later, that he'd been duped by magnets. Weiss says the meteoritic literature is rife with false magnetic findings—such as reports of extreme fields in one of the most studied meteorites of all time, Allende, which fell in Mexico in 1969. "I wasn't the first one to be fooled."

After the frustration of finding magnetic contamination in nine different Black Beauty samples, the researchers decided to confront the hand-magnet issue head-on. In their study, accepted this week by the *Journal of Geophysical Research: Planets*, they calculated how magnets of different strengths would alter a meteorite's magnetic records as they approached the rock. Study co-author France Lagroix, at the Paris Institute of Planetary Physics, helped check the calculations by measuring the fields in 13 specimens of terrestrial basalt before and after placing a typical hand magnet at various distances from them. The results showed how the magnet progressively resets fields from the outside in, giving researchers a guide for how deep they would have to cut to find a pristine sample. "Now we're 100% sure, if we weren't already, that this is what's going on," Weiss says.

But for most people—even other meteorite researchers—the magnetic records aren't as precious as they are to paleomagnetists. The "quick-and-dirty" method of meteorite identification persists because "not everybody cares about magnetic fields like Ben Weiss does," says Carl Agee, the meteoriticist at the University of New Mexico who first determined Black Beauty hailed from Mars.

For the past 2 decades, Hasnaa Chennaoui Aoudjehane, a planetary scientist at the Hassan II University of Casablanca, has been trying to educate Saharan meteorite hunters about the dangers of hand magnets. But the message doesn't always sink in. "We try explaining to hunters … 'it's the human heritage; it's the history of the Solar System," Chennaoui Aoudjehane says. "But when someone needs to buy bread and things to live every day … their priority is not the science that is conducted on those rocks. It's their source of revenue." Saïd Yousfi, a meteorite collector and dealer in Morocco, agrees magnets will remain a fixture of the Saharan meteorite-hunting culture—despite the fact that most local hunters are skilled enough to identify meteorites by eye.

In their study, Vervelidou and her colleagues recommend an alternative: susceptibility meters. These devices apply a weak magnetic field that doesn't erase the records, and they are better at identifying different types of meteorites. The catch is that commercial devices often cost a few thousand dollars, and they're not as intuitive to use as a simple magnet. Gattacceca and colleagues are now building handheld susceptibility meters that have only one button and cost a few hundred dollars.

Gattacceca hopes to make inroads with scientists. He points to the Antarctic Search for Meteorites (ANSMET), an annual expedition funded by the National Science Foundation. His collaborators there told him they weren't using magnets on their samples, so he assumed the large magnetizations he was finding were relics of the early Solar System.

But a few years ago, a colleague participating in the expedition brought back a small hand magnet adorned with the ANSMET logo. It had been distributed in the researchers' field kits. "That's what you call a smoking gun," Gattacceca says. "Once you have the gun, you're likely to use it." ■

Zack Savitsky is a journalist in New York City.

PHOTOS: (TOP TO BOTTOM) GABRIEL PINTO; NASA

Promising Alzheimer's therapies shrink brains

Effects of antiamyloid antibody drugs worry some scientists, who call for more study

By **Jennifer Couzin-Frankel**

A class of drugs meant to slow the cognitive decline of Alzheimer's disease, including one that appears to have real but modest benefits, can cause brain shrinkage, a new analysis shows. Although scientists and drug developers have documented brain volume loss in trials of the drugs for years, the scientific review, published last week in *Neurology*, is the first to look at data across numerous studies. It also links the brain shrinkage to a better known side effect of the drugs, brain swelling.

"We don't fully know what these changes might imply," says Jonathan Jackson, a cognitive neuroscientist at Massachusetts General Hospital. But, he says, "It's likely these changes are detrimental." They cast a shadow on the promise of one drug, the antibody lecanemab, which was granted accelerated approval in the United States in January after a trial showed it slowed the rate of cognitive decline by 27% after 18 months compared with people on a placebo.

The analysis alarmed Scott Ayton, a neuroscientist at the Florey Institute of Neuroscience and Mental Health in Melbourne, Australia, who led the work and has advised Eisai, which led the development of lecanemab. "We're talking about the possibility of brain damage" from treatment, Ayton says. "I find it very peculiar that these data, which are very important, have been completely ignored by the field."

A spokesperson for Eisai suggested the brain shrinkage could be benign. The company said that although participants in its pivotal trial did experience "greater cortical volume loss on lecanemab relative to placebo," those reductions may be due to the antibody clearing the protein beta amyloid from the brain and reducing inflammation.

But that's sheer speculation, some scientists worry. "We don't know what [the shrinkage] means," says Lon Schneider, director of the California Alzheimer's Disease Center at the Keck School of Medicine of the University of Southern California. It's crucial, he says, to "try to seriously understand this."

Ayton and two colleagues identified 31 published clinical trials of drugs that aim to eliminate beta amyloid, whose buildup many consider a driver of the disease. About half were trials of secretase inhibitors, traditional small-molecule drugs targeting an enzyme that produces beta amyloid from a larger protein. (Those drugs have been largely abandoned due to ineffectiveness.) The others were trials of monoclonal antibodies like lecanemab that directly target various forms of beta amyloid. Another antiamyloid antibody in the analysis, aducanumab, was approved in 2021 amid much controversy, and still others are in trials.

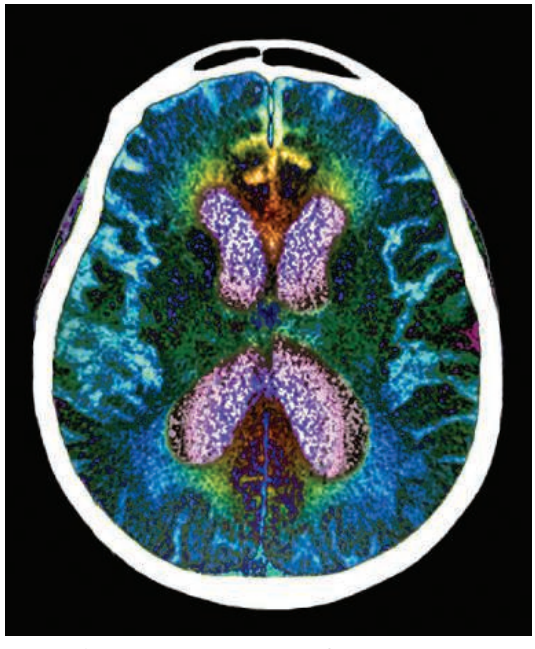

A CT scan shows the brain of a 78-year-old woman with Alzheimer's disease.

IMAGE: ZEPHYR/SCIENCE PHOTO LIBRARY

Alzheimer's disease frequently causes the brain to shrink. But the researchers found both types of antiamyloid drugs generally caused trial participants to lose brain volume faster. In two large lecanemab trials, people on the highest dose—which is the one the U.S. Food and Drug Administration (FDA) approved—recorded, on average, a 28% greater brain volume loss than people on placebo after about 18 months. This translated to a loss of an extra 5.2 milliliters (mL) in brain matter. The authors also reported that the antiamyloid antibodies—but not the secretase inhibitors—led to a greater increase in the size of the brain's fluid-filled ventricles.

Ayton's group then studied whether the shrinkage was associated with so-called amyloid-related imaging abnormalities (ARIA), a type of brain swelling and bleeding that is a well-documented side effect of the antibodies. ARIA occurred in 21% of the 898 people taking lecanemab in Eisai's pivotal trial (as well as 9% on a placebo); most had no symptoms, but some became severely ill and at least two died. Ayton and his colleagues found the experimental therapies with a higher rate of ARIA also generated a bigger average increase in the size of the ventricles.

"I was just shocked when we put these data together," Ayton says, but he sees a possible connection. ARIA shows up on brain scans as inflammation, and generally, "it's not controversial that neuroinflammation would lead to neurodegeneration," he says. As a result, patients who develop ARIA—which tends to happen early in treatment—might later be more prone to brain volume loss, he speculates.

FDA officials who approved Eisai's application for lecanemab noted the brain volume changes. Like the company, though, they weren't unduly concerned. A lead FDA reviewer "questions the clinical relevance of the changes to whole brain volume and total ventricular volume," FDA wrote in its summary review of the drug, in part because the drug met its goal of slowing cognitive decline.

But researchers note that individual patients may have had cognitive or other effects not noted across the trial population. Madhav Thambisetty, a neurologist at Johns Hopkins University and chief of the clinical and translational neuroscience section at the National Institute on Aging, says it's not clear "whether brain volume loss and increase in ventricular volume are associated with worsening clinical and cognitive outcomes" in individual patients. The "incomplete reporting of results … is very concerning to me."

Ayton shares the sentiment. "The lack of information increases my worry," he says, calling on companies, including Eisai, and drug regulators to examine this issue and share more trial data. "Tell us why we shouldn't be concerned."

FDA is planning an advisory committee meeting by July to consider whether to grant lecanemab full approval. ■

Check for updates

ASTRONOMY

Low-cost array hunts radio bursts, black holes

Closely packed telescope dishes enable wide-field, real-time sky surveys

By **Daniel Clery**

When the immense Arecibo radio telescope in Puerto Rico collapsed in 2020, it left gaping holes in astronomy. Now, a team from the California Institute of Technology (Caltech) hopes to address some of the gaps with a very different instrument: a tightly packed array of relatively inexpensive radio dishes that aims to quickly image radio sources across wide swaths of the sky. A nearly completed prototype array in California that the team calls a "radio camera" is already locating dozens of the distant, enigmatic eruptions called fast radio bursts (FRBs). Next year, the team hopes to begin construction on a much larger array with 2000 dishes that, together, will match the size of Arecibo.

Maura McLaughlin of West Virginia University is a leader of NANOGrav (the North American Nanohertz Observatory for Gravitational Waves), an effort to search for gravitational waves from supermassive black holes that relied on Arecibo for half its data. She says they took "a big sensitivity hit" when it was lost. "We really need a new telescope with a similar collecting area," she says, and Caltech's planned Deep Synoptic Array (DSA) fits that bill. "It will be a game changer."

To gain sensitivity, radio astronomers can build big dishes like Arecibo or arrays of smaller dishes. But in most such arrays, the dishes are widely spaced, which sharpens their resolution but creates "a data deluge problem," says Caltech's Gregg Hallinan, DSA principal investigator (PI). Producing an image from a scattered array is like looking through a fragmented mirror, he says, and recreating the information from the missing parts is a complex nonlinear process known as deconvolution that can take weeks—or even years.

Many astronomers just want to regularly survey the sky for new objects or monitor sources for subtle changes without a heavy processing burden. Caltech's solution, Hallinan says, is to "fill the mirror up" by packing low-cost dishes together. That makes deconvolution easier and should enable DSA to construct images in real time.

The team has nearly finished assembling its prototype, the DSA-110, a T-shaped array of 95 dishes spaced 1 meter apart at Caltech's Owens Valley Radio Observatory in California plus another 15 "outriggers" spread out more than 1 kilometer away. To keep construction costs to $4 million, the instrument uses commercially available 4.6-meter dishes, homemade amplifiers, and wave-channeling feeds fashioned out of cake tins. Most radio telescopes require expensive cryogenic cooling to reduce amplifier noise, but Caltech's engineers have squeezed similar performance out of room-temperature circuits. (Co-PI Vikram Ravi admits they perform less well in the summer heat.)

With a wide field of view, DSA-110 is good at detecting FRBs, intense blasts of radio waves lasting only milliseconds, coming from all over the sky. Several thousand have been detected, but only a dozen or so have been traced to their home galaxies, which might hold clues to what is powering the bursts. DSA-110 aims to localize many more. If a burst is detected, data from the outrigger dishes allow the telescope to zoom in and pin the FRB to its galaxy.

During 2022, with more than half the dishes in place including the outriggers, DSA-110 identified source galaxies for about 20 FRBs, overtaking the number of localized sources found by all other telescopes. When completed this summer, it should localize a couple of FRBs every week, Ravi says. "It's going to be a lot of fun."

The results so far are already confounding theorists. They predicted FRBs are most likely to come from galaxies that are rapidly forging new stars. Such galaxies are rich in massive stars that quickly run out of fusion fuel and collapse into tiny stellar remnants rippling with energy called magnetars—the favored engines for blasting out FRBs. But DSA-110 has found FRBs in quiescent galaxies whose magnetars would have fizzled out long ago. That suggests FRBs might have other sources besides magnetars, says Victoria Kaspi of McGill University. Just last week in *Nature Astronomy*, researchers reported an FRB that appeared to come from the merger of two neutron stars. "Having many FRBs localized is important," Kaspi says. "We may be able to see different populations [of FRBs] from different sources."

Meanwhile, the Caltech team is gearing up for the next phase: DSA-2000. At 19 by 15 kilometers, it will be too big for Owens Valley so the team is looking at Hot Creek

PHOTO: DSA/CALTECH

In 2022, the Deep Synoptic Array 110 traced about 20 fast radio bursts to their source galaxies.

Valley in Nevada, a sparsely populated, radio quiet region. To keep costs low, the Caltech team plans to make its own 5-meter dishes by molding sheets of aluminum. Although DSA-2000 won't be as sensitive as other planned radio observatories, such as the Square Kilometre Array in South Africa and Australia, it will beat them on survey speed. Existing surveys have logged 10 million radio sources across the sky, Hallinan says. DSA-2000 will boost that number 100-fold to 1 billion, giving astronomers, for example, a better picture of how galaxies form and grow, and allowing them to capture fleeting sources like merging neutron stars over a much wider volume.

Later this year, the team will apply to the U.S. National Science Foundation to supplement the private sources that have funded development work. If the team can raise the $144 million needed to build the array, DSA-2000 could start logging tens of thousands of FRBs in 2026. That could enable astronomers to start using FRBs as a mapping tool. As the compact radio pulses move through space, they get smeared by the gas they pass through—giving astronomers a clue to the location of gas around and between galaxies that is normally invisible to telescopes. Astronomers don't know where half the normal matter in the universe is; FRBs could help them find it.

One-quarter of its time will be devoted to eavesdropping on another hidden component of the universe: the colossal black holes with masses of millions or billions of suns that lurk at the centers of galaxies. When galaxies merge, the newly formed galaxy ought to end up with two of these lumbering giants, circling each other warily and churning out long, languorous gravitational waves. Detectors on Earth have detected the shorter, sharper waves generated by collisions of star-size black holes. But it takes a detector light-years across to pick up these long waves. NANOGrav's strategy is to studiously observe pulsars, spinning stellar fossils that emit metronomic radio pulses hundreds of times a second. A passing gravitational wave would slightly shift a pulsar's repetition rate as it ripples space between the pulsar and Earth.

More than a decade of watching several dozen pulsars has yet to turn up a firm detection. But with DSA-2000 monitoring more pulsars, more accurately and more often, a signal might emerge, says NANOGrav member Chiara Mingarelli of the University of Connecticut, Storrs. That would open "a new frontier," she says, revealing giant black holes performing a hidden pas de deux. "DSA-2000 will be transformational for gravitational wave astronomy." ■

DEVELOPMENTAL BIOLOGY

Monkey mock embryos set new development record

First embryo mimics from monkeys may boost research into early development, miscarriages

By **Mitch Leslie**

To probe the mysterious early stages of development, researchers have concocted a variety of embryo stand-ins from mouse or human stem cells. Now, scientists in China have created the first monkey versions. These pseudo-embryos should more closely reflect human development than their mouse equivalents. And unlike human embryo mimics, they can be inserted into females to help scientists better understand the beginnings of pregnancy—and why it often fails.

"The findings are a milestone in the field of stem cell–derived embryo models," says stem cell biologist Alejandro De Los Angeles of the University of Oxford, who wasn't connected to the study.

> **"The findings are a milestone in the field of stem cell–derived embryo models."**
> **Alejandro De Los Angeles**, University of Oxford

Starting with stem cells obtained from embryos or from adult cells transformed into an embryonic-like state, several groups of researchers have grown structures that resemble the blastocyst, the ball of cells that in humans takes shape about 5 days after fertilization and implants in the uterus. Termed blastoids, these imitation embryos can survive for several days in culture and develop many features of the real things. Scientists have even inserted mouse blastoids into mother rodents and shown that they induce some of the changes of pregnancy, although they don't continue to develop. But mouse blastoids can only reveal so much about human development, and it would be unethical to implant human blastoids into people.

Monkey blastoids promise to be better models, but the right recipe for culturing them proved elusive. Now, Zhen Liu of the Chinese Academy of Sciences and colleagues have generated blastoids from the embryonic stem cells of cynomolgus monkeys, they report this week in *Cell Stem Cell*. The researchers raised the cells in 3D cultures and coaxed them to divide and specialize with two kinds of media. In culture, the blastoids could survive about 18 days.

They developed further than any previous blastoids, undergoing gastrulation, the cellular reorganization that sets up the three basic layers of the embryo. They also contained many of the same types of cells genuine monkey blastocysts do and showed similar patterns of gene activity, suggesting they were faithful replicas.

In previous blastoids, certain types of "founder" cells that give rise to key embryonic structures were scarce, notes developmental biologist Jennifer Nichols of the University of Edinburgh. But the new culture system produced a better balance of these cells, suggesting it might benefit other labs trying to nurture blastoids, she says. A next step, De Los Angeles says, is to investigate ways to prolong the development of the monkey blastoids.

The researchers also inserted 7-day-old blastoids into eight mother monkeys. In three of them, hormones that signal pregnancy appeared in the blood. These three monkeys also sprouted gestational sacs, telltale structures in the uterus that indicate pregnancy. Those findings suggest that monkey blastoids can implant into the uterus and emulate aspects of pregnancy.

They did not continue to develop inside the surrogate mothers, however, suggesting they are not perfect copies. To Nichols, "It's reassuring that they didn't develop further." She thinks that failure should discourage disreputable individuals from trying to pitch human blastoids as a fertility treatment.

"This is a beautiful study," says Nicolas Rivron, a stem cell biologist at the Austrian Academy of Sciences's Institute of Molecular Biotechnology whose team engineered the first mouse blastoids in 2018. Creating simulated embryos for more species, he says, will help scientists learn more about early development and what's necessary for successful pregnancy.

In particular, Rivron hopes the monkey blastoids can provide insights into why implantation often fails in humans. "Implantation is the bottleneck of human pregnancy," he says. ■

Check for updates

In 2022, the Deep Synoptic Array 110 traced about 20 fast radio bursts to their source galaxies.

Valley in Nevada, a sparsely populated, radio quiet region. To keep costs low, the Caltech team plans to make its own 5-meter dishes by molding sheets of aluminum. Although DSA-2000 won't be as sensitive as other planned radio observatories, such as the Square Kilometre Array in South Africa and Australia, it will beat them on survey speed. Existing surveys have logged 10 million radio sources across the sky, Hallinan says. DSA-2000 will boost that number 100-fold to 1 billion, giving astronomers, for example, a better picture of how galaxies form and grow, and allowing them to capture fleeting sources like merging neutron stars over a much wider volume.

Later this year, the team will apply to the U.S. National Science Foundation to supplement the private sources that have funded development work. If the team can raise the $144 million needed to build the array, DSA-2000 could start logging tens of thousands of FRBs in 2026. That could enable astronomers to start using FRBs as a mapping tool. As the compact radio pulses move through space, they get smeared by the gas they pass through—giving astronomers a clue to the location of gas around and between galaxies that is normally invisible to telescopes. Astronomers don't know where half the normal matter in the universe is; FRBs could help them find it.

One-quarter of its time will be devoted to eavesdropping on another hidden component of the universe: the colossal black holes with masses of millions or billions of suns that lurk at the centers of galaxies. When galaxies merge, the newly formed galaxy ought to end up with two of these lumbering giants, circling each other warily and churning out long, languorous gravitational waves. Detectors on Earth have detected the shorter, sharper waves generated by collisions of star-size black holes. But it takes a detector light-years across to pick up these long waves. NANOGrav's strategy is to studiously observe pulsars, spinning stellar fossils that emit metronomic radio pulses hundreds of times a second. A passing gravitational wave would slightly shift a pulsar's repetition rate as it ripples space between the pulsar and Earth.

More than a decade of watching several dozen pulsars has yet to turn up a firm detection. But with DSA-2000 monitoring more pulsars, more accurately and more often, a signal might emerge, says NANOGrav member Chiara Mingarelli of the University of Connecticut, Storrs. That would open "a new frontier," she says, revealing giant black holes performing a hidden pas de deux. "DSA-2000 will be transformational for gravitational wave astronomy." ■

DEVELOPMENTAL BIOLOGY

Monkey mock embryos set new development record

First embryo mimics from monkeys may boost research into early development, miscarriages

By **Mitch Leslie**

To probe the mysterious early stages of development, researchers have concocted a variety of embryo stand-ins from mouse or human stem cells. Now, scientists in China have created the first monkey versions. These pseudo-embryos should more closely reflect human development than their mouse equivalents. And unlike human embryo mimics, they can be inserted into females to help scientists better understand the beginnings of pregnancy—and why it often fails.

"The findings are a milestone in the field of stem cell–derived embryo models," says stem cell biologist Alejandro De Los Angeles of the University of Oxford, who wasn't connected to the study.

> **"The findings are a milestone in the field of stem cell–derived embryo models."**
> **Alejandro De Los Angeles**, University of Oxford

Starting with stem cells obtained from embryos or from adult cells transformed into an embryonic-like state, several groups of researchers have grown structures that resemble the blastocyst, the ball of cells that in humans takes shape about 5 days after fertilization and implants in the uterus. Termed blastoids, these imitation embryos can survive for several days in culture and develop many features of the real things. Scientists have even inserted mouse blastoids into mother rodents and shown that they induce some of the changes of pregnancy, although they don't continue to develop. But mouse blastoids can only reveal so much about human development, and it would be unethical to implant human blastoids into people.

Monkey blastoids promise to be better models, but the right recipe for culturing them proved elusive. Now, Zhen Liu of the Chinese Academy of Sciences and colleagues have generated blastoids from the embryonic stem cells of cynomolgus monkeys, they report this week in *Cell Stem Cell*. The researchers raised the cells in 3D cultures and coaxed them to divide and specialize with two kinds of media. In culture, the blastoids could survive about 18 days.

They developed further than any previous blastoids, undergoing gastrulation, the cellular reorganization that sets up the three basic layers of the embryo. They also contained many of the same types of cells genuine monkey blastocysts do and showed similar patterns of gene activity, suggesting they were faithful replicas.

In previous blastoids, certain types of "founder" cells that give rise to key embryonic structures were scarce, notes developmental biologist Jennifer Nichols of the University of Edinburgh. But the new culture system produced a better balance of these cells, suggesting it might benefit other labs trying to nurture blastoids, she says. A next step, De Los Angeles says, is to investigate ways to prolong the development of the monkey blastoids.

The researchers also inserted 7-day-old blastoids into eight mother monkeys. In three of them, hormones that signal pregnancy appeared in the blood. These three monkeys also sprouted gestational sacs, telltale structures in the uterus that indicate pregnancy. Those findings suggest that monkey blastoids can implant into the uterus and emulate aspects of pregnancy.

They did not continue to develop inside the surrogate mothers, however, suggesting they are not perfect copies. To Nichols, "It's reassuring that they didn't develop further." She thinks that failure should discourage disreputable individuals from trying to pitch human blastoids as a fertility treatment.

"This is a beautiful study," says Nicolas Rivron, a stem cell biologist at the Austrian Academy of Sciences's Institute of Molecular Biotechnology whose team engineered the first mouse blastoids in 2018. Creating simulated embryos for more species, he says, will help scientists learn more about early development and what's necessary for successful pregnancy.

In particular, Rivron hopes the monkey blastoids can provide insights into why implantation often fails in humans. "Implantation is the bottleneck of human pregnancy," he says. ■

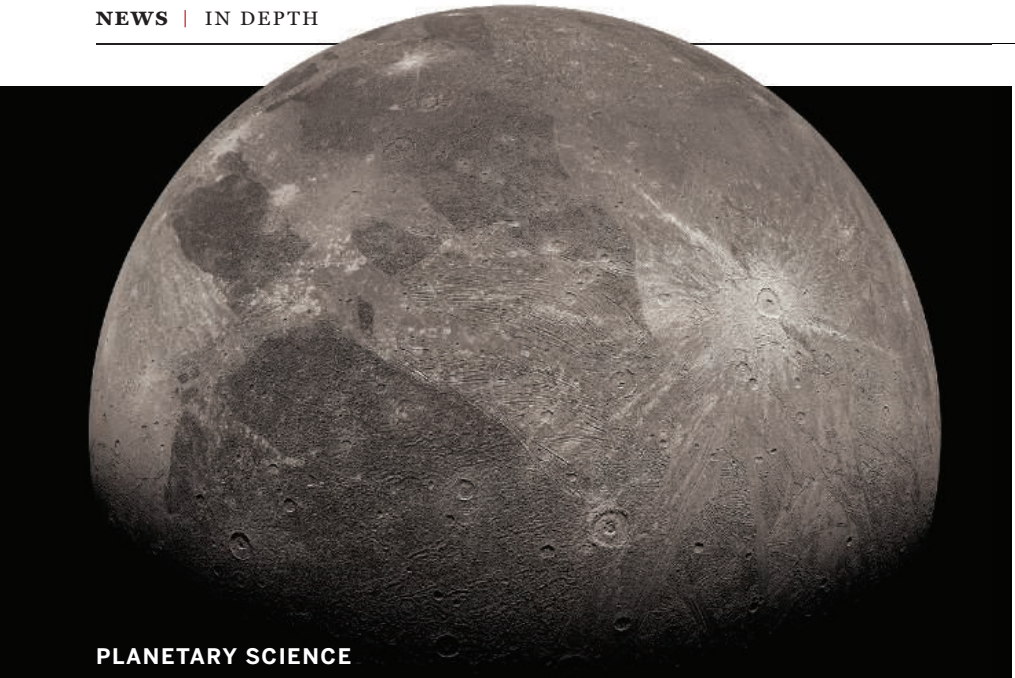

Ganymede is thought to hide a saltwater ocean beneath more than 100 kilometers of ice.

PLANETARY SCIENCE

Jupiter's ocean moons targeted by spacecraft

European Juice mission will explore icy worlds for subsurface pockets of habitability

By **Paul Voosen**

Ganymede, Jupiter's largest moon, is practically a planet. Larger than Mercury, it is the only moon with its own magnetic field, produced by churning molten iron in its core. Its icy crust, more than 100 kilometers thick, is cut by ridges and grooves, evidence of past tectonic activity. Smooth plains suggest ice-spewing cryovolcanoes may have paved over parts of the moon. And beneath the crust, many researchers believe, is a salty ocean, kept warm by the moon's inner heat and Jupiter's gravitational kneading. "It's now clear you can find liquid water much farther away from the Sun than we ever thought," says Michele Dougherty, a space physicist at Imperial College London.

Ganymede is one of three jovian moons that may hold hidden oceans, all potential habitats for life. They are the targets of the $1.6 billion Jupiter Icy Moons Explorer (Juice), a European Space Agency (ESA) mission set for a 13 April launch on an Ariane 5 rocket from French Guiana. Boosted by gravitational assists from Earth and Venus, Juice will take 8 years to reach Jupiter. It will spend another 3 years promenading among the moons, eventually ending up in a tight orbit around Ganymede—the first time a spacecraft will orbit a moon other than Earth's.

Ganymede's sister moon, Europa, has long gotten more attention as a possible home for life and is the target of another spacecraft, NASA's Europa Clipper, to launch in October 2024. Europa's icy shell is much thinner than Ganymede's, perhaps just 15 kilometers thick, and its ocean may sometimes breach the surface—perhaps even sending plumes of water erupting into space. But Europa orbits closer to Jupiter's intense radiation field, which would disrupt the electronics of any spacecraft lingering nearby. The Clipper, which will arrive a year ahead of Juice thanks to a more powerful rocket, will inspect Europa by swooping past it 50 times.

Juice will also fly past the moon, twice. If the plumes exist, Juice's mass spectrometer might be able to sample their outer reaches and hunt for organic molecules. The spacecraft's radar, capable of penetrating ice 9 kilometers thick or more, might see the ocean if the crust is thin enough, or at least subsurface pockets of water embedded in the ice. Eruptions from these pockets could be responsible for the "chaos terrains," a landscape of fissures that cover one-fourth of the moon's surface. Juice will also use a laser altimeter—an instrument Clipper doesn't possess—to search for depressions where subsurface water might be close to bursting through. "We'll switch on all the instruments to gather as much as we possibly can," says Olivier Witasse, Juice's project scientist at ESA's European Space Research and Technology Centre.

Callisto, the most distant of Jupiter's moons, is another target for Juice. It does not derive much energy from Jupiter's tidal tugs, and data from NASA's Galileo spacecraft in the 1990s suggest it never got hot enough to separate into distinct layers, leaving its ice and rock jumbled together. "We think it's not active at all, a dead moon," Witasse says. Yet Galileo's magnetometer found hints that Callisto, too, might hold an ocean: faint signs of a magnetic field, perhaps generated as Jupiter's strong magnetic field sweeps through electrically conductive saltwater in the moon's interior and induces currents and magnetism. By carefully looking for this induced field, Juice could divine whether this ocean exists.

In late 2034 Juice will finally settle into orbit 500 kilometers above Ganymede. One task will be delimiting the ocean, which some researchers think could exist in multiple layers, separated by high-pressure species of ice. Ganymede's crust is too thick for Juice's radar to penetrate, but the ocean's structure could be revealed through careful study of the way its sloshing contributes to orbital wobbles, combined with measures of induced magnetic fields. The radar can also hunt for pockets of water that could be fueling eruptive episodes that create the smooth plains, says Lorenzo Bruzzone, a remote-sensing scientist at the University of Trento. By measuring how deep the radar penetrates, the team can also learn how salty the ice is, an important factor in its freezing temperature.

Juice's mass spectrometer can provide another handle on the composition of the crust. It will sniff the moon's thin atmosphere for molecules that have escaped the surface. "You get the ground truth by directly sampling the material," says Audrey Vorburger, a planetary scientist at the University of Bern. Meanwhile, the magnetometer will help determine the size of the core and the ocean by measuring their separate contributions to the moon's field.

NASA may end the Europa Clipper by crashing it into Jupiter, lest microbes on the spacecraft seed Europa's ocean with earthly life. Ganymede's thick shell means the Juice team doesn't have to worry as much about contamination. It plans to end the mission sometime after 2035 by colliding with its target, leaving one more crater on its icy crust. ■

PHOTO: NASA/JPL-CALTECH/SWRI/MSSS/KALLEHEIKKI KANNISTO

Cage-free "layers" at a chicken ranch near San Diego receive vaccines to protect them from many diseases, but not deadly avian flus.

PHOTO: J. COHEN/SCIENCE

BIRD SHOTS

As an avian influenza virus devastates the poultry industry, the United States considers an unprecedented step: vaccinating its flocks

By **Jon Cohen**, *in Lakeside, California*

Hilliker's Ranch Fresh Eggs in this San Diego suburb has 30,000 chickens in three "cage-free," open-air barns, where birds crowd the floor like rush-hour riders on a big city subway. "A cage-free aviary is a very interesting science experiment," says Frank Hilliker, who runs the farm his grandfather started in 1942. He worries mightily about infections spreading through the massed birds. On his iPhone, he pulls up a list of the vaccines his chickens get: against Newcastle disease, infectious laryngotracheitis, coryza, colibacillosis, salmonella, infectious bronchitis, and fowlpox.

There is one disease for which his chickens have not been vaccinated: a highly pathogenic avian influenza (HPAI) that's now racing around the world, killing 90% or more of the poultry it infects. Endemic in migratory birds, this HPAI emerged in U.S. poultry in February 2022, and to date has killed or required the culling of a record 58 million chickens, turkeys, and ducks in commercial and backyard flocks.

Hilliker, who despite the unusually chilly February morning is wearing cargo shorts and a zip-up sweatshirt—this *is* San Diego—has a no-nonsense demeanor mixed with a tinge of superstition from years of worrying about his chickens. His farm has never detected an HPAI, he says, knocking on a wood wall. "We're pretty isolated here," he says, giving another rap. But he might well use an HPAI vaccine to protect his birds, he says, if it was priced right—and allowed.

The goal of vaccination is not just to protect poultry. Well before COVID-19, epidemiologists were nervously watching two kinds of highly pathogenic influenza viruses, H5 and H7, fearing they could erupt into a human pandemic reminiscent of the 1918 flu. HPAI can infect mammals, and the current, massive outbreak has killed seals, bears, and farmed mink and infected at least seven people, killing one. Thankfully, there is no evidence the virus can spread from mammal to mammal, let alone person to person—so far. But fears are growing that the more mammals it infects, the higher the odds that it will adapt to humans (see story, p. 28).

Slowing the spread among birds could reduce the risk. "I think it is time to give serious consideration to vaccinating commercial poultry in the United States," says Robert Webster, an emeritus influenza researcher at St. Jude Children's Research Hospital. But despite strong evidence that HPAI vaccine programs can work—mainly from China, which has aggressively vaccinated poultry over the past 2 decades—the U.S. Department of Agriculture (USDA) does not give farmers like Hilliker the option. Instead, the country has fought HPAI by combining intensive surveillance, strict biosecurity at farms, and culling.

Skeptics of poultry vaccination say that's the right approach. Immunizing flocks, they argue, could allow the virus to spread silently—not reducing the threat of an avian flu pandemic but simply making it more difficult to detect. And the current practice of "stamping out" outbreaks has worked: Before the current HPAI strain surfaced in U.S. flocks in February 2022, no HPAI had swept through since 2015. But in the face of the largest HPAI outbreak on record, both the United States and Europe are rethinking their hesitancy.

Many questions remain about how, exactly, to use a vaccine in countries that have relied on culling. And because of the uncertain U.S. market, companies are reluctant to invest in moving beyond the initial steps of making vaccines against the current variant and embarking on the rigorous and costly process of seeking regulatory approval. "There's no incentive at all," says microbiologist Mahesh Kumar, who heads global biologics R&D for Zoetis, which makes vaccines for pets and livestock and sells an HPAI vaccine outside the United States. "It's very, very difficult for anybody to continue to invest in that space."

And something else has kept the brakes on HPAI vaccination in both the United States and Europe: trade. Some countries—including the United States—won't allow imports of meat or eggs from vaccinated birds.

Scientific evidence doesn't support those bans. But as Nancy Reimer, a poultry veterinarian who provides care for Hilliker's birds, puts it, "Some of this is political science, not poultry science."

THE FIRST GLIMPSE of the HPAI strain now wreaking havoc came in 2010 in China's Jiangsu province, when researchers from Yangzhou University isolated a new variant of a known subtype, H5N8, from a duck sold in a market. (The H and N refer to two viral surface proteins, hemagglutinin and neuraminidase.) Three years later, a similar virus was spotted in another duck, about 300 kilometers south in Zhejiang. When relatives surfaced a third time, in Korean breeder ducks the next year, a new clade was christened: 2.3.4.4b.

The march of 2.3.4.4b took an ominous turn at an island in Qinghai Lake on the Tibetan Plateau. The lake, the largest in China, provides a temporary home to some 150,000 migratory birds each year flying between Russia and India or Australia. On 1 May 2016, researchers discovered the carcass of a brown-headed gull, the first of some 150 gulls and geese at the lake found to have been infected with variants of 2.3.4.4b. The virus was evidently headed north.

That summer and fall some of the same variants turned up near the Ural mountains in Russia, and then the virus took hold in Western Europe. The resulting HPAI epidemic in poultry, researchers wrote in the *Proceedings of the National Academy of Sciences,* was "the largest and most widespread ... ever recorded in Europe."

China has aggressively vaccinated poultry against dangerous avian flu viruses for nearly 2 decades.

PHOTO: STR/AFP/GETTY IMAGES

This Iowa farm had to cull 56,000 birds in 2015 because of highly pathogenic avian influenza. Culling flocks is a standard way to control the virus in the United States.

By October 2020, the virus had undergone a significant genetic change, swapping N8 for N1, but the new H5N1 2.3.4.4b proved just as transmissible as its predecessor. It spread to Africa and back to Asia. Then, in November 2020, came evidence it had jumped the Atlantic Ocean: Researchers documented a sick great black-backed gull on Newfoundland. In the following weeks and months it established multiple beachheads in North America.

By now, 2.3.4.4b has evolved a niche unlike any HPAI ever seen. Usually HPAI infections die out in a season, but the 2.3.4.4b clade is present year-round in migratory birds. It infects so many species in so many locales that no country's poultry flocks are ever safe.

Despite their name, HPAIs can cause mild or no disease in some avian species, including ducks. But their arrival on an unvaccinated chicken farm can be devastating. Birds may become weak and listless, stop laying eggs, develop severe diarrhea, stumble, and struggle to breathe. An entire flock can die within 2 days. By USDA regulations, just a single bird infected with HPAI requires stamping out a flock, a gruesome procedure that entails cutting off ventilation in barns or suffocating the birds with carbon dioxide or fire-fighting foam. USDA has a program that compensates producers who are forced to cull, but rebuilding the business can still mean a major financial hit.

Globally the toll is enormous. The intergovernmental World Organisation for Animal Health has tracked stamp-outs triggered by H5 and H7 infections. Between January 2005 and 2022, more than 8500 H5 outbreaks led to the culling of nearly 400 million birds, with another 30 million sacrificed to fight more than 100 outbreaks of H7s.

IN 1995, MEXICO PIONEERED an alternative approach to combating HPAI, becoming the first country to use a vaccine as well as culling to stop a virus designated H5N2. The vaccine, which cost pennies per dose, was made like the human one, by growing the virus in eggs and then inactivating it with chemicals. The campaign eliminated the virus from Mexico's flocks in short order.

China in November 2005 upped the ante in the face of a frightening H5N1 strain that spilled over to nearly 100 humans in Asia that year. In addition to culling, it set out to vaccinate all 14 billion chicken, geese, and ducks then consumed in the country each year—the largest single vaccination effort ever for any species, according to the Food and Agriculture Organization of the United Nations. The government provided the vaccine at no cost to farmers, who were required to use it. Thirteen other countries also used H5 vaccines in poultry by 2010, but China alone accounted for 91% of the total shots given to birds—nearly 100 billion doses.

Later, China faced a new threat: an H7N9 strain that spread through flocks in multiple waves starting in 2013. People caught it, too, mainly from farming or live poultry sold at markets, and by 2017 it had sickened 1500, killing 39% of them. The human tragedy and the economic loss led China in 2017 to introduce a bivalent H5/H7 vaccine for poultry.

China's HPAI vaccines have had limitations, says virologist Chen Hualan at the Harbin Veterinary Research Institute, who with her colleagues studied the country's vaccination campaign. The evolution of new variants, which immune pressure from vaccines helped to speed up, forced repeated vaccine updates. And domestic ducks—which often did not get vaccinated—provided a haven for the virus.

China's farmers rear about 4 billion ducks each year, mostly in open fields where they mingle with wild birds and are regularly exposed to flu and other viruses. But because ducks rarely become ill from HPAI, only about 30% of duck farmers vaccinated their birds. "This explains why even though the H5 vaccine has been used in poultry in China for over 10 years, H5 virus can still be detected in the live poultry markets, mainly from ducks," Chen and her colleagues wrote in 2018.

Some Chinese farmers shunned HPAI vaccination because of worries that it could allow infections to spread without being detected by surveillance. Farms that raise chickens for their meat (the "broilers" that are slaughtered when they are about 6 to 8 weeks old) also had less financial incentive to vaccinate than farms with egg layers, which typically produce for a year or longer.

Still, Chen's group found that about 70% of the chickens they sampled had antibodies from the H5N1 or the H5/H7 bivalent vaccines. As a result, she and her colleagues wrote in *Emerging Microbes & Infections* on 2 December 2022, "even though the globally circulating H5 viruses have been detected in many species of wild birds and occasionally in ducks or geese in recent years, they have never caused problems on routinely vaccinated poultry farms in China."

China's success in vaccinating against H7N9 is even more compelling. The Chen team sampled more than 50,000 poultry at some 1500 markets and farms before and after the H7N9 vaccine campaign began. They found the prevalence of the virus dropped by 93.3%, and the spread of H7N9 to humans stopped altogether. No human

PHOTO: SCOTT MORGAN/*THE NEW YORK TIMES*

case of H7N9 has been reported since 2019.

The effort benefits both poultry and farmers, Chen told *Science,* because the government does not require culling an entire farm if the virus is found in one bird. "If it is in a farm with several barns, just birds in that barn will be destroyed," she says.

Given that success, "We recommend that any unnecessary obstacles to vaccination strategies should be removed immediately and forever," she and her colleagues wrote in a review paper this year.

Webster also sees lessons in China's vaccination effort, which not only tamped down HPAI in China but likely kept H7N9 influenza viruses from spreading worldwide. "It is remarkable," he says. "I believe that Chen is justified in believing that vaccination played an important role."

The European Union in May 2022 conceded that vaccinating might make sense and is now testing candidates against 2.3.4.4b. At an October 2022 meeting in Paris, organized under the aegis of the International Alliance for Biological Standardization, participants called for "removing unnecessary barriers" for vaccination to control HPAI.

"We cannot keep doing the same thing over and over again," said David Swayne, a veterinarian who for 28 years ran USDA's main HPAI research group and co-organized the meeting, which brought together academic scientists, vaccinemakers, and representatives of European governments. "The virus has changed. We've got to change."

IN THE UNITED STATES, the National Chicken Council is not convinced. The organization, which represents broiler farmers, has long argued that using HPAI vaccines would lead to trade restrictions, based in part on fears of silent infections that could contaminate chicken products.

Swayne dismisses that concern, which his own group's experiments may have helped fuel. They gave vaccinated birds extraordinarily high "challenge" doses of virus to see how well the vaccine prevented death and reduced viral shedding. The high doses meant that vaccinated birds sometimes got infected but showed no signs of illness. But the silent infection concern is "a misinterpretation of that data," Swayne says. Vaccinated birds exposed to more realistic, real-world virus doses, he says, are unlikely to become infected.

Even if farms missed infections, the main U.S. export is meat, usually frozen—not live birds. No evidence exists that frozen meat can transmit influenza viruses. "When you look at risk analyses, they would say the chances of that happening are low or negligible," Swayne says.

The bottom line is that business worries often trump science, says James Sumner, who served as president of the USA Poultry and Egg Export Council from 1990 to 2022 and remains a consultant there. "Many countries look for excuses to restrict trade," he says—and many already have grievances against the United States. "The products that we export the most are the leg quarters, and we export those at a pretty low price because our industry makes its money on the upper half of the chicken, on the breast and the wings," which Americans prefer, Sumner explains. Farmers in foreign countries "consider that unfair trade, and it is often classified as dumping," he says. Refusing to import chicken meat from the United States if it vaccinates is a tempting retaliatory measure.

Migratory birds like snow geese, seen flying over a Maryland field, transport flu viruses from one continent to another.

PHOTO: JIM WATSON/AFP/GETTY IMAGES

On the flip side, farmers who raise turkeys, another big branch of the U.S. poultry meat market, are more pro-vaccine because their birds are particularly susceptible to HPAI and they live for up to 6 months. "There are these divided camps," Sumner says.

Still, the unprecedented H5N1 outbreak in the United States has altered the conversation. Vaccination "is discussed much more widely now, and there are some people who are pushing for it," Sumner says. "We all recognize that there are situations where vaccination would be beneficial."

Poultry vaccinemakers say they stand ready to develop products if the market exists. Kumar says it would be wise for the government to at least order doses for USDA's National Veterinary Stockpile now, as it did in 2016 to prepare for a variant of an H5N1 strain that had devastated poultry flocks the year before. (In response to a Freedom of Information Act request, USDA told *Science* that the stockpile currently contains no HPAI vaccines.)

Zoetis has produced what's known as a master seed to make vaccine against 2.3.4.4b, Kumar says, and done initial safety and efficacy studies. Boehringer Ingelheim told *Science* that it, too, had "completed efficacy tests against clade 2.3.4.4b." But both companies are waiting for a signal from USDA that it will allow use of the vaccines. "It's not like you just turn on the button, and you have vaccine ready, right? It takes time to get it done," Kumar says.

In March, USDA began to test four different HPAI vaccines made by agency scientists, Zoetis, and Merck. Erica Spackman, acting director of USDA's Exotic and Emerging Avian Viral Diseases unit, says her team will challenge vaccinated chickens to see how well they're protected against the 2.3.4.4b strain. The commercial vaccines target earlier H5 strains, but Spackman says a mismatch between a genome used to make a vaccine and the virus in circulation sometimes doesn't matter. "Some strains are very immunogenic and that overcomes the mismatches," she says.

Spackman has little concern about vaccines creating silent infections. "Within the context of a population monitored by a surveillance program, as would be the case here, infection is not silent," she says.

In a statement to *Science,* USDA said if the vaccines work, which the agency should know by June, it will look for manufacturers to produce them. (It will also consider data from European labs now testing vaccines against 2.3.4.4b, Spackman says.) Then, "there are 20 discrete stages to complete" before companies can submit data for regulatory approval, the statement says. It typically takes 2.5 to 3 years to complete that process, the agency said, but "in emergency situations manufacturers may expedite development, resulting in a shortened timeframe to licensure."

Reimer, the veterinarian who cares for the birds at Hilliker's farm, does not expect to be vaccinating chickens soon enough to protect them from the current HPAI wave. "I've had these discussions before," Reimer says. "With this particular outbreak, I'm guessing we won't resolve anything." But by the time the next HPAI outbreak hits, she says, her charges may not have to face the virus unprotected. ■

Check for updates

FROM BAD TO WORSE

How the avian flu must change before it can trigger a human pandemic

By **Kai Kupferschmidt**

The victims are varied, from th
sands of sea lions off the coast of
Peru to mink farmed for fur in Spain to grizzly bears in Montana and harbor seals in Maine. For months, the avian influenza virus that has been decimating birds across the world (see story, p. 24) has also sickened and killed a menagerie of mammals, raising fears it might evolve to spread more efficiently between these animals, and ultimately between people.

For that nightmare to unfold, however, the virus, a subtype known as H5N1, would have to undergo a major transformation, changing from a pathogen efficient at infecting cells in the guts of birds and spreading through feces-contaminated water into one adept at infecting human lung tissue and spreading through the air. So far, that has not happened. None of the few people who have caught the virus currently wiping out birds, called clade 2.3.4.4b, seems to have passed it on to other people.

"This clade … is most of all and more than all previous clades an avian virus," says virologist Martin Beer of the Friedrich Loeffler Institute. That is why it has spread so far and wide in birds, he says, and why it is so poor at infecting people. Beer and his colleagues in Berlin and Münster, Germany, have been using lung tissue taken from cancer patients undergoing surgeries, for instance, to see whether the virus can efficiently infect the human cells. So far, it cannot.

So exactly how would this virus have to mutate to cause a human pandemic? Scientists can't fully answer that yet—but they have identified some key steps. Much of what is known comes from controversial experiments more than a decade ago in which researchers coaxed an earlier strain of H5N1 to spread more efficiently between ferrets. That feat prompted restrictions on such "gain of function" experiments, which has hampered research, says Mathilde Richard, a virologist at Erasmus Medical Center, where some of that work was done. "I do think that this has really, really slowed down our knowledge." Still, researchers have found other ways to examine how avian flu adapts to mammals. For instance, when another avian flu

Dangerous steps

For the H5N1 avian influenza virus to spark a human pandemic, its genome must acquire mutations that alter several of its proteins.

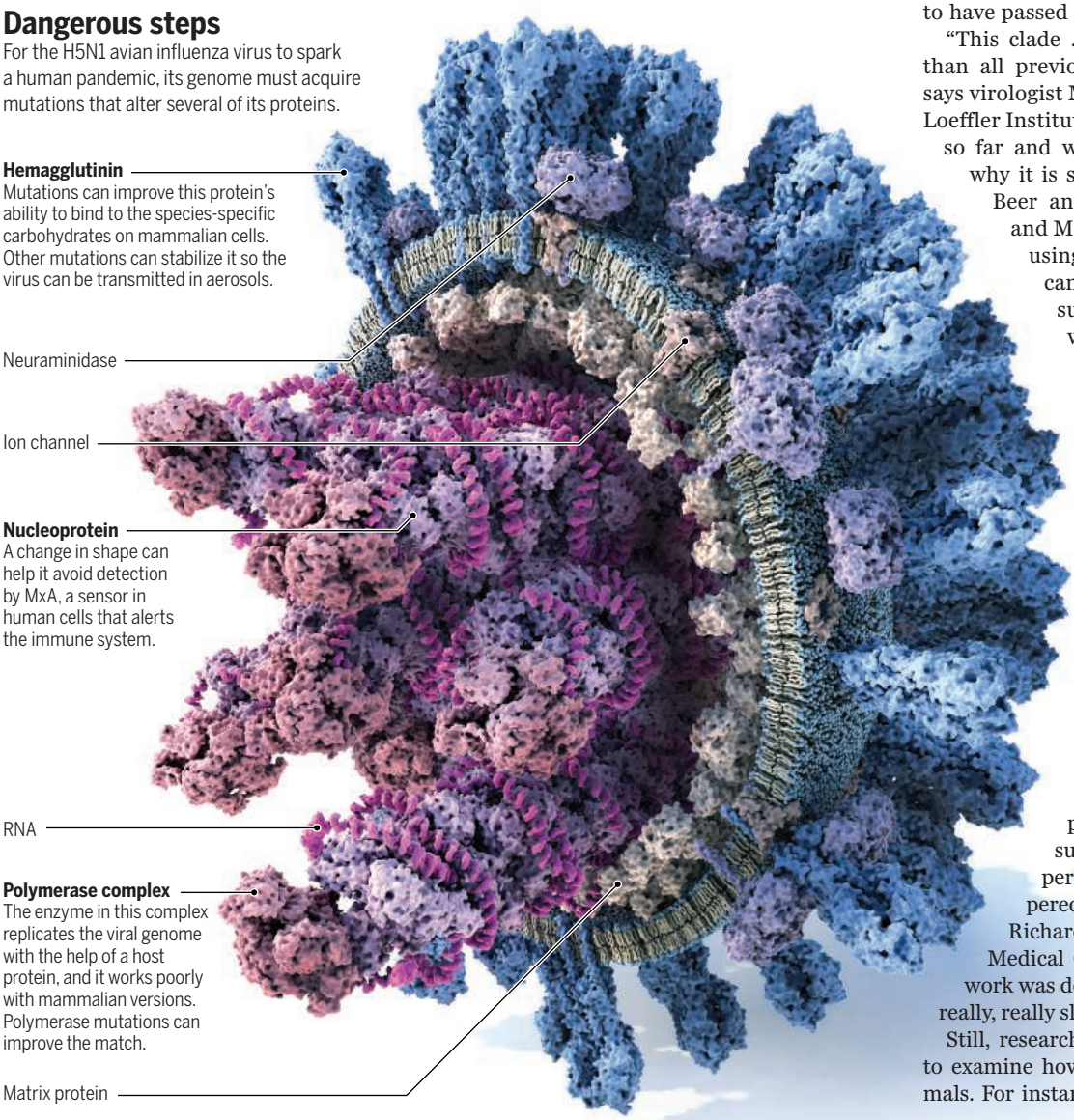
Hemagglutinin
Mutations can improve this protein's ability to bind to the species-specific carbohydrates on mammalian cells. Other mutations can stabilize it so the virus can be transmitted in aerosols.
Neuraminidase
Ion channel
Nucleoprotein
A change in shape can help it avoid detection by MxA, a sensor in human cells that alerts the immune system.
RNA
Polymerase complex
The enzyme in this complex replicates the viral genome with the help of a host protein, and it works poorly with mammalian versions. Polymerase mutations can improve the match.
Matrix protein

GRAPHIC: C. BICKEL/*SCIENCE*

subtype called H10N7 struck seals in Europe in 2014, scientists sequenced the virus at different stages of the outbreak to identify what genetic changes helped it adapt to the mammals. "That is sort of like a massive gain-of-function experiment in nature, and from those outbreaks, you can still learn quite a lot," Richard says.

Virologists now know that for H5N1 to become adept at spreading between mammals, several of its proteins must evolve. One they are watching closely is the polymerase the virus uses to replicate its RNA genome once it invades a cell. To do its job, the enzyme must co-opt a host intracellular protein, and it is currently more tailored to the avian molecule than its mammalian equivalent. Different combinations of mutations in one subunit of the polymerase, PB2, can change the enzyme to work better in mammals. But there's one known mutation, dubbed E627K, that does so in a single bound by swapping an amino acid at a key position, a glutamate, for a lysine. The mutation's first recorded appearance was in the virus causing the 1918 flu. "That PB2 was so good that it has stuck in every human influenza virus until the 2009 swine flu pandemic," says Imperial College London virologist Tom Peacock.

Whatever path the virus hits upon, H5N1 needs an altered PB2 to become a human pathogen. Think of evolving into a pandemic virus as a ladder that H5N1 has to climb, Beer says. "Then this is the first step."

It seems an easy step. H5N1 has managed it several times already in the current avian flu virus outbreak. For instance, researchers found the E627K mutation in infected foxes that were sampled in the Netherlands in late 2021 and early 2022. The mutation was also found in a sample from a New England seal, part of an outbreak of H5N1 in seals off the East Coast last year. The PB2 mutations don't seem to hamper the virus in birds, Richard says. "That's the reason why we see the polymerase mutations popping up quite often."

But for H5N1 to cause a pandemic it also needs multiple changes in hemagglutinin, a protein on the surface of the virus that helps it attach to carbohydrates on host cells. Those carbohydrates are shaped differently in birds and mammals, so H5N1's hemagglutinin has to change its shape for the virus to efficiently infect mammalian cells. "That is absolutely essential," Peacock says. "In fact, there are no influenza viruses that are transmissible between people that don't have a human-adapted hemagglutinin."

A pair of amino acid changes, Q226L and G228S, can reshape hemagglutinin to bind to mammalian cells. But in H5N1, the second amino acid change requires two nucleotide mutations very near each other in the hemagglutinin gene. "That is much rarer than single nucleotide changes," Peacock says. "But obviously, if you put it under enough selection pressure, it could maybe do that."

Bird flu recently killed seals in Maine, raising fears that the virus will begin to spread more easily among mammals.

PHOTO: MICHAEL DOOLITTLE/ALAMY STOCK PHOTO

Another crucial hemagglutinin change would make H5N1 more transmissible through the air—also a prerequisite for a pandemic. Once the virus attaches to a cell it is taken up into a vesicle that becomes more acidic, triggering a pH-dependent shape change in the hemagglutinin. This leads the virus and vesicle membranes to fuse, letting the pathogen's genetic material escape into the cell. In water, the hemagglutinin on avian viruses typically has no problem staying untriggered. But in the air, droplets of moisture carrying flu viruses often shrink and may reach that acidic threshold, so pandemic viruses need mutations that stabilize their hemagglutinin, explains Emory University virologist Seema Lakdawala, who studies airborne transmission of pathogens.

Those three steps are the minimum changes H5N1 likely needs to become transmissible between humans, Richard says. In her lab she regularly sequences H5N1 viruses isolated from mammals to see whether they carry any of these concerning mutations. Her team also directly tests the virus' polymerase activity and the binding capacity and stability of their hemagglutinin. "We really want to test the phenotypes and not just look at the genetic changes because we know that there are probably [other genetic changes] that have the same impact and we just do not know them yet."

Beer thinks a pandemic virus needs a fourth change: an ability to evade an intracellular protein called MxA. MxA alerts the immune system to an influenza infection when it detects the virus' nucleoprotein, a protein bound to its RNA. To prevent that alarm, the nucleoprotein must mutate into a form that the human MxA cannot detect. "That is the last barrier," Beer says. Although MxA's detection skills appear very weak in ferrets and some other animals, it is more sensitive in humans—and in pigs. "If an H5 virus is spreading in pigs then it really is code red," Beer says.

In an unpublished experiment Beer and his colleagues infected pigs with H5N1. Even when high doses were used, the virus barely replicated in the animals.

People likely have other defenses beyond MxA that avian flu viruses have to beat. Lakdawala thinks that even though most people have not been exposed to H5 viruses, life-long exposure to other flu viruses may have created cellular or antibody protections against H5N1, too. In an ongoing experiment she is comparing how the current avian virus grows in ferrets infected 3 months earlier with seasonal influenza versus ferrets with no prior infections. "We really want to understand how likely these viruses are to emerge in the context of pre-existing immunity," she says.

What researchers know so far about the steps needed to adapt H5N1 to humans offers some reassurance: It has one of the highest barriers to becoming a pandemic virus of any avian influenza virus, Peacock says. "It's really wrong in so many ways," he says. "But obviously it only has to get the right combination of mutations once to do to jump."

And with the virus spreading so furiously around the globe, it has more opportunities to hit the right combination than ever before. In the past, H5N1 outbreaks have faded, but this time, the virus is probably here to stay in wild birds in Europe and the Americas, Richard says. "This is the threat that's going to keep knocking at our door until it will indeed, I assume, cause a pandemic. Because there is no way back." ■

A worker (left) and queen of the yellow crazy ant, *Anoplolepis gracilipes*, are shown.

PHOTO: THE WILD MARTIN

GENETICS

The unusual genetics of invasive ants

The males of an invasive ant species are chimeras of two distinct genetic lineages

By **Daniel J. C. Kronauer**[1,2]

Species with unusual modes of reproduction are overrepresented among invasive organisms that are dispersed by humans across the globe and can wreak havoc wherever they land (*1*, *2*). Invasive species thrive in disturbed habitats as well as island ecosystems, which have evolved largely in isolation and are therefore particularly vulnerable. However, upon arrival, colonizers face their own challenges: At initially tiny numbers, finding mates can be almost impossible, and inbreeding and genetic bottlenecks can be severe. Successful invaders often overcome these challenges through ingenious innovations in their reproductive biology. On page 55 of this issue, Darras *et al.* (*3*) show that the yellow crazy ant (*Anoplolepis gracilipes*), an invasive species that has spread across Asia and the western Pacific, features workers that are hybrids between two separate genetic lineages, and males that are genetic chimeras of the same two genetic stocks.

Ants rank among the most detrimental invasive pests (*4*), and a recent study found that, among 15,969 known ant species, 359 have established stable populations outside of their native habitat (*5*). Ants are haplodiploid, with diploid (two sets of chromosomes) females and haploid (one set of chromosomes) males that develop from unfertilized eggs. They are also eusocial, with females developing into one of two castes: large queens that specialize in egg-laying or small workers that forgo reproduction and care for the queen's offspring instead. Invasive ants are a treasure trove of wonderfully weird biology. In some, like the little fire ant, *Wasmannia auropunctata*, and the longhorn crazy ant, *Paratrechina longicornis*, queens and males belong to distinct genetic lineages and clone themselves (*6*, *7*). The two lineages only merge in the workers, which are highly heterozygous and produced sexually.

The yellow crazy ant rose to infamy after extirpating populations of the charismatic red land crab, *Gecarcoidea natalis*, on Christmas Island. Cascading ecological effects spanned several trophic levels, leading to what has been described as an "invasional meltdown" (*8*). Colonies of this species contain many reproductively active queens and can occur at very high densities, forming "supercolonies" where ants travel freely between nests. The first indication that the yellow crazy ant does not conform to standard ant reproduction came from a population genetic study showing that workers were always heterozygous at some marker loci, reminiscent of the little fire ant and longhorn crazy ant (*9*). Such an excess in heterozygosity seemed incompatible with random mating. Strangely, most of the males carried genotypes that were similar, if not identical, to those of the workers—that is, they had two alleles at most of the assayed loci, and the interpretation at the time was that they must be diploid (*9*). Diploid male ants, which are sterile and therefore impose substantial fitness costs on colonies, occur occasionally under inbreeding or in genetically impoverished populations. But the yellow crazy ant males were seemingly outbred and genetically diverse, only adding to the mystery surrounding the species' reproductive mode (*9*).

The study by Darras *et al.* shows that yellow crazy ant males are not diploid, but rather are made up of haploid cells with different genetic compositions: They are chimeras of two distinct genetic lineages, "R" and "W". The queens are members of the R lineage, carrying two copies of R chromosomes. When a queen lays an R egg that is fertilized by an R sperm, it develops into a new queen. However, when it is fertilized by a W sperm, there are two possible outcomes—either the egg and sperm pronuclei fuse and the egg develops into a diploid and highly heterozygous worker, or the pronuclei fail to fuse, and the egg develops into a haploid chimeric male. Although chimeras have been described before in a number of species, including marmosets and humans, the regular production of chimeras from single fertilization events has not previously been reported.

This discovery has a number of interesting implications. There are strong genetic effects on female caste development, adding to an increasing number of examples of such systems in ants (*6*, *10*–*14*). This suggests that many ant lineages harbor genetic variants that affect caste determination, possibly through biasing or limiting the body size a given genotype can obtain (*15*). However, in

[1]Laboratory of Social Evolution and Behavior, The Rockefeller University, New York, NY, USA. [2]Howard Hughes Medical Institute, New York, NY, USA. Email: dkronauer@rockefeller.edu

all known cases, it is the smaller workers that develop from hybrid eggs, whereas the larger queens are purebred. This seems at odds with other animals and plants, where viable hybrids often show "hybrid vigor" and are bigger than their parents. Therefore, the yellow crazy ant is a promising model to elucidate how ants, with their striking morphological castes, might differ from other organisms in terms of their developmental genetics.

Chimerism opens the door to competition between different genetic lineages, with possibly detrimental effects to the organism. Indeed, Darras *et al.* found that the two genotypes in males are not evenly distributed across tissues. Most of the cells in somatic tissues were of the R type, whereas most of the sperm carried W chromosomes. This means that W cells somehow outcompete R cells in terms of their contribution to the germ line, which is what matters for a genotype's fitness. The mechanisms that drive overrepresentation of W cells in the germ line, and whether and how they negatively affect the fitness of chimeric males, are promising avenues for future investigation.

Why would such a complicated reproductive system contribute to invasive success? One possible advantage is that, as in the little fire ant and the longhorn crazy ant (*6, 7*), a single inseminated queen can carry all the genetic information required to keep the system going in perpetuity. That R/W hybrids develop into nonreproductive workers prevents admixture between R and W genomes and, therefore, genetic bottlenecks and inbreeding depression. Conversely, chimerism and germline overrepresentation in haploid males ensure that W genomes remain in circulation. ■

REFERENCES AND NOTES

1. C. Rabeling, D. J. C. Kronauer, *Annu. Rev. Entomol.* **58**, 273 (2013).
2. P.-A. Eyer, E. L. Vargo, *Curr. Opin. Insect Sci.* **46**, 24 (2021).
3. H. Darras *et al.*, *Science* **380**, 55 (2023).
4. C. Bertelsmeier, *Curr. Opin. Insect Sci.* **46**, 16 (2021).
5. M. K. L. Wong, E. P. Economo, B. Guénard, *Curr. Biol.* **33**, 566 (2023).
6. D. Fournier *et al.*, *Nature* **435**, 1230 (2005).
7. S.-P. Tseng *et al.*, *Mol. Ecol.* **32**, 1020 (2023).
8. D. J. O'Dowd, P. T. Green, P. S. Lake, *Ecol. Lett.* **6**, 812 (2003).
9. J. Drescher, N. Blüthgen, H. Feldhaar, *Mol. Ecol.* **16**, 1453 (2007).
10. J. Romiguier, A. Fournier, S. H. Yek, L. Keller, *Mol. Ecol.* **26**, 1108 (2017).
11. K. D. Lacy, D. Shoemaker, K. G. Ross, *Curr. Biol.* **29**, 1394 (2019).
12. T. Schwander, N. Lo, M. Beekman, B. P. Oldroyd, L. Keller, *Trends Ecol. Evol.* **25**, 275 (2010).
13. A. Kuhn, H. Darras, O. Paknia, S. Aron, *Mol. Ecol.* **29**, 549 (2020).
14. S. Helms Cahan, A. D. Nguyen, Y. Zhou, *Evolution* **76**, 1016 (2022).
15. W. Trible, D. J. C. Kronauer, *J. Exp. Biol.* **220**, 53 (2017).

ACKNOWLEDGMENTS

Thanks to K. Lacy for feedback on the manuscript.

10.1126/science.adh1664

CHEMISTRY

Alternating the current direction

Waveform-controlled electrolysis enables the carbon-carbon coupling of carboxylic acids

By **Peng Guo** *and* **Ke-Yin Ye**

Carbon-carbon (C–C) bonds constitute the frameworks of almost all organic compounds. The artistry of scientists modulating these chemical bonds provides a fascinating wealth of molecules with diverse functionalities. The central goal of synthetic organic chemistry is to discover more versatile and robust C–C bond-forming reactions with high fidelity. In particular, state-of-the-art transition metal–catalyzed C–C cross-coupling reactions (*1*) readily provide access to diverse molecules that are rich in arenes (aromatic rings), profoundly accelerating pharmaceutical and materials science. By contrast, efforts in pursuing general coupling of aliphatic C–C chains have been met with limited success. On page 81 of this issue, Hioki *et al.* (*2*) demonstrate an elegant solution to this challenge based on waveform-controlled electrolytic C–C coupling of aliphatic carboxylic acids.

Aliphatic carboxylic acids are ubiquitous and inexpensive feedstock chemicals from commercial and natural sources, serving as perfect aliphatic C–C coupling precursors upon decarboxylation (extrusion of carbon dioxide). Enzyme-mediated decarboxylation of amino acids (*3*) can proceed under ambient conditions, but thermal approaches are attainable only under harsh conditions, which typically involve high temperatures that are achieved through energy-intensive processes (*4*). A detour solution to the decarboxylative inertness of aliphatic carboxylic acids is preactivation, for example, to form their redox-active esters (*5*). But this solution involves the downsides of adding an extra synthetic step, generation of excessive waste, and diminished atom economy (quantity of material from the starting materials or reagents into the final product).

Radical chemistry provides innovative solutions to many synthetic challenges inherently associated with polar (ionic) chemistry. For example, single-electron oxidation of a carboxylate (the conjugate base of a carboxylic acid) gives rise to a highly reactive carboxy radical, which spontaneously extrudes carbon dioxide (*6*) and concomitantly generates a carbon-centered radical. This radical decarboxylation of carboxylic acids can be used for forging diverse C–C bonds (*7*), albeit mostly through complex reaction settings.

The Kolbe reaction (*8*) directly uses aliphatic carboxylic acids to construct saturated C–C bonds through consecutive electrochemical decarboxylation and radical-radical coupling. Unfortunately, it relies on exceptionally high current density, typically greater than 100 mA·cm^{-2}, to enhance the adsorption of carboxylate on the positive platinum electrode and generate highly concentrated radicals nearby for effective C–C coupling (*9*). Despite the simplicity and sustainability of the Kolbe reaction in forging C–C bonds, the high current precludes the compatibility of

The waveform matters

Potential waveforms for electrolysis can be direct current and rapid alternating polarity (rAP). The rAP renders the classic Kolbe reaction readily accessible with a reduced current density and sustainable carbon-based electrodes to produce previously unattainable aliphatic building blocks and unnatural amino acids.

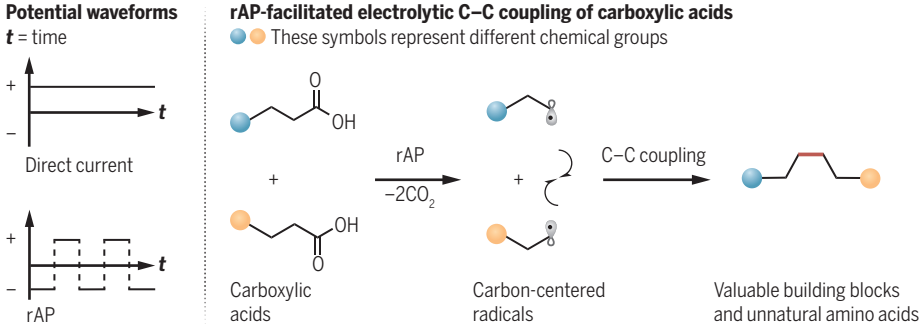

GRAPHIC: N. CARY/*SCIENCE*, BASED ON P. GUO AND K.-Y. YE

all known cases, it is the smaller workers that develop from hybrid eggs, whereas the larger queens are purebred. This seems at odds with other animals and plants, where viable hybrids often show "hybrid vigor" and are bigger than their parents. Therefore, the yellow crazy ant is a promising model to elucidate how ants, with their striking morphological castes, might differ from other organisms in terms of their developmental genetics.

Chimerism opens the door to competition between different genetic lineages, with possibly detrimental effects to the organism. Indeed, Darras *et al.* found that the two genotypes in males are not evenly distributed across tissues. Most of the cells in somatic tissues were of the R type, whereas most of the sperm carried W chromosomes. This means that W cells somehow outcompete R cells in terms of their contribution to the germ line, which is what matters for a genotype's fitness. The mechanisms that drive overrepresentation of W cells in the germ line, and whether and how they negatively affect the fitness of chimeric males, are promising avenues for future investigation.

Why would such a complicated reproductive system contribute to invasive success? One possible advantage is that, as in the little fire ant and the longhorn crazy ant (*6*, *7*), a single inseminated queen can carry all the genetic information required to keep the system going in perpetuity. That R/W hybrids develop into nonreproductive workers prevents admixture between R and W genomes and, therefore, genetic bottlenecks and inbreeding depression. Conversely, chimerism and germline overrepresentation in haploid males ensure that W genomes remain in circulation. ■

REFERENCES AND NOTES

1. C. Rabeling, D. J. C. Kronauer, *Annu. Rev. Entomol.* **58**, 273 (2013).
2. P.-A. Eyer, E. L. Vargo, *Curr. Opin. Insect Sci.* **46**, 24 (2021).
3. H. Darras *et al.*, *Science* **380**, 55 (2023).
4. C. Bertelsmeier, *Curr. Opin. Insect Sci.* **46**, 16 (2021).
5. M. K. L. Wong, E. P. Economo, B. Guénard, *Curr. Biol.* **33**, 566 (2023).
6. D. Fournier *et al.*, *Nature* **435**, 1230 (2005).
7. S.-P. Tseng *et al.*, *Mol. Ecol.* **32**, 1020 (2023).
8. D. J. O'Dowd, P. T. Green, P. S. Lake, *Ecol. Lett.* **6**, 812 (2003).
9. J. Drescher, N. Blüthgen, H. Feldhaar, *Mol. Ecol.* **16**, 1453 (2007).
10. J. Romiguier, A. Fournier, S. H. Yek, L. Keller, *Mol. Ecol.* **26**, 1108 (2017).
11. K. D. Lacy, D. Shoemaker, K. G. Ross, *Curr. Biol.* **29**, 1394 (2019).
12. T. Schwander, N. Lo, M. Beekman, B. P. Oldroyd, L. Keller, *Trends Ecol. Evol.* **25**, 275 (2010).
13. A. Kuhn, H. Darras, O. Paknia, S. Aron, *Mol. Ecol.* **29**, 549 (2020).
14. S. Helms Cahan, A. D. Nguyen, Y. Zhou, *Evolution* **76**, 1016 (2022).
15. W. Trible, D. J. C. Kronauer, *J. Exp. Biol.* **220**, 53 (2017).

ACKNOWLEDGMENTS

Thanks to K. Lacy for feedback on the manuscript.

10.1126/science.adh1664

CHEMISTRY

Alternating the current direction

Waveform-controlled electrolysis enables the carbon-carbon coupling of carboxylic acids

By **Peng Guo** *and* **Ke-Yin Ye**

Carbon-carbon (C–C) bonds constitute the frameworks of almost all organic compounds. The artistry of scientists modulating these chemical bonds provides a fascinating wealth of molecules with diverse functionalities. The central goal of synthetic organic chemistry is to discover more versatile and robust C–C bond-forming reactions with high fidelity. In particular, state-of-the-art transition metal–catalyzed C–C cross-coupling reactions (*1*) readily provide access to diverse molecules that are rich in arenes (aromatic rings), profoundly accelerating pharmaceutical and materials science. By contrast, efforts in pursuing general coupling of aliphatic C–C chains have been met with limited success. On page 81 of this issue, Hioki *et al.* (*2*) demonstrate an elegant solution to this challenge based on waveform-controlled electrolytic C–C coupling of aliphatic carboxylic acids.

Aliphatic carboxylic acids are ubiquitous and inexpensive feedstock chemicals from commercial and natural sources, serving as perfect aliphatic C–C coupling precursors upon decarboxylation (extrusion of carbon dioxide). Enzyme-mediated decarboxylation of amino acids (*3*) can proceed under ambient conditions, but thermal approaches are attainable only under harsh conditions, which typically involve high temperatures that are achieved through energy-intensive processes (*4*). A detour solution to the decarboxylative inertness of aliphatic carboxylic acids is preactivation, for example, to form their redox-active esters (*5*). But this solution involves the downsides of adding an extra synthetic step, generation of excessive waste, and diminished atom economy (quantity of material from the starting materials or reagents into the final product).

Radical chemistry provides innovative solutions to many synthetic challenges inherently associated with polar (ionic) chemistry. For example, single-electron oxidation of a carboxylate (the conjugate base of a carboxylic acid) gives rise to a highly reactive carboxy radical, which spontaneously extrudes carbon dioxide (*6*) and concomitantly generates a carbon-centered radical. This radical decarboxylation of carboxylic acids can be used for forging diverse C–C bonds (*7*), albeit mostly through complex reaction settings.

The Kolbe reaction (*8*) directly uses aliphatic carboxylic acids to construct saturated C–C bonds through consecutive electrochemical decarboxylation and radical-radical coupling. Unfortunately, it relies on exceptionally high current density, typically greater than 100 mA·cm^{-2}, to enhance the adsorption of carboxylate on the positive platinum electrode and generate highly concentrated radicals nearby for effective C–C coupling (*9*). Despite the simplicity and sustainability of the Kolbe reaction in forging C–C bonds, the high current precludes the compatibility of

The waveform matters

Potential waveforms for electrolysis can be direct current and rapid alternating polarity (rAP). The rAP renders the classic Kolbe reaction readily accessible with a reduced current density and sustainable carbon-based electrodes to produce previously unattainable aliphatic building blocks and unnatural amino acids.

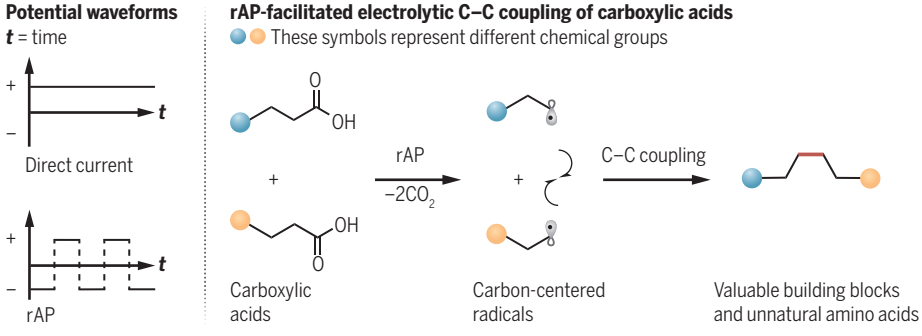

GRAPHIC: N. CARY/*SCIENCE*. BASED ON P. GUO AND K.-Y. YE

most chemical functionalities, and the use of expensive precious-metal electrodes further limits the adoption of this reaction in mainstream organic syntheses and industrial applications.

Hioki *et al.* creatively approach these long-standing challenges by rapidly alternating the current direction (see the figure). Although alternating current (in which the electric flow changes direction periodically) is pervasive in households worldwide, almost all electro-organic transformations, including constant voltage or current electrolysis, rely on direct current (in which the current only flows in one direction). By contrast, synthetic electrochemistry adapts only alternating current electrolysis to remove electrode fouling and passivation (insulation of the electrode surface). Only very recently have chemists come to recognize the importance of alternating current to minimize unproductive overoxidation and overreduction, facilitate paired electrolysis involving transient intermediates, and promote the discovery of new reactions (*10*–*12*).

"...electronic waveform is an underappreciated yet enabling handle in modulating reactivity in synthetic electrochemistry."

Although early studies did not reveal any preference for alternating current over direct current, Hioki *et al.* demonstrate that the reactivity and selectivity of the Kolbe reaction are substantially improved by using rapid alternating polarity (rAP). Using a square waveform with an optimal frequency of 50 ms for the alternating current and acetone as the proton- and electron-acceptor is pivotal to this reactivity. The use of rAP further renders the demanding Kolbe reaction readily accessible even with sustainable C-based electrodes. The up-conversion strategy of Hioki *et al.* tolerates aliphatic carboxylic acids with many previously unusable functionalities. Therefore, many trivial biomass-derived acids can be converted into highly value-added and prohibitively expensive building blocks in one step, which are otherwise elusive or tedious to prepare. Another important synthetic application of their method is hetero-coupling, which upgrades the inexpensive natural amino acids, such as glutamic acid and aspartic acid, into valuable unnatural amino acids of pharmaceutical interest. The authors show that this waveform-controlled aliphatic C–C coupling is operative on large scales simply by using technical-grade acetone under ambient conditions.

How would direct current and rAP impart the Kolbe reaction so differently? Despite a partially neutralized solution of carboxylic acids used in the Kolbe reaction, direct current electrolysis still creates a local microscopic acidic environment near the electrodes, known as the electrogenerated acid. The consequent protonation of the carboxylates into the difficult-to-oxidize carboxylic acids accounts for why such high currents are usually needed in the Kolbe reaction. By contrast, the fast polarity switching in rAP affords more concentrated carboxylates on the electrode surface. Therefore, a reduced current density is sufficient, and the platinum electrodes used in the Kolbe reaction to accumulate carboxylates are now dispensable, paving the way for sustainable future industrial adoption.

The report by Hioki *et al.* demonstrates that electronic waveform is an underappreciated yet enabling handle in modulating reactivity in synthetic electrochemistry. Future efforts will be devoted to minimizing the meticulous reaction optimization (*13*), improving energy efficiency by avoiding massive energy loss during periodical polarity switching, and establishing predictable waveform-reactivity modes (*14*). ■

Key Laboratory of Molecule Synthesis and Function Discovery (Fujian Province University), College of Chemistry, Fuzhou University, Fuzhou, China. Email: kyye@fzu.edu.cn

REFERENCES AND NOTES

1. The Royal Swedish Academy of Sciences awarded the Nobel Prize in Chemistry for 2010 to Richard F. Heck, Ei-ichi Negishi, and Akira Suzuki for "palladium-catalyzed cross couplings in organic synthesis."
2. Y. Hioki *et al.*, *Science* **380**, 81 (2023).
3. T. Li, L. Huo, C. Pulley, A. Liu, *Bioorg. Chem.* **43**, 2 (2012).
4. N. Rodríguez, L. J. Goossen, *Chem. Soc. Rev.* **40**, 5030 (2011).
5. B. Zhang *et al.*, *Nature* **606**, 313 (2022).
6. J. W. Hilborn, J. A. Pincock, *J. Am. Chem. Soc.* **113**, 2683 (1991).
7. S. B. Beil, T. Q. Chen, N. E. Intermaggio, D. W. C. MacMillan, *Acc. Chem. Res.* **55**, 3481 (2022).
8. H. Kolbe, *Justus Liebigs Ann. Chem.* **69**, 257 (1849).
9. T. Dickinson, W. F. K. Wynne-Jones, *Trans. Faraday Soc.* **58**, 400 (1962).
10. S. Rodrigo, D. Gunasekera, J. P. Mahajan, L. Luo, *Curr. Opin. Electrochem.* **28**, 100712 (2021).
11. J. Zhong, C. Ding, H. Kim, T. McCallum, K. Ye, *Green Synth. Catal.* **3**, 4 (2022).
12. M. Jamshidi *et al.*, *Synthesis* **54**, 4661 (2022).
13. D. Gunasekera *et al.*, *J. Am. Chem. Soc.* **144**, 9874 (2022).
14. L. Zeng *et al.*, *Nat. Synth.* **2**, 172 (2023).

ACKNOWLEDGMENTS

K.-Y.Y. is supported by the National Natural Science Foundation of China (22171046).

10.1126/science.adh1837

CHEMISTRY

Chemistry that allows plastic recycling

Enhancing thermal stability of polyhydroxyalkanoates for their closed-loop chemistry

By **Sophie M. Guillaume**

Polyhydroxyalkanoates (PHAs), a class of polyesters discovered nearly a century ago (*1*), have recently gained renewed industrial and academic interest because of their renewability, biocompatibility, degradability, and recyclability (*2*). Diverse PHAs are biosynthesized in nature from microorganisms. They also can be synthesized through chemical reactions, creating forms with greater variability with respect to polymer chain length, microstructure, postpolymerization reactivity, and functional properties (*3*, *4*). However, PHAs suffer from mechanical brittleness, thermal instability, and lack of the desired closed-loop chemical recyclability, which limit their widespread applications. On page 64 of this issue, Zhou *et al.* (*5*) describe a synthetic strategy based on designing PHAs with enhanced mechanical toughness and thermal stability. Moreover, the process is circular, enabling PHAs to be recycled.

An ecological circular plastics economy requires renewable and recyclable plastics as alternatives to fossil fuel–based nondegradable polymers that currently dominate the markets. Eco-designing polymers from biobased feedstocks with improved end-of-life options is nowadays mandatory to secure a sustainable future (*6*–*9*). In this context, PHAs are promising alternatives to common plastics such as polystyrene, polypropylene, and poly(ethylene terephtalate), with applications that range from packaging to biomedical and pharmaceutical devices (*2*). However, the broad commercial use of these polymers is impeded because they are mechanically brittle, not melt-processable, and not chemically recyclable to monomers (*3*, *4*). In contrast to bacterial routes, synthetic chemical (abiotic) pathways can produce functional reactive PHAs that are endowed with tunable thermomechanical and degradable or biodegradable properties. These pathways include the

most chemical functionalities, and the use of expensive precious-metal electrodes further limits the adoption of this reaction in mainstream organic syntheses and industrial applications.

Hioki *et al.* creatively approach these long-standing challenges by rapidly alternating the current direction (see the figure). Although alternating current (in which the electric flow changes direction periodically) is pervasive in households worldwide, almost all electro-organic transformations, including constant voltage or current electrolysis, rely on direct current (in which the current only flows in one direction). By contrast, synthetic electrochemistry adapts only alternating current electrolysis to remove electrode fouling and passivation (insulation of the electrode surface). Only very recently have chemists come to recognize the importance of alternating current to minimize unproductive overoxidation and overreduction, facilitate paired electrolysis involving transient intermediates, and promote the discovery of new reactions (*10*–*12*).

"...electronic waveform is an underappreciated yet enabling handle in modulating reactivity in synthetic electrochemistry."

Although early studies did not reveal any preference for alternating current over direct current, Hioki *et al.* demonstrate that the reactivity and selectivity of the Kolbe reaction are substantially improved by using rapid alternating polarity (rAP). Using a square waveform with an optimal frequency of 50 ms for the alternating current and acetone as the proton- and electron-acceptor is pivotal to this reactivity. The use of rAP further renders the demanding Kolbe reaction readily accessible even with sustainable C-based electrodes. The up-conversion strategy of Hioki *et al.* tolerates aliphatic carboxylic acids with many previously unusable functionalities. Therefore, many trivial biomass-derived acids can be converted into highly value-added and prohibitively expensive building blocks in one step, which are otherwise elusive or tedious to prepare. Another important synthetic application of their method is hetero-coupling, which upgrades the inexpensive natural amino acids, such as glutamic acid and aspartic acid, into valuable unnatural amino acids of pharmaceutical interest. The authors show that this waveform-controlled aliphatic C–C coupling is operative on large scales simply by using technical-grade acetone under ambient conditions.

How would direct current and rAP impart the Kolbe reaction so differently? Despite a partially neutralized solution of carboxylic acids used in the Kolbe reaction, direct current electrolysis still creates a local microscopic acidic environment near the electrodes, known as the electrogenerated acid. The consequent protonation of the carboxylates into the difficult-to-oxidize carboxylic acids accounts for why such high currents are usually needed in the Kolbe reaction. By contrast, the fast polarity switching in rAP affords more concentrated carboxylates on the electrode surface. Therefore, a reduced current density is sufficient, and the platinum electrodes used in the Kolbe reaction to accumulate carboxylates are now dispensable, paving the way for sustainable future industrial adoption.

The report by Hioki *et al.* demonstrates that electronic waveform is an underappreciated yet enabling handle in modulating reactivity in synthetic electrochemistry. Future efforts will be devoted to minimizing the meticulous reaction optimization (*13*), improving energy efficiency by avoiding massive energy loss during periodical polarity switching, and establishing predictable waveform-reactivity modes (*14*). ■

Key Laboratory of Molecule Synthesis and Function Discovery (Fujian Province University), College of Chemistry, Fuzhou University, Fuzhou, China. Email: kyye@fzu.edu.cn

REFERENCES AND NOTES

1. The Royal Swedish Academy of Sciences awarded the Nobel Prize in Chemistry for 2010 to Richard F. Heck, Ei-ichi Negishi, and Akira Suzuki for "palladium-catalyzed cross couplings in organic synthesis."
2. Y. Hioki *et al.*, *Science* **380**, 81 (2023).
3. T. Li, L. Huo, C. Pulley, A. Liu, *Bioorg. Chem.* **43**, 2 (2012).
4. N. Rodríguez, L. J. Goossen, *Chem. Soc. Rev.* **40**, 5030 (2011).
5. B. Zhang *et al.*, *Nature* **606**, 313 (2022).
6. J. W. Hilborn, J. A. Pincock, *J. Am. Chem. Soc.* **113**, 2683 (1991).
7. S. B. Beil, T. Q. Chen, N. E. Intermaggio, D. W. C. MacMillan, *Acc. Chem. Res.* **55**, 3481 (2022).
8. H. Kolbe, *Justus Liebigs Ann. Chem.* **69**, 257 (1849).
9. T. Dickinson, W. F. K. Wynne-Jones, *Trans. Faraday Soc.* **58**, 400 (1962).
10. S. Rodrigo, D. Gunasekera, J. P. Mahajan, L. Luo, *Curr. Opin. Electrochem.* **28**, 100712 (2021).
11. J. Zhong, C. Ding, H. Kim, T. McCallum, K. Ye, *Green Synth. Catal.* **3**, 4 (2022).
12. M. Jamshidi *et al.*, *Synthesis* **54**, 4661 (2022).
13. D. Gunasekera *et al.*, *J. Am. Chem. Soc.* **144**, 9874 (2022).
14. L. Zeng *et al.*, *Nat. Synth.* **2**, 172 (2023).

ACKNOWLEDGMENTS

K.-Y.Y. is supported by the National Natural Science Foundation of China (22171046).

10.1126/science.adh1837

CHEMISTRY

Chemistry that allows plastic recycling

Enhancing thermal stability of polyhydroxyalkanoates for their closed-loop chemistry

By **Sophie M. Guillaume**

Polyhydroxyalkanoates (PHAs), a class of polyesters discovered nearly a century ago (*1*), have recently gained renewed industrial and academic interest because of their renewability, biocompatibility, degradability, and recyclability (*2*). Diverse PHAs are biosynthesized in nature from microorganisms. They also can be synthesized through chemical reactions, creating forms with greater variability with respect to polymer chain length, microstructure, postpolymerization reactivity, and functional properties (*3*, *4*). However, PHAs suffer from mechanical brittleness, thermal instability, and lack of the desired closed-loop chemical recyclability, which limit their widespread applications. On page 64 of this issue, Zhou *et al.* (*5*) describe a synthetic strategy based on designing PHAs with enhanced mechanical toughness and thermal stability. Moreover, the process is circular, enabling PHAs to be recycled.

An ecological circular plastics economy requires renewable and recyclable plastics as alternatives to fossil fuel–based nondegradable polymers that currently dominate the markets. Eco-designing polymers from biobased feedstocks with improved end-of-life options is nowadays mandatory to secure a sustainable future (*6*–*9*). In this context, PHAs are promising alternatives to common plastics such as polystyrene, polypropylene, and poly(ethylene terephtalate), with applications that range from packaging to biomedical and pharmaceutical devices (*2*). However, the broad commercial use of these polymers is impeded because they are mechanically brittle, not melt-processable, and not chemically recyclable to monomers (*3*, *4*). In contrast to bacterial routes, synthetic chemical (abiotic) pathways can produce functional reactive PHAs that are endowed with tunable thermomechanical and degradable or biodegradable properties. These pathways include the

polycondensation reaction of substituted hydroxyacids, or the ring-opening polymerization of either substituted cyclic four-membered ring β-lactones or eight-membered ring diolides (*2*).

Fine adjustment of PHA characteristics can be specifically achieved with ring-opening polymerization of the functional cyclic esters or diesters, performed in the presence of a stereoselective catalytic system (organic or metal-based). Thus, PHAs with precise chain length, β-pendant substituents, chain end-groups, and stereomicrostructure that can be controlled in a specific manner (tacticity)—features not available with natural PHAs—can be achieved (*10*–*12*).

Zhou *et al*. tackled the thermal instability of PHAs by designing a polymer from α,α-dialkylated β-lactones. The straightforward substitution of the two α-hydrogens with alkyl groups prevented a facile cis-elimination reaction that is detrimental to thermal steadiness. This simple approach makes use of either a glucose-derived hydroxyacid {3-hydroxy-2,2-dimethylbutyric acid [3H(Me_2)BA]} or an α,α-dimethyl-α-butyrolactone (Me_2BL) monomer. The latter cyclic ester is obtained from the former hydroxyacid through direct lactonization, in which the gem-disubstituent favors ring closure and stabilization of the strained ring (*13*, *14*). Subsequent polycondensation of 3H(Me_2)BA or controlled ring-opening polymerization of (Me_2)BL, catalyzed by commercially available reagents under mild conditions (<160°C for ~20 hours), generated the desired α,α-dimethylated PHA—poly(3-hydroxy-2,2-dimethylbutyrate), or P3H(Me_2)B—of short, medium, or long chain length (see the figure). Increasing the synthesis of the monomers [up to 362 g of 3H(Me_2)BA and 232 g of (Me_2)BL] afforded as much as 115 g of pure P3H(Me_2)B (92% yield) through ring-opening polymerization under industry-relevant conditions (55 parts per million loading of a catalyst under solvent-free conditions at 70°C for 28 hours). The demonstrated compatibility of the method with other α-dialkylated monomers or a mixture of such monomers further broadens the scope of possible PHAs.

All P3H(Me_2)B samples synthesized by Zhou *et al*. were semicrystalline regardless of their tacticity (atactic or isotactic). This is a rare example of polymers exhibiting tacticity-independent crystallinity and provides a highly valuable strategy for preparing high-performance PHAs without requiring the more delicate stereocontrolled ring-opening polymerization that relies on specifically designed stereoselective catalysts. Furthermore, the P3H(Me_2)B samples exhibited thermal robustness with high melting and degradation temperatures (T_m = 167 to 243°C and T_d = 314 to 335°C) at 68°C and 85°C, respectively, higher than those of the most ubiquitous isotactic PHA, (*R*)-polyhydroxybutyrate. Additionally, these P3H(Me_2)B polymers showed high mechanical performances and enhanced melt-processability and ductility (elongation at break > 200%). Even more rewarding, P3H(Me_2)B could be chemically recycled back to its starting monomers upon either depolymerization to 3H(Me_2)BA or chain-unzipping into (Me_2)BL, establishing the highly sought monomer-polymer-monomer closed-loop chemical recyclability of PHAs.

The pathways described by Zhou *et al*. exemplify how polymers can be improved by revisiting some fundamental chemistry concepts rather than establishing complex chemistry models. Their reversible polymerization routes stand in contrast to past strategies that focused on either varying the steric, electronic, and chemical environment of the β-substituent on the lactone monomer, or on the composition, stereochemistry, and structure of the main-chain backbone, or even on the polymer topology. Furthermore, the method enables the introduction of other chemical groups at the α-position, which opens the possibility of pushing PHAs toward more diversified functional materials. Together with the scalability of the polymerization and depolymerization steps, the findings of Zhao *et al*. constitute an notable step in the PHA domain to advance sustainability and circularity of polymers and could have profound implications for the next-generation of industrial plastics. ■

Chemistry that allows plastic recycling

Two synthetic pathways can produce a stable α,α-disubstituted polyhydroxyalkanoate P3H(Me_2)B polymer. One route involves a polycondensation reaction from the dimethylbutyric acid [3H(Me_2)BA] monomer. The other route uses ring-opening polymerization of the α,α-dimethyl-β-butyrolactone [(Me_2)BL] monomer. This monomer itself is derived from the lactonization of 3H(Me_2)BA. The resulting polymer can undergo base-catalyzed hydrolysis or depolymerization, regenerating the monomers and closing the life-cycle loop.

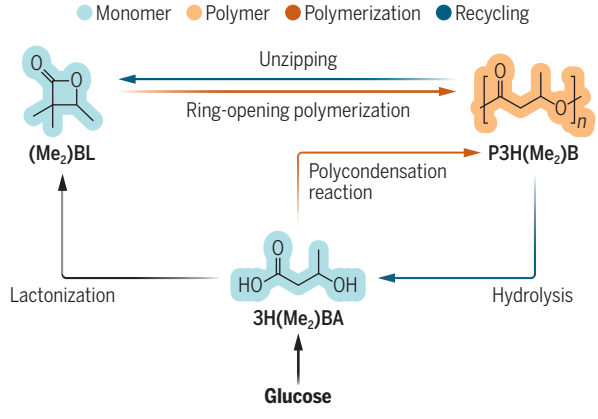

The range of products that could be made with polyhydroxyalkanoates includes straws, cups, bottles, lids, utensils, plates, and bags.

CREDITS: (GRAPHIC) A. MASTIN/*SCIENCE*; (PHOTO) JUN KRISWANTO

REFERENCES AND NOTES

1. M. Lemoigne, *Bull. Soc. Chim. Biol. (Paris)* **8**, 770 (1926).
2. M. Koller, Ed., *The Handbook of Polyhydroxyalkanoates* (CRC Press, ed. 1, 2020), vol. 1–3.
3. S. Taguchi, T. Iwata, H. Abe, Y. Doi, *Polym. Sci. A Comprehensive Ref.* **9**, 157 (2012).
4. A. H. Westlie, E. C. Quinn, C. R. Parker, E. Y.-X. Chen, *Prog. Polym. Sci.* **134**, 101608 (2022).
5. L. Zhou *et al*., *Science* **380**, 64 (2023).
6. B. von Vacano *et al*., *Angew. Chem. Int. Ed.* **62**, e202210823 (2023).
7. F. M. Haque *et al*., *Chem. Rev.* **122**, 6322 (2022).
8. L. T. J. Korley, T. H. Epps 3rd, B. A. Helms, A. J. Ryan, *Science* **373**, 66 (2021).
9. G. W. Coates, Y. D. Y. L. Getzler, *Nat. Rev. Mater.* **5**, 501 (2020).
10. X.-L. Li, K. Ma, F. Xu, T.-Q. Xu, *Chem. Asian J.* e202201167 (2023).
11. C. X. Shi *et al*., *Chem* **7**, 2896 (2021).
12. H. Li *et al*., *Chem. Eur. J.* **26**, 128 (2020).
13. W. Xiong *et al*., *Chem* **6**, 1831 (2020).
14. M. E. Jung, G. Piizzi, *Chem. Rev.* **105**, 1735 (2005).

Université de Rennes, CNRS, Institut des Sciences Chimiques de Rennes (ISCR), UMR 6226, 35042 Rennes, France.
E-mail: sophie.guillaume@univ-rennes.fr

10.1126/science.adh3072

MEDICINE

Toward a vaccine against hepatitis C virus

Recent advances aid the development of vaccines to prevent chronic liver diseases

By **Anna Offersgaard[1,2], Jens Bukh[1,2], Judith M. Gottwein[1,2]**

A vaccine protecting against chronic infection with hepatitis C virus (HCV) is urgently needed to address the ongoing public health crisis caused by this insidious pathogen—a major cause of liver cirrhosis and cancer. Efforts toward development of vaccines were initiated after the discovery of HCV in 1989, but to date, no vaccine has been licensed. An increased understanding of HCV protective immunity and HCV envelope glycoprotein structure and function is paving the way toward rational vaccine design and evaluation.

HCV is mainly transmitted through blood, but sexual and perinatal transmissions do occur. Worldwide, most transmissions are caused by unsafe medical procedures, but ~20% occur in people who inject drugs (PWID), an important risk group in high-income countries; another risk group in high-income countries is men who have sex with men (*1*). The World Health Organization (WHO) estimates that 1.5 million new infections occur annually, and incidence is increasing in many countries, including the US, where transmission is fueled by the opioid crisis. About 75% of infections progress to chronic hepatitis C, estimated to affect 58 million individuals worldwide. Chronic hepatitis C leads to liver cirrhosis in ~20% of cases, which also comes with an ~5% annual risk for the development of hepatocellular carcinoma. Annually, HCV-induced liver diseases cause ~290,000 deaths worldwide.

Efficient, curative, and direct-acting antivirals have so far had limited effect on global HCV prevalence. Without population screening programs, ~80% of chronic infections are undiagnosed because specific symptoms often only appear when severe and potentially irreversible liver damage has developed. Further, reinfections are common in risk groups. Thus, it currently appears unrealistic to achieve the WHO target of eliminating viral hepatitis as a major public health threat by 2030. In the future, achieving this target globally will likely require a vaccine, and the availability of a vaccine is predicted to result in aggregated cost savings of several billion US dollars compared with testing and treatment alone (*2*).

HCV belongs to the *Flaviviridae* family and is an enveloped positive-sense, single-stranded RNA virus classified into eight major genotypes with ~30% sequence difference. This extensive genetic heterogeneity challenges vaccine development. The virus particle contains the structural proteins Core, which encapsidates the RNA genome, and E1 and E2, which are highly heterogeneous envelope glycoproteins that form heterodimers interacting with host cell receptors during viral entry into hepatocytes. E1 and E2 are the main targets of neutralizing antibodies (nAbs) and thus of vaccine approaches that target B cells. The nonstructural (NS) proteins (p7, NS2, NS3, NS4A, NS4B, NS5A, and NS5B) mediate viral processing inside the host cell and are thus primarily targeted by vaccine approaches that aim to elicit T cell–mediated responses.

In preclinical studies, a range of HCV vaccine candidates has been explored—based on viral vectors, recombinant inactivated viruses, virus-like particles (VLPs), nanoparticles, recombinant proteins, peptides, DNA, and mRNA—showing varying immunogenicity (*1*). Among these, only one candidate has proceeded to a clinical protection study. In 2021, a phase 1/2 trial (NCT01436357) in PWID provided evidence that a viral vector vaccine encoding NS3-NS5B, based on chimpanzee adenovirus 3 for priming and modified vaccinia Ankara virus for boosting, induced HCV-specific T cells. However, this vaccine candidate did not protect against chronic HCV infection (*1*, *3*). The most advanced B cell–targeting HCV vaccine candidate, an MF59-adjuvanted E1-E2 heterodimer vaccine, was protective in chimpanzees and had the capacity to induce broadly neutralizing antibodies (bnAbs) in a phase 1 trial reported in 2010 (NCT00500747). However, immunogenicity was low, with <50% of vaccinees mounting nAbs (*1*). Rational design of next-generation vaccines is now guided by improved understanding of HCV protective immunity, viral immune escape mechanisms, and the structure of the HCV envelope glycoproteins and neutralizing epitopes.

HCV protective immunity is feasible: ~25% of acute infections are cleared, and clearance is more likely after reinfection (*1*, *4*). Early studies on protective immunity focused on evaluating T cells. Later, studies of nAbs were enabled by the development of suitable recombinant in vitro systems: Panels of HCV E1-E2 containing pseudoparticles, which allow studies of HCV cell entry, and of cell culture–adapted HCV, which allows studies of the complete viral life cycle, now represent HCV genetic and antigenic diversity (*5*–*8*). Important insights were initially gained from chimpanzee challenge studies, which are no longer feasible; studies now rely on humans at risk of infection. Together, such studies have clarified that both humoral and cellular immune responses appear to be involved in the natural clearance of HCV infection; however, they may not always contribute equally (*1*, *5*). Thus, in any individual, nAbs or T cells might be the dominant drivers of viral clearance.

Clearance has been associated with sustained $CD4^+$ and $CD8^+$ T cell responses, with low expression of inhibitory receptors, such as programmed cell death protein 1 (PD1), on T cells as well as with induction of high-titer nAbs (*1*, *5*). Both nAbs with narrow specificity and bnAbs, which target epitopes that are conserved across HCV strains, have been associated with natural clearance in humans (*1*, *5*, *8*). Such antibody responses are also induced during chronic HCV infection, which suggests that antibody titers and timing, in relation to the onset of infection and the emergence of viral immune escape variants within the infected individual, likely determine the prospects of antibody-driven clearance (*1*, *5*). The demonstration of persisting memory B and T cells after natural infection also holds promise for vaccine-induced protection (*9*).

HCV genetic heterogeneity and mutational immune escape call for vaccines that target conserved epitopes. Although the vaccine candidate eliciting T cells was not protective in the phase 1/2 trial (*3*), similar viral vector vaccines are currently being optimized to increase the magnitude and breadth of T cell responses by using conserved epitopes (*1*, *10*). Alternatively, T cell epitopes could be presented using mRNA, recombinant protein, and peptide vaccine platforms (*1*). The protective potential of nAbs was demonstrated in passive transfer experiments in chimpanzees and human liver chimeric mice (*5*, *11*). Therefore, emerging vaccine candidates that target B cells to induce potent bnAbs should be evaluated in humans.

[1]Copenhagen Hepatitis C Program (CO-HEP), Department of Infectious Diseases, Copenhagen University Hospital Hvidovre, Hvidovre, Denmark. [2]CO-HEP, Department of Immunology and Microbiology, Faculty of Health and Medical Sciences, University of Copenhagen, Copenhagen, Denmark. Email: jgottwein@sund.ku.dk

Hepatitis C virus (HCV) vaccine development

Research on HCV protective immunity, envelope glycoprotein structure, and drivers of immune escape facilitates rational vaccine design. Vaccine-induced immune responses are evaluated preclinically using animals and in vitro assays and are compared with known correlates of protection. Without an immunocompetent animal challenge model, advancing candidate vaccines will largely depend on efficient phase 2 trial design, potentially including a controlled human infection model.

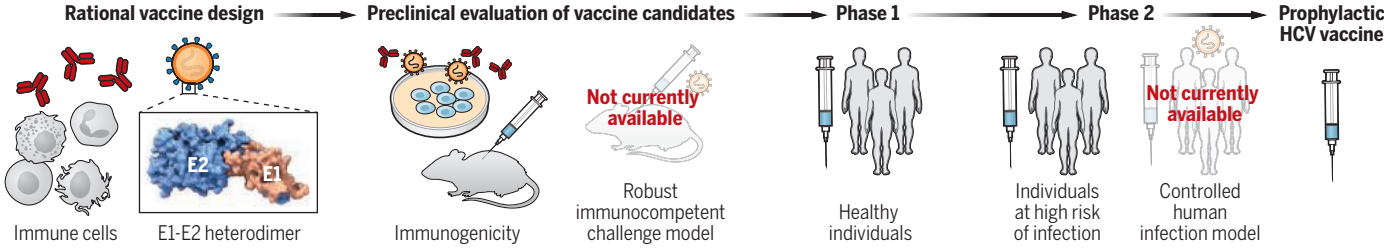

Conserved neutralizing epitopes on the envelope glycoproteins that are targeted by bnAbs include continuous epitopes in antigenic site 412 (AS412) and AS434 and noncontinuous conformation-sensitive epitopes in antigenic region 3 (AR3). These epitopes contribute to the E2 "neutralizing face" and the binding site of the key HCV receptor, CD81, on hepatocytes. Antibodies targeting this neutralizing face likely interfere with receptor binding and hepatocyte entry (*5*). Heavy-chain variable regions of such bnAbs are often encoded by the immunoglobulin heavy variable 1-69 (*IGHV1-69*) gene, making it relevant to explore germ line–targeting vaccine approaches using antigens designed to engage and guide affinity maturation of germline B cells encoding bnAb precursors—a strategy explored for HIV vaccines (*5*). Although several studies have refined the HCV E2 and AR3 structure (*5*), the structure of E1-E2 and the conserved noncontinuous conformation-sensitive epitope AR4, which is at the base of E2 but requires E1 for stable presentation, was only recently resolved (*12*). AR4-targeting antibodies might stabilize E1-E2 in a prefusion state, thereby inhibiting viral fusion with host cells (*12*). The bnAbs induced by natural HCV infection in humans often target the neutralizing face or AR4, although AS412-targeting antibodies are less frequent, and responses targeting multiple epitopes tend to have increased neutralization breadth (*13*).

How can a vaccine antigen be designed to elicit potent bnAbs? Emerging studies on the determinants of HCV immunogenicity in humans identified highly immunogenic HCV strains and revealed favorable viral features that can inform antigen engineering (*8*, *13*). During repeated infections in humans, bnAb responses were promoted by antigenically related E1-E2 that were characterized by high exposure of conserved epitopes targeted by bnAbs (*8*). However, structural flexibility of the envelope glycoproteins and limited accessibility of conserved neutralizing epitopes constitute HCV immune escape mechanisms and hamper induction of bnAbs during natural infection and vaccination (*5*). Epitope stabilization and exposure could be achieved by structure-based antigen design or by genetic modification of determinants of epitope exposure identified in recombinant cell culture–adapted HCV, such as certain E2 residues, E2 glycosylation motifs, and E2 hypervariable region 1 (HVR1) (*5*, *14*). Regions that induce nonfavorable antibody responses might be deleted from vaccine antigens. For example, HVR1 is immunodominant but leads to induction of non-nAbs or nAbs with narrow specificity that are rapidly rendered inefficient by mutational viral escape (*1*, *5*). E1-E2 could be presented by recombinant inactivated HCV. VLP, nanoparticle, mRNA, and protein vaccine platforms could be used to present E1-E2 or E2 alone, which is often more technically feasible. Alternatively, relevant epitopes could be presented on scaffolds. Adjuvants to enhance immunogenicity are also being explored.

A protective vaccine may need to engage both arms of the adaptive immune system. Vaccination of mice with a viral vector encoding conserved T cell epitopes and E2 without its three highly variable regions induced T cells and nAbs (*10*). An mRNA vaccine platform could similarly deliver T and B cell antigens, and inactivated virus and VLP vaccines can elicit not only nAbs but also T cells, modulated by an adjuvant. Alternatively, combination or prime-boost regimens could be used to activate T and B cells (*1*).

There is a critical need to facilitate the transition of promising preclinical vaccine candidates from animal immunogenicity studies to clinical efficacy trials. Currently, there is no robust immunocompetent HCV permissive animal model for vaccine efficacy evaluation. Instead, certain aspects of HCV vaccine–induced protection can be studied in transgenic immunocompromised and humanized mice. The protective potential of vaccine-induced nAbs can be evaluated in passive transfer studies in human liver chimeric mice (*11*). In addition, the overall capacity of certain vaccine approaches to induce protective immunity can be studied in surrogate animal models using HCV-related viruses (*11*). Currently, assessment of the protective potential of preclinical vaccine candidates needs to largely rely on knowledge-based evaluation of potency, breadth, and epitope specificity of vaccine-induced immune responses in vitro compared with protective immune responses. Therefore, there is a push to establish protocols for a controlled human infection model, where healthy volunteers are intentionally infected with HCV, to facilitate fast and cost-effective clinical efficacy testing of promising vaccine candidates (*15*). Additional clinical efficacy trials could then assess the protective capacity of selected candidates in individuals at risk of infection, reflecting real-world settings with regard to exposure to heterogeneous HCV strains and variable immune status of important vaccine target groups (see the figure).

Overcoming HCV immune escape mechanisms requires rational vaccine design based on the molecular understanding of viral features and host protective immunity. In the absence of robust immunocompetent animal challenge models, efforts should be directed at aligning assays for evidence-based characterization and prioritization of vaccine candidates and at facilitating accelerated clinical vaccine testing. Experiences gained on the cumbersome path toward an HCV vaccine might inform vaccine development for other complex viral targets. ■

REFERENCES AND NOTES

1. J. R. Bailey, E. Barnes, A. L. Cox, *Gastroenterology* **156**, 418 (2019).
2. N. Scott *et al.*, *BMC Med.* **17**, 175 (2019).
3. K. Page *et al.*, *N. Engl. J. Med.* **384**, 541 (2021).
4. W. O. Osburn *et al.*, *Gastroenterology* **138**, 315 (2010).
5. M. Law, *Cold Spring Harb. Perspect. Med.* **11**, a036962 (2021).
6. D. Bankwitz *et al.*, *Gut* **70**, 1734 (2021).
7. S. Ramirez, J. Bukh, *Antiviral Res.* **158**, 264 (2018).
8. N. Frumento *et al.*, *J. Clin. Invest.* **132**, e160058 (2022).
9. A. Nishio *et al.*, *Nat. Commun.* **13**, 5446 (2022).
10. T. Donnison *et al.*, *Hepatology* **76**, 1190 (2022).
11. R. Burm *et al.*, *Front. Immunol.* **9**, 1032 (2018).
12. A. Torrents de la Peña *et al.*, *Science* **378**, 263 (2022).
13. N. A. Brasher *et al.*, *J. Hepatol.* **72**, 670 (2020).
14. G. P. Alzua *et al.*, *Gut* **72**, 560 (2023).
15. T. J. Liang *et al.*, *N. Engl. J. Med.* **385**, 1235 (2021).

10.1126/science.adf2226

GRAPHIC: K. HOLOSKI/*SCIENCE*

POLICY FORUM

RENEWABLE ENERGY

Photovoltaics at multi-terawatt scale: Waiting is not an option

25% annual PV growth is possible over the next decade

By **Nancy M. Haegel, Pierre Verlinden, Marta Victoria, Pietro Altermatt, Harry Atwater, Teresa Barnes, Christian Breyer, Chris Case, Stefaan De Wolf, Chris Deline, Marwan Dharmrin, Bernhard Dimmler, Markus Gloeckler, Jan Christoph Goldschmidt, Brett Hallam, Sophia Haussener, Burkhard Holder, Ulrich Jaeger, Arnulf Jaeger-Waldau, Izumi Kaizuka, Hiroshi Kikusato, Benjamin Kroposki, Sarah Kurtz, Koji Matsubara, Stefan Nowak, Kazuhiko Ogimoto, Christian Peter, Ian Marius Peters, Simon Philipps, Michael Powalla, Uwe Rau, Thomas Reindl, Maria Roumpani, Keiichiro Sakurai, Christian Schorn, Peter Schossig, Rutger Schlatmann, Ron Sinton, Abdelilah Slaoui, Brittany L. Smith, Peter Schneidewind, BJ Stanbery, Marko Topic, William Tumas, Juzer Vasi, Matthias Vetter, Eicke Weber, A. W. Weeber, Anke Weidlich, Dirk Weiss, Andreas W. Bett**

A major renewable-energy milestone occurred in 2022: Photovoltaics (PV) exceeded a global installed capacity of 1 TW_{dc}. But despite considerable growth and cost reduction over time, PV is still a small part of global electricity generation (4 to 5% for 2022), and the window is increasingly closing to take action at scale to cut greenhouse gas (GHG) emissions while meeting global energy needs for the future. PV is one of very few options that can be dispatched relatively quickly, but discussions of TW-scale growth at the global level may not be clearly communicating the needed size and speed for renewable-energy installation. A major global risk would be to make poor assumptions or mistakes in modeling and promoting the required PV deployment and industry growth and then realize by 2035 that we were profoundly wrong on the low side and need to ramp up manufacturing and deployment to unrealistic or unsustainable levels.

PV is increasingly recognized as a "no regrets option"—a deployment pathway for the critical next 10 years that is available, cost effective, and aligned with long-term sustainable development goals. A growing number of studies are converging on the realization that PV, with electrification and a strongly sector-coupled energy system, is key to decarbonization at scale. Electrification refers to direct [e.g., heat pumps or electric vehicles (EVs)] or indirect (e.g., producing hydrogen or synthetic fuels) replacement of today's fossil fuel use. Sector-coupling is the ability to address variable-generation limitation with flexible demand, storage, and interconnection among energy sectors, including transportation, buildings, and industrial use. The resulting transition could actually lead to a sustainable future with overall lower energy supply costs (*1*).

However, just as many earlier projections consistently underestimated PV growth because of outdated cost assumptions and limited vision, concerns are raised today about maximum industry growth rates and supply chains. The availability of very-low-cost electricity from PV, in a world that prioritizes global economic development and climate goals, calls for constant reassessment of long-held assumptions and acknowledgment of the rapid rate of growth and change in the field. Plans for 2025 and 2035 not only set the path to 2050 but also increasingly constrain future options if we are not on track.

Based on a review of projections for global PV installation targets from various institutions and studies, projections of 2050 demand for PV range from 1.4 to 8 kW per capita, or 14 to 80 TW installed in the next 25 years, assuming a population of 10 billion (all PV installed or projected values are indicated in units of dc peak power). This is a large variation and does not provide clear direction to an evolving industry. Identifying a target range that is aligned with an achievable path to climate goals and economic development is critical for setting both manufacturing and policy goals.

The large variation in projections is associated with varying assumptions about future costs and preferred paths to decarbonization and often underestimates the sustained decrease in PV costs while anticipating decreased costs and rapid growth for other technologies (e.g., nuclear power and carbon capture and storage) that have yet to be realized or even begun. Low-end predictions for required PV by 2050 often also underestimate the increased energy consumption associated with development in the Global South, limit goals for broad electrification, or assume that countries, for various reasons, will adopt higher-cost technologies.

Integrating such large levels of renewable energy into the global energy system is a major challenge in such a relatively short period of time. In addition to the production capacity for PV, other renewable technologies, and storage, this will require a holistic approach that addresses transmission, grid integration, and interconnection. Infrastructure

Regional electricity demand supplied by solar PV

The data reflect annual percentages of historical regional demand (2010 and 2021) and modeled demand projections (2050). See supplementary materials for details.

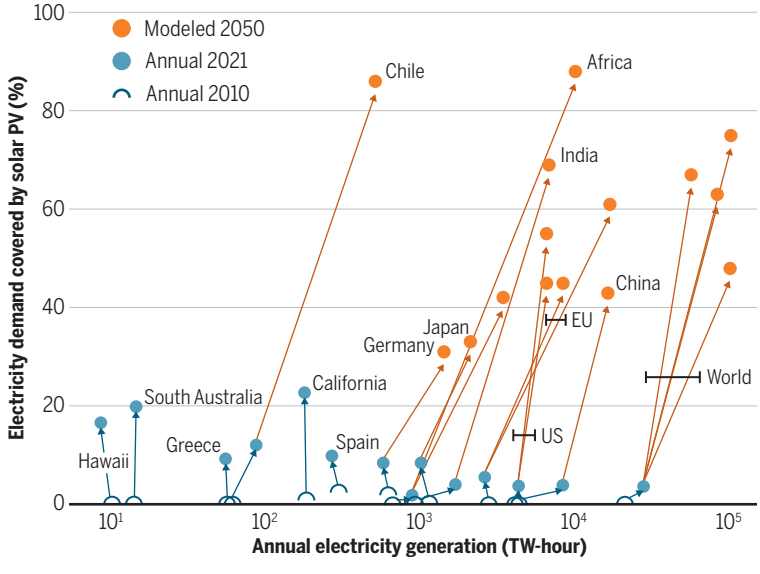

EU, European Union; PV, photovoltaics.

GRAPHIC: D. AN-PHAM/*SCIENCE*

Author affiliations are listed in the supplementary materials.
Email: nancy.haegel@nrel.gov

planning at this scale must look forward aggressively. Similarly, building and supporting supply chains for PV at the multi-TW scale requires planning and major lead times. Scenarios that substantially underestimate the required scale can limit planning and investment of governments, the PV industry, and other key stakeholders.

If climate, cost, and development goals are all kept in play, then independent modeling from multiple sources projects ambitious, but achievable, goals of 50 to 65 TW by 2050 (*2*–*4*), even before including future contributions from PV use for the chemical manufacturing sector. To identify what this total energy demand means for the PV industry and deployment, we take 75 TW as a target estimate for 2050 installed PV capacity.

PV FUTURE

This global estimate of 75 TW frames the challenge at hand. High PV growth rates from past decades must be continued. Rapid change has occurred in the past decade in the contribution of PV to the electric grid of various countries and regions (see the first figure). The fraction of electricity supplied by PV substantially increased from 2010, when it was negligible in all major power systems, to 2021, when it achieved a meaningful contribution in a growing number of power systems of different sizes. Local system records have been attained, for both annual average and instantaneous penetration of PV supply, that seemed impossible just a few years ago.

We also highlight the growth required to reach the targets identified in various 100% renewable models (see the first figure). Deployment and system flexibility and coupling challenges exist, especially for the largest power-grid systems (the United States and China), that are associated with technical challenges for high penetration of variable inverter-based energy sources. These are the focus of parallel R&D and investment, but multiple strategies exist to balance solar fluctuations. PV can be combined with wind power, which, in many world regions, shows complementary seasonal patterns. Also, dispatchable generation, such as hydropower, can accommodate operation to enable grids that have a high level of renewable power. Additionally, extended interconnections can be used to balance regional fluctuations, and storage can be used to balance fluctuations in time.

Whereas earlier discussions focused on narrowly matching PV and storage, more-recent approaches and modeling have moved to a focus on flexible demand response and broad sector coupling. The optimal required storage depends on the extent to which the other balancing strategies are used. For PV, electric batteries, which show high cost per energy capacity but also high efficiency, can effectively contribute to balancing intraday solar fluctuations. Pumped hydro storage or the conversion of solar electricity to hydrogen to be consumed in other sectors provides additional storage options. Heat pumps can be used to provide heating or cooling, with the latter having a good correlation with PV generation. Batteries can be both static and in EVs, providing an effective strategy to decarbonize land transport while bringing additional balancing options for smart charging or vehicle-to-grid operation. New battery chemistries, reduced use of critical metals such as cobalt, and increased R&D to identify alternative lithium sources, such as desalination or geothermal brines, are all moving forward to address battery materials and supply issues.

Energy system models and associated PV projections will continue to evolve. Key inputs to continuously assess include (i) up-to-date cost assumptions for PV and all other major components in the new energy system; (ii) high temporal resolution and modeling of balancing mechanisms, including storage and transmission networks; and (iii) modeling of technologies that enable direct electrification and indirect electrification of other sectors. When these requirements are fulfilled, future energy scenarios based on cost optimization project large shares of PV, regardless of the size of the energy system (see the first figure).

Organizations such as the International Energy Agency (IEA) and Intergovernmental Panel on Climate Change (IPCC), which have been and remain conservative regarding the future growth of PV, are now increasingly calling for more rapid scaling of wind and solar in the next decade. This "no regret" option can take us to major GHG emission reductions. Researching the best strategies for the final decarbonization steps, such as technologies to remove atmospheric carbon dioxide (CO_2), should be done in parallel with ambitious deployments of solar and wind to achieve a path that is compatible with the Paris Agreement.

PV MANUFACTURING AND R&D ON THE ROAD TO 2050

Reaching a target of 75 TW of globally installed PV by 2050 will place substantial demands on the manufacturing and R&D communities. Some question the ability of the PV and supporting industries to deliver components at the volume required, at low cost, and with the required quality and reliability while achieving the financial and material sustainability and production security that are expected from a critical manufacturing sector. Indeed, the PV industry over the past 50 years has shown a consistent ability

PHOTO: PATRICK HERTZOG/AFP/GETTY IMAGES

to grow, with a demonstrated doubling of annual production and cumulative capacity every 3 years. At this rate, the next TW of installed capacity is expected to be reached around 2024, and planned build-out of polysilicon capacity suggests that a production rate of 1 TW per year could be reached by 2028 or sooner. The first half of 2022 saw an annual growth in production rate in the range of 45 to 137% of the Chinese PV industry across the entire supply chain of silicon PV, from polysilicon to deployment (*5*). The cost of manufacturing has followed a typical learning curve, with a 24% cost decrease for every doubling of cumulative production.

In parallel, there has been a substantial increase in the speed of translational innovation. Since 2010, the PV industry has gone from a somewhat slow-moving and conservative industry focused on the cost of individual components, where new technologies took considerable time to replace old technologies because of cost, to a very dynamic industry that is more focused on levelized cost of electricity (LCOE, or the estimated

Double-usage of land is demonstrated at this Agrivoltaic site in Amance, France, where the simultaneous use of land for power production and agriculture can also reduce irrigation needs in arid lands.

revenue needed to build and operate a generator over a certain period), where innovations are quickly introduced to the market and where technology transitions happen in months to a few years. Examples of these include hydrogenation for defect control, diamond wire sawing, multibusbars, half-cut cells, and increases in wafer size. The latest tunnel oxide passivated contact silicon (Si) PV technology (commonly known as TOPCON) advanced in 5 years from an industrially relevant laboratory design to commercialization and mass production. Fundamental advances in materials chemistry for cadmium telluride (CdTe) PV have recently also made their way into production in record time. Recent analysis shows that it now takes about 3 years for the average cell efficiency in mass production to reach the efficiency of the champion cell fabricated in the industrial laboratory (*6*).

Rapid growth in Si PV has been enabled in part by a clustered industry, first in the United States and then in Japan, Germany, and now China, with major collaboration between industry players and research laboratories (*7*–*9*). Standardization throughout the supply chain has been an important factor to reduce cost. Over the past 10 years, the cost of building new Si PV production lines has decreased by 50% every 3 years, driven primarily by typical machine throughput doubling every 3 years. During the past 20 years, Si wafer size has increased from 125-mm pseudo-square wafers to 210-mm fully square wafers. With an efficiency increase of 0.5% absolute per year on average, this corresponds to an increase of power output per cell from 2.5 to 10 W. Module power output has increased from 150 to 400 W for residential modules and up to 700 W for large utility panels.

The PV industry, however, is at an important juncture. It needs to demonstrate that it can sustainably and reliably deploy multi-TW of PV systems every year. Supply constraints could have serious impacts on cost and the ability to grow. It is important to differentiate supply chain issues related to volume demands for components such as Si and glass from issues related to potential scarcity of materials. For the current leading Si technology, the main material sustainability issue is silver. Current industrial use is ~15 mg/W. To be sustainable at multi-TW scale, this needs to be reduced to less than 5 mg/W because today's silver consumption for PV is already 10% of worldwide production. Research to replace silver with copper or aluminum is advancing. Other scarce materials, such as indium used for Si heterojunction technologies that combine crystalline and amorphous Si layers, must be assessed in the context of TW-scale demands. Techniques to address the use of scarce materials should be approached from an ecodesign perspective and analyzed by life-cycle assessment to confirm resulting impacts, evaluating metrics such as resource depletion and GHG emissions.

Major PV manufacturers have been reducing their energy, water usage, and CO_2 emissions. Efficiency improvement, larger wafer size, increased batch size, and multilane tools have contributed to this improved footprint, but the main factor has been the reduced use of Si feedstock per unit of power, from about 14 tonnes/MW in 2000 down to less than 4 tonnes/MW in 2021, which is due to a fourfold reduction in the diameter of the steel wires used to slice the wafers. At the same time, improved high-efficiency cell architectures allow the use of thinner Si wafers without performance loss.

We provide one simple scenario for current industry growth to reach a cumulative installation of ~75 TW by 2050, with a steady-state production of ~3.4 TW/year reached in 2037 (see the second figure). Cumulative totals are estimated by adding new installation and subtracting the installation from 25 years earlier, assuming a 25-year module warranty. This means that steady-state cumulative installation, in this case ~85 TW, is not reached until close to 2060, when retirements become comparable to installation.

To reach a target of this order of magnitude in a realistic way, the PV industry must continue to grow over the next critical years at rates of ~25% per year. A 25% per year growth rate, however, is consistent with what PV has achieved in past decades. This simple model could be modified in a myriad of ways but makes clear the order of magnitude of growth that is required over the next 10 years.

INNOVATION, DEPLOYMENT, AND SECTOR COUPLING: RAPIDLY AND TOGETHER

Solar PV has become a strategic technology to fight climate change and enable global development. This suggests that its supply chain must be delocalized, not only to reduce logistics costs and embedded emissions but also to ensure uninterrupted component supply. IEA and other institutions have observed that overly concentrated production in a single country or region can limit supply and increase the risk of supply chain disruptions.

R&D for ecodesign and recycling must be ramped up now to support rapid and sustainable scaling of PV. Recycling is not a short-term solution for materials availability issues through 2035, given the relatively low current installation levels and long lifetimes compared with the demands of the next two decades. Product lifetime, reliability, and detailed life-cycle analysis are key levers in minimizing virgin materials needs, waste, carbon footprint, and environmental impact, particularly at the TW scale (*10*, *11*).

As we enter the TW scale of annual global production, the PV industry must continuously innovate to improve material sustainability and reduce the embedded carbon and energy required to manufacture and deploy PV. Increasing material circularity through many different pathways is one way to reduce the emissions, energy, and environmental impacts associated with mining, refining, and upstream manufacturing processes. Responsible scaling requires that the industry reduce embedded energy and carbon at every step (*12*). Because the energy mix used in PV production is a critical factor, increased PV installation will help decarbonize an already green technology.

Improved module efficiency will continue to be important to reduce both cost and space demands. The asymptotic approach to fundamental efficiency limits for single-junction Si solar cells is driving accelerated R&D of potential low-cost tandem structures, both for established (e.g., CdTe-Si) or emerging (perovskite-Si) material combinations. Production of thin-film modules, including CdTe, requires less energy input and produces fewer GHG emissions because they do not require individual wafers. Given the multi-TW need, there is room for a mix of technologies going forward, and thin-film PV, which is competitive for both embedded energy and GHG emissions (*12*), could increasingly contribute as it scales.

To deliver on the promise of PV at this scale, there must be comparable scaling in energy storage and electrolyzers, and PV itself should be able to provide added flexibility to the grid. Building integrated PV can help meet electricity needs in the building sector as well as contribute to heating and cooling requirements. Direct charging of EVs during times of high PV electricity generation is an efficient and sustainable means for transforming large parts of the transportation sector (*13*). Agrivoltaics, the simultaneous use of land for power production and agriculture, can integrate land use while reducing irrigation needs in arid lands (*14*). As emerging economies greatly increase their energy and electricity consumption in the coming years, PV should become the natural choice for energy system expansion. Finally, global attention to the development of hydrogen and hydrogen-based e-fuels and e-chemicals at scale as carbon-free fuels and feedstocks is only possible in a sustainable way if low-cost electricity from PV and wind are available at large scale.

The next decade will be decisive. The path to 2050 needs to include continuing policy support that addresses the real costs of climate change and air pollution and encourages a transition to broad electrification, on-going communication to address rapid change and outdated assumptions, and continued PV R&D and innovation. Of particular importance is attention to global PV supply chains to ensure support for multiple sources at all component levels, as befits a critical and strategic energy supply. Acceleration of permitting, incentives for daytime charging of EVs, and standards and net-zero goals for buildings are all examples of supportive local actions. Multiple countries and regions—including India, the United States, and Europe—have acted in recent years to focus on the complete PV supply chain, encourage distributed production, and create a broader global playing field, though selection of the highest-impact actions depends on regional and national circumstances. Policies that demonstrate long-term commitments to achieve climate change mitigation can provide a market security to support the major capital investments that are required.

Recent history and the current trajectory suggest that sustained global growth in PV of 25% per year over the next decade toward 75 TW of installed PV by 2050 can be achieved. Waiting is not an option. ■

PV installations and growth toward 75 TW by 2050

Modeled cumulative capacity going forward is based on sustaining 25% production rate growth over the next 7 years and then reducing slowly to steady state. Replacement needs are included by simple subtraction of installations 25 years before the modeled date.

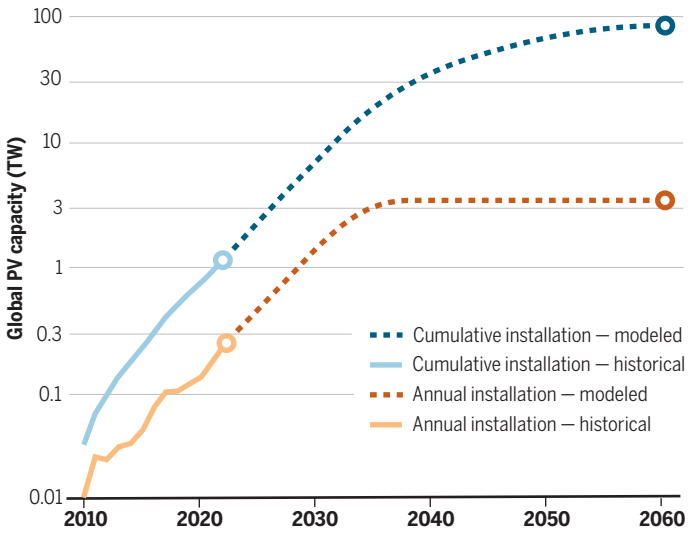

GRAPHIC: D. AN-PHAM/*SCIENCE*

REFERENCES AND NOTES

1. C. Breyer *et al.*, *IEEE Access* **10**, 78176 (2022).
2. D. Bogdanov *et al.*, *Energy* **227**, 120467 (2021).
3. E. Pursiheimo, H. Holttinen, T. Koljonen, *Renew. Energy* **136**, 1119 (2019).
4. J. C. Goldschmidt, L. Wagner, R. Pietzcker, L. Friedrich, *Energy Environ. Sci.* **14**, 5147 (2021).
5. "MIIT says China produced 123.6 GW solar modules in H1/2022 & exported 78.6 GW capacity," TaiyangNews, 21 July 2022; https://taiyangnews.info/markets/chinas-solar-pv-production-capacity-in-h1-2022/.
6. Y. Chen *et al.*, *Prog. Photovolt. Res. Appl.* 10.1002/pip.3626 (2022).
7. R. Preu *et al.*, *Appl. Phys. Rev.* **7**, 041315 (2020).
8. M. Hermle, F. Feldmann, M. Bivour, J. C. Goldschmidt, S. W. Glunz, *Appl. Phys. Rev.* **7**, 021305 (2020).
9. G. M. Wilson *et al.*, *J. Phys. D Appl. Phys.* **53**, 493001 (2020).
10. S. Ovaitt, H. Mirletz, S. Seetharaman, T. Barnes, *iScience* **25**, 103488 (2021).
11. N. J. Bartie *et al.*, *Resour. Conserv. Recycling* **169**, 105516 (2021).
12. H. M. Wikoff, S. B. Reese, M. O. Reese, *Joule* **6**, 1710 (2022).
13. S. Powell, G. V. Cezar, L. Min, I. M. L. Azevedo, R. Rajagopal, *Nat. Energy* **7**, 932 (2022).
14. G. A. Barron-Gafford *et al.*, *Nat. Sustain.* **2**, 848 (2019).

ACKNOWLEDGMENTS

This article was informed by the Third Terawatt Workshop convened in Freiburg, Germany, by the Global Alliance of Solar Energy Research Institutes on 16 and 17 May 2022. The National Renewable Energy Laboratory's portion of this effort was supported by the Alliance for Sustainable Energy, LLC, under contract no. DE-AC36-08GO28308. The views expressed are those of the authors and do not necessarily reflect those of the Department of Energy, US government, or European Commission.

SUPPLEMENTARY MATERIALS

science.org/doi/10.1126/science.adf6957

10.1126/science.adf6957

BOOKS *et al.*

The ineffable nature of transcendence proves a tricky topic for materialistic inquiry.

Check for updates

COGNITIVE SCIENCE

Making sense of the sacred

A physicist attempts to reconcile inspiring experiences with materialistic beliefs

By **Alex Gomez-Marin**

The clash between science and religion has generated more heat than light, and yet our search for meaning in life is relentless, and a sense of the sacred remains a universal part of the human experience. Matter and spirit must thus engage in dialogue rather than in feud, as the American physicist and writer Alan Lightman argues in his new book, *The Transcendent Brain*.

Lightman seeks to reconcile transcendent experiences with scientific materialism and begins the book with a personal story of a close encounter with a pair of juvenile ospreys that left him with "a feeling of being part of something much larger than myself." He then switches modes and declares: "I'm a scientist and have always had a scientific view of the world—by which I mean that the universe is made of material stuff, and only material stuff."

Lightman calls himself a "spiritual materialist" and honors experiences of enchantment, but he ultimately conflates science with a materialist worldview. His metaphysical presuppositions seem to overrule concrete experience, leaving readers with a peculiar kind of empiricism—one in which love, awe, and pain are real but molecules [and atoms (and protons)] are somehow realer.

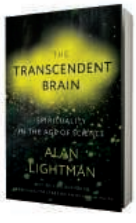

The Transcendent Brain: Spirituality in the Age of Science
Alan Lightman
Pantheon, 2023. 208 pp.

"How can the material neurons in the human nervous system give rise to feelings of spirituality?" asks Lightman. His answer (and question) draws from mainstream neuroscience and evolutionary biology: The brain makes conscious experiences, and evolution made some of these experiences transcendent. Here, he invokes the notion of "emergent phenomena," comparing fireflies flashing in synchrony with neurons producing our inner lights.

The book's introduction clearly outlines Lightman's position, while the first two chapters provide a necessarily incomplete but superficial exploration of the origin of nonmaterialist conceptions of the world. Chapters 3 and 4 form the core of the book. Here, a series of non sequiturs portrays a narrow account of current consciousness studies, which is followed by Lightman's argument that spirituality is a natural by-product of high-level conscious minds subject to natural selection.

Lightman acknowledges the epistemic insufficiency of reductionism, whereby different levels of analysis and explanation are needed; however, his ideology remains that "mind and brain are the same thing" and there is nothing but the material world. But what exactly is matter? And is lived experience secondary?

This, in turn, leads to a sophisticated naïveté: Religion becomes psychologized and human values biologized. Lightman does "not mean to diminish such a majestic and profound feeling," but, nevertheless, he sees spiritual experiences as being "as natural as hunger or love or desire, given a brain of sufficient complexity." Beauty becomes a by-product of traits with survival benefit, creativity hardly more than a consequence of the urge for exploration and discovery, and the capacity for awe just a kind of openness to the world.

Sparks of intellectual courage shine through at the end of the book. Here, Lightman addresses the counterproductivity of so-called "new atheists": "[Richard] Dawkins dismisses people of faith as 'nonthinkers' and labels religion as 'nonsense.' Such an attitude from a leading spokesperson for the scientific establishment only increases the divide between different groups of people."

Indeed, it is one thing to be intolerant of gluten, another to deny that bread exists or to insult those who eat it. The belief that science has all the answers now, or will in the future, and that what cannot be counted does not count is plain "scientism," and it does science no good.

Lightman's "spiritual materialism" will not "out-transcend" evangelical atheists like Dawkins. Even they have transcendent experiences. But as the American philosopher David Ray Griffin has argued: "The perceived conflict between science and religion (now rebranded as spirituality) is based upon a double mistake—the assumption that religion requires supernaturalism and that scientific naturalism requires atheism and materialism" (*1*).

Let us therefore put an end to the ongoing confusion whereby science, materialism, atheism, and reason are used interchangeably (*2*). We can affirm both science and spirituality without subordinating one to the other and progressively come out of the spiritual closet in our professional and personal lives (*3*). ■

The reviewer is at the Instituto de Neurociencias, Consejo Superior de Investigaciones Científicas–Universidad Miguel Hernández de Elche, Alicante, Spain. Email: agomezmarin@gmail.com

REFERENCES AND NOTES

1. D. R. Griffin, *Religion and Scientific Naturalism* (SUNY Press, 2000).
2. I. McGilchrist, *The Matter with Things* (Perspectiva Press, 2021).
3. M. Woollacott, D. Lorimer, Eds., *Spiritual Awakenings* (Academy for the Advancement of Postmaterialist Sciences, 2022).

10.1126/science.adh0532

PHOTO: ANDREW NGUYEN/EYEEM/GETTY IMAGES

Check for updates

MEDICINE

America's snake oil problem

An irreverent dive into "medical freedom" highlights the comedy and tragedy of medicine in the United States

By **Christopher Kemp**

If It Sounds Like a Quack... A Journey to the Fringes of American Medicine
Matthew Hongoltz-Hetling
PublicAffairs, 2023. 336 pp.

Something strange has happened to Project America. Slowly, we have become a population that includes a substantial number of people who drink bleach to cure bronchitis. Some of us aim lasers at our arthritic joints. A few of us speak in tongues, beseeching a higher power to fix our acid reflux.

With our latest technological advances, we can achieve what was once impossible. Astonishingly, for example, we designed, tested, and distributed a vaccine for COVID-19 within a year of its arrival in the United States. But as surely as the Sun will rise tomorrow, some people will reject both the vaccine and the best available treatments and opt to drink aquarium cleaner instead. With his book *If It Sounds Like a Quack...*, Vermont-based journalist Matthew Hongoltz-Hetling charts the reasons why.

Hongoltz-Hetling has smartly chosen to center his book on the narratives of six purveyors of quack medicine, each an archetype. There is Larry Lytle, a South Dakota dentist who, for several years, sold $12,000 laser pointers to gullible people, telling them that light could cure anything from hearing problems to HIV/AIDS. There are Pentecostal preachers fleecing their flocks through prayer. There is Toby McAdam, who made millions marketing his own homemade—and completely untested—supplements.

A Polish immigrant, Alicja Kolyszko, treats patients with leeches. She attaches them to a patient's skin—regardless, really, of medical complaint—and waits until they finally detach and fall off the patient's body, blood-fattened and exhausted. Because leeches are animals and not molecules or roots or chemical mixtures, they are surprisingly unregulated.

Jim Humble claims that he is an alien from the distant Andromeda Galaxy. For the entirety of this excellent book, Hongoltz-Hetling refers to Humble as "the alien in Humble's skin." Authorial choices like that are not for everyone, but I cannot get enough of them. The book is a genuine scream: irreverent, very often snarky, sometimes bawdy, but always insightful and well reported.

Hongoltz-Hetling tells readers that as recently as 2001, vaccines had a higher approval rating in the United States than did Dolly Parton, Tom Hanks, or Dr. Seuss. Back then, 93% of Republicans and 97% of Democrats believed in vaccine effectiveness.

Medical skepticism is often associated with broader anti-government sentiments.

Not anymore. In 2020, in the deadliest months of a global pandemic, around 66 million Americans refused to wear face masks, which had been shown to slow the spread of COVID-19. In fact, they hated the face masks. The masks, in their minds, had become the problem. It is important to understand why this happened, because it almost certainly will happen again.

Hongoltz-Hetling is an able guide. With his red umbrella held high, he takes us through the recent history of American quackery. He deftly retells the ways in which each of his protagonists first became radicalized and how poorly our regulatory institutions responded to the threat they represented.

At times, it is staggering. We have a broken health care system that leaves millions underserved and often untreated; we have a political system awash with influence from Big Pharma, which spent around $6 billion on lobbying and contributing to political campaigns between 1998 and 2018 alone. On top of this, millions of religious Americans are already primed, perhaps without knowing it, for superstition and magical thinking. By 2017, according to a Pew Research poll, 20% of Americans had rejected conventional medicine and instead relied exclusively on alternative medicine—on lasers, and prayer, and leeches, and crystals, and reiki, and drinking bleach, and herbal tinctures, and poultices.

By then, years before the arrival of COVID-19, the liberal left-wing yoga-and-crystal crowd had made an unexpected alliance with the right-wing, gun rights, "Don't Tread on Me" faction of American life. Emboldened by former US president Donald Trump—a man Hongoltz-Hetling witheringly refers to throughout the book as "the game show host"—they began to advocate for "medical freedom," or the right to reject mainstream health practices and to access nontraditional therapies.

The movement's alignment with broader anti-government groups is noteworthy. At the 6 January 2021 US Capitol insurrection, for example, one of the stages from which protesters addressed the crowd was dedicated to health freedom.

It is all here in Hongoltz-Hetling's book: the nonsense cures, the half-hearted and toothless US Food and Drug Administration injunctions, the inevitable jail time for pseudoscience purveyors, the unnecessary and painful deaths of the vulnerable and desperate. We see the religious praying over a treatable girl as she dies. We meet people who are convinced, even several days after her death, that she will rise again. It is tragic. It is comic. It is tragic. Like me, you may find yourself laughing through tears as you read. ■

The reviewer is at the Department of Translational Neuroscience, Michigan State University, Grand Rapids, MI 49503, USA, and is the author of *Dark and Magical Places: The Neuroscience of Navigation* (Norton, 2022). Email: cjkemp@gmail.com

10.1126/science.adh1865

PHOTO: MARIO TAMA/STAFF/GETTY IMAGES

INSIGHTS

Attendees socialize during a networking session at the 2023 AAAS meeting in Washington, DC.

LETTERS

NEXTGEN VOICES

The future of scientific societies

AAAS (the publisher of *Science*) turns 175 years old this year. AAAS's mission is to advance science, engineering, and innovation throughout the world for the benefit of all. To celebrate this milestone and explore AAAS's anniversary theme of "igniting progress for the next 175," we asked young scientists, "**How have scientific societies affected your career, and how can societies best support scientists in the future?**" Read a selection of the responses here. Follow NextGen Voices on Twitter with hashtag #NextGenSci. **—Jennifer Sills**

Inclusion

Scientific societies have given me the opportunity to attend events, enter contests, and start a science communication project. Ensuring more representation of neurodivergent researchers and other minorities in scientific societies is what drives me, as an autistic researcher, to pursue my goals. Scientific societies' most important role in the future will be inclusion. When scientific societies care about sharing the work and struggles of Black, LGBTQIA+, female, neurodivergent, and other underrepresented researchers, they create a more welcoming scientific community, which will encourage more individuals in minority groups to become scientists.

Camila Fonseca Amorim da Silva
School of Arts, Sciences, and Humanities, University of Sao Paulo, Sao Paulo, Brazil.
Email: camilafonsecaamorim@usp.br

Participating in meetings held by national scientific societies, such as the American Geophysical Union and the American Association of Geographers, has allowed me to better understand the research dynamics in my field and helped me to identify emerging research areas. In the future, I hope that the economic barriers to attending annual meetings will be lower. Scientific societies could work to reduce social disparities by providing equal access to science and providing pathways for members of historically underrepresented groups to access the resources required to pursue a scientific career.

Edgar Virgüez
Biosphere Sciences & Engineering Division, Carnegie Institution for Science, Stanford, CA, USA. Email: evirguez@carnegiescience.edu

As a first-generation, female, non-European academic, I did not benefit from participating in societies in my field for personal development, but joining the Global Young Academy (GYA) has provided me with a sense of belonging. The GYA connects and mobilizes young scientists from six continents

PHOTO: ROBB COHEN PHOTOGRAPHY & VIDEO

to improve the research ecosystem, from working life to public perception of science. Discipline-specific societies cannot support scientists effectively if they function as echo chambers for senior scientists. In the future, scientific institutions will inevitably evolve toward inclusivity, diversity, technological change, and employee-friendly work conditions. The societies that equip scientists with the skills and network to make this transition will play a leading role in catalyzing a better scientific community.

Sibel Eker
Radboud University, Nijmegen, Netherlands and International Institute for Applied Systems Analysis, Laxenburg, Austria.
Twitter: @sibel_eker_

Reliable information

By publicly presenting the state of the field based on the available science, scientific societies act as a positive force against false premises. My bird and reptile interests led me to join BirdLife Australia and the Australian Society of Herpetologists when I moved to Australia in 2008. These societies provided me with both a community of like-minded people and trustworthy information about taxonomy, species distributions, and ecology that continue to inform my hobbies and research interests today. In a rapidly changing world filled with uncertainty and misinformation, scientific societies' ability to provide reliable, evidence-based information and a sense of community will become increasingly important.

Christina N. Zdenek
School of Biological Sciences, The University of Queensland, Brisbane, QLD, Australia.
Twitter: @CNZdenek

Scientific societies have allowed me to share my own results and learn about research elsewhere. In a world with information overload and artificial intelligence that can create fake but convincing data, scientific societies disseminate accessible, reliable, and up-to-date information. In the future, society journals should adapt their policies to maximize accessibility and reliability. Research results should be open access. Journals should provide a platform where experts can thoroughly question research results. Publishing peer reviews could help with civility and unfair assessment as well as contribute to the recognition of younger scientists. Societies should also provide more support for preprint publication.

Cathrine Bergh
KTH Royal Institute of Technology, 11423 Stockholm, Sweden. Email: cabergh@kth.se

Social media can be used to voice scientific information but can also expose the public to anti-science movements. The presence of scientific societies on various social media platforms has helped counter misinformation. Such societies have given me the opportunity to engage online with the public as well as resources and guidance to effectively communicate my own research on social media. The involvement of scientific societies on social media platforms will be critical in the future to help build trust in scientific institutions and accurately inform the public.

Casimiro Gerarduzzi
Department of Medicine, University of Medicine, Montreal, QC, Canada. Twitter: @CasGerarduzzi

Training

Training courses and seminars held by scientific societies can support researchers who want to find practical applications for basic research. I attended a seminar, sponsored in part by the China Association for Science and Technology and the Ecological Society of China, that explained how the agriculture industry can help alleviate poverty. The course provided perspectives from government agencies, businesses, institutions of higher learning, and certification bodies. In the future, applying the results of basic research will be crucial to achieving agricultural production and food and water security. Training organized by scientific societies can help scientists and their partners meet those goals.

Yan Ge
College of Resources and Environment, Northeast Agricultural University, Harbin 150030, Heilongjiang, China. Email: amy_geyan@163.com

To prepare for the future, scientific societies should take a more active role in anticipating the directions of their field and the needs of trainees and junior scientists. Thanks to their wide-reaching networks, societies have immense but underutilized influence. They therefore have a duty to help implement effective training of younger scientists, especially students of diverse backgrounds and those who can't afford to pay for membership. Societies can help prescribe training plans, research suggestions, or coursework for universities, or they could establish conferences aimed at undergraduates.

Madeline Klinger
Helen Wills Neuroscience Institute, University of California, Berkeley, Emeryville, CA, USA.
Instagram: @madelinescientist

My scientific society, the American Association of Orthodontists, has offered everything from free lunches at annual scientific sessions to grant funding to career development workshops. Training faculty in the formative stages of their career by offering courses on advancing racial equity, conducting collaborative science, interviewing effectively, networking, handling microaggressions, and leading with sensitivity is one of the most important services societies can offer in the future.

Veerasathpurush Allareddy
Department of Orthodontics, University of Illinois Chicago College of Dentistry, Chicago, IL, USA.
Email: sath@uic.edu

Global networks

My undergraduate institution had a strong local chapter of the Society for Conservation Biology (SCB). The group connected me to volunteer work, research positions, my honors thesis adviser, and a group of students curious about the same kinds of scientific questions as I was. When the pandemic hit, we kept our SCB chapter alive. Although nothing could replace gathering in person, we found opportunities to hear from remote speakers, hold virtual events, and build an engaging community for students facing unprecedented social isolation. In the future, the most important thing a scientific society can offer to researchers at any career stage will be community. Our increasingly virtual society presents new ways to connect, even with colleagues and peers we have never met face-to-face. In some ways, this virtual shift has revealed weaknesses in these organizations, particularly in accessibility and member diversity. The best scientific societies will find a way to grow, facilitate connections, and adapt with the times to bring their communities together.

Elizabeth Hoots
Department of Science, Engineering, and Built Environment, Deakin University, Queenscliff, VIC, Australia.
Email: beth.hoots@research.deakin.edu.au

As a Latin American woman working in Europe, I know the barriers scientists face when moving abroad, including creating a collaborative network and building a reputation in a new place. Scientific societies provide opportunities to overcome these challenges. I participated in congresses and served as a junior editorial member in a society-associated journal. I expect scientific societies to maintain an active role in improving the conditions for research and facilitating connections within the scientific community.

Tania Henriquez
Department of Medical Biotechnologies, University of Siena, Siena, Tuscany, Italy.
Twitter: @Tania_H_A

Scientific societies widened my network and strengthened my research skills through mentorship programs. Scientific societies can be a critical tool that links people together across the world, ensuring that knowledge in the field moves forward as a whole. In the future, societies should continue to build bridges in the form of activities between researchers from differing backgrounds and seniority, fostering interaction and connection.

Khor Waiho
Higher Institution Centre of Excellence, Institute of Tropical Aquaculture and Fisheries, Universiti Malaysia Terengganu, Kuala Nerus, Terengganu, Malaysia. Email: waiho@umt.edu.my

Funding

Scientific society awards allowed me to take part in international conferences as a PhD student—an unbelievable opportunity for someone from a working-class background with no funding. Scientific progress is challenged by powerful forces, such as economic interests, a culture of competition, and bureaucracy, that influence the direction of research. Scientific societies must fight against these trends by defending the scientific community's right to determine its own path. Supporting early-career researchers and other disadvantaged groups through scholarships and awards would be a step toward that goal.

Carlo D'Ippoliti
Department of Statistical Sciences, Sapienza University of Rome, Rome, Italy.
Email: carlo.dippoliti@uniroma1.it

Scientific societies organize conferences at which I can share my research, exchange ideas, and network with peers and potential employers. In the future, scientific societies should encourage involvement of early-career researchers to avoid stagnation of ideas and accelerate progress toward diversity. Conferences should be affordable and accessible to researchers from economically disadvantaged areas. Societies can also use their funds and influence to support and reward efforts of science communication and the engagement of researchers with policymakers.

Ahmed Al Harraq
Cain Department of Chemical Engineering, Louisiana State University, Baton Rouge, LA, USA. Email: ahmed.95med@gmail.com
Twitter: @ahmed_alharraq

Entrepreneurship

Six years ago, as a junior majoring in management, my friends and I began an entrepreneurial project to produce rice and crayfish. When the project almost failed, scientific societies stepped in to help, recommending suppliers of high-quality production materials and providing technical guidance. Inspired by the experience, I am now a PhD student in crop cultivation and agricultural technology. Scientific societies should continue to nurture innovation by supporting entrepreneurship, especially in young scholars.

Hui Xu
School of Agronomy, Anhui Agricultural University, Hefei, Anhui 230036, China.
Email: aauxuhui@126.com

Unlike traditional symposia, scientific societies allow scientists to gain peer recognition, which is a vital incentive for doctoral students at the beginning of their academic career. In the future, scientific societies can serve as key entry points for young scientists to connect with society, experts, and other young people in their field. Scientific societies also have the potential to replace traditional startups in the Internet era, as distributed organizations jointly own and incubate cutting-edge technologies and products.

Junyu Zou
School of Environmental Science and Engineering, Southern University of Science and Technology, Shenzhen, China.
Email: zoujy2020@mail.sustech.edu.cn

Societal solutions

As a PhD student in electrical engineering, I have benefited from the activities of the Institute of Electrical and Electronics Engineers (IEEE) and the Chinese Society for Electrical Engineering. These societies can use their influence to guide the research direction of the engineering industry. For example, the special issues on low-carbon power systems in IEEE's top journal have driven the field toward research on more sustainable electricity generation, transmission, and consumption. Scientific societies have the responsibility to steer their fields toward environmentally responsible research.

Yuanxing Xia
Department of Electrical Engineering, Southeast University, Nanjing, Jiangsu Province, China.
Email: eexyx@seu.edu.cn

SUBMIT NOW

NEXTGEN VOICES: INSPIRING DISCOVERIES

The new NextGen VOICES survey is now open: In exactly six words, describe a discovery in your field that has inspired you or influenced your research.

To submit, go to www.science.org/nextgen-voices

Deadline for submissions is 21 April. A selection of the best responses will be published in the 7 July issue of *Science*.

The research opportunities provided by scientific societies have helped me secure funding and collaborators for research projects on diseases in underserved communities in my conflict-ridden country. I have also received society-sponsored travel awards to attend training courses, workshops, and conferences. However, the role of scientific societies goes beyond member benefits. Scientific societies can promote interdisciplinary and multifaceted solutions to address issues of global concern, including climate change, food security, energy, and emerging health problems, through effective communication, education, technology, collaboration, and science diplomacy.

Rashad Abdul-Ghani
Faculty of Medicine and Health Sciences, Sana'a University, Sana'a, Yemen and Faculty of Medicine and Health Sciences, Tropical Disease Research Center, University of Science and Technology, Sana'a, Yemen.
Email: rashadqb@yahoo.com

When I was an undergraduate researcher in India, scientific societies helped me connect and share my work with other biologists. Societies can also contribute to reforms in the academic community. In the future, societies should integrate more early-career researchers into leadership committees and advocate for scientists with marginalized identities. To advance inclusion while also focusing on the dangers of the planet's survival, scientific societies should collect data and resources showing how scientists can reduce their research carbon footprint. Societies should also commit to organizing sustainable and eco-friendly conferences, including eco-conscious choices for meeting size, frequency, location, transportation, accommodation, food options, and waste mitigation. As we advance toward global change, scientific societies can help adapt institutional policies by fostering green and equitable science.

Mayank Chugh
Department of Systems Biology, Harvard Medical School, Boston, MA, USA.
Twitter: @mayank_mchugh

10.1126/science.adh8182

PRIZE ESSAY

GRAND PRIZE WINNER
Jordan W. Squair

Jordan Squair received his undergraduate, master's, and PhD degrees (as part of the MD/PhD program) at the University of British Columbia. After completing his postdoctoral fellowships at the Swiss Federal Institute of Technology (EPFL) and the University of Calgary, Jordan started his group as a Swiss National Science Foundation Ambizione Fellow in the Life Sciences Department within NeuroRestore at EPFL in 2022. His research focuses on developing technological and biological interventions for neurotraumatic and neurodegenerative disorders.

www.science.org/doi/10.1126/science.adg7669

BII | Prize for Science | Innovation

INNOVATION

Invisible consequences of paralysis

Neuroprosthetic technologies can control blood pressure and restore walking

By **Jordan W. Squair**[1,2,3,4,5,6]

Individuals with spinal cord injury (SCI) demonstrate remarkable optimism, despite losing their ability to move, feel, and control many essential bodily functions. Since I started pursuing my MD/PhD in 2015, I have been passionate about the possibility of developing new therapies to improve the lives of people with SCI. I quickly learned that much of the research on SCI focuses on the restoration of movement and sensation. However, my advisers made me more aware of some less-appreciated symptoms of SCI that result from the disruption of the autonomic nervous system and have profound health consequences. These symptoms are invisible, and we often do not realize how much they affect the quality of life of people with SCI.

SCI prevents the brainstem from modulating blood pressure in response to changes in posture (*1*). Consequently, blood pressure can drop to dangerously low levels simply from sitting up in the morning. This condition, termed orthostatic hypotension, has extensive consequences, because people with SCI frequently feel dizzy and nauseated, experience regular syncope, and, in some cases, must remain bedridden (*1*). At present, our clinical toolkit to treat this condition is largely ineffective and leaves more than 90% of people with SCI constantly struggling with blood pressure complications, which increases the risk for cardiovascular disease (*2*).

For the past 8 years, I have been singularly focused on the treatment of orthostatic hypotension in SCI. Even as an optimistic young graduate student, I would have never imagined that my research would lead to multiple patents, industry-sponsored clinical trials, and the translation of our discoveries into updated guidelines and new therapies to help the worldwide community of people living with SCI.

While working on my PhD, I had the opportunity to be involved in human experiments involving individuals with SCI who had been implanted with neurostimulation systems. My colleagues and I found that epidural electrical stimulation (EES) of the spinal cord could rapidly increase blood pressure (*3*). Eager to better understand the mechanism of this response and to exploit this underlying process, I spent the next few years as a postdoctoral fellow focused on identifying the mechanisms by which EES modulates blood pressure (*4*). We found that pressor responses to EES correlate linearly with the density of sympathetic preganglionic neurons embedded in the targeted spinal segment and that there is a disproportionate enrichment of these neurons in the last three thoracic segments. We termed these locations the hemodynamic hotspots. Delivering EES over these hemodynamic hotspots enabled real-time control of blood pressure, even during severe orthostatic challenges.

The robustness of this treatment, which we called the neuroprosthetic baroreflex (*4*), encouraged us to conduct evaluations in nonhuman primate models of SCI and eventually in one human patient with severe medically refractory orthostatic hypotension. This treatment enabled the permanent cessation of medical therapies for hemodynamic stabilization and eliminated the clinical burden of orthostatic hypotension (*4*).

Our publication describing these findings (*4*) attracted substantial interest from practicing neurologists around the world. After presenting our findings to neurologists at our local hospital, I was asked whether this technology could potentially help a patient under their care. The patient presented with a diagnosis of multiple system atrophy and had severe deficits in both motor and autonomic functions, including hemodynamic instability that prevented her from standing for more than a few minutes. Given her clinical status,

[1]Defitech Center for Interventional Neurotherapies (NeuroRestore), Lausanne University Hospital (CHUV)–University of Lausanne (UNIL)–École Polytechnique Fédérale de Lausanne (EPFL), Lausanne, Switzerland. [2]NeuroX Institute, EPFL, Lausanne, Switzerland. [3]Department of Neurosurgery and Clinical Neuroscience, CHUV–UNIL, Lausanne, Switzerland. [4]Department of Clinical Neuroscience, CHUV–UNIL, Lausanne, Switzerland. [5]Hotchkiss Brain Institute and Libin Cardiovascular Institute, University of Calgary, Calgary, AB, Canada. [6]Faculty of Medicine, University of British Columbia, Vancouver, BC, Canada. Email: jordan.squair@epfl.ch

PHOTO: COURTESY OF JIMMY RAVIER

we surgically implanted an EES system to modulate the hemodynamic hotspots. Immediately after implantation, she was able to stand up and walk several hundred meters (see the figure). To this day, she remains symptom free from syncope despite the advancement of her disease (*5*).

Based on our publications, several companies became interested in our results, and we decided to license the patents describing our approach to ONWARD Medical. Our goal was to collaborate with them to develop a clinical-grade version of the neuroprosthetic baroreflex that maximizes the efficacy of this therapy, facilitates its use by people with SCI and their caretakers, and ultimately could be tested in a clinical trial. To facilitate the translation of this therapy from the laboratory to the clinic, we worked together and obtained a US Federal Drug Administration Breakthrough Device designation to manage hemodynamics based on the neuroprosthetic baroreflex, which provides a first step toward obtaining a label and reimbursement for this therapy to ensure its widespread use.

Bridging the gap between research and industry has already enabled three individuals to be implanted through a proof-of-concept clinical study, all of whom have shown robust increases in blood pressure when the neuroprosthetic baroreflex is activated. All participants reported marked improvements in their quality of life because the treatment reduces fatigue and enables them to be active throughout the day. I set out at the beginning of my training to contribute to the development of new therapies, and these findings have been extremely gratifying to witness. We are now designing a clinical trial to demonstrate the safety and efficacy of this treatment to manage hemodynamic stability in people with SCI. Moreover, our results have also led to a successful application to a Defense Advanced Research Projects Agency program, which is now supporting us with a large consortium to upgrade our technologies with sensing capabilities.

Achieving robust hemodynamic stability in people with SCI is one of the most promising ways to optimize neurological recovery in the acute phase and to reduce the burden on patients due to orthostatic hypotension and associated secondary medical complications in the chronic phase. The work I completed during my PhD and postdoctoral fellowship has now fueled international efforts by us, other scientists, and ONWARD Medical that are poised to establish a new treatment to prevent orthostatic hypotension in people with neurological disease. I plan to continue working closely with industrial partners, government agencies, and other collaborators around the world to make this treatment available to every person who needs it. ■

FINALIST

Samuel F. Bakhoum

Samuel Bakhoum received undergraduate degrees from Simon Fraser University, his PhD from Dartmouth College, and his MD from Geisel School of Medicine at Dartmouth. After completing his clinical training at Memorial Sloan Kettering Cancer Center (MSKCC) and a postdoctoral fellowship at Weill Cornell Medicine, he started his laboratory in the Human Oncology and Pathogenesis Program and the Department of Radiation Oncology at MSKCC in 2018. His research aims to understand the cellular mechanisms by which chromosomal instability drives cancer progression. **www.science.org/doi/10.1126/science.adg7671**

FINALIST

Kaira Wagoner

Kaira Wagoner received an undergraduate degree from Guilford College and her master's and PhD from the University of North Carolina Greensboro (UNC Greensboro). After completing her postdoctoral fellowship at UNC Greensboro, Kaira started her laboratory in its Biology Department in 2021. Her research focuses on insect chemical communication, pollinator behavioral ecology, and honey bee pests and diseases. **www.science.org/doi/10.1126/science.adg7672**

REFERENCES AND NOTES

1. A. A. Phillips, A. V. Krassioukov, *J. Neurotrauma* **32**, 1927 (2015).
2. J. J. Cragg, V. K. Noonan, A. Krassioukov, J. Borisoff, *Neurology* **81**, 723 (2013).
3. C. R. West *et al.*, *JAMA Neurol.* **75**, 630 (2018).
4. J. W. Squair *et al.*, *Nature* **590**, 308 (2021).
5. J. W. Squair *et al.*, *N. Engl. J. Med.* **386**, 1339 (2022).

10.1126/science.adg7669

The neuroprosthetic baroreflex restores hemodynamic stability

The x-ray image shows a participant's spinal cord, including visualization of the targeted thoracic posterior roots (T10 to T12), and implantable pulse generator (left). A chronophotograph shows a patient with multiple system atrophy walking comfortably with the neuroprosthetic baroreflex turned on (right); before surgery to implant the system, she was unable to take a step.

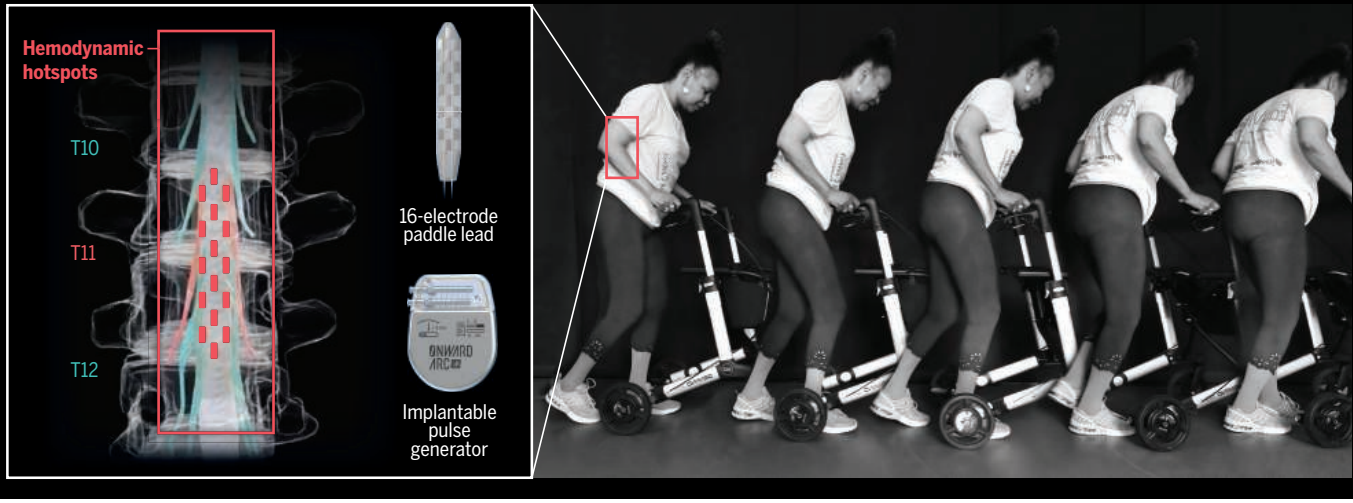

CREDITS: (GRAPHIC) ADAPTED FROM J. W. SQUAIR *ET AL.* (5); (PHOTOS, LEFT TO RIGHT) MEMORIAL SLOAN KETTERING CANCER CENTER; COURTESY OF THE UNIVERSITY OF NORTH CAROLINA GREENSBORO

PRIZE ESSAY

FINALIST

Samuel F. Bakhoum

Samuel Bakhoum received undergraduate degrees from Simon Fraser University, his PhD from Dartmouth College, and his MD from Geisel School of Medicine at Dartmouth. After completing his clinical training at Memorial Sloan Kettering Cancer Center (MSKCC) and a postdoctoral fellowship at Weill Cornell Medicine, he started his laboratory in the Human Oncology and Pathogenesis Program and the Department of Radiation Oncology at MSKCC in 2018. His research aims to understand the cellular mechanisms by which chromosomal instability drives cancer progression. **www.science.org/doi/10.1126/science.adg767**

BII | Prize for Science | Innovation

INNOVATION

Targeting the undruggable

Journey through basic biology reveals a way to treat chromosomally unstable cancers

By **Samuel F. Bakhoum**[1,2]

Cancer cells that metastasize—spread throughout the body—frequently shuffle their genomes through an ongoing process called chromosomal instability (CIN). Despite the widespread prevalence of CIN in human disease, we lack adequate therapies to target this tumor-intrinsic process. My laboratory has built on fundamental discoveries in cell and cancer biology to identify ways to selectively target CIN, with the goal of developing a new class of drugs aimed at the most lethal subset of cancer cells.

Since the first cancer genome was sequenced, our knowledge of genetic alterations that promote cancer initiation and progression has grown exponentially. That knowledge has led to the development of therapies that target individual genetic drivers of tumor progression, with the underlying assumption that tumor growth can be halted in its tracks if these drivers are inhibited. Yet we soon learned that tumors are wily and can develop resistance to these targeted therapies through CIN. This instability arises from chromosome segregation errors during mitosis and leads to widespread genomic heterogeneity that fuels tumor evolution, which can promote metastasis and therapeutic resistance.

CIN remains one of the greatest unresolved genomic challenges in cancer treatment. This is in part due to the poorly defined biological pathways that give rise to CIN, the dearth of well-controlled experimental systems, and the absence of therapies that can target complex chromosomal alterations in cancer. My team was drawn to this challenge and has used an interdisciplinary approach to systematically dissect mechanisms at the root of chromosome segregation errors in cancer (see the figure). To better understand these mechanisms, we began with the basic biology underlying chromosome segregation during cell division (*1*–*4*), then turned to computational approaches that model the behavior of tumor cell populations (*5*–*7*), and last, used experimental tools to selectively interrogate CIN in tumor evolution and metastasis (*8*–*10*).

This effort has identified several drug targets and led to the foundation of Volastra Therapeutics, a New York–based biotech startup that is focused on CIN. Volastra, which I co-founded with Lewis Cantley and Olivier Elemento, uses a comprehensive approach that ranges from synthetic lethality to uncovering immune vulnerabilities in cancers with CIN to develop therapies for advanced and metastatic cancers.

In my research team's quest to uncover how CIN drives cancer progression, we made an unexpected observation: CIN tricks cancer cells into behaving as though they were infected by a virus, leading to the activation of immune pathways that enable the cells to survive and spread (*8, 9*). When chromosomes become unstable, they often end up in cytoplasm outside of the primary nucleus, where they should normally reside. This aberrant localization of DNA triggers the activation of the cyclic guanosine monophosphate–adenosine monophosphate (GMP-AMP) synthase-stimulator of interferon genes (cGAS-STING) pathway, which has normally evolved to fight viral infection. Notably, this pathway cannot distinguish whether the DNA in the cytoplasm arises from within or is from an external viral source, and its engagement normally activates immune responses that are meant to clear viral infection. CIN is an ongoing process, like prolonged COVID-19 infection, and persistent activation of the cGAS-STING pathway leads to broad immune dysfunction, enabling cancer cells to overcome the risks associated with inflammation (*9*).

This finding motivated my team to embark on a journey to understand how cancer cells with CIN coexist with inflammation and avoid targeted destruction by the immune system. We reasoned that if we could identify and focus on proteins enabling this adaptation, we could unmask chromosomally unstable cancer cells to the immune system and allow it to unleash its antitumor potential. This approach revealed a key mechanism used by tumor cells with CIN to escape immune attack, through the expression of an extracellular enzyme called ectonucleotide pyrophosphatase/phosphodiesterase fam-

[1]Human Oncology and Pathogenesis Program, Memorial Sloan Kettering Cancer Center (MSKCC), New York, NY, USA. [2]Department of Radiation Oncology, MSKCC, New York, NY, USA. Email: samuel.bakhoum@gmail.com

PHOTO: MEMORIAL SLOAN KETTERING CANCER CENTER

ily member 1 (ENPP1). ENPP1 breaks down the immune stimulatory molecule generated by cGAS when it encounters cytoplasmic DNA. This enzyme then disrupts the crosstalk between cancer cells and the immune system, rendering the latter blind to the tumor (*8*). Intriguingly, through one additional enzymatic step, tumor cells converted this immune-stimulatory molecule into an immune-suppressive metabolite called adenosine—turning a foe into a friend.

This discovery was a watershed moment; not only do cancer cells with CIN avoid the deleterious effects of inflammation, they also use it to their advantage to survive and spread to distant organs. This led an entirely new strategy to selectively target tumor cells with CIN while sparing normal tissues. Focused on the broader approach to exploit the cancer cell–intrinsic and immune-related vulnerability created by CIN, Volastra was founded and has now grown to more than 40 employees. It has raised more than $100 million in financing in its bid to develop therapies tailored at advanced and metastatic cancers with CIN. Volastra's lead clinical-stage program aims to test the role of Kif18a inhibitors in advanced cancers and represents an opportunity to selectively target chromosomally unstable cells with minimal effect on normal genomically stable cells, including immune cells. This particular therapeutic window sets CIN-directed therapies apart from conventional chemotherapeutics, which often exhibit dose-limiting toxicities.

My deep-rooted desire to untangle the mysteries of CIN in cancer has led me down a path of unexpected yet exciting discoveries and applications. A common theme in this journey was curiosity-driven science undertaken with a readiness to translate findings to the clinic as the opportunity availed itself. Tackling an age-old problem, which has perhaps been understudied owing to the advent of new technologies, has always been appealing. Scientifically, I am drawn to unanswered fundamental questions, and as a physician, I have been motivated by the fact that too many patients with advanced and metastatic cancer still lack adequate therapies, in part because of the rampant level of CIN in the late stages of disease, which render tumors resistant to many of the therapies we have to date. This unmet need is what makes the journey—as challenging as it may be—entirely worthwhile. ■

GRAPHIC: ADAPTED FROM S. F. BAKHOUM

REFERENCES AND NOTES

1. S. F. Bakhoum, S. L. Thompson, A. L. Manning, D. A. Compton, *Nat. Cell Biol.* **11**, 27 (2009).
2. S. F. Bakhoum, G. Genovese, D. A. Compton, *Curr. Biol.* **19**, 1937 (2009).
3. S. F. Bakhoum, L. Kabeche, J. P. Murnane, B. I. Zaki, D. A. Compton, *Cancer Discov.* **4**, 1281 (2014).
4. A. L. Manning *et al.*, *EMBO J.* **29**, 3531 (2010).
5. A. M. Laughney, S. Elizalde, G. Genovese, S. F. Bakhoum, *Cell Rep.* **12**, 809 (2015).
6. S. Elizalde, A. M. Laughney, S. F. Bakhoum, *PLOS Comput. Biol.* **14**, e1006447 (2018).
7. S. F. Bakhoum *et al.*, *Nature* **553**, 467 (2018).
8. S. F. Bakhoum *et al.*, *Nat. Commun.* **6**, 5990 (2015).
9. S. F. Bakhoum, O. V. Danilova, P. Kaur, N. B. Levy, D. A. Compton, *Clin. Cancer Res.* **17**, 7704 (2011).
10. B. I. Zaki, A. A. Suriawinata, A. R. Eastman, K. M. Garner, S. F. Bakhoum, *Cancer* **120**, 1733 (2014).

ACKNOWLEDGMENTS

S.F.B. holds a patent related to some of the work described targeting CIN and the cGAS-STING pathway in advanced cancer. He owns equity in, receives compensation from, and serves as a consultant on the Scientific Advisory Board and Board of Directors of Volastra Therapeutics.

10.1126/science.adg7671

Deconstructing the multifaceted role of chromosomal instability (CIN) requires a multidisciplinary approach

(**A**) Chromosome segregation errors have a profound impact on tumor evolution. This can be through the generation of genomic copy number heterogeneity, which serves as the substrate for natural selection. Alternatively, unstable chromosomes can promote chronic inflammatory transcriptional changes that induce EMT, therapeutic resistance, and promote cancer cell migration and metastasis. (**B**) Understanding the role of CIN in cancer can be best tackled through a multidisciplinary approach that combines cell biology, mathematical modeling, single-cell analysis, tumor modeling, and clinical samples. Targeting CIN in cancer has the potential to enhance antitumor immune response, minimize the onset of therapeutic resistance, and suppress metastatic progression.

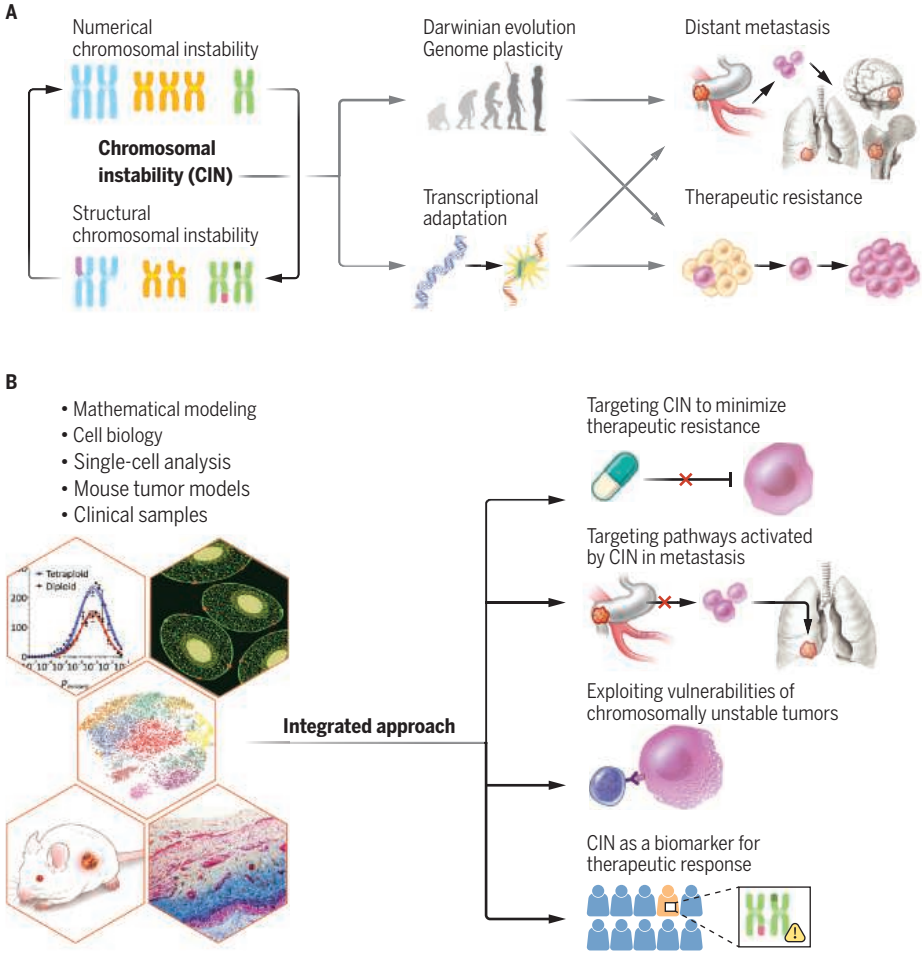

PRIZE ESSAY

FINALIST
Kaira Wagoner

Kaira Wagoner received an undergraduate degree from Guilford College and her master's and PhD from the University of North Carolina Greensboro (UNC Greensboro). After completing her postdoctoral fellowship at UNC Greensboro, Kaira started her laboratory in its Biology Department in 2021. Her research focuses on insect chemical communication, pollinator behavioral ecology, and honey bee pests and diseases. **www.science.org/doi/10.1126/science.adg7672**

BII | Prize for Science Innovation

INNOVATION

Helping honey bees help themselves

Pheromone-based technology benefits bee breeding and health to bolster food security

By **Kaira Wagoner**

Recently declared the most important beings on the planet, bees are critical pollinators of natural ecosystems and crops, contributing between $235 and $577 billion to annual global food production. Animal-dependent crop pollination relies heavily on managed honey bees and is responsible for 30% of food supplies worldwide (*1*). Despite their importance, honey bee colonies are dying at unprecedented rates.

The recent host-shift of the parasitic mite *Varroa* (*Varroa destructor*) from the eastern honey bee (*Apis cerana*) to the western honey bee (*Apis mellifera*) has brought ancient bees to their figurative knees. *Varroa* is an obligate, ectoparasitic mite that vectors numerous diseases to honey bees and completes its reproductive cycle inside the capped cells of developing honey bee brood (*2*). The first documented spillover of *Varroa* into the western honey bee took place in Japan in 1957. Since then, *Varroa* and the deadly diseases that they vector have spread to nearly all *A. mellifera* populations worldwide. Honey bee colony losses resulting from the spread of *Varroa* are expanding the land area required for crop production, increasing the environmental impact of farming, and threatening global food security.

In honey bee colonies, the high contact rate between closely related individuals increases the spread of pests and diseases. As superorganisms (i.e., a highly connected group of individuals that functions as a unified being or animal), honey bees have evolved several social immune mechanisms that boost pest and disease resistance at the colony level (*3*). Two examples include necrophoresis (*4*), the removal of dead individuals from the colony, and hygienic behavior (*5*), the detection, uncapping, and removal of unhealthy brood from the colony. In *Varroa*'s original host, *A. cerana*, high susceptibility of individual brood to *Varroa* causes mortality of parasitized brood, triggering necrophoresis (*6*). This individual susceptibility infers *Varroa* resistance at the colony level because dead brood are more easily detected and removed than unhealthy brood (*7*), and brood removal interrupts the *Varroa* reproductive cycle (*2*). By contrast, individual *A. mellifera* brood are more resistant to *Varroa*, leading to covert infestations that are less likely to trigger a hygienic response. *A. mellifera* colonies are thus more susceptible to *Varroa* than *A. cerana* colonies (*6*) because *A. mellifera* must rely on adult perception of subtle unhealthy brood odors to trigger the removal of infested brood.

My laboratory recently identified minute quantitative changes in cuticular hydrocarbons of *Varroa*-infested and virus-infected brood (*8*). We demonstrated that these unhealthy brood odors (UBOs) were elevated in brood targeted for hygienic uncapping (*8*) and confirmed that laboratory-synthesized UBOs could be applied to brood cell caps to trigger hygienic behavior (*9*). We then transformed these discoveries into a rapid, effective, and beekeeper-friendly tool to predict honey bee colony *Varroa* resistance and survival (*10*) (see the figure). This technology, called UBeeO, involves the application of synthetic pheromones to the wax caps of developing brood and subsequent quantification of honey bee hygienic response to treated cells. We have now shown that colonies capable of uncapping ≥60% of UBeeO-treated cells in a 2-hour, early season test have significantly lower *Varroa* infestations at the end of the summer and are significantly more likely to survive winter compared with lower-scoring colonies (*10*). By measuring honey bee responsiveness to UBeeO, beekeepers will be able to distinguish *Varroa*-resistant and *Varroa*-susceptible colonies earlier and more reliably to better facilitate breeding and apiary management decisions that have critical implications for honey bee health and survival.

In a beekeeping industry desperate to control *Varroa*, the selective breeding of more hygienic honey bees has been recognized as a promising (*11*) and urgently

Department of Biology, University of North Carolina Greensboro, Greensboro, NC, USA.
Email: kmwagone@uncg.edu

PHOTO: COURTESY OF THE UNIVERSITY OF NORTH CAROLINA GREENSBORO

needed alternative to temperature-sensitive organic acid treatments and the use of harmful acaricides, which are susceptible to the evolution of mite resistance (*2*) and exact heavy sublethal tolls on honey bee queens, drones, and workers (*12*). Although selective breeding for hygiene has been performed for decades, existing selection methods are insufficient, based either on prohibitively labor-intensive analysis of mite reproduction or quantification of necrophoresis, an unreliable indicator of *Varroa*-specific hygiene (*13*, *14*). As more beekeepers are able to rapidly and effectively measure colony *Varroa* resistance, UBeeO will improve breeding efforts, including localized hygiene selection that facilitates maintenance of important climate-specific traits, such as cold tolerance. UBeeO will also inform apiary management because *Varroa*-susceptible colonies can be isolated to facilitate breeding efforts, lower beekeeper labor costs, and reduce unnecessary miticide use.

With so much potential, UBeeO has created quite a buzz within the bee world, capturing the attention of social media influencers, honey bee scientists, and some of the most renowned queen breeders worldwide. Since 2020, I have established 13 UBO-related collaborations in six countries—the Netherlands, Canada, Australia, Israel, Belgium, and the United States.

Based on UBeeO's commercial potential and the success of numerous laboratory and field trials, I was recently granted three patents and joined with a former colleague to cofound the university spinout company Optera. Within 14 months, Optera raised more than $330,000 in nondilutive funding and has a growing list of customers awaiting product launch, planned for early 2024.

Although I expect UBeeO technology to improve honey bee health, I anticipate benefits beyond increased colony survival and related advantages for beekeepers, farmers, and ecosystems. Native pollinators share floral resources and pathogens with honey bees. Thus, controlling diseases in managed colonies may reduce pathogen spillover to native pollinators, further improving pollinator heath, natural ecosystem maintenance, and global food security.

Moreover, honey bees are not alone in their willingness to sacrifice individuals for the greater good. Other social insects, including ants, termites, and stingless bees, also remove sick pupae from their colonies. One compound that we identified as a hygiene trigger in honey bees is also elevated in ant pupae targeted for removal (*15*), which suggests that our contribution to the understanding of honey bee chemical communication may lead to the development of additional technologies to sustainably control pests and improve the health of other beneficial insects. What evolved from an exploration of hygiene chemistry into a practical tool now aims to revolutionize bee breeding, improve pollinator health, and boost global food security. This work is an example of how fundamental science with unknown practicality can result in real-world solutions to important global problems. ■

Better bees through hygiene chemistry

By improving selective breeding of *Varroa*-resistant bees and informing apiary management decisions, UBeeO could increase colony survival, natural ecosystem pollination, and ultimately global food security. The technology also has the potential to decrease miticide use, pathogen spillover to native bees, and total land required for crop production.

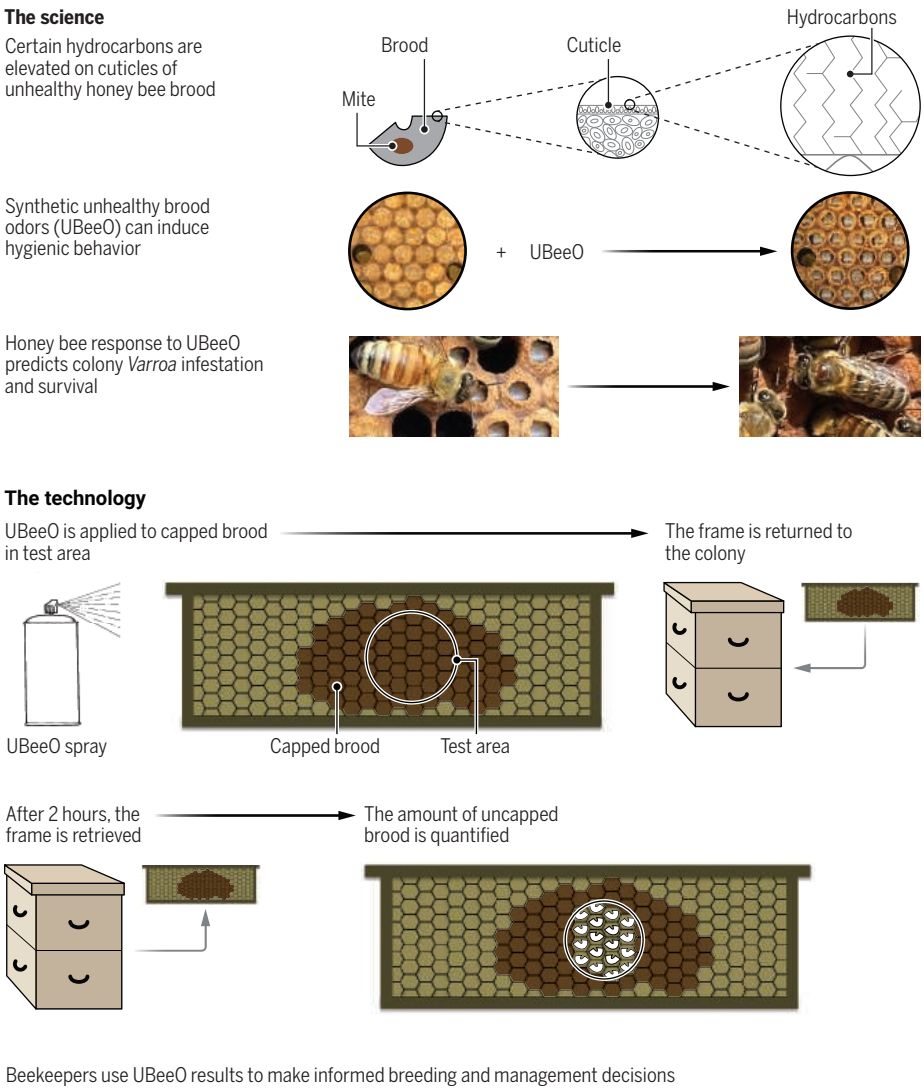
The science
Certain hydrocarbons are elevated on cuticles of unhealthy honey bee brood
Brood
Cuticle
Hydrocarbons
Mite
Synthetic unhealthy brood odors (UBeeO) can induce hygienic behavior
+ UBeeO
Honey bee response to UBeeO predicts colony Varroa infestation and survival
The technology
UBeeO is applied to capped brood in test area
The frame is returned to the colony
UBeeO spray
Capped brood
Test area
After 2 hours, the frame is retrieved
The amount of uncapped brood is quantified

GRAPHIC: ADAPTED FROM K. WAGONER

Beekeepers use UBeeO results to make informed breeding and management decisions

REFERENCES AND NOTES

1. S. L. Bushmann, F. A. Drummond, *Agronomy* **10**, 1413 (2020).
2. P. Rosenkranz, P. Aumeier, B. Ziegelmann, *J. Invertebr. Pathol.* **103**, S96 (2010).
3. M. Simone-Finstrom, *Bee World* **94**, 21 (2017).
4. P. K. Visscher, *Anim. Behav.* **31**, 1070 (1983).
5. W. C. Rothenbuhler, *Anim. Behav.* **12**, 578 (1964).
6. P. Page *et al.*, *Sci. Rep.* **6**, 27210 (2016).
7. M. Spivak, D. L. Downey, *J. Econ. Entomol.* **91**, 64 (1998).
8. K. Wagoner, M. Spivak, A. Hefetz, T. Reams, O. Rueppell, *Sci. Rep.* **9**, 8753 (2019).
9. K. M. Wagoner, J. G. Millar, C. Schal, O. Rueppell, *Sci. Rep.* **10**, 7132 (2020).
10. K. Wagoner *et al.*, *J. Insect Sci.* **21**, 4 (2021).
11. G. Leclercq, B. Pannebakker, N. Gengler, B. K. Nguyen, F. Francis, *J. Apic. Res.* **56**, 366 (2017).
12. C. Lu, Y.-T. Hung, Q. Cheng, *Curr. Pollut. Rep.* **6**, 137 (2020).
13. G. Leclercq, F. Francis, N. Gengler, T. Blacquière, *J. Apic. Res.* **57**, 663 (2018).
14. G. Leclercq, T. Blacquière, N. Gengler, F. Francis, *J. Apic. Res.* **57**, 292 (2018).
15. C. D. Pull *et al.*, *eLife* **7**, e32073 (2018).

10.1126/science.adg7672

RESEARCH

IN *SCIENCE* JOURNALS

Edited by **Michael Funk**

Artist's depiction of a T cell genetically engineered to produce chimeric antigen receptors

PHOTO: CHRISTOPH BURGSTEDT/SCIENCE PHOTO LIBRARY/GETTY IMAGES

CANCER

Tuning up CAR-T cells

A major goal for improving chimeric antigen receptor (CAR)–T cell therapy is to ensure that the CAR-T cell products infused into patients with cancer function optimally. However, standard manufacturing protocols do not enrich for cellular phenotypes associated with enhanced function. To address this limitation, Meyran et al. developed a protocol that generates TSTEM-like CAR-T cells that exhibit features of stem-like T cells. Compared with conventionally produced CAR-T cells, TSTEM-like CAR-T cells were more proliferative and produced more cytokines after CAR stimulation in vitro. They also exhibited superior control of tumor burden in vivo. Together, these results support the implementation of production strategies to generate TSTEM-like CAR T cells for clinical use. —CSM

Sci. Transl. Med. **15**, eabk1900 (2023).

PROTEOMICS

Decrypting drug actions through proteomics

Many cancer drugs aim to inhibit abnormally active proteins that drive the growth of tumors, but it is often not understood just how cancer cells react to these drugs. Zecha *et al*. devised a proteomic technology called decryptM that can measure the time- and dose-dependent response of thousands of proteins and reveal changes in response to small-molecule or antibody-based drugs. Application of decryptM to 31 drugs generated millions of measurements. These data helped to place protein modifications into new functional contexts, created fingerprints of drug response, and provided insights into how certain drugs kill cancerous blood cells. The decryptM data are available as a community resource for use in future basic biology, drug discovery, and clinical research. —PNK

Science, ade3925, this issue p. 93

COLLISION DYNAMICS

Imaging all Feshbach resonances at once

Quantum scattering resonances, and Feshbach resonances in particular, are the key features of cold collisions that can fundamentally change collision outcomes. Numerous previous experiments have mainly focused on the initial channel, providing limited insight into the resonant scattering dynamics. Margulis *et al*. developed a method in which the energetics and decay channels of Feshbach resonances, formed by collisions induced by Penning ionization of metastable helium or neon atoms and the ground-state hydrogen molecule, were mapped out by ion-electron coincidence velocity map imaging with a precision of several kelvin, enough to resolve all of the final rovibrational quantum states in a single measurement. The proposed method offers a new approach to quantum state mapping of resonant collision dynamics. —YS

Science, adf9888, this issue p. 77

METALENSES

Pushing metalenses to extremes

The fields of ultrafast spectroscopy and semiconductor photolithography rely on very short wavelengths, typically in the extreme ultraviolet (EUV) realm. However, most optical materials strongly absorb light in this wavelength regime, resulting in a lack of generally available

transmissive components. Ossiander *et al*. designed and fabricated a metalens in which a carefully engineered array of holes in a thin silicon membrane focuses ultrafast EUV pulses close to the diffraction limit by "vacuum guiding." The results open up transmissive optics to the EUV regime. —ISO

Science, adg6881, this issue p. 59

POLYMER CHEMISTRY

Methyl groups improve a plastic

Polyhydroxyalkanoates are a promising class of plastics accessible chemically or microbially from relatively sustainable feedstocks. However, their performance properties lag behind commercial petrochemically derived alternatives. Zhou *et al*. report that replacing reactive carbonyl-adjacent hydrogens in the monomer with methyl groups produces a polyhydroxyalkanoate that is more robust in multiple respects (see the Perspective by Guillaume). The dimethyl polymer is both crystalline and ductile, structurally sound during melt processing, and subject to efficient degradation to recover the monomer on treatment with base. —JSY

Science, adg4520, this issue p. 64; see also adh3072, p. 35

CATALYSIS

Mobile metal atoms underlying reactions

In heterogeneous catalysis, it is often assumed that adsorbates have minimal effects on the bonding between surface metal atoms at low temperatures and pressures. Xu *et al*. used density functional theory to find conditions in which adsorbed molecules can scavenge transition metal atoms by breaking bonds at the surface. These atoms can then form clusters, as observed in kinetic Monte Carlo simulations of carbon monoxide on copper and in scanning tunneling microscopy studies of carbon monoxide on a Ni(111) surface containing steps and dislocations. The reaction mechanisms of several catalytic systems may be dominated by in situ adsorbate-induced active site formation. —PDS

Science, add0089, this issue p. 70

PIEZOELECTRICS

A winning template

Lead zirconate titanate piezoelectrics are important for making transducers, sensors, and other components for electromechanical applications. To expand the usable temperature range and electromechanical coupling factor, Li *et al*. introduce a texturing process for lead zirconate titanate–based materials. A sacrificial template both changes the composition of the solid solution and orients the crystals to improve the piezoelectric properties. —BG

Science, adf6161, this issue p. 87

AUTOIMMUNITY

Targeting B cell migration in arthritis

COMMD3 and COMMD8, members of the copper metabolism MURR1 domain–containing (COMMD) protein family, form a heterodimer essential for chemoattractant-mediated B cell migration during the induction of humoral immune responses. By screening a compound library for molecules capable of disrupting the COMMD3/8 complex, Shirai *et al*. identified the Chinese herbal medicine celastrol as a potent inhibitor of COMMD3 association with COMMD8. In a mouse model of rheumatoid arthritis, celastrol treatment initiated at the onset of arthritis prevented disease progression. Celastrol's ability to disrupt the COMMD3/8 complex and inhibit arthritis was lost when a cysteine in COMMD3 was mutated to alanine. These findings reveal a molecular mechanism for the anti-arthritic activity of celastrol and identify the COMMD3/8 complex as a potential drug target in B cell–dependent autoimmune diseases. —IRW

Sci. Immunol. **8**, eadc9324 (2023)

IN OTHER JOURNALS

Edited by **Caroline Ash** *and* **Jesse Smith**

NEUROSCIENCE

Orientation and head direction

Proper orientation requires the brain to encode an organism's head direction in the horizontal plane, and several brain structures contain neurons selective for this function. Fallahnezhad *et al*. monitored the activity of head direction cells from two regions, the anterodorsal thalamic nucleus and the retrosplenial cortex, in the mouse brain simultaneously. They found that subsecond temporal coordination between neurons in these structures contributes to forming a unitary representation of direction. Further, neuronal coordination between multiple head direction signals and the distant head direction cell structures is mediated by the cerebellum. —PRS

Proc. Natl. Acad. Sci. U. S. A. (2023) 10.1073/pnas.2214539120.

ANXIETY

Biomarkers for behavior

Anxiety disorders are common, underdiagnosed, and disabling, yet objective measures of anxiety are lacking. Currently, clinicians assess anxiety through patients' self-ratings of anxiety and others' external ratings of their behavior. Could blood tests that measure RNA biomarkers objectively determine a person's risk for developing anxiety issues? And could such tests measure how severe a person's current state of anxiety is and match them to medication and therapies that offer effective treatment? In within-subject and between-subject designs across three independent cohorts, Roseberry *et al.* have begun to identify biomarkers that change in expression consistent with patients' self-ratings of high or low anxiety. Blood tests that track anxiety could allow

PHOTO: JOHN MOORE/GETTY IMAGES

ALSO IN *SCIENCE* JOURNALS

Edited by **Michael Funk**

IMMUNOLOGY

Changing ideas about brain immunity

Our understanding of how the brain and immune system interact has changed substantially over the past years and decades. Initially, the brain was thought to be immune privileged and isolated from the rest of the body. In a Review, Castellani *et al*. discuss recent discoveries, including attribution of central nervous system immune surveillance to tissue-resident microglia and acknowledging the existence of a complex brain-immune network that involves multiple peripheral immunological players. This complex brain-immune relationship is important during development, adulthood, and aging, as well as during various pathologies. Rethinking brain immunity could reveal new therapeutic targets for various neurological disorders. —GKA

Science, abo7649, this issue p. 52

LIPID SIGNALING

Accounting for omega-3 double bonds

In addition to being an energy source, fatty acids influence cells through their effects on membrane structure and as signaling molecules or precursors to signaling molecules. The G protein–coupled receptor GPR120 binds to various fatty acids, in particular polyunsaturated omega-3 fatty acids, which are essential components of the human diet. Mao *et al*. determined cryo–electron microscopy structures of GPR120–G protein complexes bound to natural lipids or a synthetic agonist and, in parallel, performed biochemical experiments to study biased signaling properties of the receptor. The tight binding pocket packs around the lipids, and hydrophobic and aromatic residues read out different double bonds, resulting in subtle structural changes that result in different activation and bias patterns for different ligands. These insights will be invaluable for efforts to target this receptor for drugs that treat metabolic and immune diseases. —MAF

Science, add6220, this issue p. 53

IMMUNOLOGY

Antibodies GRAB their targets

Different individuals will reproducibly generate antibodies against the same epitopes after exposure to a pathogen. However, the mechanisms driving the production of these "public antibodies" continue to be poorly understood. Shrock *et al.* used a phage display platform called VirScan to glean additional insights into this process. They found that many human V gene segments contained germline-encoded amino acid–binding (GRAB) motifs that bind particular amino acids and are essential for antibody recognition. Moreover, a comparison of mouse and human GRAB motifs uncovered only a partial overlap, which may explain the distinct public epitopes targeted by different species. —STS

Science, adc9498, this issue p. 54

MEDICINE

HCV vaccine design

Hepatitis C virus (HCV) can cause chronic hepatitis, liver cirrhosis, and hepatocellular carcinoma, together accounting for ~290,000 deaths worldwide. Attempts to develop an HCV vaccine have so far been unsuccessful, but emerging understanding of HCV envelope glycoprotein structure and protective immunity could lead to improved vaccine design. In a Perspective, Offersgaard *et al.* discuss how protective immunity against HCV involves antibodies and T cells and that both should be engaged by next-generation vaccines to ensure broad protection against genetically heterogeneous HCV strains. Such vaccine strategies could target both HCV envelope proteins and viral proteins that are involved in replication. The authors also discuss the need to improve testing of vaccine candidates given the lack of a robust animal model. —GKA

Science, adf2226, this issue p. 37

GPCR SIGNALING

Arresting interactions for chemotaxis

GPR183 is a G protein–coupled receptor (GPCR) for oxysterol ligands, including 7α,25-dihydroxycholesterol, and mediates the migration of various immune cells and their proper positioning in lymphoid tissues. Kjær *et al*. characterized the signaling and regulation of GPR183 function in cells in response to various ligands. Unlike other chemotactic GPCRs, GPR183 internalization was β-arrestin independent. Moreover, GPR183 interacted with caveolae rather than clathrin for ligand-induced internalization and required β-arrestin for 7α,25-dihydroxycholesterol–dependent chemotaxis. —JFF

Sci. Signal. **16**, eabl4283 (2023).

ELECTROCHEMISTRY

Alternate approach to Kolbe coupling

Kolbe coupling is one of the very oldest reported reactions in organic chemistry. Essentially, an electrode oxidizes two carboxylic acids to release carbon dioxide and then couples the residual carbon fragments. Although direct and simple, the conventional reaction is incompatible with many common functionalities that can undergo competing oxidation. Hioki *et al*. now report that rapidly alternating the polarity of the electrochemical cell greatly expands the range of substituents compatible with the coupling (see the Perspective by Guo and Ye). This approach avoids pH lowering near the electrode that would otherwise slow down the decarboxylative oxidation at the expense of the side reactions. —JSY

Science, adf4762, this issue p. 81; see also adh1837, p. 34

EVOLUTIONARY BIOLOGY

A new mode of reproduction in animals

Multicellular organisms typically develop from a single cell into a collection of cells that all have the same genetic material. Darras *et al*. discovered a deviation from this developmental hallmark in the yellow crazy ant, *Anoplolepis gracilipes*. Males of this species are all chimeras, a collection of haploid cells with only maternal or paternal genetic material (see the Perspective by Kronauer). These chimeras develop from fertilized eggs in which parental nuclei divide independently. Genetic analyses show that this unusual mode of reproduction is probably the result of a genetic conflict between two co-occurring lineages. —DJ

Science, adf0419, this issue p. 55; see also adh1664, p. 33

transmissive components. Ossiander *et al*. designed and fabricated a metalens in which a carefully engineered array of holes in a thin silicon membrane focuses ultrafast EUV pulses close to the diffraction limit by "vacuum guiding." The results open up transmissive optics to the EUV regime. —ISO

Science, adg6881, this issue p. 59

POLYMER CHEMISTRY

Methyl groups improve a plastic

Polyhydroxyalkanoates are a promising class of plastics accessible chemically or microbially from relatively sustainable feedstocks. However, their performance properties lag behind commercial petrochemically derived alternatives. Zhou *et al*. report that replacing reactive carbonyl-adjacent hydrogens in the monomer with methyl groups produces a polyhydroxyalkanoate that is more robust in multiple respects (see the Perspective by Guillaume). The dimethyl polymer is both crystalline and ductile, structurally sound during melt processing, and subject to efficient degradation to recover the monomer on treatment with base. —JSY

Science, adg4520, this issue p. 64; see also adh3072, p. 35

CATALYSIS

Mobile metal atoms underlying reactions

In heterogeneous catalysis, it is often assumed that adsorbates have minimal effects on the bonding between surface metal atoms at low temperatures and pressures. Xu *et al*. used density functional theory to find conditions in which adsorbed molecules can scavenge transition metal atoms by breaking bonds at the surface. These atoms can then form clusters, as observed in kinetic Monte Carlo simulations of carbon monoxide on copper and in scanning tunneling microscopy studies of carbon monoxide on a Ni(111) surface containing steps and dislocations. The reaction mechanisms of several catalytic systems may be dominated by in situ adsorbate-induced active site formation. —PDS

Science, add0089, this issue p. 70

PIEZOELECTRICS

A winning template

Lead zirconate titanate piezoelectrics are important for making transducers, sensors, and other components for electromechanical applications. To expand the usable temperature range and electromechanical coupling factor, Li *et al*. introduce a texturing process for lead zirconate titanate–based materials. A sacrificial template both changes the composition of the solid solution and orients the crystals to improve the piezoelectric properties. —BG

Science, adf6161, this issue p. 87

AUTOIMMUNITY

Targeting B cell migration in arthritis

COMMD3 and COMMD8, members of the copper metabolism MURR1 domain–containing (COMMD) protein family, form a heterodimer essential for chemoattractant-mediated B cell migration during the induction of humoral immune responses. By screening a compound library for molecules capable of disrupting the COMMD3/8 complex, Shirai *et al*. identified the Chinese herbal medicine celastrol as a potent inhibitor of COMMD3 association with COMMD8. In a mouse model of rheumatoid arthritis, celastrol treatment initiated at the onset of arthritis prevented disease progression. Celastrol's ability to disrupt the COMMD3/8 complex and inhibit arthritis was lost when a cysteine in COMMD3 was mutated to alanine. These findings reveal a molecular mechanism for the anti-arthritic activity of celastrol and identify the COMMD3/8 complex as a potential drug target in B cell–dependent autoimmune diseases. —IRW

Sci. Immunol. **8**, eadc9324 (2023)

IN OTHER JOURNALS

Edited by **Caroline Ash** *and* **Jesse Smith**

PHOTO: JOHN MOORE/GETTY IMAGES

NEUROSCIENCE

Orientation and head direction

Proper orientation requires the brain to encode an organism's head direction in the horizontal plane, and several brain structures contain neurons selective for this function. Fallahnezhad *et al*. monitored the activity of head direction cells from two regions, the anterodorsal thalamic nucleus and the retrosplenial cortex, in the mouse brain simultaneously. They found that subsecond temporal coordination between neurons in these structures contributes to forming a unitary representation of direction. Further, neuronal coordination between multiple head direction signals and the distant head direction cell structures is mediated by the cerebellum. —PRS

Proc. Natl. Acad. Sci. U. S. A. (2023) 10.1073/pnas.2214539120.

ANXIETY

Biomarkers for behavior

Anxiety disorders are common, underdiagnosed, and disabling, yet objective measures of anxiety are lacking. Currently, clinicians assess anxiety through patients' self-ratings of anxiety and others' external ratings of their behavior. Could blood tests that measure RNA biomarkers objectively determine a person's risk for developing anxiety issues? And could such tests measure how severe a person's current state of anxiety is and match them to medication and therapies that offer effective treatment? In within-subject and between-subject designs across three independent cohorts, Roseberry *et al.* have begun to identify biomarkers that change in expression consistent with patients' self-ratings of high or low anxiety. Blood tests that track anxiety could allow

PHOTO: DINAR BUDIMAN/SHUTTERSTOCK

The Australian wildfires of 2019–2020 perturbed the chlorine chemistry of the stratosphere and destroyed ozone.

OZONE DEPLETION

Organic effects

The Australian wildfires of 2019–2020 injected around one teragram of aerosols into the stratosphere, including large amounts of chlorine, causing significant ozone decreases in the lower stratosphere at southern hemisphere midlatitudes. Wang *et al.* discuss the unusual changes observed in HCl and $ClONO_2$, species involved in stratospheric ozone destruction, and what they may reveal about the heterogeneous chemistry affecting ozone under both background and wildfire conditions. The authors found that these reactions can occur at much higher temperatures than they do in the Antarctic polar vortex and suggest that chlorine processes on organic aerosols likely should be included in stratospheric ozone simulations. —HJS

Proc. Natl. Acad. Sci. U. S. A. (2023) 10.1073/pnas.2213910120.

clinicians to identify anxiety earlier to better inform their treatment decisions. —EEU

Mol. Psychiatry (2023) 10.1038/s41380-023-01998-0.

BEHAVIOR

Estrus-independent behavior

Scientists often assume that estrus influences spontaneous behavior. Therefore, until recently, behavioral experiments have mostly been performed in male animals to reduce variability. Levy *et al.* tested this assumption by characterizing spontaneous behavior in female animals during different phases of the estrous cycle and also used male mice for comparison. In both sexes, the authors identified individual-specific behaviors; however, the phase of the estrous cycle had no effect on spontaneous behavior, and male animals showed more variability compared with females. By refuting an old assumption, the results provide additional support (if it is still needed) for using animals of both sexes in behavioral research. —MM

Curr. Biol. (2023) 10.1016/j.cub.2023.02.035.

PLANT SCIENCE

Finetuning gene expression in plants

Genome-editing technology using CRISPR-Cas has profoundly changed the trajectory of biological research, medicine, and agriculture. To modulate protein expression in rice plants, Xue *et al*. used prime or base editing for precision mutation of short upstream open reading frames (uORFs) in the 5′ untranslated regions of coding mRNAs. A simple transient luciferase reporter system reliably predicted gene expression and phenotype. Sets of new uORFs can thus be engineered to incrementally modulate translation from about 85% down to 2.5% of wild-type levels. Using this technique on the brassinosteroid signaling pathway, a series of rice plants were generated that had a gradation of plant height and tiller number (stems that arise from the base of the plant). This technology could bring about rapid innovation in crop breeding. —DJ

Rice plant gene expression can be modulated to provide many different phenotypes for a range of growth conditions.

Nat. Biotechnol. (2023) 10.1038/s41587-023-01707-w.

ELECTRON EMISSION

The shape of electron emission

Electron emission finds a range of applications, from vacuum nano-electronics to ultrafast structural and surface imaging techniques for materials characterization. Yanagisawa *et al.* placed single fullerene molecules (C_{60} or buckyballs) on the end of a sharp tungsten tip and showed that by modulating the tip with ultrafast laser pulses, the resulting emission patterns could be switched. Calculations showed that the emission patterns result from the electrons passing through the different molecular orbitals of the single molecule. Being able to control the spatial profile and temporal dynamics of the emitted electrons provides a wider suite of tools with which to probe materials and additional degrees of freedom to exploit in electronic devices. —ISO

Phys. Rev. Lett. (2023) 10.1103/PhysRevLett.130.106204.

ORGANIC CHEMISTRY

Birch in a ball mill

The Birch reduction of arenes to dienes is so distinctly useful that it has been widely applied for nearly 80 years despite requiring extreme conditions: a flammable alkali metal dissolved in liquid ammonia. Recently, there has been substantial progress in tuning the conditions for improved safety and convenience. Gao *et al.* report an exceptionally rapid mechanochemical approach. Mixing the substrate in a ball mill with lithium, ethylene diamine, and in some cases tetrahydrofuran lowers the reaction time to just a minute and does not require the exclusion of air. —JSY

Angew. Chem. Int. Ed. (2023) 10.1002/anie.202217723.

REVIEW SUMMARY

IMMUNOLOGY

Transforming the understanding of brain immunity

Giulia Castellani†, Tommaso Croese†, Javier M. Peralta Ramos†, Michal Schwartz*

BACKGROUND: Beginning in the early 19th century, the brain was considered a self-contained organ behind barriers and thus as "immune privileged." This assumption was supported by experiments showing that a dye injected into the circulation did not stain the brain and by evidence of prolonged survival of tissue grafts in the brain compared with transplants into peripheral tissues. These conclusions led to the axiomatic view that the brain cannot tolerate any immune activity. The identification of brain-resident immune cells, the microglia, was often used as an additional argument to support the immunological self-sufficiency of the brain. In addition, despite the early description of brain lymphatic drainage, which dates back to 1787, the supposed absence of lymphatic vessels within the brain was, until recently, among the most common rationales used to support the view of a complete separation between the brain and the immune system.

ADVANCES: Our perception of the relationship between the brain and the immune system has completely changed over the past decades. It is now established that immune cells operate as guardians of the central nervous system (CNS), support brain function and repair, and reside in specialized immunological niches at its borders, including the meninges, the choroid plexus, and the perivascular spaces. The meninges remotely affect the brain through immune cell–derived cytokine release. The choroid plexus hosts and orchestrates the selective homing of immune cells to the CNS parenchyma. The perivascular spaces are populated by immune cells regulating cerebrospinal fluid flow. The demonstration of the CNS lymphatic system and brain drainage led to the identification of the brain-draining cervical lymph nodes as crucial supplementary sites of the interaction between the CNS and the immune system. Additional observations revealed that microscopic channels in the bone of the skull allow exposure of the bone marrow (BM) to the cerebrospinal fluid, thereby influencing cellular maturation in the BM and migration into the brain. Such an intricate communication network guarantees efficient CNS-monitoring activities by neighboring immune cells, the phenotype of which is shaped by the CNS microenvironment to which they are constantly exposed. The bidirectional nature of the CNS–immune system interplay is supported by emerging studies demonstrating the ability of neuronal cells to modulate the immune response through lymphoid organ innervation in the context of CNS diseases.

OUTLOOK: The negative side of the immune system participating in brain physiology is that imbalanced brain-immune interactions might be critical in aging and in autoimmune, neurodegenerative, and neurodevelopmental disorders. Under such conditions, the perturbed brain microenvironment might lead to a harmful immune response, which may exacerbate disease manifestations. Further advances in our understanding of brain immunity and the reciprocal ability of the CNS and the immune system to sense and influence each other will offer intervention tools for the design of new therapeutic strategies for treating brain pathologies. Understanding what goes awry in each of the brain's immune niches, including the skull BM, the meninges, and the choroid plexus, as well as in lymphatic drainage, might reveal new potential targets for therapeutic approaches in the near future. ■

Department of Brain Sciences, Weizmann Institute of Science, Rehovot, Israel.
The list of author affiliations is available in the full article online.
†These authors equally contributed to this work.
*Corresponding author. Email: michal.schwartz@weizmann.ac.il
Cite this article as G. Castellani *et al.*, *Science* **380**, eabo7649 (2023). DOI: 10.1126/science.abo7649

READ THE FULL ARTICLE AT
https://doi.org/10.1126/science.abo7649

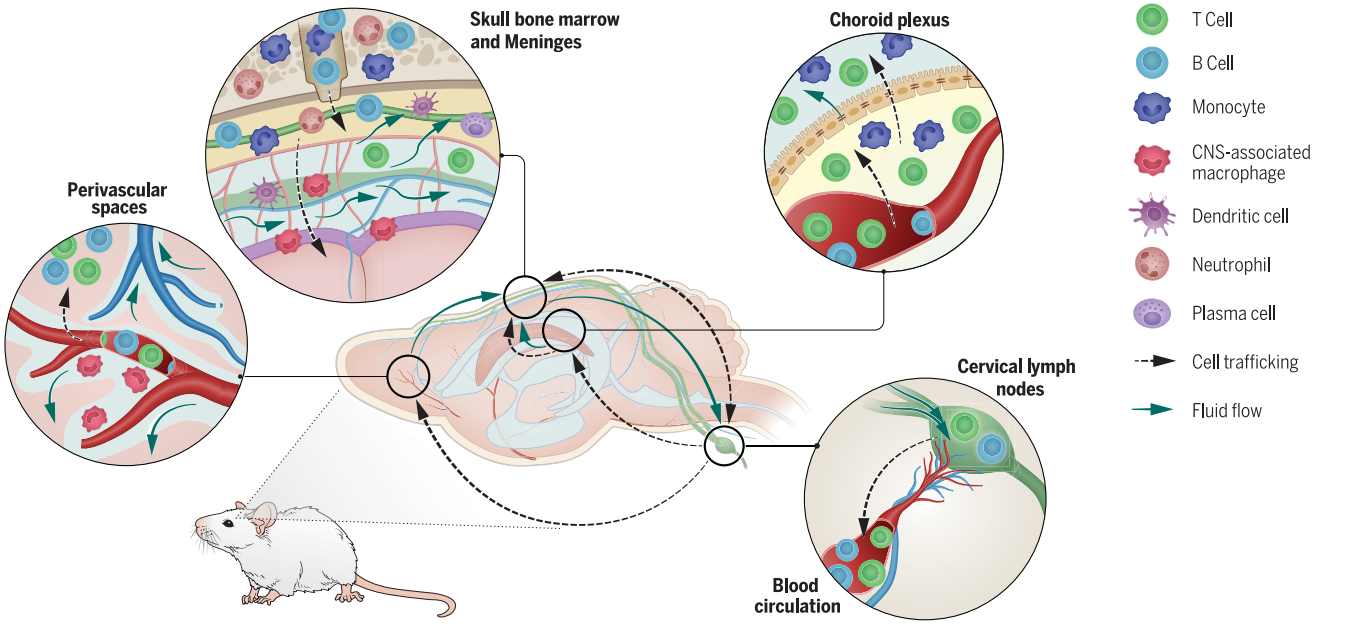

New perception of brain immunity. Shown is a representation of the communication network allowing fine-tuned brain immunosurveillance. The immune cells are strategically positioned in immunological niches, where they are constantly exposed to CNS cues transported by the intracranial interstitial, cerebrospinal, and lymphatic fluid. Upon sensing brain signals, the immune cells can migrate toward the CNS to exert their effector functions.

REVIEW

IMMUNOLOGY

Transforming the understanding of brain immunity

Giulia Castellani†, Tommaso Croese†, Javier M. Peralta Ramos†, Michal Schwartz*

Contemporary studies have completely changed the view of brain immunity from envisioning the brain as isolated and inaccessible to peripheral immune cells to an organ in close physical and functional communication with the immune system for its maintenance, function, and repair. Circulating immune cells reside in special niches in the brain's borders, the choroid plexus, meninges, and perivascular spaces, from which they patrol and sense the brain in a remote manner. These niches, together with the meningeal lymphatic system and skull microchannels, provide multiple routes of interaction between the brain and the immune system, in addition to the blood vasculature. In this Review, we describe current ideas about brain immunity and their implications for brain aging, diseases, and immune-based therapeutic approaches.

Until ~25 years ago, it was assumed that no immune activity was allowed within the brain, as evidenced by the limited rejection of tissues grafted into the brain compared with peripherally transplanted tissues (*1*, *2*). This view of the brain as "immune privileged" (*3*), together with a finding dating back to 1885 in which a dye peripherally injected into an animal was unable to penetrate the brain (*4*) because of the existence of a specialized barrier, later designated the blood–brain barrier (BBB) (*5*), led to the widely accepted belief that the brain is isolated from the peripheral immune system. Even the earlier discovery that the brain is equipped with a lymphatic system (*6*–*9*) was ignored, to the extent that the purported absence of lymphatic circulation was repeatedly mentioned in support of the brain's immune privilege (*10*, *11*).

Since the 20th century, several reports revealing the involvement of the immune system in autoimmune inflammatory diseases (e.g., multiple sclerosis) (*12*–*15*) and in neurodevelopmental disorders (*16*, *17*) have suggested a negative impact of the immune response in the central nervous system (CNS) in these contexts. Other studies focusing on neuroinflammatory diseases observed some adaptive immune cells even in the CNS of healthy mammals (*18*–*21*). Later, a physiological brain-immune interplay was suggested by the discoveries in animal models that bone marrow (BM)–derived macrophages (*22*) and T cells (*23*) support CNS protection and repair. In addition, T cells recognizing brain self-antigens were shown to be needed for normal brain function (*24*). Together, these findings led to the concept of "protective autoimmunity," indicating the beneficial properties exerted by self-recognizing immune cells in the CNS that are able to promote repair and healthy brain plasticity. It is now accepted that the lifelong formation of new neurons is supported by adaptive immune cells (*24*, *25*), whereas uncontrolled immunity, as in the case of inflammation, impairs neurogenesis (*26*, *27*). Subsequently, additional brain functions, including social behavior (*28*–*31*) and the brain's ability to cope with stress, were found to be dependent on the integrity of adaptive immunity (*32*). As a corollary, failure of immune regulation of critical processes during brain development, including neuronal synaptic pruning, results in a higher incidence of neurodevelopmental disorders (*33*–*35*).

Additional studies have identified specialized immunological compartments within the brain, including the meninges (*36*–*39*), the choroid plexus (*40*–*42*), and the perivascular spaces (*43*, *44*), forming niches from which immune cells could affect the CNS without interfering with its delicate neuronal network. These discoveries contributed to elucidating the role of various cell types of both CNS and peripheral origin strategically located at the borders of the brain (*28*–*30*, *36*, *37*, *40*, *45*) that provide remote surveillance. Other studies revealed a complex interplay between CNS immunity and the gut, as evidenced by the observation of gut-derived immunoglobulin A–expressing (IgA^+) plasma cells in murine and human meninges (*38*), and a close association between the gut microbiome and CNS disorders (*46*–*49*). With the description of brain lymphatic drainage (*50*, *51*) and the connection between the CNS and the skull BM (*52*–*54*), it is clear that the CNS has adopted mechanisms that enable tightly regulated communication with the immune system, which is crucial for a healthy brain (*36*, *38*–*40*) (Fig. 1). The innervation of lymphoid organs by the brain provides an additional route of brain-immune system communication, underlying the brain's ability to predict and suggest the appropriate immunological response required to restore homeostasis through a mechanism called immunoception (*55*–*58*).

In this Review, we describe the brain-immune relationship during development, adulthood, and aging; the recent discovery of anatomical niches in which immune cells are compartmentalized; the conditions under which such a relationship may go awry; and how such knowledge is expected to affect the next generation of therapies for CNS diseases.

Immune cells in the brain

Myeloid cells

It is now widely appreciated that brain-immune communication is needed for proper CNS function at all stages of life, from embryonic development to aging. The immune cells that support the brain include those that migrate to the CNS during embryonic development, which reside mainly in the brain parenchyma, and those that are derived from the blood circulation or potentially directly from the skull BM and home to the brain at different stages throughout life. Starting at embryonic day 9.5 (E9.5) in mice, premacrophage progenitors originating in the yolk sac migrate into the developing CNS (*59*) and gives rise to two brain-resident immune populations: parenchymal microglia (*60*) and CNS-associated macrophages (CAMs). Characterized by a low turnover, the CAMs can be distinguished by their location and transcriptomic profile (*61*, *62*). Because of their presence at the brain's borders, these cells are also known as border-associated macrophages (*63*). Only microglia and meningeal CAMs share a common prenatal origin; perivascular macrophages derive from postnatally established meningeal macrophages, and CAMs in the choroid plexus are partially renewed by blood-derived monocytes (*61*, *64*).

During brain development, microglia are involved in controlling neurogenesis, the fate of neural oligodendrocyte progenitor cells, and myelin formation (*65*, *66*). In addition, they affect neuronal survival through the phagocytosis of cellular debris, by releasing soluble factors including nerve growth factor and reactive oxygen species (*67*, *68*), by controlling synapse pruning through the complement system, and by engaging in complex interactions with various neuronal and non-neuronal cell types such as astrocytes (*33*, *69*–*74*) (Fig. 2A). Although astrocytes are not viewed as classical immune cells, they demonstrate immunological features in physiological and pathological conditions such as neuroinflammation (*74*–*78*), neurodegeneration (*79*–*83*), and brain cancer (*84*–*86*).

In adulthood, microglia serve as the sentinels of the brain. They have the capacity to morphologically and functionally adapt to their changing surroundings (*87*, *88*), and

Department of Brain Sciences, Weizmann Institute of Science, Rehovot, Israel.
*Corresponding author. Email: michal.schwartz@weizmann.ac.il
†These authors equally contributed to this work.

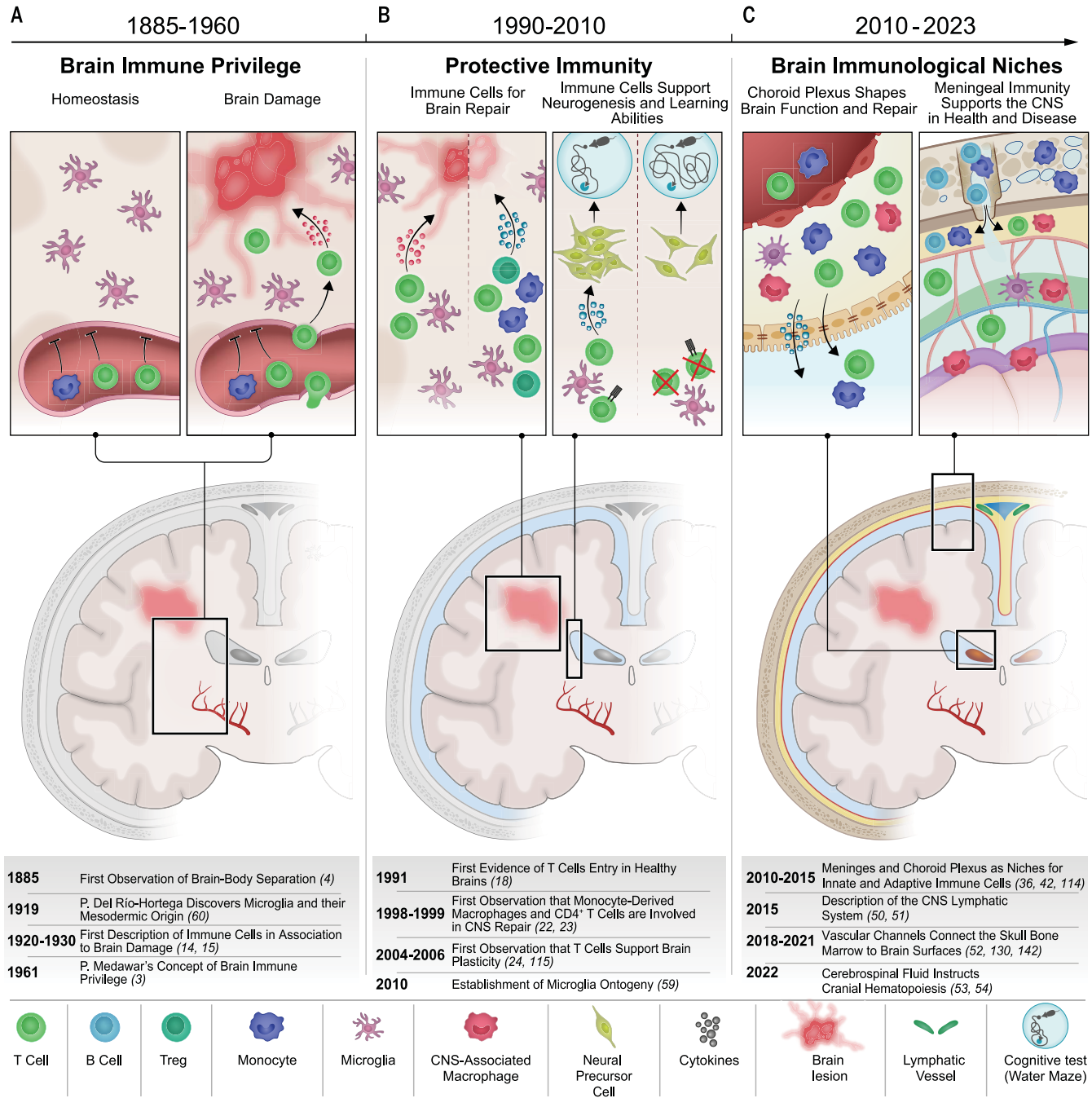
A
1885-1960
Brain Immune Privilege
Homeostasis
Brain Damage
1885 First Observation of Brain-Body Separation (4)
1919 P. Del Río-Hortega Discovers Microglia and their Mesodermic Origin (60)
1920-1930 First Description of Immune Cells in Association to Brain Damage (14, 15)
1961 P. Medawar's Concept of Brain Immune Privilege (3)
B
1990-2010
Protective Immunity
Immune Cells for Brain Repair
Immune Cells Support Neurogenesis and Learning Abilities
1991 First Evidence of T Cells Entry in Healthy Brains (18)
1998-1999 First Observation that Monocyte-Derived Macrophages and CD4+ T Cells are Involved in CNS Repair (22, 23)
2004-2006 First Observation that T Cells Support Brain Plasticity (24, 115)
2010 Establishment of Microglia Ontogeny (59)
C
2010-2023
Brain Immunological Niches
Choroid Plexus Shapes Brain Function and Repair
Meningeal Immunity Supports the CNS in Health and Disease
2010-2015 Meninges and Choroid Plexus as Niches for Innate and Adaptive Immune Cells (36, 42, 114)
2015 Description of the CNS Lymphatic System (50, 51)
2018-2021 Vascular Channels Connect the Skull Bone Marrow to Brain Surfaces (52, 130, 142)
2022 Cerebrospinal Fluid Instructs Cranial Hematopoiesis (53, 54)
T Cell
B Cell
Treg
Monocyte
Microglia
CNS-Associated Macrophage
Neural Precursor Cell
Cytokines
Brain lesion
Lymphatic Vessel
Cognitive test (Water Maze)

Fig. 1. Timeline describing the major milestones guiding the new understanding of brain immunity. The major advances that transformed the comprehension of brain immunity are classified into three periods, shown here in panels (A) to (C). (**A**) Discoveries in the first half of the 20th century that supported the concept of brain "immune privilege." According to this view, infiltration of immune cells was invariably associated with CNS inflammation and disease states. (**B**) Early discoveries starting at the end of the 20th century attributing a role in CNS maintainance and repair to the immune response and the subsequent discovery that immune cells affect neurogenesis and cognition. (**C**) Identification of distinct immune niches within the brain, from which innate and adaptive immune cells can modulate brain function and repair.

they are key players in CNS homeostasis to the extent that their dysregulation can lead to neurodegeneration in mice (*89*). Microglia are tightly controlled by several immune checkpoints, including the fractalkine–CX_3C chemokine receptor 1 (CX3CR1) axis and the OX-2 membrane glycoprotein (also called CD200)–CD200 receptor pathway (*90*). In the aged brains of both humans and mice, microglia accumulate lipid droplets, a known feature of aged microglia and impaired metabolism (*91*); lose their motility; produce high levels of reactive oxygen species and proinflammatory cytokines (*91*); and show a robust type I interferon (IFN) transcriptional signature that is associated with an impaired ability to attenuate neuroinflammation (*92*). As a result, such microglia might contribute to BBB disruption (*93*), negatively affect adult neurogenesis (*27*, *94*, *95*), and mediate the loss of functional synapses in mice (*96*). Furthermore, phagocytic

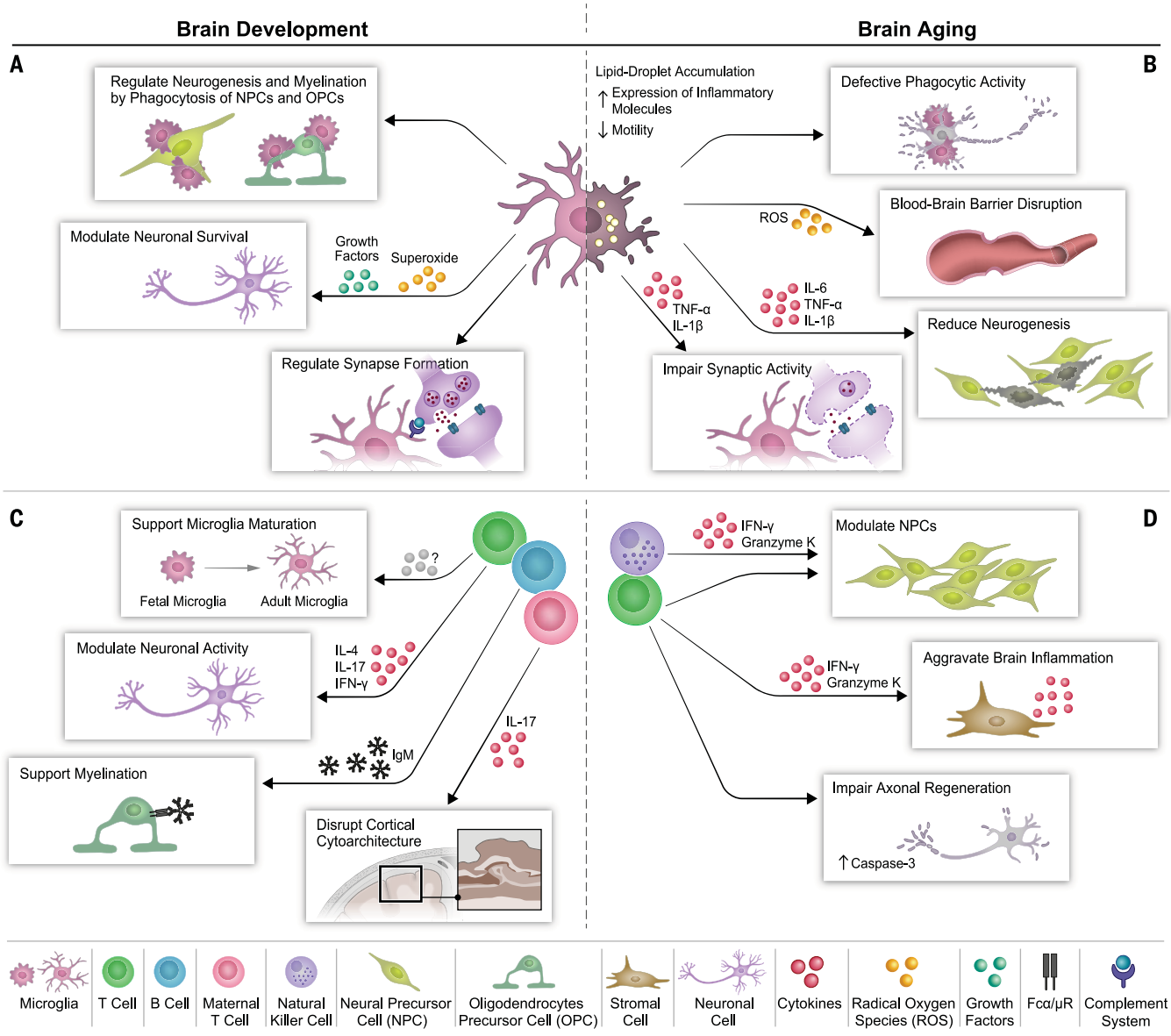

Fig. 2. Effects of microglia and adaptive immune cells during brain development and aging. Shown are schematic representations of some of the main mechanisms through which microglia [(A) and (B)] and lymphocytes [(C) and (D)] interact with neuronal and non-neuronal cell types and affect brain functions. (**A**) Mechanisms by which microglia contribute to healthy brain development. (**B**) Morphological and functional changes of aged microglia and their consequence for age-related neurodegeneration. (**C**) Effect of B and T lymphocytes during brain development. (**D**) Mechanisms by which lymphocytes that infiltrate the brain parenchyma can contribute to brain aging.

clearance of protein aggregates and cellular debris by microglia deteriorates during aging (*91*, *97*) and neurodegenerative disease (*98*, *99*), concomitant with cognitive decline (Fig. 2B). Inhibition of the B cell receptor CD22 protein, a negative regulator of phagocytosis that is up-regulated in aged microglia, was found to restore the phagocytic capacity of microglia in vivo and to improve cognition in aged mice (*97*). In addition, in aged mice, myeloid cells enter an energy-deficient state characterized by sequestration of glucose into glycogen, reduced glucose metabolic flux, and reduced mitochondrial respiration. Restoration of their metabolic function by selectively inhibiting the receptor for the lipid messenger prostaglandin E2 was sufficient to rescue hippocampal memory function and long-term potentiation in mice. A similar effect was observed when metabolic functions were restored in aged peripheral myeloid cells, but not in aged microglia, highlighting the relevance of both intact CNS and peripheral immune activity in maintaining CNS health (*100*). Transcriptome-wide association studies of human microglia show that these cells age in a generally uniform manner across brain regions (*101*, *102*). Changes in microglial gene expression in aged mice showed an overrepresentation of genes associated with Alzheimer's disease (AD) and Parkinson's disease (PD), suggesting that overlapping processes might occur in aging and neurodegenerative conditions (*91*, *101*).

Adaptive immune cells

In addition to the various myeloid cells, adaptive immune cells recruited from the circulation have been implicated in brain development, function, and aging. It is still unclear at which stage of brain development lymphocytes infiltrate the CNS. In mice, depletion of $CD4^+$

T cells at postnatal day 5 prevents microglial maturation, causing multiple behavioral abnormalities. No detrimental effect was observed in mice when T cells were depleted 3 weeks after birth (*103*), suggesting a critical time-dependent role of adaptive immune cells in brain development. Nevertheless, as much as innate and adaptive immune cells are needed for healthy brain development, their dysfunction may also negatively affect neurodevelopmental processes. For example, transient viral infection of the mouse brain in the first week of life generates long-lived T cells in the brain that confer enhanced vulnerability to autoimmune episodes, as shown in a mouse model of multiple sclerosis (*104*). Similarly, the presence of maternal interleukin-17 (IL-17)–secreting lymphocytes in the CNS of E14.5 offspring has been linked to cortical defects and abnormal behavior in mice (*34*). Conversely, murine fetal-derived γδ T cells colonize the brain before birth; persist throughout life; and control synaptic plasticity, short-term memory, and anxiety-like behavior, also through the release of IL-17 (*29*, *30*). During brain development, immune cells can also indirectly affect synapses and neuronal functions by modulating microglial activation and the activity of other non-neuronal cells (*103*, *105*–*109*). For example, B lymphocytes infiltrate the murine brain as early as E16 and contribute to oligodendrogenesis and myelination by promoting oligodendrocyte precursor cell proliferation through immunoglobulin M–Fcα/μR signaling (*110*) (Fig. 2C).

Multiple aspects of murine brain plasticity have been shown to be supported by $CD4^+$ T cells in adulthood, including coping with mental stress (*111*–*113*) and preserving cognitive function (*24*, *25*, *36*, *41*, *114*) and social behavior (*28*). Further support for the relevance of a healthy immune system in maintaining intact brain function was provided by the demonstration that replacement of BM from healthy mice with BM derived from severe combined immunodeficient (SCID) mice induces cognitive impairment (*115*). In many of the cases in which $CD4^+$ T cells were found to support healthy brain function, the observed effect was shown to be mediated, at least in part, through remote mechanisms based on the release of cytokines upon encounter of immune cells with their cognate antigens at the brain's borders (*28*, *36*, *41*). Metabolic fitness of $CD4^+$ T cells is also critical for adult brain function, because animal models carrying T cell mitochondrial dysfunction that recapitulate classic features observed in aging can develop signs of neurological disability as early as 2 months of age (*116*).

Although $CD4^+$ T cells provide crucial support for the maintenance of brain health, brain aging is often associated with local innate inflammation. Clonally expanded IFN-γ–producing $CD8^+$ T cells can infiltrate neurogenic niches of aged mice and inhibit the proliferation of neural stem cells, as shown both in co-cultures and in vivo (*117*). Conversely, cognitive impairment in aged and AD mouse models was found to be associated with the loss of IFN-γ–producing $CD4^+$ T cells at the choroid plexus (*118*, *119*). This indicates that a given cytokine can display opposite effects in aging, depending both on its cellular origin and location. Moreover, natural killer (NK) cells, a type of innate cytotoxic lymphocyte, accumulate during aging in close proximity to the neurogenic niches, where they outnumber other BM-derived cells and contribute to neurogenic decline (*47*). At late stages of life, $CD8^+$ T cells bearing markers of exhaustion have been shown to expand and secrete high amounts of granzyme K, which might then induce or perpetuate brain inflammation (*112*). These cells might also be responsible for the reduced ability of the aged CNS to recover from injury. Indeed, older mice express elevated levels of the chemokine C-X-C motif chemokine 13 (CXCL13) in the dorsal root ganglia, promoting the recruitment of $CXCR5^+$ $CD8^+$ T cells and the activation of caspase-3 in neurons, resulting in their failure to regenerate after nerve injury (*120*) (Fig. 2D).

Overall, it is becoming clear that a tight communication between the CNS and the immune cells is essential for proper functioning of the brain during both development and adulthood. Indeed, immune system aging in mice was shown to be sufficient to drive aging of solid tissues, including the brain (*121*). Therefore, an alteration in brain-immune cross talk could be considered an escalating factor in brain aging or neurodevelopmental disorders and has been shown to contribute to neurodegenerative diseases (Table 1).

Immunological niches in the CNS borders

The brain's anatomical borders, including the BBB, the meninges, and the blood–cerebrospinal fluid (CSF) barrier (BCSFB) were assumed to function solely as barriers between the periphery and the brain. With the emerging understanding of brain-immune interactions, the BBB is still considered a true barrier, whereas other anatomical interfaces function as sites that differentially host immune cells implicated in the surveillance and defense of the brain. Various innate and adaptive immune cells populate the meninges surrounding the CNS, the choroid plexus within the brain's ventricles that contain CSF, and the perivascular spaces. In addition to these, the skull BM provides rapid access of immune cells to the brain through microscopic channels within the skull, and the brain-draining cervical lymph nodes (CLNs), an additional compartment that acts as an immune interface between the CNS and systemic immunity, collect lymphatic fluid from the brain through the meningeal lymphatic system (Fig. 3). A variety of immune cells that reside in the special anatomical structures described above are involved in the surveillance of the brain, facilitating a rapid immune response upon sensing danger signals or preventing the spread of peripheral pathogens (*29*, *30*, *37*, *38*, *40*, *122*). In health, immune cells located at the brain's borders can remotely control CNS function by secreting several mediators, including cytokines and neurotrophic factors (*29*, *30*, *36*, *119*). Alternatively, they can access the CNS parenchyma to locally exert their immunomodulatory activity upon sensing chemotactic signals secreted in response to damage, providing additional support to resident microglia (*123*). Although previous studies have suggested a detrimental role for resident CAMs in mouse models of neuroinflammation (*62*) and neurodegeneration (*43*, *124*, *125*), the mechanisms through which immune cells located at the brain's borders can contribute to disease progression require further investigation.

Meninges

For decades, the meninges were assumed to provide mainly physical protection for the brain and spinal cord, but it has recently become clear that they might also serve as an immune compartment. This tissue consists of several layers: the inner pia mater, the arachnoid mater in the middle [which is divided into two functional compartments by the recently discovered subarachnoid lymphatic–like membrane (SLYM) (*126*)], and the external dura mater. The meninges are located underneath the cranium and are separated from it by an epidural space containing fat and blood vasculature. The dura is mainly composed of dense connective tissue including fibroblasts and extracellular collagen. The dural layer hosts sinuses responsible for venous drainage emptying into the internal jugular veins (*127*) and the lymphatic vasculature that connects the brain with the CLNs, ensuring the drainage of CNS waste. Residing beneath the dura, the arachnoid mater consists of an additional layer of connective tissue. More internally, the subarachnoid space, which lies between the arachnoid and pia mater, is filled with CSF and is connected to the fourth ventricle of the brain through the median aperture and paired lateral apertures. In humans, some arachnoid mater protrusions called arachnoid granulations extend into the dura mater, channeling the CSF into the dural veins and thereby connecting the different meningeal layers. Within the subarachnoid layer, the SLYM constitutes a quasi-impermeable monolayer of lymphatic cells and loosely organized collagen fibers that prevents the exchange of CSF solutes larger than 3 kDa between the inner and outer subarachnoid space compartments. The SLYM

Table 1. Brain-immune interactions: Implications for neurodevelopmental and neurodegenerative disorders. Table summarizes the findings that describe the involvement of immune cells in the pathogenesis of neurological disorders.

Disease	Cell type	Observation
ASD	$CD4^+$ T cells	ASD-like phenotypes in the poly I:C–induced maternal immune activation model are associated with $ROR\gamma t^+$ maternal T cells (*34*)
		Diminished T_{regs} in children with ASD and high levels of $CD4^+$ T_H17 cells in children with comorbidity of ASD and gastrointestinal symptoms (*160*)
		Reduced T_{regs} and higher levels of $ROR\gamma t^+$, T-bet^+, and GATA-3^+ $CD4^+$ T cells in a mouse model of ASD (*161*)
	Monocytes	Dysregulated peripheral blood monocyte response in children with ASD (*162*)
	NK cells	Highly activated and dysfunctional $NKG2C^+$ NK cells in the blood of adults with high-functioning ASD (*163*)
AD	T cells	T cell deficiency accelerates disease progression in the 5xFAD mouse model of AD (*164*)
	$CD4^+$ T cells	Transient depletion of $FOXP3^+$ T_{regs} attenuates disease pathology in the 5xFAD mouse model of AD (*165*)
	$CD8^+$ T cells	Clonally expanded $CD8^+$ T cells accumulate in the CSF of sporadic AD patients, inversely correlating with cognition (*166*)
	Neutrophils	Neutrophils have a negative impact on disease pathology and cognitive performance in the 5xFAD, 3xTg, and APP/PS1 mouse models of AD (*167*, *168*)
	Monocytes	Peripheral monocytes undergo functional alterations along disease progression in sporadic AD (*169*)
		Monocytes are disease modifying in both amyloid β- and tau-driven mouse models of AD and dementia, respectively (*170*–*172*)
	NK cells	Proinflammatory NK cells contribute to disease pathology and cognitive impairment in the 3xTg mouse model of AD (*173*)
PD and synucleinopathies	$CD4^+$ T cells	Circulating αSYN-specific $CD4^+$ T_H cells are found before symptom onset, potentially driving PD (*174*–*176*)
		Clonally expanded $CD4^+$ T_H17 cells may contribute to neurodegeneration in individuals with Lewy body dementia (*177*)
		Human MSA-derived αSYN triggers a differential $CD4^+$ T cell immune response in rat brain (*178*)
		$CD4^+$ T cells accumulate in the substantia nigra of postmortem MSA brains (*179*)
	$CD8^+$ T cells	Circulating αSYN-specific cytotoxic T cells may drive PD (*174*)
		Human MSA-derived αSYN triggers a differential $CD8^+$ T cell immune response in rat brain (*178*)
		$CD8^+$ T cells accumulate in the substantia nigra of postmortem MSA brains (*179*)
	Neutrophils	High neutrophil:lymphocyte ratio is a prognostic biomarker for poor survival in MSA but not for PD patients (*180*, *181*)
	Monocytes	αSYN-mediated degeneration of dopamine-releasing neurons is associated with infiltration of peripheral monocytes in a mouse model of PD (*182*)
	NK cells	Systemic depletion of NK cells exacerbates αSYN-associated pathology in a mouse model of α-synucleinopathy (*183*)
ALS	$CD4^+$ T cells	$CD4^+$ T cells slow disease progression in an animal model of ALS (*184*, *185*)
		Patient-derived T_{regs} exhibit impaired suppressive function, correlating with disease progression (*186*)
	Neutrophils	High neutrophil:lymphocyte ratio is proposed to predict short survival in ALS (*187*)
	Monocytes	Accumulation of monocyte-derived macrophages in the spinal cord alleviates disease progression and extends life span in an ALS mouse model (*136*)
	NK cells	NK cells exacerbate disease progression in a sex- and age-dependent manner in a mouse model of ALS (*188*)
		NK cells are linked with motor neuron loss by impairing $FOXP3^+$ T_{regs} accumulation in the spinal cord of ALS mice (*189*)
Acute injuries	T_{regs}	T_{regs} suppress astrogliosis and potentiate neurological recovery after stroke (*123*)
		Brain-specific IL-2 gene delivery drives T_{reg} expansion and potentiates neurological recovery after stroke (*77*)
	Monocytes	Monocyte-derived macrophages support recovery after stroke in patients (*190*)
		Macrophages reduce inflammation after CNS injury (*42*, *191*)

ASD, autism spectrum disorder; poly I:C, polyinosinic:polycytidylic acid; T_H, T helper; αSYN, α-synuclein; MSA, multiple system atrophy

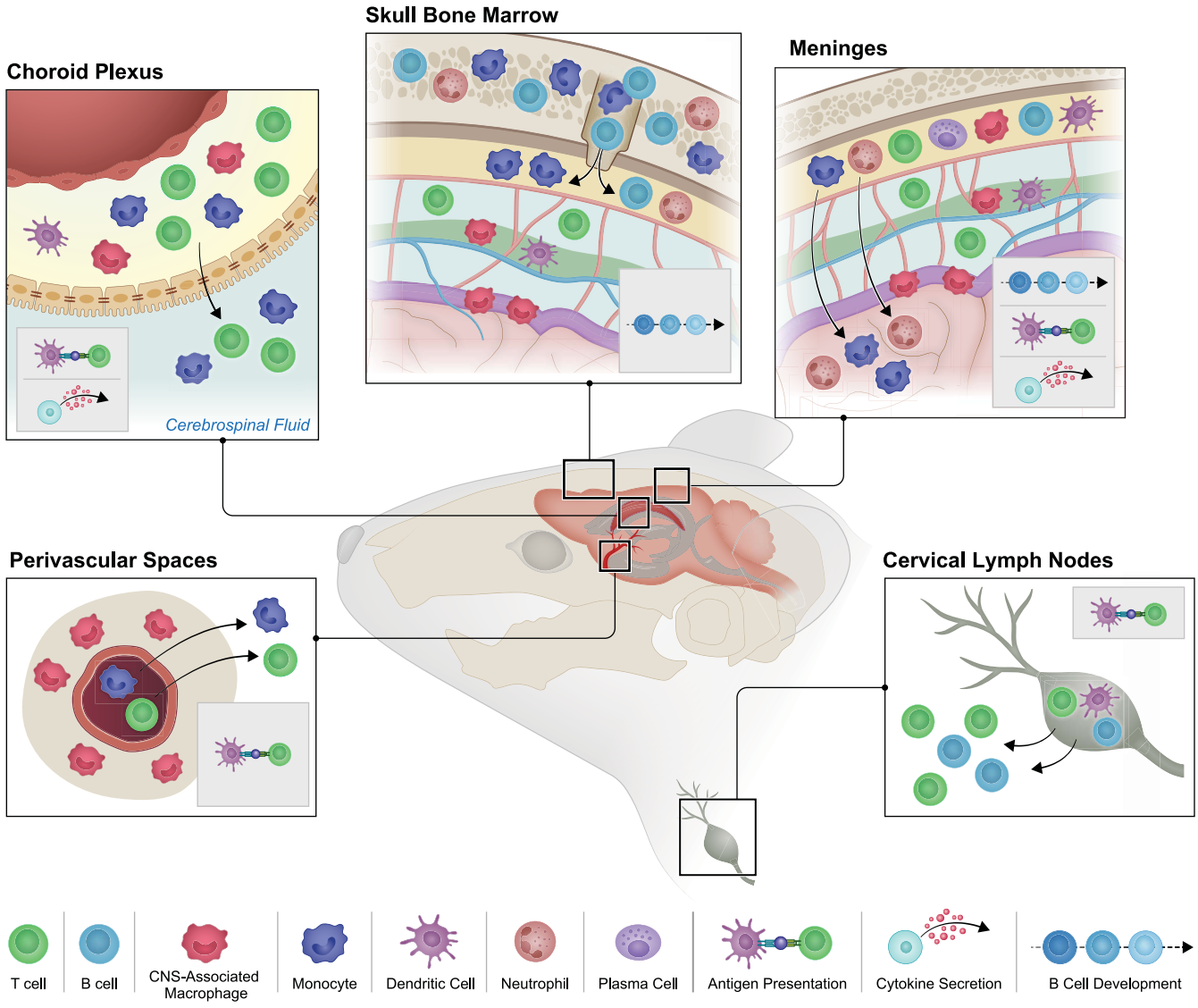

Fig. 3. The brain's borders and routes connecting the periphery to the brain. Shown is a depiction of the compartmentalization of immune cells within and near the mouse brain, illustrating the cell types homing to the various immunological niches in a homeostatic state: perivascular spaces, choroid plexus, skull bone marrow, meninges, and draining CLNs. The immunological processes that have been described at these sites in both health and disease are also shown: antigen presentation, cytokine secretion, and B cell development. Arrows indicate the preferred routes connecting these immunological niches and the brain, which have been documented under various pathological conditions.

presents traits of a mesothelium, which potentially contributes to reduce friction between the skull and brain. The juxtraposition of the SLYM and the venous endothelium represents the rodent equivalent of the arachnoid granulations (*126*). The highly vascularized pia mater is the thin inner membrane of the meninges that adheres to the surface of the CNS parenchyma.

Distinct roles have been attributed to the different meningeal layers in the context of local inflammation (*128*). The meninges were recently found to be largely populated by lymphocytes and antigen-presenting cells (APCs) such as CAMs and dendritic cells (DCs), which present antigens derived from the CSF or the parenchyma to T cells (*37*, *126*, *128*). For instance, in the dura, the formation of a specialized neuroimmune interface is supported by stromal cells including mural and endothelial cells, which are able to coordinate the recruitment and homing of CNS antigen-specific T cells, mainly through the release of chemokines. Leukocytes expressing the chemokine receptors CXCR4 and CXCR6 are then recruited by homeostatic chemokines such as CXCL12 and CXCL16, whereas CX3CR1^{+} CAMs can be attracted by fractalkine (*37*). Additionally, stromal cells were shown to produce essential factors for leukocyte survival, recruitment, and polarization. Among such factors are the KIT ligand, which is important for mast cell survival; insulin-like growth factor I (IGF1), which acts in the suppression of autoimmunity by T regulatory cells (T_{regs}); and macrophage colony–stimulating factor 1 and fractalkine, which are associated with macrophage function (*37*). This perisinusal hub provides a convenient physiological mechanism to sample CNS-derived antigens, because it is strategically positioned at the site of CSF exit into the dural sinuses, which might be associated with

local T cell activation. Gut-derived IgA$^+$ plasma cells are among the CXCR4-expressing leukocytes found under homeostatic conditions adjacent to the dural venous sinuses, a vulnerable site where they can easily encounter blood-borne pathogens and prevent their spreading into the brain (*38*).

Evidence for the association among intact meningeal immunity, behavioral traits, and brain protection comes from the demonstration that murine meningeal γδ T cells regulate anxiety by affecting a subpopulation of cortical glutamate-releasing neurons (*29*, *30*) and from the above-mentioned meningeal IgA$^+$ plasma cells that are essential for defending the brain from fungal spread (*38*). Furthermore, IFN-γ– and IL-4–producing meningeal T cells can support neuronal circuits associated with social behavior (*28*) and cognition (*36*, *129*). The meninges were recently shown to provide a niche for the development of immature B cells that migrate from the skull BM through microchannels (*39*, *45*, *130*). Additionally, it was suggested that the meninges are equipped with a mechanism that allows for the elimination of CNS-reactive B cells through a process of negative selection by apoptosis in the dura (*39*). Overall, the meninges, particularly the dura, are viewed as fundamental immunological niches where antigens can be sensed and presented and where various immune cells release cytokines that affect brain function. In addition to numerous studies describing the immunological features of the meninges, a well-defined description of dural lymphatic vessels (*50*, *51*) revealed a previously ignored interconnection between the brain and the CLNs, enabling the peripheral immune system to sense and potentially respond to CNS signals.

Choroid plexus

Positioned at the border between the vasculature and the CSF and located in each brain ventricle, the choroid plexus forms the BCSFB. Even though it was initially studied for its role in regulating the composition and volume of the CSF, its function as a unique neuroimmunological niche, engaging signals both from circulating immune cells and the CNS parenchyma, became clearer only in recent years. The choroid plexus is primarily composed of tightly connected epithelial cells surrounding a highly vascularized stroma containing mesenchymal, glial, neuronal, and immune cells (*131*). Its neuroimmunological activity relies on the ability of the choroid plexus to sense and adapt to peripheral inflammation (*122*) and its intrinsic capacity to host different immune cell populations.

Recent technical advances in imaging and single-cell transcriptomics have begun to fully elucidate the architecture, immune composition, and signaling occurring at the choroid plexus. A comprehensive single-cell and spatial atlas of the choroid plexus revealed both ventricle- and age-dependent transcriptional signatures in epithelial cells and fibroblasts, demonstrating enhanced IL-1β signaling among resident CAMs in the aged choroid plexus (*131*), ultimately leading to age-associated inflammation ("inflammaging"). Various immune cells populate the choroid plexus (*40*, *131*). Macrophages in particular are largely represented and are either localized to the apical surface as Kolmer's epiplexus cells, where they are constantly exposed to the CSF, or to the stromal space as choroid plexus CAMs, where they more closely communicate with mesenchymal cells and might sample blood-derived factors that freely diffuse from the fenestrated blood vessels within the stroma. Such environmental cues shape these specialized resident macrophages with distinct host defense and surveillance behavior, as shown after a peripheral immune challenge or local injury in mice (*132*). Although these cells exhibit relatively stationary cell bodies, their processes have high motility and continuously monitor their surroundings, showing contact-mediated retraction after interaction with other neighboring immune cells (*132*). This steady-state surveillance behavior is similar to that of other brain-resident myeloid cells such as microglia (*88*) and supports the involvement of the choroid plexus in the response to inflammatory insults coming from both the periphery and the brain (*40*, *122*). Accordingly, involvement of the choroid plexus has been reported in neuroinflammatory processes, as shown by the release of extracellular vesicles into the CSF by the choroid plexus epithelium after systemic-induced inflammation (*133*) and during AD pathogenesis in transgenic mice (*134*).

The choroid plexus is a diverse and dynamic hub of immune cell activity and has also been suggested to be a selective and tightly regulated physiological gateway to the CNS for immune cells (*42*). This niche is particularly enriched in major histocompatibility complex II–expressing APCs (*63*) and can serve as an entry site for infiltrating T cells and macrophages, as shown after acute CNS injury in mice (*42*, *135*) and in an animal model of amyotrophic lateral sclerosis (ALS) (*136*). Transepithelial migration of leukocytes through the choroid plexus is dependent on type II IFN signaling through the IFN-γ/IFN-γ receptor axis (*40*). IFN-γ, which can be produced by CD4$^+$ effector memory T cells located within the choroid plexus stroma, can stimulate the epithelium to specifically express adhesion molecules and various chemokines, which can support the mobilization of inflammation-resolving immune cells toward the CNS after injury (*40*). By contrast, increased levels of type I IFN observed in the choroid plexus during aging (*41*) and in neurodegenerative diseases such as AD (*118*, *137*) affect microglial function in a remote manner, resulting in impaired cognitive performance in mice (*92*, *137*). Moreover, single-cell transcriptomic analyses of choroid plexi isolated from post-mortem brains of patients with AD, frontotemporal dementia, and Huntington's disease revealed a common signature (*138*), implying a potentially similar cross-talk among the periphery, the choroid plexus, and the brain across different neurodegenerative conditions. Taken together, these studies highlight the role of the choroid plexus as a brain barrier and immunological hub that serves as a critical route of access for immune cells from the periphery into the brain.

Perivascular spaces

Small blood vessels (arterioles, capillaries, and venules) that supply the brain penetrate the CNS parenchyma and are surrounded by CSF-filled compartments called perivascular spaces or Virchow-Robin spaces. These compartments are bordered by an endothelial basement membrane on the abluminal side of the vessel wall and a network of astrocytic processes on the parenchymal side called the glia limitans perivascularis. The two basement membranes fuse and restrict the perivascular space at the site at which the arteries turn into arterioles and finally into small capillaries. This intricate architecture, which may also involve astrocytic aquaporin-4, serves as a "glymphatic" drainage system that provides a clearance route for CNS-derived antigens, metabolites, and molecules (*139*). Although immune cells are prevented from exiting the bloodstream through the capillaries, leukocyte recruitment occurs preferentially in postcapillary venules, which allow T cells to reach the perivascular space, where they can recognize their cognate antigen on resident APCs, leading to local activation and subsequent migration across the glia limitans and into the CNS parenchyma (*140*).

All brain-resident myeloid cells, including the specialized perivascular CAMs residing in this compartment, belong to the innate immune system, which acts as the first line of defense, surveillance, and protection during neuroimmune interactions (*63*, *64*). Recent data demonstrated that perivascular (and leptomeningeal) macrophages regulate CSF flow dynamics, which affects the circulation of cytokines and antigens through the parenchyma by arterial pulsation (*44*). Moreover, these macrophages have a role in extracellular matrix protein deposition and consequently regulate CNS perfusion and clearance, processes that are impaired in aging and AD (*44*). Accordingly, during neurodegeneration, selective activation of perivascular CAMs has been shown to reduce the levels of pathogenic amyloid-β_{42} (*141*). Overall, additional functional studies specifically focused on perivascular cells are required to better elucidate their role in the pathogenesis and progression of brain diseases.

Immunological compartments interconnected with the CNS

Skull BM

The exact source of BM-derived immune cells within the brain has not been comprehensively explored to date. Recently, it was found that immune cells from the skull BM can home directly to the meninges in mice (*52*). In vivo cell labeling and tracking showed migration of murine myeloid cells and B cells from the skull BM into the dura through microvascular channels crossing the inner skull cortex (*52*, *130*, *142*). Tracking analysis with a CSF tracer demonstrated that these conduits allow CSF outflow and flushing of the skull BM both in mice (*53*, *54*) and in humans (*143*). Thus, the CSF shapes the skull BM microenvironment, exposing BM cells to CNS cues (*53*, *54*). In turn, exposure to CSF signals was shown to promote myelopoiesis in an experimental setting of spinal cord injury (*53*, *54*) and to enable the egress of myeloid cells, particularly neutrophils. The latter are well-known responders to inflammatory signals that migrate from the BM into the murine meninges in models of both stroke and aseptic meningitis (*53*, *54*, *143*). Overall, the identification of the skull BM as a reservoir of innate immune cells uniquely exposed to CSF cues reveals a mechanism whereby the CNS can promptly mount an immune response during the early stages of an infection or sterile inflammation. In a mouse model of multiple sclerosis, CNS-reactive T cell migration in the skull and vertebral BM has been found to augment myelopoiesis (*144*), which could account for the infiltration of the myeloid cells contributing to disease progression (*144*, *145*). The relevance of BM myelopoiesis to neurodegenerative and neurodevelopmental disorders remains to be elucidated. These studies could eventually lead to new advanced approaches based on the modulation of CSF composition for the treatment of various CNS-related disorders.

CLNs

The CLNs are secondary lymphoid organs located in proximity to the jugular artery in the throat. They drain the extracellular fluid from the brain through the lymphatic vasculature arising from the dural sinuses (*50*, *51*). The first description of the brain lymphatic system was reported in 1787 (*6*), and this description was confirmed years later (*7*–*9*, *146*). However, because of the notion that the brain was immune privileged, the misconception that the brain lacks a drainage system persisted until more recent findings shed new light on meningeal lymphatics (*50*, *51*). The CLNs are sites at which peripheral lymphocytes can be primed toward brain-derived antigens. This event could lead to expansion of autoreactive immune cells, as observed in mouse models of multiple sclerosis (*147*), or to the formation of protective autoimmune T cells or T_{regs}, as shown after ischemic stroke in mice (*123*). This process can occur upon drainage of free soluble antigen from the CNS into the CLNs or by APC-mediated antigen transport, a mechanism previously described for DCs (*148*, *149*). Once an antigen enters the CLNs, as occurs in other lymph nodes, it is likely that an adaptive immune response is initiated by engaging both B and T cells (*147*, *150*). The primed T cells, together with plasma cells, might then be released from the CLNs into the circulation and reach the choroid plexus and the meninges to locally exert their function. This system is most likely aimed at mobilizing peripherally derived lymphocytes to participate in tissue protection. Indeed, CLN-derived type-1 regulatory T cells (Tr1) were shown to suppress astrocyte activation and CNS inflammation in mouse models of progressive multiple sclerosis, providing neuroprotection by reducing the recruitment of peripheral monocytes and attenuating the inflammatory milieu in the CNS (*151*). Similarly, CLN-derived T_{regs} might also suppress neurotoxic astrogliosis in a mouse model of ischemic stroke (*123*). In this experimental setting, C-C motif chemokine 1 (CCL1) and CCL20 were found to play key roles in recruiting T_{regs} into the brain, whereas IL-2, IL-33, and serotonin drove T_{reg} expansion at the infarcted brain region (*123*).

The crucial role of the draining CLNs in brain protection has been corroborated by studies in mouse models of both aging and AD, which showed reduced cognitive abilities in mice subjected to resection or ligation of CLNs (*152*–*154*). Because CLNs sense signals indicating deviation from homeostasis in the CNS by continuously scanning brain-derived lymphatic fluid, further investigation of its immune function might offer new therapeutic opportunities for neurological disorders.

The well-controlled brain immunosurveillance involving different immune niches relies on cooperation among them. For example, it is likely that CNS-derived antigens reach the CLNs through lymphatic drainage, where they can prime local lymphocytes that in turn migrate through the bloodstream and into the CNS borders, including the meninges and the choroid plexus (Fig. 4). Upon recognition of their cognate antigen within the niches at the CNS borders, T cells can become activated by DCs and macrophages, which were shown to take part in the process of sampling and antigen presentation within the dural sinuses (*37*). Additional data suggest that antigen presentation might also occur at the choroid plexus (*155*) and leptomeningeal layers, as evidenced in mouse models of multiple sclerosis (*128*). Although there is limited evidence for thymic presentation of brain-derived antigens during negative selection, it is possible that low-affinity, CNS-specific T cells might egress from the thymus as potential brain-protective T cells (*156*, *157*). This could explain the mechanism underlying the presence of $CD4^+$ T cells reported in the healthy CNS (*24*, *36*, *115*). Conversely, dysregulation of this process can give rise to encephalitogenic CNS-reactive T cells and brain autoimmunity in the context of multiple sclerosis (*156*). Although little is known about the role of autoreactive B lymphocytes in the brain, it was shown that the meninges can potentially exclude CNS-reactive B cells (*39*). In general, such a sequence of events highlights the intricate network existing between immunological niches and the occurrence of biological processes allowing the brain to be shielded from uncontrolled immune attacks.

A transformed view of the immune privilege of the brain

The emerging evidence of CNS-immune interactions, summarized above, substantially changed our understanding of the physiology of the brain, which had been assumed to be immune privileged. Several discoveries challenged this classic view of brain immunity. Among them are the notions of brain dependency on immune system integrity (*24*, *25*, *28*, *36*, *115*); of the choroid plexus as an immunological gateway regulated by immunological stimuli (*40*, *42*, *122*, *132*, *133*, *135*); and of the meninges as a site for immune surveillance, B cell development, and negative selection (*28*–*30*, *36*–*39*, *45*, *130*). Other findings include the description of the brain's lymphatic system (*50*, *51*) and the exposure of CLNs to CNS-derived signals. Additional new evidence for brain-immune interactions comes from the discoveries that the CSF can flush the skull BM and, thereby, influence hematopoiesis (*53*, *54*, *143*), and that the skull BM is a potential a reservoir of immune cells that are able to directly migrate into the CNS (*52*, *130*, *142*). Together, these discoveries helped to set the stage for an important paradigm shift, from attributing CNS immune surveillance solely to resident microglia to acknowledging the existence of a complex brain-immune network involving multiple peripheral immunological players. Because of the presence of a physical inert barrier (the BBB) and the distinct relationship of the CNS with immunological niches that are constantly exposed to danger cues, engaging in surveillance and acting as educational gates that provide active permissive immunomodulatory passageways, the brain's privilege has gained a new meaning. This revised interpretation of the immune privilege refers to the ability of the brain to access immune cells in its immediate vicinity, rather than being immune isolated.

Another tissue that is encased in several barriers separating it from the circulation and therefore is considered immune privileged is

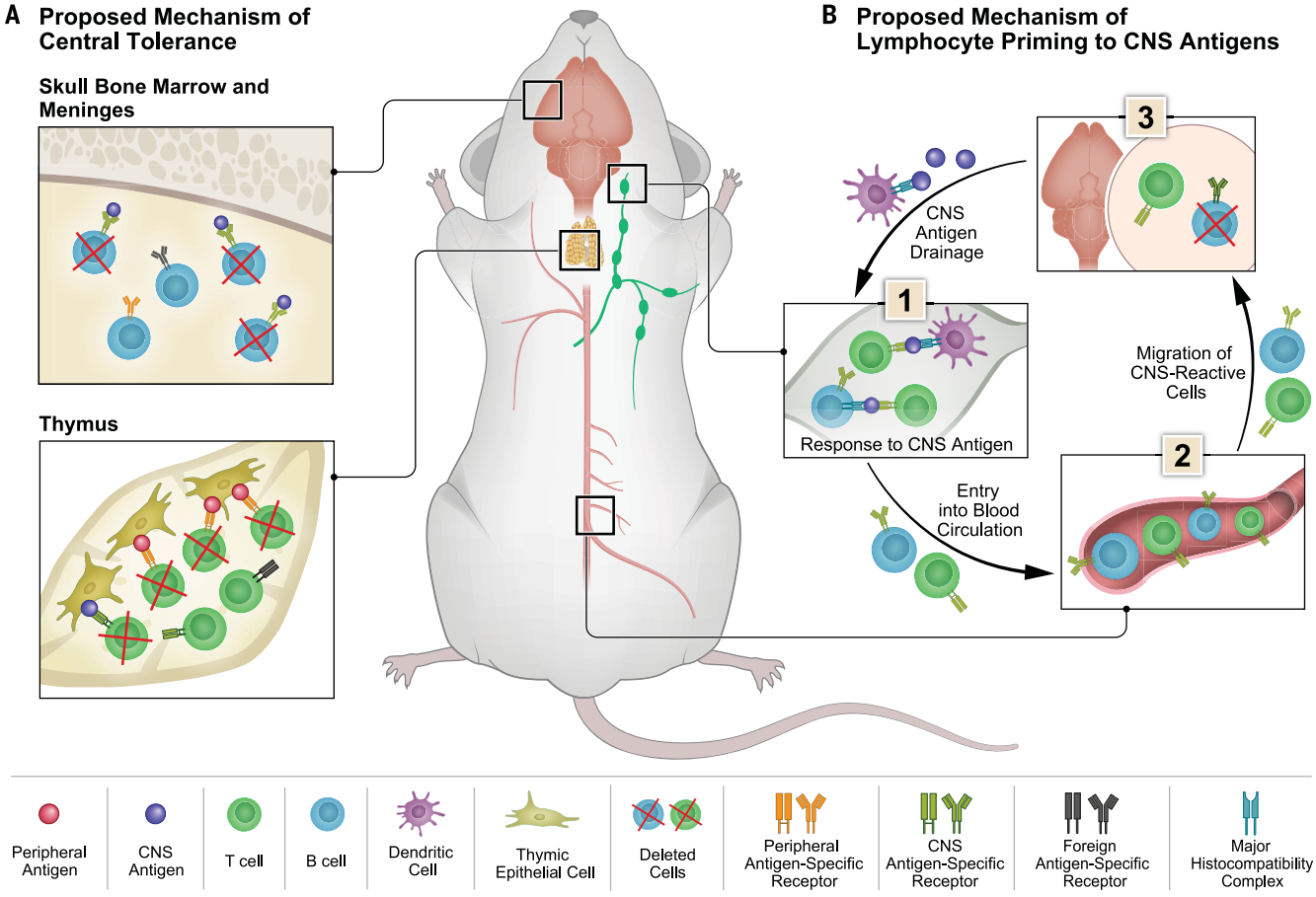

Fig. 4. Proposed mechanisms of tolerance induction, education of lymphocytes, and homing of CNS-reactive immune cells to the brain's borders. (**A**) Deletion of skull BM-derived B cells in the meninges, together with the biological processes by which high-affinity potentially autoreactive T cells are eliminated in the thymus. Although high-affinity autoreactive T cells are excluded, low-affinity autoreactive T lymphocytes might egress from the thymus. (**B**) Proposed model explaining the events after CNS antigen drainage and presentation in the draining CLNs (1); after antigen priming (2), CNS-reactive lymphocytes enter the bloodstream and finally home to the CNS borders (3).

the eye. In this organ, although the inner blood-retinal barrier functions as a physical barrier, the outer barrier, together with the blood-aqueous barrier, provides a distinct immunological milieu that dictates the immune profile of both macrophages and T cells (*158*). Other immune-privileged sites, such as the maternal-fetal interface and the testis, are also equipped with immunomodulatory properties but do not present true barriers. Instead, accumulating evidence shows that they can act as educational gates for leukocytes providing immune regulation and tolerance (*158*). Although further studies are needed to decipher the distinct immunological features of each of the immune-privileged organs, it appears that the brain has developed immunological pathways to allow for the well-controlled mobilization of the immune system in response to immunological cues, ultimately ensuring not only immune surveillance, but also its optimal functioning (*159*).

In brain pathologies, any of the immunological processes taking place at the brain's borders could potentially malfunction. For example, choroid plexus dysfunction (*41*, *118*) has been reported in mouse models of aging and AD caused by an imbalance of IFN signaling (*41*, *92*, *118*), which negatively affects cognitive performance and the fate of the microglia (*137*). Likewise, disruption of brain lymphatic drainage has been indicated as one of the underlying factors exacerbating amyloid-β load and memory impairment in AD mice and has been suggested as a therapeutic target to alleviate cognitive decline (*152*). Further experiments in aged mice showed improved learning and memory performance after the enhancement of brain drainage achieved by the administration of vascular endothelial growth factor C (*152*). Additionally, the recent finding that the skull BM serves as a reservoir for cells engaging in brain surveillance may provide new therapeutic avenues aimed at inducing the rapid recruitment of immune cells to the brain after various CNS insults. Moreover, BM myelopoiesis might represent a candidate target in multiple sclerosis, because an imbalance of this process is linked to CNS inflammation and demyelination and depends on the migration of myelin-reactive T cells in the BM, as evidenced in diseased mice (*144*). This trafficking of autoreactive T cells into the BM relies on the CXCL12-CXCR4 axis, whereas the skewing of myelopoiesis is induced through the CCL5-CCR5 axis. Therefore, these pathways might represent promising candidates for the design of therapeutic approaches to treat multiple sclerosis and potentially other CNS autoimmune disorders (*144*). The relevance of B cells in the pathogenesis of multiple sclerosis has been demonstrated by the efficacy of B cell–depleting immunotherapies, although this pathology was previously considered to be dependent on T cells (*39*). However, an interesting approach could come from the capacity of the meninges to delete CNS-autoreactive B cells (*39*), further suggesting that enhancement of dural B cell selection could be considered as a potential means to overcome brain autoimmunity.

The functions of adaptive immune cells in life-long brain maintenance, together with the network encompassing the CNS and its specialized immunological niches, provide the organism with a substantial advantage in

protecting brain health. It is hard to believe that for more than a full century, the research community ignored the possibility that brain resilience to constant perturbation and its robustness in performing endless functions were dependent on the immune system. Now, with the discoveries of the intimate connections between the two systems, multiple remaining questions may be addressed, including what is the antigenic specificity of the T cells that reside in the different brain niches and do they change during aging and under different disease conditions? The answers to these questions might direct the optimal design of efficient T cell–based immunotherapies for a wide range of brain disorders. It is still unclear whether the skull BM serves as the source of myeloid cells in health or if it is only a reservoir for these cells under pathological conditions and if the CSF milieu impairs the function of the skull BM–derived cells in pathology or aging. Such knowledge might open new intervention strategies aimed at modulating the CSF or the skull BM composition to regulate the brain immune responses. It is also unclear how the fate of the peripheral immune system affects the brain immune niches and, conversely, how the brain affects systemic immune responses. Moreover, a deep comprehension of this network is likely to lead to new functional markers for disease diagnosis in the blood or CSF, which would serve as a proxy to changes in the brain or its borders. These issues and many others are being addressed using currently available and state-of-the art approaches, with extensive progress being made with the advent of unbiased molecular, cellular, and spatial techniques of multiple-omics and high-resolution imaging methodologies. Recognition of the exceptionally interconnected nature of the CNS allows a sophisticated understanding of brain immunity, offering a wide range of new opportunities for the design of innovative therapeutic approaches and drug-delivery strategies and thus broadening the range of molecular and cellular targets for potential disease-modifying therapies.

REFERENCES AND NOTES

1. P. B. Medawar, Immunity to homologous grafted skin; the fate of skin homografts transplanted to the brain, to subcutaneous tissue, and to the anterior chamber of the eye. *Br. J. Exp. Pathol.* **29**, 58–69 (1948). pmid: 18865105
2. J. B. Murphy, E. Sturm, Conditions determining the transplantability of tissues in the brain. *J. Exp. Med.* **38**, 183–197 (1923). doi: 10.1084/jem.38.2.183; pmid: 19868782
3. P. B. Medawar, Immunological tolerance. *Nature* **189**, 14–17 (1961). doi: 10.1038/189014a0; pmid: 13768821
4. P. Ehrlich, *Über das Sauerstoffbedürfnis des Organismus* (Hirschwald, 1885).
5. E. E. Goldmann, *Vitalfärbung am Zentralnervensystem: Beitrag zur Physio-Pathologie des Plexus chorioideus und der Hirnhäute* (Königl. Akademie der Wissenschaften, 1913).
6. P. Mascagni, C. Santi, *Vasorum lymphaticorum Corporis Humani Historia etIchnographia* (Pazzini Carli, 1787).
7. G. Schwalbe, Der Arachnoidalraum, ein Lymphraum und sein Zusammenhang mit dem Perichorioidalraum. *Zentralbl. Med. Wiss.* (1869).
8. J. B. Brierley, E. J. Field, The connexions of the spinal sub-arachnoid space with the lymphatic system. *J. Anat.* **82**, 153–166 (1948). pmid: 17105055
9. M. Földi *et al*., New contributions to the anatomical connections of the brain and the lymphatic system. *Acta Anat.* **64**, 498–505 (1966). doi: 10.1159/000142849; pmid: 5957959
10. J. Y. Niederkorn, See no evil, hear no evil, do no evil: The lessons of immune privilege. *Nat. Immunol.* **7**, 354–359 (2006). doi: 10.1038/ni1328; pmid: 16550198
11. R. Dantzer, J. C. O'Connor, G. G. Freund, R. W. Johnson, K. W. Kelley, From inflammation to sickness and depression: When the immune system subjugates the brain. *Nat. Rev. Neurosci.* **9**, 46–56 (2008). doi: 10.1038/nrn2297; pmid: 18073775
12. T. L. Sørensen *et al*., Expression of specific chemokines and chemokine receptors in the central nervous system of multiple sclerosis patients. *J. Clin. Invest.* **103**, 807–815 (1999). doi: 10.1172/JCI5150; pmid: 10079101
13. U. Traugott, E. L. Reinherz, C. S. Raine, Multiple sclerosis: Distribution of T cell subsets within active chronic lesions. *Science* **219**, 308–310 (1983). doi: 10.1126/science.6217550; pmid: 6217550
14. W. S. Lazarus-Barlow, R. H. Parry, The brain and immunity reactions to Jensen's rat sarcoma - PMC. *Br. J. Exp. Pathol.* (1923).
15. G. Stuart, K. S. Krikorian, A fatal neuro-paralytic accident of antirabies treatment. *Lancet* **215**, 1123–1125 (1930). doi: 10.1016/S0140-6736(00)70779-3
16. B. E. Deverman, P. H. Patterson, Cytokines and CNS development. *Neuron* **64**, 61–78 (2009). doi: 10.1016/j.neuron.2009.09.002; pmid: 19840550
17. U. Meyer, J. Feldon, O. Dammann, Schizophrenia and autism: Both shared and disorder-specific pathogenesis via perinatal inflammation? *Pediatr. Res.* **69**, 26R–33R (2011). doi: 10.1203/PDR.0b013e318212c196; pmid: 21289540
18. W. F. Hickey, B. L. Hsu, H. Kimura, T-lymphocyte entry into the central nervous system. *J. Neurosci. Res.* **28**, 254–260 (1991). doi: 10.1002/jnr.490280213; pmid: 2033653
19. W. F. Hickey, K. Vass, H. Lassmann, Bone marrow-derived elements in the central nervous system: An immunohistochemical and ultrastructural survey of rat chimeras. *J. Neuropathol. Exp. Neurol.* **51**, 246–256 (1992). doi: 10.1097/00005072-199205000-00002; pmid: 1583531
20. M. L. Cuzner, G. M. Hayes, J. Newcombe, M. N. Woodroofe, The nature of inflammatory components during demyelination in multiple sclerosis. *J. Neuroimmunol.* **20**, 203–209 (1988). doi: 10.1016/0165-5728(88)90161-0; pmid: 3058743
21. S. H. Naqvi, L. M. Dunkle, S. Naseer, C. Barth, Significance of neutrophils in cerebrospinal fluid samples processed by cytocentrifugation. *Clin. Pediatr. (Phila.)* **22**, 608–611 (1983). doi: 10.1177/000992288302200904; pmid: 6883891
22. O. Rapalino *et al*., Implantation of stimulated homologous macrophages results in partial recovery of paraplegic rats. *Nat. Med.* **4**, 814–821 (1998). doi: 10.1038/nm0798-814; pmid: 9662373
23. G. Moalem *et al*., Autoimmune T cells protect neurons from secondary degeneration after central nervous system axotomy. *Nat. Med.* **5**, 49–55 (1999). doi: 10.1038/4734; pmid: 9883839
24. Y. Ziv *et al*., Immune cells contribute to the maintenance of neurogenesis and spatial learning abilities in adulthood. *Nat. Neurosci.* **9**, 268–275 (2006). doi: 10.1038/nn1629; pmid: 16415867
25. S. A. Wolf *et al*., CD4-positive T lymphocytes provide a neuroimmunological link in the control of adult hippocampal neurogenesis. *J. Immunol.* **182**, 3979–3984 (2009). doi: 10.4049/jimmunol.0801218; pmid: 19299695
26. M. L. Monje, H. Toda, T. D. Palmer, Inflammatory blockade restores adult hippocampal neurogenesis. *Science* **302**, 1760–1765 (2003). doi: 10.1126/science.1088417 pmid: 14615545
27. C. T. Ekdahl, J.-H. Claasen, S. Bonde, Z. Kokaia, O. Lindvall, Inflammation is detrimental for neurogenesis in adult brain. *Proc. Natl. Acad. Sci. U.S.A.* **100**, 13632–13637 (2003). doi: 10.1073/pnas.2234031100; pmid: 14581618
28. A. J. Filiano *et al*., Unexpected role of interferon-γ in regulating neuronal connectivity and social behaviour. *Nature* **535**, 425–429 (2016). doi: 10.1038/nature18626; pmid: 27409813
29. M. Ribeiro *et al*., Meningeal γδ T cell-derived IL-17 controls synaptic plasticity and short-term memory. *Sci. Immunol.* **4**, eaay5199 (2019). doi: 10.1126/sciimmunol.aay5199; pmid: 31604844
30. K. Alves de Lima *et al*., Meningeal γδ T cells regulate anxiety-like behavior via IL-17a signaling in neurons. *Nat. Immunol.* **21**, 1421–1429 (2020). doi: 10.1038/s41590-020-0776-4; pmid: 32929273
31. M. D. Reed *et al*., IL-17a promotes sociability in mouse models of neurodevelopmental disorders. *Nature* **577**, 249–253 (2020). doi: 10.1038/s41586-019-1843-6; pmid: 31853066
32. W. C. Poller *et al*., Brain motor and fear circuits regulate leukocytes during acute stress. *Nature* **607**, 578–584 (2022). doi: 10.1038/s41586-022-04890-z; pmid: 35636458
33. D. P. Schafer *et al*., Microglia sculpt postnatal neural circuits in an activity and complement-dependent manner. *Neuron* **74**, 691–705 (2012). doi: 10.1016/j.neuron.2012.03.026; pmid: 22632727
34. G. B. Choi *et al*., The maternal interleukin-17a pathway in mice promotes autism-like phenotypes in offspring. *Science* **351**, 933–939 (2016). doi: 10.1126/science.aad0314; pmid: 26822608
35. A. Sekar *et al*., Schizophrenia risk from complex variation of complement component 4. *Nature* **530**, 177–183 (2016). doi: 10.1038/nature16549; pmid: 26814963
36. N. C. Derecki *et al*., Regulation of learning and memory by meningeal immunity: A key role for IL-4. *J. Exp. Med.* **207**, 1067–1080 (2010). doi: 10.1084/jem.20091419; pmid: 20439540
37. J. Rustenhoven *et al*., Functional characterization of the dural sinuses as a neuroimmune interface. *Cell* **184**, 1000–1016.e27 (2021). doi: 10.1016/j.cell.2020.12.040; pmid: 33508229
38. Z. Fitzpatrick *et al*., Gut-educated IgA plasma cells defend the meningeal venous sinuses. *Nature* **587**, 472–476 (2020). doi: 10.1038/s41586-020-2886-4; pmid: 33149302
39. Y. Wang *et al*., Early developing B cells undergo negative selection by central nervous system-specific antigens in the meninges. *Immunity* **54**, 2784–2794.e6 (2021). doi: 10.1016/j.immuni.2021.09.016; pmid: 34626548
40. G. Kunis *et al*., IFN-γ-dependent activation of the brain's choroid plexus for CNS immune surveillance and repair. *Brain* **136**, 3427–3440 (2013). doi: 10.1093/brain/awt259; pmid: 24088808
41. K. Baruch *et al*., Aging. Aging-induced type I interferon response at the choroid plexus negatively affects brain function. *Science* **346**, 89–93 (2014). doi: 10.1126/science.1252945; pmid: 25147279
42. R. Shechter *et al*., Recruitment of beneficial M2 macrophages to injured spinal cord is orchestrated by remote brain choroid plexus. *Immunity* **38**, 555–569 (2013). doi: 10.1016/j.immuni.2013.02.012; pmid: 23477737
43. G. Faraco *et al*., Perivascular macrophages mediate the neurovascular and cognitive dysfunction associated with hypertension. *J. Clin. Invest.* **126**, 4674–4689 (2016). doi: 10.1172/JCI86950; pmid: 27841763
44. A. Drieu *et al*., Parenchymal border macrophages regulate the flow dynamics of the cerebrospinal fluid. *Nature* **611**, 585–593 (2022). doi: 10.1038/s41586-022-05397-3; pmid: 36352225
45. D. Schafflick *et al*., Single-cell profiling of CNS border compartment leukocytes reveals that B cells and their progenitors reside in non-diseased meninges. *Nat. Neurosci.* **24**, 1225–1234 (2021). doi: 10.1038/s41593-021-00880-y; pmid: 34253922
46. E. Blacher *et al*., Potential roles of gut microbiome and metabolites in modulating ALS in mice. *Nature* **572**, 474–480 (2019). doi: 10.1038/s41586-019-1443-5; pmid: 31330533
47. T. R. Sampson *et al*., Gut microbiota regulate motor deficits and neuroinflammation in a model of parkinson's disease. *Cell* **167**, 1469–1480.e12 (2016). doi: 10.1016/j.cell.2016.11.018; pmid: 27912057
48. B. D. Needham *et al*., A gut-derived metabolite alters brain activity and anxiety behaviour in mice. *Nature* **602**, 647–653 (2022). doi: 10.1038/s41586-022-04396-8; pmid: 35165440
49. D. Erny *et al*., Microbiota-derived acetate enables the metabolic fitness of the brain innate immune system during health and disease. *Cell Metab.* **33**, 2260–2276.e7 (2021). doi: 10.1016/j.cmet.2021.10.010; pmid: 34731656
50. A. Louveau *et al*., Structural and functional features of central nervous system lymphatic vessels. *Nature* **523**, 337–341 (2015). doi: 10.1038/nature14432; pmid: 26030524
51. A. Aspelund *et al*., A dural lymphatic vascular system that drains brain interstitial fluid and macromolecules. *J. Exp. Med.* **212**, 991–999 (2015). doi: 10.1084/jem.20142290; pmid: 26077718
52. F. Herisson *et al*., Direct vascular channels connect skull bone marrow and the brain surface enabling myeloid cell migration. *Nat. Neurosci.* **21**, 1209–1217 (2018). doi: 10.1038/s41593-018-0213-2; pmid: 30150661

53. J. A. Mazzitelli *et al*., Cerebrospinal fluid regulates skull bone marrow niches via direct access through dural channels. *Nat. Neurosci.* **25**, 555–560 (2022). doi: 10.1038/s41593-022-01029-1; pmid: 35301477
54. F. E. Pulous *et al*., Cerebrospinal fluid can exit into the skull bone marrow and instruct cranial hematopoiesis in mice with bacterial meningitis. *Nat. Neurosci.* **25**, 567–576 (2022). doi: 10.1038/s41593-022-01060-2; pmid: 35501382
55. T. Koren, A. Rolls, Immunoception: Defining brain-regulated immunity. *Neuron* **110**, 3425–3428 (2022). doi: 10.1016/j.neuron.2022.10.016; pmid: 36327893
56. T. Koren *et al*., Insular cortex neurons encode and retrieve specific immune responses. *Cell* **184**, 5902–5915.e17 (2021). doi: 10.1016/j.cell.2021.10.013; pmid: 34752731
57. T. L. Ben-Shaanan *et al*., Activation of the reward system boosts innate and adaptive immunity. *Nat. Med.* **22**, 940–944 (2016). doi: 10.1038/nm.4133; pmid: 27376577
58. M. Rosas-Ballina *et al*., Acetylcholine-synthesizing T cells relay neural signals in a vagus nerve circuit. *Science* **334**, 98–101 (2011). doi: 10.1126/science.1209985; pmid: 21921156
59. F. Ginhoux *et al*., Fate mapping analysis reveals that adult microglia derive from primitive macrophages. *Science* **330**, 841–845 (2010). doi: 10.1126/science.1194637; pmid: 20966214
60. P. Río-Hortega, El tercer elemento de los centros nerviosos. I. La microglia en estado normal. *Bol. Soc. Esp. Biol.* **9**, 68–82 (1919).
61. T. Masuda *et al*., Specification of CNS macrophage subsets occurs postnatally in defined niches. *Nature* **604**, 740–748 (2022). doi: 10.1038/s41586-022-04596-2; pmid: 35444273
62. M. J. C. Jordão *et al*., Single-cell profiling identifies myeloid cell subsets with distinct fates during neuroinflammation. *Science* **363**, eaat7554 (2019). doi: 10.1126/science.aat7554; pmid: 30679343
63. D. Mrdjen *et al*., High-dimensional single-cell mapping of central nervous system immune cells reveals distinct myeloid subsets in health, aging, and disease. *Immunity* **48**, 599 (2018). doi: 10.1016/j.immuni.2018.02.014; pmid: 29562204
64. T. Goldmann *et al*., Origin, fate and dynamics of macrophages at central nervous system interfaces. *Nat. Immunol.* **17**, 797–805 (2016). doi: 10.1038/ni.3423; pmid: 27135602
65. C. L. Cunningham, V. Martínez-Cerdeño, S. C. Noctor, Microglia regulate the number of neural precursor cells in the developing cerebral cortex. *J. Neurosci.* **33**, 4216–4233 (2013). doi: 10.1523/JNEUROSCI.3441-12.2013; pmid: 23467340
66. E. N. Santos, R. D. Fields, Regulation of myelination by microglia. *Sci. Adv.* **7**, eabk1131 (2021). doi: 10.1126/sciadv.abk1131; pmid: 34890221
67. J. M. Frade, Y. A. Barde, Microglia-derived nerve growth factor causes cell death in the developing retina. *Neuron* **20**, 35–41 (1998). doi: 10.1016/S0896-6273(00)80432-8; pmid: 9459440
68. J. L. Marín-Teva *et al*., Microglia promote the death of developing Purkinje cells. *Neuron* **41**, 535–547 (2004). doi: 10.1016/S0896-6273(04)00069-8; pmid: 14980203
69. B. Stevens *et al*., The classical complement cascade mediates CNS synapse elimination. *Cell* **131**, 1164–1178 (2007). doi: 10.1016/j.cell.2007.10.036; pmid: 18083105
70. P. T. Nguyen *et al*., Microglial remodeling of the extracellular matrix promotes synapse plasticity. *Cell* **182**, 388–403.e15 (2020). doi: 10.1016/j.cell.2020.05.050; pmid: 32615087
71. E. Favuzzi *et al*., GABA-receptive microglia selectively sculpt developing inhibitory circuits. *Cell* **184**, 4048–4063.e32 (2021). doi: 10.1016/j.cell.2021.06.018; pmid: 34233165
72. A. Badimon *et al*., Negative feedback control of neuronal activity by microglia. *Nature* **586**, 417–423 (2020). doi: 10.1038/s41586-020-2777-8; pmid: 32999463
73. D. He *et al*., Disruption of the IL-33-ST2-AKT signaling axis impairs neurodevelopment by inhibiting microglial metabolic adaptation and phagocytic function. *Immunity* **55**, 159–173.e9 (2022). doi: 10.1016/j.immuni.2021.12.001; pmid: 34982959
74. I. C. Clark *et al*., Barcoded viral tracing of single-cell interactions in central nervous system inflammation. *Science* **372**, eabf1230 (2021). doi: 10.1126/science.abf1230; pmid: 33888612
75. L. M. Sanmarco *et al*., Gut-licensed IFNγ^{+} NK cells drive LAMP1^{+}TRAIL^{+} anti-inflammatory astrocytes. *Nature* **590**, 473–479 (2021). doi: 10.1038/s41586-020-03116-4; pmid: 33408417
76. M. A. Wheeler *et al*., MAFG-driven astrocytes promote CNS inflammation. *Nature* **578**, 593–599 (2020). doi: 10.1038/s41586-020-1999-0; pmid: 32051591
77. L. Yshii *et al*., Astrocyte-targeted gene delivery of interleukin 2 specifically increases brain-resident regulatory T cell numbers and protects against pathological neuroinflammation. *Nat. Immunol.* **23**, 878–891 (2022). doi: 10.1038/s41590-022-01208-z; pmid: 35618831
78. J. I. Alvarez *et al*., The Hedgehog pathway promotes blood-brain barrier integrity and CNS immune quiescence. *Science* **334**, 1727–1731 (2011). doi: 10.1126/science.1206936; pmid: 22144466
79. N. Habib *et al*., Disease-associated astrocytes in Alzheimer's disease and aging. *Nat. Neurosci.* **23**, 701–706 (2020). doi: 10.1038/s41593-020-0624-8; pmid: 32341542
80. F. Endo *et al*., Molecular basis of astrocyte diversity and morphology across the CNS in health and disease. *Science* **378**, eadc9020 (2022). doi: 10.1126/science.adc9020; pmid: 36378959
81. J. Tcw *et al*., Cholesterol and matrisome pathways dysregulated in astrocytes and microglia. *Cell* **185**, 2213–2233.e25 (2022). doi: 10.1016/j.cell.2022.05.017; pmid: 35750033
82. Y. H. Ju *et al*., Astrocytic urea cycle detoxifies Aβ-derived ammonia while impairing memory in Alzheimer's disease. *Cell Metab.* **34**, 1104–1120.e8 (2022). doi: 10.1016/j.cmet.2022.05.011; pmid: 35738259
83. C. S. McAlpine *et al*., Astrocytic interleukin-3 programs microglia and limits Alzheimer's disease. *Nature* **595**, 701–706 (2021). doi: 10.1038/s41586-021-03734-6; pmid: 34262178
84. N. Priego *et al*., STAT3 labels a subpopulation of reactive astrocytes required for brain metastasis. *Nat. Med.* **24**, 1024–1035 (2018). doi: 10.1038/s41591-018-0044-4; pmid: 29892069
85. R. Perelroizen *et al*., Astrocyte immunometabolic regulation of the tumour microenvironment drives glioblastoma pathogenicity. *Brain* **145**, 3288–3307 (2022). doi: 10.1093/brain/awac222; pmid: 35899587
86. D. Henrik Heiland *et al*., Tumor-associated reactive astrocytes aid the evolution of immunosuppressive environment in glioblastoma. *Nat. Commun.* **10**, 2541 (2019). doi: 10.1038/s41467-019-10493-6; pmid: 31186414
87. D. Davalos *et al*., ATP mediates rapid microglial response to local brain injury in vivo. *Nat. Neurosci.* **8**, 752–758 (2005). doi: 10.1038/nn1472; pmid: 15895084
88. A. Nimmerjahn, F. Kirchhoff, F. Helmchen, Resting microglial cells are highly dynamic surveillants of brain parenchyma in vivo. *Science* **308**, 1314–1318 (2005). doi: 10.1126/science.1110647; pmid: 15831717
89. R. Socodato *et al*., Microglia dysfunction caused by the loss of rhoa disrupts neuronal physiology and leads to neurodegeneration. *Cell Rep.* **31**, 107796 (2020). doi: 10.1016/j.celrep.2020.107796; pmid: 32579923
90. A. Deczkowska, I. Amit, M. Schwartz, Microglial immune checkpoint mechanisms. *Nat. Neurosci.* **21**, 779–786 (2018). doi: 10.1038/s41593-018-0145-x; pmid: 29735982
91. J. Marschallinger *et al*., Lipid-droplet-accumulating microglia represent a dysfunctional and proinflammatory state in the aging brain. *Nat. Neurosci.* **23**, 194–208 (2020). doi: 10.1038/s41593-019-0566-1; pmid: 31959936
92. A. Deczkowska *et al*., Mef2C restrains microglial inflammatory response and is lost in brain ageing in an IFN-I-dependent manner. *Nat. Commun.* **8**, 717 (2017). doi: 10.1038/s41467-017-00769-0; pmid: 28959042
93. A. Montagne *et al*., Blood-brain barrier breakdown in the aging human hippocampus. *Neuron* **85**, 296–302 (2015). doi: 10.1016/j.neuron.2014.12.032; pmid: 25611508
94. M. D. Wu, S. L. Montgomery, F. Rivera-Escalera, J. A. Olschowka, M. K. O'Banion, Sustained IL-1β expression impairs adult hippocampal neurogenesis independent of IL-1 signaling in nestin + neural precursor cells. *Brain Behav. Immun.* **32**, 9–18 (2013). doi: 10.1016/j.bbi.2013.03.003; pmid: 23510988
95. A. Sierra *et al*., Microglia shape adult hippocampal neurogenesis through apoptosis-coupled phagocytosis. *Cell Stem Cell* **7**, 483–495 (2010). doi: 10.1016/j.stem.2010.08.014; pmid: 20887954
96. C. Wang *et al*., Microglia mediate forgetting via complement-dependent synaptic elimination. *Science* **367**, 688–694 (2020). doi: 10.1126/science.aaz2288; pmid: 32029629
97. J. V. Pluvinage *et al*., CD22 blockade restores homeostatic microglial phagocytosis in ageing brains. *Nature* **568**, 187–192 (2019). doi: 10.1038/s41586-019-1088-4; pmid: 30944478
98. H. Scheiblich *et al*., Microglia jointly degrade fibrillar alpha-synuclein cargo by distribution through tunneling nanotubes. *Cell* **184**, 5089–5106.e21 (2021). doi: 10.1016/j.cell.2021.09.007; pmid: 34555357
99. Y. Huang *et al*., Microglia use TAM receptors to detect and engulf amyloid β plaques. *Nat. Immunol.* **22**, 586–594 (2021). doi: 10.1038/s41590-021-00913-5;pmid: 33859405
100. P. S. Minhas *et al*., Restoring metabolism of myeloid cells reverses cognitive decline in ageing. *Nature* **590**, 122–128 (2021). doi: 10.1038/s41586-020-03160-0; pmid: 33473210
101. K. P. Lopes *et al*., Genetic analysis of the human microglial transcriptome across brain regions, aging and disease pathologies. *Nat. Genet.* **54**, 4–17 (2022). doi: 10.1038/s41588-021-00976-y; pmid: 34992268
102. K. Grabert *et al*., Microglial brain region-dependent diversity and selective regional sensitivities to aging. *Nat. Neurosci.* **19**, 504–516 (2016). doi: 10.1038/nn.4222; pmid: 26780511
103. E. Pasciuto *et al*., Microglia require CD4 T cells to complete the fetal-to-adult transition. *Cell* **182**, 625–640.e24 (2020). doi: 10.1016/j.cell.2020.06.026; pmid: 32702313
104. K. Steinbach *et al*., Brain-resident memory T cells generated early in life predispose to autoimmune disease in mice. *Sci. Transl. Med.* **11**, eaav5519 (2019). doi: 10.1126/scitranslmed.aav5519; pmid: 31243152
105. C. Garber *et al*., T cells promote microglia-mediated synaptic elimination and cognitive dysfunction during recovery from neuropathogenic flaviviruses. *Nat. Neurosci.* **22**, 1276–1288 (2019). doi: 10.1038/s41593-019-0427-y; pmid: 31235930
106. K. Somebang *et al*., CCR2 deficiency alters activation of microglia subsets in traumatic brain injury. *Cell Rep.* **36**, 109727 (2021). doi: 10.1016/j.celrep.2021.109727; pmid: 34551293
107. J. Zhang *et al*., IL4-driven microglia modulate stress resilience through BDNF-dependent neurogenesis. *Sci. Adv.* **7**, eabb9888 (2021). doi: 10.1126/sciadv.abb9888; pmid: 33731342
108. O. Matcovitch-Natan *et al*., Microglia development follows a stepwise program to regulate brain homeostasis. *Science* **353**, aad8670 (2016). doi: 10.1126/science.aad8670; pmid: 27338705
109. H. Ben-Yehuda *et al*., Maternal Type-I interferon signaling adversely affects the microglia and the behavior of the offspring accompanied by increased sensitivity to stress. *Mol. Psychiatry* **25**, 1050–1067 (2020). doi: 10.1038/s41380-019-0604-0; pmid: 31772304
110. S. Tanabe, T. Yamashita, B-1a lymphocytes promote oligodendrogenesis during brain development. *Nat. Neurosci.* **21**, 506–516 (2018). doi: 10.1038/s41593-018-0106-4; pmid: 29507409
111. M. Absinta *et al*., A lymphocyte-microglia-astrocyte axis in chronic active multiple sclerosis. *Nature* **597**, 709–714 (2021). doi: 10.1038/s41586-021-03892-7; pmid: 34497421
112. D. A. Mogilenko *et al*., Comprehensive profiling of an aging immune system reveals clonal GZMK+ CD8+ T cells as conserved hallmark of inflammaging. *Immunity* **54**, 99–115.e12 (2021). doi: 10.1016/j.immuni.2020.11.005; pmid: 33271118
113. H. Cohen *et al*., Maladaptation to mental stress mitigated by the adaptive immune system via depletion of naturally occurring regulatory CD4+CD25+ cells. *J. Neurobiol.* **66**, 552–563 (2006). doi: 10.1002/neu.20249; pmid: 16555237
114. A. Radjavi, I. Smirnov, J. Kipnis, Brain antigen-reactive CD4+ T cells are sufficient to support learning behavior in mice with limited T cell repertoire. *Brain Behav. Immun.* **35**, 58–63 (2014). doi: 10.1016/j.bbi.2013.08.013; pmid: 24012647
115. J. Kipnis, H. Cohen, M. Cardon, Y. Ziv, M. Schwartz, T cell deficiency leads to cognitive dysfunction: Implications for therapeutic vaccination for schizophrenia and other psychiatric conditions. *Proc. Natl. Acad. Sci. U.S.A.* **101**, 8180–8185 (2004). doi: 10.1073/pnas.0402268101; pmid: 15141078
116. G. Desdín-Micó *et al*., T cells with dysfunctional mitochondria induce multimorbidity and premature senescence. *Science* **368**, 1371–1376 (2020). doi: 10.1126/science.aax0860; pmid: 32439659
117. B. W. Dulken *et al*., Single-cell analysis reveals T cell infiltration in old neurogenic niches. *Nature* **571**, 205–210 (2019). doi: 10.1038/s41586-019-1362-5; pmid: 31270459
118. S. D. Mesquita *et al*., The choroid plexus transcriptome reveals changes in type I and II interferon responses in a mouse model of Alzheimer's disease. *Brain Behav. Immun.* **49**, 280–292 (2015). doi: 10.1016/j.bbi.2015.06.008; pmid: 26092102

119. K. Baruch *et al*., CNS-specific immunity at the choroid plexus shifts toward destructive Th2 inflammation in brain aging. *Proc. Natl. Acad. Sci. U.S.A.* **110**, 2264–2269 (2013). doi: 10.1073/pnas.1211270110; pmid: 23335631
120. L. Zhou *et al*., Reversible CD8 T cell-neuron cross-talk causes aging-dependent neuronal regenerative decline. *Science* **376**, eabd5926 (2022). doi: 10.1126/science.abd5926; pmid: 35549409
121. M. J. Yousefzadeh *et al*., An aged immune system drives senescence and ageing of solid organs. *Nature* **594**, 100–105 (2021). doi: 10.1038/s41586-021-03547-7; pmid: 33981041
122. S. Carloni *et al*., Identification of a choroid plexus vascular barrier closing during intestinal inflammation. *Science* **374**, 439–448 (2021). doi: 10.1126/science.abc6108; pmid: 34672740
123. M. Ito *et al*., Brain regulatory T cells suppress astrogliosis and potentiate neurological recovery. *Nature* **565**, 246–250 (2019). doi: 10.1038/s41586-018-0824-5; pmid: 30602786
124. L. Park *et al*., Brain perivascular macrophages initiate the neurovascular dysfunction of alzheimer aβ peptides. *Circ. Res.* **121**, 258–269 (2017). doi: 10.1161/CIRCRESAHA.117.311054; pmid: 28515043
125. K. Thanopoulou, A. Fragkouli, F. Stylianopoulou, S. Georgopoulos, Scavenger receptor class B type I (SR-BI) regulates perivascular macrophages and modifies amyloid pathology in an Alzheimer mouse model. *Proc. Natl. Acad. Sci. U.S.A.* **107**, 20816–20821 (2010). doi: 10.1073/pnas.1005888107; pmid: 21076037
126. K. Møllgård *et al*., A mesothelium divides the subarachnoid space into functional compartments. *Science* **379**, 84–88 (2023). doi: 10.1126/science.adc8810; pmid: 36603070
127. V. Kekere, K. Alsayouri, *Anatomy, Head and Neck, Dura Mater* (StatPearls Publishing, 2022).
128. A. Merlini *et al*., Distinct roles of the meningeal layers in CNS autoimmunity. *Nat. Neurosci.* **25**, 887–899 (2022). doi: 10.1038/s41593-022-01108-3; pmid: 35773544
129. J. Herz *et al*., GABAergic neuronal IL-4R mediates T cell effect on memory. *Neuron* **109**, 3609–3618.e9 (2021). doi: 10.1016/j.neuron.2021.10.022; pmid: 34793707
130. S. Brioschi *et al*., Heterogeneity of meningeal B cells reveals a lymphopoietic niche at the CNS borders. *Science* **373**, eabf9277 (2021). doi: 10.1126/science.abf9277; pmid: 34083450
131. N. Dani *et al*., A cellular and spatial map of the choroid plexus across brain ventricles and ages. *Cell* **184**, 3056–3074.e21 (2021). doi: 10.1016/j.cell.2021.04.003; pmid: 33932339
132. F. B. Shipley *et al*., Tracking calcium dynamics and immune surveillance at the choroid plexus blood-cerebrospinal fluid interface. *Neuron* **108**, 623–639.e10 (2020). doi: 10.1016/j.neuron.2020.08.024; pmid: 32961128
133. S. Balusu *et al*., Identification of a novel mechanism of blood-brain communication during peripheral inflammation via choroid plexus-derived extracellular vesicles. *EMBO Mol. Med.* **8**, 1162–1183 (2016). doi: 10.15252/emmm.201606271; pmid: 27596437
134. C. Vandendriessche *et al*., Importance of extracellular vesicle secretion at the blood-cerebrospinal fluid interface in the pathogenesis of Alzheimer's disease. *Acta Neuropathol. Commun.* **9**, 143 (2021). doi: 10.1186/s40478-021-01245-z; pmid: 34425919
135. G. Llovera *et al*., The choroid plexus is a key cerebral invasion route for T cells after stroke. *Acta Neuropathol.* **134**, 851–868 (2017). doi: 10.1007/s00401-017-1758-y; pmid: 28762187
136. G. Kunis, K. Baruch, O. Miller, M. Schwartz, Immunization with a myelin-derived antigen activates the brain's choroid plexus for recruitment of immunoregulatory cells to the CNS and attenuates disease progression in a mouse model of ALS. *J. Neurosci.* **35**, 6381–6393 (2015). doi: 10.1523/JNEUROSCI.3644-14.2015; pmid: 25904790
137. E. R. Roy *et al*., Concerted type I interferon signaling in microglia and neural cells promotes memory impairment associated with amyloid β plaques. *Immunity* **55**, 879–894.e6 (2022). doi: 10.1016/j.immuni.2022.03.018; pmid: 35443157
138. E. G. Stopa *et al*., Comparative transcriptomics of choroid plexus in Alzheimer's disease, frontotemporal dementia and Huntington's disease: Implications for CSF homeostasis. *Fluids Barriers CNS* **15**, 18 (2018). doi: 10.1186/s12987-018-0102-9; pmid: 29848382
139. L. Xie *et al*., Sleep drives metabolite clearance from the adult brain. *Science* **342**, 373–377 (2013). doi: 10.1126/science.1241224; pmid: 24136970
140. I. Bechmann, I. Galea, V. H. Perry, What is the blood-brain barrier (not)? *Trends Immunol.* **28**, 5–11 (2007). doi: 10.1016/j.it.2006.11.007; pmid: 17140851
141. C. A. Hawkes, J. McLaurin, Selective targeting of perivascular macrophages for clearance of beta-amyloid in cerebral amyloid angiopathy. *Proc. Natl. Acad. Sci. U.S.A.* **106**, 1261–1266 (2009). doi: 10.1073/pnas.0805453106; pmid: 19164591
142. A. Cugurra *et al*., Skull and vertebral bone marrow are myeloid cell reservoirs for the meninges and CNS parenchyma. *Science* **373**, eabf7844 (2021). doi: 10.1126/science.abf7844; pmid: 34083447
143. G. Ringstad, P. K. Eide, Molecular trans-dural efflux to skull bone marrow in humans with CSF disorders. *Brain* **145**, 1464–1472 (2022). doi: 10.1093/brain/awab388; pmid: 34849609
144. K. Shi *et al*., Bone marrow hematopoiesis drives multiple sclerosis progression. *Cell* **185**, 2234–2247.e17 (2022). doi: 10.1016/j.cell.2022.05.020; pmid: 35709748
145. B. Ajami, J. L. Bennett, C. Krieger, K. M. McNagny, F. M. V. Rossi, Infiltrating monocytes trigger EAE progression, but do not contribute to the resident microglia pool. *Nat. Neurosci.* **14**, 1142–1149 (2011). doi: 10.1038/nn.2887;pmid: 21804537
146. H. F. Cserr, C. J. Harling-Berg, P. M. Knopf, Drainage of brain extracellular fluid into blood and deep cervical lymph and its immunological significance. *Brain Pathol.* **2**, 269–276 (1992). doi: 10.1111/j.1750-3639.1992.tb00703.x; pmid: 1341962
147. A. Louveau *et al*., CNS lymphatic drainage and neuroinflammation are regulated by meningeal lymphatic vasculature. *Nat. Neurosci.* **21**, 1380–1391 (2018). doi: 10.1038/s41593-018-0227-9; pmid: 30224810
148. J. Karman, C. Ling, M. Sandor, Z. Fabry, Initiation of immune responses in brain is promoted by local dendritic cells. *J. Immunol.* **173**, 2353–2361 (2004). doi: 10.4049/jimmunol.173.4.2353; pmid: 15294948
149. X. Hu *et al*., Meningeal lymphatic vessels regulate brain tumor drainage and immunity. *Cell Res.* **30**, 229–243 (2020). doi: 10.1038/s41422-020-0287-8; pmid: 32094452
150. J. N. H. Stern *et al*., B cells populating the multiple sclerosis brain mature in the draining cervical lymph nodes. *Sci. Transl. Med.* **6**, 248ra107 (2014). doi: 10.1126/scitranslmed.3008879; pmid: 25100741
151. L. Mayo *et al*., IL-10-dependent Tr1 cells attenuate astrocyte activation and ameliorate chronic central nervous system inflammation. *Brain* **139**, 1939–1957 (2016). doi: 10.1093/brain/aww113; pmid: 27246324
152. S. Da Mesquita *et al*., Functional aspects of meningeal lymphatics in ageing and Alzheimer's disease. *Nature* **560**, 185–191 (2018). doi: 10.1038/s41586-018-0368-8; pmid: 30046111
153. S. Da Mesquita *et al*., Meningeal lymphatics affect microglia responses and anti-Aβ immunotherapy. *Nature* **593**, 255–260 (2021). doi: 10.1038/s41586-021-03489-0; pmid: 33911285
154. L. Wang *et al*., Deep cervical lymph node ligation aggravates AD-like pathology of APP/PS1 mice. *Brain Pathol.* **29**, 176–192 (2019). doi: 10.1111/bpa.12656; pmid: 30192999
155. S. Rodríguez-Lorenzo *et al*., Inflammation of the choroid plexus in progressive multiple sclerosis: Accumulation of granulocytes and T cells. *Acta Neuropathol. Commun.* **8**, 9 (2020). doi: 10.1186/s40478-020-0885-1; pmid: 32014066
156. A. E. Handel, S. R. Irani, G. A. Holländer, The role of thymic tolerance in CNS autoimmune disease. *Nat. Rev. Neurol.* **14**, 723–734 (2018). doi: 10.1038/s41582-018-0095-7; pmid: 30451970
157. D. A. Michelson, K. Hase, T. Kaisho, C. Benoist, D. Mathis, Thymic epithelial cells co-opt lineage-defining transcription factors to eliminate autoreactive T cells. *Cell* **185**, 2542–2558.e18 (2022). doi: 10.1016/j.cell.2022.05.018; pmid: 35714609
158. R. Shechter, A. London, M. Schwartz, Orchestrated leukocyte recruitment to immune-privileged sites: Absolute barriers versus educational gates. *Nat. Rev. Immunol.* **13**, 206–218 (2013). doi: 10.1038/nri3391; pmid: 23435332
159. M. Fijak, A. Meinhardt, The testis in immune privilege. *Immunol. Rev.* **213**, 66–81 (2006). doi: 10.1111/j.1600-065X.2006.00438.x; pmid: 16972897
160. D. R. Rose *et al*., T cell populations in children with autism spectrum disorder and co-morbid gastrointestinal symptoms. *Brain Behav. Immun. Health* **2**, 100042 (2020). doi: 10.1016/j.bbih.2020.100042; pmid: 34589832
161. S. A. Bakheet *et al*., Resveratrol ameliorates dysregulation of Th1, Th2, Th17, and T regulatory cell-related transcription factor signaling in a BTBR T + tf/J mouse model of autism. *Mol. Neurobiol.* **54**, 5201–5212 (2017). doi: 10.1007/s12035-016-0066-1; pmid: 27578011
162. H. K. Hughes *et al*., Dysregulated gene expression associated with inflammatory and translation pathways in activated monocytes from children with autism spectrum disorder. *Transl. Psychiatry* **12**, 39 (2022). doi: 10.1038/s41398-021-01766-0; pmid: 35082275
163. M. Bennabi *et al*., Persistence of dysfunctional natural killer cells in adults with high-functioning autism spectrum disorders: Stigma/consequence of unresolved early infectious events? *Mol. Autism* **10**, 22 (2019). doi: 10.1186/s13229-019-0269-1; pmid: 31123562
164. S. E. Marsh *et al*., The adaptive immune system restrains Alzheimer's disease pathogenesis by modulating microglial function. *Proc. Natl. Acad. Sci. U.S.A.* **113**, E1316–E1325 (2016). doi: 10.1073/pnas.1525466113; pmid: 26884167
165. K. Baruch *et al*., Breaking immune tolerance by targeting Foxp3(+) regulatory T cells mitigates Alzheimer's disease pathology. *Nat. Commun.* **6**, 7967 (2015). doi: 10.1038/ncomms8967; pmid: 26284939
166. D. Gate *et al*., Clonally expanded CD8 T cells patrol the cerebrospinal fluid in Alzheimer's disease. *Nature* **577**, 399–404 (2020). doi: 10.1038/s41586-019-1895-7; pmid: 31915375
167. E. Zenaro *et al*., Neutrophils promote Alzheimer's disease-like pathology and cognitive decline via LFA-1 integrin. *Nat. Med.* **21**, 880–886 (2015). doi: 10.1038/nm.3913; pmid: 26214837
168. J. C. Cruz Hernández *et al*., Neutrophil adhesion in brain capillaries reduces cortical blood flow and impairs memory function in Alzheimer's disease mouse models. *Nat. Neurosci.* **22**, 413–420 (2019). doi: 10.1038/s41593-018-0329-4; pmid: 30742116
169. A. D. Thome *et al*., Functional alterations of myeloid cells during the course of Alzheimer's disease. *Mol. Neurodegener.* **13**, 61 (2018). doi: 10.1186/s13024-018-0293-1; pmid: 30424785
170. Y. Koronyo *et al*., Therapeutic effects of glatiramer acetate and grafted CD115$^+$ monocytes in a mouse model of Alzheimer's disease. *Brain* **138**, 2399–2422 (2015). doi: 10.1093/brain/awv150; pmid: 26049087
171. N. Rosenzweig *et al*., PD-1/PD-L1 checkpoint blockade harnesses monocyte-derived macrophages to combat cognitive impairment in a tauopathy mouse model. *Nat. Commun.* **10**, 465 (2019). doi: 10.1038/s41467-019-08352-5; pmid: 30692527
172. H. Ben-Yehuda *et al*., Key role of the CCR2-CCL2 axis in disease modification in a mouse model of tauopathy. *Mol. Neurodegener.* **16**, 39 (2021). doi: 10.1186/s13024-021-00458-z; pmid: 34172073
173. Y. Zhang *et al*., Depletion of NK cells improves cognitive function in the alzheimer disease mouse model. *J. Immunol.* **205**, 502–510 (2020). doi: 10.4049/jimmunol.2000037; pmid: 32503894
174. D. Sulzer *et al*., T cells from patients with Parkinson's disease recognize α-synuclein peptides. *Nature* **546**, 656–661 (2017). doi: 10.1038/nature22815; pmid: 28636593
175. C. S. Lindestam Arlehamn *et al*., Widespread Tau-Specific CD4 T Cell Reactivity in the General Population. *J. Immunol.* **203**, 84–92 (2019). doi: 10.4049/jimmunol.1801506; pmid: 31085590
176. C. S. Lindestam Arlehamn *et al*., α-Synuclein-specific T cell reactivity is associated with preclinical and early Parkinson's disease. *Nat. Commun.* **11**, 1875 (2020). doi: 10.1038/s41467-020-15626-w; pmid: 32313102
177. D. Gate *et al*., CD4$^+$ T cells contribute to neurodegeneration in Lewy body dementia. *Science* **374**, 868–874 (2021). doi: 10.1126/science.abf7266; pmid: 34648304
178. A. Van der Perren *et al*., The structural differences between patient-derived α-synuclein strains dictate characteristics of Parkinson's disease, multiple system atrophy and dementia with Lewy bodies. *Acta Neuropathol.* **139**, 977–1000 (2020). doi: 10.1007/s00401-020-02157-3; pmid: 32356200
179. G. P. Williams *et al*., T cell infiltration in both human multiple system atrophy and a novel mouse model of the disease. *Acta Neuropathol.* **139**, 855–874 (2020). doi: 10.1007/s00401-020-02126-w; pmid: 31993745
180. L. Zhang *et al*., High neutrophil-to-lymphocyte ratio predicts short survival in multiple system atrophy. *NPJ Parkinsons Dis.* **8**, 11 (2022). doi: 10.1038/s41531-021-00267-7; pmid: 35058467
181. L. Muñoz-Delgado *et al*., Peripheral immune profile and neutrophil-to-lymphocyte ratio in Parkinson's disease. *Mov.*

Disord. **36**, 2426–2430 (2021). doi: 10.1002/mds.28685; pmid: 34101890
182. A. S. Harms *et al*., Peripheral monocyte entry is required for alpha-Synuclein induced inflammation and Neurodegeneration in a model of Parkinson disease. *Exp. Neurol.* **300**, 179–187 (2018). doi: 10.1016/j.expneurol.2017.11.010; pmid: 29155051
183. R. H. Earls *et al*., NK cells clear α-synuclein and the depletion of NK cells exacerbates synuclein pathology in a mouse model of α-synucleinopathy. *Proc. Natl. Acad. Sci. U.S.A.* **117**, 1762–1771 (2020). doi: 10.1073/pnas.1909110117; pmid: 31900358
184. I. M. Chiu *et al*., T lymphocytes potentiate endogenous neuroprotective inflammation in a mouse model of ALS. *Proc. Natl. Acad. Sci. U.S.A.* **105**, 17913–17918 (2008). doi: 10.1073/pnas.0804610105; pmid: 18997009
185. D. R. Beers, J. S. Henkel, W. Zhao, J. Wang, S. H. Appel, CD4+ T cells support glial neuroprotection, slow disease progression, and modify glial morphology in an animal model of inherited ALS. *Proc. Natl. Acad. Sci. U.S.A.* **105**, 15558–15563 (2008). doi: 10.1073/pnas.0807419105; pmid: 18809917
186. D. R. Beers *et al*., ALS patients' regulatory T lymphocytes are dysfunctional, and correlate with disease progression rate and severity. *JCI Insight* **2**, e89530 (2017). doi: 10.1172/jci.insight.89530; pmid: 28289705
187. S.-J. Choi *et al*., High neutrophil-to-lymphocyte ratio predicts short survival duration in amyotrophic lateral sclerosis. *Sci. Rep.* **10**, 428 (2020). doi: 10.1038/s41598-019-57366-y; pmid: 31949271
188. B. J. Murdock *et al*., Natural killer cells associate with amyotrophic lateral sclersois in a sex- and age-dependent manner. *JCI Insight* (2021). doi: 10.1172/jci.insight.147129
189. S. Garofalo *et al*., Natural killer cells modulate motor neuron-immune cell cross talk in models of amyotrophic lateral sclerosis. *Nat. Commun.* **11**, 1773 (2020). doi: 10.1038/s41467-020-15644-8; pmid: 32286313
190. E. R. Chernykh *et al*., Safety and therapeutic potential of M2 macrophages in stroke treatment. *Cell Transplant.* **25**, 1461–1471 (2016). doi: 10.3727/096368915X690279; pmid: 26671426
191. A. D. Greenhalgh *et al*., Peripherally derived macrophages modulate microglial function to reduce inflammation after CNS injury. *PLOS Biol.* **16**, e2005264 (2018). doi: 10.1371/journal.pbio.2005264; pmid: 30332405

ACKNOWLEDGMENTS

We apologize to all those colleagues whose work was discussed without citation owing to space constraints. We thank G. Brodsky for valuable help in designing the figures and S. Schwarzbaum for contributing to editing the manuscript. **Funding:** The Schwartz research group is supported by the Advanced European Research Council (grant no. 7417), the Israel Science Foundation (ISF research grant no. 991/16), and the ISF Legacy Heritage Bio-Medical Science Partnership (research grant no. 1354/15). We thank the Thompson Foundation for their generous support of our AD research. **Competing interests:** M.S. is an inventor of the intellectual property that forms the basis for the development of PD-L1 immunotherapy for AD. The remaining authors declare no competing interests. **License information:** Copyright © 2023 the authors, some rights reserved; exclusive licensee American Association for the Advancement of Science. No claim to original US government works. https://www.science.org/about/science-licenses-journal-article-reuse

Submitted 21 July 2022; accepted 28 February 2023
10.1126/science.abo7649

RESEARCH ARTICLE SUMMARY

IMMUNOLOGY

Germline-encoded amino acid–binding motifs drive immunodominant public antibody responses

Ellen L. Shrock, Richard T. Timms, Tomasz Kula, Elijah L. Mena, Anthony P. West Jr., Rui Guo, I-Hsiu Lee, Alexander A. Cohen, Lindsay G. A. McKay, Caihong Bi, Keerti, Yumei Leng, Eric Fujimura, Felix Horns, Mamie Li, Duane R. Wesemann, Anthony Griffiths, Benjamin E. Gewurz, Pamela J. Bjorkman, Stephen J. Elledge*

INTRODUCTION: Antibodies are generated by a DNA recombination mechanism occurring in the immunoglobulin heavy and light chain genes in which modular VDJ (for heavy) and VJ (for light) gene segments are combinatorially assembled. The vast complexity of the antibody repertoire allows many species to generate antibodies against virtually any protein. However, when different individuals are exposed to a given pathogen they often mount antibody responses to the same precise protein regions—or epitopes—from the pathogen. The mechanisms underlying these recurrent antibody responses to immunodominant "public epitopes" are not well understood.

RATIONALE: We set out to identify a collection of immunodominant public epitopes that would allow us to study mechanisms underlying recurrent antibody responses. We employed VirScan—a phage display platform programmed to display peptides covering the entire human virome—to identify the epitopes of antiviral antibodies from a large cohort of individuals in a high-throughput manner. Additionally, we isolated B cell receptors from different individuals that bound to model public epitopes in order to investigate their determinants of specificity. Finally, we performed a systematic analysis of antibody–antigen structures from the Protein Data Bank (PDB) to search for recurrent modes of antigen recognition.

RESULTS: We mapped 376 immunodominant public epitopes from 51 viral species to single-amino-acid resolution. Antibodies from different individuals that recognized the same public epitope often (i) shared light chain isotype (kappa or lambda) and (ii) bound the same precise critical residues in the epitope. Public epitopes showed biased amino acid composition, including a striking enrichment of lysine at the borders of public epitopes recognized by antibodies with lambda light chains. We examined 50 B cell receptors recognizing three model public epitopes in detail and observed conserved V gene segment usage but almost no conservation of heavy chain CDR3 sequences, indicating that key specificity determinants lay within the V gene segments themselves. Structural analysis of antibody–antigen complexes in the PDB uncovered 18 human V gene segments that harbor germline-encoded amino acid–binding (GRAB) motifs that specifically bind to particular amino acids. Among these were a family of six closely related lambda V gene segments with similar GRAB motifs specific for border lysines. We confirmed that the GRAB motifs we identified were critical for antibody recognition of two model public epitopes. Analysis of murine antibody–antigen structures revealed 21 V gene segment–encoded GRAB motifs that only partially overlapped with the human GRAB motifs, which may explain why there is little overlap between the public epitopes recognized across species. Thus, there appears to be a structural basis underlying the notable convergence in humoral immune responses to immunodominant public epitopes across humans and the differing public epitope selection across species.

CONCLUSION: Recurrent antibody responses to immunodominant public epitopes are a general feature of humoral immunity. We propose that they are driven by GRAB motifs, a germline-encoded component of the architecture of the antibody repertoire that predisposes antibodies to recognize particular structures and thus influences epitope selection and composition. Public epitopes likely arise in part because they are best aligned for recognition by GRAB motifs and can thus be bound by a relatively large precursor pool of B cells. GRAB motifs may have evolved to ensure efficient antibody responses to pathogens; the recurrent responses they engender across populations likely exert selective pressure on pathogens and influence host–pathogen coevolution. ■

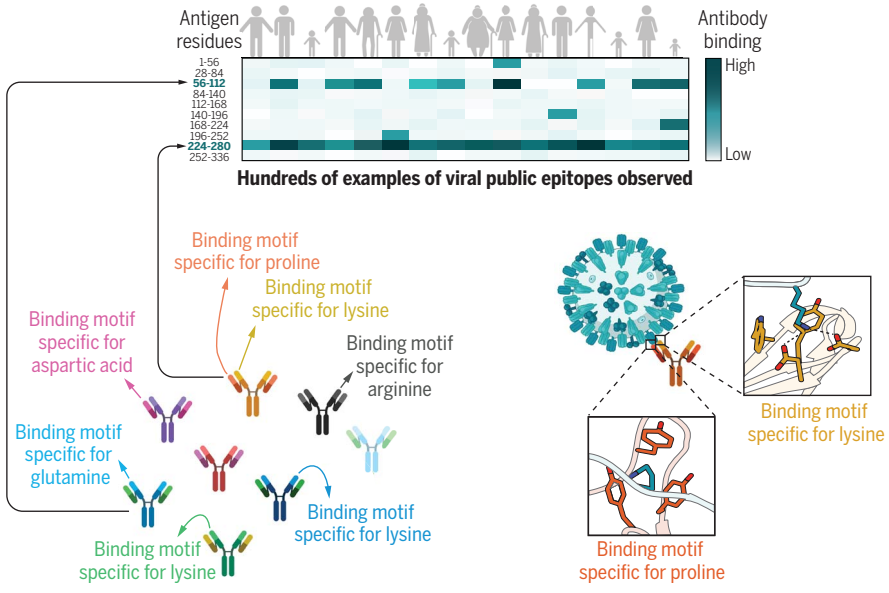

Uncovering origins of public antibody responses. VirScan reveals shared antibody responses to certain regions of viral proteins ("public epitopes") across human populations. Heatmap color represents the strength of the antibody response in each individual (columns) to each peptide of a viral protein (rows). An analysis of antibody–antigen structures reveals that antibody genes harbor germline-encoded motifs that specifically bind certain amino acids and drive recognition of public epitopes.

The list of author affiliations is available in the full article online.
*Corresponding author. Email: selledge@genetics.med.harvard.edu
Cite this article as E. L. Shrock *et al.*, *Science* **380**, eadc9498 (2023). DOI: 10.1126/science.adc9498

READ THE FULL ARTICLE AT
https://doi.org/10.1126/science.adc9498

RESEARCH ARTICLE

IMMUNOLOGY

Germline-encoded amino acid–binding motifs drive immunodominant public antibody responses

Ellen L. Shrock[1,2,3], Richard T. Timms[4]†, Tomasz Kula[1,2,3]†‡, Elijah L. Mena[1,2], Anthony P. West Jr.[5], Rui Guo[6,7,8], I-Hsiu Lee[9], Alexander A. Cohen[5], Lindsay G. A. McKay[10], Caihong Bi[11,12], Keerti[11,12], Yumei Leng[1,2], Eric Fujimura[1,2], Felix Horns[13], Mamie Li[1,2], Duane R. Wesemann[8,11,12,14], Anthony Griffiths[10], Benjamin E. Gewurz[6,7,8,15], Pamela J. Bjorkman[5], Stephen J. Elledge[1,2]*

Despite the vast diversity of the antibody repertoire, infected individuals often mount antibody responses to precisely the same epitopes within antigens. The immunological mechanisms underpinning this phenomenon remain unknown. By mapping 376 immunodominant "public epitopes" at high resolution and characterizing several of their cognate antibodies, we concluded that germline-encoded sequences in antibodies drive recurrent recognition. Systematic analysis of antibody-antigen structures uncovered 18 human and 21 partially overlapping mouse germline-encoded amino acid–binding (GRAB) motifs within heavy and light V gene segments that in case studies proved critical for public epitope recognition. GRAB motifs represent a fundamental component of the immune system's architecture that promotes recognition of pathogens and leads to species-specific public antibody responses that can exert selective pressure on pathogens.

The adaptive immune system relies on an extremely diverse antibody repertoire to mount a response to any pathogen encountered. Antibody diversity is generated by a DNA recombination mechanism occurring in the heavy and light chain genes in which modular VDJ (for heavy) and VJ (for light) gene segments are combinatorially assembled to generate a vast repertoire of variable domain sequences. Immunoglobulin G (IgG) is composed of two heavy and two light chains arranged as a heterodimer with two identical antigen-binding sites, each formed by paired heavy and light chain variable domains. A given antibody has either a kappa or a lambda light chain, which have no known functional difference. Antigen recognition is accomplished primarily by complementarity determining regions (CDRs), which are hypervariable loops within the heavy and light chain variable domains (three in each domain). The heavy and light chain CDR1s and CDR2s are encoded by the V gene segments, whereas the CDR3s span the junctions of the recombined VDJ or VJ gene segments and are thus highly diverse and generally thought to play a dominant role in determining specificity (*1*).

The complexity of the antibody repertoire enables the generation of antibodies to virtually any antigen, yet isolated examples of recurrent responses in different individuals to particular epitopes have been reported (*2*–*13*). Given the challenge of mapping antibody epitopes at high resolution, it has been unclear how common recurrent antibody responses are and how widely they are shared across human populations. Recently, we developed VirScan, a phage display platform programmed to display peptides spanning the human virome, which enabled the high-throughput identification of antiviral antibody epitopes (*14*–*18*). We used VirScan to profile hundreds of human serum samples (*14*) and found that although many viral peptides recognized by an individual were relatively specific to that person, many other viral peptides—which we termed "public epitopes"—were recognized by a substantial percentage (≤98%) of individuals seropositive for the given virus (*14*). Public epitopes were also observed in VirScan studies of antibody responses to allergens and symbiotic microbiota (*19*–*21*). These findings raised a fundamental question: what mechanisms drive recurrent responses to public epitopes?

Results

Public epitopes are a general feature of the human antibody response

To identify a collection of publicly recognized viral peptides from a VirScan analysis of 569 human sera samples (*14*), we chose the 5 most commonly recognized peptides from all viruses for which there were at least 5 seropositive individuals. This yielded a list of 363 viral peptides, 199 of which were recognized by at least 30% of seropositive individuals (Fig. 1A and table S1). These peptides were derived from 62 viral species spanning a broad range of viral classes and encompassed both structural and nonstructural proteins. Antibody responses to publicly recognized peptides appeared unrelated to donor age or geographic location and thus appeared to be a general feature of the human antibody response.

The publicly recognized viral peptides could harbor either a single epitope recognized by many different individuals or multiple epitopes. To distinguish between these possibilities and map individual epitopes more precisely, we designed an additional VirScan library containing tiled truncations and triple-alanine-scan mutations of the 363 publicly recognized 56–amino acid (AA) viral peptides (Fig. 1B and table S2). We profiled the serum antibody responses of ~70 diverse donors with a wide range of viral exposures with this library and observed that the positions of the epitopes recognized by different individuals within these peptides were often identical (fig. S1, A and B).

Antibodies recognizing public epitopes have biased light chain isotype usage

Next, we examined whether antibodies from different individuals that recognized the same public epitope were structurally similar. We adapted the VirScan assay to separately immunoprecipitate (IP) antibodies with kappa versus lambda light chains ("kappa antibodies" and "lambda antibodies," respectively) (Fig. 1B). If different individuals made structurally similar antibodies against a given public epitope, we expected to detect responses to the epitope mainly in kappa or in lambda IP fractions, but if they made structurally diverse antibodies, we would expect no light chain bias. We reprofiled the ~70 human serum samples with the public epitope truncation and alanine-scan library using the kappa- and lambda-specific IP protocol and found that antibody responses to public epitopes were strongly biased in light chain isotype usage. For example, peptides from a 56-AA region

[1]Department of Genetics, Harvard Medical School, Boston, MA 02115, USA. [2]Division of Genetics, Department of Medicine, Howard Hughes Medical Institute, Brigham and Women's Hospital, Boston, MA 02115, USA. [3]Program in Biological and Biomedical Sciences, Harvard University, Boston, MA 02115, USA. [4]Cambridge Institute of Therapeutic Immunology and Infectious Disease, Jeffrey Cheah Biomedical Centre, Cambridge Biomedical Campus, University of Cambridge, Cambridge, UK. [5]Division of Biology and Biological Engineering, California Institute of Technology, Pasadena, CA 91125, USA. [6]Division of Infectious Disease, Department of Medicine, Brigham and Women's Hospital, Harvard Medical School, Boston, MA 02115, USA. [7]Department of Microbiology, Harvard Medical School, Boston, MA 02115, USA. [8]Broad Institute of Harvard and MIT, Cambridge, MA, 02142, USA. [9]Center for Systems Biology, Department of Radiology, Massachusetts General Hospital and Harvard Medical School, Boston, MA 02114, USA. [10]National Emerging Infectious Diseases Laboratories, Boston University School of Medicine, Boston University, Boston, MA 02118, USA. [11]Division of Allergy and Immunology, Division of Genetics, Department of Medicine, Brigham and Women's Hospital, Harvard Medical School, Boston, MA 02115, USA. [12]Massachusetts Consortium on Pathogen Readiness, Boston, MA 02115, USA. [13]Department of Bioengineering, Department of Applied Physics, Chan Zuckerberg Biohub and Stanford University, Stanford, CA 94305, USA. [14]Ragon Institute of MGH, MIT, and Harvard, Cambridge, MA, 02139 USA. [15]Graduate Program in Virology, Division of Medical Sciences, Harvard Medical School, Boston, MA 02115, USA.

*Corresponding author. Email: selledge@genetics.med.harvard.edu

†These authors contributed equally to this work.

‡Present address: Society of Fellows, Harvard University, Cambridge, MA 02138, USA.

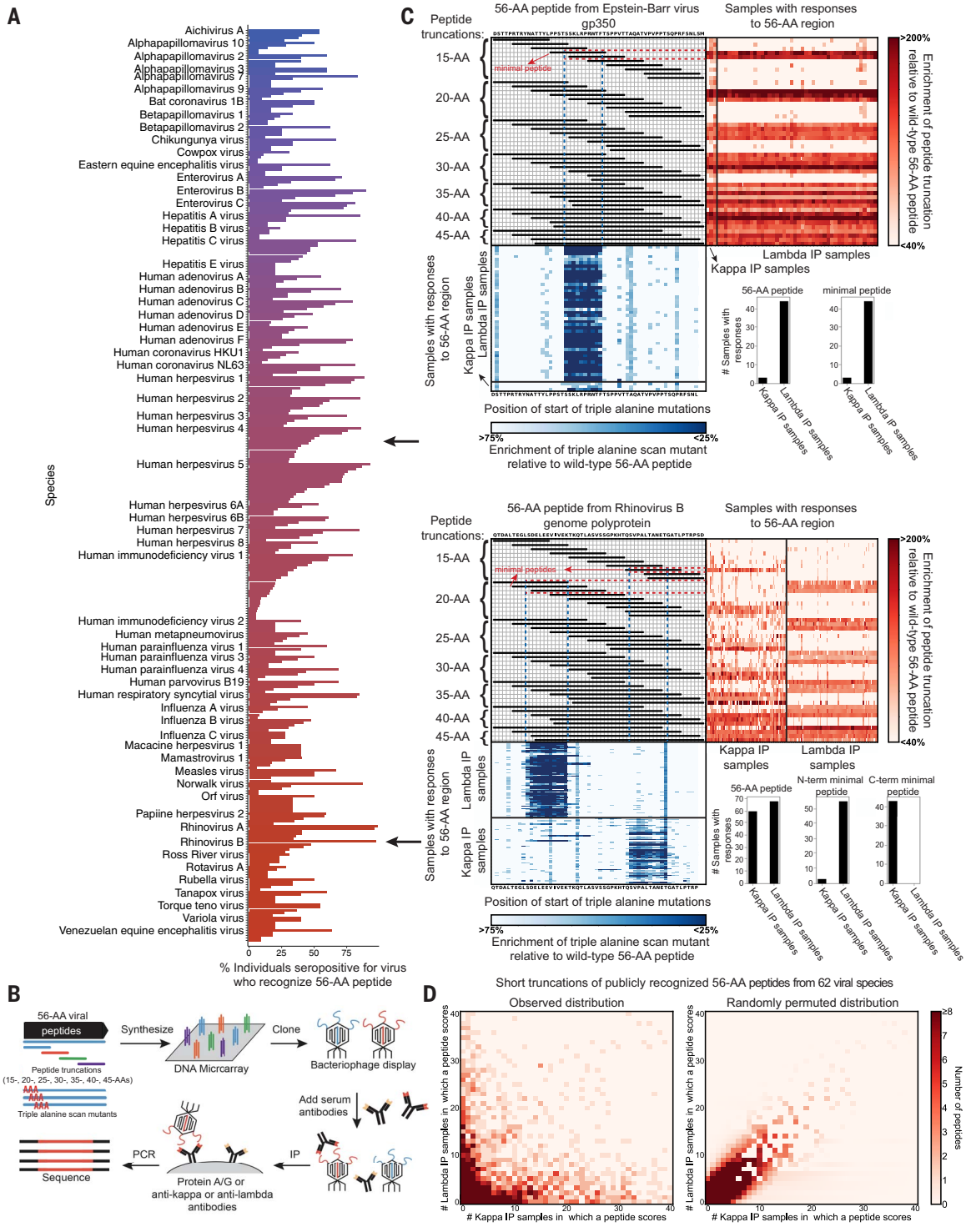

Fig. 1. Recurrent antibody responses to public epitopes are a general feature of humoral immunity and antibodies that recognize a given public epitope have biased light chain isotype usage. (**A**) Percentage of individuals seropositive for a given virus who exhibit antibody responses to each publicly recognized 56-AA peptide. For each viral species, publicly recognized 56-AA peptides are arranged in descending order by their value on the *x* axis. Arrows indicate the peptides detailed in (C). (**B**) Schematic representation of the VirScan assay using the public epitope truncation and alanine scan library (IP, immunoprecipitation). (**C**) Antibody responses to public epitopes from EBV envelope glycoprotein gp350 (top) and rhinovirus B genome polyprotein (bottom) as characterized by VirScan using the kappa and lambda isotype-specific IP protocol. The subset of serum samples exhibiting antibody responses to at least one peptide from the 56-AA region are shown; data are the mean of two technical replicates. AAs are identified by their standard one-letter abbreviations. (**D**) Number of kappa and lambda IP samples that recognize short truncations (15, 20, 25, and 30 AAs in length) of publicly recognized 56-AA peptides from 62 viral species. Observed data (left) and randomly permuted data (right) are shown. Axes are capped at 40 because most data points fell within this range.

of Human Herpesvirus 4 [Epstein-Barr virus (EBV)] were primarily recognized by lambda antibodies across individuals (Fig. 1C). Additionally, a 56-AA region from Rhinovirus B contained two distinct public epitopes, one predominantly recognized by lambda and the other by kappa antibodies across individuals (Fig. 1C and fig. S2). Overall, we observed an inverse distribution in which epitopes tended to be recognized in many donors' lambda IP samples and few kappa IP samples, or vice versa (Fig. 1D). This contrasted with the distribution expected if there were no systematic light chain isotype bias (Fig. 1D and fig. S3). In the few cases where a peptide was recognized by many kappa and many lambda IP samples, distinct kappa and lambda epitopes were evident from the triple-alanine-scan data. Thus, across human populations, antibodies specific for a given public epitope frequently use the same light chain isotype, suggesting that they may share structural similarity. Moreover, light chains appear to be important for antibody recognition of public epitopes.

Antibodies recognizing public epitopes exhibit similar high-resolution footprints

Having found that different individuals recognize similar regions within publicly recognized 56-AA peptides, we next sought to map public epitopes at even higher resolution. We designed a VirScan library with 407 short peptide truncations ("minimal peptides") that captured most of the antibody responses to the original 363 publicly recognized 56-AA peptides (Fig. 1C and table S3), as well as associated saturating mutants in which each AA was substituted with each of the other 19 possible AAs (*19*, *22*) (Fig. 2A, fig. S4, and table S4). We profiled the ~70 human serum samples with the saturating mutagenesis public epitope library, using the kappa- and lambda-specific IP protocol, thus generating a set of high-resolution antibody footprints that identified residues critical for antibody recognition.

For most minimal peptides, different human serum samples produced high-resolution footprints that were similar (Fig. 2B). In many cases, most individuals' high-resolution footprints for a given minimal peptide were highly correlated, often as much so as technical replicates. In some cases, two or more distinct groups of highly correlated high-resolution footprints for a given minimal peptide were evident. Thus, in many cases, different individuals appear to generate antibodies to precisely the same epitopes.

For each minimal peptide, we identified the dominant pattern of critical residues recognized by kappa or, separately, by lambda IP samples. This resulted in a set of 376 consensus viral public epitopes defined at AA resolution: 189 recognized by kappa antibodies ("kappa public epitopes") and 187 recognized by lambda antibodies ("lambda public epitopes") (tables S5 and S6). For 232 of the 376 consensus public epitopes, sera from more than one-third of individuals that recognized the minimal peptide targeted the same consensus pattern of critical residues (Fig. 2D and table S7). The public epitopes had an average of four critical residues and spanned an average of seven AAs from the first to last critical residue (tables S5 and S6).

Substitution of critical residues with chemically related AAs (*23*, *24*) were frequently tolerated (e.g., A-S, I-L, I-V, Y-F) (fig. S5), with some exceptions: neither K-R nor D-E swaps were particularly well tolerated. Some differences in substitution tolerance in kappa versus lambda public epitopes were observed, (e.g., for W-F, W-Y, and A-P), suggesting different modes of binding certain AAs.

Critical residues of public epitopes have a distinctive AA composition

The large number of consensus public epitopes we mapped allowed us to examine their AA composition, relative to the human viral proteome. Most notably, lysines were significantly enriched among critical residues of lambda ($P < 5 \times 10^{-33}$, binomial test) but not kappa public epitopes. Among other differences, prolines and tryptophans were strongly enriched, whereas serines, threonines, and valines were depleted in all public epitopes. (Fig. 3A). Although some of these differences may have resulted from the enrichment of particular residues on protein surfaces, others may have reflected preferential recognition of these AAs by kappa and/or lambda antibodies.

The majority of lambda public epitopes have border lysine residues

Next, we investigated whether lysine residues were preferentially situated at particular position(s) within lambda public epitopes. We examined the frequency of each AA at border (first or last critical residues) or interior (all other critical residues) positions of public epitopes, relative to their frequency in the human viral proteome (Fig. 3, B and C). Several AAs were enriched or depleted at border or interior positions of kappa and/or lambda public epitopes. Most notably, lysine was enriched at border positions of public epitopes (enrichment $P < 5 \times 10^{-69}$). Of all 135 lysines in critical residues of lambda public epitopes, 127 were located at border positions and 61% of all lambda public epitopes featured a border lysine (table S6). We hypothesized that some lambda antibodies may harbor specificity for lysine.

B cell receptors specific for three public epitopes exhibit conserved gene segment usage but distinct heavy chain CDR3 sequences

To explore sequence determinants of specificity for public epitopes, we initially selected two minimal peptides as case studies, both of which elicited highly conserved high-resolution antibody footprints across individuals: a kappa minimal peptide from influenza A hemagglutinin and a lambda minimal peptide from EBV gp350. We then isolated and sequenced B cell receptors (BCRs) specific for these peptides (Fig. 4A).

We obtained nine BCRs that recognized the influenza A minimal peptide from six donors (Fig. 4B, fig. S6, A to C, and table S8). All had kappa light chains and conserved gene segment usage: IgHV5-51 paired with IgKV4-1. They also featured similar light chain CDR3 sequences. The heavy chain CDR3 sequences were not conserved although they were longer than average (~20 versus ~15 AAs for the overall antibody repertoire) (*25*, *26*). We profiled each of these antibodies with the saturating mutagenesis public epitope VirScan library and observed similar high-resolution footprints (fig. S7). All nine antibodies bound to intact influenza A H3 hemagglutinin trimers, but none were neutralizing (fig. S8).

We obtained 19 BCRs that recognized the EBV minimal peptide from four donors (Fig. 4C, fig. S6, A, D, E, and F, and table S9). Many shared conserved gene segment usage (IgHV1-46, frequently paired with IgLV3-10) but did not share conserved heavy chain CDR3 sequences. The IgHV1-46/IgLV3-10 BCRs from different donors exhibited almost identical high-resolution footprints (fig. S9), indicating that different individuals generate BCRs that recognize the EBV minimal peptide in extremely similar ways. A representative subset of the EBV minimal peptide-specific antibodies bound to full-length gp350 (fig. S10).

As a third case study, we isolated 19 BCRs that bound a publicly recognized SARS-CoV-2 spike peptide that overlaps with the fusion peptide (Fig. 4D) (*18*). These BCRs exhibited more diverse V gene segment usage than the flu and EBV BCRs. Nevertheless, 11 BCRs featured IgHV3 genes (IgHV3-30, IgHV3-23, and IgHV3-64D) and diverse heavy chain CDR3 sequences, and these BCRs exhibited very similar high-resolution footprints (fig. S11). Thus, IgHV3-30, IgHV3-23, and IgHV3-64D may share common features that enable recognition of the spike fusion peptide epitope. All 19 antibodies bound to the S2 domain of spike though only a few bound to full-length spike, and none out of a representative subset were neutralizing (fig. S12). This was consistent with reports of other antibodies that bound to this fusion peptide epitope but only when spike was engaged with ACE2 and thus constrained in the up conformation (*27*–*29*). From these three case studies, the theme of conserved V gene segment usage in the absence of the conserved heavy chain CDR3 sequence suggested that antibodies may recognize public epitopes through germline-encoded sequences within the V gene segments.

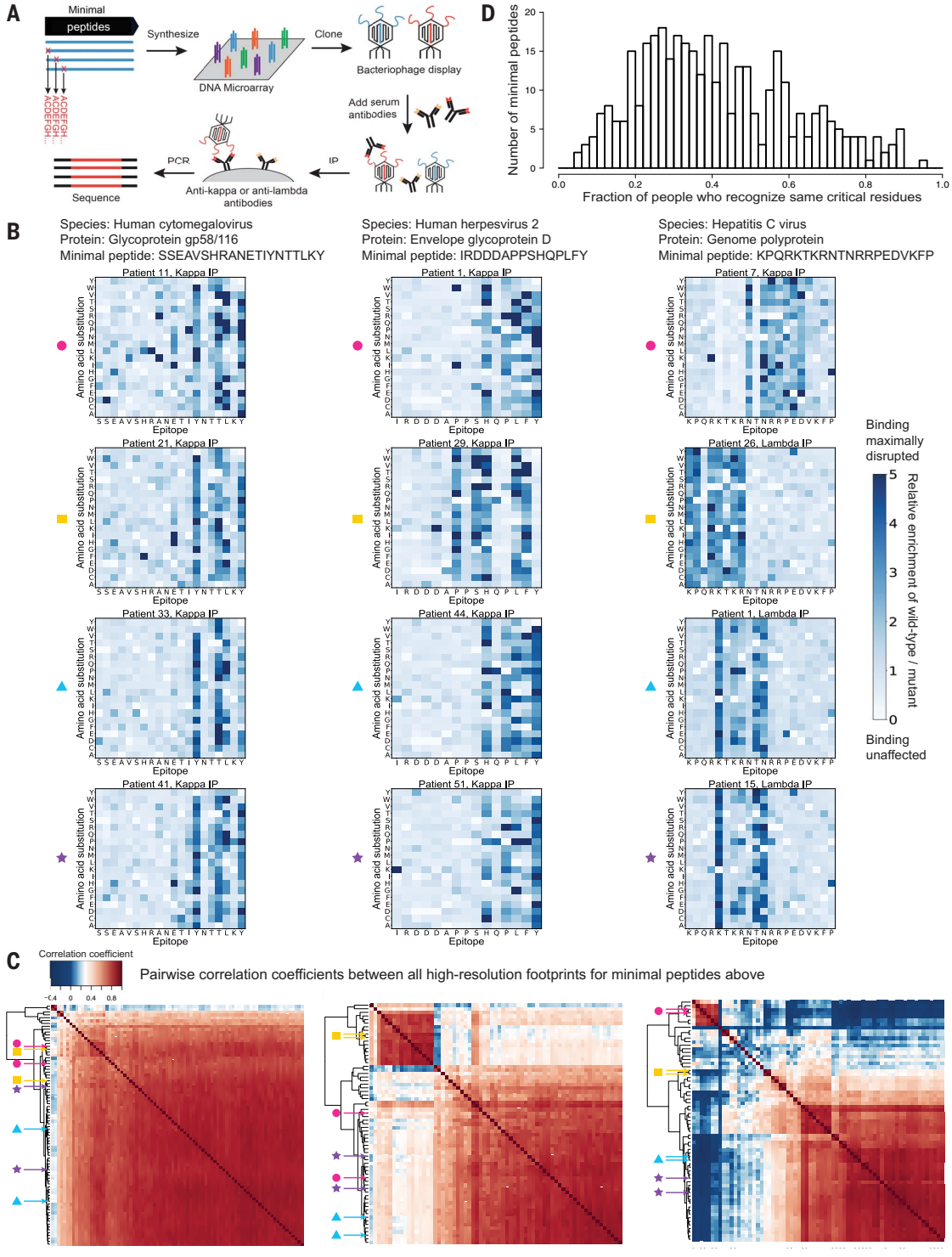

Fig. 2. Antibodies recognizing public epitopes often exhibit similar high-resolution footprints. (**A**) Construction of the saturating mutagenesis public epitope library and VirScan screening procedure. Throughout, AAs are identified by their standard one-letter abbreviations. (**B**) Representative high-resolution antibody footprints from different individuals for minimal peptides from human cytomegalovirus (left), human herpesvirus 2 (center), and hepatitis C virus (right). The sequence of the minimal peptide is shown on the *x* axis and the AA substitution on the *y* axis. The darker the blue color, the greater the disruption of antibody binding. Colored shapes to the left side of each high-resolution footprint are coordinated with colored arrows in (C) to indicate the location of the high-resolution footprints and their technical replicates within the clustered heatmaps. (**C**) Clustered heatmaps illustrating the similarities between all high-resolution antibody footprints for the three example minimal peptides in (B); these were obtained by calculating the pairwise Pearson correlation coefficients between the enrichment matrices (see methods) of each serum sample that recognized the minimal peptide. Colored arrows are coordinated with colored shapes in (B) to indicate the location of the high-resolution footprints from (B) and their technical replicates within the clustered heatmaps. (**D**) Histogram depicting the fraction of individuals whose kappa or, separately, lambda antibody responses to a given minimal peptide recognized the consensus pattern of critical residues or only differed by one position.

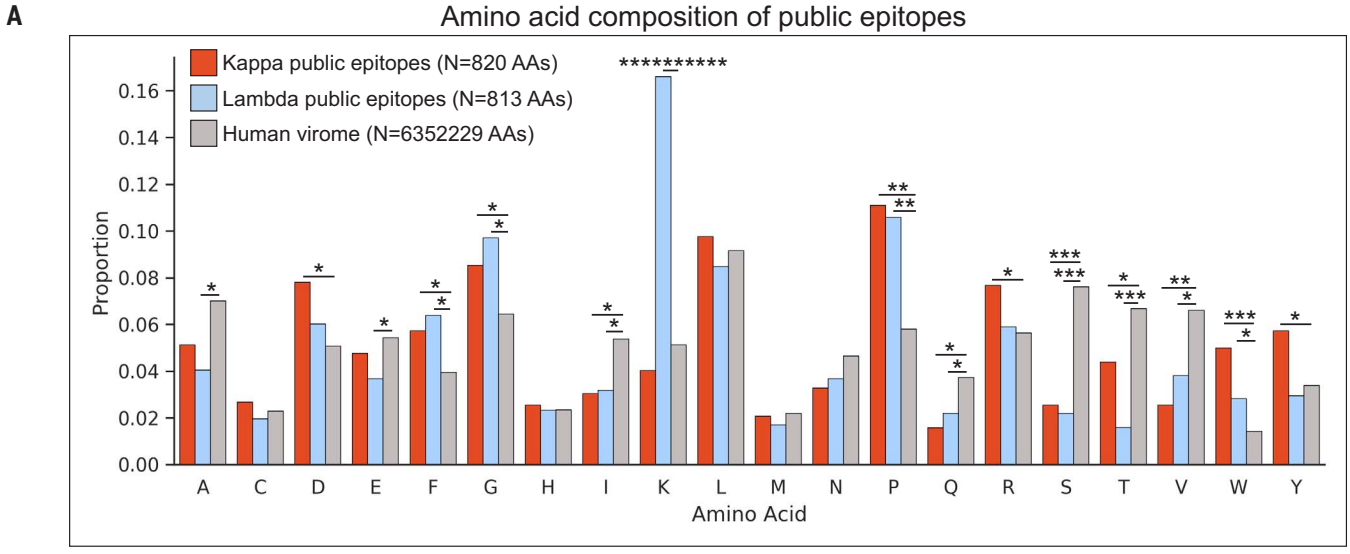
A
Amino acid composition of public epitopes
Kappa public epitopes (N=820 AAs)
Lambda public epitopes (N=813 AAs)
Human virome (N=6352229 AAs)
****
Proportion
Amino Acid
A C D E F G H I K L M N P Q R S T V W Y

	A	C	D	E	F	G	H	I	K	L	M	N	P	Q	R	S	T	V	W	Y
p-value kappa	0.034	0.41	7.8E-4	0.44	0.012	0.019	0.64	0.0019	0.18	0.54	0.91	0.068	5.5E-9	4.3E-4	0.015	8.7E-10	0.0077	2.3E-7	1.8E-11	6.5E-4
p-value lambda	5.6E-4	0.64	0.23	0.025	8.3E-4	3.4E-4	1	0.0040	5.4E-33	0.54	0.40	0.21	1.1E-7	0.020	0.70	3.2E-11	1.2E-11	6.9E-4	0.0028	0.56

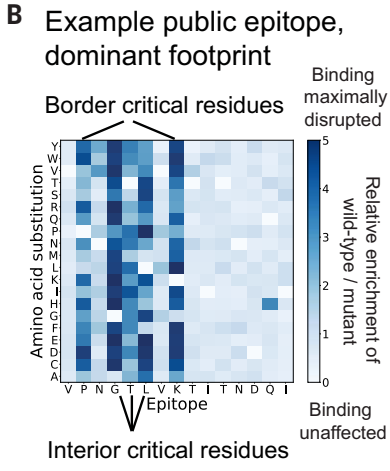
B
Example public epitope, dominant footprint
Border critical residues
Binding maximally disrupted
Amino acid substitution
Relative enrichment of wild-type / mutant
V P N G T L V K T I T N D Q I
Epitope
Binding unaffected
Interior critical residues

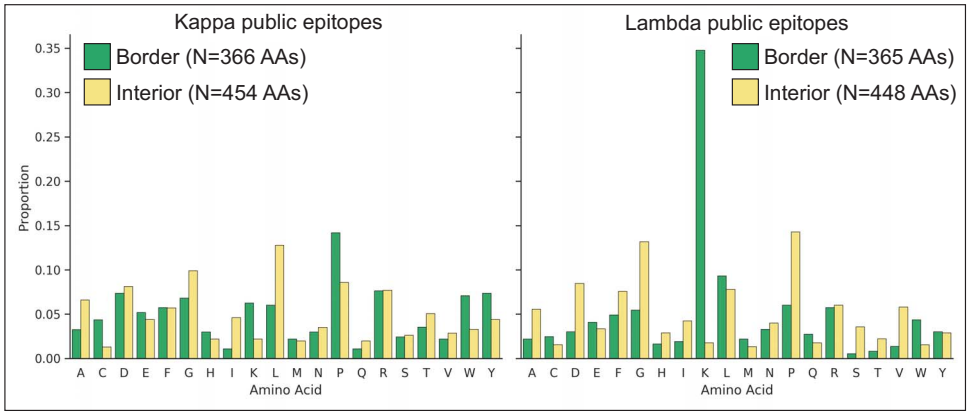
C
Amino acid composition of border vs interior residues of public epitopes
Kappa public epitopes
Border (N=366 AAs)
Interior (N=454 AAs)
Lambda public epitopes
Border (N=365 AAs)
Interior (N=448 AAs)
Proportion
Amino Acid
A C D E F G H I K L M N P Q R S T V W Y

	A	C	D	E	F	G	H	I	K	L	M	N	P	Q	R	S	T	V	W	Y
p-value kappa border	0.0038	0.014	0.055	1.0	0.082	0.75	0.39	3.6E-5	0.29	0.037	1.0	0.17	3.3E-9	0.0036	0.11	4.2E-5	0.015	1.9E-4	5.4E-11	2.1E-4
p-value kappa interior	0.85	0.21	0.0051	0.41	0.069	0.0053	1.0	0.53	0.0027	0.011	0.87	0.31	0.015	0.047	0.066	1.1E-5	0.19	6.1E-4	0.0043	0.24
p-value lambda border	5.5E-5	0.73	0.073	0.30	0.34	0.52	0.49	0.0016	6.0E-69	0.93	1.0	0.26	0.82	0.41	0.91	2.8E-10	7.8E-8	4.0E-6	1.1E-4	0.88
p-value lambda interior	0.27	0.43	0.0023	0.048	3.6E-4	2.3E-7	0.43	0.34	5.2E-4	0.37	0.26	0.65	4.3E-11	0.025	0.68	6.5E-4	2.6E-5	0.57	0.69	0.69
p-value lambda border excluding lysine	0.029	0.13	0.88	0.57	0.011	0.23	0.83	0.11		0.0093	0.26	0.76	0.036	0.61	0.047	3.4E-6	1.3E-4	0.0024	5.2E-7	0.28
p-value lambda interior excluding lysine	0.30	0.42	0.0015	0.058	3.1E-4	1.5E-7	0.43	0.40		0.46	0.33	0.65	2.2E-11	0.032	0.61	8.2E-4	4.9E-5	0.63	0.69	0.79

Fig. 3. Critical residues of public epitopes have a distinctive AA composition, including profound enrichment of lysine at the borders of lambda public epitopes. (**A**) AA composition of critical residues of lambda and kappa public epitopes, relative to the entire human virome library. *P* values (binomial test) are listed below. Those that remain below the significance threshold of 0.05 after correcting for multiple hypothesis testing with the Benjamini–Hochberg false discovery rate method are indicated with asterisks in the bar chart (*$P < 0.05$, **$P < 10^{-6}$, ***$P < 10^{-9}$, **********$P < 10^{-30}$) and colored in red (enriched AAs) or blue (depleted AAs). (**B**) Diagram indicating the positions of border and interior critical residues in a representative high-resolution antibody footprint. (**C**) AA composition of critical residues found at border or interior positions of kappa and lambda public epitopes. *P* values (binomial test) as in (A) are listed at the bottom of the figure.

To examine potential polyspecificity of public epitope-reactive antibodies we profiled each of our influenza A-, SARS-CoV-2-, and a representative subset of our EBV minimal peptide-reactive antibodies against the human virome VirScan library (>100,000 peptides from >200 viral species) (*15*). Almost all the monoclonal antibodies we tested specifically bound peptides containing their cognate public epitope sequences; some cross-reacted with peptides that shared very similar sequences (fig. S13). Thus, the phenomenon of public epitopes is due to recurrently generated antibodies specific for these epitopes rather than polyreactive antibodies.

A germline-encoded aspartic acid at position 51 of several lambda V gene segments drives specificity for border lysines

The border lysine enrichment in lambda public epitopes suggested that lysine might specifically interact with lambda light chains, possibly through pairing with a germline-encoded acidic

A

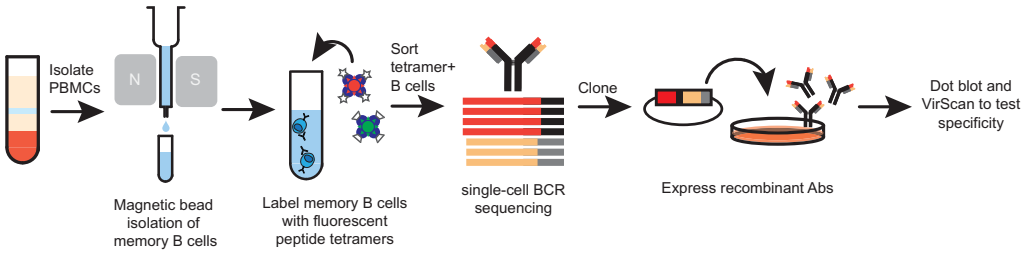

B

Organism: Influenza A virus (strain A/Memphis/3/1988 H3N2)
Protein: Hemagglutinin
Minimal peptide: V**PNGTL**V**K**TITNDQI

Donor	Clonotype ID	IgH CDR3	IgH V gene	IgH D gene	IgH J gene	IgH C gene	IgL/K CDR3	IgL/K V gene	IgL/K J gene	IgL/K C gene
1	flu_c326	CAKPYNYCNTTTCYTRGYFDFW	IGHV5-51	IGHD2-2	IGHJ4	IGHG1	CQQYYFTPYTF	IGKV4-1	IGKJ2	IGKC
2	flu_c357	CARLPHRESGNVSTTWGWFDPW	IGHV5-51	IGHD3-10	IGHJ5	IGHG1	CQQYFSTPYTF	IGKV4-1	IGKJ2	IGKC
3	flu_c504	CAMCVGSPTCYGWFDPW	IGHV5-51	IGHD2-2	IGHJ5	IGHA1	CQQYHSIPYTF	IGKV4-1	IGKJ2	IGKC
3	flu_c645	CARAPVPGMSGWFDPW	IGHV5-51	IGHD6-19	IGHJ5	IGHG1	CQQYFYTPYTF	IGKV4-1	IGKJ2	IGKC
4	flu_c3	CARPPHFIDAGGRQTPGYFDLW	IGHV5-51	IGHD2-8	IGHJ4	IGHG1	CQQYHDSPYTF	IGKV4-1	IGKJ2	IGKC
5	flu_c286	CARGVQDCDSRNCYAYNWFDPW	IGHV5-51	IGHD3-16	IGHJ5	IGHG1	CQQYYYSPYTF	IGKV4-1	IGKJ2	IGKC
6	flu_c473	CARGVQSCIRNTCSFYGWFDRW	IGHV5-51	IGHD2-2	IGHJ5	IGHG3	CQQYFYSPYTF	IGKV4-1	IGKJ2	IGKC
7	flu_c2760	CARVPEGSVVAGEVHFYYYMDVW	IGHV5-51	IGHD2-15	IGHJ6	IGHG3	CQQYYFTPYTF	IGKV4-1	IGKJ2	IGKC
7	flu_c4582	CARGAATILRGVVTSYNWFDSW	IGHV5-51	IGHD3-10	IGHJ5	IGHG1	CQQYFSTPYTF	IGKV4-1	IGKJ2	IGKC

C

Organism: Epstein-Barr virus (strain AG876) (HHV-4) (Human Herpesvirus 4)
Protein: Envelope glycoprotein gp350
Minimal peptide: PPSTSS**KLR**PRW**T**FT

	Donor	Clonotype ID	IgH CDR3	IgH V gene	IgH D gene	IgH J gene	IgH C gene	IgL/K CDR3	IgL/K V gene	IgL/K J gene	IgL/K C gene
	A	EBV_c186	CTRDRDQRLLFDYW	IGHV1-46	IGHD6-25	IGHJ4	IGHG2	CYSKDRF	IGLV3-10	IGLJ2	IGLC2
Same precursor	B	EBV_c9	CARGPDYVGISSPFDYW	IGHV1-46	IGHD4-23	IGHJ4	IGHG1	CYSGDSNGNHWVF	IGLV3-10	IGLJ3	IGLC2
Same precursor	B	EBV_c19	CARGPDYGGNSSPFDNW	IGHV1-46	IGHD4-23	IGHJ4	IGHG1	CYSGDINGNHWVF	IGLV3-10	IGLJ3	IGLC2
Same precursor	B	EBV_c61	CARGPDSSGISSPFDYW	IGHV1-46	IGHD4-23	IGHJ4	IGHG1	CYSGDTNGNHWVF	IGLV3-10	IGLJ3	IGLC2
Same precursor	B	EBV_c149	CARGPDYVGISSPFDFW	IGHV1-46	IGHD4-23	IGHJ4	IGHG1	CYSGDSNGNHWVF	IGLV3-10	IGLJ3	IGLC2
	C	EBV_c101	CARGTAVSTNLGLLFDLW	IGHV1-46	IGHD1-26	IGHJ5	IGHG1	CFSADSSGTHSVF	IGLV3-10	IGLJ1	IGLC1
	D	EBV_c150	CARVPPDDGYFDYW	IGHV1-46	IGHD1-14	IGHJ4	IGHG1	CYTTGSSVSHVVF	IGLV3-10	IGLJ2	IGLC2
	D	EBV_c40	CARARDLYGDSDFDYW	IGHV1-46	IGHD4-17	IGHJ4	IGHG1	CQAWESSNVVF	IGLV3-1	IGLJ2	IGLC2
	B	EBV_c124	CARAAEGDYGDSALDYW	IGHV1-46	IGHD4-17	IGHJ4	IGHG3	CQVWDSNTVVF	IGLV3-1	IGLJ2	IGLC2
	C	EBV_c63	CARDREQMVRGIIISNGLDVW	IGHV1-46	IGHD3-10	IGHJ6	IGHG1	CSSYTSSSTLVF	IGLV2-14	IGLJ1	IGLC1
	D	EBV_c83	CARVGYNWGSHSVSSPGAMDVW	IGHV1-46	IGHD3-16	IGHJ6	IGHA1	CQSADTGGTYVIF	IGLV3-25	IGLJ2	IGLC2
Same precursor	B	EBV_c3	CARAFCNSDRCSPELFDPW	IGHV1-8	IGHD1-26	IGHJ5	IGHG1	CATWDTSLRGVVF	IGLV1-51	IGLJ2	IGLC2
Same precursor	B	EBV_c10	CARAFCNSNRCSPELFDPW	IGHV1-8	IGHD2-2	IGHJ5	IGHG1	CATWDNSLRGVVF	IGLV1-51	IGLJ2	IGLC2
Same precursor	B	EBV_c77	CARAFCNSDRCSPELFDPW	IGHV1-8	IGHD1-26	IGHJ5	IGHG1	CATWDTSLRGVVF	IGLV1-51	IGLJ2	IGLC2
Same precursor	B	EBV_c120	CARAYCNSNRCSPELFDPW	IGHV1-8	IGHD3-22	IGHJ5	IGHG1	CATWDSSLRGVVF	IGLV1-51	IGLJ2	IGLC2
Same precursor	B	EBV_c127	CARAFCNSDRCSPELFDPW	IGHV1-8	IGHD1-26	IGHJ5	IGHG1	CATWDNSLRGVLF	IGLV1-51	IGLJ2	IGLC2
Same precursor	B	EBV_c138	CARAFCNSDRCSPELFDPW	IGHV1-8	IGHD1-26	IGHJ5	IGHG1	CATWDTSLRGVVF	IGLV1-51	IGLJ2	IGLC2
	C	EBV_c57	CEAIAAVSATEGAFDIW	IGHV1-8	IGHD6-13	IGHJ3	IGHG1	CAAWDDSLTAWVF	IGLV1-47	IGLJ3	IGLC3
	B	EBV_c98	CAKDTIFDGMDVW	IGHV3-30	IGHD3-3	IGHJ6	IGHG1	CMQSTHWPLTF	IGKV2-30	IGKJ4	IGKC

D

Organism: SARS-CoV-2
Protein: Spike glycoprotein
Minimal peptide: DPSKPSK**R**SFI**ED**L**LF**NKVTLADAG

	Clonotype ID	IgH CDR3	IgH V gene	IgH D gene	IgH J gene	IgH C gene	IgL/K CDR3	IgL/K V gene	IgL/K J gene	IgL/K C gene
Same precursor	CoV2_c0	CARGRHLTNSYDRVHMDVW	IGHV3-30	IGHD3-3	IGHJ6	IGHG1	CQHYDYPIVFTF	IGKV1-33	IGKJ3	IGKC
Same precursor	CoV2_c9	CSRGRNLKNNYHRVYLDVW	IGHV3-30	IGHD1-1	IGHJ6	IGHG1	CQHYDFPIIFTF	IGKV1-33	IGKJ3	IGKC
Same precursor	CoV2_c33	CARGRNLENNYHRVHMDVW	IGHV3-30	IGHD5-24	IGHJ6	IGHG1	CQQYDYPIIFTF	IGKV1-33	IGKJ3	IGKC
Same precursor	CoV2_c49	CARGRHLRDNYHRVHMDVW	IGHV3-30	IGHD1-1	IGHJ6	IGHG1	CQHYDYPIVFTF	IGKV1-33	IGKJ3	IGKC
Same precursor	CoV2_c55	CSRGRNLKNKYHRVYMDVW	IGHV3-30	IGHD1-14	IGHJ6	IGHG1	CQHYDYPILFTF	IGKV1-33	IGKJ3	IGKC
	CoV2_c7	CARDAFNVLTAYLSPSPSLDFW	IGHV3-30	IGHD3-9	IGHJ4	IGHG2	CQQYHDWPLITF	IGKV3-15	IGKJ5	IGKC
	CoV2_c48	CARDPYIFPTALPLDYW	IGHV3-30	IGHD3-9	IGHJ4	IGHG1	CQQYDDWPLITF	IGKV3-15	IGKJ5	IGKC
Same precursor	CoV2_c2	CAKALWVGDFNDW	IGHV3-23	IGHD3-10	IGHJ4	IGHG1	CSYGGTSTFHVVF	IGLV2-23	IGLJ2	IGLC2
Same precursor	CoV2_c11	CAKALWVGDFNDW	IGHV3-23	IGHD3-10	IGHJ4	IGHG1	CSYGGTSTFHVVF	IGLV2-23	IGLJ2	IGLC2
Same precursor	CoV2_c51	CAKALWVGDFNDW	IGHV3-23	IGHD3-10	IGHJ4	IGHG1	CSYGGTSTFHVVF	IGLV2-23	IGLJ2	IGLC2
	CoV2_IIc2	CVKTMAPPVLWFEKLRDDAFDIW	IGHV3-64D	IGHD3-10	IGHJ3	IGHG3	CMLGTHWPELTF	IGKV2-30	IGKJ4	IGKC
	CoV2_c4	CTTWWFW	IGHV3-15	IGHD2-15	IGHJ4	IGHG1	CHSRGSGDDLLVF	IGLV3-19	IGLJ1	IGLC1
Same precursor	CoV2_c18	CTTWWIW	IGHV3-15	IGHD2-15	IGHJ3	IGHG1	CQSRSTSGPHLVF	IGLV3-19	IGLJ3	IGLC2
Same precursor	CoV2_c40	CTTWWIW	IGHV3-15	IGHD2-15	IGHJ3	IGHG1	CQSRAASGSHLVF	IGLV3-19	IGLJ2	IGLC2
Same precursor	CoV2_c47	CTTWWVW	IGHV3-15	IGHD2-15	IGHJ3	IGHG3	CQSRATSGNHLLF	IGLV3-19	IGLJ3	IGLC2
	CoV2_c45	CASLNVTCW	IGHV1-2	IGHD2-8	IGHJ4	IGHG2	CYSTDSSGNHWVF	IGLV3-10	IGLJ3	IGLC2
	CoV2_c54	CATGVAPLVPIDYW	IGHV1-2	IGHD3-16	IGHJ4	IGHA1	CQRYSSAPWTF	IGKV1-27	IGKJ1	IGKC
	CoV2_c8	CARVEPTVTEGSFDYW	IGHV1-18	IGHD4-17	IGHJ4	IGHA1	CQSADSSGTYVF	IGLV3-25	IGLJ1	IGLC1
	CoV2_c50	CARQSVPLDGFDLW	IGHV3-20	IGHD2-2	IGHJ3	IGHA1	CQSGDSRGILF	IGLV3-25	IGLJ2	IGLC2

Fig. 4. BCRs specific for example public epitopes share conserved gene segment usage but not heavy chain CDR3 sequences. (**A**) Schematic representation of the workflow to isolate public epitope-specific B cells. PBMCs were isolated from multiple healthy donors and pooled. Switched (IgG^+ and IgA^+) memory B cells were then purified by magnetic-activated cell sorting, split into aliquots to be labeled with customized CITE-Seq antibody barcodes, and then stained with fluorescent peptide tetramers. Fluorescent cells were isolated by FACS and analyzed by single-cell BCR sequencing. (**B** to **D**) Sequence characteristics of BCRs validated to bind three example minimal peptides. Consensus critical residues within the minimal peptides are shown in bold and conserved gene segments and CDR3 sequences are shown in red.

residue. We searched the Protein Data Bank (PDB) (*30*–*32*) for human lambda (n = 297) and kappa (n = 631) antibody-antigen (Ab-Ag) complexes and found that light chain position 51 directly interacted with lysines in antigens much more frequently in lambda than kappa Ab-Ag complexes (Fig. 5A). In these interactions, lambda light chain position 51 was almost always a germline-encoded aspartic acid.

We selected two antibodies that bound the same EBV minimal peptide described above but that recognized distinct critical residues: EBV_c186, which recognized a border lysine, and EBV_c40, which did not (Fig. 5B and fig. S9). We individually mutated each aspartic acid (D) or glutamic acid (E) of their lambda light chains to lysine (K) (for maximal disruption) and assessed impacts on binding by dot blot. The D51K mutation disrupted the binding of EBV_c186 but not EBV_c40, suggesting that D51 was important for border lysine recognition

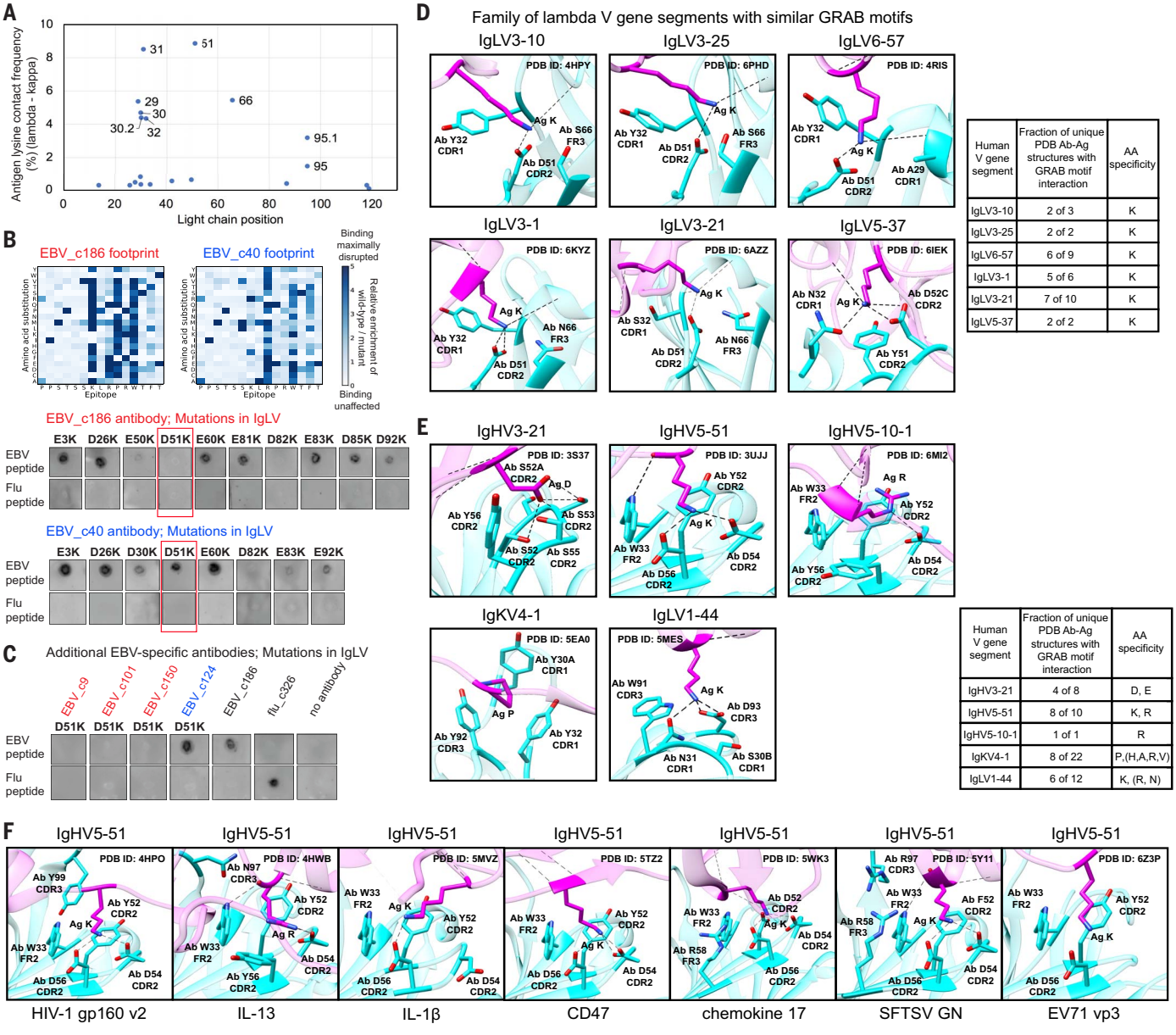

Human V gene segment	Fraction of unique PDB Ab-Ag structures with GRAB motif interaction	AA specificity
IgLV3-10	2 of 3	K
IgLV3-25	2 of 2	K
IgLV6-57	6 of 9	K
IgLV3-1	5 of 6	K
IgLV3-21	7 of 10	K
IgLV5-37	2 of 2	K

Human V gene segment	Fraction of unique PDB Ab-Ag structures with GRAB motif interaction	AA specificity
IgHV3-21	4 of 8	D, E
IgHV5-51	8 of 10	K, R
IgHV5-10-1	1 of 1	R
IgKV4-1	8 of 22	P,(H,A,R,V)
IgLV1-44	6 of 12	K, (R, N)

Fig. 5. Many antibody V gene segments feature GRAB motifs that recurrently recognize specific AAs in antigens. (**A**) An aspartic acid germline-encoded at position 51 of several lambda V gene segments drives specificity for border lysines in epitopes. Differences in frequencies (lambda-kappa) with which each position of the light chain contacts lysine residues in the antigen in human lambda (n = 297) and kappa Ab-Ag complexes (n = 631) in the PDB. (**B** and **C**) The indicated mutations were introduced into a panel of EBV minimal peptide-specific antibodies and the impacts on antigen binding assayed by dot blot. The epitopes of antibodies shown in red include border lysines, whereas the epitopes of those shown in blue do not. EBV and influenza A minimal peptides (146786 and 72153 in table S3, respectively) were spotted on the nitrocellulose membranes; flu_c326 served as a control. (**D** and **E**) Representative GRAB motif interactions for the indicated human V gene segments. The antigen residue is shown in magenta and all antibody residues whose side chains interact with the antigen residue are shown in cyan (FR, framework region). Summary tables (right) show the fraction of unique PDB Ab-Ag structures with the relevant V gene segment that feature the GRAB motif interaction. Throughout, PDB structures are visualized with UCSF Chimera (*72*). (**F**) Images of the other seven unique Ab-Ag structures involving IgHV5-51 that feature the GRAB motif interaction, labeled as in (D) and (E). Throughout, all residue positions follow the Chothia antibody numbering system. References for PDB Ab-Ag structures are provided in table S10.

(Fig. 5B). The D51K mutation also disrupted the binding of three additional antibodies (EBV_c9, EBV_c101, and EBV_c150) whose epitopes within the EBV minimal peptide contained a border lysine, but had no effect on EBV_c124, whose epitope lacked a border lysine (Fig. 5C).

At least six lambda V gene segments share similar germline-encoded lysine-specific binding motifs

Although a single salt bridge may stabilize an interaction, it alone cannot confer lysine specificity. To define additional residues involved, we investigated all Ab-Ag structures from the PDB with light chain position 51-antigen lysine interactions and uncovered a family of six lambda V gene segments (IgLV3-10, IgLV3-25, IgLV6-57, IgLV3-1, IgLV3-21, and IgLV5-37) that shared similar germline-encoded lysine-specific binding motifs. We called these germline-encoded amino acid–binding (GRAB) motifs (Fig. 5D and table S10). The GRAB motif in IgLV3-1 encompassed germline-encoded residues Y32 from CDR1, D51 from CDR2, and N66 from framework region 3 to specifically bind lysine in the antigen. D51 made a salt bridge with the lysine amine and Y32 made nonpolar interactions with the carbons of the side chain. Five of the six unique IgLV3-1 Ab-Ag complexes in the PDB featured this lysine-GRAB motif interaction (Fig. 5D and table S11, tab A). IgLV3-10, IgLV3-25, IgLV6-57, and IgLV3-21 harbored nearly identical lysine-specific GRAB motifs to IgLV3-1, whereas the IgLV5-37 GRAB motif differed somewhat, with Y51, D52C, and N32 making cation-pi, salt-bridge, and hydrogen-bond interactions with the lysine amine, respectively. Cumulatively, 75% (24 of 32) PDB Ab-Ag structures involving these six V gene segments featured a lysine-GRAB motif interaction (Fig. 5D and table S11, tab A). Of these 24 structures, 16 involved conformational epitopes, indicating that GRAB motifs are important for recognition of both conformational and linear epitopes. Additionally, the lysine was almost always found at the edge of the epitope in both conformational and linear antigens (fig. S14 and table S11, tab A), possibly because these GRAB motifs are largely encoded by CDR1 and CDR2, the loops of which are oriented on the "outside" of the variable domain structure relative to the "interior" CDR3 loops. Alignment of Ab-Ag structures with the lysine-GRAB motif interaction showed similar interaction orientations (fig. S15A). Thus, IgLV lysine GRAB motifs encode specificity for border lysines and may drive the enrichment of lysine at the borders of lambda public epitopes, profoundly influencing the AA composition of public epitopes.

In addition to the six lambda V gene segments with lysine-specific GRAB motifs, four additional lambda V gene segments (IgLV3-9*02, IgLV3-16, IgLV3-22, and IgLV3-27) had germline-encoded Y/S32, D51, and S/T66 residues that were predicted by AlphaFold2 (*33*, *34*) to fold into similar structures as the GRAB motifs described above (fig. S15B and table S11, tab C). However, there are currently no Ab-Ag complexes in the PDB involving these gene segments to confirm their specificity.

Multiple heavy, kappa, and lambda V gene segments harbor GRAB motifs specific for particular AAs

The principle of GRAB motifs is not necessarily limited to lambda V gene segments or lysines. Therefore, we expanded our PDB analysis to search all human V gene segments (heavy, kappa, and lambda) for GRAB motifs that recurrently bound any given AA. We identified five additional GRAB motifs (Fig. 5E and table S11, tab B). For example, IgHV3-21 harbored a GRAB motif encompassing germline-encoded CDR2 residues (S52, S52A, S53, S55, and Y56) to specifically bind aspartate or glutamate in the antigen. A subset of the serine residues hydrogen-bonded with the carboxylate moiety whereas the tyrosine made nonpolar interactions with the carbons in the aspartate/glutamate side chain. Four of eight distinct PDB Ab-Ag complexes involving IgHV3-21 featured this aspartate/glutamate–GRAB motif interaction. The closely related IgHV3-11 had three alleles (*03, *05, and *06) that were not represented in the PDB but had germline-encoded S52, S52A, S53, S55, and Y56 residues predicted to form the same GRAB motif (fig. S15C and table S11, tab C).

IgHV5-51 encoded a GRAB motif comprising germline-encoded CDR2 and framework region 2 residues W33, Y52, D54, D56, and sometimes R58 that specifically interacted with a lysine in the antigen in 8 of the 10 distinct PDB Ab-Ag complexes involving IgHV5-51 (Fig. 5, E and F, and table S11, tab B). Similar to the IgLV lysine GRAB motif interactions, in the IgHV5-51 GRAB motif, D54 and D56 made salt bridges with the lysine amine whereas W33 and Y52 engaged in nonpolar interactions with the carbons of the side chain.

Some GRAB motifs exhibited recognition flexibility. IgKV4-1 harbored a GRAB motif involving Y30A, Y32, and Y92, germline-encoded by the CDR1 and CDR3, which formed nonpolar interactions with antigens. Although primarily recognizing proline (four examples), this GRAB motif could also interact with histidine, valine, arginine, or alanine (one example each), underscoring the chemical utility of tyrosine for protein-protein interactions. Of the 22 distinct PDB IgKV4-1 Ab-Ag complexes, 8 featured interactions between this GRAB motif and the AAs listed above (Fig. 5E and table S11, tab B).

If GRAB motif interactions were important for antigen recognition, they should contribute substantially to the ΔG of the Ab-Ag complex. Using computational alanine scanning (*35*, *36*), we predicted the effects on the Ab-Ag complexes of mutating AAs recognized by GRAB motifs. The median predicted ΔΔG was 1.9 kcal/mol and the median predicted fold change in binding affinity (K_D) was 21.9, indicating that the GRAB motif interactions were important for Ab-Ag binding (table S11, tabs A and B).

We also observed five recurrent germline-encoded interactions present in distinct Ab-Ag structures involving the same antigen—evidence of shared antibody responses to public epitopes. For example, recent reports described a public antibody response to the receptor binding domain of SARS-CoV-2 spike that used IgHV3-53 or the closely related IgHV3-66, frequently paired with IgKV1-9 or IgKV3-20 (*10*, *11*, *37*). These antibodies had unmutated or nearly unmutated sequences, yet potently neutralized SARS-CoV-2 (*38*). We observed that IgHV3-53/IgHV3-66 engaged in multiple stereotyped interactions between germline-encoded residues from CDR1, framework region 2, CDR2, and framework region 3 and Y473, the backbone near A475, and Y421 of spike (fig. S16 and table S11, tab D). Additionally, IgKV1-9/IgKV3-20 exhibited stereotyped interactions between germline-encoded residues of framework region 1, CDR1, framework region 3 (for IgKV3-20 only), and CDR3 and Y505 of spike (fig. S16 and table S11, tab D). These germline-encoded interactions appeared to contribute to the prevalence of the IgHV3-53/IgHV3-66 + IgKV1-9/IgKV3-20 neutralizing antibody response among individuals exposed to SARS-CoV-2 (*10*, *11*), much in the way we hypothesize that GRAB motif interactions do. These stereotyped germline-encoded interactions were included in our count of GRAB motifs, with the caveat that their generalizability to other antigens was uncertain.

GRAB motifs mediate recognition of an influenza A public epitope

If GRAB motifs mediate antibody recognition of public epitopes, mutation of GRAB motif residues should weaken this recognition. As a test case, we used influenza A public epitope-specific antibodies, because these shared conserved IgHV5-51 and IgKV4-1 gene segments, which we knew harbored GRAB motifs specific for lysine and proline, respectively. We individually mutated each AA of the IgHV5-51 and IgKV4-1 GRAB motifs to alanine in flu_c504 and flu_c3 and observed that these mutations often severely reduced binding, whereas mutations of nearby non–GRAB motif or of CDR3 residues often did not affect binding (Fig. 6, A and B, and fig. S17, A and B). We profiled the mutant versions of flu_c504 and flu_c3 using the saturating mutagenesis public epitope VirScan library. Use of substantial quantities of monoclonal antibody allowed us to obtain high-resolution antibody footprints for most mutants despite weakened binding. Although flu_c504 and flu_c3 originally recognized

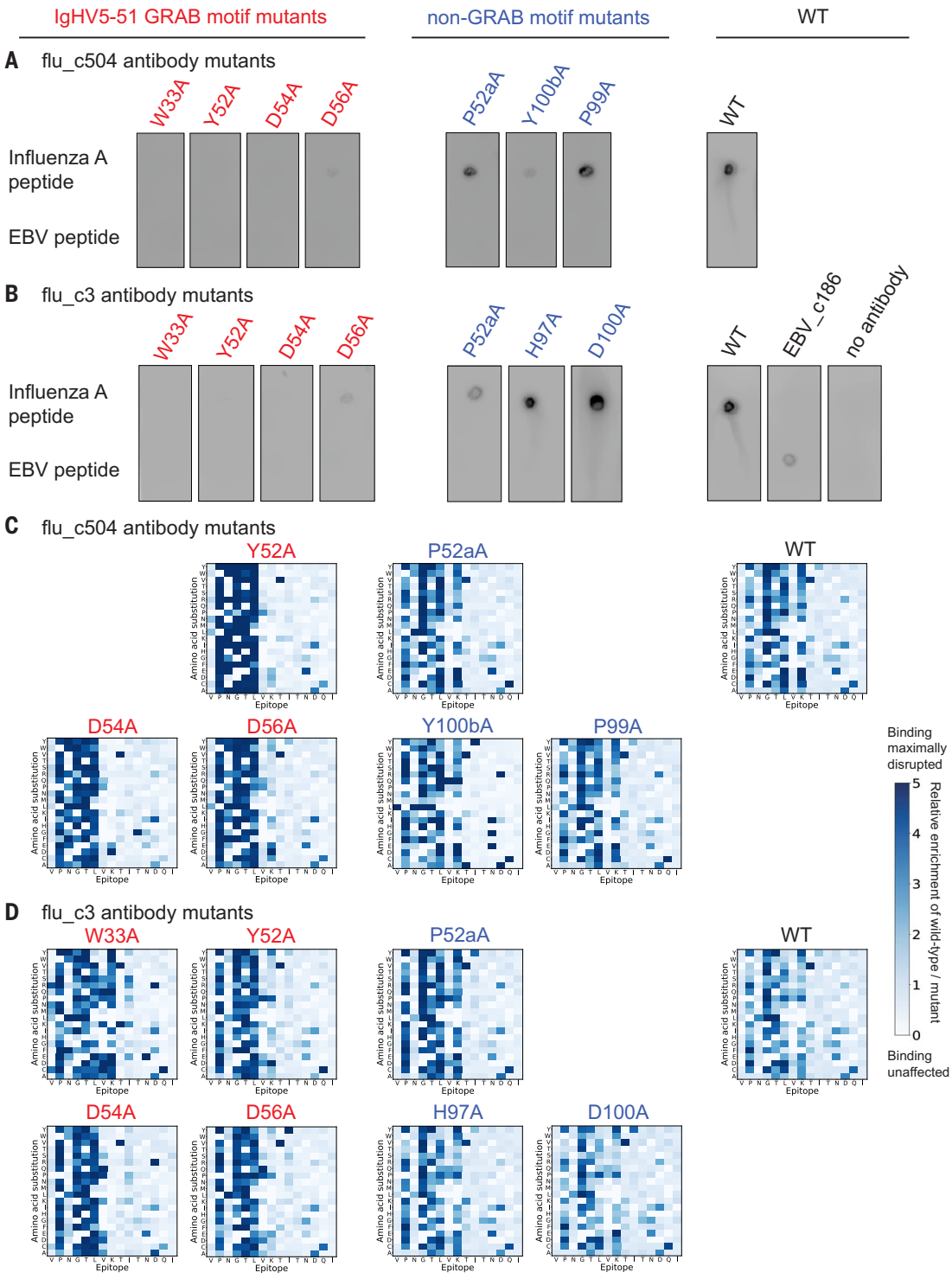

Fig. 6. The IgHV5-51 GRAB motif mediates antibody recognition of an influenza A public epitope. (**A** and **B**) Mutation of IgHV5-51 GRAB motif residues in influenza A public epitope-specific antibodies severely weakens recognition of the epitope. The indicated mutations were introduced into two influenza A public epitope-specific antibodies, flu_c504 (A) and flu_c3 (B) and the impact on binding assayed by dot blot. Influenza A and EBV minimal peptides (146786 and 72153 in table S3, respectively) were spotted onto the nitrocellulose membranes; the EBV_c186 antibody served as a control. (**C** and **D**) High-resolution footprints for the monoclonal antibodies from (A and B). Heatmaps are labeled as described in Fig. 2B. Note that the heatmaps do not depict absolute enrichment values, but rather the relative enrichment of the wild-type peptide compared with the mutant peptide for a given sample.

the critical residues P-GTL-K, mutation of IgHV5-51 GRAB motif residues specifically abolished recognition of the lysine while increasing the dependence on the other critical residues (Fig. 6, C and D). Likewise, IgKV4-1 GRAB motif mutations reduced proline recognition (fig. S17, C and D). In all cases, mutations outside of GRAB motifs did not affect the high-resolution antibody footprints. Thus, the IgHV5-51 and IgKV4-1 GRAB motifs likely mediate binding to the influenza A public epitope through specific recognition of lysine and proline, respectively, as predicted by the PDB analysis of these V gene segments.

Public epitopes are largely species-specific

We next asked whether different species recognized the same or distinct public epitopes. We used VirScan to map antibody responses to peptides from SARS-CoV-2 spike in 30 SARS-CoV-2–infected humans (*18*), 9 SARS-CoV-2–infected nonhuman primates (NHPs) (*39*), and 8 C57BL/6 mice vaccinated with adeno-associated virus (AAV) encoding SARS-CoV-2 spike (*40*). The general regions of spike recognized by all three species were similar (Fig. 7A), but when we reprofiled these samples using a SARS-CoV-2

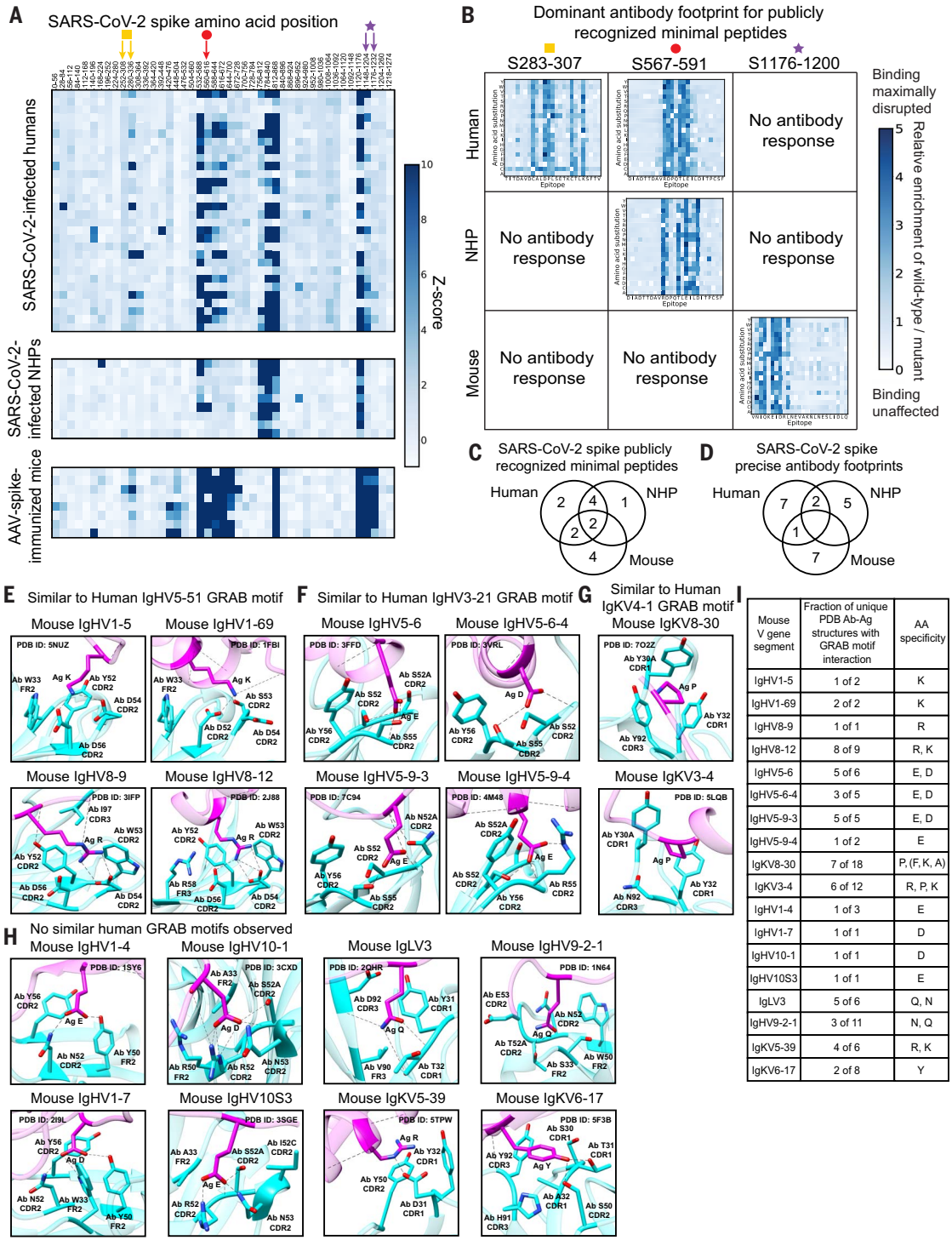

I

Mouse V gene segment	Fraction of unique PDB Ab-Ag structures with GRAB motif interaction	AA specificity
IgHV1-5	1 of 2	K
IgHV1-69	2 of 2	K
IgHV8-9	1 of 1	R
IgHV8-12	8 of 9	R, K
IgHV5-6	5 of 6	E, D
IgHV5-6-4	3 of 5	E, D
IgHV5-9-3	5 of 5	E, D
IgHV5-9-4	1 of 2	E
IgKV8-30	7 of 18	P, (F, K, A)
IgKV3-4	6 of 12	R, P, K
IgHV1-4	1 of 3	E
IgHV1-7	1 of 1	D
IgHV10-1	1 of 1	D
IgHV10S3	1 of 1	E
IgLV3	5 of 6	Q, N
IgHV9-2-1	3 of 11	N, Q
IgKV5-39	4 of 6	R, K
IgKV6-17	2 of 8	Y

Fig. 7. Public epitopes are largely species-specific, consistent with only partially overlapping sets of GRAB motifs. (**A**) Antibody responses to peptides from SARS-CoV-2 spike in SARS-CoV-2-infected humans (n = 30) (*18*), SARS-CoV-2–infected NHPs (n = 9) (*39*), and C57BL/6 mice immunized with an AAV vector carrying stabilized prefusion SARS-CoV-2 spike (n = 8) (*40*). Each row represents a unique individual and each column represents a peptide tile. Darker colors indicate greater enrichment (Z-score) of a peptide in a given sample. Colored arrows are coordinated with colored shapes in (B) to show the positions of select public epitopes within spike. (**B**) Representative high-resolution footprints for minimal public epitope peptides recognized by one or more of the indicated species. Heatmaps are labeled as in Fig. 2B. Colored shapes are coordinated with colored arrows in (A) to show the positions of these public epitopes within spike. (**C** and **D**) Venn diagrams depicting the number of public epitopes recognized by one or more of the indicated species. (C) shows the number of publicly recognized minimal peptides, whereas (D) shows the number of precise antibody footprints (these were only considered to be shared if different species recognized the same pattern of critical residues). (**E** to **H**) Representative GRAB motif interactions for the indicated mouse V gene segments (table S13). Mouse GRAB motifs for which we found analogous human GRAB motifs are shown in (E) to (G). Those for which we did not find analogous human GRAB motifs are shown in (H). Images are labeled as in Fig. 5, D and E. (**I**) Summary table showing the fraction of unique PDB Ab-Ag structures with the relevant V gene segment that feature the GRAB motif interaction.

public epitope saturating mutagenesis VirScan library (table S12), we observed that the precise public epitopes recognized by each species were most often distinct (Fig. 7, B to D, and fig. S18). Thus, mice and NHPs do not recapitulate the human antibody response to public epitopes.

Different species have partially overlapping sets of GRAB motifs

We hypothesized that different species might recognize different public epitopes in part because of distinct sets of GRAB motifs. To investigate, we performed a similar analysis of PDB Ab-Ag complexes as described above, for mouse V gene segments (we analyzed V gene segments from several different mouse strains). This revealed 21 murine GRAB motifs, which partially overlapped with human GRAB motifs (Fig. 7, E to I, figs. S19 to S21, and table S13).

For example, four mouse V gene segments (denoted with "m")—mIgHV1-5, mIgHV1-69, mIgHV8-9, and mIgHV8-12—had germline-encoded lysine/arginine-specific GRAB motifs resembling the human IgHV5-51 GRAB motif (Fig. 7, E and I, and table S13). Although the AAs (W, Y, D, and D) that constituted the human IgHV5-51, mIgHV8-9, and mIgHV8-12 GRAB motifs were equivalent, in mIgHV8-9 and mIgHV8-12, the W was encoded by the CDR2 whereas in human IgHV5-51 it was encoded by the framework region 2, illustrating convergent strategies to form similar GRAB motifs.

Several mouse GRAB motifs had no discernable human equivalents (Fig. 7, H and I, and table S13). These included similar aspartate/glutamate–specific GRAB motifs in mIgHV1-4 and mIgHV1-7, a distinct set of aspartate/glutamate-specific GRAB motifs in mIgHV10-1 and mIgHV10S3, asparagine/glutamine–specific GRAB motifs in mIgLV3 and mIgHV9-2-1, an arginine/lysine–specific GRAB motif in mIgKV5-39, and a tyrosine-specific GRAB motif in IgKV6-17, among others. Furthermore, mice have only three functional lambda V gene segments and these did not share the lysine GRAB motifs present in human lambda V gene segments. In several cases, additional mouse V gene segments shared conserved residues with known mouse GRAB motifs (table S13, tab B), but Ab-Ag structures were not present in the PDB to validate their specificity. Thus, only partially overlapping sets of GRAB motifs in mice and humans, potentially coupled with distinct CDR3 sequences and subtle differences in the positions of GRAB motif residues within CDR loops and framework regions, could affect the geometry of antibody binding and hence epitope selection, thereby explaining why human and mice antibodies rarely recognize the same public epitopes.

Discussion

A fundamental question in immunology is why antibodies recognize particular regions of proteins more frequently than others. Our data support a model in which public epitopes arise in part because they are best aligned for recognition by GRAB motifs. A certain threshold binding energy is required to initiate an antibody response to an epitope. If a GRAB motif within a particular germline V gene segment provides a substantial portion of this binding energy, a larger number of CDR3 sequences would be compatible in the antibody because the CDR3 would need to contribute less binding energy to reach the threshold to progress to affinity maturation. Thus, there would be a relatively abundant precursor population of naïve B cells with adequate affinity for the epitope, and this could lead to an immunodominant, public antibody response (*41*, *42*). Conversely, if a specific CDR3 sequence were required to provide most of the binding energy for a particular epitope, the antibody response to this epitope would be rarer because of the low precursor frequency of naïve B cells with this CDR3 sequence (Fig. 8). This model is supported by evidence of precursor frequency and binding affinity affecting antibody selection for VRC01-class HIV neutralizing antibodies from quantitative B cell transfer experiments in studies of immunodominance (*43*).

The evolution of antibody genes with germline-encoded sequences that bind AAs commonly found on the surface of proteins is clearly advantageous, allowing the immune system to recognize pathogens quickly and efficiently. However, given their prevalence, shared antibody responses can exert population-wide selective pressures on pathogens. This has been observed clearly for SARS-CoV-2: variants of concern have evolved to evade recognition by the public IgHV3-53/IgHV3-66 + IgKV1-9/IgKV3-20 class of neutralizing antibodies described above, among others (*44*–*48*).

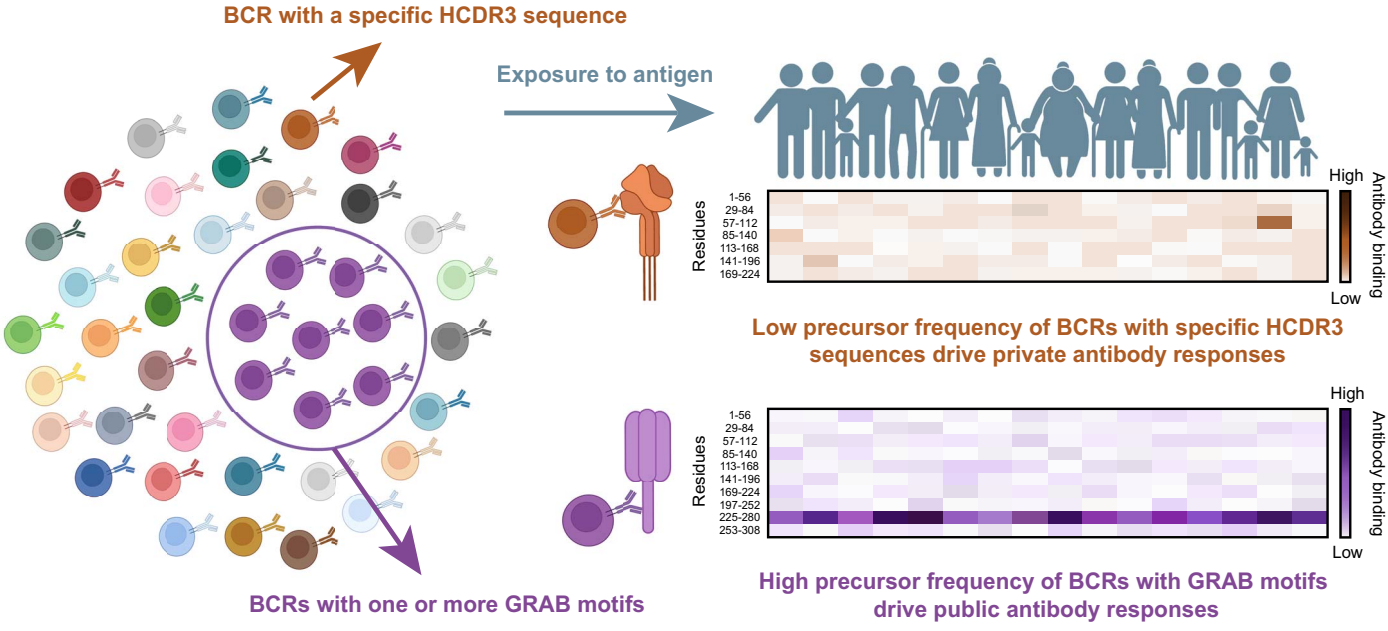

Fig. 8. Proposed model for development of recurrent antibody responses to public epitopes through recognition by GRAB motifs. The B cell repertoire has a relatively low precursor frequency of BCRs with a specific heavy chain CDR3 (HCDR3) sequence, but a relatively high precursor frequency of BCRs with a certain combination of V gene segments (e.g., IgHV5-51 and IgKV4-1). If GRAB motifs within these V gene segments are sufficient to bind a certain epitope, this can lead to a public antibody response. By contrast, if a specific HCDR3 sequence is required to bind an epitope, this will likely lead to a private antibody response.

Alternatively, if public antibody responses are nonprotective to the host, in principle viruses could exploit this by conserving the cognate epitopes. They could also evolve additional non-neutralizing epitopes easily recognized by host GRAB motifs, thereby eliciting frequent nonprotective antibody responses across the host population and potentially delaying the production of more protective antibodies. Such epitopes could be removed from vaccine formulations.

An outstanding question is what selective pressure drove the expansion of lambda V gene segments with lysine-specific GRAB motifs in humans. Although mice do not share these GRAB motifs, 8 rhesus macaque lambda V gene segments share the same residues as known human lysine-specific GRAB motifs (*49*, *50*) and as many as 39% (12 of 31, including hypothetical GRAB motifs) of the functional human lambda V gene segments have germline-encoded specificity for lysine. The expansion of lysine-specific GRAB motifs in primates suggests adaptation to pathogens, which in turn suggests an advantage for pathogens to be enriched in lysines. Notably, in the SARS-CoV-2 omicron BA.1 variant, 8 of the 30 AA substitutions in spike involve mutation to lysine (*51*). Recent modeling has suggested that positive charges on viruses may recruit heavily sialated mucins to enhance survival in aerosols or aid in interactions with lung surfaces (*52*, *53*), providing a hypothesis for further study.

We have likely discovered only a fraction of all GRAB motifs as our analysis was limited by available PBD Ab-Ag structures (*54*). Indeed, 39% of human V gene segments (50 of 127 annotated by IMGT) were not represented and an additional 15% were only represented in one or two distinct Ab-Ag structures. Additional structural data and enhanced computational approaches will be needed to bridge this gap. Furthermore, GRAB motifs may have specificity for combinations of AAs or more complex topological structures, which were beyond the scope of our current analysis. Nevertheless, the GRAB motifs we identified—18 human, 21 mouse with structural evidence, and an additional 6 human and 27 mouse predicted GRAB motifs based on conservation to known motifs—likely influence the selection and composition of public epitopes, as illustrated by the profound enrichment of border lysines in lambda public epitopes and potentially also the enrichment of proline in kappa public epitopes.

This work has several implications: first, it suggests that private rather than public neutralizing antibodies may be superior candidates for inclusion in therapeutic monoclonal antibody cocktails, because private antibodies are less likely to exert population-wide selective pressures on pathogens and may thus retain efficacy for future variants. Second, the fact that public, immunodominant antibody responses appear to be largely species-specific may limit our ability to consistently predict how vaccines tested in nonhuman species will perform in humans, especially with respect to cross protection to variants. However, in another context species specificity may prove beneficial: vaccines administered to nonhuman species may elicit neutralizing antibody responses to epitopes that are not publicly recognized by humans. Because human viruses are not under evolutionary pressure to evade these antibodies, they may have therapeutic efficacy for humans against a broad range of variants. Third, the data presented here may enable exploration of the functional consequences of antibody responses to public epitopes, with relevance to vaccine design. Fourth, the set of viral public epitopes may be useful in diagnostic applications. Fifth, knowledge of the GRAB motifs should aid species-specific B cell epitope prediction algorithms and computational methods to predict and design Ab-Ag interactions. Overall, this study reveals a fundamental structural code inherent in our humoral immune response that shapes epitope selection and composition and drives recurrent antibody responses across individuals and differing epitope selection among species, thus affecting host-pathogen coevolution and human health. Additionally, as T cell receptors are structurally similar to BCRs, it is highly likely that a similar structural code exists within T cell receptor V gene segments that contributes to T cell epitope immunodominance.

Materials and Methods

Human donor samples

Human specimens were collected in accordance with the local protocol governing human research after obtaining informed written consent from the donors. Secondary use of all human samples for the purposes of this work was exempted by the Brigham and Women's Hospital Institutional Review Board (protocol number 2013P001337). Samples included serum and plasma from donors residing in Peru (n = 24), France (n = 2), and the United States (n = 52) (*14*). The United States cohort included donors with hepatitis C virus (n = 24), donors with human immunodeficiency virus 1 (n = 24), and healthy donors (n = 4). Human serum and plasma samples were stored in aliquots at −80°C until use. Apheresis leukoreduction collars from healthy platelet donors were obtained from the Brigham and Women's Hospital Specimen Bank under protocol T0276. Access to COVID-19 patient samples was facilitated by the MassCPR.

Design and cloning of the public epitope truncation and alanine scanning library

We designed peptide sequences of 15, 20, 25, 30, 35, 40, and 45 AAs in length, tiling through all of the 56-AA publicly recognized peptides with 5-AA overlap. For these shorter peptide truncations, we added random filler AA sequences after the stop codon so that downstream PCR steps would produce amplicons of the same size for all the members of the library. Additionally, we made triple-mutant sequences scanning through the 56-AA peptides. Non-alanine AAs were mutated to alanine, and alanines were mutated to glycine. We reverse-translated the peptide sequences into DNA sequences that were (a) codon-optimized for expression in *Escherichia coli*, (b) lacked restriction sites used in downstream cloning steps (EcoRI and XhoI), and (c) were unique in the 50 nucleotides (nt) at the 5′ end to allow for unambiguous mapping of the sequencing reads. Then we added the adapter sequences AGGAATTCCGCTGCGT to the 5′ end and CAGGGAAGAGCTCGAA to the 3′ end or ATGAATTCGGAGCGGT to the 5′ end and CACTGCACTCGAGACA to the 3′ end to form the 200-nt oligonucleotide sequences, which were synthesized on a releasable DNA microarray (Agilent). We PCR-amplified the DNA oligonucleotide library with the primers T7-PFA 5′-AATGATACGGCGGGAATTCCGCTGCGT-3′ and T7-PRA 5′-CAAGCAGAAGACTCGAGCTCTTCCCTG-3′ and, separately, with the primers T7-Pep2-PFb 5′-AATGATACGGCGTGAATTCGGAGCGGT-3′ and T7-Pep2-PRb 5′-CAAGCAGAAGACGTCTCGAGTGCAGTG-3′, digested the products with EcoRI and XhoI, and cloned them into the EcoRI/SalI site of the T7FNS2 vector (*17*). We packaged the resultant library into T7 bacteriophage using the T7 Select Packaging Kit (EMD Millipore) and amplified the library according to the manufacturer's protocol.

VirScan

We performed VirScan (*14*–*16*), which is based on the phage immunoprecipitation and sequencing (PhIP-Seq) methodology (*17*), as described previously (*14*–*16*, *18*) or with slight modifications. For the light chain isotype-specific IPs, we substituted magnetic protein A and protein G Dynabeads (Invitrogen) with 5 μg of biotinylated goat anti-human kappa (Southern Biotech) or 4 μg of biotinylated goat anti-human lambda (Southern Biotech) antibodies. The day after establishing the phage and serum mixtures, we added these antibodies and incubated the reactions overnight at 4°C. Afterward, we added 20 μl of Pierce streptavidin magnetic beads (Thermo Fisher Scientific), incubated the reactions for 4 hours at room temperature, then continued with the washing steps and the remainder of the protocol, as previously described (*14*–*16*, *18*).

For the isotype-specific depletions, we substituted magnetic protein A and protein G Dynabeads with 15 μg of biotinylated goat anti-human kappa or 10 μg of biotinylated goat anti-human lambda antibodies. The day

after establishing the phage and serum mixtures, we added these antibodies to the phage and serum mixtures and let the reactions incubate overnight at 4°C. We then added 60 μl (for kappa depletions) or 40 μl (for lambda depletions) of Pierce streptavidin magnetic beads, incubated the reactions for 4 hours at room temperature, then moved the supernatants into new plates. We added 40 μl of mixed protein A and protein G Dynabeads to the supernatants, incubated the reactions for 4 hours at room temperature, and continued with the IPs and library preparation for multiplexed Illumina sequencing as described previously (*14*–*16*, *18*).

To test whether we could successfully profile antibody responses to the saturating mutagenesis public epitope library, we used the following antibodies against HA tag (which was included in the saturating mutagenesis public epitope library as a control): mouse anti-HA-biotin clone HA-7 (Sigma), rat anti-HA-biotin clone 3F10 (Sigma), and anti-HA magnetic beads clone 2-2.2.14 (Thermo Fisher Scientific) (fig. S4).

For mouse serum samples, 0.6 μl of mouse serum was used for each VirScan reaction and 40 μl of mixed protein A and protein G Dynabeads were used as the IP reagent. For NHP samples, 0.2 μl of NHP serum was used for each VirScan reaction and 40 μl of mixed protein A and protein G Dynabeads were used as the IP reagent. For monoclonal antibodies, ~50 μl of cell culture supernatant was used as input for VirScan reactions involving the saturating mutagenesis public epitope library to generate high-resolution footprints. Unless otherwise specified, 20 ng of purified antibody was used as input for VirScan reactions involving the human virome library to investigate potential polyspecificity. Forty microliters of mixed protein A and protein G Dynabeads were used as the IP reagent. All samples were run in duplicate except for the mouse sera samples profiled with the CoV 56-AA library (however, this library contains duplicate barcoded versions of each peptide, and the measurements for each of the duplicate peptides were averaged).

Statistical analysis of VirScan data generated with the public epitope truncation and alanine scanning library

We first mapped the sequencing reads to the reference library sequences using Bowtie (*55*) and counted the number of reads corresponding to each peptide in the input library and each sample "output". For each sample, we normalized the read counts for each peptide by the total read counts for the sample. Then, we divided the normalized read counts of each peptide in the sample by the normalized read counts of each peptide in the input library to obtain an enrichment value. We averaged enrichment values for technical replicates of a sample.

For each truncation and alanine scanning mutant peptide, we calculated relative-to-wild-type enrichment values as follows: we first calculated the average enrichment value of the middle 50% of the alanine scanning mutants of a given 56-AA peptide, as we assumed most alanine scanning mutations throughout the peptide would not disrupt the epitope. We found this to be a more robust (i.e., less noisy) representation of the enrichment of the wild-type 56-AA peptide than the enrichment value of the single wild-type 56-AA peptide. Next, we divided the enrichment value of a given peptide truncation or alanine scanning mutant by the average enrichment value of the middle 50% of the alanine scanning mutants to obtain a relative-to-wild-type enrichment value. Finally, for each 56-AA peptide, we generated a heatmap using Python matplotlib to illustrate the relative-to-wild-type enrichment values of the peptide truncations and alanine scanning mutants for all the samples that recognized the wild-type version of the 56-AA peptide (i.e., where the enrichment value of the wild-type 56-AA peptide was >1.5). For the alanine scanning mutants, the values in the heatmap were 1 / (relative-to-wild-type enrichment value), with darker blue colors indicating greater disruption of the epitope.

Permutation analysis

We limited this analysis to the short peptide truncations (15, 20, 25, and 30-AA in length) as some 56-AA peptides contained more than one distinct public epitope, and we sought to isolate these with the shorter peptides. To perform one permutation, we randomized the kappa and lambda assignments of the pair of IPs for each serum sample. We then counted the number of kappa and lambda IP fractions in which each short peptide truncation was enriched. We performed a total of 1000 permutations. Based on these permutations, we calculated an average distribution of kappa and lambda IP samples in which the short peptide truncations were expected to score, and used this distribution to calculate the fold-enrichment of each value in the observed distribution. We also calculated a *P*-value for each observed value based on how many random permutations had resulted in at least such a high number of peptides scoring in the given numbers of kappa and lambda IP samples.

Design and cloning of the saturating mutagenesis public epitope library

From the VirScan data generated with the public epitope truncation and alanine scanning library using the kappa and lambda isotype-specific IP protocol, we identified peptide truncations whose relative-to-wild-type enrichment values were at least 0.75 in at least half of the samples in which the wild-type 56-AA peptide scored. We filtered for peptide truncations with read counts of at least 5 in the input library to avoid spurious enrichment values, and peptide truncations for which at least 6 samples recognized the wild-type 56-AA peptide. We first chose 15-AA and 20-AA peptide truncations that met these requirements. This was a relatively stringent set of criteria, so to capture the remaining epitopes within the 56-AA peptides of the public epitope truncation and alanine scanning library, we next set the threshold for the relative-to-wild-type enrichment values to 0.5 and chose the shortest peptide truncation that captured at least half of the samples' responses to the wild-type 56-AA peptide.

With this list of minimal public epitope-containing peptides ("minimal peptides"), we designed saturating mutants such that each AA of the peptide was mutated to the other 19 AAs. As a positive control and to calibrate how antibody responses to saturating mutants would be detected in a VirScan assay, we included HA tag and saturating mutants of this epitope. Because the public epitope peptides were of varying sizes, we added random filler AA sequences after the stop codon so that downstream PCR steps would yield products of the same size for all the members of the library. We reverse-translated the peptide sequences into DNA sequences that were codon-optimized for expression in *E. coli*, that lacked restriction sites used in downstream cloning steps (EcoRI and XhoI), and that were unique in the 50 nt at the 5′ end to allow for unambiguous mapping of the sequencing reads. Then we added the adapter sequence GGAATTCCGCTGCGT to the 5′ end and CAGG- GAAGAGCTCGA to the 3′ end to form the 198-nt oligonucleotide sequences. These oligonucleotide sequences were synthesized on a releasable DNA microarray (Agilent). We PCR-amplified the DNA oligonucleotide library with the primers T7-PFA 5′-AATGATACGGCGGGAATTCCGCTGCGT-3′ and T7-PRA 5′-CAAGCAGAAGACTCGAGCTCT-TCCCTG-3′, digested the product with EcoRI and XhoI, and cloned it into the EcoRI/SalI site of the T7FNS2 vector (*17*). We packaged the resultant library into T7 bacteriophage using the T7 Select Packaging Kit (EMD Millipore) and amplified the library according to the manufacturer's protocol.

Statistical analysis of VirScan data generated with the saturating mutagenesis public epitope library and the SARS-CoV-2 public epitope saturating mutagenesis library

We first mapped the sequencing reads to the reference library sequences using Bowtie (*55*) and determined the read counts of each peptide in the input library and each sample "output". For each sample, we normalized the read counts corresponding to each peptide by the total read counts for the sample. Then, for each peptide, we divided the normalized read

counts of each peptide in the sample by the normalized read counts of each peptide in the input library in order to obtain the enrichment value.

For each minimal peptide and for each sample, we next calculated relative-to-wild-type enrichment values for each AA substitution mutant as follows: we first calculated the average enrichment value of the middle 50% of the alanine substitution mutants, most of which we assumed would be minimally disruptive to the epitope contained in the peptide. We found that the average enrichment value of the middle 50% of the alanine substitution mutants was a more robust representation of the enrichment of the wild-type peptide than the enrichment value of the single wild-type peptide. Next, we divided the enrichment value of a given substitution mutant by the average enrichment value of the middle 50% of the alanine substitution mutants in order to obtain a relative-to-wild-type enrichment value. Finally, for each minimal peptide, if a sample recognized the wild-type version of the peptide (i.e., the enrichment value of the wild-type peptide was >1 and the average enrichment value of the middle 50% of all substitution mutants of the peptide was >1), we then generated an "enrichment matrix" with the relative-to-wild-type enrichment values of all the substitution mutants of the peptide. We also generated a heatmap using Python matplotlib displaying values of 1 / (relative-to-wild-type enrichment value + 0.2) for all the substitution mutants of the peptide.

Statistical analysis of VirScan data generated with the human virome library and the CoV 56-AA library

VirScan data generated with the human virome library and the CoV 56-AA library were analyzed as previously described (*15*, *16*, *18*).

Critical residue analysis and definition of kappa and lambda public epitopes

For every minimal peptide in the saturating mutagenesis public epitope library, we converted all enrichment matrices from samples that recognized the given peptide into binary matrices: if the relative-to-wild-type enrichment value of a given mutant peptide was <0.5 (i.e., the mutant enriched less than half as well as the middle 50% of all alanine substitution mutants for that peptide), then the mutant was considered to disrupt the epitope and given a value of "1". Alternatively, the mutant was considered to be permitted and given a value of "0". Next, we collapsed each binary enrichment matrix into a one-row summary by adding the number of mutants at each position that disrupted the epitope. Then, for each minimal peptide, we converted the one-row summaries into binary one-row summaries: if at least one third of the 19 substitutions at a given position disrupted the epitope, then the position was considered a critical residue and given a value of "1". Alternatively, the position was given a value of "0". These data are available on the Harvard Dataverse, doi: 10.7910/DVN/AIXWW2. Next, for each minimal peptide, we counted the number of samples that exhibited the same binary summaries (i.e., that recognized the same pattern of critical residues). The pattern of critical residues shared by the greatest number of samples was considered to be the consensus public epitope, also called the dominant footprint. Thus, we defined the critical residues of the kappa and lambda public epitopes. Samples that recognized the consensus public epitope or a pattern of critical residues that only differed from the consensus public epitope by one position were considered to be part of the dominant footprint group. The counts and proportions of kappa or lambda IP samples that recognized each minimal peptide and that were part of the dominant footprint group are provided in table S7. We performed this analysis separately for kappa samples and lambda samples and limited the analysis to minimal peptides recognized by at least five kappa samples or at least five lambda samples.

Analysis of tolerated AA substitutions

For each minimal peptide, we took the average of all the binary matrices for samples that were part of the dominant footprint group. Then, for every critical residue of a given public epitope, we determined which AA substitutions were permitted (i.e., the AA substitutions for which the average of the binary matrices was >0.5). Finally, for each of the 20 AAs, we calculated the frequency at which each of the other 19 AA substitutions were permitted at a critical residue.

Public epitope-specific memory B cell isolation and sequencing

For most experiments, ~10 fresh (<6 hours from collection) apheresis leukoreduction collars from healthy platelet donors were obtained from the Brigham and Women's Hospital Specimen Bank under protocol T0276. For the experiment to isolate SARS-CoV-2 public epitope-specific memory B cells, five cryopreserved peripheral blood mononuclear cell (PBMC) samples and one fresh leukopak sample from COVID-19-recovered donors were purchased from Cellero and obtained from the MassCPR COVID-19 Biorepository, respectively. PBMCs were purified on a Ficoll-Paque density gradient. Briefly, 8 ml of donor blood was diluted 1:1 with PBS, slowly layered on 16 ml of Ficoll-Paque (Thermo Fisher Scientific) and centrifuged at 400*g* for 30 min with the brake off. The upper layer containing plasma and platelets was removed and frozen, and the mononuclear cell layer at the interface was extracted and washed four times with PBS at 400*g* for 10 min with the brake on. PBMCs from the different apheresis collars were counted, pooled together, and switched memory B cells were purified using the Human Switched Memory B cell Kit (Miltenyi) according to the manufacturer's instructions. We used this kit, which employs a negative-selection protocol, rather than a kit that positively selects for IgG^+ memory B cells, to avoid labeling the BCR with an antibody and potentially influencing the ability of the BCR to bind the viral peptide. Purified memory B cells were resuspended in RPMI 1640 (Life Technologies) with 10% (v/v) FBS (Hyclone), 100 U/ml of penicillin, 100 μg/ml of streptomycin, and incubated at 37°C and 5% CO_2 for a few hours (≤6 hours, to ensure high cell viability). Memory B cells were stained with biotinylated minimal peptides conjugated to fluoresceinated streptavidin and then fluorescent cells were isolated by FACS using the MoFlo Astrios EQ Cell Sorter (Beckman Coulter) (*56*) (Fig. 4A). We typically began with 8×10^9 PBMCs from ~10 donors and ultimately purified 5×10^7 switched memory B cells. In cases where we wanted to sort for multiple minimal peptide specificities, we split the switched memory B cells into multiple aliquots, and labeled the different aliquots with distinct CITE-seq barcodes (*57*) customized to be compatible with the Chromium 5′ V(D)J solution (10x Genomics). We sorted ~0.002% of the switched memory B cells for any given minimal peptide specificity, then sequenced their BCRs using the Chromium 5′ V(D)J solution (10x Genomics) according to the manufacturer's instructions. In addition to amplifying and sequencing the BCR transcripts, we designed custom primers to amplify MHC transcripts and the customized CITE-seq barcodes (*58*, *59*). SARS-CoV-2 public epitope-reactive BCRs were sequenced using the Chromium Next GEM Single Cell 5′ Kit v2 (10x Genomics). MHC transcripts were not sequenced for these cells.

Minimal peptides used for staining and sorting memory B cells were designed to have an N-terminal biotin or biotin-Ahx modification followed by a GGGGS linker sequence, and neutral charge. If a minimal peptide sequence was not neutral, the linker was extended with charged AAs to achieve net neutral charge. Biotinylated peptides were ordered from Thermo Fisher Scientific or GenScript, reconstituted in a small amount of DMSO (20–40 μl, or 2 to 4% of the final volume), then diluted to a final concentration of 1 mg/ml in ultrapure water and stored at −20°C in aliquots. The sequences of the biotinylated public epitope peptides were as follows:

146786_neutral_linker_flu: N terminus-Biotin-Ahx-GGGGSVPNGTLVKTITNDQI-C terminus

72153_neutral_linker_EBV: N terminus-Biotin-Ahx-EGEGGGGSPPSTSSKLRPRWTFT-C terminus

SARS-CoV-2_S807-832: N terminus- Biotin-GGGGSDPSKPSKRSFIEDLLFNKVTLADAG -C terminus

Biotinylated peptides were conjugated to fluorescent streptavidin by combining the reagents in the following ratios:

For a 20-AA peptide:

6.3 μg of public epitope peptide: 9.0 μg of streptavidin-APC (Thermo Fisher Scientific)

19 μg of public epitope peptide: 9.5 μg of steptavidin-488 (Thermo Fisher Scientific)

3.9 μg of irrelevant peptide: 10.5 μg of streptavidin-PE (Thermo Fisher Scientific)

3.3 μg of irrelevant peptide: 10 μg of streptavidin-BV421 (Biolegend)

For a 25-AA biotinylated peptide:

7.7 μg of public epitope peptide: 9.0 μg of streptavidin-APC

23.4 μg of public epitope peptide: 9.5 μg of streptavidin-488

4.7 μg of irrelevant peptide: 10.5 μg of streptavidin-PE

4.0 μg of irrelevant peptide: 10 μg of streptavidin-BV421

Streptavidin-peptide complexes were incubated at 4°C for ~4 hours on a rotator, then purified using a Bio-Spin® P-30 Gel Column into Tris Buffer (Bio-Rad) according to the manufacturer's instructions.

Immediately prior to staining switched memory B cells, two customized CITE-Seq ADTs per memory B cell aliquot were pooled and cleaned on a 50 kDa cutoff column as previously described (*57*). Switched memory B cells were centrifuged at 300*g* for 10 min, then washed once with 1 ml of staining buffer (PBS + 2% BSA + 0.02% Tween 20) and centrifuged at 400*g* for 4 min. Next, cells were resuspended in 100 μl of staining buffer and 100 μl of cleaned ADT pool (containing ~1–2 μg of each ADT) and incubated with end-over-end mixing for 30 min at 4°C. ADT-labeled switched memory B cells were washed once with staining buffer, then resuspended in purified streptavidin-peptide complexes plus 150 μl of staining buffer and incubated with end-over-end mixing for 1 hour at 4°C. Then, cells were centrifuged at 400*g* for 4 min, washed twice in staining buffer, resuspended in 750 μl of staining buffer, and filtered over a 35-μm nylon mesh cell strainer. Cells that were negative for the two fluorophores conjugated to irrelevant peptides and positive for the two fluorophores conjugated to the minimal public epitope peptide were sorted using the MoFlo Astrios EQ Cell Sorter (Beckman Coulter) into 4 μl of RPMI-1640 supplemented with 0.2% BSA, 100 U/ml of penicillin, 100 mg/ml of streptomycin in one well of a 96-well plate. After sorting, cells were immediately used as input for single cell BCR sequencing using the Chromium 5′ V(D)J solution (10x Genomics) according to the manufacturer's protocol with slight modifications (described below) to amplify ADT barcodes and MHC transcripts in addition to BCR transcripts. V, D, and J gene segments assigned by Cell Ranger (10x Genomics) were double checked by entering the nucleotide sequence of the BCR variable region as a query sequence in IgBlast (*60*), using the IMGT human V, D, and J (F + ORF) germline gene databases. Where the IgBlast and Cell Ranger gene segment assignments differed, the IgBlast assignments were used.

CITE-Seq ADT customization for Chromium 5′ V(D)J solution (10x Genomics)

ADT barcodes were designed as follows to be compatible with the Chromium 5′ V(D)J solution (10x Genomics):

5′ to 3′: 4 nt linker–10xVDJ_ADT_inner primer binding site–Read 2 adaptor sequence–random barcode–13 nt homology to the template switch oligo (10x Genomics)

An example sequence is given below:

5′- /5AmMC12/ATCT–GCGTTCGAGCTCTTCCTG–GTGACTGGAGTTCAGACGTGTGCTCTTCCGATCT–ATGGACCTTAAGCGCTACCGGAATGGTTCG–CCCATATAAGAAA -3′

This design allowed for a two-step PCR enrichment, the first step using SI-PCR primer (10x Genomics) and 10xVDJ_ADT_inner, and the second using SI-PCR primer and a Sample Index PCR primer (10x Genomics).

After the cDNA amplification step of the Chromium 5′ V(D)J solution (10x Genomics) protocol, amplification products above 400 bp, including MHC and BCR transcripts, were captured on SPRI beads (Beckman Coulter) using 0.6X SPRI. The supernatant containing amplification products under 400 bp, including ADT barcodes, was removed to a separate tube, 1.4X SPRI was added to obtain a final SPRI volume of 2X SPRI, and purified in parallel with the amplification products over 400 bp. ADT Target Enrichment 1 from Amp cDNA was performed using SI-PCR primer and 10xV(D)J_ADT_inner primer. Amplification products from nine cycles of PCR were purified with 2X SPRI. ADTs were indexed and purified using the conditions given by the Chromium 5′ V(D)J solution (10x Genomics) protocol. The Sample Index PCR served both to index the ADTs and to perform a second step of target enrichment. The sequence of the 10xV(D)J_ADT_inner primer was as follows:

10xV(D)J_ADT_inner: 5′- GCGTTCGAGCTCTTCCCTG -3′

After quantification, libraries were mixed (50% BCR transcripts, 25% MHC I transcripts, 12.5% MHC II transcripts, 12.5% ADT barcodes). Sequencing was performed with a NextSeq 500 (Illumina) per manufacturer's instructions.

Next-generation sequencing reads corresponding to ADTs were separated by cell barcode. For each cell's ADT reads, the number of times each ADT barcode appeared was counted. The ADT pair with the greatest counts indicated the peptide for which the cell was sorted.

MHC enrichment primer design and donor identification strategy

Primers to amplify MHC I and DR transcripts were designed by downloading CDS sequences of all HLA-A, HLA-B, HLA-C, DRA, and DRB alleles from the Immuno Polymorphism Database-ImMunoGeneTics information system® / Human Leukocyte Antigen (IPD-IMGT/HLA) (*58*, *59*), aligning all alleles of each gene, and designing primers in conserved regions to cover over 95% of alleles and produce reverse transcription products whose lengths would be compatible with the downstream Chromium 5′ V(D)J solution (10x Genomics) protocol. The sequences of the primers designed to amplify the MHC transcripts were as follows:

HLA_A_Outer_1_346 bp: 5′- CAGGGCGATGTAATCCTTGC -3′

HLA_A_Outer_2_450: 5′- CAAGGCGATGTAATCCTTGC -3′

HLA_B_Outer_385bp: 5′- TCCTCGTTCAGGGCGATGT -3′

HLA_C_Outer_360bp: 5′- GCGATGTAATCCTTGCCGTC -3′

HLA_A_Inner_1_346bp: 5′- AACCGGCCTCGCTCTGG -3′

HLA_A_Inner_2_450bp: 5′- GAACCGTCCTCGCTCTGGT -3′

HLA_B_Inner_279bp: 5′- TGTGAGACCCGGCCTCG -3′

HLA_C_Inner_250bp: 5′- CTCGCTCTGGTTGTAGTAGC -3′

DRA_outer: 5′- ATGAAACAGATGAGGACGHLA_C_Inner_250TTGG - 3′

DRB_outer_1: 5′- CTCGCCGCTGCACTGTG - 3′

DRB_outer_2: 5′- CCCCGTAGTTGTGTCTGCA - 3′

DRA_inner: 5′- CTCTCTCAGTTCCACAGGGC - 3′

DRB_inner_1: 5′- CCCAGCTCCGTCACCGC - 3′

DRB_inner_2: 5′- GTCCTTCTGGCTGTTCCAG - 3′

MHC I Target Enrichment 1 from Amp cDNA was performed using SI-PCR primer and MHC I PCR1 RV "outer" mixture (consisting of HLA-A outer 1, HLA-A outer 2, HLA-B outer, HLA-C outer). Amplification products from 10 cycles of PCR were purified with 0.8X SPRI. MHC II Target Enrichment 1 from Amp cDNA was performed using SI-PCR primer and MHC II PCR1 RV "outer" mixture (consisting of DRA_outer, DRB_outer_1, and DRB_outer_2). Amplification products from 10 cycles of PCR were purified with 0.8X SPRI. MHC I Target Enrichment 2 was performed using 10xV(D)J_PCR2F primer and MHC I inner primer mix 2 (consisting of HLA-A inner 1, HLA-A inner 2, HLA-B inner, HLA-C inner). Amplification products from 10 cycles of PCR were purified with a double-sided size selection using 0.5X SPRI

and 0.8X SPRI. MHC II Target Enrichment 2 was performed using 10xV(D)J_PCR2F primer and MHC II inner primer mix 2 (consisting of DRA_inner, DRB_inner_1, and DRB_inner_2). Amplification products from 10 cycles of PCR were purified with a double-sided size selection using 0.5X SPRI and 0.8X SPRI. MHCI and MHCII samples were indexed and purified using the conditions given by the Chromium 5′ V(D)J solution (10x Genomics) protocol. The sequence of the 10xV(D)J_PCR2F is as follows:

10xV(D)J_PCR2F: 5′- AATGATACGGCGACCACCGAGATCT- 3′

After quantification, libraries were mixed (50% BCR transcripts, 25% MHC I transcripts, 12.5% MHC II transcripts, 12.5% ADT barcodes). Sequencing was performed with a NextSeq 500 (Illumina) per manufacturer's instructions.

Next-generation sequencing reads corresponding to MHC I and MHC II transcripts were separated by cell barcode. For each cell's MHC I and MHC II reads, we searched for unique sequences ~90 nt in length that appeared in at least 8% of reads. These unique sequences were considered the MHC alleles for the donor from which the cell originated. Cells with identical MHC alleles were considered to come from the same individual.

Identification of influenza A minimal peptide-specific memory B cells

We performed two rounds of sorting for memory B cells that bound the influenza A minimal peptide VPNGTLVKTITNDQI, the first using 11 donor blood collars and the second using a new set of 10 donor blood collars. During the first round, we obtained 30 paired heavy and light chain sequences and chose seven to clone and recombinantly express, including four that featured similar gene segment usage. Using dot blot and VirScan with the saturating mutagenesis public epitope library, we validated that only these four antibodies: flu_c326, flu_c357, flu_c504, and flu_c645, originating from three different donors, were specific for the VPNGTLVKTITNDQI peptide (Fig. 4B, fig. S6A). These four antibodies exhibited highly conserved gene segment usage: they all featured IgHV5-51 in the heavy chain and IgKV4-1 and IgKJ2 in the light chain. These antibodies also shared highly similar light chain CDR3s, but very poorly conserved heavy chain CDR3 sequences. During the second round of the experiment, we obtained 71 paired heavy and light chain sequences and chose 12 of these to clone and recombinantly express, including three that contained the IgHV5-51 / IgKV4-1 / IgKJ2 gene segment combination, as well as all antibodies with either IgHV5-51 or IgKV4-1, but not the combination of both. Using dot blot VirScan with the saturating mutagenesis public epitope library, we validated that only the three antibodies with the IgHV5-51 / IgKV4-1 / IgKJ2 combination: flu_c3, flu_c286, and flu_c473, originating from three different individuals, were specific for VPNGTLVKTITNDQI (Fig. 4B, fig. S6C). None of the antibodies with only IgHV5-51 or only IgKV4-1 bound the influenza A minimal peptide. Of the 101 BCR sequences obtained from VPNGTLVKTITNDQI-sorted memory B cells from the two sorting experiments, the IgHV5-51 / IgKV4-1 / IgKJ2 gene segment combination was only found in the seven antibodies that we ultimately validated as specific for the peptide. The full list of antibodies we tested for specificity for VPNGTLVKTITNDQI is provided in table S8.

Identification of additional influenza A minimal peptide-specific BCRs from a dataset of BCRs from an individual pre- and post-influenza vaccination

To investigate whether we could identify additional BCRs specific for the influenza A minimal peptide VPNGTLVKTITNDQI by simply selecting for the conserved V gene segments and light chain CDR3 characteristics of known binders, we searched a dataset of ~100,000 BCR sequences from an individual pre- and post-influenza vaccination (*61*, *62*) for those with IgHV5-51, IgKV4-1, IgKJ2, and a light chain CDR3 similar to our example set. We identified five such class-switched BCRs and found that two (flu_c2760 and flu_c4582) bound the influenza A minimal peptide and exhibited similar high-resolution footprints to those of the peptide-tetramer-sorted BCRs (Fig. 4B, fig. S6B, fig. S7; table S8). Flu_c2760 and flu_c4582 were the only BCRs of the set of five with long heavy chain CDR3s (23 and 22 AA, respectively). Flu_c2760 was flu-responsive, expanding in the post-influenza vaccination repertoire (*62*).

Identification of EBV minimal peptide-specific memory B cells

We also performed two rounds of sorting for the EBV minimal peptide PPSTSSKLRPRWTFT, the first using 11 donor blood collars and the second using a new set of 11 donor blood collars. During the first round, we obtained 54 paired heavy and light chain sequences and chose 6 to clone and recombinantly express. Using dot blot and VirScan with the saturating mutagenesis public epitope library, we validated that one antibody, EBV_c186, was specific for the PPSTSSKLRPRWTFT peptide (Fig. 4C and fig. S6A). During the second round of sorting, we obtained 94 paired heavy and light chain sequences. We initially chose 10 of these to clone and recombinantly express, including six antibodies from three different donors that featured the same V gene segment usage as EBV_c186, namely, IgHV1-46 / IgLV3-10. These six antibodies: EBV_c9, EBV_c19, EBV_c61, EBV_c149, EBV_c101, and EBV_c150, validated as specific for PPSTSSKLRPRWTFT, as well as three other antibodies: EBV_c40, which featured a IgHV1-46 / IgLV3-1 gene segment combination, and EBV_c3 and EBV_c120, which were from the same B cell precursor and donor and featured a IgHV1-8 / IgLV1-51 combination (Fig. 4C, fig. S6D). Because most of the antibodies from this initial selection validated as specific for the PPSTSSKLRPRWTFT peptide, we selected 23 additional antibodies from the same dataset to clone and recombinantly express, including every remaining antibody that shared the IgHV1-46 / IgLV3-1 or IgHV1-8 / IgLV1-51 combinations, several antibodies with either IgHV1-46 or IgLV3-10 but not both, and several antibodies chosen at random. Using dot blot and VirScan with the saturating mutagenesis public epitope library, we validated that nine of these 23 antibodies were specific for the PPSTSSKLRPRWTFT peptide: three antibodies: EBV_c63, EBV_c83, and EBV_c124, which featured IgHV1-46; four antibodies: EBV_c10, EBV_c77, EBV_c127, and EBV_c138, which were from the same B cell precursor and donor as EBV_c3 and EBV_c120 and featured the IgHV1-8 / IgLV1-51 combination; one antibody, EBV_c57, which featured a IgHV1-8 / IgLV1-47 combination; and one additional antibody: EBV_c98, which featured a IgHV3-30 / IgKV2-30 combination (Fig. 4C, fig. S6E). Of all the cells we sorted and sequenced for the EBV minimal peptide, the IgHV1-46 / IgLV3-10 combination was only found among the antibodies we ultimately validated as specific for the peptide and one other antibody, EBV_c626, which exhibited weak binding to the peptide by dot blot (fig. S6F). The full list of antibodies we tested for specificity for the PPSTSSKLRPRWTFT is provided in table S9.

Recombinant expression of antibodies

Heavy and light chain sequences of BCRs of interest were synthesized as gene fragments (IDT, Gene Universal) and cloned into human IgG, IgK, and IgL expression vectors (Human IgG Vector Set, Sigma) according to the manufacturer's instructions. Recombinant expression of antibodies was performed as previously described using the Expi293 Expression System Kit (Thermo Fisher Scientific) (*63*) or the ExpiCHO Expression System (Thermo Fisher Scientific). Filtered cell culture supernatant was used for dot blot and VirScan characterization. Antibody purification was performed using NAb Protein A Plus Spin Column (Thermo Fisher Scientific) according to the manufacturer's instructions.

Dot blot

Nitrocellulose membrane was marked with pencil to indicate the regions where the peptides would be spotted. Four micrograms of recombinant peptide was spotted onto each marked region of the nitrocellulose membrane, then the membrane was cut into strips and blocked in Tris Buffered Saline with Tween

20 (Cell Signaling Technology) and 5% bovine serum albumin (TBST 5% BSA) for 30 min at room temperature. The membrane was next incubated in cell culture supernatant from recombinant antibody expression diluted 1:20 in TBST 5% BSA for 1 hour at room temperature. Nitrocellulose was washed three times with TBST for 5 min per wash, then incubated with anti-human IgG-HRP (Southern Biotech) diluted 1:500 in TBST 5% BSA for 1 hour at room temperature. Nitrocellulose was washed three times with TBST for 5 min per wash, then once with TBS for 5 min. Nitrocellulose was incubated with SuperSignal West Femto Maximum Sensitivity Substrate enhanced chemiluminescent substrate (Thermo Fisher Scientific) according to the manufacturer's instructions and chemiluminescent signals were captured using a CCD camera-based imager.

Influenza A hemagglutinin ELISA

Expression and purification of hemagglutinin (HA) trimers and antibodies: Cloning, expression, and purification of HA ectodomain trimers were carried out as previously described (*64*). Briefly, HAs were expressed as soluble trimers with a C-term foldon trimerization domain and a 6x-His tag (HA1-HA2-glyser-thrombin-glyser-foldon-glyser-HHHHHH) (*65*). HA1-HA2 sequences (residue 1-504 H3 numbering) from A/Aichi/02/1968 Aichi (H3), A/Shanghai/1/2013 SH13 (H7), A/Jiangxi-Donghu/346/2013 JX346 (H10), A/swine/HuBei/06/2009 HB09 (H4N1), A/California/04/2009 CA09 (H1N1), A/Vietnam/1203/2004 Viet04 (H5N1), A/Japan/305/1957 JP57 (H2N2) and A/guinea fowl/Hong Kong/1999 WF10 (H9N2) were cloned into a pTT5 expression vector containing the C-term tags. Soluble HA trimers were expressed by transient transfection in the Expi293 Expression System and purified from supernatants by Ni-NTA chromatography followed by size exclusion chromatography (SEC). Purified soluble HA trimers were stored in TBS buffer (20 mM Tris pH 8.0, 150 mM NaCl and 0.02% sodium azide) at 4°C and used for at least one month. FI6 (*65*) antibody was produced as described for hemagglutinin trimers. Briefly, antibody genes were cloned into the pTT5 expression vector, expressed by transient transfection in Expi293T cells, and purified from cell supernatants using Ni-NTA chromatography followed by SEC. Proteins were stored in TBS buffer at 4°C and used for up to 6 months.

Influenza A hemagglutinin ELISA: The binding of the recombinant IgG influenza A minimal peptide-specific antibodies to hemagglutinin ectodomain trimers was measured by ELISA as described previously (*64*). Briefly 384-well plates (Sigma) were coated with 10 μg/ml of recombinant HAs in 0.1 M $NaHC0_3$ pH 9.8 and stored overnight at 4°C. Plates were then blocked with 3% BSA in TBS-T (TBS with 0.1% Tween 20) for 1 hour at room temperature. Plates were washed with TBS-T after each step. Antibodies were diluted to 10 μg/ml with TBS-T and serially diluted fourfold for a total of eight dilutions and added for 3 hours at room temperature. Secondary HRP-conjugated goat anti-human IgG (Southern Biotech) diluted 1:10,000 was added for 1 hour at room temperature. The SuperSignal ELISA Femto Maximum Sensitivity Substrate (Thermo Fisher Scientific) was used to develop the plates, and the plates were read at 425 nm. ELISA binding curves were plotted using Graphpad Prism 8.3.

In vitro influenza A neutralization assay

Neutralization assays were conducted as described previously (*64*). Briefly, live PB1flank-eGFP virus were used for BSL 2 strains A/Aichi/02/1968 (X31; H3N2), A/California/04/2009 (CA09; H1N1) (*66*), using reagents kindly provided by Dr. J. Bloom (Fred Hutchinson). MDCK cells were used for live neutralization assays. Purified antibodies were diluted to 50 μg/ml except for flu_c3 and flu_c286, which were at 30 μg/ml and 6.7 μg/ml, respectively, and then serially diluted fivefold for a total of eight dilutions. Pseudovirus assays (*67*) were conducted for BSL 3 strains A/Shanghai/1/2013 (SH13; H7), A/Jiangxi-Donghu/346/2013 (JX346; H10) and A/Vietnam/1203/2004 (Viet04; H5). TZM-bl cells were used for the pseudoviral neutralization assays. Antibodies were diluted to 50 μg/ml except for flu_c3 and flu_c286, which were at 30 μg/ml and 6.7 μg/ml, respectively, and then serially diluted fourfold for a total of eight dilutions. Percent neutralization was then determined for each concentration of antibody and plotted using Graphpad Prism 8.3.

Live cell immunofluorescence

The EBV+ Burkitt lymphoma cell line P3HR-1-ZHT was used for EBV lytic reactivation (*68*). P3HR1-ZHT cells stably express a conditional BZLF1 allele (BZLF1-HT), in which the ligand binding domain of a modified estrogen receptor responsive to 4HT is fused to the BZLF1 C terminus. In the absence of 4HT, BZLF1-HT is retained in the cytosol and is destabilized. 4HT addition stabilizes BZLF1-HT and drives its rapid nuclear translocation which leads to lytic reactivation. P3HR1-ZHT cells (1×10^6 cells/ml) were reactivated with 4HT (1 μM) for 24 hours. For live cell staining, 1×10^6 cells were washed twice with live cell staining buffer (PBS with 1 mM EDTA and 0.5% BSA), followed by incubation with primary antibodies at 2 μg/ml for 30 min on ice. Cells were then washed with the staining buffer twice and subsequently stained with Alexa Fluor 488-conjugated anti-human IgG secondary antibody (Jackson Immunoresearch) at 6 μg/ml and Cy5-conjugated anti-gp350 mouse monoclonal antibody 72A1 (gift of Dr. E. Kieff) at 2 μg/ml for 30 min on ice. Labeled cells were washed three more times with FACS buffer and the nucleus was stained by Hoechst 33258 at 1 μg/ml prior to confocal microscopy using the LSM800 system with an Apochromat 63x/1.4 Oil DIC M27 objective lens (Zeiss). Images were analyzed with Adobe Photoshop.

SARS-CoV-2 spike ELISA

Ninety-six-well maxisorp ELISA plates (Thermo Fisher Scientific) were coated with 2 μg of full-length SARS-CoV-2 (2019-nCoV) spike protein (S, gift of B. Chen, Ragon Institute of MGH, MIT and Harvard) or S2 (purchased from GenScript) in 35 μl of PBS overnight at 4°C. After discarding coating buffer, ELISA plates were blocked with 50 μl of PBS with 3% BSA at room temperature for 2 hours. During the time of incubation, monoclonal antibodies were serially diluted twofold using 1 μg/ml as a starting concentration in 1% BSA prepared in PBS with 0.03% Tween 20. The anti-peanut PT275-H40 monoclonal antibody (gift of Dr. D.R. Wesemann) was used as a negative control. After blocking, the solution was discarded and ELISA plates were washed once in PBS containing 0.05% Tween 20. Monoclonal antibody dilutions were transferred into the plates in duplicates along with standards and incubated overnight at room temperature. Afterward, primary antibody solution was decanted and plates were washed thrice in PBS containing 0.05% Tween 20. Secondary antibody solutions of anti-human IgG alkaline phosphatase (AP) (Southern Biotech) diluted 1:2000 in PBS containing 1% BSA and 0.03% Tween 20 were added to each plate at 30 μl per well. Plates were incubated for 90 min at room temperature and then washed thrice. Alkaline phosphatase substrate p-nitrophenyl phosphate tablets (Sigma, St. Louis, MO) were dissolved in 0.1 M glycine, pH 10.4, with 1 mM $MgCl_2$ and 1 mM $ZnCl_2$, pH 10.4, to a concentration of 1.6 mg/ml. One hundred microliters of this development/substrate solution was then added to each well in a 96-well plate. Plates were kept in the dark and allowed to develop for 2 hours prior to reading. Absorbance at 405 nm was measured using a microplate reader (Biotek Synergy H1). All samples were run in duplicate wells.

In vitro SARS-CoV-2 neutralization assay

Cell culture: NR-596 VeroE6 cells (BEI Resources) were maintained in Dulbecco's modified Eagle medium (DMEM) (Gibco™) with the following additives: 10% heat inactivated fetal bovine serum (Gibco™), GlutaMAX (Gibco™), non-essential amino acids (Gibco™), and sodium pyruvate (Gibco™). The day prior to the assay, 8.0×10^5 VeroE6 cells were seeded per well of a six-well plate in 2 ml of media.

Virus propagation: Authentic SARS-CoV-2 viruses were propagated as previously described

(*46*) from passage 4 SARS-CoV-2 USA-WA1/2020 (*69*).

Viral plaque reduction neutralization assay: All viral infection quantification assays were performed at biosafety level 4 (BSL-4) at the National Emerging Infectious Disease Laboratories (NEIDL). In brief, an Avicel plaque reduction assay was used to quantify plaques as follows: Antibody samples were serially diluted in Dulbecco's Phosphate Buffered Saline (DPBS) (Gibco™) using half-log or threefold dilutions. Each dilution was incubated at 37°C and 5% CO_2 for 1 hour with 1000 plaque forming units/ml (PFU/ml) of SARS-CoV-2 (isolate USA-WA1/2020 – described above). The maintenance media was then removed from each plate and 200 µl of each inoculum dilution was added to confluent monolayers of NR-596 Vero E6 cells (including 1000 PFU/ml SARS-CoV-2 incubated with DPBS as a positive control and a mock DPBS negative control) in triplicate and incubated for 1 hour at 37°C/5% CO_2 with gentle rocking every 10–15 min to prevent monolayer drying. The overlay was prepared by mixing by inversion Avicel 591 overlay (DuPont Nutrition & Biosciences, Wilmington, DE) and 2X Modified Eagle Medium (Temin's modification, Gibco™) supplemented with 2X antibiotic-antimycotic (Gibco™), 2X GlutaMAX (Gibco™) and 10% fetal bovine serum (Gibco™) in a 1:1 ratio. After 1 hour, 2 ml of overlay was added to each well and the plates were incubated for 48 hours at 37°C/5% CO_2. Six-well plates were then fixed using 10% neutral buffered formalin prior to removal from BSL-4 space. The fixed plates were then stained with 0.2% aqueous Gentian Violet (RICCA Chemicals, Arlington, TX) in 10% neutral buffered formalin for 30 min, followed by rinsing and plaque counting. The half maximal inhibitory concentrations (IC50) were calculated using GraphPad Prism 8.

PDB analysis to identify GRAB motifs

Nucleotide sequences of human and mouse V gene segments were obtained from IMGT V-QUEST (*49*, *50*) and translated to AA sequences. The mouse V gene segment sequences were from multiple strains of mice. We used the RCSB PDB Search API (Number of Distinct Protein Entities ≥3, Sequence = the AA sequence of the relevant V gene segment with an identity cutoff of 93%) to identify relevant structures of Ab–Ag complexes involving the V gene segment. The following json query was used:

```
"query": {
"type": "group",
"logical_operator": "and",
"nodes": [
{
"type": "group",
"logical_operator": "and",
"nodes": [
{
"type": "terminal",
"service": "text",
"parameters": {
"operator": "greater_or_equal",
"negation": False,
"value": 3,
"attribute": "rcsb_entry_info.polymer_entity_count_protein"
}
}
]
},
{
"type": "terminal",
"service": "sequence",
"parameters": {
"evalue_cutoff": 0.1,
"identity_cutoff": 0.93,
"target": "pdb_protein_sequence",
"value": seq
}
},
]
}
```

Next, for each PDB structure, we loaded the Chothia numbered version of the PDB file from SAbDab (*70*, *71*) into UCSF Chimera (*72*) and used the command findclash (with parameters VDW overlap −1, hbond 0.0) to detect residues in the antigen chain that interacted with the relevant antibody heavy or light chain. For each PDB structure, we generated a row-by-row summary of each antigen residue (in column "Antigen_Residue") that interacted with the relevant antibody chain, the antibody residues it interacted with (in column "Interacts_With"), and the subset of those antibody residues whose side chain atoms interacted with the antigen AA (in column "Interacts_With_SC"). Next, using SAbPred ANARCI (*73*, *74*), we annotated the subset of the residues in the column "Interacts_With_SC" that were germline-encoded (in column "Interacts_With_Germline_SC"). We also included counts of the number of interacting residues (in columns "Num_Interactions", "Num_SC_Interactions", "Num_Germline_SC_Interactions"). As a quality control, we entered the relevant antibody heavy or light sequence into IgBlast and annotated the top hit, % alignment, and Evalue (in columns "IgBlast_TopHit", "Alignment", and "Evalue", respectively), and performed a sequence match between the top hit and the original V gene segment query name (in column "Check") in order to confirm the identity of the V gene segment. We also annotated whether the antigen was a protein or peptide in the column "Antigen_Type". Then, we collected the output for all the structures with the relevant V gene segment into a file ("_antigenSummary.csv"). We performed a similar analysis for all the antibody residues that interacted with the antigen and collected the output into a file ("_antibodySummary.csv"). These files are available on the Harvard Dataverse, doi: 10.7910/DVN/WZCLMB; 10.7910/DVN/DXWJ2Y.

Finally, we searched each "_antigen.csv" V gene segment file for recurrent interactions found in multiple unique Ab-Ag structures between certain germline-encoded residues in the antibody and a given AA (or a small set of biochemically similar AAs) in the antigen. These recurrent interactions were considered GRAB motif interactions. V gene segments for which there was a single example of an Ab-Ag interaction that strongly resembled a GRAB motif interaction present in another V gene segment were also considered to harbor GRAB motifs.

AlphaFold2 predictions

BCR sequences containing IgLV3-16, IgLV3-27, IgLV1-47, and IgHV3-11*06 were identified from our single-cell sequencing datasets. If residues of the predicted GRAB motifs were somatically hypermutated, we reverted them to the germline-encoded residues at those positions. We could not find BCRs containing IgLV3-22 or IgLV3-9*02 in our datasets, so we substituted these germline V gene segments within the sequence of the BCR containing IgLV3-27. A (GGS)x12 linker was inserted between the heavy variable and light variable region of each BCR sequence, and the structures of these "fusion proteins" predicted using AlphaFold2 (*33*, *34*).

Quantification and Statistical Analysis

Statistical details of experiments can be found in the figure legends and materials and methods. Data analysis was performed in Python, R, Graphpad Prism, and Excel.

REFERENCES AND NOTES

1. J. L. Xu, M. M. Davis, Diversity in the CDR3 region of V(H) is sufficient for most antibody specificities. *Immunity* **13**, name 37–45 (2000). doi: 10.1016/S1074-7613(00)00006-6; pmid: 10933393
2. G. R. McLean *et al*., Recognition of human cytomegalovirus by human primary immunoglobulins identifies an innate foundation to an adaptive immune response. *J. Immunol.* **174**, 4768–4778 (2005). doi: 10.4049/jimmunol.174.8.4768; pmid: 15814702
3. M. Zhang, D. Zharikova, K. Mozdzanowska, L. Otvos, W. Gerhard, Fine specificity and sequence of antibodies directed against the ectodomain of matrix protein 2 of influenza A virus. *Mol. Immunol.* **43**, 2195–2206 (2006). doi: 10.1016/j.molimm.2005.12.015; pmid: 16472860
4. C. A. Thomson *et al*., Germline V-genes sculpt the binding site of a family of antibodies neutralizing human cytomegalovirus. *EMBO J.* **27**, 2592–2602 (2008). doi: 10.1038/emboj.2008.179; pmid: 18772881
5. R. Robert *et al*., Restricted V gene usage and VH/VL pairing of mouse humoral response against the N-terminal immunodominant epitope of the amyloid β peptide. *Mol. Immunol.* **48**, 59–72 (2010). doi: 10.1016/j.molimm.2010.09.012; pmid: 20970857
6. M. K. Gorny *et al*., Human anti-V3 HIV-1 monoclonal antibodies encoded by the VH5-51/VL lambda genes define a conserved antigenic structure. *PLOS ONE* **6**, e27780 (2011). doi: 10.1371/journal.pone.0027780; pmid: 22164215
7. A. P. West Jr., R. Diskin, M. C. Nussenzweig, P. J. Bjorkman, Structural basis for germ-line gene usage of a potent class of antibodies targeting the CD4-binding site of HIV-1 gp120. *Proc. Natl. Acad. Sci. U.S.A.* **109**, E2083–E2090 (2012). doi: 10.1073/pnas.1208984109; pmid: 22745174

8. D. F. Robbiani *et al*., Recurrent Potent Human Neutralizing Antibodies to Zika Virus in Brazil and Mexico. *Cell* **169**, 597–609.e11 (2017). doi: 10.1016/j.cell.2017.04.024; pmid: 28475892
9. K.-W. Chan *et al*., Structural Comparison of Human Anti-HIV-1 gp120 V3 Monoclonal Antibodies of the Same Gene Usage Induced by Vaccination and Chronic Infection. *J. Virol.* **92**, e00641-18 (2018). doi: 10.1128/JVI.00641-18; pmid: 29997214
10. M. Yuan *et al*., Structural basis of a shared antibody response to SARS-CoV-2. *Science* **369**, 1119–1123 (2020). doi: 10.1126/science.abd2321; pmid: 32661058
11. C. O. Barnes *et al*., Structures of Human Antibodies Bound to SARS-CoV-2 Spike Reveal Common Epitopes and Recurrent Features of Antibodies. *Cell* **182**, 828–842.e16 (2020). doi: 10.1016/j.cell.2020.06.025; pmid: 32645326
12. W. N. Voss *et al*., Prevalent, protective, and convergent IgG recognition of SARS-CoV-2 non-RBD spike epitopes. *Science* **372**, 1108–1112 (2021). doi: 10.1126/science.abg5268; pmid: 33947773
13. M. Mukhamedova *et al*., Vaccination with prefusion-stabilized respiratory syncytial virus fusion protein induces genetically and antigenically diverse antibody responses. *Immunity* **54**, 769–780.e6 (2021). doi: 10.1016/j.immuni.2021.03.004; pmid: 33823129
14. G. J. Xu *et al*., Viral immunology. Comprehensive serological profiling of human populations using a synthetic human virome. *Science* **348**, aaa0698 (2015). doi: 10.1126/science.aaa0698; pmid: 26045439
15. M. J. Mina *et al*., Measles virus infection diminishes preexisting antibodies that offer protection from other pathogens. *Science* **366**, 599–606 (2019). doi: 10.1126/science.aay6485; pmid: 31672891
16. E. L. Shrock, C. L. Shrock, S. J. Elledge, VirScan: High-throughput Profiling of Antiviral Antibody Epitopes. *Biol. Protoc.* **12**, e4464 (2022). doi: 10.1126/science.aay6485; pmid: 31672891
17. H. B. Larman *et al*., Autoantigen discovery with a synthetic human peptidome. *Nat. Biotechnol.* **29**, 535–541 (2011). doi: 10.1038/nbt.1856; pmid: 21602805
18. E. Shrock *et al*., Viral epitope profiling of COVID-19 patients reveals cross-reactivity and correlates of severity. *Science* (2020). doi: 10.1126/science.abd4250
19. G. Chen *et al*., High-resolution epitope mapping by AllerScan reveals relationships between IgE and IgG repertoires during peanut oral immunotherapy. *Cell Rep. Med.* **2**, 100410 (2021b). doi: 10.1016/j.xcrm.2021.100410; pmid: 34755130
20. D. R. Monaco *et al*., Profiling serum antibodies with a pan allergen phage library identifies key wheat allergy epitopes. *Nat. Commun.* **12**, 379 (2021). doi: 10.1038/s41467-020-20622-1; pmid: 33483508
21. T. Vogl *et al*., Population-wide diversity and stability of serum antibody epitope repertoires against human microbiota. *Nat. Med.* **27**, 1442–1450 (2021). doi: 10.1038/s41591-021-01409-3; pmid: 34282338
22. K. W. Barber, E. Shrock, S. J. Elledge, CRISPR-based peptide library display and programmable microarray self-assembly for rapid quantitative protein binding assays. *Mol. Cell* **81**, 3650–3658.e5 (2021). doi: 10.1016/j.molcel.2021.07.027; pmid: 34390675
23. S. Henikoff, J. G. Henikoff, Amino acid substitution matrices from protein blocks. *Proc. Natl. Acad. Sci. U.S.A.* **89**, 10915–10919 (1992). doi: 10.1073/pnas.89.22.10915; pmid: 1438297
24. V. E. Gray, R. J. Hause, D. M. Fowler, Analysis of Large-Scale Mutagenesis Data To Assess the Impact of Single Amino Acid Substitutions. *Genetics* **207**, 53–61 (2017). doi: 10.1534/genetics.117.300064; pmid: 28751422
25. M. Zemlin *et al*., Expressed murine and human CDR-H3 intervals of equal length exhibit distinct repertoires that differ in their amino acid composition and predicted range of structures. *J. Mol. Biol.* **334**, 733–749 (2003). doi: 10.1016/j.jmb.2003.10.007; pmid: 14636599
26. B. J. DeKosky *et al*., Large-scale sequence and structural comparisons of human naive and antigen-experienced antibody repertoires. *Proc. Natl. Acad. Sci. U.S.A.* **113**, E2636–E2645 (2016). doi: 10.1073/pnas.1525510113; pmid: 27114511
27. J. S. Low *et al*., ACE2-binding exposes the SARS-CoV-2 fusion peptide to broadly neutralizing coronavirus antibodies. *Science* **377**, eabq2679 (2022). doi: 10.1126/science.abq2679; pmid: 35857703
28. C. Dacon *et al*., Broadly neutralizing antibodies target the coronavirus fusion peptide. *Science* **377**, eabq3773 (2022). doi: 10.1126/science.abq3773; pmid: 35857439
29. X. Sun *et al*., Neutralization mechanism of a human antibody with pan-coronavirus reactivity including SARS-CoV-2. *Nat. Microbiol.* **7**, 1063–1074 (2022). doi: 10.1038/s41564-022-01155-3; pmid: 35773398
30. H. M. Berman *et al*., The Protein Data Bank. *Nucleic Acids Res.* **28**, 235–242 (2000). doi: 10.1093/nar/28.1.235; pmid: 10592235
31. H. Berman, K. Henrick, H. Nakamura, Announcing the worldwide Protein Data Bank. *Nat. Struct. Biol.* **10**, 980 (2003). doi: 10.1038/nsb1203-980; pmid: 14634627
32. S. K. Burley *et al*., RCSB Protein Data Bank: Powerful new tools for exploring 3D structures of biological macromolecules for basic and applied research and education in fundamental biology, biomedicine, biotechnology, bioengineering and energy sciences. *Nucleic Acids Res.* **49**, D437–D451 (2021). doi: 10.1093/nar/gkaa1038; pmid: 33211854
33. J. Jumper *et al*., Highly accurate protein structure prediction with AlphaFold. *Nature* **596**, 583–589 (2021). doi: 10.1038/s41586-021-03819-2; pmid: 34265844
34. M. Varadi *et al*., AlphaFold Protein Structure Database: Massively expanding the structural coverage of protein-sequence space with high-accuracy models. *Nucleic Acids Res.* **50**, D439–D444 (2022). doi: 10.1093/nar/gkab1061; pmid: 34791371
35. T. Kortemme, D. E. Kim, D. Baker, Computational alanine scanning of protein-protein interfaces. *Sci. STKE* **2004**, pl2 (2004). doi: 10.1126/stke.2192004pl2; pmid: 14872095
36. T. Kortemme, D. Baker, A simple physical model for binding energy hot spots in protein-protein complexes. *Proc. Natl. Acad. Sci. U.S.A.* **99**, 14116–14121 (2002). doi: 10.1073/pnas.202485799; pmid: 12381794
37. D. F. Robbiani *et al*., Convergent antibody responses to SARS-CoV-2 in convalescent individuals. *Nature* **584**, 437–442 (2020). doi: 10.1038/s41586-020-2456-9; pmid: 32555388
38. C. Kreer *et al*., Longitudinal Isolation of Potent Near-Germline SARS-CoV-2-Neutralizing Antibodies from COVID-19 Patients. *Cell* **182**, 843–854.e12 (2020). doi: 10.1016/j.cell.2020.06.044; pmid: 32673567
39. A. Chandrashekar *et al*., SARS-CoV-2 infection protects against rechallenge in rhesus macaques. *Science* **369**, 812–817 (2020). doi: 10.1126/science.abc4776; pmid: 32434946
40. N. Zabaleta *et al*., An AAV-based, room-temperature-stable, single-dose COVID-19 vaccine provides durable immunogenicity and protection in non-human primates. *Cell Host Microbe* **29**, 1437–1453.e8 (2021). doi: 10.1016/j.chom.2021.08.002; pmid: 34428428
41. D. Angeletti, J. W. Yewdell, Understanding and Manipulating Viral Immunity: Antibody Immunodominance Enters Center Stage. *Trends Immunol.* **39**, 549–561 (2018). doi: 10.1016/j.it.2018.04.008; pmid: 29789196
42. A. Akram, R. D. Inman, Immunodominance: A pivotal principle in host response to viral infections. *Clin. Immunol.* **143**, 99–115 (2012). doi: 10.1016/j.clim.2012.01.015; pmid: 22391152
43. R. K. Abbott *et al*., Precursor Frequency and Affinity Determine B Cell Competitive Fitness in Germinal Centers, Tested with Germline-Targeting HIV Vaccine Immunogens. *Immunity* **48**, 133–146.e6 (2018). doi: 10.1016/j.immuni.2017.11.023; pmid: 29287996
44. S. A. Clark *et al*., SARS-CoV-2 evolution in an immunocompromised host reveals shared neutralization escape mechanisms. *Cell* **184**, 2605–2617.e18 (2021). doi: 10.1016/j.cell.2021.03.027; pmid: 33831372
45. Q. Zhang *et al*., Potent and protective IGHV3-53/3-66 public antibodies and their shared escape mutant on the spike of SARS-CoV-2. *Nat. Commun.* **12**, 4210 (2021). doi: 10.1038/s41467-021-24514-w; pmid: 34244522
46. P. Tong *et al*., Memory B cell repertoire for recognition of evolving SARS-CoV-2 spike. *Cell* **184**, 4969–4980.e15 (2021). doi: 10.1016/j.cell.2021.07.025; pmid: 34332650
47. Q. Li *et al*., The Impact of Mutations in SARS-CoV-2 Spike on Viral Infectivity and Antigenicity. *Cell* **182**, 1284–1294.e9 (2020). doi: 10.1016/j.cell.2020.07.012; pmid: 32730807
48. Y. Cao *et al*., Omicron escapes the majority of existing SARS-CoV-2 neutralizing antibodies. *Nature* **602**, 657–663 (2022). doi: 10.1038/s41586-021-04385-3; pmid: 35016194
49. X. Brochet, M.-P. Lefranc, V. Giudicelli, IMGT/V-QUEST: The highly customized and integrated system for IG and TR standardized V-J and V-D-J sequence analysis. *Nucleic Acids Res.* **36**, W503-8 (2008). doi: 10.1093/nar/gkn316; pmid: 18503082
50. V. Giudicelli, X. Brochet, M.-P. Lefranc, IMGT/V-QUEST: IMGT standardized analysis of the immunoglobulin (IG) and T cell receptor (TR) nucleotide sequences. *Cold Spring Harb. Protoc.* **2011**, pdb.prot5633 (2011). doi: 10.1101/pdb.prot5633; pmid: 21632778
51. R. Viana *et al*., Rapid epidemic expansion of the SARS-CoV-2 Omicron variant in southern Africa. *Nature* **603**, 679–686 (2022).
52. A. Dommer *et al*., #COVIDisAirborne: AI-Enabled Multiscale Computational Microscopy of Delta SARS-CoV-2 in a Respiratory Aerosol. bioRxiv 2021.11.12.468428 [Preprint] (2021); doi: 10.1101/2021.11.12.468428
53. B. A. Symmes, A. L. Stefanski, C. M. Magin, C. M. Evans, Role of mucins in lung homeostasis: Regulated expression and biosynthesis in health and disease. *Biochem. Soc. Trans.* **46**, 707–719 (2018). doi: 10.1042/BST20170455; pmid: 29802217
54. R. Akbar *et al*., A compact vocabulary of paratope-epitope interactions enables predictability of antibody-antigen binding. *Cell Rep.* **34**, 108856 (2021). doi: 10.1016/j.celrep.2021.108856; pmid: 33730590
55. B. Langmead, C. Trapnell, M. Pop, S. L. Salzberg, Ultrafast and memory-efficient alignment of short DNA sequences to the human genome. *Genome Biol.* **10**, R25 (2009). doi: 10.1186/gb-2009-10-3-r25; pmid: 19261174
56. A. P. Kodituwakku, C. Jessup, H. Zola, D. M. Roberton, Isolation of antigen-specific B cells. *Immunol. Cell Biol.* **81**, 163–170 (2003). doi: 10.1046/j.1440-1711.2003.01152.x; pmid: 12752679
57. M. Stoeckius *et al*., Simultaneous epitope and transcriptome measurement in single cells. *Nat. Methods* **14**, 865–868 (2017). doi: 10.1038/nmeth.4380; pmid: 28759029
58. J. Robinson, A. Malik, P. Parham, J. G. Bodmer, S. G. Marsh, IMGT/HLA database—A sequence database for the human major histocompatibility complex. *Tissue Antigens* **55**, 280–287 (2000). doi: 10.1034/j.1399-0039.2000.550314.x; pmid: 10777106
59. J. Robinson *et al*., The IPD and IMGT/HLA database: Allele variant databases. *Nucleic Acids Res.* **43**, D423–D431 (2015). doi: 10.1093/nar/gku1161; pmid: 25414341
60. J. Ye, N. Ma, T. L. Madden, J. M. Ostell, IgBLAST: an immunoglobulin variable domain sequence analysis tool. *Nucleic Acids Res.* **41**, W34–40 (2013).
61. F. Horns, C. Vollmers, C. L. Dekker, S. R. Quake, Signatures of selection in the human antibody repertoire: Selective sweeps, competing subclones, and neutral drift. *Proc. Natl. Acad. Sci. U.S.A.* **116**, 1261–1266 (2019). doi: 10.1073/pnas.1814213116; pmid: 30622180
62. F. Horns, C. L. Dekker, S. R. Quake, Memory B Cell Activation, Broad Anti-influenza Antibodies, and Bystander Activation Revealed by Single-Cell Transcriptomics. *Cell Rep.* **30**, 905–913.e6 (2020). doi: 10.1016/j.celrep.2019.12.063; pmid: 31968262
63. R. Vazquez-Lombardi *et al*., Transient expression of human antibodies in mammalian cells. *Nat. Protoc.* **13**, 99–117 (2018). doi: 10.1038/nprot.2017.126; pmid: 29240734
64. A. A. Cohen *et al*., Construction, characterization, and immunization of nanoparticles that display a diverse array of influenza HA trimers. *PLOS ONE* **16**, e0247963 (2021). doi: 10.1371/journal.pone.0247963; pmid: 33661993
65. D. C. Ekiert *et al*., A highly conserved neutralizing epitope on group 2 influenza A viruses. *Science* **333**, 843–850 (2011). doi: 10.1126/science.1204839; pmid: 21737702
66. J. D. Bloom, L. I. Gong, D. Baltimore, Permissive secondary mutations enable the evolution of influenza oseltamivir resistance. *Science* **328**, 1272–1275 (2010). doi: 10.1126/science.1187816; pmid: 20522774
67. N. J. Temperton *et al*., A sensitive retroviral pseudotype assay for influenza H5N1-neutralizing antibodies. *Influenza Other Respir. Viruses* **1**, 105–112 (2007). doi: 10.1111/j.1750-2659.2007.00016.x; pmid: 19453415
68. R. Guo *et al*., MYC Controls the Epstein-Barr Virus Lytic Switch. *Mol. Cell* **78**, 653–669.e8 (2020). doi: 10.1016/j.molcel.2020.03.025; pmid: 32315601
69. J. Harcourt *et al*., Isolation and characterization of SARS-CoV-2 from the first US COVID-19 patient. *bioRxiv* (2020). doi: 10.1101/2020.03.02.972935
70. J. Dunbar *et al*., SAbDab: The structural antibody database. *Nucleic Acids Res.* **42**, D1140–D1146 (2014). doi: 10.1093/nar/gkt1043; pmid: 24214988
71. C. Schneider, M. I. J. Raybould, C. M. Deane, SAbDab in the age of biotherapeutics: Updates including SAbDab-nano, the nanobody structure tracker. *Nucleic Acids Res.* **50**, D1368–D1372 (2022). doi: 10.1093/nar/gkab1050; pmid: 34986602
72. E. F. Pettersen *et al*., UCSF Chimera—A visualization system for exploratory research and analysis. *J. Comput.*

Chem. **25**, 1605–1612 (2004). doi: 10.1002/jcc.20084; pmid: 15264254
73. J. Dunbar *et al*., SAbPred: A structure-based antibody prediction server. *Nucleic Acids Res.* **44**, W474-8 (2016). doi: 10.1093/nar/gkw361; pmid: 27131379
74. J. Dunbar, C. M. Deane, ANARCI: Antigen receptor numbering and receptor classification. *Bioinformatics* **32**, 298–300 (2016b). doi: 10.1093/bioinformatics/btv552; pmid: 26424857

ACKNOWLEDGMENTS

We thank L. Vandenberghe, N. Zabaleta, D. Barouch, and A. Chandrashekar for providing sera samples; S. Quake, D. Grishin, J. Bloom, C. O'Leary, C. Glassman, and M. Steffen for helpful discussions; A. Kohlgruber for designing initial versions of the schematics in Fig. 1B, Fig. 2A, and Fig. 4A; C. Araneo and the Immunology Flow Cytometry Facility and A. Ciulla Hurst and the BioPolymers Genomics Core Facility at Harvard Medical School for supporting this work; J. Q. O'Brien for contributing to revision experiments; and R. E. Shrock for reviewing the manuscript. Access to COVID-19 patient samples was facilitated by the MassCPR. We thank the Resource for Biocomputing, Visualization, and Informatics at the University of California, San Francisco, with support from NIH P41-GM103311 for help with molecular graphics. Fig. 8 and the print page summary figure were created with BioRender.com. **Funding:** This research was supported by the SARS-CoV-2 Viral Variants Program and the Value of Vaccine Research Network to S.J.E.; the MassPCR and the NIH 1P01AI165072 to S.J.E., A.G., and D.R.W.; and the NIH 1R01AI129784 to P.J.B. E.L.S. and T.K. were supported by the NSF Graduate Research Fellows Program. R.T.T. is supported by a Pemberton-Trinity Fellowship and a Sir Henry Wellcome Fellowship (201387/Z/16/Z). E.L.M. is supported by a Jane Coffin Childs Postdoctoral Fellowship. R.G. is supported by an NIH Pathway to Independence Award (K99/R00) K99DE031016. D.R.W. is also supported by AI139538, AI169619, AI170715, and AI170580. B.E.G. is supported by a Burroughs Wellcome Career Award in Medical Sciences. S.J.E. is an Investigator with the Howard Hughes Medical Institute. **Author contributions:** Conceptualization: S.J.E., E.L.S., and T.K. Formal analysis: E.L.S., R.T.T., T.K., A.P.W., I.L., A.A.C., L.G.A.M., C.B., and K. Investigation: E.L.S., T.K., R.G., A.A.C., L.G.A.M., C.B., K., Y.L., and M.L. Methodology: E.L.S., R.T.T., T.K., E.L.M., and A.P.W. Resources: E.F. and F.H. Supervision: S.J.E., P.J.B., B.E.G., A.G., and D.R.W. Visualization: E.L.S., T.K., E.L.M., I.L., A.A.C., R.G., A.P.W., L.G.A.M., C.B., and K. Writing – original draft: E.L.S. and S.J.E. Writing – review and editing: E.L.S., S.J.E., R.T.T., T.K., E.L.M., and P.J.B. **Competing interests:** S.J.E. and T.K. are founders of TSCAN Therapeutics and ImmuneID. SJ.E. is a founder of MAZE Therapeutics and Mirimus, and serves on the scientific advisory board of Homology Medicines, TSCAN Therapeutics, MAZE Therapeutics, none of which impact this work. E.L.S. was a consultant for ImmuneID. S.J.E., and T.K. are inventors on a patent application filed by the Brigham and Women's Hospital (US20160320406A) that covers the use of the VirScan library to identify pathogen antibodies in blood. **Data and materials availability:** All data necessary to interpret our findings are available in supplemental tables or on the Harvard Dataverse, digital object identifiers: 10.7910/DVN/AIXWW2; 10.7910/DVN/WZCLMB; 10.7910/DVN/DXWJ2Y. All reasonable requests for materials will be fulfilled. **License information:** Copyright © 2023 the authors, some rights reserved; exclusive licensee American Association for the Advancement of Science. No claim to original US government works. https://www.sciencemag.org/about/science-licenses-journal-article-reuse

SUPPLEMENTARY MATERIALS

science.org/doi/10.1126/science.adc9498
Figs. S1 to S21
Tables S1 to S17
MDAR Reproducibility Checklist
References (*75*)

View/request a protocol for this paper from *Bio-protocol*.

Submitted 11 May 2022; accepted 3 March 2023
10.1126/science.adc9498

RESEARCH ARTICLE SUMMARY

LIPID SIGNALING

Unsaturated bond recognition leads to biased signal in a fatty acid receptor

Chunyou Mao†, Peng Xiao†, Xiao-Na Tao†, Jiao Qin†, Qing-Tao He†, Chao Zhang†, Sheng-Chao Guo, Ya-Qin Du, Li-Nan Chen, Dan-Dan Shen, Zhi-Shuai Yang, Han-Qiong Zhang, Shen-Ming Huang, Yong-Hao He, Jie Cheng, Ya-Ni Zhong, Pan Shang, Jun Chen, Dao-Lai Zhang, Qian-Lang Wang, Mei-Xia Liu, Guo-Yu Li, Yongyuan Guo, H. Eric Xu, Chuanxin Wang, Cheng Zhang, Shiqing Feng*, Xiao Yu*, Yan Zhang*, Jin-Peng Sun*

INTRODUCTION: Hormones regulate most aspects of human physiology and are generally divided into four groups: protein and peptides, monoamines, steroids, and free fatty acids (FAs). Unsaturated FAs, those with C–C double bonds, exert physiological functions through engagement with membrane receptors, many of which are G protein–coupled receptors (GPCRs). Omega-3 (ω-3) FAs, which are a main component of fish oil, bind to the receptor GPR120, which mediates insulin sensitization, stimulates glucagon-like peptide 1 (GLP-1) secretion, and controls adipogenesis and anti-inflammatory effects through coupling to distinct downstream effectors, including the guanine nucleotide–binding (G) proteins G_s, G_i, and G_q and β-arrestins. The association of the p.R270H missense mutation of GPR120 in obesity suggests therapeutic potential for GPR120 in the treatment of metabolic diseases.

RATIONALE: How natural fatty acid hormones—which are amphipathic molecules, distinguished mainly by number and position of double bonds—interact with GPCRs such as GPR120 has been unclear. Both saturated and unsaturated FAs are able to activate GPR120, but only certain unsaturated FAs are beneficial for metabolism. It is therefore important to understand whether GPR120 can recognize selective double-bond decorations in FAs and, if so, translate binding to specific biological signaling pathways, including different G protein subtypes and arrestins. The lack of GPCR structures in complex with natural fatty acid hormones and downstream effectors has hampered our understandin double-bond recognition, which is one c lenge in developing therapeutics that might act through this receptor.

RESULTS: By profiling G protein and arrestin activities of GPR120 stimulated by saturated and unsaturated endogenous FAs or the synthetic compound TUG891, we found that these molecules exhibited different biased signaling properties. In particular, only the beneficial ω-3 FAs were able to activate G_s signaling. We determined six cryo–electron microscopy (cryo-EM) structures of GPR120-G_i/G_{iq} with 9-hydroxystearic acid (9-HSA), linoleic acid (LA), oleic acid (OA), the natural agonist ω-3 eicosapentaenoic acid (EPA), and the synthetic agonist TUG891. All fatty acid hormones and TUG891 assumed an overall "L" configuration and were buried inside the seven-transmembrane (7TM) helix bundle of the receptor. Through structural and mutational analysis, biochemical characterization, and molecular simulations, we identified aromatic residues in the ligand pocket of GPR120 that specifically recognize the C–C double bonds present in unsaturated FAs through π:π interactions and translate this recognition into different signaling outcomes. A propagating path connects the double-bond recognition of GPR120 inside the ligand pocket of the cytoplasmic side, and common and distinct features of G_s and G_q coupling interfaces were investigated. We also analyzed the structural basis for selectivity of TUG891 toward GPR120 and a disease-associated single-nucleotide polymorphism of GPR120. The separation of TUG891 into two regions by a linker oxygen suggests that fragment-based drug design could be exploited for GPR120 ligand design.

CONCLUSION: Our cryo-EM structures reveal how fatty acid hormones bind the orthosteric site within the 7TM domain of GPCRs and how specific aromatic residues inside the ligand pocket recognize the C–C double bonds. We also investigated mechanisms underlying signaling bias of GPR120 in response to various ligands. This work will serve as a foundation for the development of molecules that bind and activate GPR120 for potential therapeutic uses as well as to better understand how ligand-induced conformational changes bias signaling outcomes in GPRCs. ■

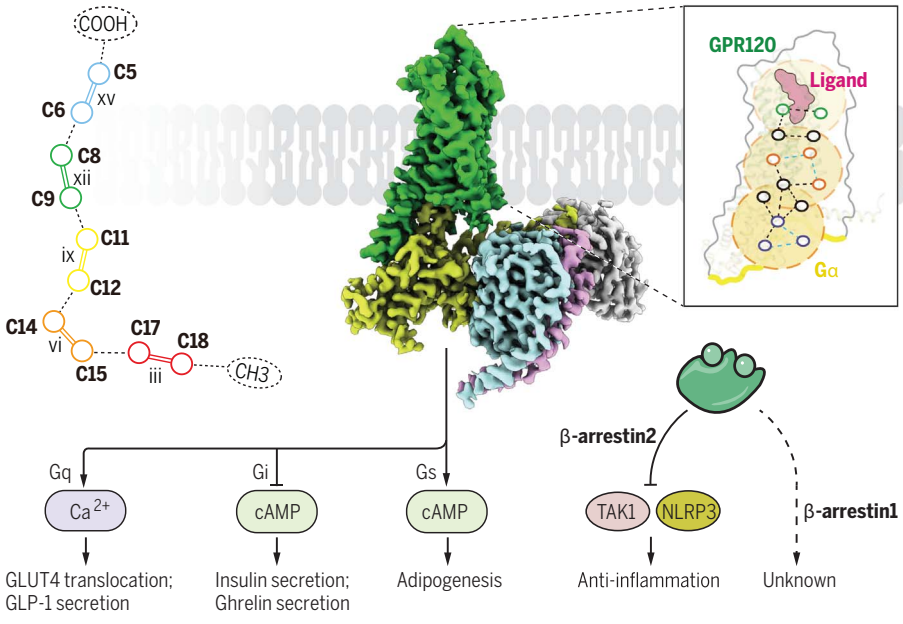

Fish oil membrane receptor GPR120 recognizes different unsaturated FAs and couples to distinct downstream effectors. The membrane receptor GPR120 specifically recognizes the C–C double bonds present in unsaturated FAs, such as those in the ω-3 FAs found in fish oil, through π:π interactions. The interaction patterns of different FAs or ligands inside of the ligand pocket of GPR120 are translated into different signaling outcomes via distinct propagating paths. GLUT4, glucose transporter member 4; cAMP, cyclic adenosine monophosphate; TAK1, transforming growth factor-β–activated kinase 1; NLRP3, NLR family pyrin domain containing 3.

The list of author affiliations is available in the full article online.
*Corresponding author. Email: shiqingfeng@sdu.edu.cn (S.F.); yuxiao@sdu.edu.cn (X.Y.); zhang_yan@zju.edu.cn (Y.Z.); sunjinpeng@sdu.edu.cn (J.-P.S.)
†These authors contributed equally to this work.
Cite this article as C. Mao *et al.*, *Science* **380**, eadd6220 (2023). DOI: 10.1126/science.add6220

READ THE FULL ARTICLE AT
https://doi.org/10.1126/science.add6220

RESEARCH ARTICLE

LIPID SIGNALING

Unsaturated bond recognition leads to biased signal in a fatty acid receptor

Chunyou Mao[1]†, Peng Xiao[2]†, Xiao-Na Tao[2,3,4]†, Jiao Qin[1]†, Qing-Tao He[5]†, Chao Zhang[2]†, Sheng-Chao Guo[2], Ya-Qin Du[3], Li-Nan Chen[1], Dan-Dan Shen[1], Zhi-Shuai Yang[2], Han-Qiong Zhang[2], Shen-Ming Huang[3], Yong-Hao He[2], Jie Cheng[6,7], Ya-Ni Zhong[2], Pan Shang[7], Jun Chen[2], Dao-Lai Zhang[8], Qian-Lang Wang[2], Mei-Xia Liu[2], Guo-Yu Li[2], Yongyuan Guo[5], H. Eric Xu[9], Chuanxin Wang[4], Cheng Zhang[10], Shiqing Feng[4,5]*, Xiao Yu[7]*, Yan Zhang[1,11,12,13]*, Jin-Peng Sun[2,3,6]*

Individual free fatty acids (FAs) play important roles in metabolic homeostasis, many through engagement with more than 400 protein–coupled receptors. Searching for receptors to sense beneficial omega-3 FAs of fish oil enabled the identification of GPR120, which is involved in a spectrum of metabolic diseases. Here, we report six cryo–electron microscopy structures of GPR120 in complex with FA hormones or TUG891 and G_i or G_{iq} trimers. Aromatic residues inside the GPR120 ligand pocket were responsible for recognizing different double-bond positions of these FAs and connect ligand recognition to distinct effector coupling. We also investigated synthetic ligand selectivity and the structural basis of missense single-nucleotide polymorphisms. We reveal how GPR120 differentiates rigid double bonds and flexible single bonds. The knowledge gleaned here may facilitate rational drug design targeting to GPR120.

Individual free fatty acids (FAs) are important signaling molecules that modulate body weight, insulin secretion and sensitivity, inflammation, and many other metabolic processes (*1*–*3*), in addition to being critical energy sources. Omega-3 FAs (ω-3 FAs), in particular, have well-documented benefits, including anti-inflammatory effects (*4*), preventing metabolic disorder (*5*), and enabling homeostasis of healthy fat tissue (*6*), as do alterations in the unsaturated-to-saturated FA ratio using Fat1 transgenic mice (*3*, *4*). Searching for receptors mediating the anti-inflammatory effects of ω-3 FAs enabled the identification of GPR120 (also known as FFAR4, free fatty acid receptor 4) (*7*, *8*), a receptor that can sense long-chain FAs (LCFAs) and promote insulin sensitization (*9*, *10*), anti-inflammatory effects (*5*, *11*), glucagon-like peptide 1 (GLP-1) secretion stimulation (*11*, *12*), and the control of adipogenesis (*6*). Further research using synthetic GPR120 agonists and GPR120-deficient mouse models, as well as the manifestation of the association of the p.R270H missense mutation of GPR120 in obesity (*13*), supported the therapeutic potential of GPR120 for the treatment of metabolic diseases (*2*, *14*–*18*).

The activation of GPR120 is known to be coupled to multiple downstream effectors, including guanine nucleotide–binding (G) proteins G_s, G_i, G_q, and β-arrestins (*6*, *8*). While G_q-mediated signaling is required for GPR120-mediated glucose transporter member 4 (GLUT4) translocation in adipose tissues and GLP-1 secretion (*7*, *12*), the G_i function of GPR120 plays critical roles in promoting insulin secretion in pancreatic islets and inhibiting ghrelin secretion in stomach cells (*19*, *20*). Moreover, mechanistic studies revealed that the anti-inflammatory effects of GPR120 are mediated by its association with β-arrestin2, which blocks the activities of transforming growth factor-β–activated kinase 1 (TAK1) and the NLR family pyrin domain containing 3 (NLRP3) inflammasome (*5*, *7*). In addition, the G_s signaling of GPR120 at cilia potentially controls adipogenesis (Fig. 1A) (*6*). Although both saturated and unsaturated FAs were able to activate GPR120, and only certain unsaturated FAs are known to be beneficial for metabolism (*7*, *11*), the signaling bias of GPR120 in response to different saturated or unsaturated FAs, as well as synthetic compounds, has just begun to be appreciated (Fig. 1A) (*16*).

In the present study, we set out to delineate the bias properties of GPR120 in response to stimulation with endogenous saturated 9-hydroxystearic acid (9-HSA), unsaturated linoleic acid (LA) and oleic acid (OA), the natural agonist ω-3 eicosapentaenoic acid (EPA), and the synthetic agonist TUG891 [3-(4-{[5-fluoro-2-(4-methylphenyl)phenyl]methoxy}phenyl)propanoic acid] (*18*, *21*). We determined six GPR120 structures in complex with these agonists and G_i or G_{iq} transducers, which, along with pharmacological profiling, mutations, and computational work, provided in-depth insights into double-bond recognition and signaling bias by GPR120.

Bias property of GPR120 agonists

Different downstream effectors play key roles in mediating distinct GPR120 (FFAR4) functions. We found previously that two endogenous FAs, OA and LA, were up-regulated in pancreatic islets in response to glucose and exhibited functional and signaling bias in the activation of mouse GPR120 (*16*), but the bias properties of different endogenous or natural FAs toward human GPR120 have not been characterized. We exploited arrestin recruitment and G protein dissociation assays to profile the bias properties of GPR120 toward a panel of agonists, including the ω-6 FA LA and the ω-9 FA OA (two endogenous agonists); the natural product ω-3 FA, EPA (a component of fish oil); and the synthetic agonist TUG891, using the saturated FA 9-HSA as a reference (*22*) (Fig. 1, B to F; fig. S1, A to E; and table S1). By direct comparison of the representative concentration-dependent curves of GPR120 ligands, bias differences could be identified in selective ligand sets and particular signaling pairs. For instance, 9-HSA, EPA, and TUG891 showed similar maximal efficacy response (E_{max}) and median effective concentration (EC_{50}) values in G_i signaling, but the G_q activities of TUG891 were higher than those of 9-HSA and EPA (Fig. 1, C to E; fig. S1, A to E; and table S1). We next used a two-dimensional (2D) differential σ plot to enable full visualization of the bias property between the G_q and G_i signaling pair (Fig. 1F). A positive σ value indicated stronger activity of the agonist than the reference compound in the selective signaling pathway (x axis or y axis). A ligand above the diagonal line indicated bias toward

[1]Department of Biophysics and Department of Pathology of Sir Run Run Shaw Hospital, Zhejiang University School of Medicine, Hangzhou 310058, China. [2]Key Laboratory Experimental Teratology of the Ministry of Education and Department of Biochemistry and Molecular Biology, School of Basic Medical Sciences, Cheeloo College of Medicine, Shandong University, Jinan 250012, China. [3]Beijing Key Laboratory of Cardiovascular Receptors Research, Beijing 100191, China. [4]The Second Hospital of Shandong University, Cheeloo College of Medicine, Shandong University, Jinan 250012, China. [5]Department of Orthopedics, Qilu Hospital of Shandong University, Cheeloo College of Medicine, Shandong University, Jinan 250012, China. [6]Advanced Medical Research Institute, Cheeloo College of Medicine, Shandong University, Jinan 250012, China. [7]Key Laboratory Experimental Teratology of the Ministry of Education and Department of Physiology, School of Basic Medical Sciences, Shandong University, Jinan 250012, China. [8]School of Pharmacy, Binzhou Medical University, Yantai 264003, China. [9]CAS Key Laboratory of Receptor Research, Center for Structure and Function of Drug Targets, Shanghai Institute of Materia Medica, Chinese Academy of Sciences, Shanghai 201203, China. [10]The Key Laboratory of Cardiovascular Remodeling and Function Research, Chinese Ministry of Education, Chinese National Health Commission and Chinese Academy of Medical Sciences, the State and Shandong Province Joint Key Laboratory of Translational Cardiovascular Medicine, Department of Cardiology, Qilu Hospital of Shandong University, Jinan 250012, China. [11]Liangzhu Laboratory, Zhejiang University Medical Center, Hangzhou 311121, China. [12]MOE Frontier Science Center for Brain Research and Brain-Machine Integration, Zhejiang University School of Medicine, Hangzhou 310058, China. [13]Research and Development Center for E-Learning, Ministry of Education, Beijing 100816, China.
*Corresponding author. Email: shiqingfeng@sdu.edu.cn (S.F.); yuxiao@sdu.edu.cn (X.Y.); zhang_yan@zju.edu.cn (Y.Z.); sunjinpeng@sdu.edu.cn (J.-P.S.)
†These authors contributed equally to this work.

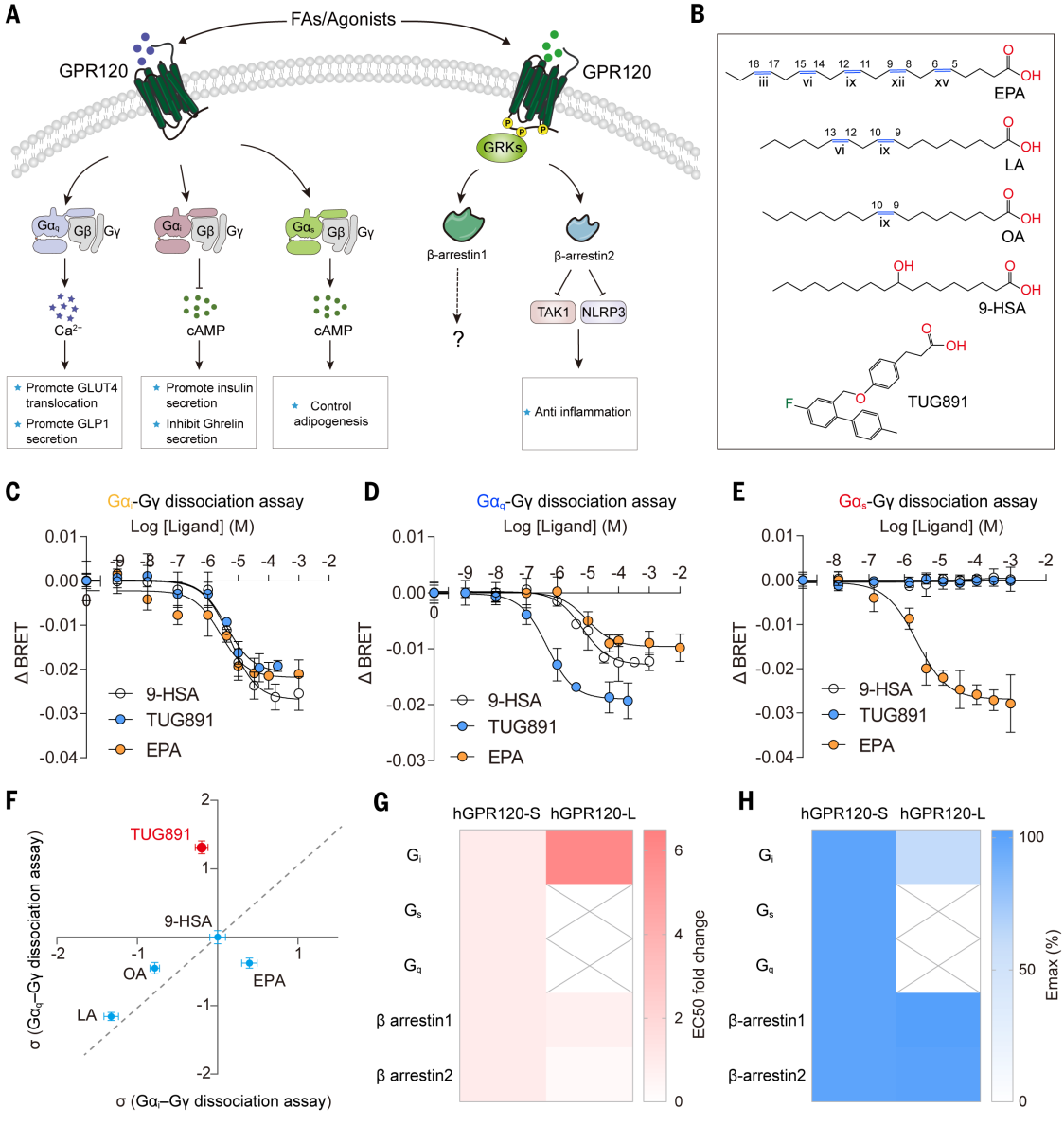

Fig. 1. Biased properties of different GPR120 ligands. (**A**) Schematic overview of G protein– and arrestin–mediated GPR120 signaling and related functions. (**B**) Chemical structures of fatty acid ligands and synthetic ligand TUG891. (**C** to **E**) Concentration-dependent response curves of GPR120 in response to ligands by $G\alpha_i$-$G\gamma$ dissociation assay (C), $G\alpha_q$-$G\gamma$ dissociation assay (D), or $G\alpha_s$-$G\gamma$ dissociation assay (E). Values are mean ± standard deviation (SD) from three independent experiments (n = 3) performed in triplicates. (**F**) Two-dimensional differential σ plot comparing effective signaling (σ) in $G\alpha_q$-$G\gamma$ dissociation and $G\alpha_i$-$G\gamma$ dissociation for a set of GPR120 ligands (9-HSA, TUG891, OA, LA, and EPA) using saturated FA 9-HSA as the reference. Ligands on the gray dashed diagonal line showed balanced signaling properties. The plot was generated on the basis of σ values shown in table S2. (**G** and **H**) Heatmap representation of activities comparison between two splice variants of GPR120 in response to EPA stimulation, via G protein dissociation assays or β-arrestin1/2 recruitment assay. Heatmap shows the EC_{50} (G) and E_{max} (H) differences. The heatmaps are generated according to the data shown in fig. S1 (refer to table S4 for details). hGPR120-L showed no detectable G_s or G_q activity and had weaker G_i coupling efficacy compared with hGPR120-S.

a particular type of signaling (y-axis signaling) over the other type of signaling (x-axis signaling), whereas a ligand below the diagonal line suggested a bias toward the x axis. Notably, TUG891 is a G_q-bias ligand, whereas EPA showed weak G_i bias when we compared G_q activation with G_i activation using 9-HSA as a reference (Fig. 1F, fig. S2, and table S2) (*22*–*24*). In particular, only ω-3 FAs, including EPA, alpha-linolenic acid (ALA), and docosahexaenoic acid (DHA), were able to activate G_s signaling, suggesting a strong G_s versus G_i or G_q bias property of EPA compared with TUG891 or 9-HSA (Fig. 1E, fig. S1E, and table S1).

Human GPR120 has two alternative splicing forms, with one long (L) GPR120 splice variant (hGPR120-L) containing a 16–amino acid insertion in the third intracellular loop of the short (S) human GPR120 splice variant (hGPR120-S) (fig. S3A). hGPR120-L showed no detectable G_s or G_q activity in response to EPA, TUG891, or LA and much less G_i activity than hGPR120-S, possibly because of steric hindrance of intracellular loop 3 (ICL3) precluding G_i or G_q protein coupling (Fig. 1, G and H; figs. S1, F to N, and S3; and tables S1 and S3).

Structural determination and overall structure

We then solved the cryo–electron microscopy (cryo-EM) structures of the TUG891-, 9-HSA–, LA-, EPA-, and OA-bound GPR120-G_i complexes and the TUG891-bound GPR120-G_{iq} complex at 3.0, 3.1, 3.1, 2.8, 2.8, and 2.6 Å, respectively (figs. S4 to S9 and table S5). The cryo-EM densities allowed assignment of the bound ligands and most residues of the GPR120 receptor, G_i or G_q heterotrimer, and scFv16 (Fig. 2, A to C, and figs. S4H, S5F, S6F, S7G, S8G, and S9G). The binding modes of the ligands in the corresponding structures were further supported by molecular dynamics (MD) simulations (fig. S10).

GPR120 assumed a classic seven-transmembrane (7TM) bundle topology (Fig. 2, A and B). Compared to other FA or lipid G protein–coupled receptors (GPCRs), including GPR40 [Protein Data Bank (PDB) ID 5TZR] (*25*), lysophosphatidic acid receptor 6 (LPA6) (PDB ID 5XSZ) (*26*), and sphingosine 1–phosphate receptor 1 (S1PR1) (PDB ID 3V2Y) (*27*), GPR120 showed prominent differences at its N terminus and

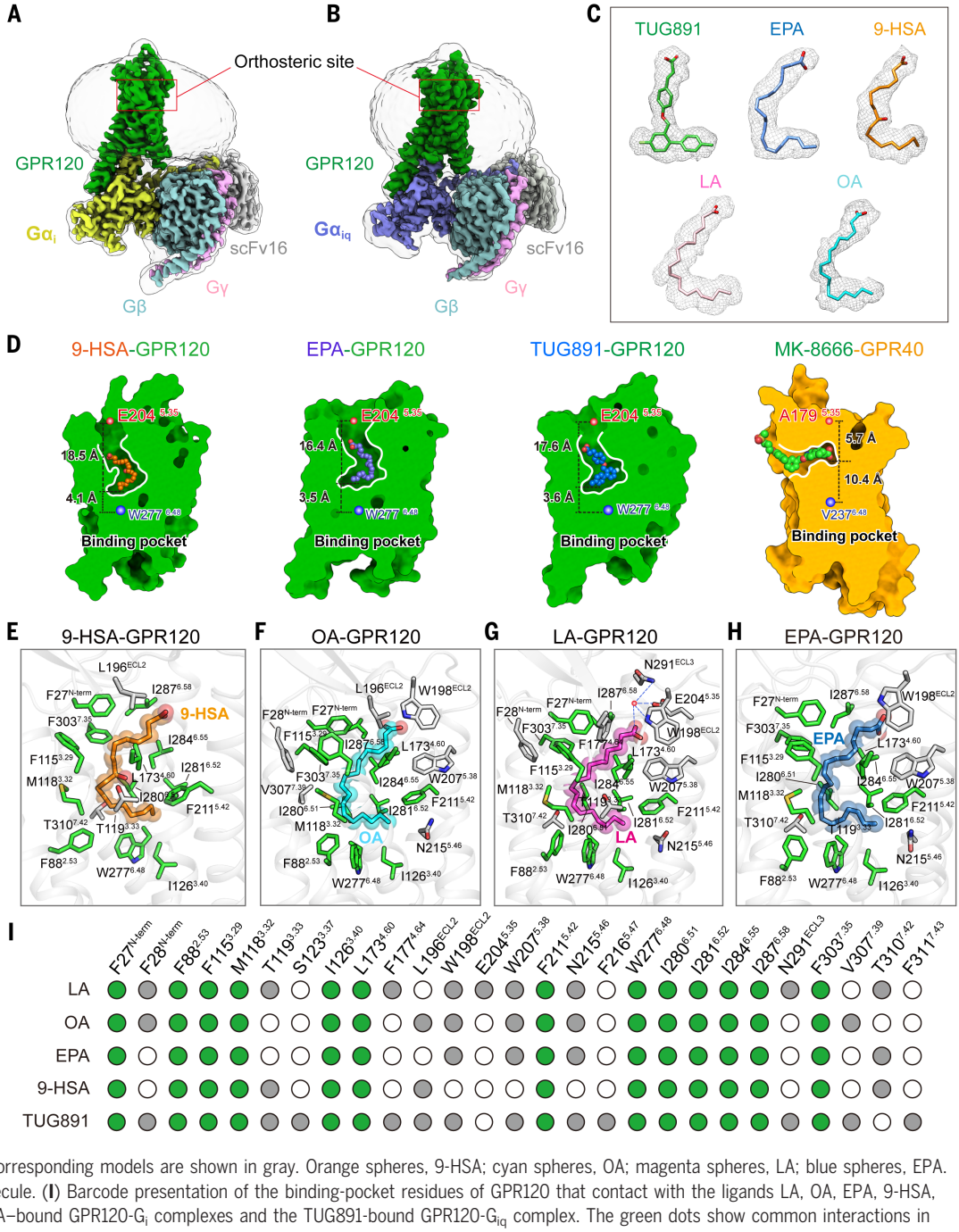

Fig. 2. Overall cryo-EM structures of the GPR120-G_i/G_{iq} heterotrimer bound with LA, OA, EPA, 9-HSA, or TUG891 and the intramolecular interaction between ligands and its binding pocket. (**A** to **C**) Cryo-EM density map of representative GPR120-G_i (exemplified by 9-HSA-GPR120-G_i complex) (A) and TUG891-GPR120-G_{iq} (B) complexes. Ligands with different colors from TUG891-GPR120-G_{iq}, EPA-GPR120-G_i, 9-HSA-GPR120-G_i, LA-GPR120-G_i, and OA-GPR120-G_i complexes (C) are shown, with surrounding density maps. TUG891, green; EPA, sky blue; 9-HSA, orange; LA, pink; OA, cyan. See also figs. S4H, S5F, S6F, S7G, S8G, and S9G. (**D**) Binding of ligands 9-HSA (orange), LA (pink), and TUG891 (blue) in the ligand pockets of GPR120 from 9-HSA-GPR120-G_i, LA-GPR120-G_i, and TUG891-GPR120-G_{iq} complexes (green) compared with binding of MK-8666 in GPR40 (PDB ID 5TZR) (*25*) (orange). The depths of the ligand pockets are highlighted. The conserved "toggle switch" and the TM5 residue of $E204^{5.35}$ (GPR120)/$A179^{5.35}$ (GPR40) were used as a reference. (**E** to **H**) The detailed interactions between 9-HSA (E), OA (F), LA (G), and EPA (H) and residues in the ligand-binding pocket of GPR120 in complex with G_i. The H-bonds and polar interactions are depicted as blue dashed lines. Common interaction residues in all four ligand-bound GPR120-G_i complex structures are shown in green, whereas specific interaction residues within corresponding models are shown in gray. Orange spheres, 9-HSA; cyan spheres, OA; magenta spheres, LA; blue spheres, EPA. The red ball represents a water molecule. (**I**) Barcode presentation of the binding-pocket residues of GPR120 that contact with the ligands LA, OA, EPA, 9-HSA, and TUG891 in LA-, OA-, EPA-, 9-HSA–bound GPR120-G_i complexes and the TUG891-bound GPR120-G_{iq} complex. The green dots show common interactions in five ligands. The gray dots show nonconserved interactions. The white dots mean that there is no interaction between ligands and GPR120. Single-letter abbreviations for the amino acid residues are as follows: A, Ala; C, Cys; D, Asp; E, Glu; F, Phe; G, Gly; H, His; I, Ile; K, Lys; L, Leu; M, Met; N, Asn; P, Pro; Q, Gln; R, Arg; S, Ser; T, Thr; V, Val; W, Trp; and Y, Tyr.

extracellular loop 2 (ECL2) (table S6). Whereas the N terminus of LPA6 or GPR40 was in proximity to ECL3, the N terminus of GPR120 assumed a "U" configuration lying across the 7TM bundle and inserted under ECL2, creating one side of the upper barrier of the ligand pocket (figs. S11, A and B, and S12A). ECL2 contained two β sheets and covered the N terminus of GPR120 (fig. S11A). In contrast, the N terminus of S1PR1 assumed an α-helical configuration and covered the ligand-binding pocket by juxtaposition with ECL2 (fig. S13A). The GPR120 ligand pocket was deeper than that of MK-8666–bound GPR40, and all agonists were buried deep inside the 7TM bundle (Fig. 2D and fig. S11, C and D). Whereas the ligand pockets of GPR120 were sealed, the GPR40 agonist MK-8666 was inserted diagonally into the receptor from an entrance created between TM3 and TM4 on the receptor side (Fig. 2D and fig. S12, B and C). For other comparisons, a proposed ligand pocket was formed between TM4 and TM5 of LPA6 to accommodate the main body of the LPA with an open entrance at the top (fig. S11, E and F) (*26*). Whereas the polar group of S1P was closer to TM1 and TM2, the polar groups of

FAs were near TM5 in GPR120 (fig. S13, B and C). Compared with the LPA6, GPR40, and S1PR1 structures on the intracellular sides, GPR120 had a longer TM5 and TM6 to hold ICL3, and TM6 was shifted outward (figs. S11G, S12D, and S13D).

Fatty acid–binding pockets

Inside the ligand pocket, all FAs assumed an overall "L" configuration (Fig. 2, C and D). The convex side of these FAs is accommodated by a hydrophobic surface created by $F27^{N\text{-}term}$, $F115^{3.29}$, $M118^{3.32}$, $L196^{ECL2}$, $I287^{6.58}$, and $F303^{7.35}$. In contrast, the concave surfaces of the FAs faced a combination of hydrophobic and polar residues of TM3-TM4-TM5-TM6, including $T119^{3.33}$, $L173^{4.60}$, $W207^{5.38}$, $F211^{5.42}$, and $I284^{6.55}$. The hydrophobic aryl chain ends of these FAs were in contact with $I281^{6.52}$ and reached the bottom of the pocket formed by $I126^{3.40}$ and the toggle switch $W277^{6.48}$ (Fig. 2, E to I). Thirteen hydrophobic residues along the GPR120 ligand pocket contributed to interactions with all these FAs, thus potentially representing a common mechanism of recognition of FAs by GPR120 (Fig. 2, E to I; figs. S14, B and C, and S15; and table S7). The C termini of both 9-HSA and OA formed polar contacts with the main chain carbonyl of $I284^{6.55}$ and the main chain amine of $L288^{6.59}$ (fig. S16, A and B). In contrast, the C terminus of LA formed a water-mediated H-bond network with $W198^{ECL2}$, $E204^{5.35}$, and $N291^{ECL3}$, and that of EPA formed only a hydrogen bond with the main chain carbonyl of $I284^{6.55}$ (Fig. 2G and fig. S16C). Consistent with these observations, mutation of the $F115^{3.29}$, $I126^{3.40}$, $L173^{4.60}$, or $L196^{ECL2}$ hydrophobic residue to alanine (Ala) decreased the G_i coupling activity of GPR120 in response to LA, OA, 9-HSA, or EPA. Although the $W198^{ECL2}$A and $E204^{5.35}$A mutations had no effects on 9-HSA–induced GPR120 activation, disrupting the H-bond network between LA and GPR120 through either of these two residues impaired LA-induced GPR120 activation (fig. S16, D to K, and table S8). The hydrophobic corridor formed by 14 common hydrophobic amino acids may thus serve as a general mechanism for the recognition of FAs by GPR120, whereas the polar networks may contribute to FA recognition specificity.

Recognition of double bonds of unsaturated FAs by GPR120

9-HSA is a saturated FA, whereas LA, OA, and EPA are unsaturated FAs and have double bonds in specific locations along carbon chains (Fig. 1B). Inspection of the structures of LA-, OA-, and EPA-bound GPR120 offered detailed information on the interaction modes of the pocket residues with these unsaturated double bonds. Comparisons of the mutation effects of residues in contact with unsaturated double bonds between unsaturated FA-induced GPR120 activation and 9-HSA–induced GPR120 activation also provided us with an opportunity to define the contributions of pocket residues to specific double-bond recognition because the corresponding double bonds in unsaturated FAs were replaced by carbon-carbon single bonds in 9-HSA.

Notably, each double bond in OA (one double bond), LA (two double bonds), and EPA (five double bonds) interacts with three to six hydrophobic residues of GPR120 (Fig. 3, A to K). We systematically mutated contacting residues and inspected whether they contributed to double-bond recognition by comparing their effects on GPR120 activation induced by unsaturated FAs with those induced by 9-HSA. Mutations of aromatic residues led to decreased potency of unsaturated FAs compared with saturated FAs through recognition of these double bonds. For instance, the mutations $F211^{5.42}$A or $W207^{5.38}$A specifically decreased EPA-induced GPR120 activity more than the activity induced by 9-HSA and other unsaturated FAs. These mutational effects are consistent with specific interactions between $W207^{5.38}$ and $F211^{5.42}$ and the double bonds xv and iii of EPA, respectively. The mutation $F88^{2.53}$V led to a larger decrease in the activity of LA and EPA, which both had a double bond at the vi position, than in the activity of 9-HSA and OA (Fig. 3, L and M; fig. S17, A to H; and table S10). Specifically, $F27^{N\text{-}term}$, $F115^{3.29}$, and $F303^{7.35}$ constituted the central aromatic core to accommodate the aliphatic chain of the FAs, forming contacts with bond ix to xv in EPA and bond ix in OA and LA. Consistent with these observations, upon the mutation $F27^{N\text{-}term}$V, $F115^{3.29}$A, or $F303^{7.35}$V, the potency of EPA, LA, and OA decreased more than that of saturated 9-HSA (Fig. 3, L and M; fig. S17, A to H; and table S10). In contrast, the nonaromatic hydrophobic residues seem to prefer single bonds over double bonds; for example, the activity of $M118^{3.32}$A decreased approximately 50-, 5-, 4-, and 2-fold in response to stimulation with 9-HSA, OA, LA, and EPA, respectively. $I280^{6.51}$A led to approximately 25-, 10-, 2-, and 2-fold decreases in the potency of 9-HSA, OA, LA, and EPA with regard to GPR120, respectively (Fig. 3L; fig. S17, A to G; and table S10). We speculated that these effects were due to the greater flexibility of the single-bond/nonaromatic hydrophobic side chain than the double-bond/aromatic side chain, enabling easier fitting of the single bond to the flexible conformations of nonaromatic residues for favorable interactions.

To further investigate the mechanisms of double-bond recognition by GPR120, we performed MD simulations. The π:π interactions between aromatic residues and double bonds are known to contribute to intermolecular interactions in organic compounds or proteins (*28*, *29*). We performed long-term MD simulations of the LA-GPR120, OA-GPR120, and EPA-GPR120 complex systems using constraint algorithms and simulated annealing by GROMACS (fig. S18). The software's own gmx distance module was used to analyze the distances between aromatic residues and double bonds in the simulation trajectories. Our calculations indicated that aromatic residues were more prone to forming stable contacts with double bonds via π:π interactions than their interactions with single bonds at the same position (Fig. 3, N and O, and fig. S17, I to N). Moreover, the mutations of the corresponding aromatic residues to nonaromatic Leu residues also notably decreased their stable interactions with the double bonds (Fig. 3P and fig. S19).

Collectively, our studies indicated that the π:π interactions contributed by aromatic residue arrays located in ligand pockets may be an important mechanism for selective double-bond recognition by GPR120. In particular, each of these aromatic residue arrays, such as $F27^{N\text{-}term}$, $F88^{2.53}$, $F115^{3.29}$, $W198^{ECL2}$, $W207^{5.38}$, $F211^{5.42}$, and $F303^{7.35}$, recognizes one to three double bonds at specific positions of these unsaturated FAs.

Recognition of synthetic TUG891 and ligand pocket selectivity of GPR120

Selective activation of GPR120 has therapeutic potential for the treatment of many diseases, including type 2 diabetes mellitus, osteoporosis, inflammation, and obesity (*1*, *2*, *7*–*9*, *11*, *13*–*15*, *30*). The GPR120-selective agonist TUG891 has been widely used in functional studies of GPR120 (*18*, *21*). To understand the structural basis of the ligand selectivity of GPR120 and facilitate the future design of selective GPR120 agonists, we determined the cryo-EM structures of the TUG891-GPR120-G_i and TUG891-GPR120-G_{iq} complexes (figs. S5 and S9). The EM density for the O10 of TUG891 is lacking in the TUG891-GPR120-G_i complex structure, whereas the EM density for TUG891 in the TUG891-GPR120-G_{iq} complex is continuous, and the modeled compound fits well with the EM density (Fig. 2, B and C, and fig. S20). The binding pose of TUG891 in the ligand pocket of GPR120 was further confirmed by MD simulation (fig. S10A). This superior EM map for TUG891 in the GPR120-G_{iq} complex in comparison to the EM map in the GPR120-Gi complex may be consistent with TUG891 having better G_q activity than G_i (TUG891 may have a more stable conformation in the GPR120-G_{iq} complex) (Fig. 1, C, D, and F). Therefore, we mainly used the TUG891-GPR120-G_{iq} structure to describe the interaction between TUG891 and GPR120 and performed computational simulation of the potential position of TUG891 in the TUG891-GPR120-G_i complex structure (Fig. 4A and fig. S10E).

The presence of three aromatic rings in TUG891 rendered the compound more rigid

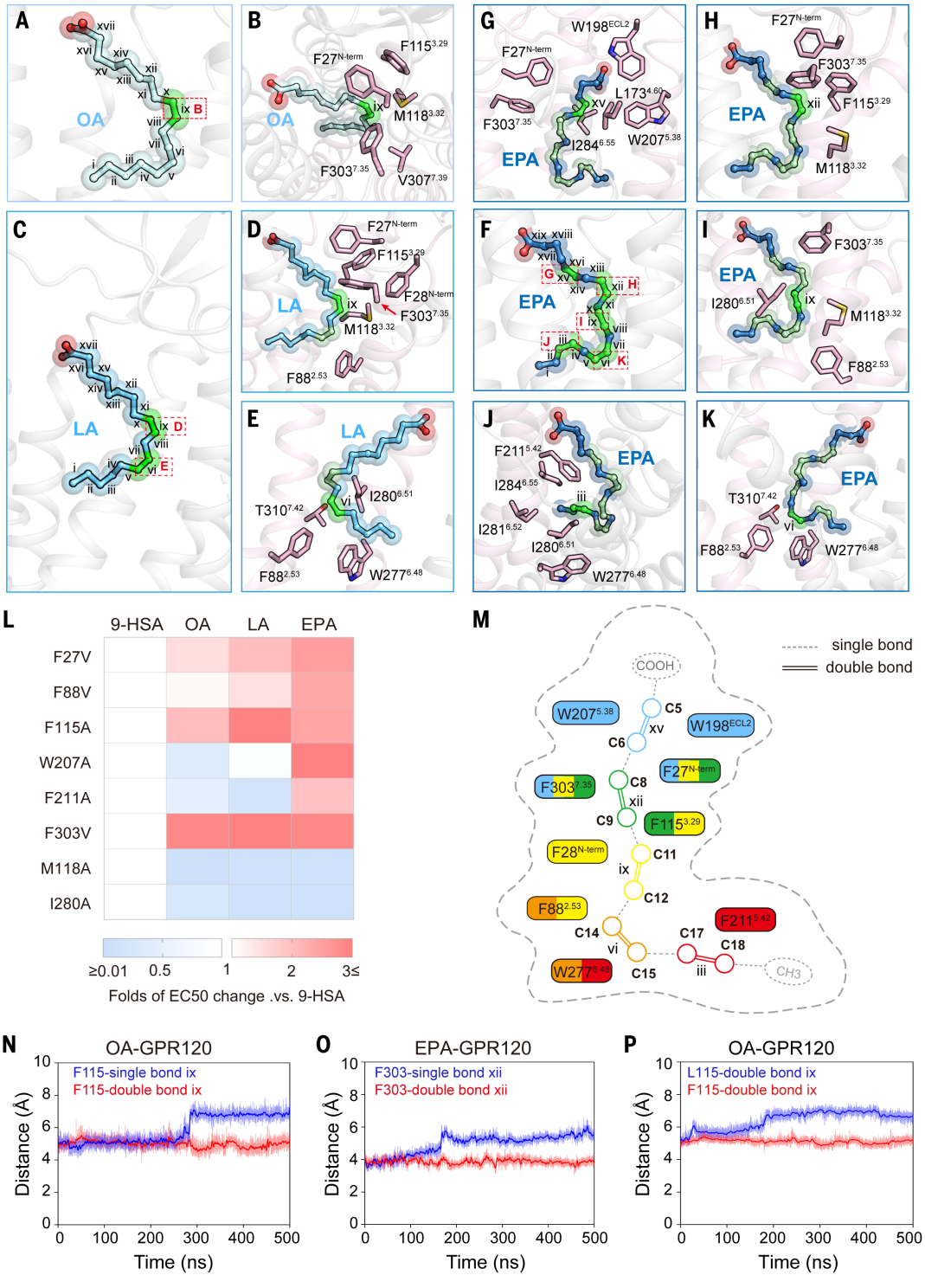

Fig. 3. Double-bond recognition by aromatic residues of GPR120. (**A** and **B**) GPR120 with bonds i to xvii (C1 to C18) in OA (A) and the double bond ix (C9 and C10) in OA (B). OA, pale cyan; double bond is highlighted in green. Bonds are labeled from i to xvii according to their position relative to the carbon end, and C atoms are labeled from C1 to C18 according to their position relative to the C terminal. Double bonds are highlighted in green. (**C** to **E**) GPR120 with bonds i to xvii (C1 to C18) in LA (C) with residues around double bond ix (C9 and C10) (D) or double bond vi (C12 and C13) (E). LA, cyan. (**F** to **K**) GPR120 with bonds i to xix (C1 to C20) in EPA (F) with residues around double bond xv (C5 and C6) (G), double bond xii (C8 and C9) (H), double bond ix (C11 and C12) (I), double bond iii (C17 and C18) (J), and double bond vi (C14 and C15) (K). EPA, blue. (**L**) Differential effects of mutations of double-bond contacting residues on unsaturated FAs (OA, LA, and EPA) compared with those on 9-HSA–induced GPR120 activation by $G\alpha_i$-Gγ dissociation assay. Heatmap shows the folds of EC_{50} changes between designated ligand and 9-HSA. The heatmap was generated using data shown in fig. S17, A to G (refer to table S11 for details). (**M**) Schematic showing the recognition of double bonds at specific positions of FAs by aromatic amino acids of GPR120. The double bonds interacting with aromatic residues of GPR120 are shown, highlighted using color-shaded boxes corresponding to individual double bonds. Here, the double bonds of EPA are shown as an example. Dashed single lines represent omitted carbon atoms and corresponding single bonds; double segments with different colors represent double bonds. Double bond iii, red; double bond vi, orange; double bond ix, yellow; double bond xii, green; double bond xv, blue. Refer to fig. S17H for details. The curved dotted line segment represents the ligand-binding pocket. (**N** to **P**) The distance change between F115 and bond ix in the OA-GPR120 system (N), the distance change between F303 and bond xii in EPA-GPR120 system (O), and the distance change between L115 or F115 and bond ix in OA-GPR120 system (P) during a 500-ns MD simulation. The red line represents the double bond ix system [(N) and (P)] and the double bond xii system (O); and the blue line represents the double bond ix (N) and xii (O) mutated to a single bond, or F115 mutated to L115 (P). The shaded area represents the original, unsmoothed value, with reduced transparency, and the thick line was the result of smoothing the original distance value every 200 points.

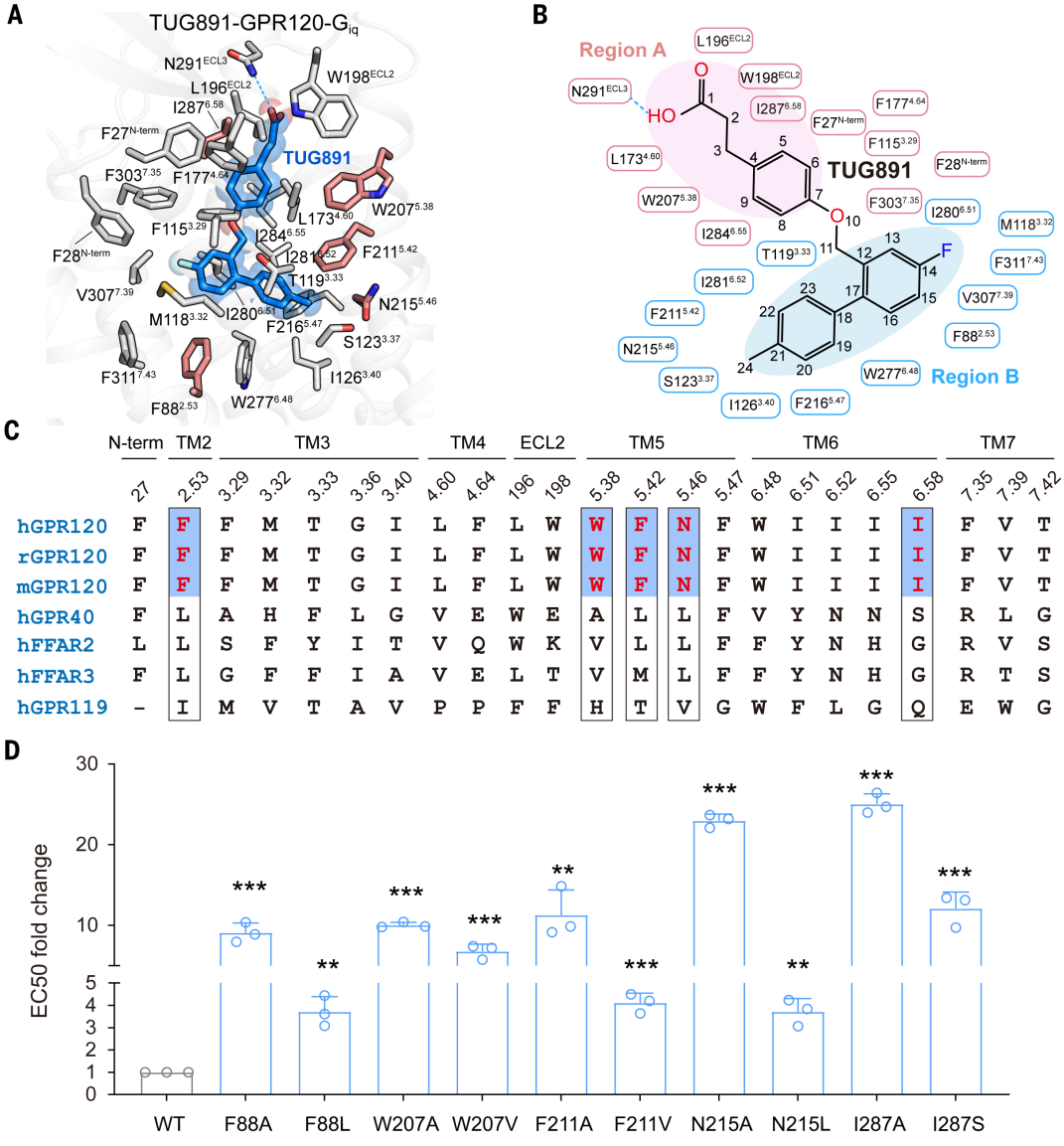
A
TUG891-GPR120-Giq
TUG891
B
Region A
Region B
TUG891
C
N-term
TM2
TM3
TM4
ECL2
TM5
TM6
TM7
hGPR120 F F F M T G I L F L W W F N F W I I I I F V T
rGPR120 F F F M T G I L F L W W F N F W I I I I F V T
mGPR120 F F F M T G I L F L W W F N F W I I I I F V T
hGPR40 F L A H F L G V E W E A L L F V Y N N S R L G
hFFAR2 L L S F Y I T V Q W K V L L F F Y N H G R V S
hFFAR3 F L G F F I A V E L T V M L F F Y N H G R T S
hGPR119 - I M V T A V P P F F H T V G W F L G Q E W G
D
EC50 fold change
WT
F88A
F88L
W207A
W207V
F211A
F211V
N215A
N215L
I287A
I287S

Fig. 4. Structural basis of ligand selectivity of TUG891. (**A**) Detailed interactions between TUG891 (blue) and residues in the binding pocket of GPR120 (gray and salmon) in TUG891-GPR120-G_{iq} complex structure. The residues highlighted in salmon are distinct compared with other GPCRs known to sense LCFAs as shown in (C). H-bond depicted as a blue dashed line. (**B**) 2D representation of contacts between GPR120 and the ligand TUG891 shown in (A). Residues that were implicated in interactions within the region A subpocket were presented in pink, those within the region B subpocket were presented in blue. H-bond was depicted as a blue dashed line. (**C**) Sequence alignment of GPR120 from different species and with other lipid receptors. Note that the residues F88$^{2.53}$, W207$^{5.38}$, F211$^{5.42}$, N215$^{5.46}$, and I287$^{6.58}$ of TM2, TM5, and TM6 in GPR120 are unique compared with other lipid receptors. (**D**) Mutational effects of GPR120 pocket residues on TUG891 induced $G\alpha_i$-Gγ dissociation activities. Statistical differences between wild type (WT) and mutants were determined by two-sided, one-way analysis of variance (ANOVA) with Tukey's test. $^{**}P < 0.01$; $^{***}P < 0.001$; ns, no significant difference. Values are the mean ± SD of three independent experiments for WT and mutants (n = 3).

than endogenous FA agonists. Divided by oxygen O10, the compound was separated into two parts, the phenylpropionic acid in the upper region (region A) and the 4-fluoro-phenyl ring and the 4-methyl phenyl ring in the lower region (region B) (Fig. 4, A and B). Notably, TUG891 is a selective GPR120 agonist. Sequence alignment indicated that at least five residues of TM2 and TM5-TM6, including F88$^{2.53}$, W207$^{5.38}$, F211$^{5.42}$, N215$^{5.46}$, and I287$^{6.58}$, are distinct compared with other GPCRs known to sense LCFAs (Fig. 4C). Mutation of these residues in GPR120 to allelic residues in GPR40, FFAR2, FFAR3, and GPR119 receptors, including F88$^{2.53}$A/L, W207$^{5.38}$A/V, I287$^{6.58}$A/S, F211$^{5.42}$A/V, and N215$^{5.46}$A/L, all decreased GPR120 activity in response to TUG891 stimulation (Fig. 4, C and D; fig. S21; and table S12). It may thus be possible to target these pocket residues for selective GPR120 agonist design. Moreover, the separation of TUG891 into two segments occupying different hydrophobic pockets by the O10 linker suggested that fragment-based chemical synthesis could be exploited to develop selective GPR120 agonists (Fig. 4, B and D; fig. S21; and table S12).

Contribution of pocket residues to signaling bias of GPR120

The diverse bias patterns of endogenous and synthetic agonists made GPR120 a good example for investigation of the structural and molecular mechanisms underlying the signaling bias of an FA GPCR (Fig. 1). TUG891 has three aromatic rings, which were found to form extensive π:π interactions with aromatic residues of GPR120 and to show obvious G_q bias compared with EPA and 9-HSA (Fig. 1, C, D, and F). We therefore profiled effects of mutations of residues surrounding TUG891 on G_q and G_i activation downstream of GPR120. The mutations F27$^{N\text{-term}}$A, F28$^{N\text{-term}}$L, F88$^{2.53}$A, F115$^{3.29}$A, F177$^{4.64}$A, F216$^{5.47}$A, F303$^{7.35}$A, and F311$^{7.43}$A induced much more loss of G_q activation by TUG891 than of G_i activation (Fig. 5, A and B; fig. S22, A to C; and table S13). These results suggested that interactions of TUG891 with an array of eight aromatic residues in the GPR120 ligand pocket may serve as an important mechanism for the G_q bias activity of TUG891, and this aromatic residue array could be exploited for design of G_q-biased agonists targeting GPR120 (Fig. 5, A and B; fig. S22, A to C; and table S13).

In particular, only the ω-3 FAs, but not other FAs among our tested FAs or synthetic TUG891, showed G_s activity, indicating a strong G_s bias of ω-3 FAs compared with other tested FAs. Compared with 9-HSA, a saturated FA with similar G_i activation, EPA formed multiple additional π:π interactions with F27$^{N\text{-term}}$, F115$^{5.39}$, W198$^{5.38}$, W207$^{5.38}$, F211$^{5.42}$, and F303$^{7.35}$ via its double bonds along the carbon chain (Fig. 3,

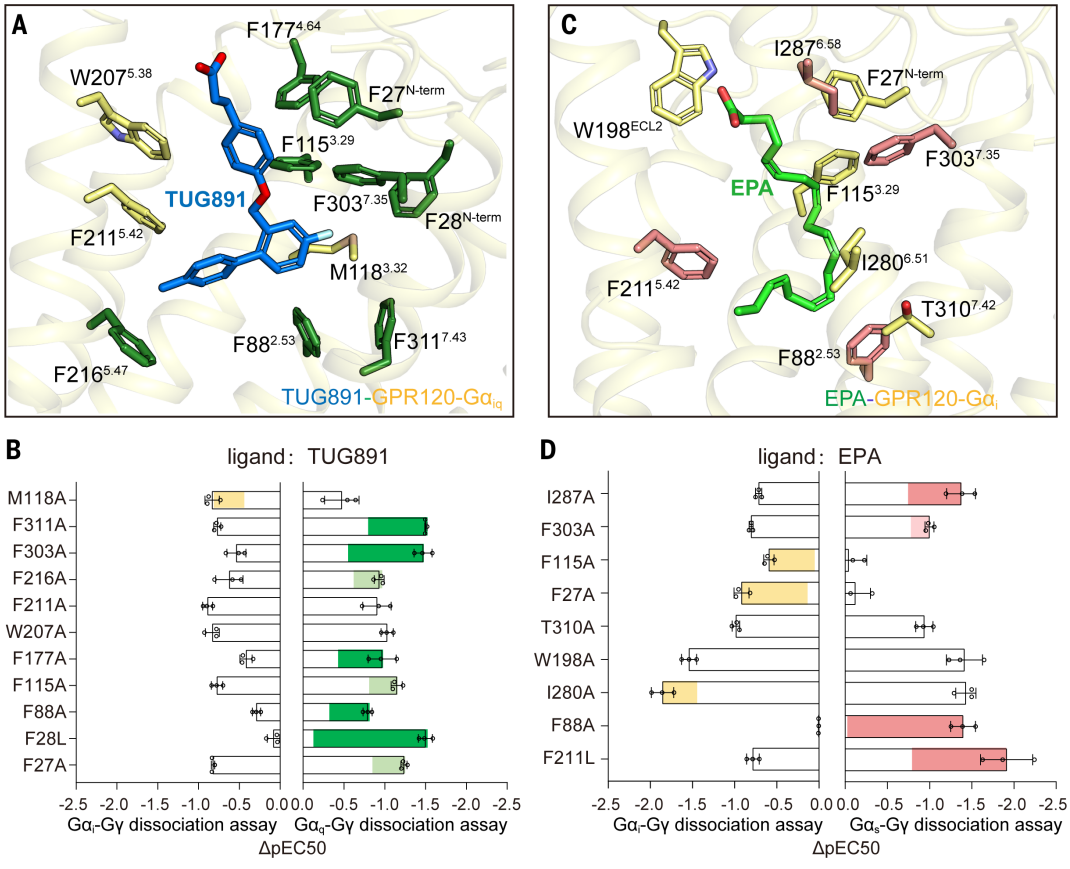

Fig. 5. Contribution of pocket residues to signaling bias of GPR120. (**A**) The detailed interactions between TUG891 and pocket residues in the ligand-binding pocket of GPR120 in complex with G_{iq}. Residues showing larger effects on G_q activation than on G_i activation are highlighted in green. TUG891, blue. (**B**) Mutational effects of the aromatic residues contacting with TUG891 or EPA double bonds on TUG891 induced GPR120-G_q or GPR120-G_i coupling activity measured by $G\alpha_q$-Gγ or $G\alpha_i$-Gγ dissociation assays, respectively. The bar graphs show the differences of potency (ΔpEC50) between wild-type GPR120 and its mutants, which were generated according to data shown in fig. S22, B and C. Residues contributing to biased signaling to either G_i or G_q pathways are shown as light green bars ($0 < \Delta\Delta$pEC50 < 0.5), green bars ($0.5 < \Delta\delta$pEC50), or yellow bars ($\Delta\Delta$pEC50 < 0). $\Delta\Delta$pEC50 is calculated by subtraction of the ΔpEC50 of G_q activity from the ΔpEC50 of G_i activity. Values are mean ± SD from three independent experiments ($n = 3$) performed in triplicates. (**C**) The detailed interactions between EPA and pocket residues in the ligand-binding pocket of GPR120 in complex with G_i. Residues showing larger effects on G_s activation than on G_i activation are highlighted in pink. EPA, green. (**D**) Mutational effects of residues contacting EPA double bonds on EPA induced GPR120-G_s or GPR120-G_i coupling activity measured by $G\alpha_s$-Gγ or $G\alpha_i$-Gγ dissociation assays, respectively. The bar graphs show the differences of potency (ΔpEC50) between wild-type GPR120 and its mutants, which were generated according to data shown in fig. S22, E and F. Residues contributing to biased signaling to either G_i or G_s pathways are shown as light pink bars ($0 < \Delta\Delta$pEC50 < 0.5), pink bars ($0.5 < \Delta\delta$pEC50), or yellow bars ($\Delta\Delta$pEC50 < 0). $\Delta\Delta$pEC50 is calculated by subtraction of the ΔpEC50 of G_s activity from the ΔpEC50 of G_i activity. Values are mean ± SD from three independent experiments ($n = 3$) performed in triplicates.

G to J). Mutations of F88$^{2.53}$A, F211$^{5.42}$L, and F303$^{7.35}$A in particular showed larger effects on the EPA-induced G_s activation of GPR120 than on G_i activation, suggesting that the recognition of double bonds iii, vi, and xii by these three residues determines the G_s bias property (Fig. 5, C and D; fig. S22, D to G; and table S14). In addition, I287$^{6.58}$ formed stronger hydrophobic interactions with EPA, and the I287$^{6.58}$A mutation caused a larger loss of EPA-induced G_s activation than G_i activation (Fig. 5D). Therefore, not only π:π interactions mediated by the double-bond decorations of unsaturated FAs but also other hydrophobic interactions within the ligand pocket contribute to the specific G_s activation of EPA (fig. S22, E to G, and table S14).

Collectively, our data suggested that the π:π interactions between the unsaturated double bonds presented by the unsaturated FAs and the specific combinations of arrays of aryl amino acids located in pockets of GPR120 and other specific hydrophobic contacts played important roles in determining G_q versus G_i and G_s versus G_i signaling bias.

Active states of GPR120

In all six GPR120-G_i or GPR120-G_{iq} structures in complex with either endogenous or natural FAs, as well as the synthetic compound TUG891, the agonists were in direct contact with the toggle switch W277$^{6.48}$, which assumed similar configurations (fig. S23, A to G). Below W277$^{6.48}$, the triad connector P$^{5.50}$-I$^{3.40}$-F$^{6.44}$ motif formed tight packing (fig. S23, H to M), which has been proposed to be essential for maintaining the active state in many class A GPCRs (*23*, *31*–*33*). On the cytoplasmic side, separation of the cytoplasmic termini between TM3 and TM6, breakage of the ionic lock [constituted by the ERM motif (D/ERY motif in class A GPCRs) and D259$^{6.30}$], and packing of the N317$^{7.49}$P318$^{7.50}$XXY321$^{7.53}$ motif with R136$^{3.50}$ were observed (fig. S23, N to Y), which are all hallmarks of the active state of class A GPCRs.

Coupling between GPR120 and G_i

The overall interaction mode between G_i and GPR120 was mostly similar to the binding of G_i with the lipid receptor S1PR1; however, the detailed contact residues and the orientation of second structural elements still showed substantial differences (Fig. 6, A to D, and fig. S24, A to C). For example, the C-terminal tail of the α5 helix was rotated away from TM3 and toward TM6 by ~8° in the 9-HSA-GPR120-G_i complex (Fig. 6A). The C-terminal wavy hook of G_i was inserted into the cavity formed by TM2-TM3 and TM5-TM7 of GPR120 (fig. S24A) and formed specific hydrophobic, polar, and charge-charge interactions (figs. S24B and S25, A to F). Another notable feature of the GPR120-G_i interface is the involvement of all three intracellular loops (ICLs), composed by ~8 to 11 residues in each of five GPR120-G_i complex structures and occupying approximately half the total G_i trimer–contacting amino acids of GPR120 (fig. S24C and table S15). In GPR120, there are five positively charged

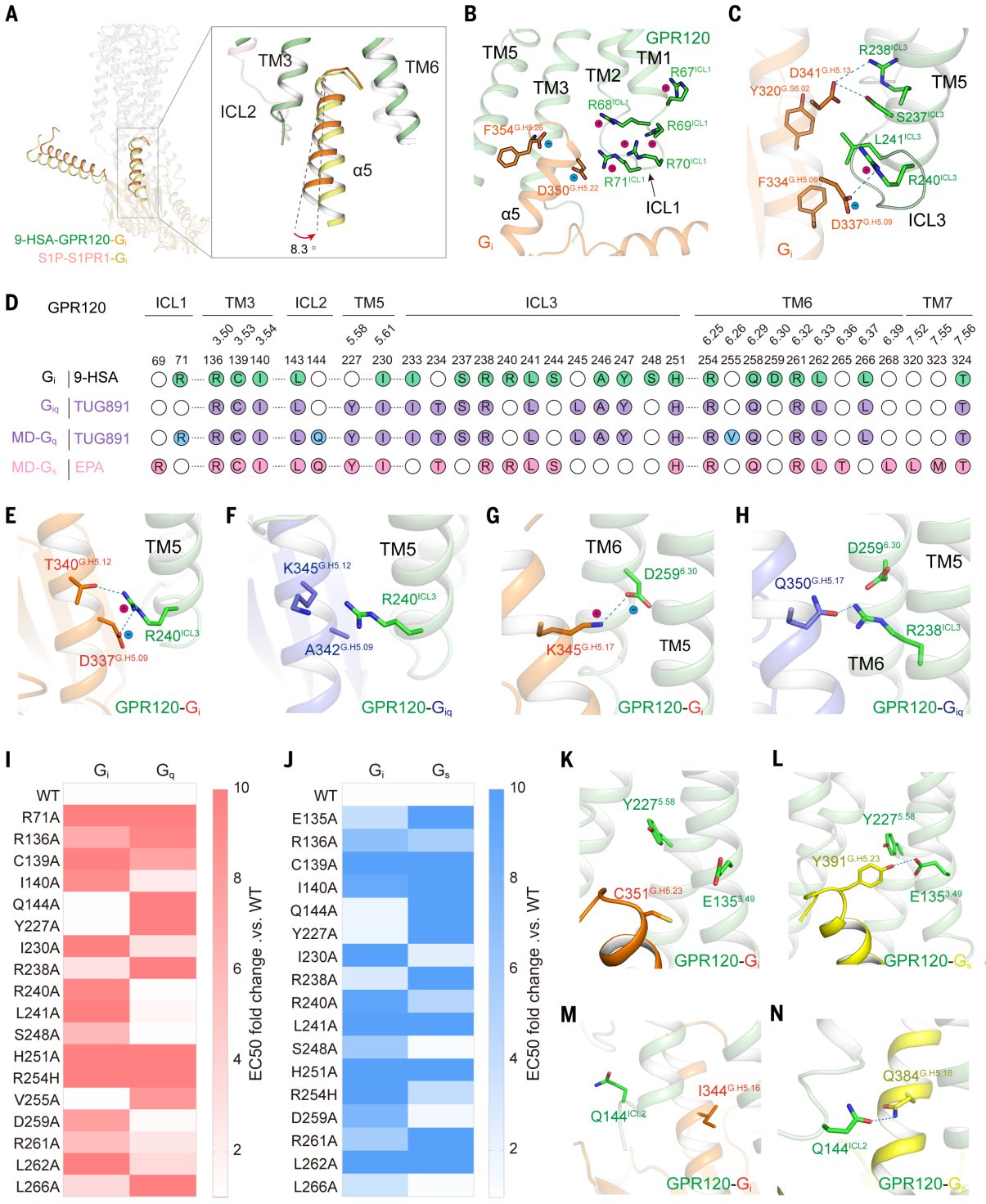

Fig. 6. GPR120-G_i interface and coupling of G_q or G_s to GPR120 by MD simulation. (**A**) Comparison of the overall interaction mode of the 9-HSA-GPR120-G_i complex with that of the S1P-S1PR1-G_i complex structure (PDB ID 7EVY) (*66*). The C-tail of the α5 helix was rotated away from TM3 and toward TM6 by ~8°. (**B** and **C**) Interactions between residues on ICL1 and ICL2 of GPR120 and $G\alpha_i$ (B). The ICL3 residues of GPR120 form interactions with G_i (C). (**D**) Interaction differences in the interface of 9-HSA-GPR120 with G_i, TUG891-GPR120 with G_q, and EPA-GPR120 with G_s in corresponding EM structures or simulated structures, respectively. Residues of GPR120 that interact with G_i are indicated by a green circle. Residues of GPR120 that interact with G_q are indicated by a purple circle. Residues of GPR120 that interact with G_s are indicated by a pink circle. Residues of GPR120 showing no interaction with G_i, G_q, or G_s are indicated by an empty circle. Note that residues of R71, Q144, and V255 in TUG891-GPR120-G_q simulated structure–formed interactions were verified by mutagenesis data and marked as blue circles. (**E** to **H**) Comparison of the TUG891-GPR120-G_{iq} and 9-HSA-GPR120-G_i complex structures revealed different interactions. (**I**) Heatmap representation of the effect of mutations in the GPR120 interface on G_i or G_q coupling in response to 9-HSA stimulation by $G\alpha_i$-Gγ dissociation assay (left column) or TUG891 stimulation by $G\alpha_q$-Gγ dissociation assay (right column). The effects of mutations on EC_{50} changes in response to 9-HSA or TUG891 for

corresponding pathways are indicated by the red color scale. The heatmap was generated according to the data shown in fig. S27, B and C (refer to table S17 for details). (**J**) Heatmap representation of the effect of mutations in the GPR120 interface on G_i or G_s coupling in response to 9-HSA stimulation by $G\alpha_i$-$G\gamma$ dissociation assay (left column) or EPA stimulation by $G\alpha_s$-$G\gamma$ dissociation assay (right column). The effects of mutations on EC_{50} changes in response to 9-HSA or EPA for corresponding pathways are indicated by the blue color scale. The heatmap was generated according to the data shown in fig. S27, B and D (refer to table S17 for details). (**K**) Structural representation showing no interactions between $E135^{3.49}$ or $Y227^{5.58}$ and $C351^{G.H5.23}$ in the 9-HSA-GPR120-G_i complex. (**L**) Structural representation of the interaction of $E135^{3.49}$ and $Y227^{5.58}$ with $Y391^{G.H5.23}$ in GPR120-G_s according to MD simulation. The blue dotted line represents a hydrogen bond. (**M**) Structural representation showing no interactions between $Q144^{ICL2}$ and $I344^{G.H5.16}$ in the 9-HSA-GPR120-G_i complex. (**N**) Structural representation of the interaction of $Q144^{ICL2}$ with $Q384^{G.H5.16}$ in GPR120-G_s according to MD simulation. The blue dotted line represents a potential hydrogen bond.

arginine residues located in ICL1, which is close to an acidic patch of $D350^{G.H5.22}$ and carboxylic end of $F354^{G.H5.26}$ of α5 helix of $G\alpha_i$ (Fig. 6B and figs. S25A and S26A). Although ICL3 of most class A GPCRs is disordered, ICL3 of GPR120 has a well-defined EM density and forms extensive interactions with the G_i protein (Fig. 6D and fig. S24C). Whereas the N-terminal residues of ICL3 formed polar, charge, or hydrophobic interactions mainly with the α5 helix of $G_{\alpha i}$, several positively charged or hydrophobic residues of the C terminus of ICL3 and initial helix of TM5 of GPR120 folded inside the 7TM bundles and formed contacts with β-strand 6 and α4-α5 helix of $G_{\alpha i}$ (Fig. 6C and figs. S24D and S25, B and G). These observations were further supported by mutational analysis of G_i coupling activity of GPR120 in response to 9-HSA stimulation (Fig. 6I; fig. S27, A and B; and table S16).

Coupling between GPR120 and G_q

Inspection of the G protein interface of the TUG891-GPR120-G_{iq} complex revealed that 21 residues of GPR120 contacted with 15 residues of $G\alpha_{iq}$ (Fig. 6D). Among these $G\alpha_{iq}$ residues, 12 are identical in native $G\alpha_q$ and three are different (fig. S26B). We therefore substituted these three nonidentical $G\alpha_{iq}$ interface residues with native $G\alpha_q$ residues and performed computational simulation (Fig. 6D and fig. S24, E and F). The simulation results revealed that three additional GPR120 residues may contact $G\alpha_q$, in addition to the other 21 residues identified in the GPR120-G_{iq} interface (Fig. 6D). Further extensive mutagenesis analysis indicated at least 14 residues of GPR120 on the GPR120-G_q interface affected $G\alpha_q$ coupling in response to TUG891 stimulation (Fig. 6I; fig. S27, A and C; and table S16). Comparison of the TUG891-GPR120-G_{iq}, simulated TUG891-GPR120-G_q, and 9-HSA-GPR120-G_i complex structures revealed both shared and different interactions (Fig. 6, D to H, and figs. S24, E to J, and S25, H to J). Notably, 19 out of 24 residues that mediated both G_i and G_q coupling formed conserved interactions with αN and α5 of both $G\alpha_i$ and $G\alpha_q$, thus perhaps accounting for the ability of GPR120 to induce both types of G protein signaling (Fig. 6, D and I; fig. S27, A to C; and tables S15 and S18). Differences between the GPR120-G_q interface and the GPR120-G_i interface were also observed (Fig. 6, E to H, and fig. S24, G to J). For example, the replacement of $D337^{G.H5.09}$ and $T340^{G.H5.12}$ of $G\alpha_i$ by $A342^{G.H5.09}$ and $K345^{G.H5.12}$ of $G\alpha_{iq}$ introduced charge-charge repulsion and destroyed previous charge-charge and polar interactions formed between $R240^{ICL3}$ of GPR120 with $D337^{G.H5.09}$ and $T340^{G.H5.12}$ of $G\alpha_i$ in the 9-HSA-GPR120-G_i complex (Fig. 6, E and F); the replacement of $K345^{G.H5.17}$ of $G\alpha_i$ by $Q350^{G.H5.17}$ of $G\alpha_{iq}$ eliminated its charge interaction with $D259^{6.30}$ but enabled the formation of a new hydrogen bond with $R238^{ICL3}$ (Fig. 6, G and H, and fig. S25, C and D). Conversely, the replacement of $G352^{G.H5.24}$ and $C351^{G.H5.23}$ of $G\alpha_i$ by $N357^{G.H5.24}$ and $Y356^{G.H5.23}$ of $G\alpha_{iq}$ allowed new H-bond formation and hydrophobic packings in the TUG891-GPR120-G_{iq} complex structure, respectively (figs. S24, I and J, and S25, I and J). Consistent with these observations, the mutation of $R240^{5.71}$A, $S248^{ICL3}$A, or $D259^{6.30}$A of GPR120 greatly impaired G_i but not G_q coupling in response to TUG891 stimulation (Fig. 6I; fig. S27, A to C; and table S16). In contrast, specific mutations of charged or hydrophobic residues of TM3 or TM5 of GPR120 impaired $G\alpha_q$ coupling more than $G\alpha_i$ coupling (Fig. 6I and fig. S27, A to C).

Interfaces between GPR120 and G_s characterized by MD simulation and mutagenesis

Among the 23 residues of GPR120 in contact with G_s in our simulated EPA-GPR120-$G\alpha_s$ complex structure, 15 residues also contacted $G\alpha_i$, suggesting that common interfaces of GPR120 are shared by these two different G protein subtypes (Fig. 6D and fig. S28). Computational simulation and mutagenesis analysis also suggested different features of the GPR120-G_s interface compared with those of the GPR120-G_i interface (Fig. 6, D and J to N; figs. S25E and S27, A, B, and D, and S28; and table S16). For instance, the replacement of the α5 helical end residue C351 of $G\alpha_i$ by Y391 of $G\alpha_s$ allowed the formation of a potential H-bond with $E135^{3.49}$ and potential π:π interactions with $Y227^{5.58}$ in the simulated EPA-GPR120-$G\alpha_s$ structure (Fig. 6, K and L, and fig. S25). The replacement of I344 in the α5 helix of $G\alpha_i$ by Q384 from $G\alpha_s$ enabled the formation of a potential H-bond with $Q144^{ICL2}$ (Fig. 6, M and N, and fig. S25E). Consistent with these predictions, the mutations $E135^{3.49}$A, $Q144^{ICL2}$A, and $Y227^{5.58}$A of GPR120 showed larger decreases in G_s activation than of G_i activation in response to EPA stimulation (Fig. 6J; fig. S27, A, B, and D; and table S16). Although the computational simulations and biochemical results allowed us to propose a preliminary model, the details of the interactions between GPR120 and G_q or between GPR120 and G_s require further structural characterization.

Potential propagation paths underlie differential G protein subtype coupling

In the TUG891-GPR120-G_q complex structure, the multiple π:π interactions of three phenyl rings of TUG891 with the aromatic array of five phenylalanines in the ligand pocket of GPR120 enabled combined conformational rearrangements of these residues compared with those in the 9-HSA-GPR120-G_i complex structure (fig. S29A). In particular, the rotations of $F88^{2.53}$ and $F311^{7.43}$ connected to the conformational changes of $L86^{2.51}$ and $I89^{2.54}$, disrupting the H-bond formed between $N313^{7.45}$ and $N317^{7.49}$ and enabling constitution of the underlying polar network by residues $N58^{1.50}$, $D85^{2.50}$, and $N317^{7.49}$ (Fig. 7, A and B). These conformational changes were linked to structural rearrangements of hydrophobic packings starting from $F82^{2.47}$ and ending with $R68^{ICL1}$ and $V65^{1.57}$, allowing outward tilting of TM7 and inward tilting of TM1 to enable a tighter insertion of the α5 helix of $G\alpha_q$ (Fig. 7C and fig. S29B). These structural changes propagated to a stronger hydrophobic packing between $Y227^{5.58}$, $Y321^{7.53}$, and $R136^{3.50}$, enabling the formation of cation-π interactions between $R136^{3.50}$ of GPR120 and Y356 of $G\alpha_q$ (Fig. 7, A and C). Consistent with these predictions, the G_q-biased property of TUG891 was reduced by mutations of propagating path connected to $F88^{2.53}$ and $F311^{7.43}$ in the ligand-binding pocket of GPR120 and the cytoplasmic side $Y227^{5.58}$ and $Y321^{7.53}$ (Fig. 7D; figs. S22, B and C, and S29, C to E; and tables S13 and S19).

Comparison of the 9-HSA-GPR120-G_i structure with our simulated EPA-GPR120-G_s model identified potential conformational locks connecting specific π:π interactions inside the ligand pocket to the cytoplasmic G protein–coupling interface of GPR120, contributing to G protein subtype selectivity (Fig. 7E). The engagement with the ω-3 double bond enabled flipping of the aromatic ring of $F211^{5.42}$, accompanied by upward movements of the side chains of $N215^{5.46}$ and $S123^{3.37}$ in the MD

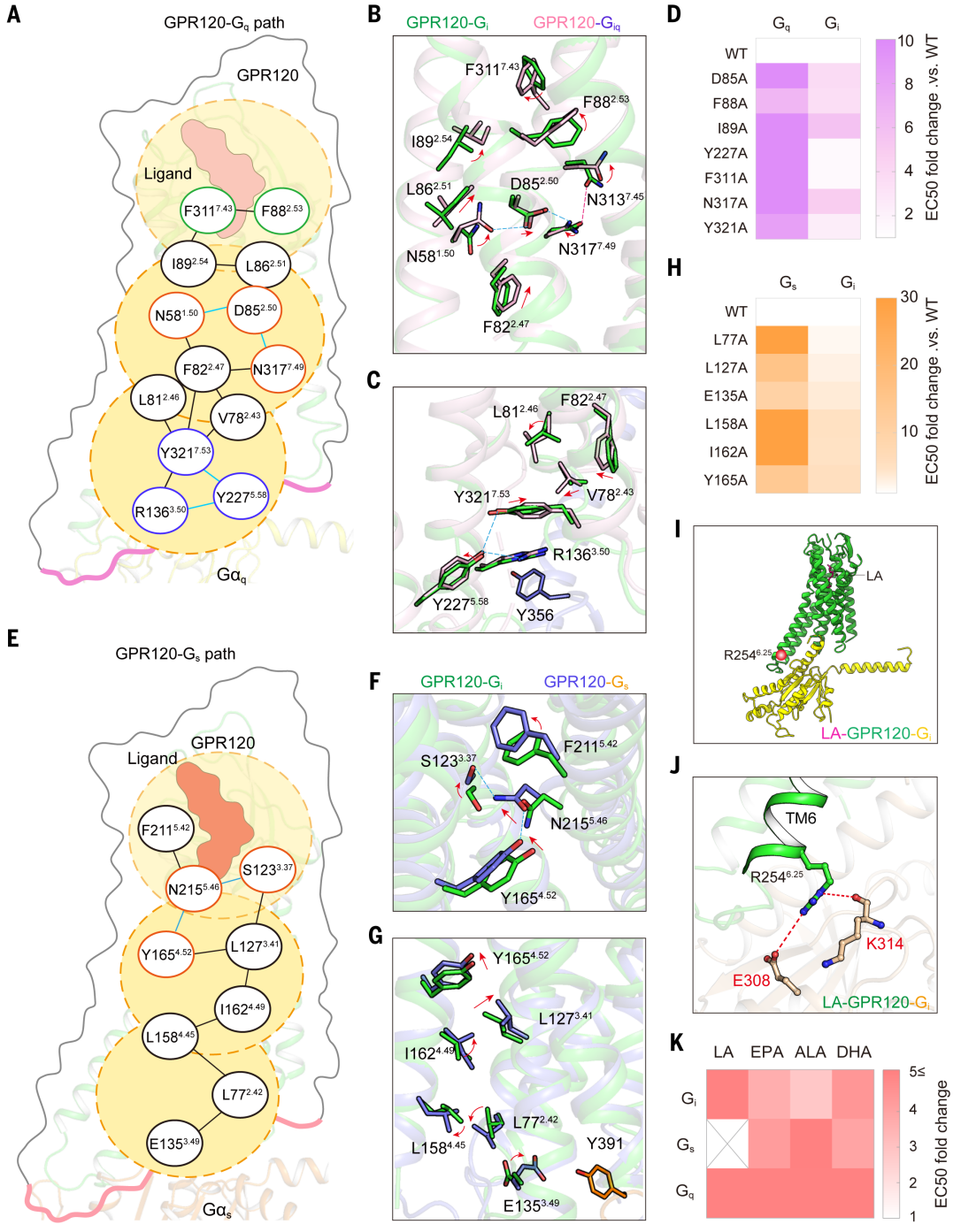

Fig. 7. The propagating paths of GPR120-G_s/G_q and SNP in GPR120. (**A**) Schematic diagram representing the propagating paths that contribute to the G_q versus G_i bias decision mechanism by comparing the structures of the 9-HSA-GPR120-G_i and TUG891-GPR120-G_q complexes. The propagating paths start with the engagement with the ligand-binding pockets and extend to the G_q protein interface region. The green cartoon represents GPR120. The yellow cartoon represents $G\alpha_q$. The bold purple curve represents the interface region between GPR120 and G_q. (**B** and **C**) The structural rearrangements of key residues along the propagating paths connected the ligand-binding pocket (B) to cytoplasmic side (C) by comparison of the 9-HSA-GPR120-G_i complex and TUG891-GPR120-G_{iq} complex structures. Hydrogen bonds or polar interactions are depicted as blue dashed lines. The hydrogen bond formed between N317 and N313 in 9-HSA-GPR120-G_i structure is highlighted as a red dashed line. (**D**) Heatmap representation of the effect of mutations in the propagating paths of GPR120-G_q or GPR120-G_i in response to TUG891 stimulation by $G\alpha_q$-Gγ and $G\alpha_i$-Gγ dissociation assay. The changes of EC_{50} in corresponding pathways are indicated by the purple color scale. The heatmap was generated according to the data shown in figs. S22, B and C, and S29, D and E (refer to table S20 for details). (**E**) Schematic diagram representing the propagating paths that contribute to the G_s versus G_i bias decision mechanism by comparing the structures of the 9-HSA-GPR120-G_i complex and simulated EPA-GPR120-G_s complex. The propagating paths start with the engagement with the ligand-binding pockets and extend to the G_s protein interface region. The green cartoon represents GPR120. The orange cartoon represents $G\alpha_s$. The bold pink curve represents the interface region between GPR120 and G_s. (**F** and **G**) The structural rearrangements of key residues along the propagating paths connected the ligand-binding pocket (F) to cytoplasmic side (G) by comparison of 9-HSA-GPR120-G_i complex and simulated EPA-GPR120-G_s complex structures. Hydrogen bonds are depicted as blue dashed lines. (**H**) Heatmap representation of the effect of mutations in the propagating paths of GPR120-G_s or GPR120-G_i in response to EPA stimulation by $G\alpha_s$-Gγ and $G\alpha_i$-Gγ dissociation assay. The changes of EC_{50} in corresponding pathways are indicated by the orange color scale. The heatmap was generated according to the data shown in figs. S22, E and F, and S29, F and G (refer to table S22 for details). (**I**) Structural representation of the position of the GPR120 SNP $R254^{6.25}$ (R270H in the long isoform of GPR120) in the LA-GPR120-G_i complex structure model, which is located in the TM6 of the receptor and participated in the GPR120-G_i trimer interface. The red ball marks the $R254^{6.25}$ site. (**J**) Detailed interaction of $R254^{6.25}$ of GPR120 with G_i, forming contacts with the side chains of E308 and main chain carbonyl group of K314 via charge-charge or polar interactions, respectively. The charge-charge and polar interactions were depicted as red dashed lines. (**K**) Heatmap representation of R254H mutation effects on ligands (LA, EPA, ALA, and DHA) induced GPR120 activities by $G\alpha_i$-Gγ, $G\alpha_s$-Gγ, or $G\alpha_q$-Gγ dissociation assays. Notably, R254H mutation significantly reduced the G_i, G_q, and G_s coupling of GPR120 in response to stimulations of these FAs. The cross indicates that no G_s activity could be detected for GPR120 in response to stimulation with LA. The heatmap is generated according to the data shown in fig. S30, G to Q (refer to table S24 for details).

model of EPA-GPR120-G_s (Fig. 7, E and F). These conformational changes were then propagated through a pathway connected by Y165$^{4.52}$-L127$^{3.41}$-I162$^{4.49}$-L158$^{4.45}$-L77$^{2.42}$ and finally led to structural rearrangement of the ionic lock residue of E135$^{3.49}$, which enabled hydrogen bonding with Y391 of G_s (Fig. 7, E to G). Consistent with this proposed model, the biased property of G_s is acutely sensitive to mutagenesis of the propagation path connected to F211$^{5.42}$ in the ligand-binding pocket of GPR120 and the cytoplasmic side of E135$^{3.49}$ (Fig. 7H; fig. S29, C, F, and G; and table S21).

Taken together, our studies suggested that the propagation path connecting the double-bond recognition of GPR120 inside the ligand pocket to specific structural features of the cytoplasmic side responsible for G_s and G_i signaling differentiation is mainly dependent on conformational locks located at TM3 and TM4. In contrast, the conformational locks at TM1-TM2 and TM7 linked the specific π:π interactions within the ligand pocket of GPR120 to cytoplasmic structural rearrangement for selective G_q versus G_i coupling.

Disease-associated SNP of GPR120

It has been reported that the naturally occurring single-nucleotide polymorphism (SNP) p.R270H, rs116454156 resulted in a missense mutation of R270 in TM6 of GPR120, which was coupled with increased fasting glucose levels and decreased homeostasis of pancreatic β cells (*13*, *34*). Previous biochemical analyses have shown that p.R270H of GPR120 decreased G_q activity in response to ALA stimulation. The side chain of R254$^{6.25}$ of the GPR120 short isoform (the allele residue of p.R270H in the GPR120-long isoform) (Fig. 7I) directly interacts with the side chains of E308 and the main chain carboxyl group of K314 of $G\alpha_i$ via charge-charge or polar interactions in the LA-GPR120- G_i complex (Fig. 7J and fig. S25K). Similar interactions were observed in all other GPR120-G_i complex structures bound to different ligands (figs. S30, A to D, and S25, L to O). The computational simulation suggested that the replacement of R254$^{6.25}$ with His abolished the charge-charge interactions formed between R254$^{6.25}$ and E308 of $G\alpha_i$ (fig. S30, E and F). The mutation R254H reduced G_i coupling of GPR120 in response to either LA or EPA stimulation (Fig. 7K; fig. S30, G to I; and table S23), in line with recent reports that p.R270H may disturb islet homeostasis (*34*). In our simulated TUG891-GPR120-G_q complex structure, R254 formed an H-bond with the main chain of S314 of $G\alpha_q$ (fig. S31A). Consistently, the G_q activity of GPR120 was decreased by more than threefold by the mutation R254H (Fig. 7K; fig. S30, H and L to N; and table S23). In addition to impaired G_i and G_q signaling, all three tested ω-3 FAs induced G_s-Gγ dissociation responses that were approximately two-fold lower in HEK293 cells overexpressing the GPR120 R254H mutant than in cells overexpressing wild-type GPR120 (Fig. 7K; fig. S30, O to Q; and table S23), which may be involved in adipogenesis in response to stimulation by ω-3 FAs. This effect was consistent with our simulation results, which indicated that R254H may impair the H-bonding between R254 of GPR120 and T350 of $G\alpha_s$ (fig. S31B).

Discussion

FAs with unsaturated double C–C bonds, such as ω-3 unsaturated long FAs, are able to promote beneficial cellular signaling to modulate metabolism via direct action on membrane receptors, including GPR120 (*3*, *5*–*7*). In this study, we identified an array of aromatic residues that were able to individually recognize specific double C–C bonds present in unsaturated FAs. Further structural analysis, biochemical characterization, and MD simulation suggested that these aromatic residues mainly recognize double bonds through π:π interactions and maintain a relatively stable binding mode with defined angles and distances, thus providing a structural framework for how membrane receptors can sense unsaturated FAs decorated with double bonds at different positions. The recognition of double bonds of unsaturated FAs by individual aromatic residues of GPR120 was connected to selective downstream G protein activation or β-arrestin recruitment and modulated the bias properties of GPR120. We characterized the potential propagating paths connecting the π:π interactions located in the ligand pocket to selective cytoplasmic structural features to differentiate downstream G protein subtype coupling. Whereas the conformational locks in TM3 and TM4 played important roles in transducing the specific double-bond recognition of GPR120 to cytoplasmic G_s coupling, the conformational locks in TM1-TM2 and TM7 contributed substantially to linking the ligand pocket to downstream G_q versus G_i discrimination. We recently found that an endogenous FA-GPR120 circuit with biased signaling properties was present in pancreatic islets and that a β-arrestin2–biased GPR120 endogenous agonist was able to improve islet functions and glucose metabolism in diabetic db/db mice (*16*). Now we see that unsaturated endogenous FAs and natural products show bias compared with saturated FA 9-HSA. Our pharmacological profiling indicated that only fatty acids harboring the ω-3 double bond were able to exhibit G_s activities. This might be one of the key features of these ω-3 unsaturated FAs that contribute to their beneficial effects on metabolism, as suggested by recent studies (*6*). Structural analysis indicated that the specific recognition of the double bonds in FAs by corresponding aromatic residues, such as the recognition of the ω-3 double bond by F211$^{5.42}$, is a determinant for their biased signaling. We speculate that unsaturated FAs may contribute to their beneficial effects by acting on specific aromatic residues of GPR120, which could be exploited for the development of selective GPR120 agonists. A complete structural understanding of the GPR120 bias properties will require the future determination of the complex structures of GPR120 with G_s and β-arrestin1/2 and even with downstream effectors of arrestins, such as TAB1 and NLRP3 (*5*, *7*).

In addition to revealing mechanisms underlying unsaturated FA differentiation and signaling bias, our structure of the TUG891-GPR120-G_i and TUG891-GPR120-G_{iq} complexes afforded a structural basis for the agonist selectivity of GPR120. Most of the TUG891-interacting residues showed great diversity compared with other known FA receptors. Biochemical analysis indicated at least five residues governing the agonist selectivity of GPR120. In particular, the linker oxygen O10 separated TUG891 into two segments fitting into two binding pockets. These observations indicate that separate optimization of the two fragments individually could be exploited for future synthetic agonist design for GPR120-targeted therapies.

Materials and methods

Cells

Human embryonic kidney (HEK) 293 cells were obtained from the Cell Resource Center of Shanghai Institute for Biological Sciences (Chinese Academy of Sciences). *Spodoptera frugiperda* (Sf9) insect cells were purchased from the Expression Systems (catalog number: 94-001S).

Construct

The cDNA of human GPR120 short isoform (GPR120-S, NP 001182684.1) and human GPR120 long isoform (GPR120-L, NP 859529.2) were synthesized at BGI (Beijing, China). For structural determination, the sequence encoding for human GPR120-S (hereafter referred to as GPR120), residues from 1 to 361, was cloned into a modified pFastBac1 vector with a hemagglutinin (HA) signal sequence at the N terminus. To facilitate expression and purification, a FLAG tag (DYKDDDDA) and cytochrome b_{562}RIL (BRIL) (*35*) followed by a three amino acid (Gly-Ser-Ala) linker was inserted into the N terminus of GPR120. The fusion of BRIL into the N terminus of GPR120 does not substantially affect the ability of ligand-induced activation of GPR120 downstream signaling (fig. S32). The human $G\alpha_{i1}$ used in GPR120-G_i complexes was described in previous studies (*36*). For the GPR120-G_q complex, an engineered $G\alpha_{iq}$ construct was generated on the basis of $G\alpha_{i1}$, in which the 26 residues on α5 helix of $G\alpha_{i1}$ (residues 329 to 354) were replaced by that of $G\alpha_q$ (residues 334 to 359). Human Gβ1 and Gγ2 were cloned into the pFastBac-Dual

vector. It is well established that the C-terminal region of a Gα subunit is one of the main determinants of coupling specificity (*37*, *38*), and similar strategy (using G_{sq} chimera) has been extensively used by B. Roth's and E. Xu's group in determination of series of structures of GPCR-G_q complexes, including 5HTR2A-Gq, MRGPRX2-Gq, B1R-Gq, and B2R-Gq (*39*–*41*). Moreover, additional computational simulation for the TUG891-GPR120-G_q complex using the TUG891-GPR120-G_{iq} complex as a template was performed and further validated by extensive mutagenesis analysis. For cell-based functional assays in HEK293 cells, human GPR120-L or GPR120-S was cloned into pcDNA3.1, with an N-terminal HA signal peptide followed by a FLAG tag, resulting in pcDNA3.1-GPR120-L and pcDNA3.1-GPR120-S, respectively. For β-arrestin recruitment assay, a yellow fluorescent protein (YFP) tag was added to the C terminus of the corresponding GPR120 constructs. The GPR120 mutants were generated using the QuikChange mutagenesis kit (Stratagene). All constructs were verified by DNA sequencing.

Protein expression

The *S. frugiperda* (Sf9) insect cells were infected at a density of 2.5×10^6 cells per milliliter; four separate baculoviruses (GPR120, $G\alpha_{i1}$ or $G\alpha_{iq}$, Gβ1γ2, and scFv16) were co-added at a ratio of 1:1:1:1 into the insect cells (*36*). After culturing for 48 hours at 27°C, the cells were harvested by centrifugation, and cell pellets were stored at −80°C.

GPR120-G_i and GPR120-$G\alpha_{iq}$ complex formation and purification

For purification of the GPR120-G_i or GPR120-$G\alpha_{iq}$ complexes, cell pellets were resuspended in buffer containing 20 mM HEPES pH 7.5, 100 mM NaCl, 10 mM $CaCl_2$, and 5 mM $MgCl_2$, supplemented with complete Protease Inhibitor Cocktail tablets (Roche). Complex formation was initiated by adding 10 μM of TUG891 and apyrase (25 mU/ml, NEB) for both GPR120-G_i and GPR120-$G\alpha_{iq}$ complexes, or by adding 10 μM 9-HSA or 50 μM LA or 50 μM OA or 50 μM EPA and apyrase (25 mU/ml, NEB) for GPR120-G_i complexes. The suspension was incubated for 1 hour at room temperature and then solubilized by 0.5% (w/v) lauryl maltose neopentyl glycol (LMNG, Anatrace) supplemented with 0.05% (w/v) cholesteryl hemisuccinate (CHS) (Anatrace) for 2 hours at 4°C. Insoluble material was removed by centrifugation at 65,000*g* for 45 min, and the solubilized GPR120-G_i or GPR120-$G\alpha_{iq}$ complex was incubated with M1 anti-Flag affinity resin for 3 hours at 4°C. The resin was collected and washed with 20 column volumes of 20 mM HEPES pH 7.4, 100 mM NaCl, 2 mM $MgCl_2$, 5 mM $CaCl_2$, 10 μM TUG891 or 10 μM 9-HSA or 50 μM LA or 50 μM OA or 50 μM EPA, 0.01% (w/v) LMNG and 0.001% (w/v) CHS. The GPR120-G_i or GPR120-$G\alpha_{iq}$ complex was then eluted with buffer containing 20 mM HEPES pH 7.4, 100 mM NaCl, 2 mM $MgCl_2$, and 10 μM TUG891 or 10 μM 9-HSA or 50 μM LA or 50 μM OA or 50 μM EPA, 0.01% (w/v) LMNG, 0.001% (w/v) CHS, 5 mM EGTA and 0.2 mg/ml Flag peptide. Finally, the complex was concentrated and loaded onto a size exclusion chromatography on a Superose 6 Increase 10/300GL column (GE Healthcare) equilibrated with the buffer containing 20 mM HEPES, pH 7.5, 50 mM NaCl, 3 mM $MgCl_2$, 0.0005% LMNG, 0.00001% CHS, and 10 μM TUG891 or 10 μM 9-HSA or 50 μM LA or 50 μM OA or 50 μM EPA. The peak fractions of GPR120-G_i or GPR120-$G\alpha_{iq}$ complexes were collected and concentrated to 8 mg/ml using a 100 kDa cut-off Amicon Ultra Centrifugal Filter (Millipore) for making the cryo grid.

Cryo-EM grid preparation and data collection

The purified GPR120-G_i or GPR120-$G\alpha_{iq}$ complex samples (concentrated to ~8 mg/ml) were applied onto holey carbon grids (Quantifoil, R1.2/1.3, 300 mesh), which were glow-discharged at 25 mA for 1 min using PELCO easiGlow. Excess samples were blotted for 3.5 s with a blot force of 8 with Ted Pella filter papers (catalog number: 47000-100). Afterward, the grids were vitrified by plunging into liquid ethane using a Vitrobot Mark IV (Thermo Fischer Scientific). Cryo-EM movies of all the six samples was performed on a Titan Krios at 300 kV in the Center of Cryo-Electron Microscopy, Zhejiang University (Hangzhou, China). Micrographs were recorded using a Gatan K2 Summit detector in counting mode with a pixel size of 1.014 Å using the SerialEM software (*42*). Movies were obtained at an exposure dose rate of ~8.0 e^- Å^{-2} s^{-1} with a defocus ranging from −0.5 to −2.5 μm. A total of 2600, 1992, 6075, 5441, and 4844 movies were collected for the TUG891-, 9-HSA–, LA-, EPA-, and OA-bound GPR120-G_i complexes, respectively.

For TUG891-bound GPR120-$G\alpha_{iq}$ complex, cryo-EM data collection was performed on a Titan Krios at 300 kV accelerating voltage at the Core Facilities, Zhejiang University Medical Center/Liangzhu laboratory. Micrographs were recorded using a Falcon 4 direct electron detector at a pixel size of 0.93 Å with EPU software. Image stacks were obtained at an exposure dose rate of about 8.7 e^- Å^{-2} s^{-1} with a defocus ranging from −1.0 to −2.0 μm. The total exposure time was 6 s, resulting in a total exposure of 52 electrons per Å^2. A total of 7093 movies were collected for TUG891-bound GPR120-$G\alpha_{iq}$ complex.

Cryo-EM data processing

Cryo-EM image stacks were aligned using MotionCor2.1 (*43*). Contrast transfer function (CTF) parameters were estimated by Gctf-v1.18 (*44*). The following data processing was performed using Relion-3.0.8 (*45*), Relion-4.0-beta (*45*, *46*), and CryoSPARC4.0.3 (*47*). For the TUG891-, 9-HSA–, LA-, and OA-bound GPR120-G_i complexes, automated particle picking using Gaussian blob detection yielded particles that were subjected to reference-free 2D classifications (classes = 100; Regularisation parameter, T = 2; mask diameter = 160 Å) or 3D classifications (classes = 4 or 6; T = 4; mask diameter = 160 Å) to discard bad particles for further processing. The map of neurotensin receptor 1–G_{i1} complex (EMD-20180) or the density map of TUG891-bound complex low-pass filtered to 40 Å were used as the reference maps for 3D classifications. Further focused 3D classifications (classes = 3 to 6; T = 4; mask diameter = 160 Å) produced well-defined subsets that were subsequently subjected to 3D refinement (initial low-pass filter = 20 Å; mask diameter = 160 Å), CTF refinement, and Bayesian polishing. The final refinement generated maps with indicated global resolutions of 3.0 Å (TUG891-bound complex), 3.1 Å (9-HSA–bound complex), 3.1 Å (LA-bound complex), and 2.8 Å (OA-bound complex) at a Fourier shell correlation of 0.143. Local resolution was determined using the Bsoft package with half maps as input maps. For OA-bound GPR120-Gi complex, the final particles were subjected to another round of local refinement with a soft mask on the 7TM region of GPR120 to further improve the map quality of receptor region.

For EPA-bound GPR120-G_i complex and TUG891-bound GPR120-G_{iq} complex, the picked particle projections were imported to CryoSPARC for 2D classification (classes = 100; batchsize = 200) to discard poorly defined particles. The selected particle projections were further subjected to ab initio reconstruction and heterogeneous refinement (classes = 3 or 4; batchsize = 2000) in CryoSPARC. The well-defined subsets were re-extracted for further processing in Relion, which were subsequently subjected to 3D refinement (initial low-pass filter = 20 Å; mask diameter = 160 Å), CTF refinement, and Bayesian polishing. The following nonuniform refinement of the complexes in CryoSPARC generated a map with an indicated global resolution of 2.81 Å (EPA-bound) and 2.64 Å (TUG891-bound) at a Fourier shell correlation of 0.143. To further improve the map quality of the complex especially for receptor, local 3D reconstruction (batchsize = 200) focusing on the receptor and G protein complex were performed in CryoSPARC. The locally refinement maps for the receptor and G protein complex were combined on the basis of the global refinement map using "vop maximum" command in UCSF Chimera.

Model building and structure refinement

The initial homology model of GPR120 receptor was generated using SWISS-MODEL (*48*).

The initial coordinates of G_{i1} and scFv16 were generated from the Dopamine D3 receptor–G_{i1}-scFv16 complex (PDB ID 7CMV). Agonists coordinates and geometry restraints were generated using phenix.elbow (*49*). Models were docked into the EM density map using UCSF Chimera (*50*) and Chimera X (*51*, *52*). This initial model was then subjected to iterative rounds of manual adjustment and automated refinement in Coot (*53*) and real-space refinement in Phenix (*49*), using minimization_global, local_grid_search, and ADP refinement with secondary structure and Ramachandran restraints. The final refinement statistics were validated using the module "comprehensive validation (cryo-EM)" in Phenix (*49*). The final refinement statistics are provided in table S5. The EM densities for these structures enabled the construction of models of major receptor and G protein regions (see table S25 for details). Helix 8 is not visible in the GPR120 receptor owing to poor EM density. For those residues with ambiguous side-chain densities, corresponding side-chain atoms were removed from the final model of EPA-GPR120-G_i, 9-HSA-GPR120-G_i, LA-GPR120-G_i, OA-GPR120-G_i, and TUG891-GPR120-G_{iq} complexes; all those residues were summarized and listed in table S26. To avoid overstatement of the potential interactions, all those indicated residues were not described or discussed in our manuscript.

Gα-Gγ dissociation assay

The gene of wild-type human GPR120 short splicing isoform (hGPR120-S) or GPR120 long splicing isoform (hGPR120-L) was cloned into pcDNA3.1 vector with N-terminal HA signal sequence and FLAG tag for Gα-Gγ dissociation assays in HEK293 cells. G protein bioluminescence resonance energy transfer (BRET) probes, including Gα-Nluc [$G\alpha_i$- Nluc (insertion of Nluc after Ala87 in $G\alpha_i$), $G\alpha_q$- Nluc (insertion of Nluc after Leu97 in $G\alpha_q$), and $G\alpha_s$- Nluc (insertion of Nluc after Leu113 in $G\alpha_s$)], Gβ1, and Gγ2-GFP10, were generated as previously described (*36*, *54*, *55*). HEK293 cells were transiently cotransfected with GPR120 WT or mutants and G protein BRET probes. Twenty-four hours after transfection, cells were distributed into 96-well microplates at a density of 5×10^4 cells per well and incubated for another 24 hours at 37°C. The cells were washed twice with Tyrode's buffer (140 mM NaCl, 2.7 mM KCl, 1mM $CaCl_2$, 12 mM $NaHCO_3$, 5.6 mM D-glucose, 0.5 mM $MgCl_2$, 0.37 mM NaH_2PO_4, and 25 mM HEPES, pH 7.4) and stimulated with different FAs at different concentrations for 2 min. BRET signal was measured after the addition of the luciferase substrate coelenterazine 400a (5 μM) using a Mithras LB940 microplate reader equipped with BRET filter sets. The BRET signal was calculated as the ratio of light emission at 510 nm/400 nm.

β-arrestin1/β-arrestin2 recruitment assay

The gene of wild-type human GPR120 short splicing isoform (hGPR120-S) or GPR120 long splicing isoform (hGPR120-L) was cloned into pcDNA3.1 vector with N-terminal HA signal sequence and FLAG tag and a C-terminal YFP tag for β-arrestin1 or β-arrestin2 recruitment assays in HEK293 cells. HEK293 cells were transiently cotransfected with β-arrestin1–Rluc or β-arrestin2–Rluc and YFP-tagged receptor (GPR120 WT or mutants) as previously described (*23*, *54*, *56*). Twenty-four hours after transfection, the cells were distributed into 96-well microplates at a density of 5×10^4 cells per well. After another 24 hours of incubation at 37°C, the cells were washed twice with Tyrode's buffer and stimulated with different FAs at different concentrations for 10 min. Luciferase substrate coelenterazine-h (5 μM) was added before light emissions were recorded using a Mithras LB940 microplate reader (Berthold Technologies) with BRET filter sets. The BRET signal was determined by calculating the ratio of luminescence at 530 nm/485 nm.

cAMP accumulation assay

To examine the intracellular cyclic adenosine monophosphate (cAMP) levels of HEK293 cells overexpressing GPR120-S or GPR120-L in response to different ligands, the GloSensor-based cAMP accumulation assay was performed as described previously (*23*, *57*, *58*). The similar cell surface expression levels of GPR120 WT or mutants were accomplished by adjusting the amount of plasmid used for transfection and confirmed by enzyme-linked immunosorbent assay (ELISA) and Western blot. In brief, pcDNA3.1-GPR120-S, pcDNA3.1-GPR120-L, or control vehicle pcDNA3.1 was cotransfected with the GloSensor plasmid into HEK293 cells with PEI, followed by incubation in six-well plates at 37°C for 24 hours, 5% CO_2 atmosphere. Twenty-four hours after transfection of GPR120 WT or corresponding mutants, the cells were seeded into 96-well microplates at a density of 5×10^4 cells per well. After another 24 hours incubation at 37°C, the cells were washed twice with Tyrode's buffer. Fifty microliters of serum-free Dulbecco's minimum essential medium containing fluorogenic substrate was added to each well of the 96-well plate 2 hours before measurement and stimulated with different FAs. The cells were pretreated with 100 ng/ml PTX for 16 hours before stimulation with different FAs. Luminescence signal was measured using an EnVision multimode plate reader (Perkin Elmer).

Inositol triphosphate measurement

The intracellular inositol triphosphate (IP3) levels of HEK293 cells overexpressing GPR120-S or GPR120-L in response to TUG891 or other GPR120 agonists were evaluated using IP3 kit (Cloud-Clone, CEC037Ge) according to the manufacturer's protocol. Briefly, HEK293 cells were transfected with either GPR120-L, GPR120-S, or control vehicle pcDNA3.1 and incubated at 37°C, 5% CO_2 atmosphere. Forty-eight hours after transfection, the cells were washed twice with Tyrode's buffer and stimulated with TUG891 at different concentrations for 20 min. The cells were then lysed by the lysis reagent provided in the ELISA Kit (Cloud-Clone), and the intracellular IP3 levels were measured according to the manufacturer's instructions. Luminescence intensity at 450 nm was measured using an EnVision multimode plate reader (Perkin Elmer).

Data analysis for bias properties

For direct comparison of GPR120 ligands on particular signaling (effector) pairs, the "Operational Model" was used as previously described (*24*, *59*). The coupling efficiency (τ) of selected GPR120 ligand to designated downstream signaling pathways is calculated by fitting the concentration-dependent data into Eq. 1 using GraphPad Prism 8 as previously described (*24*)

$$\frac{E}{E_m} = \frac{\tau[A]}{\tau[A] + ([A] + K_d)} \quad (1)$$

where $[A]$ and E are the concentration and efficacy of the designated ligand, respectively; K_d is the dissociation constant of the ligand determined from a fluorescein isothiocyanate (FITC)–ligand competition binding assay; and E_m is the maximal efficacy response (E_{max}) by a full agonist in this system.

The effective signaling (σ) for ligand (lig) over a selected reference compound (ref) in a particular signaling pathway can be calculated using Eq. 2 as previously described (*24*)

$$\sigma_{lig} = \log\left(\frac{\tau_{lig}}{\tau_{ref}}\right) \quad (2)$$

FITC-ligand competition binding assay

To determine the dissociation constant of individual ligands to GPR120, BRET-based ligand competition binding assay was used as described previously (*23*, *57*). In brief, the plasmid containing GPR120 with a Nluc fused at its N terminus (pcDNA3.1-Nluc-GPR120) was transiently transfected into HEK293 cells with Lipofectamine 2000 (Thermo Fisher). Twenty-four hours after transfection, cells were seeded into a black 96-well plate (3.5×10^4 cells per well) and further incubated for 24 hours. The saturation binding curve of FITC-TUG891 (FITC conjugated labeled at the carboxyl end of the TUG891) to GP120 was determined by treating the transfected cells with FITC-TUG891 ranging from 0 to 20 μM and with or without the presence of 200 μM TUG891 for 40 min at 37°C (fig. S2A). For the competition experiments,

the transfected cells were incubated with 2.5 μM of FITC-TUG891 and various concentrations of target competing ligands in Hanks' balanced salt solution (HBSS) buffer for 40 min at 37°C (fig. S2, B to F). Luciferase substrate coelenterazine-h (5 μM) was added before light emissions were recorded using a Mithras LB940 microplate reader (Berthold Technologies) with BRET filter sets. The BRET signal was determined by calculating the ratio of luminescence at 535 nm/460 nm.

The inhibition constants (K_i) for respective ligands were calculated using Eq. 3 as previously described (*23*)

$$K_i = \frac{IC_{50}}{1 + \frac{[L]}{K_d}} \quad (3)$$

where [*L*] is the FITC-TUG891 concentration (nanomolar), IC_{50} is the median inhibitory concentration, and K_d is the dissociation constant of FITC-TUG891 generated from the saturation binding experiment.

Enzyme-linked immunosorbent assay

To evaluate cell surface expression of the wild-type GPR120 or its mutants, HEK293 cells were transfected the plasmid of GPR120 wild-type or mutants using Lipofectamine 2000 (Thermo Fisher Scientific) as previously described (*23*, *36*). Twenty-four hours after transfection, cells were divided into 24-well plates at a density of 2 ×10^5 cells per well and further incubated for 24 hours at 37°C in 5% CO_2. The cells were washed three times with phosphate-buffered saline then fixed by 4% (w/v) paraformaldehyde for 5 min at room temperature and blocked with 5% (w/v) bovine serum albumin for another 1 hour. Afterwards, the cells were washed and incubated with the mouse monoclonal anti-FLAG M2 primary antibody (Sigma-Aldrich, Cat# F1804, 1:1000) at 4°C for 1 hour and then incubated with secondary goat anti-mouse antibody (Thermo Fisher, Cat# A-21235, 1:5000) for 1 hour at room temperature. After washing, TMB (3,3′,5,5′-tetramethylbenzidine) solution was added for color reaction, which was then stopped by adding an equal volume of 0.25 M HCl. The absorbance at 450 nm was determined using a TECAN luminescence counter (Infinite M200 Pro NanoQuant). Similar cell surface expression levels of corresponding GPR120 or its mutants determined by ELISA assay.

Western blotting analysis

Comparative plasma membrane expression levels of GPR120-S and GPR120-L, or GPR120 mutants were accomplished by adjusting of the amount of plasmids transfected into in HEK293 cells, and confirmed by Western blotting. HEK293 cells were transiently transfected with pcDNA3.1-GPR120-S, pcDNA3.1-GPR120-L, pcDNA3.1-GPR120-S-YFP, pcDNA3.1-GPR120-L-YFP, or control vehicle plasmid pcDNA3.1, respectively. Forty-eight hours after transfection, the transfected HEK293 cells were washed in pre-colded HBSS buffer twice. The cells were then scraped and pelleted by centrifugation at 600*g* at 4°C for 5 min. The cell pellets were disrupted by homogenization and centrifugated at 600*g* at 4°C for 30 min to remove fractions of nuclei and cell apparatus. To collect cell membranes, the supernatant was further centrifugated at 60,000*g* at 4°C for 30 min. The collected cell membranes were homogenized and solubilized with HBSS buffer containing 1% (w/v) DDM and protease inhibitor cocktail (Roche, 11697498001) for 2 hours at 4 °C with end-to-end rotation. After removing the insolubilized precipitate with centrifugation at 60,000*g* for 30 min, the supernatant was subjected to SDS–polyacrylamide gel electrophoresis and Western blot for further analysis. For detection of the GPR120 and ATP1A1, the anti-FLAG (Sigma, F1804) or anti-ATP1A1 (Proteintech, 14418-1-AP) primary antibodies were used at 1:1000 dilution, respectively. The HRP-conjugated goat anti-mouse IgG (Thermo-Fisher, A-21235) or goat anti-rabbit IgG (Sigma Aldrich, A6154) was used as the secondary antibody at a 1:5000 dilution.

Molecular dynamics simulations

To verify the stability of the various ligands in the binding pocket of GPR120, we performed MD simulations of the OA-GPR120-G_i, LA-GPR120-G_i, EPA-GPR120-G_i, 9-HSA-GPR120-G_i, TUG891-GPR120-G_i, and TUG891-GPR120-G_{iq} wild system. The CHARMM36m force field (*60*) was used for OA-GPR120-G_i, LA-GPR120-G_i, EPA-GPR120-G_i, TUG891-GPR120-G_i, 9-HSA-GPR120-G_i, TUG891-GPR120-G_{iq}, lipids, ions, and the TIP3P model water molecules, as described by our previous studies (*36*). All of the MD input files were generated by CHARMM-GUI (*61*) website, in which the force field parameters of ligands were generated by the CHARMM General Force Field (CGenFF) (*62*). The structures of the OA-GPR120-G_i, LA-GPR120-G_i, EPA-GPR120-G_i, 9-HSA-GPR120-G_i, TUG891-GPR120-G_i, and TUG891-GPR120-G_{iq} complexes were embedded into a preequilibrated and periodic structure of 1-palmitoyl-2-oleoyl-sn-glycero-3-phosphatidylcholine membrane. Then, 0.15 M NaCl was added to balance the charge of the OA-GPR120-G_i, LA-GPR120-G_i, EPA-GPR120-G_i, TUG891-GPR120-G_i, 9-HSA-GPR120-G_i, and TUG891-GPR120-G_{iq} complex system using the Monte Carlo Method (*63*). Next, the systems were solvated into periodic hexagonal type TIP3P water box with a size of around 80 Å by 80 Å by 100 Å by replacement methods using the membrane orientation calculated by the Orientations of Proteins in Membranes database. The OA-GPR120-G_i, LA-GPR120-G_i, EPA-GPR120-G_i, 9-HSA-GPR120-G_i, TUG891-GPR120-G_i, and TUG891-GPR120-G_{iq} complex systems were first processed for energy minimization for 10,000 steps using gmx mdrun module in Gromacs2019.6 (*64*) software, of which the first 5000 steps were performed using the steepest descent method, and the remaining 5000 steps using the conjugated gradient method. The OA-GPR120-G_i, LA-GPR120-G_i, EPA-GPR120-G_i, 9-HSA-GPR120-G_i, TUG891-GPR120-G_i, and TUG891-GPR120-G_{iq} complex systems were heated from 0 K to 310 K in the NVT ensemble (number of particles, volume, and temperature are conserved) for more than 1000 ps. Next, production simulations were run at 1 atm in the NPT ensemble (number of particles, pressure, and temperature are conserved) for more than 1000 ps with 10.0 kcal mol^{-1} $Å^{-2}$ harmonic restraints. The NVT ensemble, NPT ensemble, and the 500-ns MD production with a time step of 2 fs were performed using Gromacs2019.6. The particle mesh Ewald method was used to calculate electrostatic interactions with a cut-off of 12 Å. The bonds involving hydrogen were kept fixed using the SHAKE algorithm during each integration time step of 2 fs. All analyses were completed in Gromacs2019.6 and VMD (*65*).

To investigate the effect of π:π interactions between double bonds and aromatic residues on ligand recognition by GPR120, we constructed eight systems in which the double bond vi in LA-GPR120 was mutated to a single bond vi, the double bond ix in OA-GPR120 was mutated to a single bond ix, the double bond iii or double bond xii or double bond xv in EPA-GPR120 was mutated into single bond iii or single bond ix or single bond xv. We also constructed additional sixteen systems in which the F28 or F88 or F177 or W277 in LA-GPR120 was mutated to L28 or L88 or L177 or L277, the F28 or F115 or F303 in OA-GPR120 was mutated to L28 or L115 or L303, the F27 or F28 or F115 or F177 or W198 or W207 or F211 W277 or F303 in EPA-GPR120 was mutated to L27 or L28 or L115 or L177 or L198 or L207 or L211 or W277 or L303.

To further investigate the receptor–G protein interactions according to our experimental TUG891-GPR120-G_{iq} complex, we performed MD simulations for TUG891-GPR120-G_q complex using our experimental model as the initial template. In our MD simulations, we mutated the residues on the loop connecting helix 4 (H4) and β-sheet 6 (S6) of $G\alpha_{i1}$, including $K312^{G.h4s6.03}$, $R313^{G.h4s6.04}$, $K314^{G.h4s6.08}$, $D315^{G.h4s6.09}$, $T316^{G.h4s6.10}$, to Pro, Asp, Ser, Asp of the corresponding $G\alpha_q$ sequence. We also mutated $E308^{G.h4.16}$ and $E318^{G.h4s6.12}$ of $G\alpha_{i1}$ to their corresponding G_q residues Val and Ile, respectively. The interactions observed by experiments and MD simulations were further validated by extensive mutagenesis analysis. For analysis of the coupling of G_s to GPR120, the receptor region of EPA-GPR120-G_i complex and G_s region of the ADGRG2-β-G_s complex (PDB ID 7WUI) were extracted and merged to construct

the EPA-GPR120-G_s complex. The same MD simulation method was used for the 9-HSA-GPR120-G_i, OA-GPR120-G_i, LA-GPR120-G_i, EPA-GPR120-G_i, TUG891-GPR120-G_i, and TUG891-GPR120-G_{iq} complexes.

REFERENCES AND NOTES

1. T. Ulven, E. Christiansen, Dietary fatty acids and their potential for controlling metabolic diseases through activation of FFA4/GPR120. *Annu. Rev. Nutr.* **35**, 239–263 (2015). doi: 10.1146/annurev-nutr-071714-034410; pmid: 26185978
2. G. Milligan, E. Alvarez-Curto, B. D. Hudson, R. Prihandoko, A. B. Tobin, FFA4/GPR120: Pharmacology and therapeutic opportunities. *Trends Pharmacol. Sci.* **38**, 809–821 (2017). doi: 10.1016/j.tips.2017.06.006; pmid: 28734639
3. J. X. Kang, J. Wang, L. Wu, Z. B. Kang, *Fat-1* mice convert *n*-6 to *n*-3 fatty acids. *Nature* **427**, 504 (2004). doi: 10.1038/427504a; pmid: 14765186
4. C. A. Hudert *et al*., Transgenic mice rich in endogenous omega-3 fatty acids are protected from colitis. *Proc. Natl. Acad. Sci. U.S.A.* **103**, 11276–11281 (2006). doi: 10.1073/pnas.0601280103; pmid: 16847262
5. Y. Yan *et al*., Omega-3 fatty acids prevent inflammation and metabolic disorder through inhibition of NLRP3 inflammasome activation. *Immunity* **38**, 1154–1163 (2013). doi: 10.1016/j.immuni.2013.05.015; pmid: 23809162
6. K. I. Hilgendorf *et al*., Omega-3 fatty acids activate ciliary FFAR4 to control adipogenesis. *Cell* **179**, 1289–1305.e21 (2019). doi: 10.1016/j.cell.2019.11.005; pmid: 31761534
7. D. Y. Oh *et al*., GPR120 is an omega-3 fatty acid receptor mediating potent anti-inflammatory and insulin-sensitizing effects. *Cell* **142**, 687–698 (2010). doi: 10.1016/j.cell.2010.07.041; pmid: 20813258
8. H. D. Liu *et al*., FFA4 receptor (GPR120): A hot target for the development of anti-diabetic therapies. *Eur. J. Pharmacol.* **763**, 160–168 (2015). doi: 10.1016/j.ejphar.2015.06.028; pmid: 26123847
9. V. A. Paschoal *et al*., Positive reinforcing mechanisms between GPR120 and PPARγ modulate insulin sensitivity. *Cell Metab.* **31**, 1173–1188.e5 (2020). doi: 10.1016/j.cmet.2020.04.020; pmid: 32413335
10. J. M. Houthuijzen *et al*., Fatty acid 16:4(n-3) stimulates a GPR120-induced signaling cascade in splenic macrophages to promote chemotherapy resistance. *FASEB J.* **31**, 2195–2209 (2017). doi: 10.1096/fj.201601248R; pmid: 28183801
11. M. M. Yore *et al*., Discovery of a class of endogenous mammalian lipids with anti-diabetic and anti-inflammatory effects. *Cell* **159**, 318–332 (2014). doi: 10.1016/j.cell.2014.09.035; pmid: 25303528
12. A. Hirasawa *et al*., Free fatty acids regulate gut incretin glucagon-like peptide-1 secretion through GPR120. *Nat. Med.* **11**, 90–94 (2005). doi: 10.1038/nm1168; pmid: 15619630
13. A. Ichimura *et al*., Dysfunction of lipid sensor GPR120 leads to obesity in both mouse and human. *Nature* **483**, 350–354 (2012). doi: 10.1038/nature10798; pmid: 22343897
14. D. Y. Oh *et al*., A Gpr120-selective agonist improves insulin resistance and chronic inflammation in obese mice. *Nat. Med.* **20**, 942–947 (2014). doi: 10.1038/nm.3614; pmid: 24997608
15. J. Ghislain, V. Poitout, Targeting lipid GPCRs to treat type 2 diabetes mellitus — progress and challenges. *Nat. Rev. Endocrinol.* **17**, 162–175 (2021). doi: 10.1038/s41574-020-00459-w; pmid: 33495605
16. Y. Q. Du *et al*., Endogenous lipid-GPR120 signaling modulates pancreatic islet homeostasis to different extents. *Diabetes* **71**, 1454–1471 (2022). doi: 10.2337/db21-0794; pmid: 35472681
17. G. Milligan, E. Alvarez-Curto, K. R. Watterson, T. Ulven, B. D. Hudson, Characterizing pharmacological ligands to study the long-chain fatty acid receptors GPR40/FFA1 and GPR120/FFA4. *Br. J. Pharmacol.* **172**, 3254–3265 (2015). doi: 10.1111/bph.12879; pmid: 25131623
18. B. D. Hudson *et al*., The pharmacology of TUG-891, a potent and selective agonist of the free fatty acid receptor 4 (FFA4/GPR120), demonstrates both potential opportunity and possible challenges to therapeutic agonism. *Mol. Pharmacol.* **84**, 710–725 (2013). doi: 10.1124/mol.113.087783; pmid: 23979972
19. V. M. Stone *et al*., GPR120 (FFAR4) is preferentially expressed in pancreatic delta cells and regulates somatostatin secretion from murine islets of Langerhans. *Diabetologia* **57**, 1182–1191 (2014). doi: 10.1007/s00125-014-3213-0; pmid: 24663807
20. M. S. Engelstoft *et al*., Seven transmembrane G protein-coupled receptor repertoire of gastric ghrelin cells. *Mol. Metab.* **2**, 376–392 (2013). doi: 10.1016/j.molmet.2013.08.006; pmid: 24327954
21. B. Shimpukade, B. D. Hudson, C. K. Hovgaard, G. Milligan, T. Ulven, Discovery of a potent and selective GPR120 agonist. *J. Med. Chem.* **55**, 4511–4515 (2012). doi: 10.1021/jm300215x; pmid: 22519963
22. A. Li *et al*., Discovery of novel FFA4 (GPR120) receptor agonists with β-arrestin2-biased characteristics. *Future Med. Chem.* **7**, 2429–2437 (2015). doi: 10.4155/fmc.15.160; pmid: 26653412
23. F. Yang *et al*., Structural basis of GPBAR activation and bile acid recognition. *Nature* **587**, 499–504 (2020). doi: 10.1038/s41586-020-2569-1; pmid: 32698187
24. S. Rajagopal *et al*., Quantifying ligand bias at seven-transmembrane receptors. *Mol. Pharmacol.* **80**, 367–377 (2011). doi: 10.1124/mol.111.072801; pmid: 21610196
25. J. Lu *et al*., Structural basis for the cooperative allosteric activation of the free fatty acid receptor GPR40. *Nat. Struct. Mol. Biol.* **24**, 570–577 (2017). doi: 10.1038/nsmb.3417; pmid: 28581512
26. R. Taniguchi *et al*., Structural insights into ligand recognition by the lysophosphatidic acid receptor LPA_6. *Nature* **548**, 356–360 (2017). doi: 10.1038/nature23448; pmid: 28792932
27. M. A. Hanson *et al*., Crystal structure of a lipid G protein–coupled receptor. *Science* **335**, 851–855 (2012). doi: 10.1126/science.1215904; pmid: 22344443
28. A. M. Sarotti, I. Fernández, R. A. Spanevello, M. A. Sierra, A. G. Suárez, π-stacking effect on levoglucosenone derived internal chiral auxiliaries. A case of complete enantioselectivity inversion on the Diels–Alder reaction. *Org. Lett.* **10**, 3389–3392 (2008). doi: 10.1021/ol801140g; pmid: 18630916
29. V. Corne, A. M. Sarotti, C. Ramirez de Arellano, R. A. Spanevello, A. G. Suárez, Experimental and theoretical insights in the alkene–arene intramolecular π-stacking interaction. *Beilstein J. Org. Chem.* **12**, 1616–1623 (2016). doi: 10.3762/bjoc.12.158; pmid: 27559414
30. N. H. Moniri, Free-fatty acid receptor-4 (GPR120): Cellular and molecular function and its role in metabolic disorders. *Biochem. Pharmacol.* **110-111**, 1–15 (2016). doi: 10.1016/j.bcp.2016.01.021; pmid: 26827942
31. P. Xiao *et al*., Ligand recognition and allosteric regulation of DRD1-Gs signaling complexes. *Cell* **184**, 943–956.e18 (2021). doi: 10.1016/j.cell.2021.01.028; pmid: 33571432
32. Y. Q. Ping *et al*., Structures of the glucocorticoid-bound adhesion receptor GPR97-G_o complex. *Nature* **589**, 620–626 (2021). doi: 10.1038/s41586-020-03083-w; pmid: 33408414
33. B. L. Roth, Molecular pharmacology of metabotropic receptors targeted by neuropsychiatric drugs. *Nat. Struct. Mol. Biol.* **26**, 535–544 (2019). doi: 10.1038/s41594-019-0252-8; pmid: 31270468
34. A. Bonnefond *et al*., Contribution of the low-frequency, loss-of-function p.R270H mutation in FFAR4 (GPR120) to increased fasting plasma glucose levels. *J. Med. Genet.* **52**, 595–598 (2015). doi: 10.1136/jmedgenet-2015-103065; pmid: 26025001
35. E. Chun *et al*., Fusion partner toolchest for the stabilization and crystallization of G protein-coupled receptors. *Structure* **20**, 967–976 (2012). doi: 10.1016/j.str.2012.04.010; pmid: 22681902
36. F. Yang *et al*., Structure, function and pharmacology of human itch receptor complexes. *Nature* **600**, 164–169 (2021). doi: 10.1038/s41586-021-04077-y; pmid: 34789875
37. M. Sandhu *et al*., Conformational plasticity of the intracellular cavity of GPCR–G-protein complexes leads to G-protein promiscuity and selectivity. *Proc. Natl. Acad. Sci. U.S.A.* **116**, 11956–11965 (2019). doi: 10.1073/pnas.1820944116; pmid: 31138704
38. A. Inoue *et al*., Illuminating G-protein-coupling selectivity of GPCRs. *Cell* **177**, 1933–1947.e25 (2019). doi: 10.1016/j.cell.2019.04.044; pmid: 31160049
39. K. Kim *et al*., Structure of a hallucinogen-activated Gq-coupled 5-HT_{2A} serotonin receptor. *Cell* **182**, 1574–1588.e19 (2020). doi: 10.1016/j.cell.2020.08.024; pmid: 32946782
40. C. Cao *et al*., Structure, function and pharmacology of human itch GPCRs. *Nature* **600**, 170–175 (2021). doi: 10.1038/s41586-021-04126-6; pmid: 34789874
41. Y. L. Yin *et al*., Molecular basis for kinin selectivity and activation of the human bradykinin receptors. *Nat. Struct. Mol. Biol.* **28**, 755–761 (2021). doi: 10.1038/s41594-021-00645-y; pmid: 34518695
42. M. Schorb, I. Haberbosch, W. J. H. Hagen, Y. Schwab, D. N. Mastronarde, Software tools for automated transmission electron microscopy. *Nat. Methods* **16**, 471–477 (2019). doi: 10.1038/s41592-019-0396-9; pmid: 31086343
43. S. Q. Zheng *et al*., MotionCor2: Anisotropic correction of beam-induced motion for improved cryo-electron microscopy. *Nat. Methods* **14**, 331–332 (2017). doi: 10.1038/nmeth.4193; pmid: 28250466
44. K. Zhang, Gctf: Real-time CTF determination and correction. *J. Struct. Biol.* **193**, 1–12 (2016). doi: 10.1016/j.jsb.2015.11.003; pmid: 26592709
45. S. H. Scheres, RELION: Implementation of a Bayesian approach to cryo-EM structure determination. *J. Struct. Biol.* **180**, 519–530 (2012). doi: 10.1016/j.jsb.2012.09.006; pmid: 23000701
46. D. Kimanius, L. Dong, G. Sharov, T. Nakane, S. H. W. Scheres, New tools for automated cryo-EM single-particle analysis in RELION-4.0. *Biochem. J.* **478**, 4169–4185 (2021). doi: 10.1042/BCJ20210708; pmid: 34783343
47. A. Punjani, J. L. Rubinstein, D. J. Fleet, M. A. Brubaker, cryoSPARC: Algorithms for rapid unsupervised cryo-EM structure determination. *Nat. Methods* **14**, 290–296 (2017). doi: 10.1038/nmeth.4169; pmid: 28165473
48. A. Waterhouse *et al*., SWISS-MODEL: Homology modelling of protein structures and complexes. *Nucleic Acids Res.* **46**, W296–W303 (2018). doi: 10.1093/nar/gky427; pmid: 29788355
49. P. D. Adams *et al*., *PHENIX*: A comprehensive Python-based system for macromolecular structure solution. *Acta Crystallogr. D* **66**, 213–221 (2010). doi: 10.1107/S0907444909052925; pmid: 20124702
50. E. F. Pettersen *et al*., UCSF Chimera—A visualization system for exploratory research and analysis. *J. Comput. Chem.* **25**, 1605–1612 (2004). doi: 10.1002/jcc.20084; pmid: 15264254
51. T. D. Goddard *et al*., UCSF ChimeraX: Meeting modern challenges in visualization and analysis. *Protein Sci.* **27**, 14–25 (2018). doi: 10.1002/pro.3235; pmid: 28710774
52. E. F. Pettersen *et al*., UCSF ChimeraX: Structure visualization for researchers, educators, and developers. *Protein Sci.* **30**, 70–82 (2021). doi: 10.1002/pro.3943; pmid: 32881101
53. P. Emsley, K. Cowtan, *Coot*: Model-building tools for molecular graphics. *Acta Crystallogr. D* **60**, 2126–2132 (2004). doi: 10.1107/S0907444904019158; pmid: 15572765
54. J. Cheng *et al*., Autonomous sensing of the insulin peptide by an olfactory G protein-coupled receptor modulates glucose metabolism. *Cell Metab.* **34**, 240–255.e10 (2022). doi: 10.1016/j.cmet.2021.12.022; pmid: 35108512
55. R. H. J. Olsen *et al*., TRUPATH, an open-source biosensor platform for interrogating the GPCR transducerome. *Nat. Chem. Biol.* **16**, 841–849 (2020). doi: 10.1038/s41589-020-0535-8; pmid: 32367019
56. C. H. Liu *et al*., Arrestin-biased AT1R agonism induces acute catecholamine secretion through TRPC3 coupling. *Nat. Commun.* **8**, 14335 (2017). doi: 10.1038/ncomms14335; pmid: 28181498
57. P. Xiao *et al*., Tethered peptide activation mechanism of the adhesion GPCRs ADGRG2 and ADGRG4. *Nature* **604**, 771–778 (2022). doi: 10.1038/s41586-022-04590-8; pmid: 35418677
58. Y. Q. Ping *et al*., Structural basis for the tethered peptide activation of adhesion GPCRs. *Nature* **604**, 763–770 (2022). doi: 10.1038/s41586-022-04619-y; pmid: 35418678
59. J. W. Black, P. Leff, Operational models of pharmacological agonism. *Proc. R. Soc. London Ser. B* **220**, 141–162 (1983). doi: 10.1098/rspb.1983.0093; pmid: 6141562
60. J. Huang *et al*.., CHARMM36m: An improved force field for folded and intrinsically disordered proteins. *Nat. Methods* **14**, 71–73 (2017). doi: 10.1038/nmeth.4067; pmid: 27819658
61. J. Lee *et al*., CHARMM-GUI Input Generator for NAMD, GROMACS, AMBER, OpenMM, and CHARMM/OpenMM simulations using the CHARMM36 additive force field. *J. Chem. Theory Comput.* **12**, 405–413 (2016). doi: 10.1021/acs.jctc.5b00935; pmid: 26631602
62. K. Vanommeslaeghe *et al*.., CHARMM general force field: A force field for drug-like molecules compatible with the CHARMM all-atom additive biological force fields. *J. Comput. Chem.* **31**, 671–690 (2010). pmid: 19575467
63. N. Metropolis, S. Ulam, The Monte Carlo method. *J. Am. Stat. Assoc.* **44**, 335–341 (1949). doi: 10.1080/01621459.1949.10483310; pmid: 18139350
64. D. Van Der Spoel *et al*., GROMACS: Fast, flexible, and free. *J. Comput. Chem.* **26**, 1701–1718 (2005). doi: 10.1002/jcc.20291; pmid: 16211538
65. W. Humphrey, A. Dalke, K. Schulten, VMD: Visual molecular dynamics. *J. Mol. Graph.* **14**, 33–38 (1996). doi: 10.1016/0263-7855(96)00018-5; pmid: 8744570
66. Y. Yuan *et al*., Structures of signaling complexes of lipid receptors S1PR1 and S1PR5 reveal mechanisms of activation and drug recognition. *Cell Res.* **31**, 1263–1274 (2021). doi: 10.1038/s41422-021-00566-x; pmid: 34526663

ACKNOWLEDGMENTS

The cryo-EM data were collected at the Cryo-Electron Microscopy Facility, Zhejiang University Medical Center/Liangzhu laboratory, the Cryo-Electron Microscopy Center, Zhejiang University; and at the Cryo-EM Center for Structural Determination and Characterization, Shandong University. The cryo-EM grids were frozen and initially checked at the Cryo-Electron Microscopy Facility, Zhejiang University Medical Center/Liangzhu laboratory, and Research Center for Medical and Structural Biology of School of Basic Medical Sciences, Shandong University, with assistance from L. Qi and L. Wang. The molecular stimulations were performed on the HPC Cloud Platform of Shandong University. **Funding:** This work was supported by the National Natural Science Foundation of China (32130055 to J.-P.S.), National Key R&D Program of China (2019YFA0112100 to S.F., 2019YFA0904200 to J.-P.S. and P.X., 2019YFA050880 to Y.Z. and P.X.), National Natural Science Foundation of China (92057121 to X.Y., 31971195 to P.X., 32100959 to C.M., 32200990 to Q.-T.H.), National Science Fund for Distinguished Young Scholars Grant (81825022 to J.-P.S., 82225011 to X.Y.), National Science Fund for Excellent Young Scholars (32222038 to P.X.), Shandong Provincial Natural Science Fund for Excellent Young Scholars (ZR2021YQ18 to P.X.), Key Research and Development Program of Shandong Province (2021CXGC011105 and 2021ZLGX02 to J.-P.S.), the Key Research Project of the Natural Science Foundation of Beijing, China (Z200019 to J.-P.S.), Major Fundamental Research Program of Natural Science Foundation of Shandong Province, China (ZR2021ZD18 to X.Y.), Fundamental Research Funds for the Central Universities (2021JCG020 to J.-P.S. and P.X.), the China Postdoctoral Science Foundation Grant (2022M711954 to Q.-T.H.), Zhejiang Province Natural Science Fund for Excellent Young Scholars (LR22C050002 to C.M.), and the Key R&D Projects of Zhejiang Province (2021C03039 to Y.Z.). **Author contributions:** J.-P.S., Y.Z., and X.Y. initiated the project for investigation of the activation mechanism and ligand recognition of GPR120. X.Y., Y.Z., S.F., and J.-P.S. supervised the overall project. X.Y. and J.-P.S. provided the conceptual design for understanding the recognition of double bonds of unsaturated FA by GPR120 and its connection to biased signaling. X.Y., J.-P.S., P.X., X.-N.T., J.Q., and Q.-T.H. participated in data analysis and interpretation. X.-N.T. participated in the initial Sf9 cell preparation for GPR120. P.X., X.-N.T., and Q.-T.H. developed the procedure for LA-GPR120- G_i, OA-GPR120-G_i, EPA-GPR120-G_i, TUG891-GPR120-G_i, 9-HSA-GPR120-G_i, and TUG891-GPR120-G_{iq} complex formation and purification under the supervision of J.-P.S. and S.F. S.F. contributed to the development of the strategy for GPR120-Giq complex formation, and acquired the accession to cryo-EM facility for collecting cryo-EM data for TUG891-GPR120-Giq complex during the revision of the manuscript. X.-N.T. P.X., and Q.-T.H. prepared LA-GPR120-G_i, OA-GPR120-G_i, EPA-GPR120-G_i, TUG891-GPR120-G_i, 9-HSA-GPR120-G_i, and TUG891-GPR120-G_{iq} complex samples for cryo-EM. C.M., P.X., and J.Q. prepared cryo-EM grids with assistance of L.-N.C. and D.-D.S. C.M. performed the cryo-EM data collection. C.M. and J.Q. processed cryo-EM data with assistance of Y.Z. and generated the cryo-EM density map under the supervision of J.-P.S. and Y.Z. C.M., J.Q., Q.-T.H., S.-C.G., and D.-L.Z. built and refined the cryo-EM structures. Chao.Z. performed MD simulation for the GPR120 complexes using Gromacs software with assistance of Jun.C. and under the supervision of S.F. X.-N.T., P.X., Q.-T.H., Z.-S.Y., H.-Q.Z., S.F., Y.G., Jie.C., Y.-N.Z., P.S., Cheng.Z., H.E.X., and C.W. performed cell-based functional assays including G protein dissociation assay and β-arrestins recruitment assay. X.-N.T., Q.-L.W., M.-X.L., and G.-Y.L. generated all constructs used in this study. J.-P.S., X.Y., P.X., Q.-T.H., X.-N.T., Chao.Z., S.-M.H., and Y.-H.H. prepared figures with assistance from Y.-Q.D. J.-P.S., Y.Z., and X.Y. wrote the manuscript, with input from all authors. **Competing interests:** The authors declare no competing interests. **Data and materials availability:** All data are presented in the main text or supplementary materials of the manuscript. For protein structures, the atomic coordinates and their corresponding cryo-EM maps have been deposited in the Protein Data Bank with accession codes 8G59, 8ID9, 8ID3, 8ID4, 8ID8, and 8ID6 or in the Electron Microscopy Data Bank with accession codes EMD-29736, EMD-35360, EMD-35356, EMD-35357, EMD-35359, and EMD-35358 for the TUG891-GPR120-G_{iq} complex, EPA-GPR120-G_i complex, 9-HSA-GPR120-G_i complex, LA-GPR120-G_i complex, TUG891-GPR120-G_i complex, and OA-GPR120-G_i complex, respectively. **License information:** Copyright © 2023 the authors, some rights reserved; exclusive licensee American Association for the Advancement of Science. No claim to original US government works. https://www.science.org/about/science-licenses-journal-article-reuse

SUPPLEMENTARY MATERIALS

science.org/doi/10.1126/science.add6220
Figs. S1 to S32
Tables S1 to S26
MDAR Reproducibility Checklist

View/request a protocol for this paper from *Bio-protocol*.

Submitted 19 July 2022; resubmitted 21 December 2022
Accepted 16 February 2023
10.1126/science.add6220

RESEARCH ARTICLE

EVOLUTIONARY BIOLOGY

Obligate chimerism in male yellow crazy ants

H. Darras[1,2]*, C. Berney[2], S. Hasin[3], J. Drescher[4], H. Feldhaar[4,5], L. Keller[2]*†

Multicellular organisms typically develop from a single fertilized egg and therefore consist of clonal cells. We report an extraordinary reproductive system in the yellow crazy ant. Males are chimeras of haploid cells from two divergent lineages: R and W. R cells are overrepresented in the males' somatic tissues, whereas W cells are overrepresented in their sperm. Chimerism occurs when parental nuclei bypass syngamy and divide separately within the same egg. When syngamy takes place, the diploid offspring either develops into a queen when the oocyte is fertilized by an R sperm or into a worker when fertilized by a W sperm. This study reveals a mode of reproduction that may be associated with a conflict between lineages to preferentially enter the germ line.

A fundamental law of biological inheritance posits that in multicellular organisms, somatic tissues are composed of clonal cells arising from a single zygote that is usually formed by the fusion of two haploid gametes. We report that this law has been broken by the yellow crazy ant (*Anoplolepis gracilipes*), one of the worst invasive species in the world (*1*). Previous genetic studies of *A. gracilipes* had exposed unresolved discrepancies among queen, male, and worker genotypes (*2*–*4*), prompting us to conduct detailed follow-up experiments. The latter revealed the existence of a reproductive mode unknown to science: Males are chimeras of haploid cells from two divergent lineages. As in other ant species, queens and workers are diploid. However, they are genetically distinct: Queens have a pure lineage genome, whereas workers are interlineage hybrids.

Queens are genetically distinct from workers

After collecting *A. gracilipes* at 14 locations in the field, we genotyped 53 reproductive queens and 91 workers at 16 microsatellite loci (Fig. 1A and tables S1 and S2). Differences between queen ants and workers generally result from environmental or maternal factors rather than from genetic differences (*5*, *6*). However, our analyses revealed that the queens and the workers belonged to two very different genetic groups [genetic distance (R_{ST}) = 0.37, permutation p value < 0.0001; Fig. 1B and table S3)]. The workers also exhibited an extremely high level of heterozygosity (H) of 99% (SD = 2%), whereas the queens had only a moderate level (H = 19%, SD = 12%). Moreover, at each of the 16 loci, the workers possessed an allele that was rare or absent in the queens. The most likely explanation was that workers developed from crosses between two divergent lineages, whereas queens arose from crosses between parents of the same lineage, a pattern described in a few other ant species (*7*–*9*). We found support for this hypothesis through mother–daughter analyses, which showed that the queens and workers had developed from eggs fertilized by sperm from two divergent lineages (hereafter, R as in "reproductive queen" and W as in "worker"). These lineages had no shared alleles at 12 of the 16 loci and exhibited substantially different allele frequencies at the other 4 loci (Fisher's exact tests, $p < 0.001$ for all loci; supplementary text S1 and table S4). These analyses suggested that queens inherit one copy of the R genome from each of their parents, whereas workers receive one copy of the R genome from their mother and one copy of the W genome from their father. Indeed, all field-collected queens had an R/R genome, whereas all the field-collected workers had an R/W genome.

Males are chimeras of haploid cells from the two divergent lineages

In ants and other hymenopterans, males are normally haploid and develop from unfertilized eggs (*10*). Thus, we hypothesized that the genetic differences between the queens and workers could be explained by the presence of R and W males in the population. To test this supposition, we genotyped 574 males using DNA extracted from one leg per individual. We found that 34% of the males carried solely R-lineage alleles and 1% of the males carried solely W-lineage alleles but that 65% of the males were heterozygous and bore alleles from both lineages (R/W males), as the workers did. The presence of R/W males could be explained if they were diploid, which sometimes occurs because of the complementary sex-determination system used by ants. More specifically, individuals that are homozygous at the sex-determining locus develop into diploid males that are usually nonfunctional, whereas haploid individuals develop into functional males (*11*). This idea was not supported by our flow cytometry results, which revealed that the males' nuclei had half the DNA content of the workers' nuclei, irrespective of male genotype. All the males were therefore haploid (Fig. 2A and table S5).

The finding that R/W males were haploid led us to hypothesize that these males could be chimeric, carrying both haploid R and haploid W cells. To test this idea, we conducted single-cell genotyping of the nuclei of the workers and the R/W males. As expected, the workers all possessed nuclei with a diploid R/W genome.

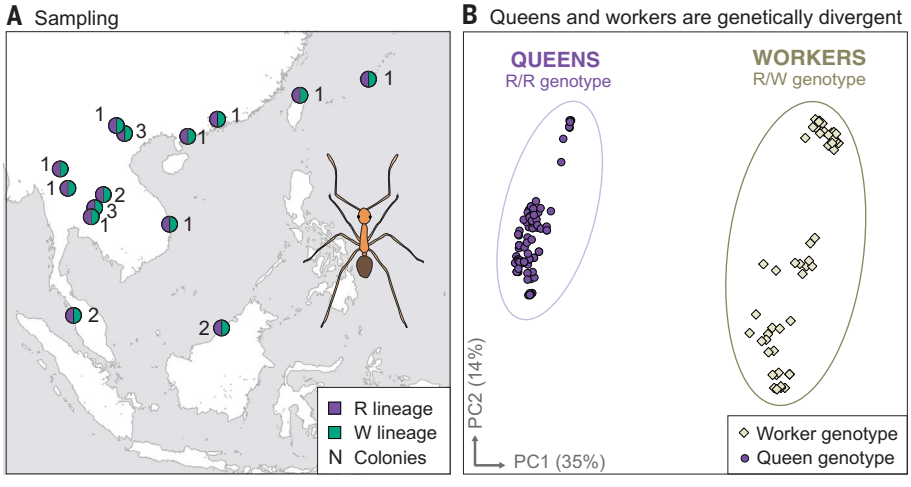

Fig. 1. Phylogeographic analyses reveal two cryptic, sympatric lineages. (**A**) Locations and number of colonies sampled (map: Esri, Earthstar Geographics; see also tables S1 and S2). (**B**) Principal coordinates analysis (PCoA) of the genetic variation among the queens (n = 53) and workers (n = 91). The percentage of the total variation explained by each of the PCoA axes is indicated.

[1]Institute of Organismic and Molecular Evolution, Johannes Gutenberg University, Mainz, Germany. [2]Department of Ecology and Evolution, University of Lausanne, Lausanne, Switzerland. [3]Valaya Alongkorn Rajabhat University, Pathum Thani, Thailand. [4]Department of Animal Ecology, Göttingen University, Göttingen, Germany. [5]Animal Ecology I, University of Bayreuth, Bayreuth, Germany.
***Corresponding author. Email: hdarras@uni-mainz.de (H.D.); laurent.keller01@gmail.com (L.K.)**
†Present address: Social Evolution Unit, Cornuit 8, BP 855, Chesières, Switzerland.

By contrast, in the R/W males, 50% of the nuclei had only the R genome and 45% had only the W genome (Fig. 2B). The remaining 5% of nuclei (randomly distributed across the males) had alleles from both lineages, a result that most likely arose because of cross-contamination between different samples. A certain degree of such contamination is expected because it is challenging to accurately sort and genotype individual nuclei (*12*, *13*). To corroborate these results, we used whole-genome sequencing to identify R- and W-specific sequences and carried out in situ hybridization using probes targeting these sequences on male tissue sections. This analysis showed that the males' tissues consisted of large cell clusters displaying only R or W staining (Fig. 3). In situ hybridization also confirmed that the 5% of nucleus genotypes with

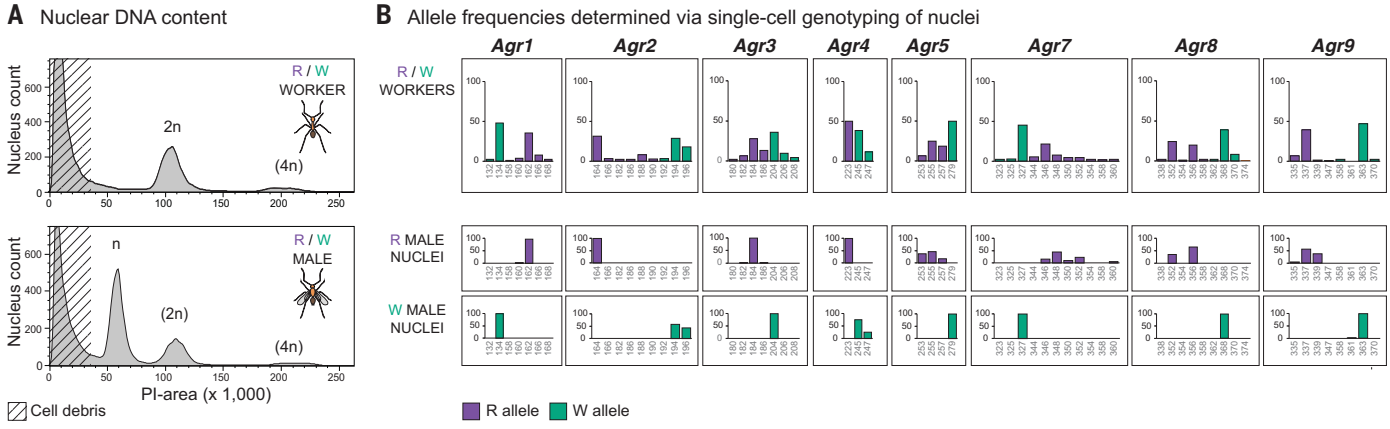

Fig. 2. Males and workers display the same genomes but differ in ploidy. (**A**) Flow cytometry analysis of nuclear DNA content for one representative worker and one representative R/W male. The nucleus count is plotted against the intensity of fluorescence. PI-area, propidium iodide fluorescence pulse area. All the males (n = 30) were haploid, as they had half the DNA content of the diploid workers (n = 15) (table S5). The main peak in each plot corresponds to sample ploidy. n, haploid; 2n, diploid. The additional peaks stem from mitotic divisions and from endoreduplication events that occur in muscle cells (*23*). (**B**) Allele frequencies for workers and males as determined by the single-cell genotyping of nuclei at eight diagnostic loci. Allele sizes are expressed in base pairs. The frequencies were inferred with 91 workers (leg genotypes), 596 nuclei from males with an R genome, and 542 nuclei from males with a W genome. The alleles originating from the R and W lineages are shown in purple and green, respectively.

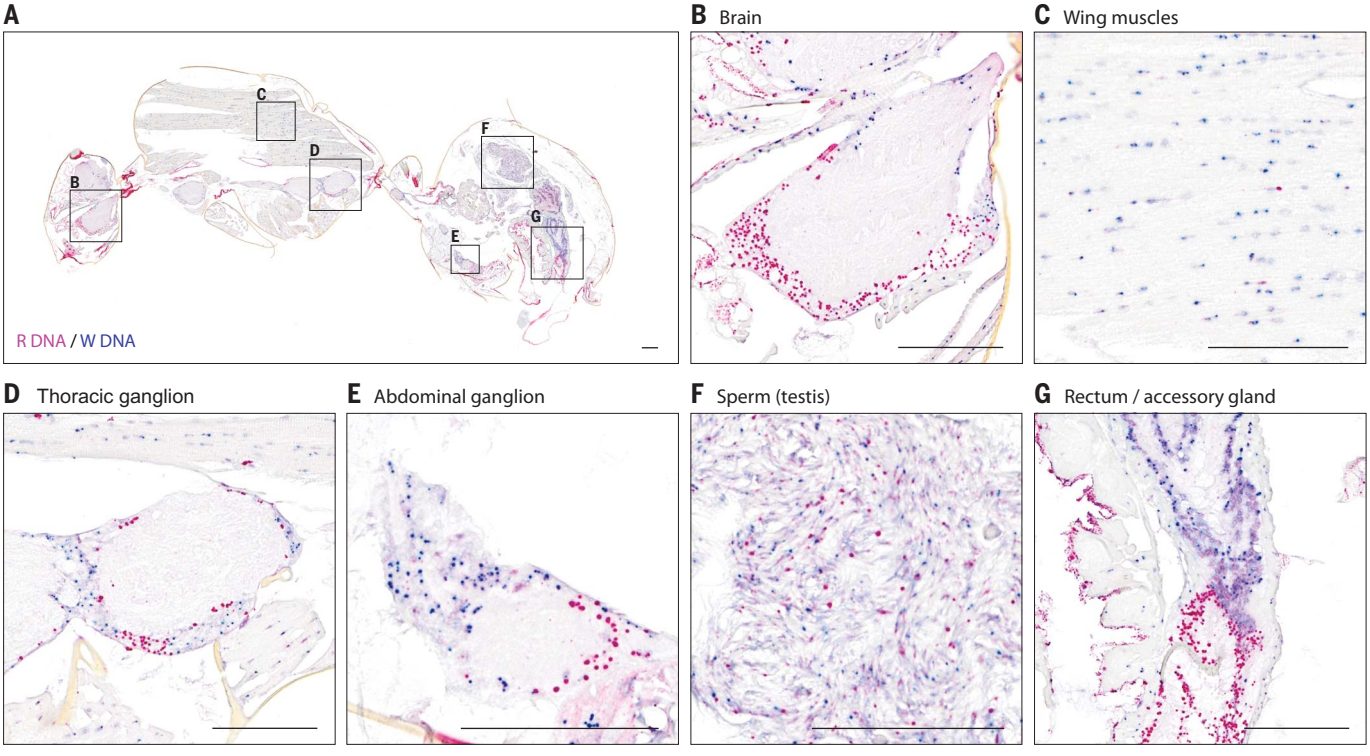

Fig. 3. Males are chimeric mixtures of cells with R and W genomes. Detection of R and W nuclei through in situ hybridization (DNAscope, Advanced Cell Diagnostics) in a male (R nuclei: pink; W nuclei: blue). (**A**) Longitudinal section with the head facing left. (**B** to **G**) Magnified views of different tissues. Scale bars, 100 μm. All the males (n = 6) were chimeras with R and W cells in different body parts (data S5).

alleles from both genomes arose from contamination because there was no colocalization between the chromogens associated with the R and W probes. Finally, mother–offspring analyses of a different set of R/W males showed that the R genome is maternally inherited whereas the W genome is paternally inherited (table S6). These findings indicate that the R/W males developed from R eggs fertilized by W sperm. Thus, in the yellow crazy ant, when these sperm and egg pronuclei fuse, diploid workers are produced. When they do not fuse, the result is haploid males that are chimeras of R and W haploid cells (Fig. 4).

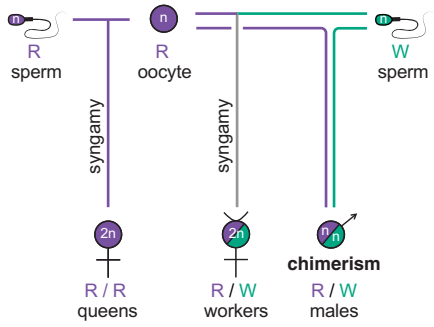

Fig. 4. Reproductive system of *A. gracilipes*. Queens are pure lineage, workers are hybrid, and males are chimeric. Schematic representation of the reproductive system used by *A. gracilipes*. Queens have an R/R genome and store both R and W sperm in their spermathecae. Queens and workers develop from eggs fertilized with R and W sperm, respectively. Males arise from eggs fertilized with W sperm in which the parental nuclei do not fuse and develop separately. The resulting adults are chimeras with haploid R cells and haploid W cells in different body parts.

Overrepresentation of the W lineage in sperm versus somatic tissues in males

To determine the distribution of the R and W genomes in the chimeric males, we analyzed 12 somatic tissues using a competitive polymerase chain reaction (PCR) assay that amplified diagnostic microsatellites. We observed that substantial variation existed in the percentages of R and W cells across males and across tissues in males (Fig. 5A and fig. S1). Overall, 51% of the 437 samples (10 to 12 tissue samples per male from 37 males) contained exclusively R or W cells. This finding that specific tissues of

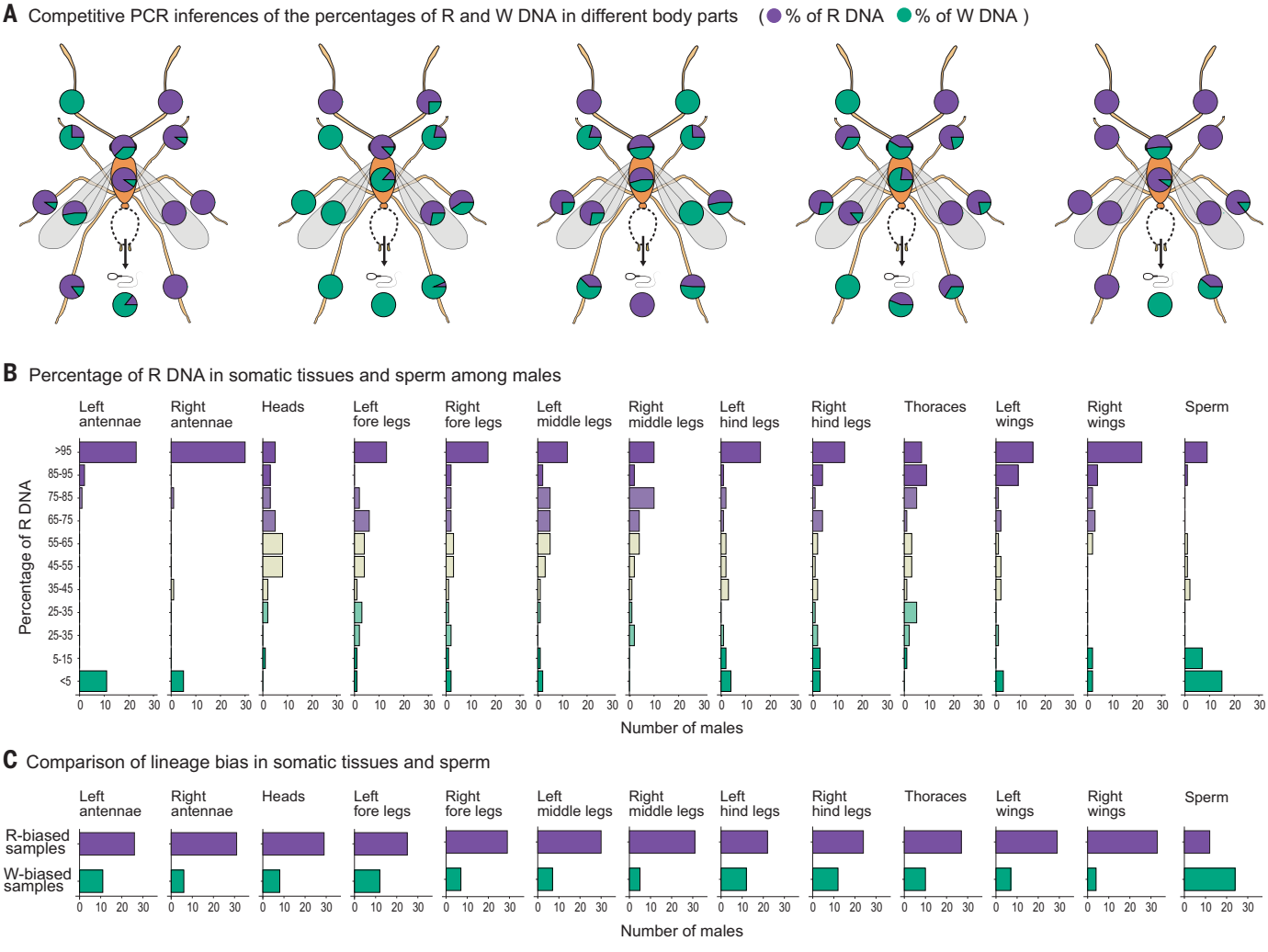

Fig. 5. R cells are more common in somatic tissues, and W cells are more common in sperm. (**A**) Pie charts showing the relative percentages of R DNA (purple) and W DNA (green) in the heads, thoraces, antennae, legs, wing pairs, and sperm of 5 representative R/W males (complete data for 37 males in fig. S1). The percentages were estimated with a competitive PCR assay using seven microsatellite markers. (**B**) Horizontal bar graphs showing the percentage of R DNA in the 12 somatic tissues and sperm of different numbers of males (n = 37). The color scale expresses the degree of bias: purple [high percentage of R cells (R-biased)] to green [low percentage of R cells (W-biased)]. (**C**) Horizontal bar graphs of the different tissues showing the number of males with more R than W cells (R-biased; in purple) and more W than R cells (W-biased; in green).

R/W males frequently contained only R or W cells has important implications for our earlier finding that 35% of the males genotyped with the DNA from a single leg had only R or W cells. These males were most likely R/W males that carried solely R-lineage or W-lineage alleles within the leg analyzed. Consequently, these data indicate that chimerism is the predominant or exclusive mode for producing males.

The fitness of the R and W genomes depends on their relative representation in the germ line. We therefore explored whether R and W cells were equally represented in the somatic tissues and sperm. In the R/W males, 73% (SD = 33%) of somatic cells were R, and 77% of the tissue samples contained more R cells than W cells (Fig. 5, B and C). The percentage of R cells was similar across the 12 somatic tissues analyzed (χ^2 test, Benjamini-Hochberg adjusted p values > 0.52 for all comparisons). By contrast, only 35% (SD = 43%) of sperm cells were R, and 67% of the sperm sampled had more W cells than R cells. The sperm were thus significantly more W-biased than any of the 12 somatic tissues (χ^2 test, Benjamini-Hochberg adjusted p values < 0.01 for all comparisons). This finding was confirmed by the results of competitive PCR analyses of legs and sperm from a larger set (n = 252) of randomly chosen males: On average, 77% (SD = 30%) of the leg cells were R, whereas just 36% (SD = 42%) of the sperm cells were R. These results indicate that the W genome is disproportionately represented in the germ line of R/W males. Because males are haploid and do not use meiosis to produce gametes (*14*), this bias is most likely driven by the spatial polarity of maternal and paternal nuclei in the early zygote. For example, in *Drosophila*, primordial germ cells form early during embryonic cellularization, arising from the first dividing nuclei to reach the germ plasm at the posterior pole of the embryo (*15*).

Forty-three percent of the males had only W sperm, and 26% had only R sperm (n = 252). Most mating events should therefore result in the transmission of only one type of sperm. However, 96% of the queens had both R and W sperm in their sperm stores, kept in a dedicated organ called the spermatheca. Ant queens mate early in adulthood and use the sperm acquired to fertilize their eggs for the rest of their lives. Given that only 31% of the males had both R and W sperm, the high proportion of queens having both types of sperm most likely reflects multiple matings. An effective mate number of four would account for 96% of queens carrying both R and W sperm (materials and methods).

The yellow crazy ant has a distinctive mode of reproduction

This study has revealed a mode of reproduction so far unknown to science. Although chimerism has been observed in a wide range of eukaryotes, it usually stems from rare developmental accidents (*16*–*18*) or the fusion of different individuals later in development (*19*, *20*). The only other known exception has been seen in marmosets: Females frequently give birth to dizygotic twins, which exchange stem cells in utero via their shared placenta. These exchanges lead to extensive chimerism in both the somatic tissues and germ lines of the adults (*21*, *22*). By contrast, chimerism in *A. gracilipes* is associated with a single fertilization event at the onset of development. The parental nuclei bypass syngamy and divide separately within the same egg, giving rise to a haploid individual that develops into a male. In contrast, when syngamy does occur, there are two other outcomes: The resulting diploid organism develops into a queen if the egg is fertilized by an R sperm or into a worker if the egg is fertilized by a W sperm. The mechanisms controlling syngamy remain unknown and may be deterministic (e.g., maternal) or stochastic in nature. The unusual mode of male development described here is likely facilitated by a combination of two factors: (i) haplodiploid sex determination, which allows functional haploids to develop in the absence of nuclear fusion, and (ii) the strong antagonistic selective pressures associated with the production of males, queens, and workers from one genome.

Chimerism appears to provide two related fitness advantages to the W genome, which persists in the population despite its association with female sterility (the production of workers instead of queens) (supplementary text S2). First, because the two parental gametes are prevented from fusing, the embryo's developmental trajectory switches tracks from sterile worker to reproductive male, allowing the W genome to propagate itself. Second, the W genome behaves as a selfish genetic element in R/W males, as seen in its disproportionate representation in the germ line. This study has not only uncovered a previously undescribed reproductive system, it has also demonstrated that this mode of reproduction is associated with a conflict between lineages over representation in the germ line versus the soma.

REFERENCES AND NOTES

1. S. Lowe, M. Browne, S. Boudjelas, M. De Poorter, *100 of the world's worst invasive alien species: A selection from the Global Invasive Species Database*, booklet, IUCN/SSC Invasive Species Specialist Group, 2004; https://portals.iucn.org/library/sites/library/files/documents/2000-126.pdf.
2. J. Drescher, N. Blüthgen, H. Feldhaar, *Mol. Ecol.* **16**, 1453–1465 (2007).
3. M. A. M. Gruber, B. D. Hoffmann, P. A. Ritchie, P. J. Lester, *Insectes Soc.* **60**, 135–145 (2013).
4. M. L. Thomas, K. Becker, K. Abbott, H. Feldhaar, *Biol. Invasions* **12**, 677–687 (2010).
5. D. E. Wheeler, *Am. Nat.* **128**, 13–34 (1986).
6. T. Schwander, N. Lo, M. Beekman, B. P. Oldroyd, L. Keller, *Trends Ecol. Evol.* **25**, 275–282 (2010).
7. J. Romiguier, A. Fournier, S. H. Yek, L. Keller, *Mol. Ecol.* **26**, 1108–1117 (2017).
8. S. Helms Cahan, S. B. Vinson, *Evolution* **57**, 1562–1570 (2003).
9. S. Helms Cahan, L. Keller, *Nature* **424**, 306–309 (2003).
10. G. E. Heimpel, J. G. de Boer, *Annu. Rev. Entomol.* **53**, 209–230 (2008).
11. L. Cournault, S. Aron, *Naturwissenschaften* **96**, 1393–1400 (2009).
12. P. F. Ray, M. Vekemans, A. Munnich, *Mol. Hum. Reprod.* **7**, 489–494 (2001).
13. B. Sun *et al.*, *Cell Rep. Methods* **1**, 100008 (2021).
14. T. Palomeque, M. A. Cano, E. Chica, R. Diaz de la Guardia, *Cytobios* **62**, 71–80 (1990).
15. A. C. Santos, R. Lehmann, *Curr. Biol.* **14**, R578–R589 (2004).
16. K. Madan, *Eur. J. Med. Genet.* **63**, 103971 (2020).
17. G. Dewald, M. W. Haymond, J. L. Spurbeck, S. B. Moore, *Science* **207**, 321–323 (1980).
18. L. Strain, J. P. Warner, T. Johnston, D. T. Bonthron, *Nat. Genet.* **11**, 164–169 (1995).
19. L. W. Buss, *Proc. Natl. Acad. Sci. U.S.A.* **79**, 5337–5341 (1982).
20. B. Rinkevich, I. L. Weissman, *Symbiosis* **4**, 117–134 (1987).
21. C. N. Ross, J. A. French, G. Ortí, *Proc. Natl. Acad. Sci. U.S.A.* **104**, 6278–6282 (2007).
22. K. Benirschke, J. M. Anderson, L. E. Brownhill, *Science* **138**, 513–515 (1962).
23. S. Aron, L. de Menten, D. R. Van Bockstaele, S. M. Blank, Y. Roisin, *Curr. Biol.* **15**, 824–827 (2005).

ACKNOWLEDGMENTS

We thank M. Nipitwattanaphon, S. Dobata, A. S. Mikheyev, C.-C. S. Yang, C. Lebas, A. Lenoir, I. Voraphab, Ju. Rattanatip, and Ja. Rattanatip for assistance with the sample collection; C. La Mendola, F. Dolivo, and J. Romiguier for help with the genotyping and sequencing; Q. M. Pan for aiding with the data visualization and statistics; S. Aron for conducting the preliminary analyses showing that there were no diploid males in *A. gracilipes*; R. Bedel, K. Blackney, and F. Sala de Oyanguren (Flow Cytometry Facility, University of Lausanne) for their cell-sorting services and technical advice; the Genomic Technologies Facility at the University of Lausanne for performing the library preparation and sequencing; J. Sordet-Dessimoz, A. Hautier, G.-F. Mancini, and N. Müller (Histology Core Facility, Swiss Federal Institute of Technology Lausanne) for setting up and optimizing the histological approaches; and S. Helms Cahan, K. G. Ross, T. Schwander, K. Van Doninck, J. Goudet, T. Kay, J. Pearce-Duvet and three anonymous reviewers for comments on an earlier version of the manuscript. **Funding:** This work was supported by an ERC grant (L.K.), a Swiss NSF grant (L.K.), and a Marie Skłodowska-Curie fellowship (H.D.). **Author contributions:** H.D., C.B., and L.K. designed the research. J.D. and H.F. ran preliminary analyses that facilitated the study. H.D. and S.H. collected field samples. H.D. and C.B. performed the research. H.D. analyzed the data and wrote the manuscript with L.K. All the authors commented on the manuscript. **Competing interests:** The authors declare that they have no competing interests. **Data and materials availability:** All the microsatellite data generated during this study are provided in the supplementary materials (data S1 to S3). The sequencing data and genome assemblies generated during this study have been deposited at NCBI (SRR21232720-SRR21232722, SRR21231522, SRR21231523, JAOBUF000000000, and JAOBUE000000000). **License information:** Copyright © 2023 the authors, some rights reserved; exclusive licensee American Association for the Advancement of Science. No claim to original US government works. https://www.science.org/about/science-licenses-journal-article-reuse

SUPPLEMENTARY MATERIALS

science.org/doi/10.1126/science.adf0419
Materials and Methods
Supplementary Text
Figs. S1 to S3
Tables S1 to S9
References (*24*–*43*)
MDAR Reproducibility Checklist
Data S1 to S6

View/request a protocol for this paper from *Bio-protocol*.

Submitted 26 September 2022; accepted 17 February 2023
10.1126/science.adf0419

METALENSES

Extreme ultraviolet metalens by vacuum guiding

Marcus Ossiander[1]*†, Maryna Leonidivna Meretska[1]†, Hana Kristin Hampel[2]†, Soon Wei Daniel Lim[1], Nico Knefz[2], Thomas Jauk[2], Federico Capasso[1]*, Martin Schultze[2]*

Extreme ultraviolet (EUV) radiation is a key technology for material science, attosecond metrology, and lithography. Here, we experimentally demonstrate metasurfaces as a superior way to focus EUV light. These devices exploit the fact that holes in a silicon membrane have a considerably larger refractive index than the surrounding material and efficiently vacuum-guide light with a wavelength of ~50 nanometers. This allows the transmission phase at the nanoscale to be controlled by the hole diameter. We fabricated an EUV metalens with a 10-millimeter focal length that supports numerical apertures of up to 0.05 and used it to focus ultrashort EUV light bursts generated by high-harmonic generation down to a 0.7-micrometer waist. Our approach introduces the vast light-shaping possibilities provided by dielectric metasurfaces to a spectral regime that lacks materials for transmissive optics.

Dielectric metasurfaces consist of transparent nanostructures with subwavelength separation, which manipulate the phase of light on the nanoscale (*1*). This elaborate control is revolutionizing modern optics: Metasurfaces can replace bulk optics by thin and flat elements (*2*, *3*), combine multiple functions in single optical elements (*4*, *5*), and be used to realize innovative optical components that induce, for example, freely designable optical angular momentum (*6*) and polarization (*7*, *8*). Technology, including modern semiconductor lithography, demands this design liberty for innovative optical elements for ever-shorter wavelength radiation, but this development has been stalled at ultraviolet frequencies where dielectrics stop being transparent. To our knowledge, linear metaoptics have only been demonstrated down to a wavelength of ≈250 nm (*9*–*11*). Nonlinear metasurfaces reach further into the ultraviolet spectrum at the cost of indirect light-shaping mechanisms and have, at present, been demonstrated down to a wavelength of 185 nm (*12*–*15*).

Inaccessible to metasurface design has been extreme ultraviolet radiation (EUV), which covers the wavelength range from 10 to 121 nm and corresponds to a photon energy of 10 to 124 eV (*16*). This wavelength regime receives appreciable attention as a gateway to achieving attosecond temporal resolution in ultrafast spectroscopy (*17*) and lithographically fabricating nanometer-scale transistors in state-of-the-art semiconductor industry (*18*). However, today, all fields that use EUV radiation are encumbered by handling problems that arise from being limited to reflective or binary optics [e.g., toroidal mirrors or Fresnel zone plates; see (*19*) for an overview of existing technology]. Here, we present a new physical mechanism for metasurface design and demonstrate how linear metasurfaces can be realized at a wavelength of 50 nm, thus providing the foundation for general-purpose transmissive optics technology for EUV radiation.

[1]John A. Paulson School of Engineering and Applied Sciences, Harvard University, Cambridge, MA 02138, USA. [2]Institute of Experimental Physics, Graz University of Technology, 8010 Graz, Austria.
*Corresponding author. Email: mossiander@g.harvard.edu (M.O.); capasso@seas.harvard.edu (F.C.); schultze@tugraz.at (M.S.)
†These authors contributed equally to this work.

Principle of vacuum guiding and metalens design

In the EUV, the strong absorption of most materials and their near-unity real part of the refractive indexes (*20*) usually prevent effective refraction or waveguiding. The refractive indexes of most dielectrics in the visible spectrum are determined by electronic transitions in the ultraviolet, that is, by resonances whose frequencies are higher than the frequency ω of visible light. In the Drude-Lorentz oscillator model, this results in a complex refractive index $\tilde{n}(\omega) = n(\omega) + i\kappa(\omega)$ for visible light, with a real part $n \geq 1$, the imaginary unit i, and a negligible absorption coefficient κ. By contrast, EUV light oscillates faster than these electronic resonance frequencies, resulting in $n \leq 1$ and a large absorption coefficient κ, which renders conventional transmissive metaoptics design unfeasible. For the same reason, EUV manipulation must rely on reflective glancing-angle mirrors in vacuum. The concept for metasurface design introduced here is visualized in Fig. 1: In the EUV spectrum, vacuum or air ($n = 1$) has a refractive index that is larger than that of a pillar made from $n < 1$ material; therefore, the pillar cannot guide or confine light. However, a void or hole ($n = 1$), that is, the absence of material, in a layer with material index $n < 1$ can act as a waveguide core surrounded by a lower-index cladding. Therefore, truncated waveguide metasurfaces are possible in the EUV by following an inverted design scheme that tunes nanohole dimensions instead of the shapes of free-standing nanostructures.

Materials with $n < 1$ that can be used to realize such metasurfaces exist throughout the EUV; for example, aluminum, silicon, and beryllium allow optics for the wavelength range from 40 to 90 nm; scandium and boron cover 20 to 40 nm; and rhenium, molybdenum, and zirconium cover 10 to 20 nm. Figure S1 compiles the refractive indexes and the transmission of these materials. Because of the availability of high-brightness laser-driven tin plasma sources, 13.5 nm is a wavelength of major importance for semiconductor lithography (*18*). At this wavelength, for example, ruthenium has the complex refractive index $\tilde{n} = 0.88 + 0.02i$ (*21*).

For the implementation of this concept, we chose a thin membrane of crystalline silicon as the base material and a cylindrical hole as the polarization-independent guiding structure. These are schematically shown (Fig. 1, A and C) together with the real part of the silicon refractive index in the EUV (*22*) and the transmission through a 220-nm-thick silicon layer (Fig. 1B). To highlight the vacuum-guiding behavior of the holes, the simulated intensity profile of light with a vacuum wavelength of λ_{vac} = 50 nm incident on such a perforated silicon membrane [80-nm hole diameter in a square 120-nm–by–120-nm unit cell, periodic boundary conditions; see section 1 of (*19*) for simulation details] is plotted in Fig. 1D: At the center of the membrane (110 nm after its front surface), 84% of the energy of an incident plane wave is transmitted within the hole, whereas 16% of its energy is transmitted in the silicon. However, the hole only covers 34% of the unit-cell area. Because most power is transmitted in vacuum, absorption in silicon is limited, and the overall transmission is enhanced relative to that of the unstructured film: An unstructured 220-nm-thick silicon membrane transmits 28% of incoming 50-nm light. Accounting for the 80-nm-diameter hole using its area coverage would increase transmission to 52%. Vacuum guiding increases the transmission further to 67%.

Although perforations have been used in nano-optics before, the presented guiding mechanism is fundamentally different from antiguiding in holes (*23*), low-index guiding in air (*24*), or hollow-core fibers (*25*). Furthermore, the enhancement does not require a periodic structure, which distinguishes the effect from extraordinary optical transmission (*26*).

To realize our EUV metasurface (Fig. 1A), with full design flexibility to emulate the phase profile of a desired optical element, we numerically created a library of meta-atoms based on the transmission phase of holes with 20- to 80-nm diameters in a 220-nm-thick silicon membrane [see section 1 of (*19*) for simulation details]. Notably, between wavelengths of 50 and 62 nm, the photon energy–dependent transmission phase is widely tunable by the

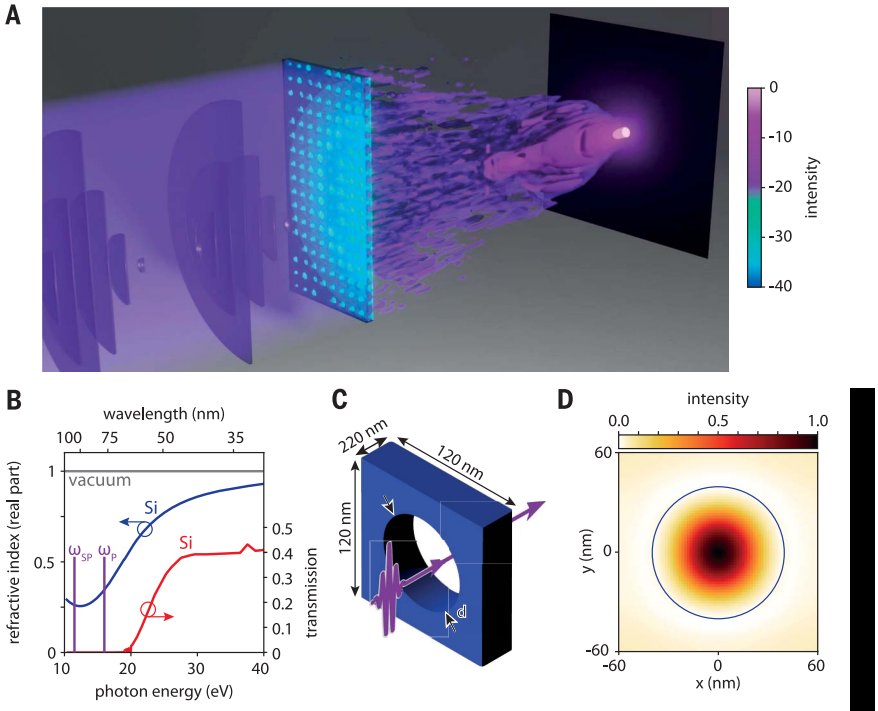

Fig. 1. Vacuum-guiding enables EUV metalenses. (**A**) Concept and simulation of a metalens that is focusing EUV: We impart the phase profile of an aspheric focusing lens on light pulses with a vacuum wavelength of 50 nm (purple disks) using holes through a silicon membrane (rectangular area). Because the refractive index of silicon is smaller than unity in parts of the EUV spectrum, holes through silicon concentrate incoming light. This effect relaxes subwavelength requirements for creating metasurfaces, allows us to impart a hole size–dependent phase shift using feature sizes on the order of the vacuum wavelength, and increases transmission through the absorbing membrane. The false color plot illustrates this light concentration in the holes and how the ultraviolet radiation collapses into a focus after propagating the focal length. For better visibility, we cut the displayed metasurface and the light-intensity distribution along a plane that includes the optical axis. Further simulation details are presented in Fig. 4. (**B**) Photon energy–dependent real part of the refractive index of crystalline silicon [blue line, data from (*22*)] in the EUV spectrum and intensity transmission of a 220-nm-thick silicon membrane (red line). The frequencies of the bulk ω_P and surface plasmon ω_{SP} are marked in purple. (**C**) Schematic and setup for meta-atom simulation: EUV light (purple arrow) passes through a 220-nm-thick crystalline silicon membrane (blue) with a hole with diameter *d*. We model a single unit cell (120 nm by 120 nm) with periodic boundary conditions. (**D**) Finite-difference time-domain simulation of EUV vacuum-guiding through an 80-nm-diameter hole in a 220-nm-thick silicon membrane. The false color plot shows the transverse beam intensity profile of light with a vacuum wavelength of 50 nm at the midpoint of the silicon membrane along the propagation direction, that is, 110 nm after the front surface. The hole is indicated as a blue circle. The simulation setup in three dimensions is shown in (C). The hole covers 34% of the total area; however, 84% of the energy is transmitted within the hole and only 16% of the energy is found in silicon. The intensity decays exponentially into the silicon cladding because of the refractive index contrast. The overall transmission of the patterned 220-nm-thick silicon membrane is 67%.

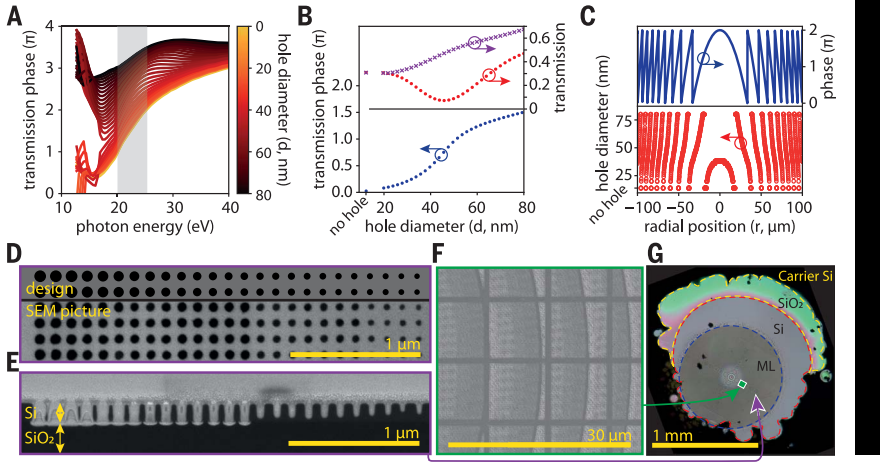

Fig. 2. Design and fabrication of an EUV metalens. (**A**) Photon energy–dependent transmission phase of holes in a 220-nm-thick silicon membrane (see Fig. 1C for the unit cell), color coded for different hole sizes. The gray area indicates the region where hole diameters from 20 to 80 nm offer phase coverage larger than 1.5π, which is enough to achieve efficient and diffraction-limited focusing (*27*). (**B**) Overall hole diameter–dependent intensity transmission (purple crosses) and transmission phase in the forward direction (blue circles) of the resulting meta-atom library at 50-nm wavelength (25-eV photon energy). Because the 120-nm–by–120-nm unit-cell size is comparable to the wavelength, low diffraction orders can be generated for holes that cause a transmission phase shift close to π (diameters around 45 nm). When plotting only the transmission into the zeroth diffraction order (red circles) of a periodic array of same-diameter holes, this causes a dip in the transmission. Because hole diameters spatially vary in a metalens and light from all holes interferes constructively to a focus, the more uniform overall transmission (purple crosses) is a better gauge to judge transmission uniformity. (**C**) Target transmission-phase profile (blue line) of a metalens with focal length *f* = 10 mm at 50-nm wavelength, calculated from Eq. 1 modulo 2π, and the corresponding matched hole diameter (red circles) using the library of (B) to realize the metalens. (**D**) Shown at the bottom is a scanning electron microscope (SEM) picture of a 3-μm–by–0.5-μm portion of the metalens with 1-mm diameter and 10-mm focal length designed for 50-nm wavelength. The position where the picture was taken on the metalens is marked by the purple arrow in (G). Shown at the top is the design of the metalens in this area [compare with (C)]. (**E**) Cross section of a metalens fabricated using the same recipe as the lens in (D) on the silicon-on-insulator carrier wafer obtained using focused-ion-beam milling and SEM. The position where the picture was taken on the metalens is marked by the purple arrow in (G). (**F**) Zoomed-out SEM picture of a 34-μm–by–31-μm portion of the metalens. The position where the picture was taken on the metalens is marked by the green rectangle in (G). The focusing pattern of the metalens is apparent from the ring segments, which show decreasing width from left to right. Every 10 μm, holes are omitted to increase the stability of the metalens, which is visible as a square scaffolding pattern. The symmetry of the scaffolding is intentionally different from the symmetry of the metasurface to increase stability. (**G**) Optical microscope picture of the final metalens membrane. The metalens (ML) is encircled by the dashed blue line. Because its features are too small to be resolved at this magnification, the metalens shows a moiré pattern (ring patterns and bright area at the center; an enlarged image is provided in fig. S4). The unpatterned silicon membrane area appears solid gray (encircled by the dashed red line). Areas with a remaining buried oxide layer appear red and green because of thin-film interference (encircled by the dashed yellow line). The silicon carrier wafer appears black.

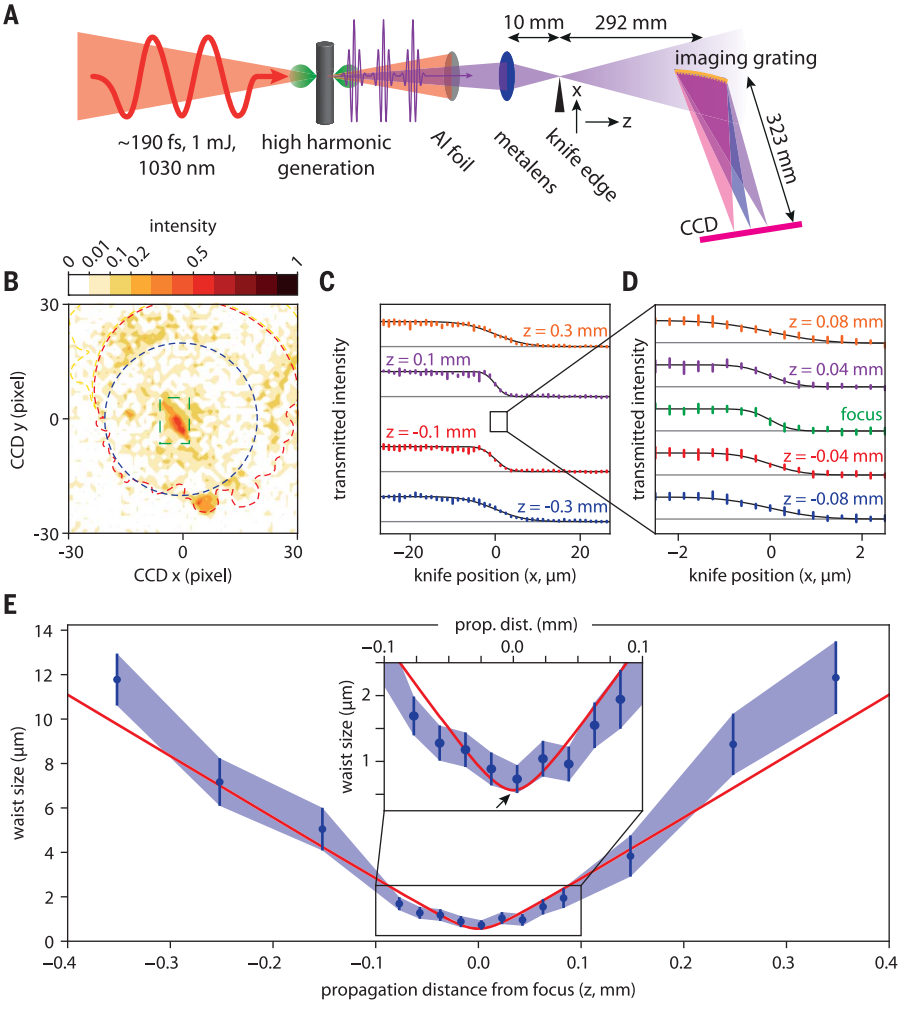

Fig. 3. Experimental demonstration of EUV metalens focusing. (**A**) An intense near-infrared femtosecond laser pulse (red arrow and area) is focused into an argon gas target (green) to generate an attosecond pulse train (purple arrow and area) by high-harmonic generation. Near-infrared radiation is blocked using an aluminum filter foil (gray). The attosecond pulse train is then focused using the metalens (blue) pictured in Fig. 2. At the position of the focus along the propagation direction (marked *z*), a knife-edge scan is performed using a razor blade mounted on a piezo stage moving along the transverse beam direction (marked *x*). Afterward, the attosecond pulse train's spectral components are split using a grazing incidence toroidal grating, and the focal plane is imaged on a charge-coupled device (CCD) camera. (**B**) EUV beam profile after the metasurface (false color plot) at 25.3-eV photon energy (21st harmonic of the driving laser at 1030-nm wavelength) detected by the CCD. For comparison, we repeat the outlines from the microscopy image in Fig. 2G: The dashed blue line marks the metasurface, and the dashed red line marks the unpatterned silicon area. The granular structure with low intensity is already present in the incoming beam profile, which is plotted in fig. S5. The focal spot created by the metalens, which is imaged onto the CCD using the toroidal grating, is marked by the green dashed rectangle. It appears larger than the real focus because of the limited numerical aperture of the toroidal grating and aberrations caused by the imaging system. (**C**) Knife-edge scans for different positions along the propagation direction of the metasurface-focused beam [movement direction marked *z* in (A)]. The colored lines show the knife position–dependent [movement direction marked *x* in (A)] integrated photon flux detected by the CCD camera in the focus area. As the razor blade moves into the focus, it blocks part of the transmitted radiation and decreases the transmitted flux. A large negative derivative of the flux represents a small focus. The error bars represent the standard deviation of three measurements. The black lines are least-squares fits to the data assuming a Gaussian focus profile. (**D**) Same as (C) but in close proximity to the focus. The error bars represent the standard deviation of 10 measurements. (**E**) Propagation direction–dependent waist sizes extracted from the fits in (C) and (D) (blue dots). The error bars represent the 95% confidence interval. The red line is a fit to the waist sizes assuming Gaussian beam propagation. The inset shows a zoomed-in view of the propagation direction–dependent waist size close to the focus [extracted only from the fits in (D)]. The minimum waist sizes reported in the text are marked by the black arrow.

hole diameter and offers more than 1.5π transmission phase coverage with an average transmission of 40% at 50 nm (see Fig. 2A for the photon energy–dependent transmission phase, Fig. 2B for the transmission and transmission phase at 50 nm, and fig. S2 for the photon energy dependent transmission). This transmission-phase coverage is enough to achieve efficient and diffraction-limited focusing, as explored, for example, in (*27*). The metasurface unit cell is shown in Fig. 1C, and the corresponding library is shown in Fig. 2B.

Experimental results

To experimentally prove that the vacuum-guiding concept yields viable EUV metalenses, we forward-designed a focusing EUV metasurface by mimicking the wavelength-dependent transverse hyperbolic phase profile (*28*)

$$\varphi(r,\lambda_{vac}) = -\frac{2\pi}{\lambda_{vac}}\left(\sqrt{r^2+f^2}-f\right) \quad (1)$$

of an aspheric lens with focal length $f = 10$ mm in vacuum at transverse position $r = \sqrt{x^2+y^2}$ (x and y are the cartesian coordinates centered at the beam axis). This analog phase profile is matched by a simulated digital phase profile (sampled at positions x, y; $x = k\Delta x$; $y = l\Delta y$; $k, l \in \mathbb{Z}$; and $\Delta x = \Delta y = 120$ nm; k and l are integer indexes) using the hole library (Fig. 2B), yielding a recipe for the required hole-diameter distribution (Fig. 2C). The metalens is designed for a central vacuum wavelength of $\lambda_{vac} = 50$ nm, where silicon features a refractive index $\tilde{n} = 0.77 + 0.02i$. The smaller-than-unity real part at this wavelength partially relaxes the necessity for true subwavelength patterning, which facilitates the manufacturing of the meta-optical element. In the given implementation, the maximum feature size (80 nm) and unit cell size (120 nm) correspond to 1.2 and 1.8 times the inside-silicon wavelength λ_{Si}, respectively. Although this does not entirely prevent the formation of low diffraction orders that contain up to 53% of the transmitted light, it still allows the realization of numerical apertures up to NA $< \frac{\lambda_{vac}}{2\Delta x} = 0.2$ following the Nyquist theorem (*29*).

The demonstration sample, a free-standing metalens with a 1-mm diameter (numerical aperture $NA_{max} = 0.05$), is realized from silicon-on-insulator wafers [see section 2 of (*19*) and fig. S3 for fabrication details]. Figure 2, D and F, shows scanning-electron microscopy pictures of the final sample after metasurface etching but before membrane isolation. Figure 2G shows a light microscopy picture of the finished membrane, with thin-film interference colors confirming the complete removal of the buried oxide layer in the lens area. We achieved the designed hole diameters (see Fig. 2D) using both diameter-dependent electron beam lithography doses and diameter-dependent fabrication offsets [see section 2 of (*19*)]. A focused-ion-beam cut (Fig. 2E) through a sample reveals holes

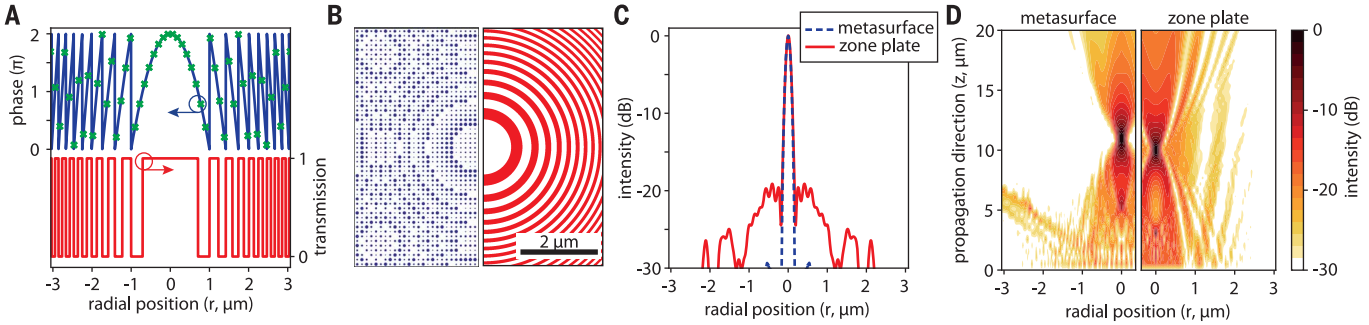

Fig. 4. Finite-difference time-domain modeling and benefits of an EUV metalens. (**A**) Target transverse-phase profile (blue line) of a diffraction-limited metalens (focusing length f = 10 μm, size 6 μm by 6 μm) designed for incoming light with 50-nm wavelength (25-eV photon energy) and sampling of this phase profile with the library presented in Fig. 2 (green crosses). As a comparison, the transmission profile of a binary intensity Fresnel zone plate with the same numerical aperture, focal length, and size is also shown (red line). (**B**) On the left is a two-dimensional design of a metasurface that realizes the phase profile in (A). White areas represent a 220-nm-thick silicon membrane, and blue areas represent holes through the silicon membrane. On the right is a two-dimensional design of a binary intensity Fresnel zone plate that realizes the transmission profile in (A). White areas are perfectly transmitting, and red areas are perfectly absorbing. (**C**) Modeled transverse intensity cuts through the focus generated by the metasurface (blue dashed line) and the zone plate in (B) (red line) for incoming light with 50-nm wavelength (25-eV photon energy) and illumination by a Gaussian beam with a 2-μm waist. The zone-plate focus has characteristic side lobes that are not present in the metasurface focus. (**D**) Shown on the left is the modeled light-intensity evolution (false color plot) after the metasurface pictured in (B) focuses the Gaussian beam described in the caption of (C). Shown on the right is the modeled light-intensity evolution (false color plot) after the zone plate pictured in (B) focuses the same Gaussian beam.

with square sidewalls and a partial etch of the smallest diameter holes. Because of the small transmission-phase difference between a membrane with small holes and a solid membrane (see Fig. 2B), the resulting phase error is smaller than 0.1π and can be corrected during meta-atom library calculation.

For experimental verification of the focusing power of the metalens, we generated diverging EUV attosecond pulse trains through near-infrared femtosecond laser pulse–driven high-harmonic generation in argon gas (*30*–*32*) [Fig. 3A and section 3 of (*19*)]. The frequency up-conversion extends up to the 35th order (42.1-eV photon energy, 29-nm wavelength) of the driving laser pulses (1.2-eV photon energy, 1030-nm wavelength), with spectral power concentrated around the laser's odd harmonics. A toroidal EUV grating disperses the spectral components of the attosecond pulse train and creates a frequency-resolved image of the focal plane on an EUV-sensitive camera where the metasurface's effect at the design wavelength can be inspected.

Figure 3B shows the beam profile at the focal plane of the metalens of the 21st harmonic with 25.3-eV photon energy and 49-nm wavelength (close to the design wavelength of the optics). The outline of the circular metasurface (dashed blue line) and features caused by the remaining silica aperture (dashed red and yellow lines; compare with Fig. 2G and fig. S4) are also visible. The bright focal spot at the metasurface center (dashed green line) presents experimental evidence for the viability of the EUV metalens to focus incident light.

Because the grazing incidence toroidal imaging grating provides a considerably smaller numerical aperture than the metasurface and introduces aberrations and astigmatism, the obtained image does not determine the focal spot diameter and underestimates the focusing power of the optical element. To determine the real focal spot size produced by the metasurface, we implemented a knife-edge scan [see Fig. 3A and (*33*)], where part of the focused beam in the focal plane is gradually blocked by a razor blade translated along the x direction indicated in Fig. 3A and the position-dependent transmitted intensity is recorded. As focusing concentrates the beam intensity along the transverse direction, the negative spatial derivative of the recorded x-dependent intensity reveals the beam profile. Figure 3, C and D, displays scan results for different planes along the propagation direction around the focus. Figure 3D includes a knife-edge scan that features a maximum negative spatial derivative, which is indicative of the focal plane. Under the assumption of a cylindrically symmetric Gaussian beam, the corresponding beam size is extracted by fitting an error function to the data at each position along the propagation direction (Fig. 3E) (*33*).

We observe that the metasurface focuses the illuminating beam to a minimum waist of $w_0^{\text{metasurface}} = 0.7 \pm 0.3$ μm [all reported waists w are measured using the $1/e^2$ intensity, that is, $I(r = \sqrt{x^2 + y^2} = w) = I(r = 0)/e^2$]. Using the Rayleigh-Sommerfeld diffraction integral (*34*), we calculated the minimum achievable waist $w_0^{\text{diffractionlimit}} = 0.45$ μm, assuming diffraction-limited focusing of our incoming beam (see fig. S5), which highlights that the metalens already performs within 1.6 times of the diffraction limit. For further comparison, the measured propagation distance–dependent waist size $w(z)$ can be fitted to that of a focused Gaussian beam with minimum waist w_0 (*35*) in vacuum:

$$w(z) = w_0\sqrt{1 + \left(\frac{z\lambda_{\text{vac}}}{\pi w_0^2}\right)^2} \qquad (2)$$

The fit (see Fig. 3E) suggests a minimum possible waist size of $w_0^{\text{metasurface}} = 0.56 \pm 0.03$ μm, which is even closer to the diffraction limit. Both results overlap within the experimental uncertainty. We attribute the deviation from the diffraction limit to imperfections in the EUV beam guiding and filtering optics and possible residual corrugations of the silicon membrane. For comparison, achieving similar spot sizes using the near-infrared driving laser would require close-to-unity numerical apertures; in the EUV, only a numerical aperture of 0.05 is required (*36*).

Aside from the focusing power, the transmission properties are crucial for future applications. Photons with wavelengths shorter than 100 nm possess enough energy to overcome the bandgap of all known dielectrics; therefore, large absorption is unavoidable (*37*). Nonetheless, owing to the vacuum guiding concept, our sample transmits more than 10% of all incoming 49-nm light and focuses 48% of the transmitted 49-nm light, which limits the root-mean-squared metalens wavefront error (*38*) due to fabrication accuracy to $\lambda_{\text{vac}}/10$ [λ_{vac} = 49 nm; see section 4 of (*19*) for details]. Such fine-granular phase control not only is a prerequisite for focusing but also opens the door for the future demonstration of optical angular

momentum plates and general holograms at EUV wavelengths.

Simulation of Nyquist-limited focusing

To further explore the potential of EUV metalenses, we investigated a metalens design with focal length f = 10 μm and overall optics diameter d = 6 μm (see Fig. 4A for the phase profile and Fig. 4B for the final design). We then simulated the focusing of a linearly polarized Gaussian beam using finite-difference time-domain modeling [illuminating Gaussian beam waist $w^{\text{illum.}}$ = 2 μm, and effective numerical aperture $\text{NA}_{\text{eff}} = \sin\left[\tan^{-1}\left(\frac{w^{\text{illum.}}}{f}\right)\right] \approx \frac{w^{\text{illum.}}}{f} = 0.2$ (*36*), which corresponds to the maximum realizable numerical aperture given by the Nyquist sampling theorem and our unit cell size (*29*); see section 1 of (*19*) for simulation details].

Figure 4D shows the formation of the metasurface focus. Even under these challenging conditions, the metasurface focus closely approaches the diffraction limit ($w_0^{\text{diffractionlimit}}$ = 85 nm) with a minimum beam waist $w_0^{\text{metasurface}}$ = 94 nm. The metalens focusing properties for a light pulse with extended bandwidth are explored in section 5 of (*19*) and fig. S6. Having the unit cell size be of the order of the design wavelength causes diffraction of ~53% of the incident power away from the beam axis into the diffraction orders of the quasi-periodic unit-cell arrangement. Adding an unpatterned layer of silicon with a refractive index n = 0.77 and a thickness on the order of half a wavelength after the metalens changes the grating condition in transmission and would prevent the creation of most of these propagating diffraction orders [because it limits the grating indices $p, q \in \mathbb{Z}$ that satisfy the transverse momentum wavevector condition $nk_0 = \sqrt{\left(\frac{2\pi p}{\Delta x}\right)^2 + \left(\frac{2\pi q}{\Delta y}\right)^2 + (nk_z)^2}$, with the overall momentum k_0 and the momentum along the layer normal k_z].

For thorough comparison, we also modeled the focal profile of a binary absorption zone plate with equal numerical aperture (see Fig. 4A for the absorption profile and Fig. 4B for the design). The juxtaposition of the focal profiles generated by the zone plate and the metalens shown in Fig. 4D highlights notable differences in focus quality and corroborates the benefit of the innovative metalens. A comparison with state-of-the-art technology [see (*39*) for a zone plate with comparable outermost zone width and section 6 of (*19*) for a summary of EUV focusing optics] highlights that the zone plate creates side lobes in its focal plane, which is an unavoidable property of zone plate foci (*40*). By contrast, because the metasurface realizes the focusing phase profile accurately by suppressing spherical aberrations, no sidelobes are visible. Furthermore, because vacuum guiding decreases absorption and no energy is lost to sidelobes, the maximum intensity in the metasurface focus exceeds that of the zone plate by 9%. The transverse focal cuts in Fig. 4C highlight this behavior: Unwanted features present in the focal plane are suppressed by more than 10 dB for the metasurface compared with the zone plate.

Concluding remarks

The transfer of metasurface technology, with its associated superior design freedom to the EUV spectral region, provides a general route to manufacture transmissive optics in this frequency range. This capability should lead to applications such as microscopy with unprecedented spatial and temporal resolution, orbital angular momentum beams with ultrahigh frequency, and structured light that has direct access to core-level electronic transitions in atoms and molecules. EUV lithography has become the main enabling fabrication technology that allows us to keep up with Moore's law (*18*); conversely, metasurface-based optics can be fabricated with deep ultraviolet lithography in the same semiconductor foundries of mainstream complementary metal-oxide-semiconductor (CMOS) technology (*27*). This convergence of semiconductor-processing technology and optics will expand to the realization of metaoptics using EUV lithography, further shrinking feature sizes and increasing the complexity of nanostructure shapes. In turn, with metasurfaces operating in the EUV, they will enable a new generation of lithography optics.

REFERENCES AND NOTES

1. S. M. Kamali, E. Arbabi, A. Arbabi, A. Faraon, *Nanophotonics* **7**, 1041–1068 (2018).
2. N. Yu *et al*., *Science* **334**, 333–337 (2011).
3. M. Khorasaninejad *et al*., *Science* **352**, 1190–1194 (2016).
4. N. Mahmood *et al*., *Nanoscale* **10**, 18323–18330 (2018).
5. C. Spägele *et al*., *Nat. Commun.* **12**, 3787 (2021).
6. R. C. Devlin, A. Ambrosio, N. A. Rubin, J. P. B. Mueller, F. Capasso, *Science* **358**, 896–901 (2017).
7. N. A. Rubin *et al*., *Science* **365**, eaax1839 (2019).
8. Y. Intaravanne, X. Chen, *Nanophotonics* **9**, 1003–1014 (2020).
9. Y. Deng *et al*., *Adv. Mater.* **30**, e1802632 (2018).
10. K. Huang *et al*., *Laser Photonics Rev.* **13**, 1800289 (2019).
11. C. Zhang *et al*., *Light Sci. Appl.* **9**, 55 (2020).
12. H. Liu *et al*., *Nat. Phys.* **14**, 1006–1010 (2018).
13. A. Ahmadivand *et al*., *Nano Lett.* **19**, 605–611 (2019).
14. M. Semmlinger *et al*., *Nano Lett.* **19**, 8972–8978 (2019).
15. M. L. Tseng *et al*., *Sci. Adv.* **8**, eabn5644 (2022).
16. W. K. Tobiska, A. Nusinov, in *35th COSPAR Scientific Assembly* (Committee on Space Research, 2004), pp. 1–10.
17. F. Krausz, M. Ivanov, *Rev. Mod. Phys.* **81**, 163–234 (2009).
18. B. Turkot, S. Carson, A. Lio, in *2017 IEEE International Electron Devices Meeting (IEDM)* (IEEE, 2017), pp. 14.4.1–14.4.3.
19. Materials and methods are available as supplementary materials.
20. A. Thompson *et al*., "X-ray data booklet" (LBNL/PUB 490 Rev. 3, Lawrence Berkeley National Laboratory, 2009).
21. D. L. Windt, *Comput. Phys.* **12**, 360–370 (1998).
22. E. D. Palik, G. Ghosh, Eds., *Handbook of Optical Constants of Solids* (Academic Press, 1998).
23. S. W. D. Lim, M. L. Meretska, F. Capasso, *Nano Lett.* **21**, 8642–8649 (2021).
24. M. Hentschel *et al*., *Light Sci. Appl.* **12**, 3 (2023).
25. C. M. Smith *et al*., *Nature* **424**, 657–659 (2003).
26. T. W. Ebbesen, H. J. Lezec, H. F. Ghaemi, T. Thio, P. A. Wolff, *Nature* **391**, 667–669 (1998).
27. J.-S. Park *et al*., *Nano Lett.* **19**, 8673–8682 (2019).
28. W. T. Chen *et al*., *Nat. Nanotechnol.* **13**, 220–226 (2018).
29. S. M. Kamali, E. Arbabi, A. Arbabi, Y. Horie, A. Faraon, *Laser Photonics Rev.* **10**, 1002–1008 (2016).
30. P. B. Corkum, *Phys. Rev. Lett.* **71**, 1994–1997 (1993).
31. M. Lewenstein, P. Balcou, M. Y. Ivanov, A. L'Huillier, P. B. Corkum, *Phys. Rev. A* **49**, 2117–2132 (1994).
32. A. L'Huillier, K. J. Schafer, K. C. Kulander, *J. Phys. At. Mol. Opt. Phys.* **24**, 3315–3341 (1991).
33. A. H. Firester, M. E. Heller, P. Sheng, *Appl. Opt.* **16**, 1971–1974 (1977).
34. R. L. Lucke, "Rayleigh-Sommerfeld diffraction vs Fresnel-Kirchhoff, Fourier propagation, and Poisson's spot" (NRL/FR/7218-04-10,001, Naval Research Laboratory, 2004).
35. B. E. A. Saleh, M. C. Teich, *Fundamentals of Photonics* (Wiley, 2007).
36. H.-S. Chon *et al*., *J. Opt. Soc. Am. A Opt. Image Sci. Vis.* **24**, 60–67 (2007).
37. M. Ossiander *et al*., *Nat. Commun.* **13**, 1620 (2022).
38. M. Rimmer, *Appl. Opt.* **9**, 533–537 (1970).
39. J. Zhu *et al*., *Chin. Phys. B* **29**, 047501 (2020).
40. G. W. Webb, I. V. Minin, O. V. Minin, *IEEE Antennas Propag. Mag.* **53**, 77–94 (2011).
41. M. Ossiander *et al*., figshare (2023); https://doi.org/10.6084/m9.figshare.22191457.

ACKNOWLEDGMENTS

Funding: This work was performed, in part, at the Center for Nanoscale Systems (CNS), a member of the National Nanotechnology Coordinated Infrastructure (NNCI), which is supported by the NSF under award no. ECCS-2025158. CNS is a part of Harvard University. The computations in this paper were run on the FASRC Cannon cluster supported by the FAS Division of Science Research Computing Group at Harvard University. M.O. acknowledges funding by the Alexander von Humboldt Foundation (Feodor-Lynen Fellowship), the Austrian Science Fund (FWF, Start Grant Y1525), and the European Union (grant agreement 101076933 EUVORAM). The views and opinions expressed are, however, those of the author(s) only and do not necessarily reflect those of the European Union or the European Research Council Executive Agency. Neither the European Union nor the granting authority can be held responsible for them. S.W.D.L. is supported by A*STAR Singapore through the National Science Scholarship Scheme. F.C. acknowledges financial support from the Air Force Office of Scientific Research (AFOSR) under award number FA9550-21-1-0312. **Author contributions:** M.O. developed the project, designed the metalenses, and conducted the numerical modeling. M.L.M. fabricated the samples. M.L.M., S.W.D.L., and M.O. imaged the samples. H.K.H., M.O., N.K., T.J., and M.S. designed, conducted, and analyzed the experiment. M.O., M.S., and F.C. wrote the manuscript. All authors discussed the final version of the manuscript. **Competing interests:** M.O., M.L.M., S.W.D.L., and F.C. have filed a provisional patent application (US 63/385,066). The authors declare no other competing interests. **Data and materials availability:** The data that support the findings of this study are included in the manuscript and the supplementary materials and are archived at figshare (*41*). **License information:** Copyright © 2023 the authors, some rights reserved; exclusive licensee American Association for the Advancement of Science. No claim to original US government works. https://www.science.org/about/science-licenses-journal-article-reuse

SUPPLEMENTARY MATERIALS

science.org/doi/10.1126/science.adg6881
Materials and Methods
Figs. S1 to S6
References (*42*–*62*)

Submitted 15 January 2023; accepted 7 March 2023
10.1126/science.adg6881

POLYMER CHEMISTRY

Chemically circular, mechanically tough, and melt-processable polyhydroxyalkanoates

Li Zhou[1]†, Zhen Zhang[1]†, Changxia Shi[1], Miriam Scoti[1,2], Deepak K. Barange[1], Ravikumar R. Gowda[1], Eugene Y.-X. Chen[1]*

Polyhydroxyalkanoates (PHAs) have attracted increasing interest as sustainable plastics because of their biorenewability and biodegradability in the ambient environment. However, current semicrystalline PHAs face three long-standing challenges to broad commercial implementation and application: lack of melt processability, mechanical brittleness, and unrealized recyclability, the last of which is essential for achieving a circular plastics economy. Here we report a synthetic PHA platform that addresses the origin of thermal instability by eliminating α-hydrogens in the PHA repeat units and thus precluding facile cis-elimination during thermal degradation. This simple α,α-disubstitution in PHAs enhances the thermal stability so substantially that the PHAs become melt-processable. Synergistically, this structural modification also endows the PHAs with the mechanical toughness, intrinsic crystallinity, and closed-loop chemical recyclability.

Polyhydroxyalkanoates (PHAs) are a class of polyester naturally accumulated biologically by living microorganisms (*1*–*8*) or synthetically produced chemocatalytically (*9*, *10*) from diverse feedstocks, especially biorenewable sources. They possess tunable thermomechanical properties and are biodegradable in the ambient environment, thus offering a more sustainable alternative to petroleum-derived and/or nondegradable plastics. Over the past 60+ years, the ring-opening polymerization (ROP) of four-membered β-lactones, such as β-butyrolactone (β-BL), and their derivatives with different substituents at α and β positions has been extensively studied to enable the chemical synthesis of PHAs, particularly poly(3-hydroxybutyrate) (P3HB), with atactic, iso-rich, syndio-rich, or syndiotactic stereomicrostructures (tacticities) (*9*–*16*). More recently, purely isotactic P3HB that has a number-average molar mass (M_n) of 154 kDa, a narrow dispersity ($Đ$) of 1.01, and a high melting-transition temperature (T_m) of 171° to 175°C (*17*); stereo-sequenced PHAs (*18*); polyolefin-like PHA copolymers (*19*); and alternating isotactic PHAs (*20*) have also been realized through the ROP of eight-membered dialkyl diolides ($8DL^R$). In addition to its isotactic polypropylene (*it*-PP)–like high T_m, the highly crystalline *it*-P3HB exhibits excellent barrier properties that are superior to those of commodity plastics widely used in packaging, such as polyethylene (PE) and polyethylene terephthalate (PET) (*21*). These attractive properties of PHAs, coupled with their biorenewability and biodegradability, offer a promising solution to combat the global plastics problem (*22*–*27*).

However, three long-standing challenges facing PHAs must be addressed before broad commercial implementation and applications can be realized. First, current PHAs are intrinsically thermally unstable, with a relatively low degradation temperature (T_d, the temperature at 5% weight loss) of ~250°C, owing to the presence of α-hydrogens that promote facile cis-elimination via the six-membered transition state to form an internal alkene and a carboxylic acid (Fig. 1A) (*28*–*31*), causing a large, continuous drop in shear viscosity under melt-processing conditions (Fig. 1B). Second, the mechanical performance of PHAs is generally inferior to that of commonly used plastics; for example, *it*-P3HB is extremely brittle with an elongation at break (ε_b) ~4%, which is much lower than that of *it*-PP (ε_b > 400%). Third, synthetic PHAs lack the desired closed-loop chemical recyclability. For example, the acid-catalyzed depolymerization of P3HB leads to formation of cyclic oligomers (which can be repolymerized to only oligomers with M_n ~5 kDa) (*32*, *33*), rather than its readily polymerizable monomer β-BL or $8DL^{Me}$ to close the loop, whereas the base-catalyzed depolymerization yields crotonic acid (*34*). Although biodegradability in the ambient environment is a distinct advantage of PHAs for protecting our environment if they are disposed there, they should not be landfilled as accumulation of degraded intermediates and eventual CO_2 will cause unintended environmental and climate problems. Additionally, the inability to recover the PHA building blocks represents a considerable loss of energy and resources that are still endowed in the postconsumer PHAs. Hence, it is critical to install the chemical circularity to the biodegradable PHAs toward an ultimate goal of establishing a circular plastics economy (*35*, *36*).

Strategies to suppress thermal degradation and achieve melt processability

A straightforward strategy to suppress thermal degradation due to cis-elimination enabled by α-hydrogens in conventional PHAs is to substitute both α-hydrogens with alkyl or aryl groups. When substituting only one α-hydrogen in the parent P3HB with a methyl group, the resulting poly(3-hydroxy-2-methylbutyrate) indeed shows improved thermal stability, but only by ~20°C relative to the P3HB used in that study (*37*). However, substituting both α-hydrogens yields poly(3-hydroxy-2,2-dimethylbutyrate) [P3H$(Me)_2$B], the thermal and mechanical properties of which are drastically enhanced: P3H$(Me)_2$B is not only semicrystalline, with high T_m's of 167° to 243°C as well as being thermally stable with high T_d's of 314° to 335°C (i.e., 56° to 85°C enhancement) and melt-processable, but also ductile, with ε_b >200% (Fig. 1, C and D). Moreover, P3H$(Me)_2$B can be chemically recycled back to its starting monomer, α,α-dimethyl-β-butyrolactone [$(Me)_2$BL], which is used in the chain-growth ROP, or 3-hydroxy-2,2-dimethylbutyric acid [3H$(Me)_2$BA], which is used in the step-growth polycondensation (SGP), thus accomplishing closed-loop chemical recyclability (Fig. 1C). Poly(3-hydroxy-2,2-dimethylpropionate), P3H$(Me)_2$P (M_n = 162 kDa, prepared from the ROP of α,α-dimethyl-β-propiolactone, table S1) also exhibits high T_d (up to 373°C) and T_m (up to 232°C) values, but it is extremely brittle with ε_b < 4% (figs. S1 to S3). The ROP of $(Me)_2$BL (prepared from highly reactive dimethyl ketene and acetaldehyde) was attempted, but only oligomeric species (M_n = 2.9 kDa) were obtained in 35% yield after 10 days (*38*). The method reported herein enabled the rapid synthesis of high–molar mass P3H$(Me)_2$B in quantitative yield and with M_n up to 554 kDa, T_m up to 243°C, and T_d up to 335°C. Overall, such thermal robustness of α,α-dimethylated PHAs enables their melt processability, despite further enhanced T_m values, and such PHAs exhibit the desired chemical circularity through closing the monomer-polymer-monomer loop.

Dual closed loops to achieve chemical circularity

The α,α-dimethylated PHA can be synthesized through either the SGP of hydroxyacid (HA) 3H$(Me)_2$BA or the ROP of lactone $(Me)_2$BL (Fig. 1C). The HA, 3H$(Me)_2$BA, was obtained in one step from acetaldehyde, which is produced at a large industrial scale and can also be biosourced, and isobutyric acid, a commercial chemical that can be obtained biologically from glucose (*39*), in 88% yield (see materials and methods for its synthesis at 362-g scale from methyl isobutyrate), whereas the lactone $(Me)_2$BL was prepared via one-step lactonization of the HA [e.g., 232 g of $(Me)_2$BL was

[1]Department of Chemistry, Colorado State University, Fort Collins, CO 80523-1872, USA. [2]Dipartimento di Scienze Chimiche, Università di Napoli Federico II, Complesso Monte S. Angelo, Via Cintia, 80126 Napoli, Italy.
*Corresponding author: Email: eugene.chen@colostate.edu
†These authors contributed equally to this work.

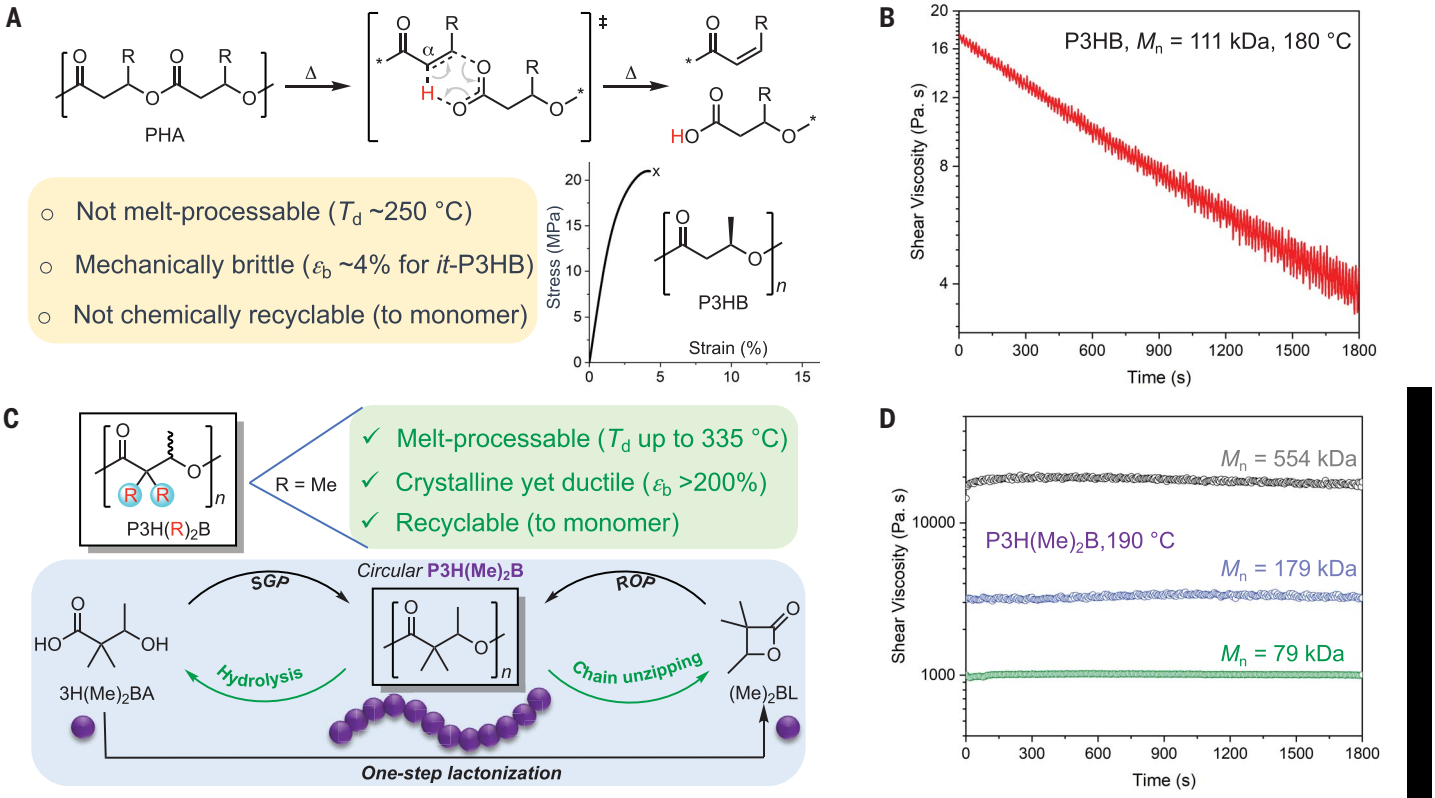

Fig. 1. Progress in PHA design. (**A**) Three challenges facing the current PHA (P3HB, in particular). (**B**) Shear viscosity (shear rate $\dot{r}$ = 1 s^{-1}) in melt (180°C) of *it*-P3HB (M_n = 111 kDa), showing a large, continuous drop in viscosity over 30 min owing to rapid degradation. Data were acquired from this study. (**C**) Redesigned α,α-disubstituted PHAs, P3H(R)$_2$B, devoid of α-hydrogens synergistically combine three desirable properties. Chemical circularity was achieved through closing both the hydroxyacid SGP, base-catalyzed hydrolysis and lactone ROP, based-catalyzed chain-unzipping loops for P3H(Me)$_2$B. (**D**) Shear viscosity ($\dot{r}$ = 1 s^{-1}) in melt (190°C) of P3H(Me)$_2$B with medium to high molar mass (M_n = 79 – 554 kDa), showing no decrease in viscosity over 30 min, indicating melt processability.

prepared in 93% yield]. The diethyl derivative, (Et)$_2$BL, was synthesized by use of the same lactonization method. Notably, the HA and lactone monomers can be prepared or recovered in good to quantitative yields from selective depolymerization of the PHA (see below).

At the outset, the ROP of (Me)$_2$BL (as a racemate) was explored by using different organic base catalysts and reaction conditions, and the ROP was optimized with superbase catalyst ^{t}Bu-P$_4$ {1-*tert*-butyl-4,4,4-tris(dimethylamino)-2,2-bis[tris(dimethylamino)phosphoranyliden-amino]2λ^5,4λ^5-catenadi(phosphazene)} in tetrahydrofuran (THF) at 70°C (table S1). Thus, the ROP in THF, with ^{t}Bu-P$_4$ as the catalyst and benzyl alcohol (BnOH) as the initiator, afforded P3H(Me)$_2$B with low M_n (22.1 kDa, $Đ$ = 1.02) to medium M_n (43.0 kDa, $Đ$ = 1.05) to high M_n (179 kDa, $Đ$ = 1.04; 554 kDa, $Đ$ = 1.06). Likewise, the ROP of (Et)$_2$BL in THF also led to the corresponding high–molar mass P3H(Et)$_2$B (M_n = 468 kDa, $Đ$ = 1.18) in near-quantitative yield (table S1). In a separate set of experiments that investigated the degree of control in the ROP, the molar mass was found to increase linearly with an increase of the [(Me)$_2$BL]/[^{t}Bu-P$_4$] ratio from 200:1 to 1600:1, whereas the dispersity of the resulting P3H(Me)$_2$B remained extremely narrow ($Đ$ ≤ 1.04), indicating the well-controlled ROP of (Me)$_2$BL (Fig. 2, A and B). The scalability of this ROP was tested in a polymerization using 125 g of (Me)$_2$BL under industrially relevant conditions: with a low catalyst loading [55 parts per million (ppm) ^{t}Bu-P$_4$], neat (solvent-free), and at 70°C. This scaled-up run achieved 96% monomer conversion and afforded 115 g of the pure P3H(Me)$_2$B in a 92% isolated yield.

To prepare a purely isotactic polymer sample for stereomicrostructural and thermal property analysis, we synthesized (*S*)-P3H(Me)$_2$B (M_n= 34.9 kDa, $Đ$ = 1.15) via the ROP of enantiopure (*S*)-(Me)$_2$BL. The perfect tacticity was characterized by the presence of only one carbonyl signal at 176.4 ppm and also a single signal at 46.9 and 12.6 ppm in ^{13}C nuclear magnetic resonance (NMR) spectra for the quaternary and methyl carbons, respectively (Fig. 2C). In comparison, the P3H(Me)$_2$B derived from (Me)$_2$BL with a 70:30 (*S*)/(*R*) ratio showed multiple signals in those regions, but most informatively, the new minor signal appeared at 45.91 ppm next to the 45.87-ppm major signal, indicative of an iso-rich tacticity. As predicted, those two signals present in the P3H(Me)$_2$B that was prepared from a 50:50 (*S*)/(*R*) ratio are approximately in equal abundance (Fig. 2C), indicating an atactic structure.

We envisioned another synergistic benefit of α,α-disubstitution that could endow the α,α-dialkylated PHA with chemical recyclability by direct depolymerization to its monomer, enabled by the *gem*-disubstituted Thorpe–Ingold effect that promotes ring closure and stabilization of strained rings (*40*–*44*). At the outset, depolymerization of a ROP-derived P3H(Me)$_2$B sample was screened at temperatures below 240°C under vacuum with different base catalysts (table S2), affording (Me)$_2$BL and side-product 2-methyl-2-butene with different ratios (fig. S18). For example, heating the sample with NaOH (5 wt %) at 210°C under

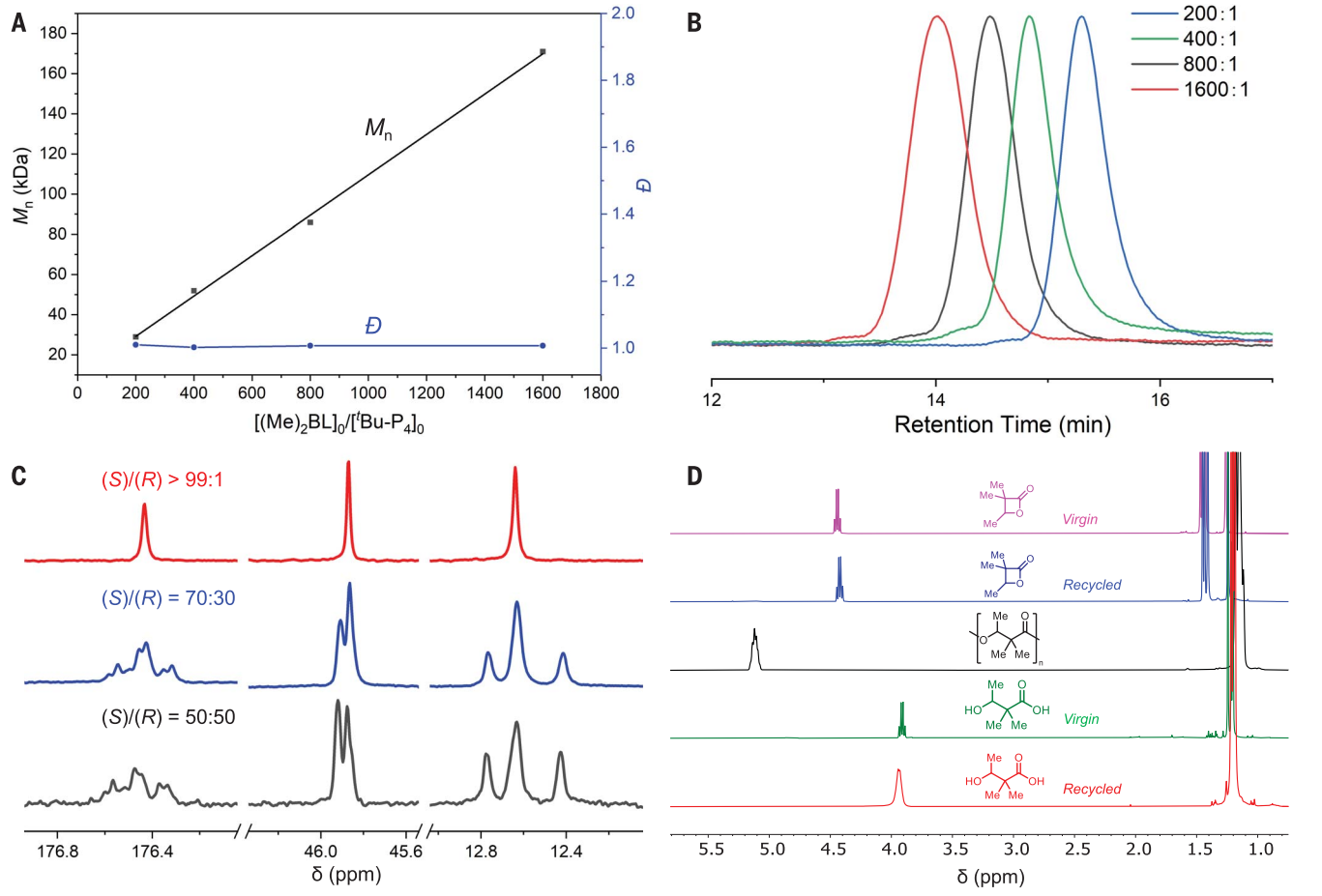

Fig. 2. ROP characteristics and chemical circularity. (**A**) Plots of M_n and $Đ$ values of the resulting P3H(Me)$_2$B as a function of the [(Me)$_2$BL]/[^{t}Bu-P$_4$] ratio (Me)$_2$BL/^{t}Bu-P$_4$ = 200:1, 400:1, 800:1, 1600:1; M_n ($Đ$) = 28.9 kDa (1.01), 51.9 kDa (1.01), 85.9 kDa (1.01), 179 kDa (1.04). (**B**) Size exclusion chromatography (SEC) curves for the P3H(Me)$_2$B samples produced at the different [(Me)$_2$BL]/[^{t}Bu-P$_4$] ratios. (**C**) Overlays of ^{13}C NMR spectra [(CF$_3$)$_2$CDOD] of P3H(Me)$_2$B derived from (Me)$_2$BL/^{t}Bu-P$_4$/BnOH = 800:0.5:1: (*S*)-(Me)$_2$BL/(*R*)-(Me)$_2$BL > 99:1 (red), = 70:30 (blue), = 50:50 (black). (**D**) Overlays of ^{1}H NMR spectra (23°C, CDCl$_3$) of the virgin (pink) and recycled (blue) lactone (Me)$_2$BL, virgin P3H(Me)$_2$B (black), and virgin (green) and recycled (red) HA monomer 3H(Me)$_2$BA.

vacuum recovered the pure (Me)$_2$BL monomer in 60% isolated yield (Fig. 2D and fig. S19) after the quick release of 2-methyl-2-butene as a gas, which was also recovered and could be reused. Next, through consecutive polymerization-depolymerization cycles, we achieved the circular monomer-polymer-monomer loop.

The second pathway to establish the closed-loop chemical recycling is through hydrolytic depolymerization of the PHA to the HA. For example, hydrolysis of P3H(Me)$_2$B (table S3) by aqueous LiOH enabled its depolymerization to form pure 3H(Me)$_2$BA in quantitative yield (Fig. 2D and fig. S21). The recovered HA can be transformed to (Me)$_2$BL via one-step lactonization (Fig. 1C). (Me)$_2$BL can also be obtained through NaOH (2 wt %)–catalyzed depolymerization of the oligomeric P3H(Me)$_2$B prepared through the SGP of 3H(Me)$_2$BA catalyzed by $BF_3{\cdot}OEt_2$ (Fig. 1C and fig. S22). These results demonstrate that the SGP of the HA can be used to obtain oligomers or polymers with low to medium molar mass, which are effectively depolymerized to form the lactone for the rapid ROP to high–molar mass PHAs.

Thermal properties and tacticity-independent (intrinsic) crystallinity

The isotactic (*R*)-P3H(Me)$_2$B exhibits a notably high T_m of 243°C (Fig. 3A and fig. S24), which is 68°C higher than that of (*R*)-P3HB (T_m = 175°C) (*17*). Moreover, the atactic *at*-P3H(Me)$_2$B, which is produced by the ROP of *rac*-(Me)$_2$BL catalyzed by the achiral organic catalyst ^{t}Bu-P$_4$, is also semicrystalline, with T_m values of 167° and 176°C (Fig. 3A and fig. S25). Thus, P3H(Me)$_2$B adds to rare examples of polymers exhibiting tacticity-independent crystallinity—a class of polymers that are intrinsically semicrystalline, having a similar degree of crystallinity regardless of the backbone tacticity, although the absolute T_m value varies as the tacticity changes (*45*, *46*). To probe the possibility of stereocomplex formation, we prepared a 1:1 physical blend of enantiomeric *it*-polymers derived from enantiomeric monomers, (*R*)-(Me)$_2$BL and (*S*)-(Me)$_2$BL, and found the resulting blend to display the same thermal properties as the homochiral polymers, suggesting the absence of stereocomplexation (fig. S27). Furthermore, the iso-rich P3H(Me)$_2$B derived from (Me)$_2$BL with a 70/30 (*S*)/(*R*) ratio showed T_m values of 189° and 204°C, which are between those of the *it*- and *at*-P3H(Me)$_2$B samples (Fig. 3A and fig. S28).

The two melting peaks observed in all the melt-crystallized P3H(Me)$_2$B samples present in the second heating scan (but not in the first heating scan) on the differential scanning calorimetry (DSC) thermograms, which become more pronounced as the tacticity decreases (Fig. 3A), could be due to the melting of two different polymorphic forms crystallized by cooling from the melt; to a transformation between two different crystalline forms; or

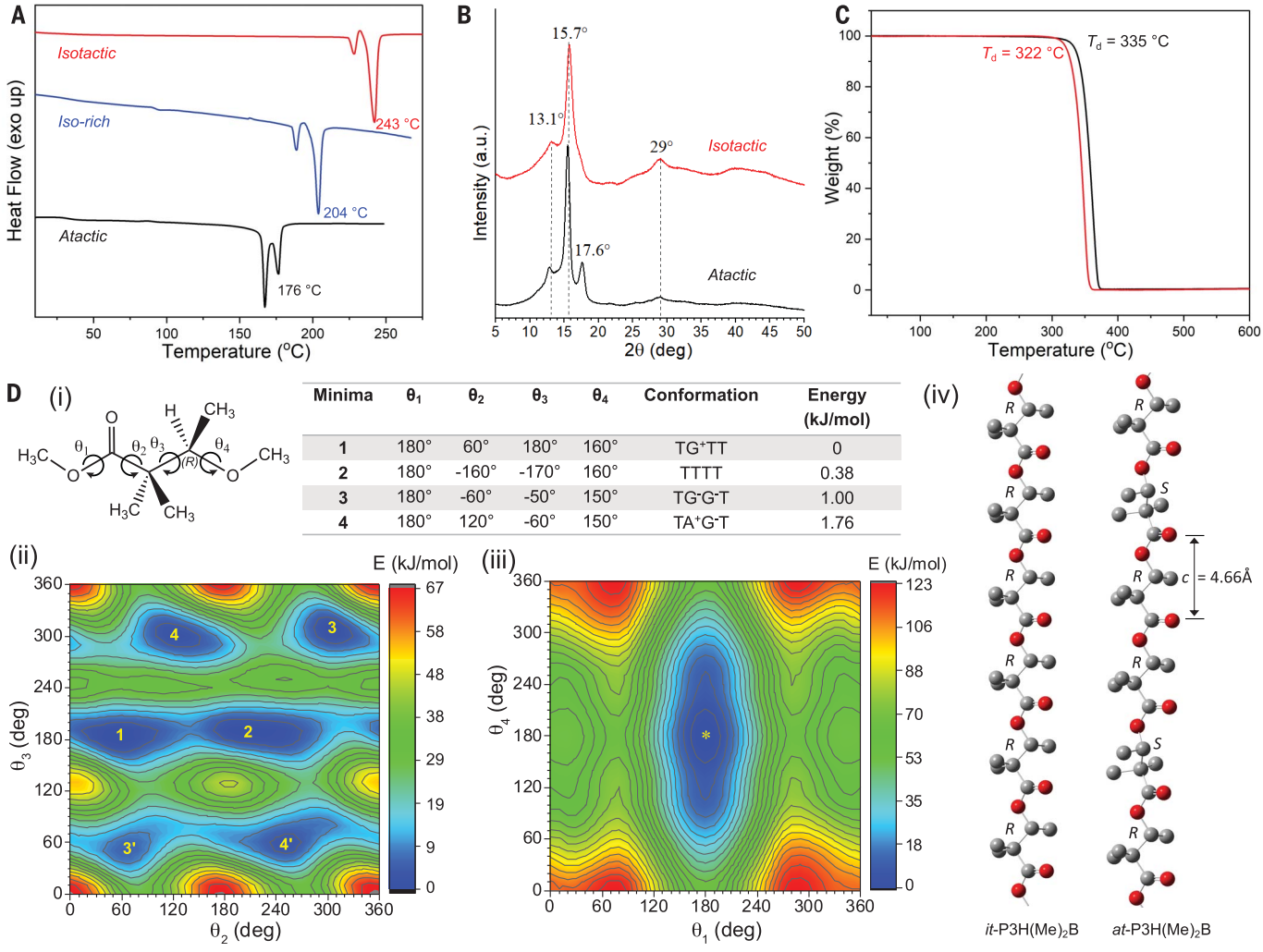

Minima	θ_1	θ_2	θ_3	θ_4	Conformation	Energy (kJ/mol)
1	180°	60°	180°	160°	TG^+TT	0
2	180°	-160°	-170°	160°	TTTT	0.38
3	180°	-60°	-50°	150°	TG^-G^-T	1.00
4	180°	120°	-60°	150°	TA^+G^-T	1.76

Fig. 3. Intrinsic crystallinity and high thermal stability. (**A**) Second heating DSC scan (10°C/min) curves for isotactic (red), iso-rich (blue), and atactic (black) P3H(Me)$_2$B materials. (**B**) WAXS profiles of *it*-P3H(Me)$_2$B (red) and *at*-P3H(Me)$_2$B (black), showing nearly identical diffraction patterns and a similar degree of crystallinity. (**C**) TGA curves for *it*-P3H(Me)$_2$B (red) and *at*-P3H(Me)$_2$B (black), showing a 13°C higher T_d for *at*-P3H(Me)$_2$B. (**D**) (i) Definition of the fragment of the chain of *it*-(*R*)-P3H(Me)$_2$B and torsion angles θ_1, θ_2, θ_3, and θ_4, with their values corresponding to the four conformational models and relative energy. (ii) Conformational energy map as a function of the torsion angles θ_2 and θ_3 scanned every 10° with θ_1 and θ_4 fixed at 180°. The energy levels are reported every 5 kJ/mol, and the energy minima are indicated with numbers. The scale of the values of energy is indicated on the right with different colors, with the energy increasing from blue (the energy minima) to red. The energy values are scaled with respect to the absolute minimum at E = 0 kJ/mol. The minima corresponding to a number and its prime number (**3** and **3'**, **4** and **4'**) are symmetrically equivalent. (iii) Conformational energy map as a function of θ_1 and θ_4 scanned every 10° with θ_2 and θ_3 fixed at θ_2 = −160° and θ_3 = −170° (minimum **2**). The energy levels are reported every 5 kJ/mol, and the value of the absolute energy minimum is indicated with an asterisk. (iv) Low-energy models of the transplanar conformation (TTTT) for the chains of *it*-(*R*)-P3H(Me)$_2$B and *at*-P3H(Me)$_2$B viewed along the chain axis.

simply to melting and recrystallization into the same crystalline form. To clarify this point, three DSC experiments with second heating scans performed at different heating rates (2.5, 10, and 20°C/min) were carried out. The decrease in the area of the higher T_m peak and the simultaneous increase in the area of the lower T_m peak with increasing the heating rate (figs. S32 and S33) suggest that the two peaks are not due to the melting of two different crystalline phases formed upon cooling from the melt, but rather indicate that melting and recrystallization phenomena occur during heating. To further test this hypothesis, we also collected wide-angle x-ray scattering (WAXS) profiles at different temperatures during heating of the melt-crystallized sample (fig. S34), showing the identical profiles between those collected at room temperature before the first heating scan and after the crystallization from the melt. These results confirm the absence of two different polymorphic forms and suggest that the two melting peaks are due to melting at nearly 167° to 169°C and fast recrystallization of the melt with formation of more-ordered and thick crystals of the same crystalline form that melt at higher temperatures of 177° to 181°C. The result that the temperatures of both melting peaks increase with decreasing heating rate is a further confirmation of the occurrence of recrystallization during heating.

The WAXS profile of the as-synthesized *at*-P3H(Me)$_2$B (M_n = 554 kDa) displays three major diffraction peaks centered at 2θ ≈ 13.1°, 15.7°, and 17.6°, and other minor diffraction

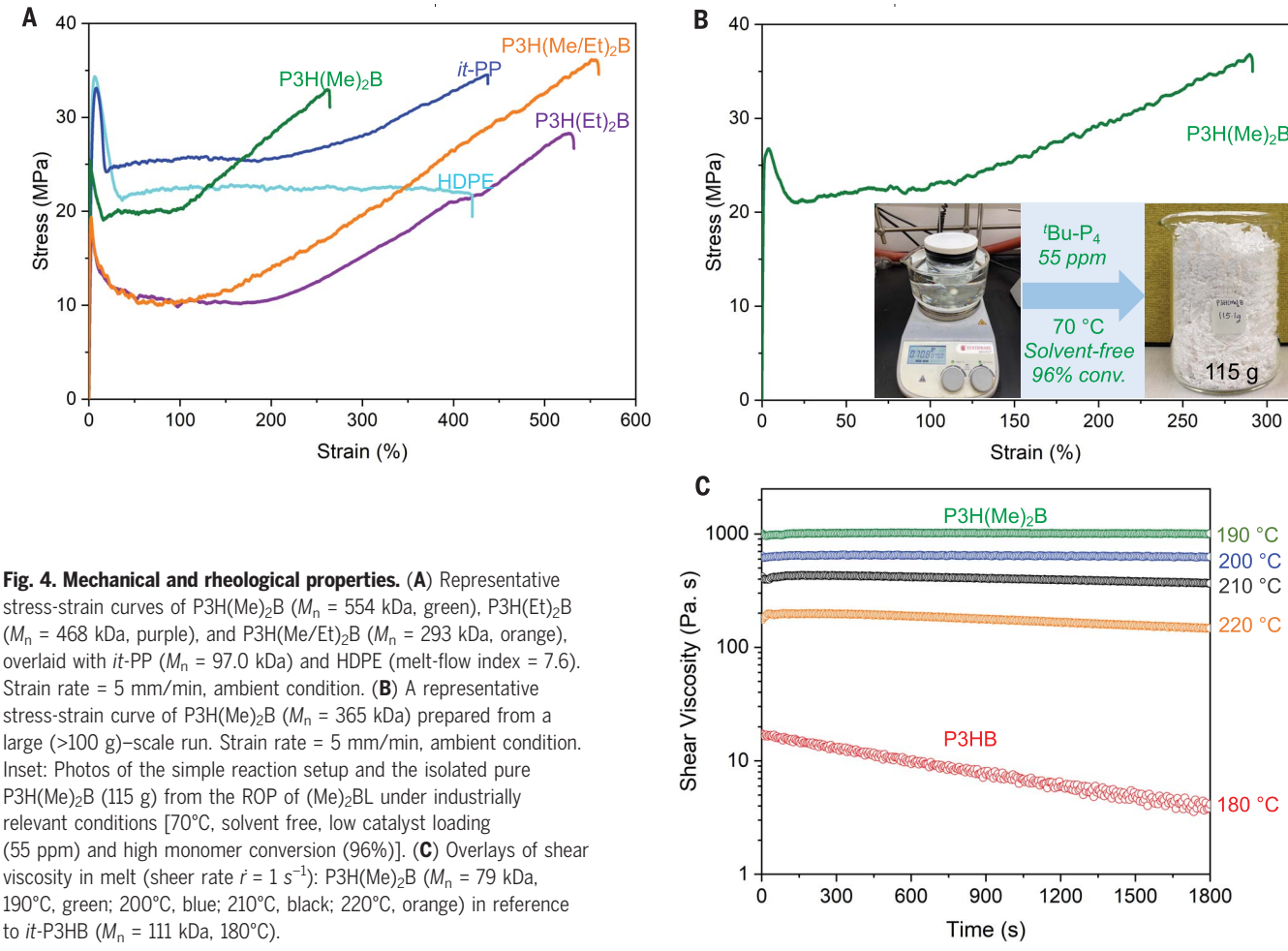

Fig. 4. Mechanical and rheological properties. (**A**) Representative stress-strain curves of P3H(Me)$_2$B (M_n = 554 kDa, green), P3H(Et)$_2$B (M_n = 468 kDa, purple), and P3H(Me/Et)$_2$B (M_n = 293 kDa, orange), overlaid with *it*-PP (M_n = 97.0 kDa) and HDPE (melt-flow index = 7.6). Strain rate = 5 mm/min, ambient condition. (**B**) A representative stress-strain curve of P3H(Me)$_2$B (M_n = 365 kDa) prepared from a large (>100 g)–scale run. Strain rate = 5 mm/min, ambient condition. Inset: Photos of the simple reaction setup and the isolated pure P3H(Me)$_2$B (115 g) from the ROP of (Me)$_2$BL under industrially relevant conditions [70°C, solvent free, low catalyst loading (55 ppm) and high monomer conversion (96%)]. (**C**) Overlays of shear viscosity in melt (sheer rate $\dot{\gamma}$ = 1 s^{-1}): P3H(Me)$_2$B (M_n = 79 kDa, 190°C, green; 200°C, blue; 210°C, black; 220°C, orange) in reference to *it*-P3HB (M_n = 111 kDa, 180°C).

peaks of much lower intensities at higher 2θ values (Fig. 3B), with the calculated crystallinity (x_c) of 67% (fig. S35). When the as-synthesized *it*- and *at*-P3H(Me)$_2$B materials are compared, they display essentially the same main diffraction peaks with slightly different intensities at the higher 2θ region (Fig. 3B); indeed, the degree of crystallinity of *at*-P3H(Me)$_2$B (x_c = 67%) was found to be even higher than that of *it*-P3H(Me)$_2$B (x_c = 58%, fig. S36). To understand the origin of crystallinity manifested in *at*-P3H(Me)$_2$B, we performed conformational analysis, first on chain models of *it*-P3H(Me)$_2$B [Fig. 3D, (i) to (iii)] with opposite chirality—namely, (*R*)-P3H(Me)$_2$B and (*S*)-P3H(Me)$_2$B—and then extended to a chain model of *at*-P3H(Me)$_2$B characterized by a random succession of *R* and *S* units along the chain (supplementary text and figs. S37 to S42). Oriented fibers of *at*-P3H(Me)2B were obtained by stretching the compression-molded sample at ~150°C and annealing the fiber under tension at 143°C for 35 min. The two-dimensional x-ray fiber diffraction pattern of *at*-P3H(Me)2B (fig. S40) reveals three strongest reflections that are polarized on the equator and centered at the same 2θ position as those observed in the powder profile (Fig. 3B). These results indicate that the fiber is crystallized in the same crystalline form of the as-prepared and melt-crystallized samples and that upon stretching, no polymorphic transformations occur. Other reflections are polarized on the first layer line and further weak reflections on the second layer line. From the separation between the different layer lines observed in the fiber pattern, a value of the chain axis *c* of 4.66 Å was determined. This value is consistent with a transplanar conformation corresponding to one of the energy minima found by the conformational analysis [Fig. 3D, (i) to (iii), and figs. S37 to S42]. Overall, this study showed that the shape of the chain and the projection normal to the chain axis of *at*-P3H(Me)$_2$B are very similar to the ordered models of the *R*-enantiomer [Fig. 3D, (iv), and figs. S40 to S42], which explains the fact that the *at*-P3H(Me)$_2$B chains can crystallize, despite the configurational disorder, and that the *at*-P3H(Me)$_2$B shows a WAXS profile similar to that of the pure enantiomeric (*R*)-P3H(Me)$_2$B. Indeed, they likely crystallize in the same crystalline form (Fig. 3B).

The thermal stability of the PHA samples was analyzed and compared by thermogravimetric analysis (TGA). Despite the largely different T_m values between *it*- and *at*-P3H(Me)$_2$B materials, they displayed similarly high T_d values of 322° and 335°C, respectively (Fig. 3C and figs. S44 and S45). These values are considerably higher than the T_d value (~250°C) of *it*-P3HB (*17*). The molar mass has a substantial effect on T_d, but it hardly affects T_m. For example, the T_d of P3H(Me)$_2$B increased from 314° to 335°C as the M_n increased from 179 to 554 kDa, whereas the T_m remained the same.

Mechanical and rheological properties

When compared to *it*-P3HB (ε_b ~4%), semicrystalline *at*-P3H(Me)$_2$B (M_n = 554 kDa) displays a significantly enhanced ductility (ε_b = 228 ± 24.6%), a higher elastic modulus (E = 2.94 ± 0.40 GPa), and a higher stress (σ = 31.6 ± 1.8 MPa), showing that the α,α-dimethyl substitution also overcomes the brittleness of *it*-P3HB (Fig. 4A, table S4, and fig. S56). With incorporation of more flexible diethyl groups, P3H(Et)$_2$B achieved further enhanced ductility with ε_b = 501 ± 36%, while maintaining a high modulus of E = 1.22 ± 0.27 GPa (Fig. 4A, table S5, and fig. S57). The Me/Et random copolymer

P3H(Me/Et)$_2$B, synthesized by copolymerizing (Me)$_2$BL and (Et)$_2$BL (figs. S17 and S58), exhibited an even higher fracture strain (ε_b = 517 ± 35%) and stress (σ = 34.1 ± 2.1 MPa) relative to P3H(Et)$_2$B, which outperformed both high-density PE (HDPE) and *it*-PP (Fig. 4A, table S6, and fig. S59). Also, the mechanical performance of the P3H(Me)$_2$B material (M_n = 332 kDa) prepared from a large (115 g)–scale run was further improved relative to the polymer prepared at 5-g scale, exhibiting higher elastic modulus (E = 3.08 ± 0.18 GPa), stress (σ = 33.9 ± 2.1 MPa), and ductility (ε_b = 252 ± 30.1%) (Fig. 4B, table S7, and fig. S60). These results further indicate the scalability of the polymerization to produce high-performance P3H(Me)$_2$B.

The third synergy as a result of removing the two cis-elimination–prone α-protons by α,α-dialkyl substitution to enhance the PHA thermal stability in the solid state is the realization of melt processability. To test the possibility of melt processing, we monitored the shear viscosity change over time for P3H(Me)$_2$B at temperatures above T_m in a continuous-flow mode at a shear rate of 1 s^{-1}. As a reference, *it*-P3HB (M_n = 111 kDa, T_m = 170°C) was also subjected to the same shear viscosity test in melt (180°C). The shear viscosity for P3H(Me)$_2$B (M_n = 79 kDa) remained constant without any obvious decrease over a time frame of 30 min at temperatures up to 210°C (Fig. 4C), which is well above the corresponding melting temperature. Furthermore, P3H(Me)$_2$B samples with a wide molar mass range, from M_n = 79 to 554 kDa, behaved similarly and showed a stable shear viscosity at 190°C over the same time period (Fig. 1D), further demonstrating melt-processing feasibility. By contrast, *it*-P3HB, known for rapid degradation in melt, displayed a substantial decay in its shear viscosity, from 17 to 4 Pa·s (76%), after 30 min at 180°C (Fig. 4C). P3H(Me)$_2$B (M_n = 79 kDa) evidenced a small but noticeable decrease in its shear viscosity at 220°C, indicating its upper-limit melt-processing temperature (Fig. 4C). Overall, the studies in shear viscosity presented here consolidate the effectiveness of the strategy of removing the α-protons of the PHA repeat units to enhance their thermal stability and enable their melt processability.

A large body of studies have focused on fine-tuning the PHA thermal and mechanical properties by varying the main-chain compositions and stereomicrostructures, as well as the β-pendent group chain length and functionality, achieving notable success in addressing some aspects of the PHA's long-standing challenges but leaving inherent issues with thermal stability and chemical circularity unresolved. The α,α-dialkylated PHA platform described in this study is designed to address the root cause of the PHA thermal instability—the facile cis-elimination process during thermal degradation involving the α-hydrogens in the repeat units—by substituting both α-hydrogens with alkyl groups. This simple α,α-dialkyl substitution not only enhances the thermal stability so substantially that the PHAs become melt processable but also synergistically endows the PHAs with the high ductility and toughness that are comparable with or superior to *it*-PP and HDPE. Furthermore, this platform offers ease of synthesis as, in contrast to the parent P3HB, the α,α-dimethylated P3H(Me)$_2$B is always semicrystalline, regardless of its tacticity, thanks to its fascinating tacticity-independent, intrinsic crystallinity, thereby allowing for the synthesis of semicrystalline high-performance PHAs without the need to control the polymerization stereochemistry that often requires specifically designed chiral catalysts. Above all, this design achieves chemical circularity through closing both the ROP and SGP loops in PHA production and chemical recycling to monomer, thereby solving the three challenges facing the current PHAs.

REFERENCES AND NOTES

1. D. K. Bedade, C. B. Edson, R. A. Gross, *Molecules* **26**, 3463 (2021).
2. D. Tan, Y. Wang, Y. Tong, G.-Q. Chen, *Trends Biotechnol.* **39**, 953–963 (2021).
3. A. Anjum *et al*., *Int. J. Biol. Macromol.* **89**, 161–174 (2016).
4. S. Muhammadi, Shabina, M.Afzal, S.Hameed, *Green Chem. Lett. Rev.* **8**, 56–77 (2015).
5. B. Laycock, P. Halley, S. Pratt, A. Werker, P. Lant, *Prog. Polym. Sci.* **38**, 536–583 (2013).
6. S. Taguchi, T. Iwata, H. Abe, Y. Doi, in *Polymer Science: A Comprehensive Reference*, K. Matyjaszewski, M. Möller., Eds. (Elsevier B.V., 2012), vol. 9, pp. 157–182 .
7. R. W. Lenz, R. H. Marchessault, *Biomacromolecules* **6**, 1–8 (2005).
8. K. Sudesh, H. Abe, Y. Doi, *Prog. Polym. Sci.* **25**, 1503–1555 (2000).
9. H. Li, R. M. Shakaroun, S. M. Guillaume, J. F. Carpentier, *Chem. Eur. J.* **26**, 128–138 (2020).
10. A. H. Westlie, E. C. Quinn, C. R. Parker, E. Y.-X. Chen, *Prog. Polym. Sci.* **134**, 101608 (2022).
11. A. Amgoune, C. M. Thomas, S. Ilinca, T. Roisnel, J. F. Carpentier, *Angew. Chem. Int. Ed.* **45**, 2782–2784 (2006).
12. E. W. Dunn, G. W. Coates, *J. Am. Chem. Soc.* **132**, 11412–11413 (2010).
13. T. Ebrahimi, D. C. Aluthge, S. G. Hatzikiriakos, P. Mehrkhodavandi, *Macromolecules* **49**, 8812–8824 (2016).
14. L. R. Rieth, D. R. Moore, E. B. Lobkovsky, G. W. Coates, *J. Am. Chem. Soc.* **124**, 15239–15248 (2002).
15. J. C. Yang, J. Yang, W. B. Li, X. B. Lu, Y. Liu, *Angew. Chem. Int. Ed.* **61**, e202116208 (2022).
16. M. Zintl *et al*., *Angew. Chem. Int. Ed.* **47**, 3458–3460 (2008).
17. X. Tang, E. Y.-X. Chen, *Nat. Commun.* **9**, 2345 (2018).
18. X. Tang, A. H. Westlie, E. M. Watson, E. Y.-X. Chen, *Science* **366**, 754–758 (2019).
19. X. Tang *et al*., *Angew. Chem. Int. Ed.* **132**, 7955–7964 (2020).
20. Z. Zhang, C. Shi, M. Scoti, X. Tang, E. Y.-X. Chen, *J. Am. Chem. Soc.* **144**, 20016–20024 (2022).
21. A. Sangroniz *et al*., *Nat. Commun.* **10**, 3559 (2019).
22. C. Jehanno *et al*., *Nature* **603**, 803–814 (2022).
23. L. D. Ellis *et al*., *Nat. Catal.* **4**, 539–556 (2021).
24. B. A. Abel, R. L. Snyder, G. W. Coates, *Science* **373**, 783–789 (2021).
25. J.-B. Zhu, E. M. Watson, J. Tang, E. Y.-X. Chen, *Science* **360**, 398–403 (2018).
26. K. P. Sullivan *et al*., *Science* **378**, 207–211 (2022).
27. M. Häußler, M. Eck, D. Rothauer, S. Mecking, *Nature* **590**, 423–427 (2021).
28. Y. Aoyagi, K. Yamashita, Y. Doi, *Polym. Degrad. Stabil.* **76**, 53–59 (2002).
29. N. Grassie, E. Murray, P. Holmes, *Polym. Degrad. Stabil.* **6**, 127–134 (1984).
30. H. Morikawa, R. H. Marchessault, *Can. J. Chem.* **59**, 2306–2313 (1981).
31. C. DePuy, R. King, *Chem. Rev.* **60**, 431–457 (1960).
32. D. Seebach, H. M. Müller, H. M. Bürger, D. A. Plattner, *Angew. Chem. Int. Ed.* **31**, 434–435 (1992).
33. M. Melchiors, H. Keul, H. Höcker, *Macromolecules* **29**, 6442–6451 (1996).
34. H. Ariffin, H. Nishida, Y. Shirai, M. A. Hassan, *Polym. Degrad. Stab.* **95**, 1375–1381 (2010).
35. M. Hong, E. Y.-X. Chen, *Green Chem.* **19**, 3692–3706 (2017).
36. G. W. Coates, Y. D. Getzler, *Nat. Rev. Mater.* **5**, 501–516 (2020).
37. S. Furutate *et al*., *NPG Asia Mater.* **13**, 31 (2021).
38. M. Brestaz, N. Desilles, G. Le, C. Bunel, *J. Polym. Sci. A Polym. Chem.* **49**, 4129–4138 (2011).
39. K. Lang, J. Zierow, K. Buehler, A. Schmid, *Microb. Cell Fact.* **13**, 2 (2014).
40. S. M. Bachrach, *J. Org. Chem.* **73**, 2466–2468 (2008).
41. M. E. Jung, G. Piizzi, *Chem. Rev.* **105**, 1735–1766 (2005).
42. W. Xiong *et al*., *Chem* **6**, 1831–1843 (2020).
43. X.-L. Li, R. W. Clarke, J.-Y. Jiang, T.-Q. Xu, E. Y.-X. Chen, *Nat. Chem.* **15**, 278–285 (2023).
44. J. Zhou, D. Sathe, J. Wang, *J. Am. Chem. Soc.* **144**, 928–934 (2022).
45. L.-B. W. Lee, R. A. Register, *Macromolecules* **38**, 1216–1222 (2005).
46. C. Shi *et al*., *Sci. Adv.* **6**, eabc0495 (2020).

ACKNOWLEDGMENTS

We thank C. Lincoln and J. Miscall of the National Renewable Energy Laboratory (NREL) for SEC analysis of polymer samples that need hexafluoro-2-propanol to solubilize them. **Funding:** We gratefully acknowledge support by the US Department of Energy, Office of Energy Efficiency and Renewable Energy, Advanced Manufacturing Office (AMO) and Bioenergy Technologies Office (BETO). This work was performed as part of the BOTTLE Consortium and funded under contract no. DE-AC36-08GO28308 with NREL, operated by the Alliance for Sustainable Energy. In the early stage of the PHA project, the work was supported by the US National Science Foundation (NSF-1955482). **Author contributions.** E.Y.-X.C. conceived the project and directed research. L.Z., Z.Z., and C.S. designed and conducted experiments and analyzed the results. D.K.B. and R.R.G. carried out scale-up synthesis of the lactone monomer and polymers. M.S. performed crystallinity characterization and conformational analysis. L.Z. and Z.Z. wrote the initial manuscript and revised subsequent versions of the manuscript. E.Y.-X.C. edited the initial draft, and all authors contributed to drafting various sections of the manuscript and reviewed the entire manuscript. **Competing interests:** E.Y.-X.C. and L.Z. have filed patent applications (US2022 63/340,168 and 63/434,550) on the findings reported here. **Data and materials availability:** The data that support the finding of this study are present in the paper and/or the supplementary materials. **License information:** Copyright © 2023 the authors, some rights reserved; exclusive licensee American Association for the Advancement of Science. No claim to original US government works. https://www.sciencemag.org/about/science-licenses-journal-article-reuse

SUPPLEMENTARY MATERIALS

science.org/doi/10.1126/science.adg4520
Materials and Methods
Supplementary Text
Figs. S1 to S60
Tables S1 to S7
References (*47*–*57*)

Submitted 25 December 2022; accepted 15 February 2023
10.1126/science.adg4520

CATALYSIS

Formation of active sites on transition metals through reaction-driven migration of surface atoms

Lang Xu[1]†, Konstantinos G. Papanikolaou[1]†, Barbara A. J. Lechner[2,3], Lisa Je[1], Gabor A. Somorjai[3,4], Miquel Salmeron[3,5], Manos Mavrikakis[1]*

Adopting low-index single-crystal surfaces as models for metal nanoparticle catalysts has been questioned by the experimental findings of adsorbate-induced formation of subnanometer clusters on several single-crystal surfaces. We used density functional theory calculations to elucidate the conditions that lead to cluster formation and show how adatom formation energies enable efficient screening of the conditions required for adsorbate-induced cluster formation. We studied a combination of eight face-centered cubic transition metals and 18 common surface intermediates and identified systems relevant to catalytic reactions, such as carbon monoxide (CO) oxidation and ammonia (NH_3) oxidation. We used kinetic Monte Carlo simulations to elucidate the CO-induced cluster formation process on a copper surface. Scanning tunneling microscopy of CO on a nickel (111) surface that contains steps and dislocations points to the structure sensitivity of this phenomenon. Metal-metal bond breaking that leads to the evolution of catalyst structures under realistic reaction conditions occurs much more broadly than previously thought.

Understanding the nature of the active sites on catalytic surfaces is central to understanding and improving catalysis (*1*). Low-index metal surfaces, such as the (111), (100), and (110) facets, are commonly adopted models of supported metal catalysts, particularly in computational studies, but have limitations in describing the active site under realistic reaction conditions (*2*). For example, such simple models do not account for low coordination atoms found in point defects, atomic steps, and grain boundaries in catalyst surfaces that can play a key role in determining catalytic properties (*3*). Recent scanning tunneling microscopy (STM) studies showed that subnanometer metal clusters that expose increased numbers of low coordinated atoms can be formed in situ on low-index surfaces when molecules are adsorbed on them. Such metal clusters exhibit distinct catalytic (*4*–*11*) and electronic properties and dynamic structural fluxionality (*12*) compared with those of nanoparticles (NPs) with diameters >2 nm, and NPs can also restructure during reaction (*13*, *14*). Adsorbate-induced cluster formation hints at the dynamic nature of catalytic surfaces and suggests that the active sites that are formed under practically relevant reaction conditions can be substantially different from those in extended facets or in pristine NP models that are commonly used in mechanistic studies of thermal catalysis and electrocatalysis (*15*).

Although highly dispersed small metal clusters are generally prepared using controlled synthesis techniques (*16*, *17*), the formation of clusters on bulk crystals induced by adsorbates under realistic reactive conditions, to our knowledge, has not been explicitly included in previous studies. The main reason has been the difficulty of experimentally characterizing catalyst structures under the conditions that are encountered in industrial catalysis, which include high pressures and temperatures (*18*). Some of the systems that have been experimentally characterized at torr-level pressures exhibit adsorbate-induced cluster formation. CO-induced clustering has been reported on Cu(111) (*19*), Cu(100) (*20*), and CuCo (*21*) alloy surfaces. However, no CO-induced cluster formation was observed on Rh(111) when the surface was exposed to CO up to atmospheric pressure (*22*). Mixed results were reported for Pt. On a flat Pt(111) single crystal with few steps, no cluster formation was observed up to atmospheric CO pressure (*23*), whereas on vicinal (regularly stepped) Pt(557) and Pt(332), clustering was observed at torr-level CO exposures (*24*). Interestingly, on Pt(997), which has a vicinal surface with a terrace size ~1.5 times larger than that of Pt (557), step doubling, but no cluster formation, was observed (*25*).

These results point to a potential role of step-step interactions in the surface evolution under reactive environments. Accordingly, adsorbate-induced cluster formation depends on the identity of the metal surface as well as the adsorbate-metal interactions (*26*). Here, we developed an efficient framework for the prediction of adsorbate-induced cluster formation using energetics derived from density functional theory (DFT) calculations. We first discuss how we correlate the adsorbate-induced clustering effect to a single energetic parameter that can be easily computed. We then demonstrate how this methodology leads to predictions in agreement with experimental results, as well as its limitations. Next, we present a comprehensive database that includes eight transition metals and 18 adsorbates that are commonly involved in heterogeneous catalysis and discuss examples of catalytic systems that should be dominated by in situ adsorbate-induced active-site formation, thereby warranting a revisitation of their detailed reaction mechanisms. Subsequently, using kinetic Monte Carlo (KMC) simulations, we conduct a case study for CO-induced cluster formation on Cu(111). We conclude with STM data for CO adsorption on a Ni(111) surface that contains steps and dislocations, pointing to the rich structure sensitivity of this phenomenon.

Theoretical modeling of bare surfaces and surfaces with adsorbed CO

The adsorbate-induced cluster formation observed by Eren *et al.* (*19*) can be described as a three-step process (Fig. 1A): (i) ejection of step-edge or kink atoms leading to adatom formation on an adjacent terrace, (ii) adatom diffusion, and (iii) aggregation of adatoms to form subnanometer clusters. Because the first step of this process requires the breaking of surface metal-metal bonds, the energy cost of atom ejection must be overcome for this three-step process to proceed. We defined the adatom formation energy (E_{form}) as the descriptor for the initial screening of systems that could exhibit clustering. Our procedure to evaluate the adatom formation energy involved the use of two infinitely separated slab models (Fig. 1, B and C), where one is the source for the surface atom to be ejected and the other is the sink where the adatom lands after ejection from the first slab. Detailed definitions are provided in the supplementary materials (SM).

Here, we considered three types of possible ejection sources: (i) a kink site [modeled with the (874) slab; Fig. 1, B and C]; (ii) a regular, defect-free step edge [modeled with the (211) slab; fig. S8A]; and (iii) the (111) terrace (fig. S8B). Because E_{form} is a thermodynamic parameter, it does not fully capture the kinetics of adatom formation, which is determined by the energy barrier. Accordingly, E_{form} values calculated here can be considered as lower bounds for the activation energy barriers for adatom formation. We later demonstrate, using results on Cu(874), that the difference between E_{form} and the true activation energy barrier for atom ejection is very small (<0.02 eV). Total energies were evaluated by using periodic DFT calculations (GGA-PBE) with the Vienna ab initio simulation package (see SM for computational details).

[1]Department of Chemical and Biological Engineering, University of Wisconsin–Madison, Madison, WI 53706, USA. [2]Department of Chemistry and Catalysis Research Center, School of Natural Sciences, Technical University of Munich, 85748 Garching, Germany. [3]Division of Materials Science, Lawrence Berkeley National Laboratory, Berkeley, CA 94720, USA. [4]Department of Chemistry, University of California, Berkeley, Berkeley, CA 94720, USA. [5]Department of Materials Science and Engineering, University of California, Berkeley, Berkeley, CA 94720, USA.
*Corresponding author. Email: emavrikakis@wisc.edu
†These authors contributed equally to this work.

As a case study, we first examined the adatom formation process under vacuum (Fig. 2A) and in the presence of CO (Fig. 2B), a common reactive species in catalytic applications. In the absence of adsorbates, adatom formation on unreconstructed (111) surfaces of eight face-centered cubic (fcc) transition metals (Ag, Cu, Au, Pd, Ni, Rh, Pt, and Ir) by ejection of a (874) kink atom was always the most energetically preferred among the three aforementioned ejection sources ($E^{vac}_{form\ (111)}{}^{(874)}_{\downarrow} < E^{vac}_{form\ (111)}{}^{(211)}_{\downarrow} < E^{vac}_{form\ (111)}{}^{(111)}_{\downarrow}$; see Fig. 2A). Further, the magnitude of the E^{vac}_{form} followed the same trend as that of the bulk cohesive energies (*27*) of the metals (pink squares in Fig. 2A). Two notable exceptions were Au and Pt, whereby despite increasing the cohesive energy (i.e., the "hardness" of a bulk metal) with respect to the previous metal in the series (Cu and Rh, respectively), the respective atom ejection energy decreased compared with that of the previous metal. This result demonstrates that the bulk metal hardness does not entirely capture atom ejection energetics.

We then investigated the effect of CO adsorption on the adatom formation from (874) kink atom ejection (Fig. 2B) at the dilute limit [one adsorbate per (874) unit cell, or 1/14 monolayer (ML) because each unit cell consists of 14 surface metal atoms; see fig. S1 for the structure of the (874) surface model]. On Ag(874), Cu(874), and Au(874) (ranked in the order of increasing bulk-metal cohesive energy), CO facilitated adatom formation ($E^{ad}_{form} < E^{vac}_{form}$), whereas on the remaining five metals studied, CO inhibited adatom formation. This mixed adsorbate effect was caused by the varying binding properties of the adsorbates across different metal surfaces (see SM for a detailed discussion).

The calculated E_{form} values on the eight metal surfaces (Fig. 2B) spanned a wide energy range from 0.42 to 2.11 eV, demonstrating the large variance in cluster formation potential across the periodic table. We expect CO to induce adatom formation from Ag(874), Cu(874), and Au(874) at near-ambient temperatures because the calculated $E^{ad}_{form\ (111)}{}^{(874)}_{\downarrow}$ values (0.58, 0.68, and 0.42 eV, respectively) were below the 0.75-eV threshold, defined as the energy barrier for a room-temperature reaction with a rate constant of 1 s^{-1} (see SM) (*26*); additionally, the $E^{ad}_{form\ (111)}{}^{(874)}_{\downarrow}$ values were also below the desorption barriers of CO [i.e., the absolute value of CO binding energy on the (874) surface of the corresponding metal; see table S8], indicating that CO-induced atom ejection should occur before CO desorption. On the remaining five metal surfaces, the adsorption of CO at low coverages hindered adatom formation; additionally, because the $E^{vac}_{form\ (111)}{}^{(874)}_{\downarrow}$ values are well above 0.75 eV, even without the presence of CO, clustering might only occur at higher temperatures. We note that adatom formation could depend strongly on the adsorbate coverage. We later demonstrate that adatom formation from Cu(874), Ni(874), and Pt(874) occurs more readily at higher CO coverages (see SM for a detailed discussion).

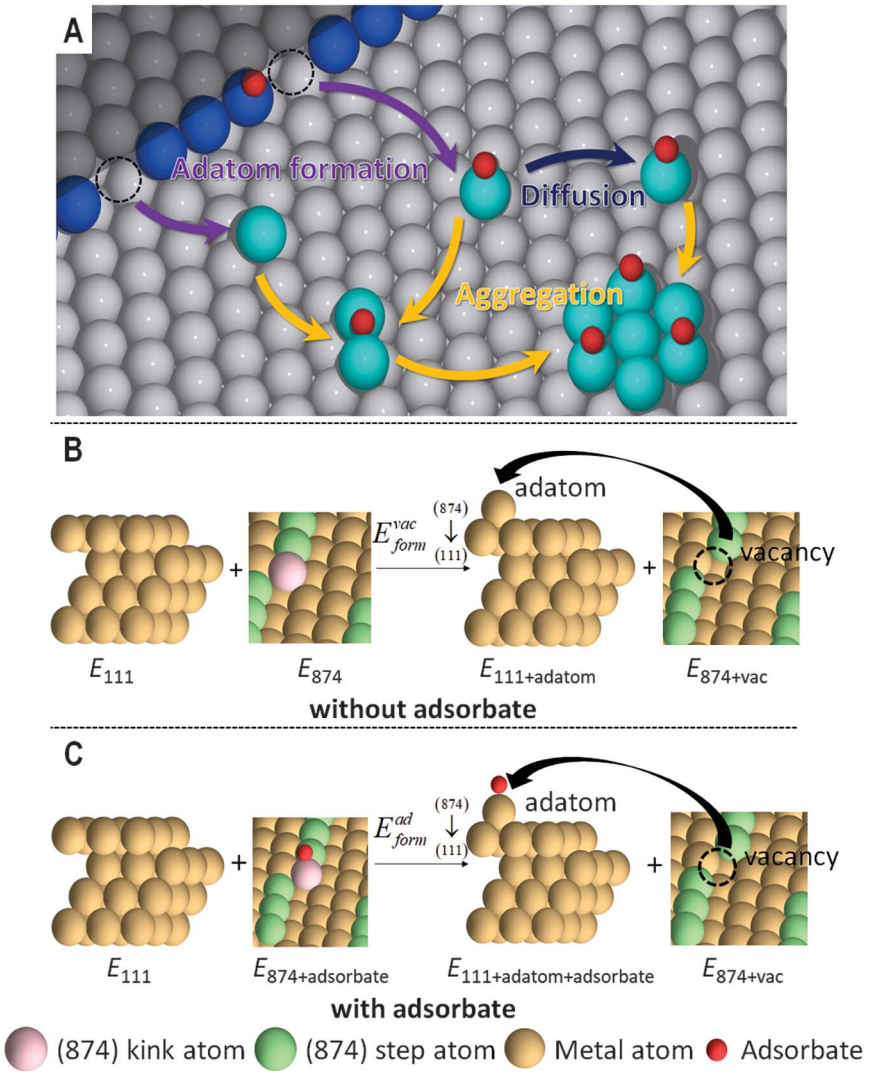

Fig. 1. Definition of adatom formation energy. (**A**) A simplified, atomic-scale illustration of the cluster formation process on a close-packed transition-metal surface due to ejection of step-edge atoms. Dashed circles indicate step-edge vacancies formed after metal atom ejection. Blue, metal atoms on a step edge; turquoise, adatoms and clusters on the terrace; gray, terrace metal atoms (the shaded area denotes the upper terrace atoms at the top-left corner); red, adsorbate species (atomic or molecular). (**B** and **C**) Schematic representations of the definitions for the adatom formation energy due to ejection of (874) kink atoms. The adatom formation energy is defined under vacuum (B) and with an adsorbate involved in the process (C) (E^{vac}_{form} and E^{ad}_{form}, respectively). All graphics represent cross-sectional views of the respective slabs used in the calculations.

Our predictions based on results shown in Fig. 2B are in agreement with ambient-temperature high-pressure (0.1 to 10 torr) STM (HP-STM) results indicating that CO could induce cluster formation on Cu(111) (*19*) but not on Rh(111) (*22*). The mixed CO-induced clustering behavior on vicinal Pt stepped surfaces [i.e., surfaces with (211)-like step-edge structures] that was observed experimentally (*24*, *25*) could be explained by taking into account the CO coverage effect on Pt steps (see SM for a detailed discussion). Specifically, a fully CO-covered step edge substantially destabilized Pt(211) step-edge atoms and facilitated atom ejection. (Note that CO coverage had a minimal effect on the energy of the final state after adatom formation.) Stress energy at steps and the vicinity of surface dislocations, as well as interactions between steps, could also considerably affect the energetics of step atom ejection (*28*). Explicit modeling of high coverage on vicinal surfaces would be suitable for a more detailed

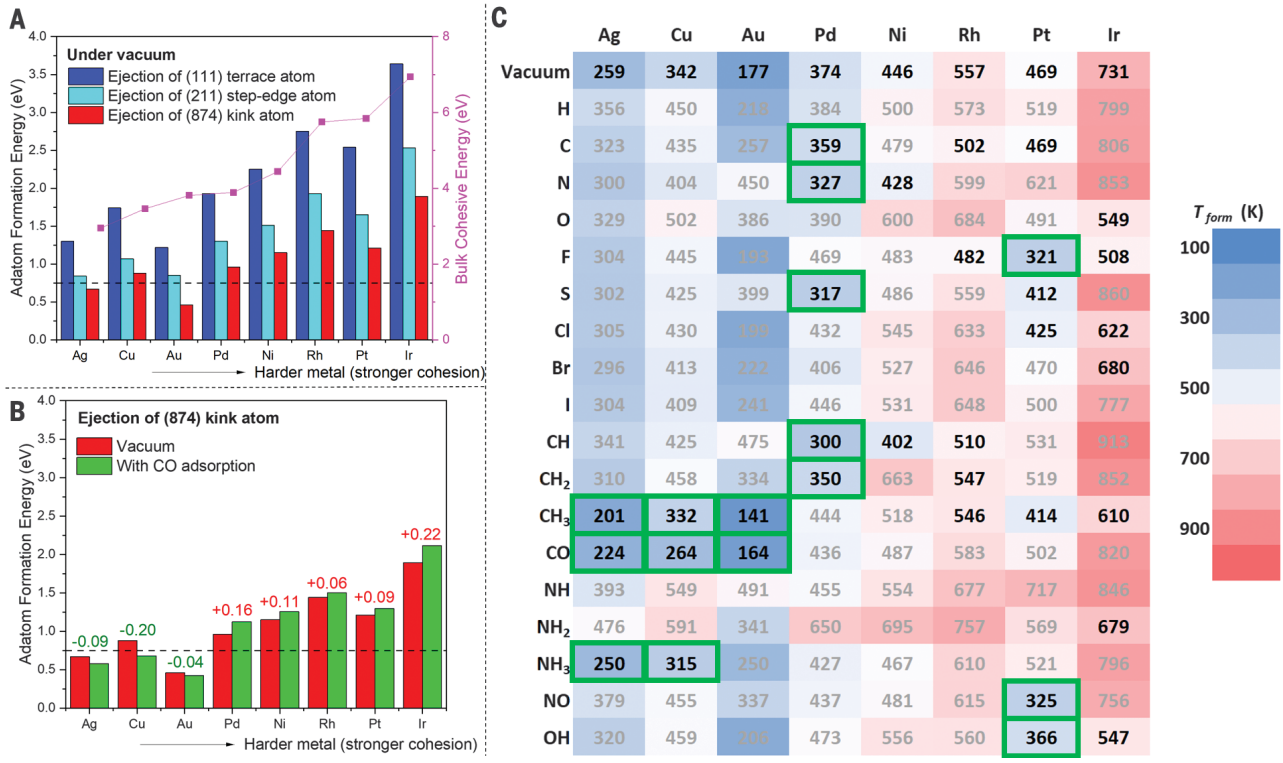

Fig. 2. Adatom formation energies and temperatures. (**A**) Comparison of calculated adatom formation energies under vacuum on the (111) facets of eight fcc transition metals by atom ejection from a (874) kink, a (211) step edge, and a (111) terrace. The experimental bulk cohesive energies from (*27*) (pink squares) are provided for comparison. (**B**) Comparison of calculated adatom formation energies on the (111) facets of fcc transition metals from the ejection of a (874) kink atom under vacuum and in the presence of CO at 1/14 ML (low-coverage limit). The numbers above the bars indicate the difference between adatom formation energy values under vacuum and in the presence of CO. In (A) and (B), the horizontal dashed line indicates the 0.75-eV threshold below which a typical surface deformation event may be expected to occur per second at ambient temperature. (**C**) Heatmap of estimated adsorbate-induced adatom formation temperatures (T^{ad}_{form}; in K) on the (111) surfaces of fcc transition metals. Except for NH_2-induced atom ejection on Au, where (111) ejection is preferred, (874) kink is the preferred atom ejection source for all the other cases. Gray-faded numbers indicate systems in which the adsorbate hinders adatom formation. Systems with both a favorable adsorbate effect for adatom formation and T^{ad}_{form} < 373 K are marked with green boxes. The eight transition metals are listed from left to right in ascending order of experimental bulk cohesive energy.

investigation of specific systems. Nonetheless, our model serves as an indicator of the tendency toward adatom and/or cluster formation and is suitable for large-scale screening purposes.

Modeling the effect of reaction intermediates on cluster formation

Next, we extended the investigation to a wide range of adsorbed reaction intermediates (H, C, N, O, F, S, Cl, Br, I, CH, CH_2, CH_3, CO, NH, NH_2, NH_3, NO, and OH) that are commonly involved in heterogeneous catalysis. An adatom formation energy database for the above eight fcc transition metals and 18 adsorbates at their low-coverage limit [1/9 ML for (111) and (211); 1/14 ML for (874)] was constructed [tables S3 to S5 for atom ejection from (111) terrace, (211) step edge, and (874) kink, respectively]. The metal adatom formation event was always endothermic regardless of the elemental nature of the adsorbate or metal and the source facet of the metal adatom. The effect of an adsorbate on adatom formation depended strongly on its binding properties (tables S6 to S9) on the corresponding metal surfaces (figs. S9 and S10; see SM for a detailed discussion).

We did not observe any generalized adsorbate effect regarding an adsorbate facilitating or inhibiting adatom formation. Except for NH_2-induced adatom formation on Au(111), where atom ejection from the (111) terrace was preferred (see SM for a discussion of adsorbate effect on adatom formation), the (874) kink was the most energetically favorable ejection source for all other cases at the low-coverage limit of the adsorbate (tables S10 and S11), as expected given the undercoordinated nature of the kink atom. The presence and fraction of kink sites on an actual catalyst surface may strongly depend on its synthesis procedure. Therefore, ejection from the other two sources (regular step and terrace) may still be relevant (see SM for a detailed discussion).

To establish a connection with realistic catalytic reaction conditions, we estimated the temperature at which these adsorbate-induced adatom formation events might occur (T^{ad}_{form}; Fig. 2C). T^{ad}_{form} is defined as the temperature at which a rate constant of 1 s^{-1} is achieved for the adatom formation event if the reaction barrier for this elementary step can be approximated by its thermochemistry (i.e., E^{ad}_{form} for the energetically preferred source of the adatom; see SM for a detailed definition). We identified systems where adsorbate-induced adatom formation might occur at near-ambient temperature based on the following two criteria: (i) the adsorbate should facilitate the adatom formation ($E^{ad}_{form} < E^{vac}_{form}$), and (ii) the estimated T^{ad}_{form} value is lower than 373 K (100°C). Sixteen adsorbate-metal systems fell into this category (table S13), which were associated with Ag, Cu, Au, Pd, and Pt. At increased temperatures, adsorbate-induced adatom formation on the other three metals (Ni, Rh, and Ir) was also possible; examples included CH/Ni (402 K), C/Rh (502 K), and O/Ir (549 K).

One notable system we identified was CO-induced adatom formation on Cu [T^{ad}_{form} = 264 K for atom ejection from Cu(874)]. The near-ambient T^{ad}_{form} value for CO/Cu, as well as the previous HP-STM evidence for cluster

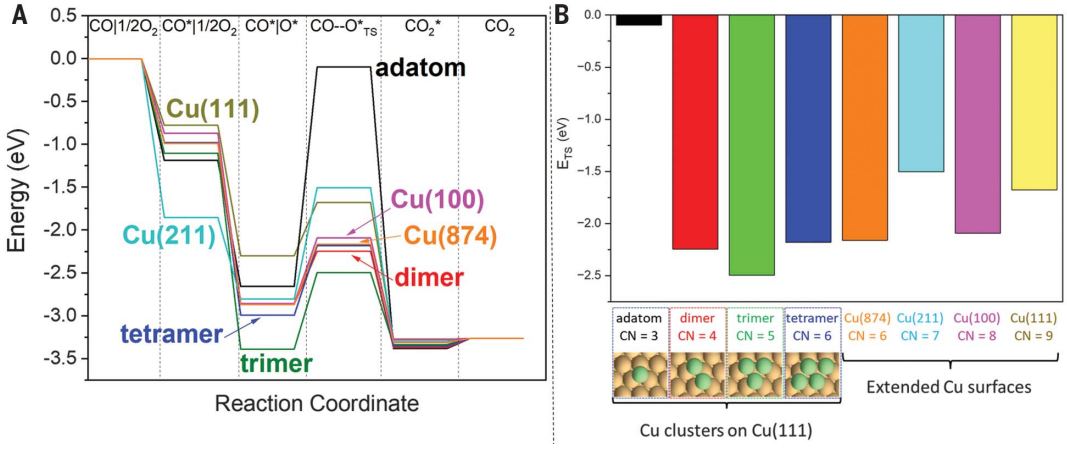

Fig. 3. Cluster effect on Cu-catalyzed CO oxidation. (**A**) Calculated potential energy diagram for CO oxidation by atomic oxygen on Cu(111)-supported Cu clusters and on pristine Cu slab models. Asterisks denote adsorbed surface species, and vertical bars denote infinite separation between adsorbed species. Zero energy is defined as the total energy of the respective clean surface plus CO and 1/2 O_2 in the gas phase. (**B**) Comparison of the calculated transition-state energy for CO--O*$_{TS}$ (E_{TS}) on Cu(111) plus adclusters and pristine Cu slab models, as compiled from data shown in (A). CN stands for the coordination number of the surface site on which the CO oxidation reaction takes place. The inset images show the atomic structures of the Cu(111) plus adcluster models. All energy values were evaluated at the low-coverage limit [1/9 ML for the (111) and (211) surfaces; 1/14 ML for the (874) surface] of each adsorbate. Green, cluster Cu atom or adatom; orange, Cu atom belonging to Cu(111).

formation on Cu(111) in the presence of CO (*19*), suggested the potential relevance of CO-induced clustering for CO oxidation on Cu catalysts. To test that hypothesis, we calculated the activation energy barrier for CO oxidation to CO_2 on Cu_n (n = 1 to 4) clusters formed on Cu(111) (Fig. 3, A and B; see SM for a detailed discussion). Among these Cu(111)-supported clusters, a Cu trimer (Cu_3) exhibited the lowest transition-state energy for CO oxidation (E_{TS}; referenced to gas-phase CO and 1/2 O_2), which was also smaller than the E_{TS} value on any extended Cu facet studied here. At room temperature, based on our DFT results, Cu_3 was estimated to be ~2×10^6 more active toward CO oxidation than Cu(874), the most active extended Cu facet. This result demonstrated the potential role of CO-induced Cu cluster sites in catalyzing CO oxidation. CO-induced clustering could also be relevant for other Cu-catalyzed industrially important catalytic reactions such as low-temperature water-gas shift (~450 to 550 K) (*29*) and methanol synthesis (~473 to 573 K) (*30*), both of which involve CO as a reactant.

Other systems with likely clustering behavior include (i) NH_3 on Ag and Cu (T^{ad}_{form} = 250 and 315 K, respectively) for ammonia oxidation (typically carried out at 383 to 553 K) (*31*); (ii) NO on Pt (T^{ad}_{form} = 325 K) for NO reduction by H_2 (~400 to 550 K); (iii) CH, CH_2, and C on Pd (T^{ad}_{form} = 300, 350, and 359 K, respectively) for methane oxidation (~673 K); and (iv) CH on Ni (T^{ad}_{form} = 402 K) and CH_3 and C on Pt (T^{ad}_{form} = 414 and 469 K, respectively) for methane steam-reforming catalysis (~973 K). If adsorbate-induced cluster formation leads to the in situ formation of the optimal cluster-type active sites for these catalytic systems, then the T^{ad}_{form} might become a limiting factor; that is, the reaction will not happen until the temperature has been raised sufficiently for adatom and active cluster-type site formation to become possible.

KMC simulations for active-site formation on Cu surfaces

To probe the kinetics of the atom ejection and cluster formation processes as a function of adsorbate coverage, we studied the CO-induced cluster formation on Cu(111) caused by the ejection of Cu atoms from Cu(874) kinks, the preferred ejection source. At different CO coverages, the activation energy barrier for kink atom ejection from Cu(874) scaled linearly with the ejection energy with a slope of near unity, thus indicating a late transition state (Fig. 4A). The ejection activation energy barrier was at most 0.02 eV larger than the respective ejection energy. Therefore, the kinetics of CO-induced atom ejection from Cu(874) was described well by its thermochemistry alone. Further, we determined that the ejection kinetics was most strongly affected by the CO coverage of the Cu(874) kink and step sites and was easiest when the kink and step sites were fully covered by CO (see SM for a detailed discussion).

We examined the overall thermochemistry associated with the formation of finite-size small clusters on Cu(111) starting from the ejection of a Cu(874) kink atom under the following three scenarios: (i) vacuum, (ii) intermediate CO coverage, and (iii) high CO coverage (Fig. 4B; see SM for a detailed definition of the cluster formation energy). As shown in Fig. 4B, the presence of CO enhanced the stability of the final clusters that formed, making the overall cluster formation process thermodynamically favorable. For intermediate CO coverage [5/14 ML on Cu(874)] corresponding to a saturated Cu step edge and kink site, the calculated adatom diffusion barrier and the activation energy barrier for adatom attachment to a preexisting Cu_5 cluster on Cu(111) to form Cu_6 (the most thermodynamically driven process for cluster size <8) were 0.04 and 0.05 eV, respectively, compared with the atom ejection barrier of 0.37 eV (Fig. 4C). At room temperature, the atom ejection should be at least five orders of magnitude slower than the diffusion and attachment processes, which confirmed that the initial adatom formation was rate limiting for the overall cluster formation process that includes atom ejection and cluster formation.

To better connect our theoretical results with experimental observations from STM, we conducted on-lattice KMC simulations facilitated by a cluster expansion to predict the energetics of nanocluster formation on Cu(111) (see SM for detailed methods) (*32*). Variation to the atom ejection energy from Cu(874) within the typical DFT error (0.2 eV) was allowed (*2*). When the ejection energy was lowered by 0.15 eV, we observed the best agreement with experimental STM measurements (Fig. 4D) at 0.3-torr CO exposure and room temperature (*19*). During a simulation period of 105.0 min, which is approximately three times the equilibration time allowed in the experiments (*19*), we observed small-sized clusters (<5 atoms) forming at early stages of the simulation. These clusters later grew to 20 to 50 atoms and were decorated with CO molecules predominantly on the peripheral sites of the clusters (Fig. 4D), similar to what was observed during the experiment (*19*). Despite the growth in cluster sizes over time, Cu_3 clusters, which are predicted to be highly active for CO oxidation (Fig. 3, A and B), were present throughout the simulation (Fig. 4D). The 0.15-eV adjustment to the ejection energy can be rationalized not only by the DFT error but also by the presence of other defects that were not accounted for in the Cu(874) surface model, which may further

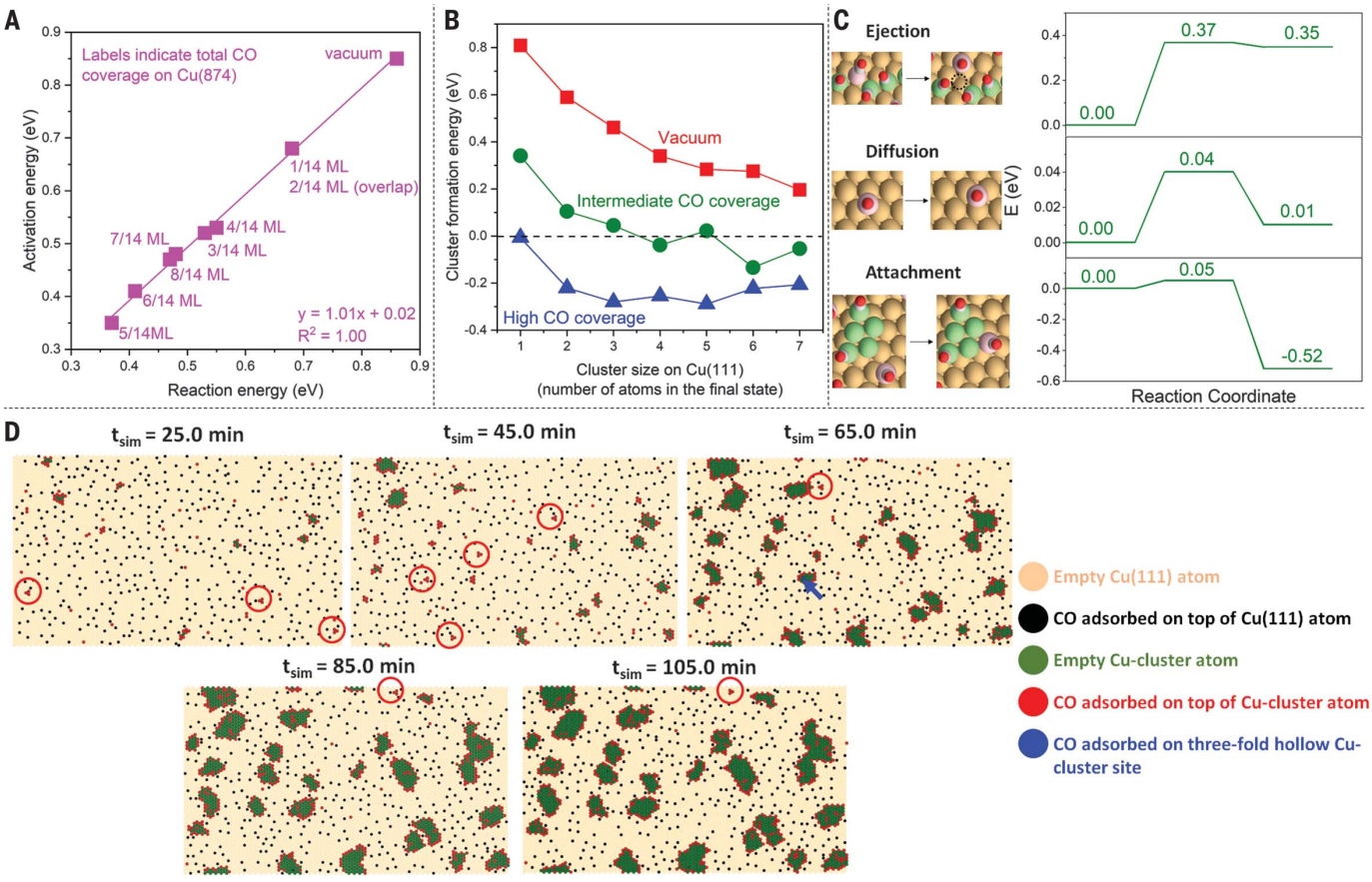

Fig. 4. CO-induced cluster formation on Cu(111) due to ejection of Cu(874) kink atoms. (**A**) Correlation between the calculated activation energy barrier and reaction energy for the kink atom ejection from Cu(874) at various CO coverages. R^2 denotes the coefficient of determination for the linear fit. (**B**) Calculated cluster formation energies (see SM for definition) due to Cu(874) kink atom ejection as a function of the Cu cluster size in the final state on Cu(111) under vacuum as well as at intermediate CO coverages [i.e., 5/14 ML CO coverage on Cu(874); half of the Cu cluster atoms formed on Cu(111) were covered by CO adsorbates] and high CO coverages (7/14 ML CO adsorbed on Cu(874); all peripheral Cu atoms and the center Cu atom of each cluster on Cu(111) were occupied by one CO molecule each]. (**C**) Potential energy diagrams for the Cu(874) kink atom ejection, Cu adatom diffusion on Cu(111), and Cu adatom addition to a Cu_5 cluster to form a Cu_6 cluster on Cu(111) at intermediate CO coverage. The minimum energy atomic structures of the initial and final states for each process are shown in the inset images. Pink, ejected Cu kink atoms; green, regular step atoms on Cu(874) and the preexisting Cu_5 cluster on Cu(111); orange, other Cu atoms; red, O; gray, C. (**D**) KMC snapshots of Cu(111) surface exposed to 0.3-torr CO at room temperature at various simulation times (t_{sim}) over a total period of 105.0 min. A fully CO-covered Cu(874) kinked step edge, with 25% of the total number of Cu(111) terrace atoms, was assumed to be implicitly present and available for atom ejection. Red circles in individual snapshots indicate Cu_3 clusters that are highly active for CO oxidation. CO adsorption at hollow sites on Cu clusters (blue circles) are very rare and indicated by the blue arrow. CO adsorbed on Cu(111) is indicated by small black circles, located in between Cu adatoms and clusters. Very many small black circles located in between Cu adatoms and/or clusters represent CO adsorbed on top of Cu(111) atoms.

facilitate local atom ejection (see discussion of the CO/Ni system in the next section).

Structure sensitivity from STM

The results in Fig. 2, A and B, point to a substantial structure sensitivity of the adatom formation, suggesting that the ejection energy decreased as the coordination number of the atom to be ejected decreased. To explore the role of defect sites and strain, we investigated the effect of CO on a Ni(111) single crystal that exhibited edge and screw dislocation defects using STM. Two types of steps, straight and undulating ones, were observed, both of atomic height (~0.2 nm). Unexpectedly, we observed that Ni adatoms and small clusters formed upon exposure to CO even at 77 K (Fig. 5). At low CO exposures, the undulating step edges became decorated by what appeared as bright protrusions, whereas straight step edges remained pristine (Fig. 5A). Several bright protrusions appeared on the terraces, exhibiting an apparent height larger than that of CO adsorbates (typically around 50 pm) and smaller than that of a full atomic step. We propose that these bright spots contain a few Ni atoms covered with CO.

Upon further CO exposure, the decoration of the undulating steps became denser and the number of clusters on the terraces increased (Fig. 5B). The streaky appearance of many clusters indicates that they were mobile under the STM tip and thus not strongly bound to the terrace sites (movie S1). As the CO exposure increased further, the straight steps also became decorated with CO molecules on every other Ni step atom (Fig. 5C). The unchanged step brightness suggests that Ni atoms were not involved in the decoration of the straight steps, in contrast to that of the undulating steps. Among some of the smallest clusters (see Fig. 5D), individual protrusions, dimer, and trimer species could be observed, which could be interpreted as one, two, and three Ni adatoms covered with CO molecules, respectively.

To better understand the formation process of the Ni adatoms and clusters, we followed the evolution of the surface during continuous exposure to ~4×10^{-9} torr CO in situ (see movie S2). Figure 5, E and F, shows derivative images (to enhance the contrast) of two frames from movie S2, which indicate that clusters were first limited to the terrace in the top

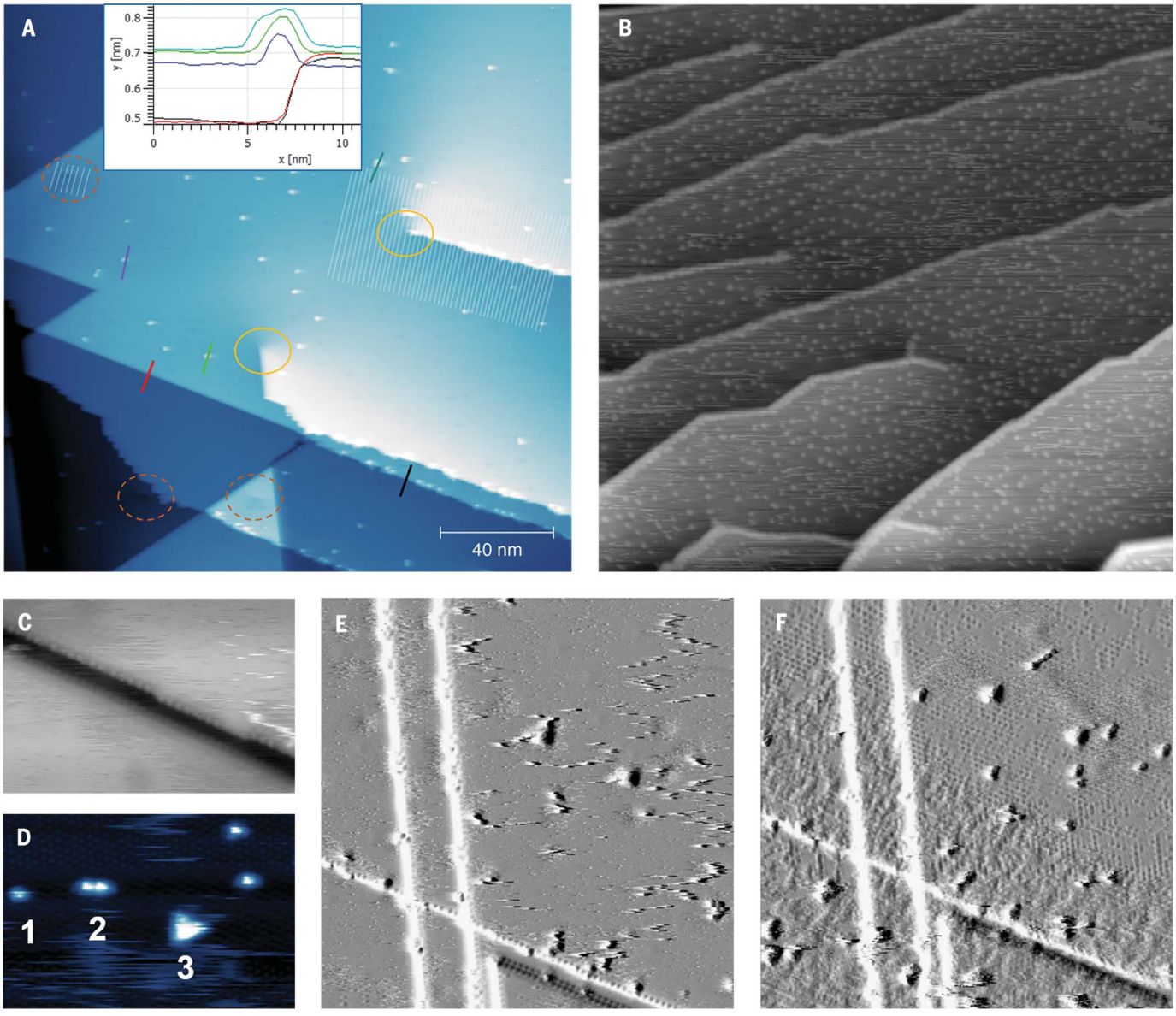

Fig. 5. STM images showing the effect of CO exposure on a defective Ni(111) surface. (**A**) At low CO exposure (background pressure of $<1 \times 10^{-10}$ torr), step-edge decoration and a few clusters on terraces are observed. Several screw and edge dislocations are present on the surface, which are indicated by yellow circles and red dashed circles, respectively. A series of line profiles across one of each type of dislocation is hinted at by semitransparent white lines, which were used to determine the change in step height (see SM). For comparison, line profiles are shown in the inset, which illustrate that straight (red) and wiggly (black) steps are of comparable height namely ~0.2 nm, and that clusters on the surface (green to blue) are of smaller heights. (**B**) Upon exposure to 3×10^{-10} torr CO for 20 s, the density of step decoration and clusters increases. Note that many clusters are mobile under the STM tip, resulting in a streaky appearance. (**C**) Upon exposure to 2×10^{-9} torr CO for 15 s, the straight steps exhibit adsorbate molecules in a p(2 × 2) arrangement, but the apparent step brightness remains the same. (**D**) Small clusters often appear as individual protrusions, dimer, and trimer species, which might be interpreted as one, two, and three Ni adatoms covered with CO molecules (recorded after extended exposure to 4×10^{-9} torr CO). (**E** and **F**) Derivative images of two frames from an STM movie recorded during exposure to ~4×10^{-9} torr CO show the progression of the interaction between CO and the defective Ni surface. Imaging parameters were as follows: temperature of 77 K [(A) to (F)]; bias voltages and tunneling currents of V_b = 100 mV and I_t = 150 pA [(A) and (C) to (F)] and V_b = 200 mV and I_t = 50 pA (B); and image sizes of 200 nm by 200 nm [(A) and (B)], 15 nm by 10 nm [(C) and (D)], and 30 nm by 30 nm [(E) and (F)].

right (Fig. 5E) but start to cover the rest of the surface after longer CO exposure (Fig. 5F). As the CO coverage increases, some clusters became locked into place by adsorbed CO molecules and appeared less streaky. An increase in apparent background roughness indicates that CO adsorption started from the step edges and then propagated into the terraces; p(2 × 2) chains along the steps and some molecules in the bottom left of Fig. 5E turn into a mostly covered bottom left half of Fig. 5F.

Based on our theoretical results (see Fig. 2C), the estimated T_{form}^{ad} value for CO-induced atom ejection from unstrained Ni(874) should be 487 K, which is well above the experimental temperature of 77 K. We propose that the large local strain near dislocations combined with a high degree of undercoordination characterizing the step defect sites could lead to a substantial decrease in the cluster formation temperature. To this end, we conducted

additional DFT calculations using a strained Ni (874) kink slab as a model for local dislocation defects (see SM for details). Our results demonstrate that the atom ejection from a kinked step site [$E^{ad}_{form\ \downarrow_{(111)}}{}^{(874)}$ = 1.26 eV for CO-induced atom ejection from the Ni(874) kink at the low-coverage limit of 1/14 ML; see table S5] would be energetically favored compared with that from a regular step [$E^{ad}_{form\ \downarrow_{(111)}}{}^{(211)}$ = 1.67 eV for CO-induced atom ejection from the Ni(211) step edge at the low-coverage limit of 1/9 ML; see table S4]. Further, combined with high CO coverage and large local compressive strain, the adatom formation energy could be markedly reduced, which potentially leads to Ni adatom formation even at 77 K. Our calculations also predict a similar strain effect for Pt because large local compressive strain would also facilitate CO-induced adatom ejection from a Pt(874) kink (fig. S19).

Discussion

We constructed a framework for the prediction of adsorbate-induced metal-metal bond breaking in solid surfaces and subsequent cluster formation on these surfaces. The insights about the nature of the active site could serve as a starting point for the screening of catalytic systems (e.g., CO oxidation, water-gas shift, and methanol synthesis on Cu, ammonia oxidation on Ag and Cu, NO reduction by H_2 on Pt, methane oxidation on Pd, and methane steam reforming on Ni) with potential adsorbate-induced clustering behavior. The rich structure sensitivity of the cluster formation process greatly adds to the complexity of this phenomena. The energetics associated with the initial adatom formation is not only affected by the structure of the atom ejection source (low-index terrace versus step versus kink) but can also vary considerably in the presence of surface defects. In the CO/Ni case, we demonstrated that compared with pristine (211) step edges, ejection from (874) kink sites could facilitate adatom formation by 0.41 eV. Strain induced by local defects such as screw dislocations could further reduce the adatom formation energy by 1 eV or more, which resulted in cluster formation at unexpectedly low temperatures. Therefore, the DFT-based predictions for reaction-driven active-site formation that are presented in this study, particularly those based on defect-free surface models, should only serve as initial guides. Given the wide range of local defect structures on metal catalyst surfaces, it is not practical to construct a universal model that accounts for all possible atom-ejection sources. Defect-rich catalysts, on which cluster formation could take place much more easily than estimated from predictions made based on defect-free surface models, should be treated with caution on a case-by-case basis.

Importantly, our results may reshape our understanding of the nature of active sites on metal NPs under catalytic reaction conditions. The low-index crystal-surface models that are widely used to calculate reaction parameters should not be taken for granted as providing the right energetic parameters; instead, nature allows for the formation of more and new types of active surface sites in reactive environments. Although the focus of our study is on the adatom formation energetics, the size of the small clusters formed by the aggregation of ejected atoms and possible sintering of those clusters would also be determined by the reactive conditions under consideration, which, in return, can alter the coverage of surface reaction intermediates under relevant temperature and pressure. This type of insight can be obtained through more in-depth investigations of specific systems, such as our KMC case-study for CO/Cu. Our approach could be easily expanded to investigate other combinations of adsorbate and catalytic surfaces—including bulk alloys (*33*), near-surface alloys (*34*, *35*), and metal oxides (*36*, *37*)—and to further explore coverage, elemental surface composition, and strain effects.

The in situ generated cluster-type active sites tend to bridge the gap between heterogeneous and homogeneous catalysis. In the latter, metal centers consisting of one or up to a few metal atoms are often responsible for catalytic transformations (*38*). Our framework should be useful for designing more accurate active-site models in theoretical studies, as well as for guiding sophisticated in situ experimental studies on the more practically relevant catalytic systems. Further, and from the catalytic active-site synthesis perspective, we suggest that we have elucidated a bottom-up approach to nanoclusters that naturally complements the top-down approach of size-selected nanocluster synthesis (*10*, *16*). We expect that this approach will have important ramifications for both thermal catalysis and electrocatalysis.

REFERENCES AND NOTES

1. J. K. Nørskov *et al*., *Chem. Soc. Rev.* **37**, 2163–2171 (2008).
2. B. W. J. Chen, L. Xu, M. Mavrikakis, *Chem. Rev.* **121**, 1007–1048 (2021).
3. W. Huang *et al*., *Science* **373**, 1518–1523 (2021).
4. Z. Xu *et al*., *Nature* **372**, 346–348 (1994).
5. C. T. Campbell, S. C. Parker, D. E. Starr, *Science* **298**, 811–814 (2002).
6. A. A. Herzing, C. J. Kiely, A. F. Carley, P. Landon, G. J. Hutchings, *Science* **321**, 1331–1335 (2008).
7. H.-G. Boyen *et al*., *Science* **297**, 1533–1536 (2002).
8. M. Turner *et al*., *Nature* **454**, 981–983 (2008).
9. A. S. Crampton *et al*., *Nat. Commun.* **7**, 10389 (2016).
10. W. E. Kaden, T. Wu, W. A. Kunkel, S. L. Anderson, *Science* **326**, 826–829 (2009).
11. K. Ding *et al*., *Science* **350**, 189–192 (2015).
12. H. Häkkinen, S. Abbet, A. Sanchez, U. Heiz, U. Landman, *Angew. Chem. Int. Ed.* **42**, 1297–1300 (2003).
13. F. F. Tao *et al*., *Nano Lett.* **16**, 5001–5009 (2016).
14. P. L. Hansen *et al*., *Science* **295**, 2053–2055 (2002).
15. V. R. Stamenkovic *et al*., *Science* **315**, 493–497 (2007).
16. S. Vajda *et al*., *Nat. Mater.* **8**, 213–216 (2009).
17. J. Jones *et al*., *Science* **353**, 150–154 (2016).
18. G. A. Somorjai, Y. Li, *Introduction to Surface Chemistry and Catalysis* (Wiley, ed. 2, 2010).
19. B. Eren *et al*., *Science* **351**, 475–478 (2016).
20. M. Roiaz *et al*., *J. Phys. Chem. C* **123**, 8112–8121 (2019).
21. B. Eren *et al*., *J. Am. Chem. Soc.* **140**, 6575–6581 (2018).
22. P. Cernota, K. Rider, H. A. Yoon, M. Salmeron, G. Somorjai, *Surf. Sci.* **445**, 249–255 (2000).
23. S. R. Longwitz *et al*., *J. Phys. Chem. B* **108**, 14497–14502 (2004).
24. F. Tao *et al*., *Science* **327**, 850–853 (2010).
25. O. Balmes, G. Prevot, X. Torrelles, E. Lundgren, S. Ferrer, *ACS Catal.* **6**, 1285–1291 (2016).
26. B. Eren, M. Salmeron, *J. Phys. Chem. C* **123**, 8171–8176 (2019).
27. C. Kittel, *Introduction to Solid State Physics* (Wiley, ed. 8, 2004).
28. B. L. M. Hendriksen *et al*., *Nat. Chem.* **2**, 730–734 (2010).
29. A. A. Gokhale, J. A. Dumesic, M. Mavrikakis, *J. Am. Chem. Soc.* **130**, 1402–1414 (2008).
30. S. Kuld *et al*., *Science* **352**, 969–974 (2016).
31. F. Wang *et al*., *ACS Catal.* **8**, 2670–2682 (2018).
32. K. G. Papanikolaou, M. T. Darby, M. Stamatakis, *ACS Catal.* **10**, 1224–1236 (2020).
33. D. Kim, J. Resasco, Y. Yu, A. M. Asiri, P. Yang, *Nat. Commun.* **5**, 4948 (2014).
34. J. Greeley, M. Mavrikakis, *Nat. Mater.* **3**, 810–815 (2004).
35. M. Lischka, C. Mosch, A. Groß, *Electrochim. Acta* **52**, 2219–2228 (2007).
36. Z. Liang, T. Li, M. Kim, A. Asthagiri, J. F. Weaver, *Science* **356**, 299–303 (2017).
37. M. Van den Bossche, H. Grönbeck, *J. Am. Chem. Soc.* **137**, 12035–12044 (2015).
38. E. Gross, G. A. Somorjai, *Top. Catal.* **57**, 812–821 (2014).

ACKNOWLEDGMENTS

Funding: The theoretical work was supported by the US Department of Energy (DOE), Office of Basic Energy Sciences, Division of Chemical Sciences, Catalysis Science Program, under grant DE-FG02-05ER15731. The experimental work was supported by the DOE, Office of Basic Energy Sciences, Division of Materials Sciences and Engineering, under contract no. DE-AC02-05CH11231, through the Structure and Dynamics of Materials Interfaces program (FWP KC31SM). B.A.J.L. acknowledges financial support from the Young Academy of the Bavarian Academy of Sciences and Humanities and Deutsche Forschungsgemeinschaft (DFG, German Research Foundation) under Germany's Excellence Strategy EXC 2089/1-390776260 during analysis of the CO on Ni(111) adsorption and diffusion. M.M. acknowledges financial support from the Miller Institute at the University of California, Berkeley, through a Visiting Miller Professorship with the Department of Chemistry. We used resources at the National Energy Research Scientific Computing Center, a DOE Office of Science User Facility that is supported by the DOE, Office of Science, under contract no. DE-AC02-05CH11231 using NERSC award BES-ERCAP0022773. Part of the computational work was carried out using supercomputing resources at the Center for Nanoscale Materials (CNM), a DOE Office of Science User Facility located at Argonne National Laboratory that is supported by DOE contract DE-AC02-06CH11357. **Author contributions:** Conceptualization: L.X., K.G.P., B.A.J.L., G.A.S., M.S., M.M.; Methodology: L.X., K.G.P., B.A.J.L., M.S., M.M.; Investigation: L.X., K.G.P., L.J., B.A.J.L.; Funding acquisition: M.M.; Supervision: M.M.; Writing – original draft: L.X., K.G.P., M.M.; Writing – review and editing: L.X., K.G.P., B.A.J.L., G.A.S., M.S., M.M. **Competing interests:** The authors declare that they have no competing interests. **Data and materials availability:** All data are available in the main text or the supplementary materials. **License information:** Copyright © 2023 the authors, some rights reserved; exclusive licensee American Association for the Advancement of Science. No claim to original US government works. https://www.science.org/about/science-licenses-journal-article-reuse

SUPPLEMENTARY MATERIALS

science.org/doi/10.1126/science.add0089
Materials and Methods
Supplementary Text
Figs. S1 to S28
Tables S1 to S13
References (*39*–*71*)
Movies S1 and S2
Data S1

Submitted 14 May 2022; resubmitted 21 December 2022
Accepted 14 March 2023
10.1126/science.add0089

COLLISION DYNAMICS

Tomography of Feshbach resonance states

Baruch Margulis[1], Karl P. Horn[2], Daniel M. Reich[2], Meenu Upadhyay[3], Nitzan Kahn[1], Arthur Christianen[4,5], Ad van der Avoird[5], Gerrit C. Groenenboom[5], Christiane P. Koch[2]*, Markus Meuwly[3]*, Edvardas Narevicius[1,6]*

Feshbach resonances are fundamental to interparticle interactions and become particularly important in cold collisions with atoms, ions, and molecules. In this work, we present the detection of Feshbach resonances in a benchmark system for strongly interacting and highly anisotropic collisions: molecular hydrogen ions colliding with noble gas atoms. The collisions are launched by cold Penning ionization, which exclusively populates Feshbach resonances that span both short- and long-range parts of the interaction potential. We resolved all final molecular channels in a tomographic manner using ion-electron coincidence detection. We demonstrate the nonstatistical nature of the final-state distribution. By performing quantum scattering calculations on ab initio potential energy surfaces, we show that the isolation of the Feshbach resonance pathways reveals their distinctive fingerprints in the collision outcome.

In atomic and molecular collisions, elastic, inelastic, and reactive scattering compete with resonance pathways. In particular, Feshbach scattering resonances that arise from the coupling between different degrees of freedom are instrumental for the transfer of energy from internal to relative motion (*1*, *2*). Feshbach resonances have been observed in atom-atom (*3*–*5*), atom-ion (*6*), atom-molecule (*7*–*9*), bimolecular (*10*, *11*), and field-dressed bimolecular collisions (*12*) by tuning either the collision energy or the magnetic field strength in the case of trapped ultracold particles. Alternatively, a single resonance path can be selected by spectroscopic excitation, as in predissociation (*13*–*16*) or electron photodetachment (*17*, *18*). However, one is then limited to the Franck-Condon region close to the equilibrium geometry that represents a rather small part of the overall phase space. In this work, we combined the advantage of ultracold molecular collisions exploring a large part of the phase space with the preparation of isolated resonances that allowed us to follow collision pathways. We achieved this by populating vibrational Feshbach resonances at long range, just below the threshold. In contrast with predissociation and similar to full collisions, the colliding particles possess a set of well-defined, unperturbed internal quantum numbers. As in reactive bialkali systems (*7*, *9*, *19*), we explored the collision regime where the short range intermolecular interaction is strong, leading to the mixing between tens of rovibrational quantum states coupled by anisotropic interactions.

Our method is complementary to and expands the capabilities of electron photodetachment spectroscopy (EPDS) (*17*, *18*) (supplementary materials). In EPDS, the electron is stripped away from an anion through interaction with laser radiation. The electron kinetic energy distribution contains information about the energy levels of the neutral product. However, the detection of subsequent dynamics is challenging. In our method, the starting point is a cold collision between an electronically excited atom and a neutral molecule. The electron is emitted during a charge transfer process that results in ionic molecular products with a well-defined set of internal quantum numbers. Because of the low collision energy, we populated a narrow momentum band during the ionization step. In such a case, the distribution of initial and final molecular ion states can be simply detected through energy conservation. The kinetic energy distribution of the molecular ions provides additional information that encodes the final quantum-state distribution resulting from the decay of Feshbach resonances populated upon the ionization step. The nonselective nature of the ionization process leads to the formation of molecular ions in many vibrational states. As a result, the ionic kinetic energy distribution contains contributions from all the accessible vibrational branches of Feshbach resonances. We disentangled the contribution of individual initial molecular ionic states using ion-electron coincidence detection. This scheme allowed us to simultaneously detect all the possible quantum states in a tomographic manner. Our results show that each Feshbach resonance has a distinctive signature reflected in the final quantum-state distribution. In a similarly strongly interacting system, it has been shown (*20*) that the final-state distribution follows statistical arguments. In earlier reactive scattering experiments in which Feshbach resonances were detected (*21*, *22*), the measured final-state distribution was found to be insensitive to the collision energy up to 180 K and did not depend on the total angular momentum (*23*). By contrast, in our case, the quantum signatures of vibrational resonances are sensitive to the details of the interaction. We confirmed this by carrying out full ab initio–based quantum scattering calculations for the benchmark system of H_2^+ colliding with a noble gas atom. Our work shows that quantum signatures can be observed even in strongly interacting and anisotropic systems if the resonance pathway can be isolated.

The method

We present a schematic description of our approach in Fig. 1. The starting point is the collision between a metastable noble gas atom and a ground-state molecule, which leads to Penning ionization (PI). The ionization is a sudden, nonadiabatic transition of the initial neutral state onto the manifold of ionic states (*24*). It can be described by projecting the scattering wave function of the neutrals Ψ (R), scaled by the ionization probability Γ (R), onto the full set of states describing the molecular ion–neutral atom interactions. Because ionization occurs at large intermolecular distances, the initial state is projected in the region where the long-range part of the intermolecular potential dominates. As a result, the Feshbach states are characterized by the free molecule basis with no change in the rotational quantum number (j) of the molecule. The populated states differ asymptotically by the vibrational energy of the molecular ion. Because of the electron's small mass, it carries away most of the excess energy released at the ionization step. Therefore, the initial vibrational state (v) of the molecular ion is encoded in the electron kinetic energy. The energy distribution of electrons represents the vibrational spectrum of the molecular ion with near Franck-Condon probabilities (*25*, *26*). In Fig. 1B, we show the resulting dynamics of such a Feshbach resonance state in which a single quantum of vibrational excitation is converted into a combination of kinetic and rotational energy. In this system, the closed channel is the vibrationally excited state, whereas the open channels are the vibrationally ground, rotationally excited states. The final quantum-state distribution is reflected in the velocity distribution of the molecular ion. The electron-ion coincidence measurement completes the quantum state-to-state mapping because every detected electron-ion pair is generated during the same collision event.

The ionization step is governed by a charge transfer process that depends exponentially

[1]Department of Chemical and Biological Physics, Weizmann Institute of Science, Rehovot 7610001, Israel. [2]Dahlem Center for Complex Quantum Systems and Fachbereich Physik, Freie Universität Berlin, Arnimallee 14, 14195 Berlin, Germany. [3]Department of Chemistry, University of Basel, Basel, Switzerland. [4]Max-Planck-Institut für Quantenoptik, Hans-Kopfermann-Strasse 1, D-85748 Garching, Germany. [5]Theoretical Chemistry, Institute for Molecules and Materials, Radboud University, Heyendaalseweg 135, 6525 AJ Nijmegen, Netherlands. [6]Department of Physics, Technische Universität, Dortmund, Germany.
*Corresponding author. Email: edvardas.narevicius@tu-dortmund.de (E.N.); m.meuwly@unibas.ch (M.M.); christiane.koch@fu-berlin.de (C.P.K.)

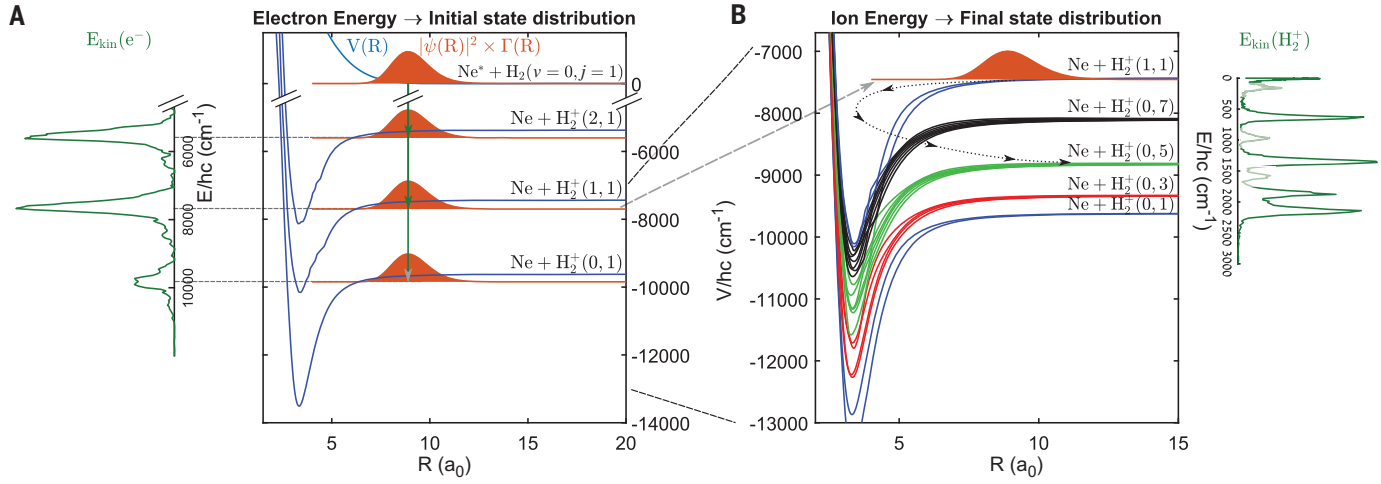

Fig. 1. Adiabatic potential energy curves and wave functions describing Penning collisions at total angular momentum state J = 6 and partial wave l = 5 between metastable neon and ortho-H_2 in its ground rovibrational state. Each adiabatic curve corresponds to the vibrational and rotational quantum numbers (v, j), of H_2^+. R, intermolecular separation in Bohr radii (a_0). Same-color curves indicate adiabatic curves with different partial wave quantum number l, but with the same molecular rotation quantum number j. (**A**) Representation of the ionization step. The green curve represents the measured kinetic energy (E) of electrons and provides the initial-state distribution of the Feshbach states. The energy positions of the projected states are set relative to the center of the measured peaks. (**B**) Representation of the decay of Feshbach states formed upon ionization. The measured ionic kinetic energy distribution (green curve) corresponds to the final-state distribution. The contribution of para-H_2 to the kinetic energy distribution is indicated in light green. The energy position of the projected state is set by the measured resonance energy. *hc*, Planck constant times the speed of light.

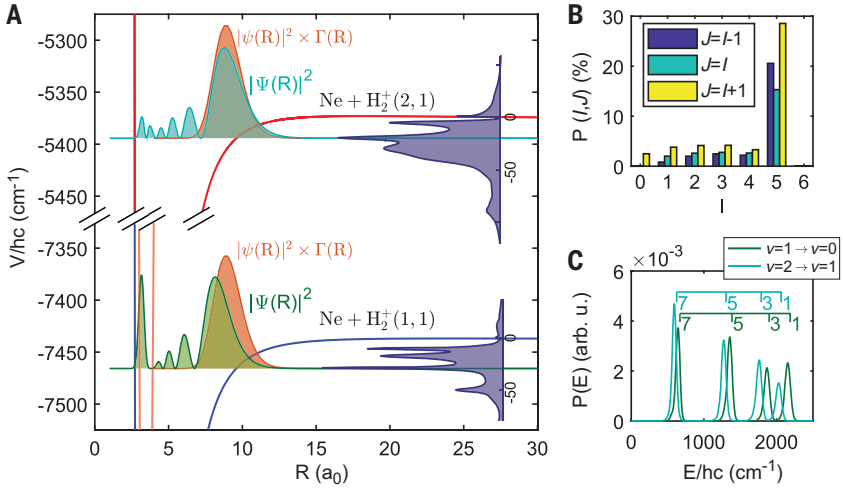

Fig. 2. Computational characteristics of Feshbach resonance states. (**A**) Zoomed-in view of adiabatic PES together with corresponding radial wave functions Ψ (R). Shown on the right side of the figure are computed overlap plots for total angular momentum J = 6 and initial partial wave l = 5, which represent the energy distribution of populated Feshbach states. The presented ionic energy eigenstates have the largest overlap with the initial neutral state, which describes the Penning collisions, $|\Psi(R)|^2 \times \Gamma(R)$. (**B**) Relative contribution of each angular momentum state of collision for Ne(^{3}P)-ortho-H_2 collisions considering the experimental collision energy and spread. P(l,J), ionization probability per initial l and J. (**C**) Computed ionic energy distributions that represent final-state distribution corresponding to initial vibrational states v = 2 and v = 1. The threshold energies are labeled by the final rotational state of free ortho − H_2^+ ions. The distributions are normalized to unity. $P(E)$, probability as a function of energy, E; *Arb. u.*, arbitrary units.

on the intermolecular distance. As such, the part of the scattering wave function that undergoes ionization is strongly localized in the vicinity of the classical turning point of the neutral potential energy surface (Fig. 1A). Such a strong localization of the initial wave function is essential for the resolution of our measurement because it determines the energy spread in the distribution of populated ionic states. After ionization, the initial scattering wave function spans a narrow, 50-cm^{-1}-wide energy band located 30 cm^{-1} away from the dissociation threshold of the molecular ion–neutral atom interaction potential energy surface. This energy window constitutes a small fraction of the total interaction strength reflected by a deep potential well of 4450 cm^{-1} in the case of Ne − H_2^+. This energy window contains only a few Feshbach resonances, associated to triatomic rovibrational states (Shown in Fig. 2A for two initial vibrational states, v = 2 and v = 1, of the molecular hydrogen ion). Moreover, the total angular momentum and parity of the Feshbach resonance are set during the PI step. By tuning the collision energy of the neutral collision system to match a shape resonance, we were able to control the total angular momentum distribution, which peaked around the resonant partial wave (*27*, *28*). Notably, the near-threshold Feshbach resonance wave functions are sensitive to both the short- and the long-range parts of the interaction potential. While in the short range, all of the degrees of freedom are strongly coupled by the anisotropy of the potential energy surface (PES), the resonance wavefunction at large separation is nearly separable into the molecular ion and neutral atom. Whereas the strength of the leading term of the anisotropic interaction is 1300 cm^{-1} at an intermolecular separation of 2 a_0, it falls to 1 cm^{-1} at 10 a_0. We demonstrate that each Feshbach resonance state has a distinctive signature in the final-state distribution depending on the Feshbach state energy,

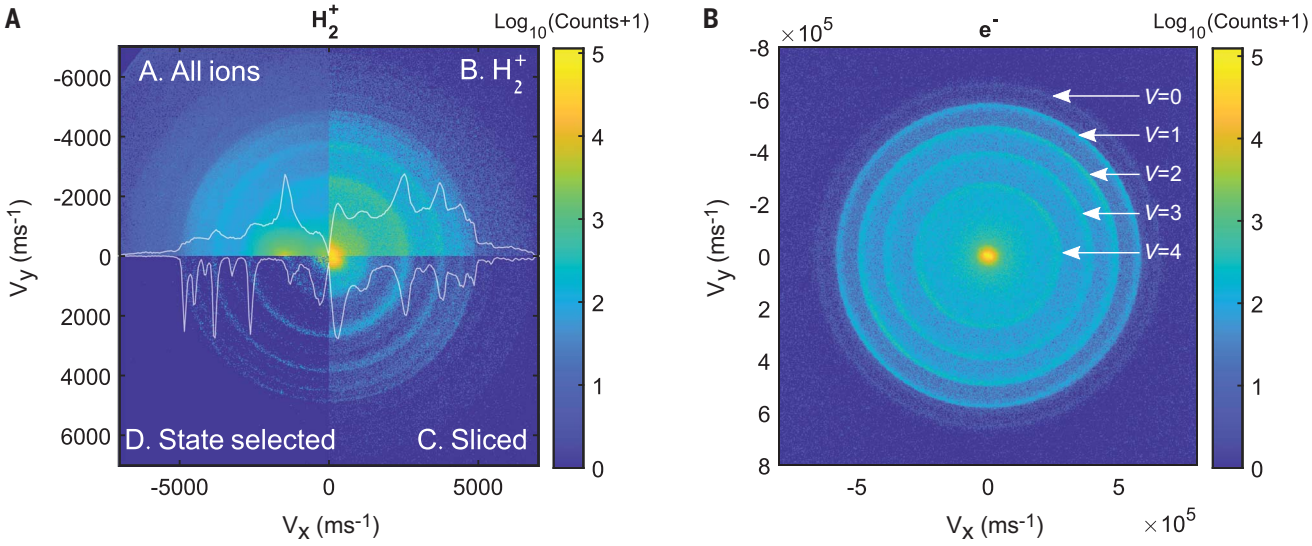

Fig. 3. VMI images of ions and coincidence electrons. (**A**) In clockwise order from the top left corner of the image, the first quadrant presents the overall accumulated ionic VMI image, which includes all ionic masses; the second quadrant shows the VMI image of H_2^+ ions alone, obtained with electron-ion coincidence; the third quadrant presents a sliced image using ion time-of-flight information; and the last quadrant presents the sliced VMI image of ions related to initial vibrational state $v = 1$ with ion-electron correlations. Angle-integrated velocity distributions are indicated with white curves at each quadrant. (**B**) VMI image of coincidence electrons corresponding to H_2^+.

the total angular momentum, and the vibrational quantum number (Fig. 2C).

Results and discussion

We studied two benchmark molecular ion collision systems, Ne − H_2^+ and He − H_2^+, by measuring the correlated energy distributions of the products of Ne*-H_2 and He*-H_2 PI collisions. The experimental setup is described in (*29*). In short, we generated two supersonic beams of metastable noble gas atoms and ground-state molecules using two Even-Lavie (*30*) valves that were positioned at a relative angle of 4.5°. We excited the noble gas atoms to a metastable state by means of a dielectric discharge that was located directly after the valve orifice (*31*). We determined the beam mean velocity by the valve temperature and the gas mixture composition. We performed PI collisions at an energy that matched the position of one of the shape resonances that occur at a few Kelvin (*27*). We first located the shape resonance positions with a complementary measurement by using the merged beam approach (supplementary materials). We present the angular momentum–state distribution for Ne*-ortho-H_2 and Ne*-para-H_2 and He*-H_2 collisions in Fig. 2B and fig. S2, respectively. For Ne*+H_2, we chose a collision energy that matches the position of the $l = 5$ shape resonance. As a result, scattering states with total angular momenta $J = 4$, 5, and 6 had the highest contribution.

We detected the product ion and electron velocities using a coincidence double velocity map imaging apparatus (*29*). Coincidence detection was the most important aspect of our experiment. The correlation between ions and electrons allowed us to extract the mass, identify the initial state, and determine the velocity magnitude distribution instead of just the projection. It also allowed us to correct the ionic velocity map imaging (VMI) images for electron recoil. Such a correction was essential for He-H_2 where the electron recoil blurred the ionic VMI image by about 100 m/s.

We present the ion and electron VMI images as measured in coincidence during the Ne*-H_2 collisions in Fig. 3. The ion VMI image is divided into quadrants that represent the various steps in the analysis of the raw, accumulated data. We started with the raw accumulated VMI image, which includes all of the ionic products in Fig. 3A. We used time-of-flight (TOF) information to obtain the VMI image of H_2^+ ions alone (Fig. 3B). During the next step, we selected the central part of H_2^+ TOF distribution to time-slice the VMI image (Fig. 3C). This procedure enabled us to construct the velocity-magnitude distribution by means of angle integration of a sliced image without the need of inverse Abel transformation–based techniques. The mass-selected and time-sliced ionic VMI image consists of a series of concentric rings indicating a set of discrete final quantum state channels in which the internal vibrational molecular ion energy is converted into a combination of the final rovibrational state and translational energy. However, this image contains information from all of the five initial vibrational states of the H_2^+ molecular ion that are populated during the quenching process. We constructed the ionic VMI image that corresponds to an individual initial quantum state of H_2^+ by postselecting only those ions that correlate with the electrons within a certain kinetic energy window. Our tomography procedure required us to eliminate the effect of high-energy electrons on rings associated with the lower-energy electrons. We have developed a "peeling" algorithm that corrects an individual ionic image because of the overlap of its coincidence electrons with higher-energy electrons. A detailed description of the peeling algorithm can be found in the supplementary materials.

We obtained the energy distribution of the molecular ions by angular integration of the sliced, initial state–selected VMI images (Fig. 4, blue curves). The energy scale corresponds to the kinetic energy release, E, which was partitioned between the molecular ion and the neutral atom according to momentum conservation. We observed sharp peaks indicating the quenching of Feshbach resonances to different continuum states that were labeled by the final quantum state (v', j') of the free molecular ion. The final-state distribution thus represents the observation of the projection of the Feshbach resonance onto the continuum-basis set, which we refer to as tomography. The threshold energies are depicted in Fig. 4 with black and green lines for $\Delta v = 1$ and $\Delta v = 2$ transitions, respectively. Each threshold energy is labeled by the final rotational state, j', of the free H_2^+ ion. We observed a higher probability of odd final

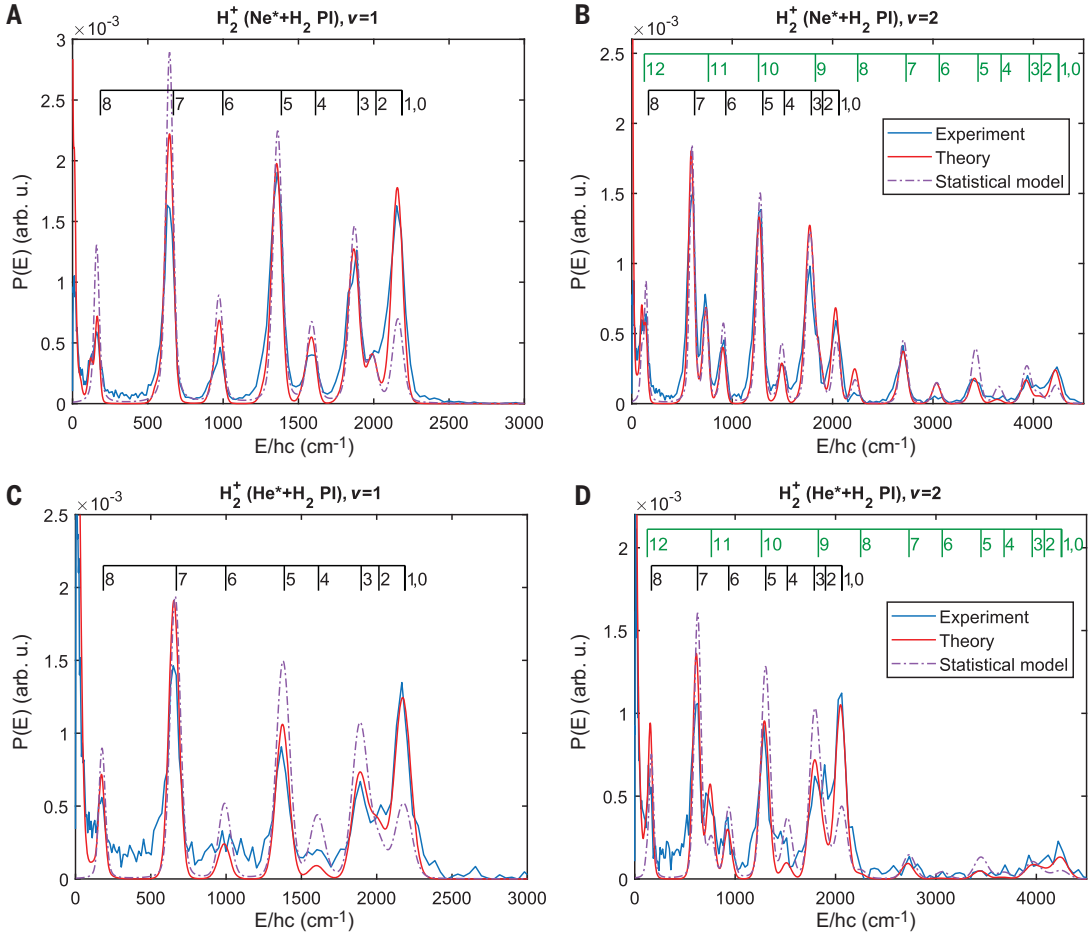

Fig. 4. Experimental and theoretical kinetic energy distributions that show the decay of Feshbach states into various continuum states. (**A** and **B**) Ne − H_2^+ at (A) $v = 1$ and (B) $v = 2$. (**C** and **D**) He − H_2^+ at (C) $v = 1$ and (D) $v = 2$. Theoretical curves are convoluted by the experimental resolution. Experimental and theoretical kinetic energy distributions indicated with blue and red curves, respectively. Distributions based on the statistical model are indicated with the pink dashed curves. *Arb. u.*, arbitrary units.

rotational states because of the spin statistics of ortho- versus parahydrogen spin isomers with the 3:1 statistical population ratio. In addition to the resonance state tomography, we obtained the resonance energy that is reflected by the shift of all peaks relative to the threshold energies. For the $v = 1$ state, we found the mean resonance energies to be −28.9 ± 3.6 cm^{-1} for Ne − H_2^+ and −20.8 ± 3.1 cm^{-1} for He − H_2^+. We report all resonance energies relative to the position of the noble gas atom and rotational ground-state molecule dissociation threshold.

To confirm the nature of the resonances and to provide additional characterization, we carried out quantum wave packet calculations on an available full configuration interaction (FCI) PES for He − H_2^+ (*32*) and a new PES for Ne − H_2^+. We determined the new $^2A'$ Ne − H_2^+ PES using 38,200 reference energies at the coupled-cluster single-, double-, and perturbative triple-excitations [CCSD (T)]/aug-cc-pV5z level of theory. We performed full coupled-channel calculations of the He − H_2^+ and Ne − H_2^+ cross sections with converged bases, with rotational states going up to and including $j = 25$ and vibrational states going up to and including $v = 5$, respectively. For He − H_2^+, fewer rotational states were required to obtain convergence. The numerical results were convoluted with the experimental uncertainty and are in excellent agreement with the experimental data (Fig. 4, blue versus red traces). Together with earlier work on the near-dissociative states of He − H_2^+ (*32*), the present agreement between experiment and theory points to near-spectroscopic accuracy of the FCI PES. Similarly, for Ne − H_2^+, the agreement between computational and experimental results is very encouraging. Further improvement could be obtained from morphing the underlying PES (*33*, *34*).

Because of the strong and highly anisotropic intermolecular interaction, one could expect a statistical description to be sufficient to describe the final-state distribution. Both interaction strength and anisotropy are comparable to the case of KRb + KRb bimolecular reactions (*20*). In the bimolecular case, we found deviations from the statistical model at the limit of the reaction exothermicity at which the centrifugal barrier hinders the reaction rate. In our case, the level of initial excitation relative to the centrifugal barrier height in the exit channel (Fig. 1B) allows all vibrational and rotational transitions to occur. In a purely statistical approach, the decay probability is proportional to the number of energetically accessible exit channels (*20*, *35*). The level of degeneracy in each continuum state is set by the initial total angular momentum J and by parity $(-1)^{j+l}$, which are conserved quantities. For a final rotational state j', the number of exit channels is determined by the number of available partial waves that fulfill the relation $J = |j' - l'|, |j' - l'| + 1, \ldots, j' + l'$ and maintain the right parity. We have constructed a statistical model in which we assumed a single Feshbach resonance, at position and width obtained with exact calculations, for which the decay probability to each final rovibrational state is given by the number of allowed partial waves. The resulting energy distribution was convoluted by the experimental resolution and is shown as pink dashed lines in Fig. 4. Comparing the results of this procedure to the experimental data shows clear deviations from the statistical model. We show a quantitative comparison of the results of the statistical model and exact calculations to the experimental data in fig. S10. In particular, the statistical model underestimates the decay to states with low final j' and overestimates the decay to states with high final j'. This observation

suggests that certain transition probabilities are preferred rather than statistical.

Outlook

Although we probed a collision system with strong interactions (charge-induced dipole) and high anisotropy, the Feshbach resonance states have a distinct quantum signature in the final-state distribution. This property may be useful for control over the final-state distribution by manipulating the quantum state of the Feshbach state itself. One way to do so is by tuning the total angular momentum, which is difficult to control. However, an effective way to select states with a certain amount of total angular momentum is to leverage different shape resonances of the neutral collision complex. This could be done with the merged beam approach, in which collision dynamics could be tuned down to a single quantum of angular momentum (*36*). Performing coincidence experiments in the *p*-wave limit will demonstrate the control of the final-state distribution. Moreover, because of the reduction in participating quantum states, individual Feshbach states that correspond to the triatomic rovibrational spectrum could be resolved.

REFERENCES AND NOTES

1. H. Feshbach, *Ann. Phys.* **5**, 357–390 (1958).
2. U. Fano, *Phys. Rev.* **124**, 1866–1878 (1961).
3. A. Frisch *et al*., *Nature* **507**, 475–479 (2014).
4. V. Barbé *et al*., *Nat. Phys.* **14**, 881–884 (2018).
5. C. Chin, R. Grimm, P. Julienne, E. Tiesinga, *Rev. Mod. Phys.* **82**, 1225–1286 (2010).
6. P. Weckesser *et al*., *Nature* **600**, 429–433 (2021).
7. H. Son *et al*., *Science* **375**, 1006–1010 (2022).
8. T. de Jongh *et al*., *Science* **368**, 626–630 (2020).
9. H. Yang *et al*., *Science* **363**, 261–264 (2019).
10. J. J. Park, Y.-K. Lu, A. O. Jamison, T. V. Tscherbul, W. Ketterle, *Nature* **614**, 54–58 (2023).
11. S. Chefdeville *et al*., *Science* **341**, 1094–1096 (2013).
12. X.-Y. Chen *et al*., *Nature* **614**, 59–63 (2023).
13. F. F. Crim, *Science* **249**, 1387–1392 (1990).
14. R. E. Miller, *Science* **240**, 447–453 (1988).
15. A. Rohrbacher, N. Halberstadt, K. C. Janda, *Annu. Rev. Phys. Chem.* **51**, 405–433 (2000).
16. C. D. Foley, C. Xie, H. Guo, A. G. Suits, *Science* **374**, 1122–1127 (2021).
17. J. B. Kim *et al*., *Science* **349**, 510–513 (2015).
18. R. Otto *et al*., *Science* **343**, 396–399 (2014).
19. K.-K. Ni *et al*., *Science* **322**, 231–235 (2008).
20. Y. Liu *et al*., *Nature* **593**, 379–384 (2021).
21. R. T. Skodje *et al*., *Phys. Rev. Lett.* **85**, 1206–1209 (2000).
22. M. Qiu *et al*., *Science* **311**, 1440–1443 (2006).
23. T. Wang *et al*., *J. Phys. Chem. Lett.* **5**, 3049–3055 (2014).
24. W. H. Miller, *J. Chem. Phys.* **52**, 3563–3572 (1970).
25. P. Siska, *Rev. Mod. Phys.* **65**, 337–412 (1993).
26. S. Tanteri, S. D. S. Gordon, J. Zou, A. Osterwalder, *J. Phys. Chem. A* **125**, 10021–10034 (2021).
27. A. B. Henson, S. Gersten, Y. Shagam, J. Narevicius, E. Narevicius, *Science* **338**, 234–238 (2012).
28. A. Klein *et al*., *Nat. Phys.* **13**, 35–38 (2017).
29. B. Margulis, J. Narevicius, E. Narevicius, *Nat. Commun.* **11**, 3553 (2020).
30. U. Even, J. Jortner, D. Noy, N. Lavie, C. Cossart-Magos, *J. Chem. Phys.* **112**, 8068–8071 (2000).
31. K. Luria, N. Lavie, U. Even, *Rev. Sci. Instrum.* **80**, 104102 (2009).
32. D. Koner, J. C. San Vicente Veliz, A. van der Avoird, M. Meuwly, *Phys. Chem. Chem. Phys.* **21**, 24976–24983 (2019).
33. M. Meuwly, J. M. Hutson, *J. Chem. Phys.* **110**, 8338–8347 (1999).
34. J. M. Bowman, B. Gazdy, *J. Chem. Phys.* **94**, 816–817 (1991).
35. P. Pechukas, J. C. Light, C. Rankin, *J. Chem. Phys.* **44**, 794–805 (1966).
36. B. Margulis *et al*., *Phys. Rev. Res.* **4**, 043042 (2022).
37. B. Margulis *et al*., Zenodo (2023); https://doi.org/10.5281/zenodo.7633162.

ACKNOWLEDGMENTS

We thank F. Gianturco for sharing preliminary cross sections that allowed us to test our own wave packet simulation code. E.N. acknowledges support from the Cluster of Excellence RESOLV. **Funding:** We gratefully acknowledge financial support from the European Research Council Advanced Grant (E.N.), the NCCR MUST and the University of Basel (M.M.), and the Deutsche Forschungsgemeinschaft (Project "Efficient Quantum Control of Molecular Rotations," grant 505622963) (C.P.K.). **Author contribution:** B.M., N.K., and E.N. designed, constructed, and conducted the experiment and analyzed the results. M.U. and M.M. designed, computed, and tested the potential energy surfaces. K.P.H. and D.M.R. wrote the scattering software with the help of A.C., A.v.d.A., and G.C.G. and calculated theoretical cross sections, which were analyzed by K.P.H., D.M.R., A.C., and C.P.K. All authors contributed to writing and revising the manuscript. **Competing interests:** The authors declare that they have no competing interests. **Data and materials availability:** All data underlying the figures are deposited at Zenodo (*37*). The information for the potential energy surfaces is available at https://github.com/MMunibas/rgh2. **License information:** Copyright © 2023 the authors, some rights reserved; exclusive licensee American Association for the Advancement of Science. No claim to original US government works. https://www.science.org/about/science-licenses-journal-article-reuse

SUPPLEMENTARY MATERIALS

science.org/doi/10.1126/science.adf9888
Materials and Methods
Supplementary Text
Figs. S1 to S10
Table S1
References (*38*–*51*)

Submitted 25 November 2022; accepted 8 March 2023
10.1126/science.adf9888

ELECTROCHEMISTRY

Overcoming the limitations of Kolbe coupling with waveform-controlled electrosynthesis

Yuta Hioki[1,2]†, Matteo Costantini[1]†, Jeremy Griffin[3], Kaid C. Harper[3], Melania Prado Merini[1], Benedikt Nissl[1], Yu Kawamata[1]*, Phil S. Baran[1]*

The Kolbe reaction forms carbon-carbon bonds through electrochemical decarboxylative coupling. Despite more than a century of study, the reaction has seen limited applications owing to extremely poor chemoselectivity and reliance on precious metal electrodes. In this work, we present a simple solution to this long-standing challenge: Switching the potential waveform from classical direct current to rapid alternating polarity renders various functional groups compatible and enables the reaction on sustainable carbon-based electrodes (amorphous carbon). This breakthrough enabled access to valuable molecules that range from useful unnatural amino acids to promising polymer building blocks from readily available carboxylic acids, including biomass-derived acids. Preliminary mechanistic studies implicate the role of waveform in modulating the local pH around the electrodes and the crucial role of acetone as an unconventional reaction solvent for Kolbe reaction.

The Kolbe reaction, described by Faraday in 1834 and established by Kolbe in 1849, is one of the oldest electrochemical reactions and possibly the first carbon-carbon (C–C) bond-forming reaction in organic synthesis (Fig. 1) (*1*). Despite the appeal of making Csp^3–Csp^3 bonds from simple carboxylic acids through direct oxidation at an electrode, its use in mainstream organic synthesis is exceedingly rare. In its canonical form, a high current density is required to ensure high anodic potential for initiating oxidative radical generation over solvent oxidation, followed by immediate dimerization on a platinum (Pt) electrode surface. Such harsh oxidative conditions undermine its synthetic utility, with even dormant terminal unactivated olefins such as **1** (*2*) or benzylic systems such as **2** (*3*) and **3** (*4*) being incompatible (Fig. 1A). These limitations are seldom advertised, although numerous reviews on this classic reaction make it clear that minimally functionalized hydrocarbons are the best substrates (*5*–*9*), and barely any practical industrial applications exist (*10*). Interest in this potentially powerful transformation has reemerged with studies from the Lam group applying it to the synthesis of functionalized pyrrolidinones (*11*), and the Sevov group studying self-assembled monolayers to mitigate the harshly oxidative conditions (*3*). A reductive, electrocatalytic variant of the Kolbe reaction has also appeared by using in situ–generated redox active esters to enable controlled heterocoupling of different carboxylic acids (*12*).

One of the most industrially promising applications of the Kolbe reaction involves the upconversion of biomass-derived chemicals to reduce reliance on petroleum-based products. Thus far, reactions used in this space are mostly simple functional group manipulations such as hydrogenation, condensation, and elimination, with the exception of olefin cross metathesis for C–C bond formation (*13*, *14*). In this context, the Kolbe reaction has long been recognized as a potentially disruptive transformation because it forges saturated C–C bonds directly from carboxylic acids, which are ubiquitous in biomass-derived chemicals. No alternative reaction currently exists to form a saturated C–C bond with this level of simplicity and sustainability. This exciting prospect, which has generated intense study in the area of sustainable synthesis (*15*), still remains an unanswered challenge for the field, with the issues of limited substrate scope and reliance on precious metal–based electrodes presenting roadblocks for adoption.

We describe a promising solution to the chemoselectivity challenge posed by the strongly oxidative Kolbe reaction through the use of rapid alternating polarity (rAP), a waveform that is implemented on a commercial potentiostat. The rAP-Kolbe reaction features a wide substrate scope, inexpensive and sustainable C-based electrodes, operability in both dimerization and heterocoupling modes, and practicality for scale-up applications (Fig. 1B). As evidence of the practicality and dramatic cost-savings of this protocol, heretofore cost-prohibitive building blocks are now easily accessible, such as unnatural amino acids and highly coveted polymer building blocks derived from biomass-derived carboxylic acids. As a proof of concept, a distinctive acid-degradable polymer was constructed from these building blocks. Last, preliminary mechanistic studies explain why the rAP-Kolbe reaction conquers chemoselectivity constraints and the requirements of a Pt-based electrode encountered for more than 100 years.

Advantage of alternating electrode polarity

The use of different waveforms for electric current delivery as a means to improve reactivity and selectivity has only recently been recognized in the field of synthetic organic electrochemistry (*16*, *17*). Early studies were suggestive that such an approach might have potential, despite having minimal benefit in synthesis (*16*). Whereas certain reactions have been shown to benefit from alternating current in terms of achieving higher reaction efficiency (*17*, *18*), drastic changes in product distribution were unknown. In 2021, the rAP waveform was shown to enable chemoselectivity in carbonyl reduction that could not be replicated in other ways, including both electrochemical and chemical means (*19*). A completely different outcome was obtained by simply changing the waveform from direct current (dc) to rAP even when identical reaction conditions were used. The same phenomenon was also applied to chemoselective Birch-type reductions in which competing proton-reduction could be largely suppressed (*20*). Those prior studies both involved reductive processes, and thus our attention pivoted to the Kolbe reaction, one of the oxidative electrochemical processes most in need of a chemoselective variant.

Reaction development and chemoselectivity

Toward this end, we began our explorations with 10-undecenoic acid (**1**), a seemingly trivial biomass-derived acid that is not amenable to Kolbe electrolysis (Fig. 1C) (*2*). However, its dimerization product (1,19-eicosadiene; **4**) could have high utility as a polymer building block. Despite its simple structure, the price of **4** is prohibitive owing to the lack of practical access ($10,000/gram, Oakwood Chemical), whereas **1** is readily obtained from castor oil (~$20/kg). In good agreement with the prior report (*2*), conventional conditions that used Pt electrodes with direct current electrolysis led to no observable formation of **4** (entry 1), presumably because of electrode passivation (in which the surface becomes insulating, blocking current from passing) (*2*, *3*). The Kolbe reaction was previously studied with an ac waveform, and the detailed result was published in 1939 by Shipley and Rogers (*21*). The Shipley and Rogers report says they observed little difference between dc and ac, which is consistant with our observation that **4** was not formed in either case (entries 1 and 2). Altering the base, solvent, and electrodes under dc electrolysis gave no improvement on the product formation (entries 3 and 4). Notably, simply switching the waveform from dc to rAP under the identical conditions of entry 4 led to formation of **4** in 63% isolated yield (entry 5).

[1]Department of Chemistry, Scripps Research, La Jolla, CA 92037, USA. [2]Science and Innovation Center, Mitsubishi Chemical Corporation, Aoba-ku, Yokohama, Kanagawa, 227-8502, Japan. [3]Abbvie Process Research and Development, North Chicago, IL 60064, USA.
*Corresponding author. Email: yukawama@scripps.edu (Y.K.); pbaran@scripps.edu (P.S.B.)
†These authors contributed equally to this work.

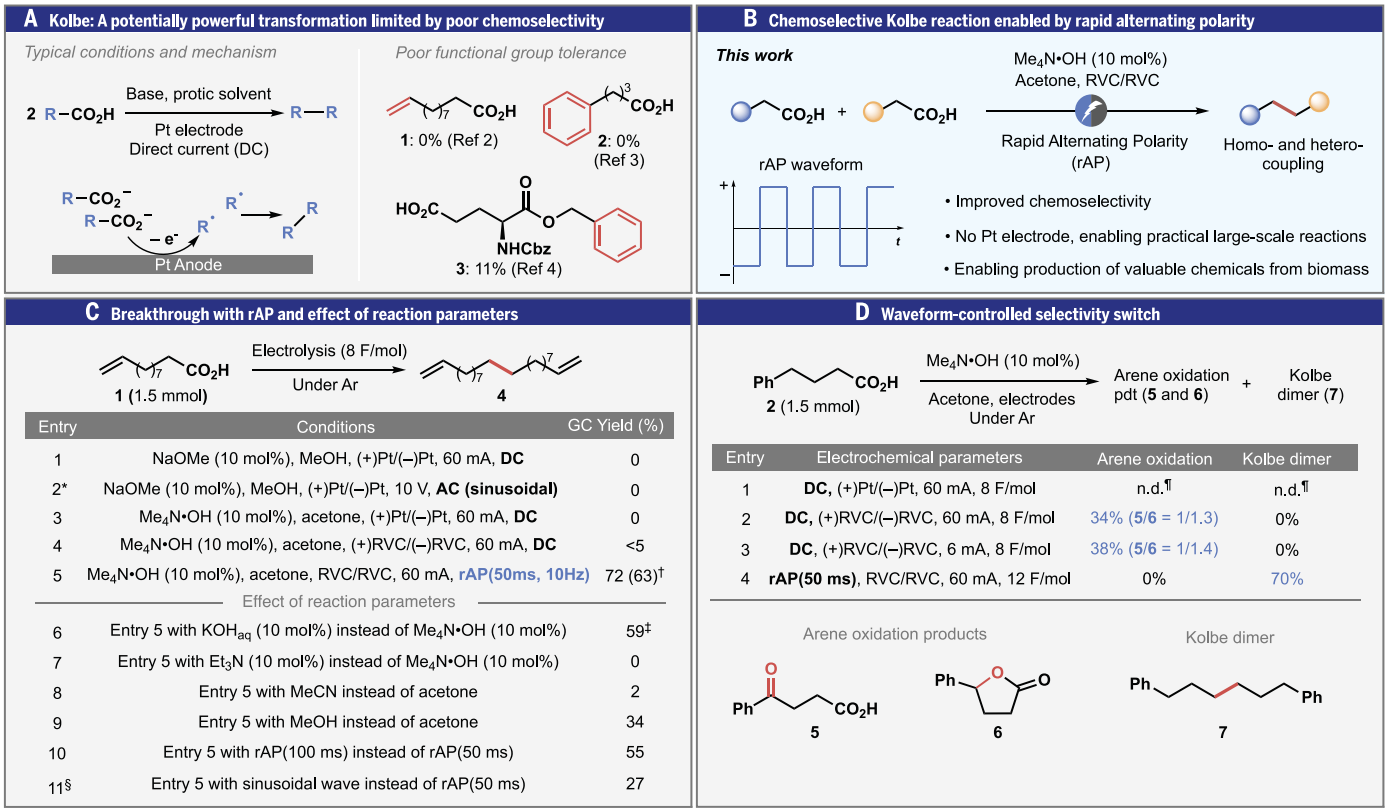

Entry	Conditions	GC Yield (%)
1	NaOMe (10 mol%), MeOH, (+)Pt/(–)Pt, 60 mA, **DC**	0
2*	NaOMe (10 mol%), MeOH, (+)Pt/(–)Pt, 10 V, **AC (sinusoidal)**	0
3	Me_4N•OH (10 mol%), acetone, (+)Pt/(–)Pt, 60 mA, **DC**	0
4	Me_4N•OH (10 mol%), acetone, (+)RVC/(–)RVC, 60 mA, **DC**	<5
5	Me_4N•OH (10 mol%), acetone, RVC/RVC, 60 mA, **rAP(50ms, 10Hz)**	72 (63)†
	Effect of reaction parameters	
6	Entry 5 with KOH_{aq} (10 mol%) instead of Me_4N•OH (10 mol%)	59‡
7	Entry 5 with Et_3N (10 mol%) instead of Me_4N•OH (10 mol%)	0
8	Entry 5 with MeCN instead of acetone	2
9	Entry 5 with MeOH instead of acetone	34
10	Entry 5 with rAP(100 ms) instead of rAP(50 ms)	55
11§	Entry 5 with sinusoidal wave instead of rAP(50 ms)	27

Entry	Electrochemical parameters	Arene oxidation	Kolbe dimer
1	**DC**, (+)Pt/(–)Pt, 60 mA, 8 F/mol	n.d.¶	n.d.¶
2	**DC**, (+)RVC/(–)RVC, 60 mA, 8 F/mol	34% (**5**/**6** = 1/1.3)	0%
3	**DC**, (+)RVC/(–)RVC, 6 mA, 8 F/mol	38% (**5**/**6** = 1/1.4)	0%
4	**rAP(50 ms)**, RVC/RVC, 60 mA, 12 F/mol	0%	70%

Fig. 1. Challenges in classic Kolbe reaction and the breakthrough by using rapid alternating polarity (rAP). (**A**) Minimal functional group compatibility of the classic Kolbe reaction owing to its strongly oxidative nature. (**B**) Overcoming this limitation by applying the rAP waveform. (**C**) Trivial yet challenging substrates in Kolbe reaction. (**D**) Waveform-controlled chemoselectivity switch. *10 V–60 Hz ac was applied according to (*21*). †Isolated yield. ‡30 mA was applied instead of 60 mA because of high resistance of the solution. §10 V–10 Hz ac was applied to be consistent with the frequency and cell voltage to entry 5. Reaction time was 18 hours. ¶Electrode passivation occcurred in both MeOH and acetone as the solvent, causing termination of the reaction before achieving meaningful conversion.

The reaction proceeds by using technical-grade acetone as a solvent without any precaution to remove water and uses only a catalytic amount of inexpensive Me_4N•OH as a soluble base. On a small scale, we used an argon (Ar) or dinitrogen (N_2) balloon, but this precaution was not necessary on larger scales. It was unexpected that Pt electrodes were not required because Pt has for more than a century been considered as essential for radical-based Kolbe reactivity (*5*, *22*); C-based electrodes are known to promote carbocation reactivity instead, leading to Hofer-Moest products (*23*). However, the type of C-based electrode seems to be important; amorphous C electrodes such as reticulated vitreous carbon (RVC) was found to be optimal, and we observed no extensive degradation of electrodes. Glassy carbon, which is essentially the same material as RVC with less surface area, could also be used under similar conditions. By contrast, graphite and boron-doped diamond electrodes were found to be ineffective under several conditions examined (table S5). Me_4N•OH is available in bulk quantity and widely used in silicon-etching (*24*) but can also be replaced by the even less expensive base potassium hydroxide (KOH) (entry 6). An organic base [triethylamine (Et_3N)] and other solvents were found to deteriorate the reaction, probably because of competing oxidation (entries 7 to 9). The beneficial role of acetone is attributed to its ability to act as an electron and proton acceptor to balance oxidative decarboxylation, which is supported by the detection of isopropanol in the crude mixture (fig. S11). The optimal frequency of polarity switch for rAP-enabled reactivity is 50 ms (for example, entry 5), but a lower frequency is also effective (entry 10). Last, the use of a conventional sinusoidal ac waveform under otherwise identical conditions showed a similar effect to rAP, albeit with lower reaction efficiency that is consistent with previous reports (entry 11) (*19*, *20*, *25*).

Before exploring the scope of the rAP-Kolbe reaction, we also evaluated 4-phenylbutyric acid (**2**) (Fig. 1D) because of its documented tendency to undergo arene oxidation that leads to the benzylic functionalization in addition to productive dimerization to **7** (*3*). Under conventional Kolbe reaction conditions with Pt electrodes (entry 1), the reaction was discontinued because of electrode passivation, whereas arene oxidation products (**5** and **6**) were predominant with RVC electrodes regardless of the current density (entries 2 and 3). In stark contrast, the rAP-Kolbe reaction led to the desired dimer **7** in 70% isolated yield without detectable amount of arene oxidation (Entry 4).

Reaction generality and product utilities

With a general protocol established, we explored the scope of the chemoselective rAP-Kolbe reaction (Fig. 2A). In broad terms, this reaction is ideally suited toward the coupling of primary carboxylic acids because secondary and tertiary systems mainly lead to Hofer-Moest reactivity (supplementary materials). Performing the reaction with dc instead of rAP is detrimental (Fig. 1C). Unlike the classic Kolbe reaction, this reaction tolerates several synthetically useful functional groups such as esters (**8** to **10** and **16** to **18**), carbamates (**11** and **17** to **19**), free hydroxy (**12**), ketones (**13**), both electron-deficient (**15**) and electron-rich arenes (**16**), aryl halides (**15**), and terminal and internal olefins (**4** and **14**). Presumably because of the free-radical nature of the Kolbe reaction, the hindered neopentyl unit can also be readily coupled to afford diester **10** in 69% yield.

Many of the substrates shown in Fig. 2A are high-value building blocks that can now be accessed in much simpler or considerably

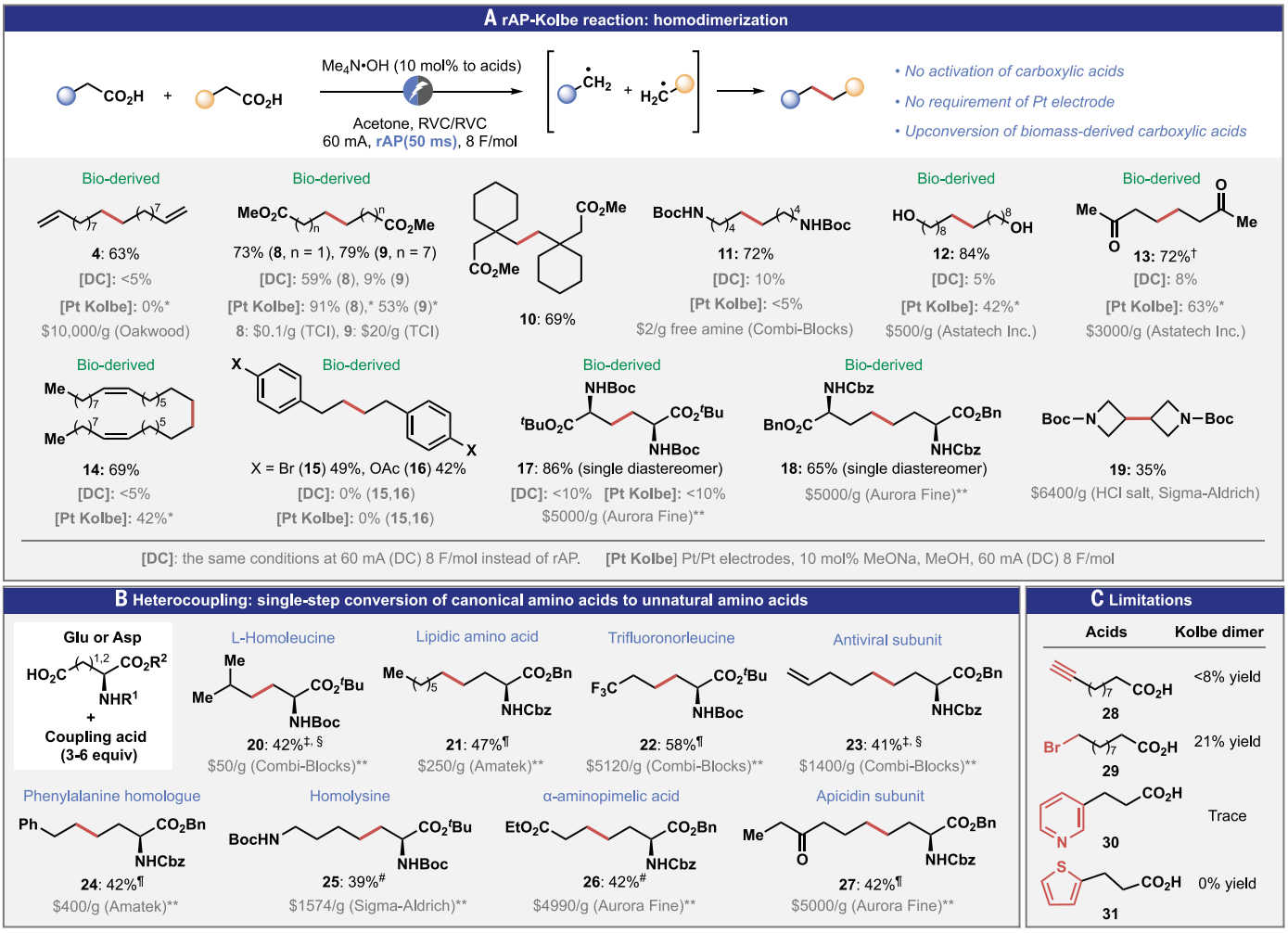

Fig. 2. Reaction generality of rAP-Kolbe reaction. (**A**) Scope of homodimerization. Reactions were performed on 1.5 mmol scale under the conditions described. (**B**) Scope of heterocoupling. Detailed reaction conditions for each substrate are provided in the supplementary materials. *Literature yield of Pt-based Kolbe reaction. Compound **4**, (*2*); compound **8**, (*28*); compound **9**, (*2*); compound **12**, (*2*); compound **13**, (*48*); compound **14**, (*2*). †NMR yield due to volatility of the product. ‡Acetone/toluene = 30/1 was used as solvent. §5 equiv of the coupling acid was used. ¶6 equiv of the coupling acid was used. #3 equiv of the coupling acid was used. **Price of free amino acid. (**C**) Redox-sensitive functionalities were not well tolerated.

different ways. These substrates serve as yet another demonstration of how labor-intensive $2e^-$-based approaches can be replaced with routes arising from radical retrosynthesis logic (*26*). For example, dimethyl adipate **8**, an important precursor for adipic acid, can be prepared from biomass-derived material by means of four-step functional group manipulations involving hydroformylation with precious metal catalysis (*27*). By contrast, the rAP-Kolbe reaction afforded **8** in a single step from monomethyl succinate (*28*), which could also be derived from bio-based succinic acid. The diamine parent of **11** is a valuable building block for polyamide 1010 and is currently prepared from sebacic acid after three functional group manipulation steps. By contrast, the rAP-Kolbe reaction opens a new avenue to access this compound from ε-caprolactam, a commodity chemical (~$3/kg), through efficient C–C bond formation. Diol **12** is an essential building block for a promising degradable surrogate of polyethylene, yet it is currently synthesized through hazardous lithium aluminum hydride (LAH) reduction of the corresponding diacid (*29*). By contrast, 10-hydroxydecanoic acid (derived from castor oil) can be converted to **12** in 84% isolated yield under rAP without any protection of the terminal alcohol. Diketone **13**, a potentially useful building block ($3000/g), can be easily derived from levulinic acid, one of the top-12 platform chemicals that can be mass produced from biorefineries, according to the US Department of Energy (*30*). Compounds **15** and **16**, now easily available by using rAP, represent a new derivatization method of hydrocinnamic acid derivatives, bio-based aromatic acids available from lignin (*31*). Amino acid dimer **17** (currently sold for ~$5000/g) is known to be an important intermediate for a potent allosteric inhibitor (*32*) and has been previously synthesized in seven steps as a racemate, whereas rAP dimerization of protected aspartate delivers it as a single diastereomer in 86% isolated yield. Similarly, dimeric amino acid **18**, a known carbon-isostere of disulfide linkages in peptides, can be easily accessed through glutamate dimerization. Past approaches to structures such as these are through a low-yielding Kolbe reaction (*4*) or olefin metathesis from unnatural amino acids (*33*, *34*). Last, bisazetidine **19** [$1600 for 250 mg; as hydrogen chloride (HCl) salt], a useful piperazine isostere in medicinal chemistry, is an example of a workable secondary coupling.

The reaction is also amenable to heterocoupling (Fig. 2B) to facilitate the rapid conversion of inexpensive natural amino acids (glutamic acid and aspartic acid) into valuable unnatural amino acids (of either absolute stereochemistry) without racemization (confirmation of no racemization is provided in figs. S7 and S8). Although 3 to 6 equiv of coupling acid is

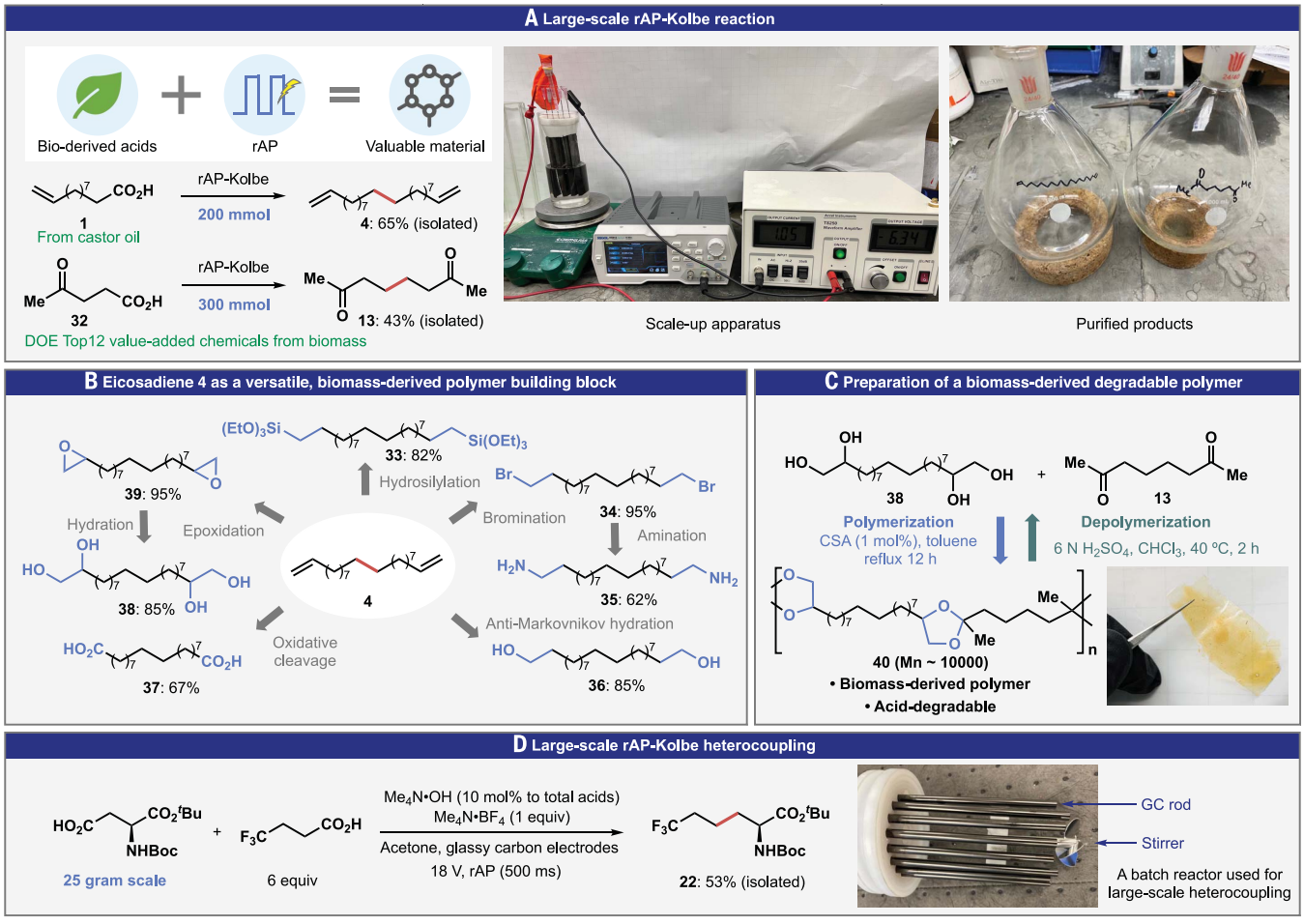

Fig. 3. Large-scale rAP-Kolbe reaction to produce biomass-derived polymers and fine chemicals. (**A**) Transforming biomass-derived carboxylic acids into useful polymer building blocks. Individual reaction conditions are provided in the supplementary materials. (**B**) Diene **4** as a biomass-derived versatile building block for various polymers. (**C**) Synthesis of an acid-degradable polymer from rAP-Kolbe reaction products. (**D**) Single-step access to a high-value unnatural amino acid on scale.

needed to achieve a synthetically useful yield (excess acid forms the homocoupling product), all the reagents as well as starting materials are inexpensive. Despite its simplicity and obvious utility, Kolbe heterocoupling of amino acids has been a formidable challenge for a conventional Kolbe reaction (*35*, *36*), and the rAP-based method exhibits the broadest reaction generality thus far. For example, lipophilic noncanonical side chains for **20** (~$50/g) and **21** (~$520/g) are readily accessible. Yet, a direct one-step access from a readily available starting material did not exist, and the most common ways of accessing such structures involve resolution, biocatalysis, asymmetric hydrogenation, and chiral auxiliary or chiral pool chemistry (a graphical compilation of prior approaches is available in the supplementary materials). Trifluoronorleucine (**22**; ~$5000/g) is a fluorinated analog of norleucine, and its only published enantioselective synthesis requires a stoichiometric amount of a chiral nickel complex (*37*). Olefin-containing amino acid **23** is a key building block to construct antiviral agents. Despite its importance, it is prohibitively expensive (~$1000/g) for practical use, and the previous syntheses require laborious preparation of a key intermediate before asymmetric hydrogenation (*38*) or a bespoke ligand for asymmetric coupling (*37*). **24** is an example of a phenyl alanine homolog that is useful for structure-activity relationship study (*39*, *40*). Homolysine **25** (~$1600/g) is a useful analog of lysine for fine-tuning peptide side chains (*41*), and α-aminopimelic acid **26** (~$5000/g) has documented bioactivity (*42*). Ketone-containing unnatural amino acid **27** (~$5000/g) is found in bioactive cyclic tetrapeptides (histone deacetylase inhibitors) (*43*). Direct access to **25** to **27** has been elusive thus far, leading to application of numerous indirect $2e^-$ strategies such as cross metathesis from an unnatural amino acid (*44*, *45*), chiral auxiliary-based α-amination of a carboxylic acid (*41*), or repurposing of chiral pool materials such as Garner's aldehyde (*46*) or glutamic acid (*47*). Although functional group compatibility was markedly improved by using rAP, redox-sensitive functionalities such as terminal alkynes (**28**), alkyl halides (**29**), as well as heterocycles (**30** and **31**) were not well tolerated (Fig. 2C).

Applications into biomass-derived polymer synthesis

As we described, one of the most sought-after applications of the Kolbe reaction involves upgrading biomass-derived carboxylic acids to high-value products, an aspiration yet to be realized (*15*). The practical conditions and broad reaction generality achieved with a rAP-Kolbe reaction can finally address this long-standing challenge, even on scale. As shown in Fig. 3A, we used biomass-derived acids **1** and **32** to produce 1,19-eicosadiene **4** and 2,7-octadione **13** (*48*, *49*) on a 200 and 300 mmol scale, respectively. No protection from air and moisture was necessary when performing large-scale reactions. Thus, **4** can now be considered a biomass-derived material that can potentially be accessible in bulk quantities. The terminal olefins can be readily converted into a variety of functional groups by using well-established

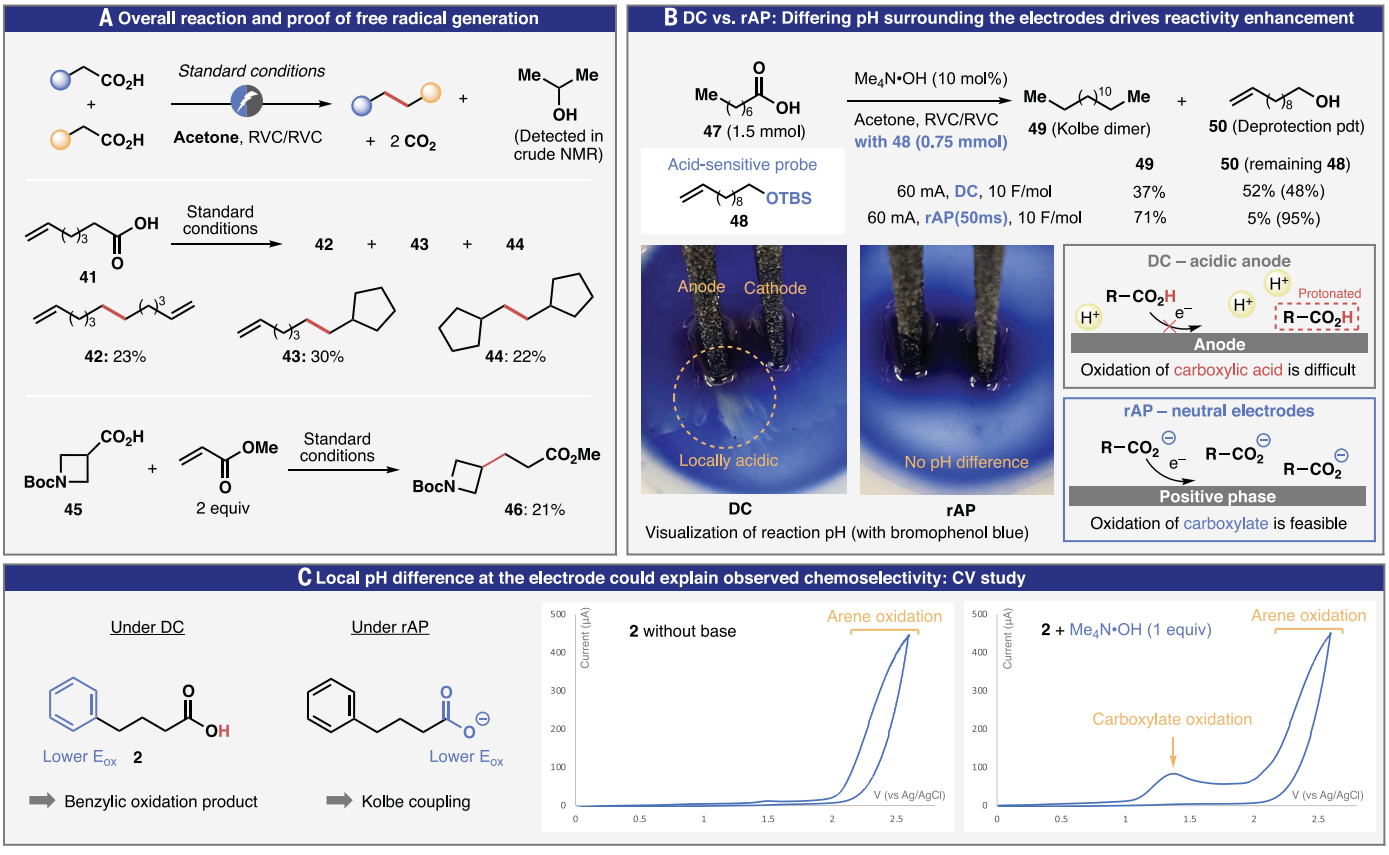

Fig. 4. Mechanistic studies on rAP-Kolbe reaction. (**A**) Overall reaction scheme and proof for free-radical generation. (**B**) Probing reaction acidity under dc and rAP as well as visualization of reaction pH. (**C**) Cyclic voltammograms of **2** with or without addition of a base.

reactions, providing additional building blocks **33** to **39**, with potential use for polymer additives or constructing degradable alternative of commodity polymers (Fig. 3B) (*50*). Degradable polymers are becoming increasingly more important to realize closed-loop recycling. Accessing such polymers from biomass-derived building blocks is attracting strong interest, as evidenced in the recent disclosure of biomass-derived polyesters and polycarbonates (*29*). As a proof of concept for this possibility, we synthesized a new polymer **40** from monomers **13** and **38** derived from a rAP-Kolbe reaction by connecting them through a ketal linkage under anhydrous conditions (catalytic camphorsulfonic acid, toluene)—an underused motif in degradable polymers (Fig. 3C) (*50*, *51*). Polymer **40** can be subsequently degraded under aqueous acidic conditions, an orthogonal degradation to polyesters or polycarbonates that require basic conditions. Furthermore, the highly practical conditions can be easily adapted to access to unnatural amino acid **22** on scale, demonstrating potential adoption of this reaction to the fine-chemical industry (Fig. 3D).

Mechanistic investigations

In Fig. 4, we outline a series of experiments that provide a qualitative mechanistic rationale for the rAP-Kolbe reaction. The net transformations are oxidative decarboxylation balanced by acetone reduction (Fig. 4A). As expected, oxidative decarboxylation invariably generated free radicals, as evidenced by cyclization of the 5-hexenyl radical derived from acid **41** as well as the Giese-type adduct **46** produced from the decarboxylation of **45** in the presence of methyl acrylate. Acetone reduction was confirmed with the detection of 0.5 equiv of isopropanol in crude proton nuclear magnetic resonance (^{1}H NMR) spectra, indicating that acetone is used as sacrificial electron- and proton-acceptor (fig. S11). How does the rAP-Kolbe reaction achieve substantially different levels of chemoselectivity relative to the classic Kolbe reaction? Unexpectedly, this fundamental reactivity difference may stem in large part from the local acidity at the electrode surface. In general, dc electrolysis creates local areas of enhanced acidity surrounding the anode at the microscopic level (regardless of stirring rate) through oxidation of solvent, water, or the substrate itself, known as electrogenerated acid (*52*). Counterintuitive to the reaction solution being partially neutralized, this phenomenon leads to protonation of carboxylate at the anode. Because the direct oxidation of a carboxylic acid is not favored, electrode passivation or oxidation of other functional groups outcompetes decarboxylative processes (that require a carboxylate). By contrast, rAP skirts this issue through fast polarity switching so that an anodic phase does not last long enough to create a persistent acidic electrode surface (because of rapid oscillation). As a result, oxidation of the deprotonated form (carboxylate) readily takes place in preference to other functional groups. To support this hypothesis, we added a compound sensitive to acidic deprotection (**48**) in both dc- and rAP-Kolbe reactions (Fig. 4B). With dc electrolysis, we generated the parent alcohol **50** in 52% yield with the formation of Kolbe dimer **49** in 37% yield, whereas the probe **48** was almost intact under rAP conditions, with a much higher yield of **49**. In addition to these experiments, we added a pH indicator (bromophenol blue) to the reaction solution to visualize the pH. As expected, a low pH was detected around the anode during dc electrolysis, whereas no visible pH difference was observed under rAP. Last, a cyclic voltammogram of **2** was recorded with or without base to understand the correlation between pH and the functional groups to be oxidized (Fig. 4C). An oxidation peak appeared above 2 V without addition of a base (Fig. 4C, left graph), which is in good agreement with the

arene oxidation potential reported in the literature (*53*). Upon addition of 1 equiv of Me_4N•OH, a new peak appeared around 1.3 V (Fig. 4C, right graph), which is the typical oxidation potential of alkyl carboxylates (*53*). Taken together, these observations explain the reactivity switch illustrated in Fig. 1D: **2** is oxidized in its neutral form under dc electrolysis because of the locally acidic anode environment, resulting in arene oxidation. By contrast, **2** is oxidized as its deprotonated form under rAP, leading to selective decarboxylation without oxidizing the arene. The modulation of electrode pH is an overlooked phenomenon in synthetic organic electrochemistry that further illustrates the profound effect that altered waveforms can have on the course of a reaction.

REFERENCES AND NOTES

1. M. Yan, Y. Kawamata, P. S. Baran, *Chem. Rev.* **117**, 13230–13319 (2017).
2. A. Weiper-Idelmann *et al*., *Acta Chem. Scand.* **52**, 672–682 (1998).
3. H. A. Hintz, C. S. Sevov, *Nat. Commun.* **13**, 1319 (2022).
4. J. Hiebl *et al*., *Tetrahedron* **54**, 2059–2074 (1998).
5. H. J. Schäfer, *Chem. Phys. Lipids* **24**, 321–333 (1979).
6. K. D. Moeller, *Tetrahedron* **56**, 9527–9554 (2000).
7. H.-J. Schäfer, *Top. Curr. Chem.* **152**, 91–151 (1990).
8. H. J. Schäfer, *Angew. Chem. Int. Ed.* **20**, 911–934 (1981).
9. G. E. Svadkovskaya, S. A. Voitkevich, *Russ. Chem. Rev.* **29**, 161–180 (1960).
10. M. C. Leech, A. D. Garcia, A. Petti, A. P. Dobbs, K. Lam, *React. Chem. Eng.* **5**, 977–990 (2020).
11. M. Quertenmont, I. Goodall, K. Lam, I. Markó, O. Riant, *Org. Lett.* **22**, 1771–1775 (2020).
12. B. Zhang *et al*., *Nature* **606**, 313–318 (2022).
13. B. M. Stadler, C. Wulf, T. Werner, S. Tin, J. G. de Vries, *ACS Catal.* **9**, 8012–8067 (2019).
14. A. Corma, S. Iborra, A. Velty, *Chem. Rev.* **107**, 2411–2502 (2007).
15. F. J. Holzhäuser, J. B. Mensah, R. Palkovits, *Green Chem.* **22**, 286–301 (2020).
16. S. Rodrigo, D. Gunasekera, J. P. Mahajan, L. Luo, *Curr. Opin. Electrochem.* **28**, 100712 (2021).
17. J. Zhong, C. Ding, H. Kim, T. McCallum, K. Ye, *Green Synth. Catal.* **3**, 4–10 (2022).
18. D. Gunasekera *et al*., *J. Am. Chem. Soc.* **144**, 9874–9882 (2022).
19. Y. Kawamata *et al*., *J. Am. Chem. Soc.* **143**, 16580–16588 (2021).
20. K. Hayashi, J. Griffin, K. C. Harper, Y. Kawamata, P. S. Baran, *J. Am. Chem. Soc.* **144**, 5762–5768 (2022).
21. J. W. Shipley, M. T. Rogers, *Can. J. Res.* **17b**, 147–158 (1939).
22. M. C. Leech, K. Lam, *Acc. Chem. Res.* **53**, 121–134 (2020).
23. J. Xiang *et al*., *Nature* **573**, 398–402 (2019).
24. P. Papet *et al*., *Sol. Energy Mater. Sol. Cells* **90**, 2319–2328 (2006).
25. S. Rodrigo *et al*., *Org. Lett.* **22**, 6719–6723 (2020).
26. J. M. Smith, S. J. Harwood, P. S. Baran, *Acc. Chem. Res.* **51**, 1807–1817 (2018).
27. A. Marckwordt *et al*., *Angew. Chem. Int. Ed.* **58**, 3486–3490 (2019).
28. H. Kurihara, T. Fuchigami, T. Tajima, *J. Org. Chem.* **73**, 6888–6890 (2008).
29. M. Häußler, M. Eck, D. Rothauer, S. Mecking, *Nature* **590**, 423–427 (2021).
30. T. A. Werpy, J. E. Holladay, J. F. White, Top value added chemicals from biomass: I. Results of screening for potential candidates from sugars and synthesis gas (2008), doi:10.2172/926125.
31. V. I. Timokhin *et al*., *ACS Sustain. Chem. & Eng.* **8**, 17427–17438 (2020).
32. Y. V. Skovpen, C. J. T. Conly, D. A. R. Sanders, D. R. J. Palmer, *J. Am. Chem. Soc.* **138**, 2014–2020 (2016).
33. M. Liu *et al*., *J. Med. Chem.* **59**, 6059–6069 (2016).
34. K. K. Kuhn *et al*., *J. Med. Chem.* **59**, 6045–6058 (2016).
35. J. Hiebl, H. Kollmann, F. Rovenszky, K. Winkler, *Bioorg. Med. Chem. Lett.* **7**, 2963–2966 (1997).
36. R. F. Nutt, R. G. Strachan, D. F. Veber, F. W. Holly, *J. Org. Chem.* **45**, 3078–3080 (1980).
37. Z.-P. Yang, D. J. Freas, G. C. Fu, *J. Am. Chem. Soc.* **143**, 8614–8618 (2021).
38. A.-M. Faucher *et al*., *Org. Lett.* **6**, 2901–2904 (2004).
39. M. Amblard *et al*., *J. Med. Chem.* **36**, 3021–3028 (1993).
40. M. D. Morin *et al*., *J. Med. Chem.* **59**, 4812–4830 (2016).
41. K. J. Kennedy, J. T. LundquistIV, T. L. Simandan, C. C. Beeson, T. A. Dix, *Bioorg. Med. Chem. Lett.* **7**, 1937–1940 (1997).
42. D. A. Berges *et al*., *J. Med. Chem.* **29**, 89–95 (1986).
43. S. K. Chattopadhyay, S. Sil, J. P. Mukherjee, *Beilstein J. Org. Chem.* **13**, 2153–2156 (2017).
44. G. W. Langley *et al*., *ACS Chem. Biol.* **11**, 755–762 (2016).
45. S. J. Ryan, Y. Zhang, A. J. Kennan, *Org. Lett.* **7**, 4765–4767 (2005).
46. P. L. Beaulieu, P. W. Schiller, *Tetrahedron Lett.* **29**, 2019–2021 (1988).
47. M. Linares, F. Agejas, R. Alajarín, J. Vaquero, J. Alvarez-Builla, *Synthesis* **12**, 2069–2073 (2006).
48. L. Wu, M. Mascal, T. J. Farmer, S. P. Arnaud, M. A. Wong Chang, *ChemSusChem* **10**, 166–170 (2017).
49. N. Kurig, J. Meyers, F. J. Holzhäuser, S. Palkovits, R. Palkovits, *ACS Sustain. Chem. & Eng.* **9**, 1229–1234 (2021).
50. F. Stempfle, P. Ortmann, S. Mecking, *Chem. Rev.* **116**, 4597–4641 (2016).
51. A. Hufendiek, S. Lingier, F. E. Du Prez, *Polym. Chem.* **10**, 9–33 (2019).
52. M. F. Nielsen, in *Encyclopedia of Electrochemistry*, (Wiley, 2007).
53. H. Roth, N. Romero, D. Nicewicz, *Synlett* **27**, 714–723 (2015).

ACKNOWLEDGMENTS

We are grateful to D.-H. Huang and L. Pasternack (Scripps Research) for NMR spectroscopic assistance. We acknowledge the use of facilities and instrumentation supported by NSF through the University of California, San Diego Materials Research Science and Engineering Center (UCSD MRSEC), grant DMR-2011924. We also thank A. F. Garrido-Castro, S. Gnaim, G. Laudadio, and S. B. J. Kan for helpful discussions. **Funding:** This work was supported by National Science Foundation Center for Synthetic Organic Electrochemistry CHE-2002158 (P.S.B.); Abbvie (P.S.B. and Y.K.); Mitsubishi Chemical (Y.H.); Wenner-Gren Stiftelserna, WGF2022-0050 (M.C.); Deutsche Forschungsgemeinschaft (DFG; German Research Foundation) under Germany's Excellence Strategy—EXC-2033 RESOLV, 390677874 (M.P.M.); and a DAAD Scholarship (to B.N.). **Author contributions:** Conceptualization: Y.H., Y.K., and P.S.B. Methodology: Y.H., M.C., and Y.K. Investigation: Y.H., M.C., J.G., K.C.H., M.P.M., Y.K., and B.N. Funding acquisition: Y.K. and P.S.B. Project administration: Y.K. and P.S.B. Supervision: Y.K. and P.S.B. Writing – original draft: Y.H., M.C., Y.K., and P.S.B. Writing – review and editing: Y.H., M.C., Y.K., and P.S.B. **Competing interests:** K.C.H. and J.G. are employees of AbbVie and may own AbbVie stock. Y.H., Y.K., and P.S.B. are the inventors of US patent application no. 63/352,091. **Data and materials availability:** All data are available in the main text or supplementary materials. **License information:** Copyright © 2023 the authors, some rights reserved; exclusive licensee American Association for the Advancement of Science. No claim to original US government works. https://www.science.org/about/science-licenses-journal-article-reuse

SUPPLEMENTARY MATERIALS

science.org/doi/10.1126/science.adf4762
Materials and Methods
Supplementary Text
Figs. S1 to S16
Tables S1 to S9
References (*54*–*67*)

Submitted 24 October 2022; accepted 14 February 2023
10.1126/science.adf4762

PIEZOELECTRICS

Lead zirconate titanate ceramics with aligned crystallite grains

Jinglei Li[1], Wanbo Qu[2], John Daniels[3], Haijun Wu[2], Linjing Liu[4], Jie Wu[1], Mingwen Wang[1], Stefano Checchia[5], Shuai Yang[1], Haobin Lei[1], Rui Lv[4], Yang Zhang[6], Danyang Wang[3], Xuexin Li[1], Xiangdong Ding[2], Jun Sun[2], Zhuo Xu[1], Yunfei Chang[4]*, Shujun Zhang[7]*, Fei Li[1]*

The piezoelectric properties of lead zirconate titanate [$Pb(Zr,Ti)O_3$ or PZT] ceramics could be enhanced by fabricating textured ceramics that would align the crystal grains along specific orientations. We present a seed-passivated texturing process to fabricate textured PZT ceramics by using newly developed $Ba(Zr,Ti)O_3$ microplatelet templates. This process not only ensures the template-induced grain growth in titanium-rich PZT layers but also facilitates desired composition through interlayer diffusion of zirconium and titanium. We successfully prepared textured PZT ceramics with outstanding properties, including Curie temperatures of 360°C, piezoelectric coefficients d_{33} of 760 picocoulombs per newton and g_{33} of 100 millivolt meters per newton, and electromechanical couplings k_{33} of 0.85. This study addresses the challenge of fabricating textured rhombohedral PZT ceramics by suppressing the otherwise severe chemical reaction between PZT powder and titanate templates.

Piezoelectric materials mechanically respond to electric fields and vice versa and are the core elements for transducers and sensors in many electromechanical applications. Lead zirconate titanate (PZT) ceramics [$Pb(Zr,Ti)O_3$, where Pb is at the A site and Zr and Ti are at the B site of the ABO_3 perovskite structure] with morphotropic phase boundary (MPB) compositions have large figures of merit (FOMs) of piezoelectric activity, such as a piezoelectric coefficient d_{33} > 200 pC N^{-1}, an electromechanical coupling factor k_{33} > 0.60, and a relatively high Curie temperature T_C (~350°C). They are also easy to manufacture at low cost. Therefore, PZT-based ceramics, as the most classical and pioneering perovskite solid solution, are the materials of choice for numerous piezoelectric devices, such as high-precision actuators for micro-nano manufacturing, ultrasonic transducers for medical imaging and therapy, and mechanical energy harvesters powering remote Internet of Things devices (*1*–*7*).

Given the ever-increasing demands of modern medical diagnostics and precision manufacturing, piezoelectric materials with even better performance are required (e.g., excellent piezoelectricity with high-temperature stability and/or broad-usage temperature ranges), and great efforts have been made to optimize the piezoelectric activity of PZT ceramics. One of the most effective approaches is to induce structural instability, which can include adding a relaxor endmember into the composition, such as $Pb(Mg_{1/3}Nb_{2/3})O_3$ (PMN) and $Pb(Ni_{1/3}Nb_{2/3})O_3$ (PNN) into PZT ceramics (*8*–*11*). This approach, however, will decrease T_C and reduce the coercive field E_C because both PMN and PNN have higher tolerance factors (t) compared with $PbZrO_3$ (PZ), following the general observation that lower t corresponds to higher T_C in PT-based perovskite ferroelectrics (*12*). The reduced T_C deteriorates the thermal stability of the electromechanical properties and limits the usable temperature range of piezoelectric devices (*13*). The decreased E_C incurs easier depolarization of piezoelectric ceramics, reduces the output energy density, and increases the complexity in the architecture of piezoelectric transducers (for example, a *dc* bias field in the devices is required to avoid depolarization). Replacing PZ with a Bi-based relaxor endmember—e.g., $BiScO_3$-$PbTiO_3$ (BS-PT)—will lead to higher T_C (~450°C) because of the lower tolerance factor of $BiScO_3$ (*12*); however, BS-PT has some downsides, such as the difficulties in fabrication, low electromechanical coupling factor, and high cost of scandium oxides, which limit further investigation on its modification.

Studies of perovskite ferroelectric crystals have provided clues for enhancing the piezoelectricity of PZT ceramics without sacrificing T_C and E_C because these materials exhibit strong piezoelectric anisotropy (*14*–*18*). For example, rhombohedral PMN-$PbTiO_3$ and $BaTiO_3$ crystals with spontaneous polarization directions along the <111> orientation have the highest reported d_{33} along the <001> crystallographic orientation, which is three to s[illegible] times as high as that of their ceramic counterparts, but with the same T_C (*14*, *15*). However, growing PZT single crystals with a usable size (>5 mm) is still impracticable because of the incongruent melting of ZrO_2, TiO_2, and PbO (*19*).

To exploit crystal anisotropy to achieve high piezoelectricity, an alternative approach is to engineer the ceramic grains along a specific crystallographic orientation through the fabrication of textured ceramics (*20*–*22*). The progress in PZT solid solution, however, has been very slow because of the vigorous reaction between PZT powder and conventionally used titanate templates ($BaTiO_3$ and $SrTiO_3$). This challenge also exists in other perovskite systems, including lead-free ceramics. Previous studies have shown that titanate templates are thermally unstable in PZT powder if the PZ content is >35% (*23*, *24*), which leads to great difficulties in the fabrication of textured PZT ceramics with the MPB composition that requires a PZ content of ~52%.

Fabrication of textured ceramics

We addressed the above challenge in two ways. First, we replaced the generally used titanate templates ($BaTiO_3$ and $SrTiO_3$) by synthesizing plate-like, <100>-oriented $Ba(Zr_{0.1}Ti_{0.9})O_3$ (BZT) microcrystals based on a modified topological chemical method (see the materials and methods for details). The morphology of these templates is shown in fig. S1. Compared with $BaTiO_3$ templates, BZT templates are more stable in PZT powder and can be used to fabricate textured PZT ceramics with a PZ content up to 45%, which is 10% higher than that with $BaTiO_3$ templates (fig. S2). However, further increasing the $BaZrO_3$ content in the $Ba(ZrTi)O_3$ template (such as 20%) destroyed the plate-like morphology of templates (fig. S3) and would make fabrication of textured PZT ceramics with PZ >45% unfeasible.

Second, we developed a seed-passivated texturing process (Fig. 1A and movie S1), where two different slurries were used for tape casting—$Pb(Zr_{0.4}Ti_{0.6})O_3$ powder with 3 vol % BZT templates and PZ powder without templates. The two different layers were alternately stacked to form the final green tape that was designed to guarantee the template-induced grain growth in the Ti-rich layer [that is, $Pb(Zr_{0.4}Ti_{0.6})O_3$] while achieving the desired MPB composition through Zr and Ti diffusion between different layers during sintering.

To experimentally realize our proposed texturing process, balancing the template-induced grain growth rate and cation diffusion rate is critical to ensure that the BZT templates do not react with the PZT powder before completion of the template-induced PZT grain growth. These rates mainly depend on the PZT powder particle size, sintering temperature, and dwell time. The detailed powder particle size and

[1]Electronic Materials Research Laboratory (Key Lab of Education Ministry), State Key Laboratory for Mechanical Behavior of Materials and School of Electronic and Information Engineering, Xi'an Jiaotong University, Xi'an 710049, China. [2]State Key Laboratory for Mechanical Behavior of Materials, Xi'an Jiaotong University, Xi'an 710049, China. [3]School of Materials Science and Engineering, University of New South Wales, Sydney, NSW, Australia. [4]Functional Materials and Acousto-Optic Instruments Institute, School of Instrumentation Science and Engineering, Harbin Institute of Technology, Harbin 150080, China. [5]European Synchrotron Radiation Facility (ESRF), 38000 Grenoble, France. [6]Instrumental Analysis Center of Xi'an Jiaotong University, Xi'an Jiaotong University, Xi'an 710049, China. [7]Institute of Superconducting and Electronic Materials, Australian Institute for Innovative Materials, University of Wollongong, Wollongong, NSW, Australia.
*Corresponding author. Email: changyunfei@hit.edu.cn (Y.C.); shujun@uow.edu.au (S.Z.); ful5@xjtu.edu.cn (F.L.)

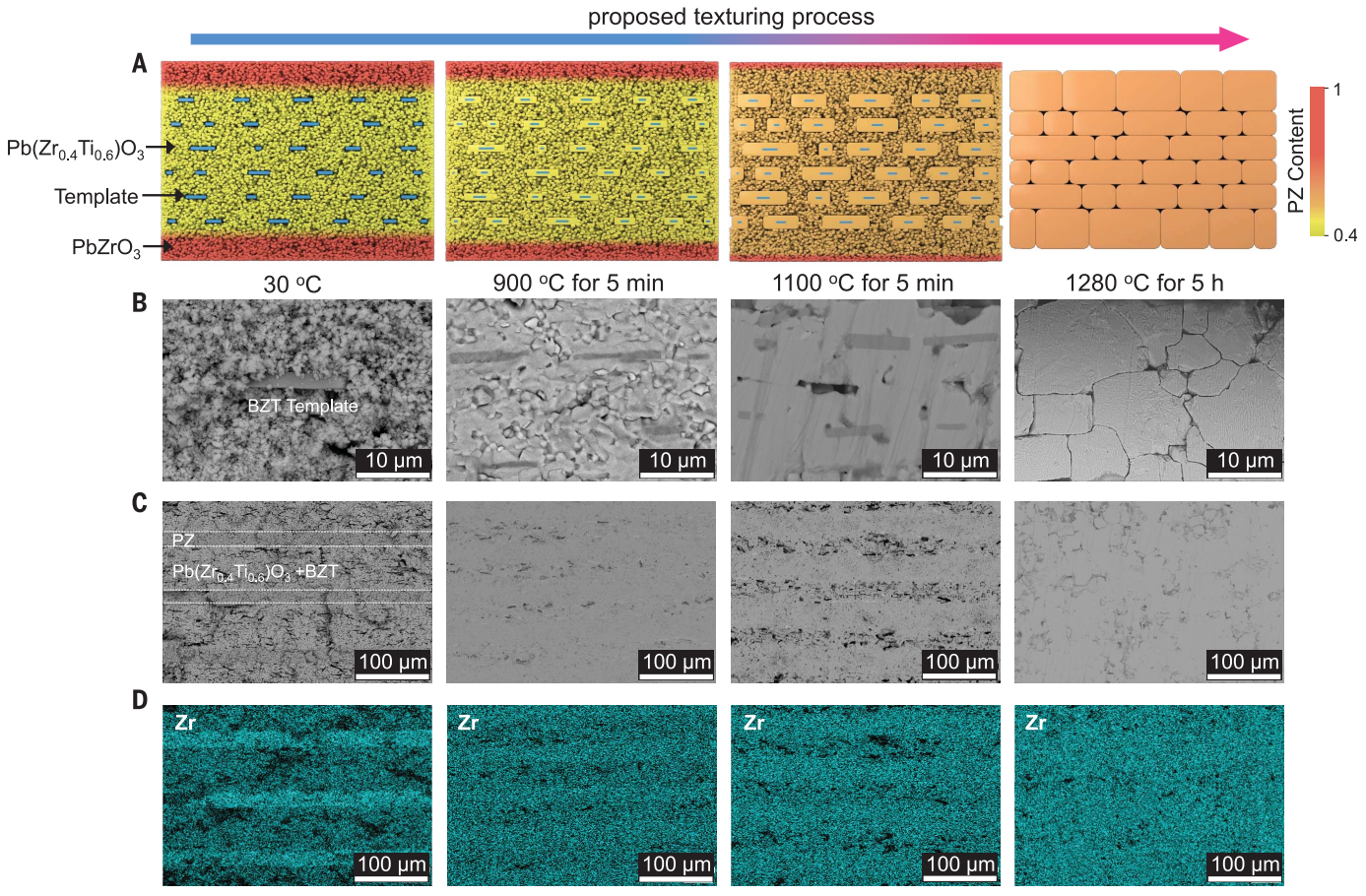

Fig. 1. Schematic illustration and experimental realization of the seed-passivated texturing process. (**A**) Schematic illustration of the proposed texturing process. The color of the PZT matrix indicates its composition. (**B** and **C**) SEM cross-sectional images for the samples with the average Zr:Ti ratio of 55:45 sintered at different temperatures, where (B) is an enlarged image of the layer with 3 vol % BZT templates in (C). (**D**) The SEM-EDS images of the Zr element, where the sample is the same as that in (C).

sintering process are outlined in the materials and methods (*25*). As shown in Fig. 1B, BZT template–induced PZT grain growth could be observed by scanning electron microscopy (SEM) at the beginning of the sintering process. The template-induced aligned grains gradually grow during sintering, accompanied by the consumption of randomly oriented grains. Meanwhile, the BZT templates start to react with the surrounding PZT matrix because the composition diffusion between the $Pb(Zr_{0.4}Ti_{0.6})O_3$ and PZ layers leads to higher PZ content in the PZT matrix around the templates (Fig. 1, C and D). Based on the proposed method, we fabricated a series of textured PZT ceramics with PZ contents up to 70% compared with the current bottleneck of ~35%. The averaged grain size of the textured PZT ceramics is in the range of 22 to 26 μm (fig. S4), with a high texture quality and a relative bulk density above 95% (table S1).

Structural characterizations

Taking the $Pb(Zr_{0.55}Ti_{0.45})O_3$ textured ceramic as an example, we verified the composition uniformity by three different methods: (i) SEM combined with energy-dispersive spectroscopy (SEM-EDS), (ii) electron probe microanalysis (EPMA), and (iii) scanning transmission electron microscopy (STEM) with EDS and electron energy-loss spectroscopy (EELS). The SEM-EDS experiment (the rightmost panel in Fig. 1D and fig. S5) showed a highly uniform distribution of Pb and Zr ions with minimal Zr segregation. To quantitatively characterize the composition distribution, we used EPMA, in which 30 points were tested along the sample thickness (fig. S6). The fluctuations [standard deviation (SD)] of Pb and Ba ions are <0.2%. Compared with Pb and Ba ions, variation in spatial concentration of Ti and Zr ions is slightly larger (SD ~ 0.7%, with maximum deviation of ~2.5%), which is consistent with those observed in conventional PZT ceramics (fig. S6).

To examine the composition homogeneity at a higher resolution, we performed STEM combined with EDS or EELS and aberration-corrected STEM experiments. The STEM–EDS/EELS measurements showed similar results to SEM-EDS and revealed no obvious composition segregation in the textured ceramic (figs. S7 and S8). We used an aberration-corrected STEM experiment to characterize the variation of lattice parameters for textured $Pb(Zr_{0.55}Ti_{0.45})O_3$ (fig. S9). The SDs in the A and B sublattice parameters are ~4 pm, similar to that observed for a PMN-PT single crystal (*18*), which again corroborates that the textured PZT ceramics have an acceptable composition uniformity.

The effect of the observed composition fluctuations on the dielectric and piezoelectric properties of the textured $Pb(Zr_{0.55}Ti_{0.45})O_3$ ceramic was analyzed by phase-field simulation. In fig. S10, we show that the variations in the dielectric and piezoelectric properties are very small (<5%) because the SD of composition for the <001>-oriented $Pb(Zr_{0.55}Ti_{0.45})O_3$ is in the range of 1 to 3%. We concluded that the present PZT textured ceramics had acceptable composition uniformity and could produce the desired electromechanical properties.

The x-ray diffraction (XRD) of all the textured PZT ceramic samples (Fig. 2A) exhibits high Lotgering texturing degree F_{001} of >99%. The high texturing quality of the $Pb(Zr_{0.55}Ti_{0.45})O_3$ ceramic is also verified by the {200} pole figure from the synchrotron x-ray experiments (Fig. 2B), where multiples of random density (MRD)

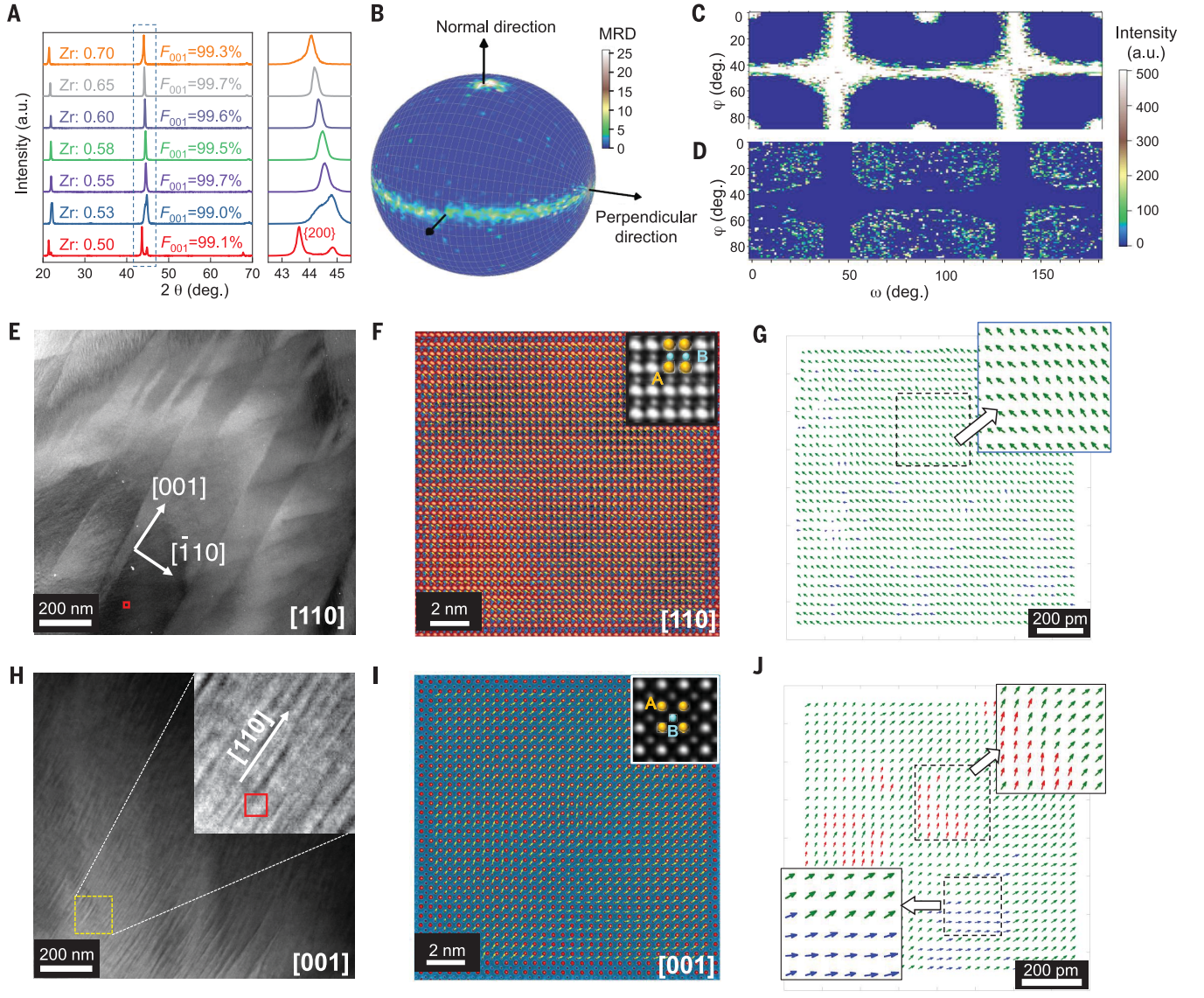

Fig. 2. Microstructural analysis of PZT textured ceramics. (**A**) XRD patterns of the PZT textured ceramics, where the texturing degree F_{001} was calculated on the basis of the XRD patterns. The enlarged (200)/(002) peaks are given on the right. a.u., arbitrary units. (**B**) The {002} pole figure obtained from the synchrotron XRD experiment, where MRD denotes the intensity of a crystallite orientation. (**C** and **D**) The {002} peak intensity as a function of sample orientation space obtained from the synchrotron XRD experiment, where (C) only includes the intensities ~15° around the tape normal direction and (D) gives intensities of the remaining orientation space. (**E**) Bright-field TEM images showing the ferroelectric domains of the $Pb(Zr_{0.55}Ti_{0.45})O_3$ textured ceramic. (**F**) Atomic-resolution STEM image of the $Pb(Zr_{0.55}Ti_{0.45})O_3$ textured ceramic [the position is shown by the red box in (E)] recorded along the crystallographic [110] direction. The A- and B-site cations are marked in the figure, where polar vectors (arrows) for each unit-cell column are derived from the A-site and B-site atomic positions. (**G**) Colorized polarization arrow map of (F), where the R-like polar vectors are marked by green, and blue indicates the polar vectors deviating 20° from the <111> direction. (**H**) Bright-field TEM images showing the ferroelectric domains of the $Pb(Zr_{0.53}Ti_{0.47})O_3$ textured ceramic. (**I**) Atomic-resolution STEM image of the $Pb(Zr_{0.53}Ti_{0.47})O_3$ textured ceramic [the position is shown by the red box in (H)] recorded along the crystallographic [001] direction. (**J**) Colorized polarization arrow map of (I), where the R-like polar vectors are marked by green, and T-like polar vectors are marked by blue and red. The cation displacement modulus is represented by the length of the arrows in (G) and (J) relative to the scale bars located in the lower right corners.

denotes the intensity of a crystallite orientation. The maximum MRD intensity occurs around the tape normal direction, which indicates that the majority of the grains are aligned by the seed templates. Additionally, the MRD intensities are evenly distributed in the perpendicular directions, again revealing that the templates are aligned with no secondary texture orientation. Some sparse grains are aligned in other directions, which indicates that these grains may have grown from misaligned templates or may have grown independently of the templates. By comparing the total {200} peak intensities of the aligned and misaligned grains (Fig. 2, C and D), we concluded that the fraction of the misaligned grains was ~6%. Electron backscatter diffraction (EBSD) further reveals that most grains of the textured PZT ceramics are oriented along the <001> direction (fig. S4), where the volume fraction of oriented grains (f) was found to be 94 to 95% for PZT textured ceramics by fitting the 00l pole figure data to the March-Dollase texture model.

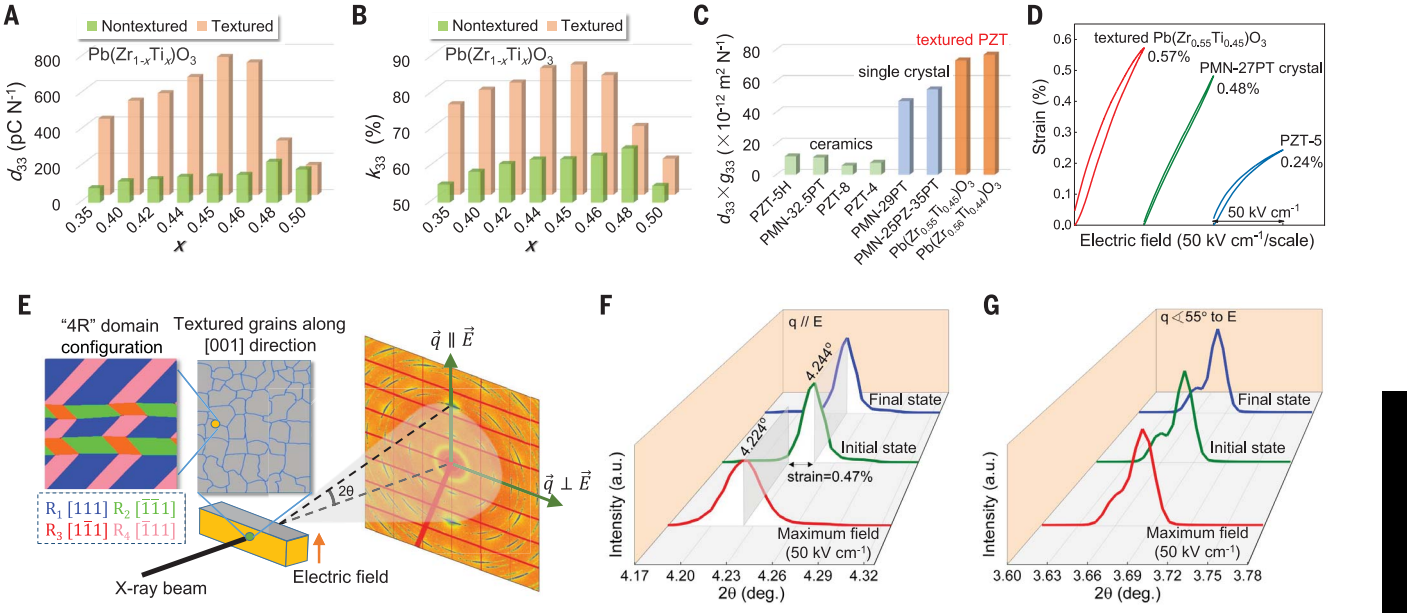

Fig. 3. Electromechanical properties and in situ synchrotron XRD analysis of electric field–induced strains for PZT textured ceramics. (**A**) The piezoelectric coefficient d_{33} of the nontextured and textured $Pb(Zr_{1-x}Ti_x)O_3$ (x between 0.35 and 0.50) ceramics. (**B**) The electromechanical coupling factor k_{33} of nontextured and textured $Pb(Zr_{1-x}Ti_x)O_3$ ceramics. (**C**) The FOM $d_{33} \times g_{33}$ of PZT textured ceramics compared with representative state-of-the-art piezoelectric ceramics and crystals. (**D**) A comparison of the electric field–induced strains between the textured $Pb(Zr_{0.55}Ti_{0.45})O_3$ ceramic, <001>-oriented PMN–27PT single crystal, and commercial PZT-5 ceramic. The frequency of the electric field is 1 Hz. (**E**) Schematic of the experimental setup showing a high-energy x-ray beam transmitting the sample and diffracting to a large area detector. The schematics of the grains and domain structures in a grain are given on the upper left. (**F**) (002) diffraction peak profiles based on synchrotron XRD measurements for the initial unpoled sample (green), final poled sample (blue), and the sample upon the electric field of 50 kV cm^{-1} (red). In this test, the x-ray scattering vector, $\vec{q}$, is parallel to the electric field—i.e., $\vec{q} \| \vec{E}$. (**G**) (111) diffraction peak profiles with $\vec{q}$ oriented 55° to the direction of the electric field. For the <001>-textured ceramic, the maximum of the (111) intensity is at 54.1° from the electric field direction; thus, integrating a 5° segment at 55° away from the electric field direction includes the maximum (111) peak intensity.

The {200} XRD peak of textured PZT ceramics (Fig. 2A) exhibits a split or distortion at a Zr content of 0.50 or 0.53, respectively, whereas the other compositions exhibit a single and symmetric {200} diffraction peak. This result indicates that the MPB of textured PZT ceramics is around a Zr content of 0.53. On the basis of Rietveld-refinement analysis (fig. S11 and table S2), the XRD patterns of textured PZT ceramic powder can be well fitted by a pure rhombohedral phase at a Zr content ≥0.55, whereas a mixture of tetragonal and rhombohedral phases must be considered to achieve acceptable fitting results for the Zr content of 0.53 or 0.50.

The ferroelectric domain structure of the textured $Pb(Zr_{0.55}Ti_{0.45})O_3$ ceramic was characterized by TEM (Fig. 2E), where a typical lamellar-type domain configuration with a domain width of tens to hundreds of nanometers was observed. The atomic image within a ferroelectric domain was characterized by aberration-corrected STEM (recorded along the [110] direction) (Fig. 2, F and G). The images show the positions of the A-site (Pb or Ba) and B-site (Zr or Ti) atomic columns. According to the positions, atomic displacements are presented as vectors pointing from a B-site cation to the center of its nearest-neighbor A-site cations. These atomic displacements represent the magnitudes and directions of the polar vectors for each unit-cell column. For $Pb(Zr_{0.55}Ti_{0.45})O_3$, almost all vectors were approximately along the <111> direction (Fig. 2G), which is the spontaneous polar direction of the rhombohedral phase. Combined with the synchrotron XRD data (splitting of the {111} peak in fig. S12) and Rietveld-refinement analysis (fig. S11), the long-range ferroelectric domains of $Pb(Zr_{0.55}Ti_{0.45})O_3$ can be inferred to be in a rhombohedral phase. After poling along the [001] direction, these ferroelectric domains are expected to form a so-called 4R domain configuration (*15*), in which the longitudinal piezoelectricity will be greatly enhanced by the contribution of the polarization rotation process (*26*, *27*).

By contrast, for $Pb(Zr_{0.53}Ti_{0.47})O_3$ with an MPB composition, very fine and striped ferroelectric domains were observed (Fig. 2H), which are attributed to the coexistence of multiple ferroelectric phases (rhombohedral, tetragonal, and/or monoclinic phases) (*28*). As expected, the polar vector directions are more diverse in $Pb(Zr_{0.53}Ti_{0.47})O_3$ when compared with $Pb(Zr_{0.55}Ti_{0.45})O_3$—i.e., R-like, T-like, or monoclinic polar vectors can be observed (Fig. 2, I and J). Thus, after poling, many polar vectors in $Pb(Zr_{0.53}Ti_{0.47})O_3$ textured ceramic may switch to the directions in proximate to the poling direction, thereby reducing the contribution of polarization rotation to longitudinal piezoelectricity (*14*).

Piezoelectric properties

The piezoelectric coefficient d_{33} and electromechanical coupling factor k_{33} for the textured PZT ceramics are shown in Fig. 3, A and B, and table S3. Compared with their nontextured counterparts, the <001>-textured PZT ceramics exhibit greatly enhanced d_{33} values in the rhombohedral phase and lower values in the tetragonal phase. This enhancement in <001>-textured rhombohedral PZT is a result of the polar vectors rotating from the <111> directions toward the [001] direction upon application of an [001] electric field (as phase-field simulated in fig. S13), which can greatly enhance the longitudinal piezoelectric response (*26*, *27*).

For <001>-textured tetragonal PZT, on the contrary, the spontaneous polarizations are already along the [001] direction after poling, and d_{33} cannot benefit from the polarization rotation process. Notably, enhanced electromechanical coupling factors k_{33} were observed for both the rhombohedral and tetragonal textured PZT ceramics, which can be explained by the

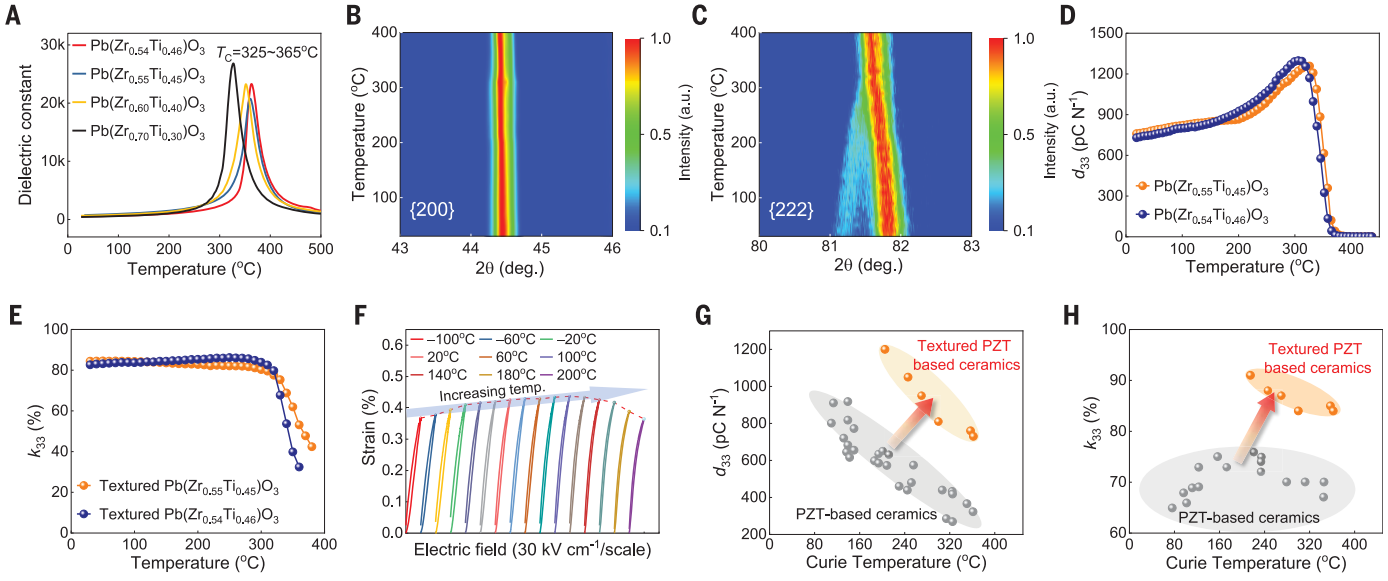

Fig. 4. Thermal stability of electromechanical properties for textured PZT ceramics. (**A**) Dielectric constant as a function of temperature for PZT textured ceramics. The dielectric constants were measured at 1 kHz. (**B** and **C**) The {200} and {222} XRD patterns as a function of temperature on the ground powder of textured $Pb(Zr_{0.55}Ti_{0.45})O_3$ ceramic, respectively. The colors indicate the intensity of XRD peaks. (**D** and **E**) Temperature dependence of piezoelectric coefficient d_{33} and electromechanical coupling factor k_{33} of textured Pb $(Zr_{0.55}Ti_{0.45})O_3$ and $Pb(Zr_{0.54}Ti_{0.46})O_3$ ceramics. (**F**) Electric field–induced strains of $Pb(Zr_{0.55}Ti_{0.45})O_3$ textured ceramic over the temperature range of −100° to 200°C. The frequency and amplitude of the electric field are 1 Hz and 30 kV cm^{-1}, respectively. (**G** and **H**) Piezoelectric coefficient d_{33} and electromechanical coupling factor k_{33} as a function of Curie temperature, respectively. The data of the representative state-of-the-art piezoelectric ceramics are given for comparison.

fact that perovskite crystals generally exhibit the highest k_{33} along the B-O (B-site cation and oxygen anion) chain direction—that is, the <001> crystallographic direction (*29*, *30*). As expected, the d_{33} and k_{33} of the textured PZT ceramics increased as the composition approached the MPB, where the maximum values were observed in the <001>-textured $Pb(Zr_{0.55}Ti_{0.45})O_3$ ceramic: 760 pC N^{-1} and 0.85, respectively.

Of particular importance is that the textured PZT ceramics exhibit a very high piezoelectric voltage coefficient g_{33} (a key factor for piezoelectric receiving transducers), up to ~100 mV m N^{-1}, as shown in table S3. This value is superior to that of most ferroelectric ceramics and crystals. From phenomenological analysis, g_{33} is equal to $2P_SQ_{33}$, where P_S is the spontaneous polarization and Q_{33} is the electrostrictive coefficient. For perovskite ferroelectric oxides, the highest Q_{33} usually exists along the <001> orientation, leading to the highest g_{33} along the same direction. In addition, compared with <001>-oriented PMN-PT crystals, the <001>-textured PZT ceramics have a larger P_S (0.36 versus 0.24 C m^{-2}; fig. S14) and a higher electrostrictive coefficient Q_{33} (0.09 versus 0.055 m^4 C^{-2}) (*30*), which accounts for the greatly improved g_{33}. We compared the $d_{33} \times g_{33}$ values (FOMs for piezoelectric energy harvesters) of the textured PZT ceramics with those of representative piezoelectric materials in Fig. 3C. As a result of the ultrahigh g_{33} and relatively high d_{33}, the textured PZT ceramics have the highest FOM (*31*, *32*), which is favorable for potential piezoelectric energy–harvesting applications.

We compare the electric field–induced strain for a textured PZT ceramic, a commercial "soft" PZT-5 ceramic, and <001>-oriented PMN-27PT crystal in Fig. 3D. At an electric field of 50 kV cm^{-1}, the strain of the textured $Pb(Zr_{0.55}Ti_{0.45})O_3$ is 0.57%, which is larger than that of the PMN-27PT crystal (0.48%) and more than twice that of the soft PZT-5 ceramic (0.24%). In situ synchrotron XRD experiments were performed on the textured PZT ceramic under an applied electric field to analyze the origin of the high electric field–induced strain. High-energy x-rays were used in transmission geometry with a large area detector (Fig. 3E) to provide simultaneous texture and strain information at multiple orientations within the sample. Radial integration of the detector image with the scattering vector, $\vec{\mathbf{q}}$, aligned with the electric field vector provided information on the lattice plane spacing for planes parallel to the electrode surfaces. In Fig. 3F, we show the (002) peak for this orientation at the initial (unpoled) state, the state with a maximum field of 50 kV cm^{-1}, and the final state after removing the electric field. As shown, a lattice strain of 0.47% is induced with the electric field, and no measurable remnant strain exists upon release of the field. The lack of remnant strain is expected because the spontaneous strains of the eight rhombohedral domains are equivalent along the [001] crystallographic orientation.

Radial integration of a 5° detector segment demonstrates that a distribution of grain orientations with a full width at half maximum (FWHM) of 7.7° exists around 54.1° (fig. S15) from the electric field and texture direction. At these orientations, the observation of any ferroelectric or ferroelastic domain switching upon field application is generally not expected (*33*, *34*). We also confirmed that no prominent domain switching was observed despite the small variation in grain orientation—i.e., the intensities of two {111} diffraction peaks are not obviously changed under the electric field (Fig. 3G). Because the rhombohedral lattice will approach the tetragonal phase under the electric field along the [001] crystallographic orientation, the splitting of the {111} peak pair is reduced from 0.022° to 0.019° with the electric field (Fig. 3G). The in situ synchrotron XRD results demonstrate that the strain mechanism in textured PZT is primarily a polarization rotation process, from the <111> R-phase polar directions toward the [001] crystallographic direction of textured grains (i.e., the direction of applied electric field), which accounts for the large electric field–induced strain.

The strain hysteresis of the textured PZT ceramic is larger than that of the PMN-27PT single crystal (Fig. 3D). This phenomenon is generally observed in <001>-textured rhombohedral perovskite ceramics, such as PMN-PZT and PIN-PSN-PT (*35*, *36*). We believe that the strain hysteresis is mainly associated with the

following three factors. (i) The orientation fluctuation of the textured grains (fig. S15) leads to slightly different free energies across domain variants under applied electric field, and thus a small amount of domain switching is expected in textured grains to accommodate the intergranular strains. (ii) Because of the presence of nontextured grains (~6 vol %), the domain switching within these nontextured grains can contribute to the observed hysteresis. (iii) Owing to the confinement of the grain boundary, the domain wall density in textured ceramics should be much higher than in their crystal counterparts, which also suggests a higher possibility of hysteresis associated with domain walls, such as domain wall motion and broadening, etc. (*37*).

Thus, the high domain wall density is believed to be a critical factor responsible for the large strain hysteresis in textured ceramics. Therefore, finding a way to remove the 71° domain walls in <001>-textured rhombohedral ceramics is one of the interesting research directions in textured ceramics.

Thermal stability

The thermal stability of piezoelectric materials is an important feature in applications in addition to their electromechanical properties, and Fig. 4A shows the dielectric constant versus temperature for the textured PZT ceramics. The T_C of the rhombohedral textured PZT ceramics (PZ content of 0.54 to 0.70) is between 365° and 325°C. The frequency dependence of T_C is minimal (fig. S16), which demonstrates a normal ferroelectric feature in PZT textured ceramics. To characterize the temperature-induced ferroelectric-ferroelectric phase transition, we performed XRD experiments on the ground powder of textured $Pb(Zr_{0.55}Ti_{0.45})O_3$ as a function of temperature (Fig. 4, B and C). The {200} diffraction peak was not split over the entire temperature range. Additionally, considering the obvious splitting or asymmetry of the {222} peak from room temperature to 300°C, the $Pb(Zr_{0.55}Ti_{0.45})O_3$ textured ceramic remained in a rhombohedral phase up to 300°C, benefiting from the straight MPB curve in the PZT solid solution (*1*, *38*).

To further explore the temperature-dependent electromechanical properties of the textured PZT ceramics, the piezoelectric coefficient d_{33}, electromechanical coupling factor k_{33}, and electric field–induced strain were studied as a function of temperature (Fig. 4, D to F). As expected, the d_{33} of the $Pb(Zr_{0.55}Ti_{0.45})O_3$ and $Pb(Zr_{0.54}Ti_{0.46})O_3$ textured ceramics first increase with increasing temperature, but a substantial decrease was observed as the temperature approached T_C, where the samples were depolarized. Compared with d_{33}, k_{33}—which can be expressed as $\frac{d_{33}}{\sqrt{s_{33}^E \times \varepsilon_{33}^T}}$—was stable as a function of temperature below T_C because d_{33}, ε_{33}^T, and s_{33}^E all followed the same trend in this temperature range.

The electric field–induced strain of the $Pb(Zr_{0.55}Ti_{0.45})O_3$ textured ceramic slightly increased with increasing temperature from −100° to 20°C and maintained a constant value between 20° and 160°C. Above this temperature range, the strain gradually decreased, with an overall variation of <15% over the broad temperature range of −100° to 200°C. The increase in electric field–induced strain with increasing temperature indicated that the field-induced polarization rotation becomes more energetically favorable with increasing temperature.

Rayleigh analysis (fig. S17) showed that both the reversible and irreversible piezoelectric contributions increase with increasing temperature from −100° to 20°C, which indicates that the extrinsic contribution of piezoelectricity also increases with temperature. This temperature dependence likely arose because the increased strain arising from polarization rotation required more domain wall motion to accommodate the intergranular stress, the energy barrier for irreversible domain wall motion lowered with increasing temperature, or both effects occurred. As the temperature approaches T_C, however, the strain slightly decreases because the reductions in spontaneous polarization and spontaneous strain weakens the contribution of polarization rotation to the electric field–induced strain. Compared with the commercial soft PZT-5 (fig. S18), the textured ceramics exhibits two to three times larger electric field–induced strains between −100° and 200°C, which further demonstrates the advantages of textured PZT ceramics for piezoelectric actuator applications.

To meet the requirements of various piezoelectric devices, we use the concept of introducing structure instability and the proposed strategy to achieve higher piezoelectric properties (*18*, *26*) by adding a PMN endmember into PZT and aligning the ceramic grains by texturing. The properties of the PZT and PMN-PZT textured ceramics can be compared with those of representative state-of-the-art piezoelectric ceramics in d_{33}-versus-T_C and k_{33}-versus-T_C charts (Fig. 4, G and H). At the same Curie temperature, PZT-based textured ceramics exhibit d_{33} that are higher by 60 to 100% and much larger k_{33} (0.82 to 0.87 versus 0.65 to 0.75) compared with those of nontextured counterparts (*38*). Thus, textured PZT-based ceramics may offer opportunities to improve the performance of next-generation piezoelectric devices.

Discussion

Using our proposed seed-passivated texturing process, we successfully fabricated a range of PZT-based textured ceramics having both high electromechanical properties and high T_C that have not been achievable during the past decades. Our approach resolves the dilemma that the piezoelectricity and Curie temperature can only be enhanced at the expense of each other. In addition to the anticipated encouraging electromechanical properties and their implications for the fundamental understanding of the most important and widely used ferroelectric solid solution, this work also provides a generalized route to fabricate textured ceramics that have not yet been manufactured because of the inevitable chemical reaction between the template and ceramic powder.

REFERENCES AND NOTES

1. B. Jaffe, W. R. Cook, H. Jaffe, *Piezoelectric Ceramics* (Academic Press, 1971).
2. J. Rödel *et al*., *J. Am. Ceram. Soc.* **92**, 1153–1177 (2009).
3. H. Cui *et al*., *Science* **376**, 1287–1293 (2022).
4. M. G. Kang, W. S. Jung, C. Y. Kang, S. J. Yoon, *Actuators* **5**, 5 (2016).
5. C. Meng *et al*., *Sci. Adv.* **7**, eabg5639 (2021).
6. Z. Li *et al*., *Adv. Funct. Mater.* **31**, 2005012 (2021).
7. M. Kimura, A. Ando, D. Maurya, S. Priya, *Advanced Piezoelectric Materials* (Elsevier, 2010).
8. A. Kumar *et al*., *Nat. Mater.* **20**, 62–67 (2021).
9. X. Gao *et al*., *Adv. Funct. Mater.* **28**, 1706895 (2018).
10. C. A. Randall, A. Kelnberger, G. Y. Yang, R. E. Eitel, T. R. Shrout, *J. Electroceram.* **14**, 177–191 (2005).
11. H. Thomann, *Adv. Mater.* **2**, 458–463 (1990).
12. R. E. Eitel *et al*., *Jpn. J. Appl. Phys.* **40**, 5999 (2001).
13. A. J. Bell, T. P. Comyn, T. J. Stevenson, *APL Mater.* **9**, 010901 (2021).
14. M. Davis, M. Budimir, D. Damjanovic, N. Setter, *J. Appl. Phys.* **101**, 054112 (2007).
15. S. Zhang, F. Li, *J. Appl. Phys.* **111**, 031301 (2012).
16. Z.-G. Ye, *MRS Bull.* **34**, 277–283 (2009).
17. Y. Yamashita *et al*., *IEEE Trans. Ultrason. Ferroelectr. Freq. Control* **69**, 3048–3056 (2022).
18. F. Li *et al*., *Science* **364**, 264–268 (2019).
19. J. A. Perez de la Torre *et al*., *Mater. Sci. Forum* **514-516**, 184–187 (2006).
20. G. L. Messing *et al*., *Crit. Rev. Solid State Mater. Sci.* **29**, 45–96 (2004).
21. M. M. Seabaugh, I. H. Kerscht, G. L. Messing, *J. Am. Ceram. Soc.* **80**, 1181–1188 (1997).
22. Y. Saito *et al*., *Nature* **432**, 84–87 (2004).
23. M. Kim, A. Upadhyay, K. W. Lim, T. T. Zate, J. H. Jeon, *J. Eur. Ceram. Soc.* **41**, 7639–7644 (2021).
24. Y. K. Yan, K. H. Cho, S. Priya, *Appl. Phys. Lett.* **100**, 132908 (2012).
25. Materials and methods are available as supplementary materials online.
26. D. Damjanovic, *IEEE Trans. Ultrason. Ferroelectr. Freq. Control* **56**, 1574–1585 (2009).
27. H. Fu, R. E. Cohen, *Nature* **403**, 281–283 (2000).
28. A. G. Khachaturyan, *Philos. Mag.* **90**, 37–60 (2010).
29. T. Yamada, *J. Appl. Phys.* **43**, 328–338 (1972).
30. F. Li, L. Jin, Z. Xu, S. J. Zhang, *Appl. Phys. Rev.* **1**, 011103 (2014).
31. Y. Yan, J. E. Zhou, D. Maurya, Y. U. Wang, S. Priya, *Nat. Commun.* **7**, 13089 (2016).
32. G. M. Sessler, J. Hillenbrand, *Appl. Phys. Lett.* **103**, 122904 (2013).
33. Y. Li, Y. Chen, Z. Zhang, A. Kleppe, D. A. Hall, *Acta Mater.* **168**, 411–425 (2019).
34. M. Hinterstein *et al*., *Phys. Rev. Lett.* **107**, 077602 (2011).
35. H. Amorín *et al*., *J. Am. Ceram. Soc.* **97**, 420–426 (2014).
36. S. Yang *et al*., *Nat. Commun.* **12**, 1414 (2021).
37. G. Liu, S. Zhang, W. Jiang, W. Cao, *Mater. Sci. Eng. R Rep.* **89**, 1–48 (2015).
38. T. R. Shrout, S. J. Zhang, *J. Electroceram.* **19**, 113–126 (2007).

ACKNOWLEDGMENTS

S.C. acknowledges the ESRF for the provision of beamtime (proposal BLC-13892) and the technical staff of beamline ID15A for assistance during beamtime. The authors thank Z. J. Ren

(Instrument Analysis Center of Xi'an Jiaotong University), Z. Wang (Australian Nuclear Science and Technology Organisation), and X. Hao (Shaanxi University of Science and Technology, China) for their assistance with SEM-EBSD analysis, texture magnitude quantification, and EELS experiments, respectively. **Funding:** F.L. and J.L. acknowledge the support of the National Key R&D Program of China (2021YFB3800602), the National Natural Science Foundation of China (grant nos. 51922083 and 52172129), and the Natural Science Foundation of Shaanxi Province (no. 2021GXLH-Z-025). Y.C. acknowledges the support of the National Natural Science Foundation of China (52072092) and the Natural Science Foundation of Heilongjiang Province (YQ2019E026).
Author contributions: The work was initially conceived by J.L., S.Z., and F.L.; F.L. supervised the investigations on PZT textured ceramics; Y.C. supervised the works on PMN-PZT textured ceramics; J.L., J.W., and S.Y. fabricated PZT textured ceramics and performed the microstructural experiments and electromechanical property measurements; L.L. and R.L. fabricated PMN-PZT textured ceramics; H.W., W.Q., and Y.Z. performed the TEM and STEM experiment and quantitative analysis; X.D. and J.S. assisted with the interpretation of TEM and STEM data; M.W. and X.L. prepared the templates; J.D. and S.C. performed the synchrotron XRD experiments; H.L. and F.L. performed phase-field simulations; F.L. drafted the manuscript; S.Z., J.D., and D.W. revised the manuscript; and all authors discussed the results. **Competing interests:** The authors have filed a provisional Chinese patent related to this work (no. 2022106809141). The authors declare no other competing interests. **Data and materials availability:** All data are available in the main text or the supplementary materials.
License information: Copyright © 2023 the authors, some rights reserved; exclusive licensee American Association for the Advancement of Science. No claim to original US government works. https://www.science.org/about/science-licenses-journal-article-reuse

SUPPLEMENTARY MATERIALS

science.org/doi/10.1126/science.adf6161
Materials and Methods
Figs. S1 to S18
Tables S1 to S3
References (*39*–*43*)
Movie S1

Submitted 2 November 2022; accepted 15 March 2023
10.1126/science.adf6161

RESEARCH ARTICLE SUMMARY

PROTEOMICS

Decrypting drug actions and protein modifications by dose- and time-resolved proteomics

Jana Zecha†, Florian P. Bayer†, Svenja Wiechmann†, Julia Woortman, Nicola Berner, Julian Müller, Annika Schneider, Karl Kramer, Mar Abril-Gil, Thomas Hopf, Leonie Reichart, Lin Chen, Fynn M. Hansen, Severin Lechner, Patroklos Samaras, Stephan Eckert, Ludwig Lautenbacher, Maria Reinecke, Firas Hamood, Polina Prokofeva, Larsen Vornholz, Chiara Falcomatà, Madeleine Dorsch, Ayla Schröder, Anton Venhuizen, Stephanie Wilhelm, Guillaume Médard, Gabriele Stoehr, Jürgen Ruland, Barbara M. Grüner, Dieter Saur, Maike Buchner, Benjamin Ruprecht, Hannes Hahne, Matthew The, Mathias Wilhelm, Bernhard Kuster*

INTRODUCTION: Most drugs act on proteins and engage cellular pathways regulated by protein posttranslational modifications (PTMs), such as phosphorylation, acetylation, or ubiquitinylation, to exert their therapeutic effects. Because polypharmacology is common, it is important to characterize drugs on a proteome-wide scale to understand all their mechanisms of action.

RATIONALE: There is a lack of dose- and time-dependent drug characterization at the level of proteins and PTMs, arguably the most important characteristics of drug action in any biological context. To address this gap, this study presents a quantitative proteomic approach called decryptM, which is able to assess drug target and pathway engagement as well as cellular mechanism of action by measuring thousands of PTM responses in a dose- and time-resolved fashion.

RESULTS: DecryptM profiling of 31 cancer drugs in 13 human cancer cell line models resulted in 1.8 million dose-response curves, including 47,502 regulated phosphopeptides, 7316 ubiquitinylated peptides, and 546 regulated acetylated peptides, all of which can be explored in ProteomicsDB (www.proteomicsdb.org/decryptM).

The observed close coherence between drug-target affinity and drug-PTM modulation potency enabled placing functionally uncharacterized PTM sites into known pathways and thus decrypting them on the grounds of guilt by association. Examples include previously uncharacterized phosphorylation sites linking chemotherapeutic drugs to the DNA damage response, regulated phosphorylation sites indicating breakdown of oncogenic signaling in response to phosphatase and kinase inhibitors, or activation of the unfolded protein response upon proteasome inhibition. Similarly, decryptM profiles enabled the identification of previously unknown substrates of kinases as well as lysine acetyltransferases and deacetylases. Each drug appeared to leave a cell line–specific decryptM signature that may constitute a pharmacodynamic marker for target and pathway engagement, identify points of conversion of signaling axes, or distinguish closely related compounds.

DecryptM analysis of therapeutic anti-HER2 antibodies revealed differences in their mechanisms of action. Whereas pertuzumab [illegible] off the HER3–mitogen-activated protein kinase (MAPK) and HER3-PI3K/AKT signaling axis in breast cancer cells, trastuzumab had no effect on any of the phosphoproteomes investigated. By contrast, the anti-CD20 antibody rituximab massively activates signaling in B cells. The collective decryptM and functional evidence supports a model in which rituximab binds to CD20, located in lipid rafts alongside the B cell receptor complex, and leads to strong activation of the MAPK and calcineurin–nuclear factor of activated T cells (NFAT) axis, tipping the signaling balance toward apoptotic cell death.

CONCLUSION: The examples presented in this study illustrate the potential of decryptM to characterize drugs' mechanisms of action, generate drug-specific PTM signatures, study resistance mechanisms, and place drug-regulated PTM sites of unclear significance into a functional context. The workflow developed supports decryptM profiling at scale and should be extendable to any molecule that modulates cellular activity by affecting PTMs or protein expression. This may include G protein–coupled receptor (GPCR) ligands, cytokines, chemokines, cofactors, metabolites, biologics, peptides, and hormones among many other factors. In the future, decryptM profiles may also serve to monitor and potentially predict drug responses in vivo. Looking further, we envision that matching decryptM profiles of cancer drugs with PTM profiles of cancer patients will become important for evidence-based treatment recommendations by molecular tumor boards. ■

The list of author affiliations is available in the full article.
***Corresponding author. Email: kuster@tum.de**
†These authors contributed equally to this work.

READ THE FULL ARTICLE AT
https://doi.org/10.1126/science.ade3925

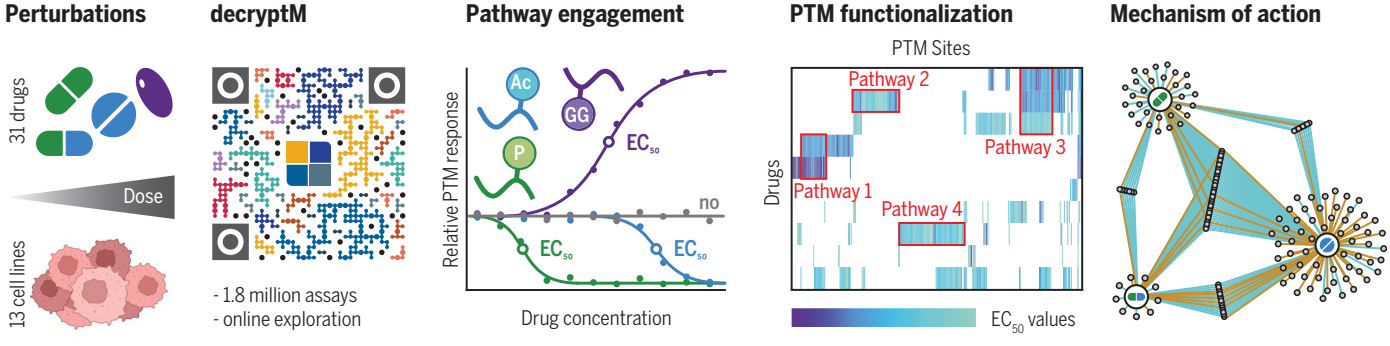

Schematic representation of the decryptM approach. Following the dose-dependent treatment of cancer cells with molecularly targeted drugs, quantitative mass spectrometry can record the dose-response characteristics of thousands of posttranslationally modified peptides in parallel. Such drug profiles can be used to place previously uncharacterized modification sites into a functional context and elucidate the cellular mechanism of action of a given drug. EC_{50}, half-maximal effective concentration; Ac, acetylation; GG, ubiquitinylation; P, phosphorylation.

PROTEOMICS

Decrypting drug actions and protein modifications by dose- and time-resolved proteomics

Jana Zecha[1,2]†, Florian P. Bayer[1]†, Svenja Wiechmann[1,2]†, Julia Woortman[1], Nicola Berner[1,2], Julian Müller[1], Annika Schneider[1], Karl Kramer[1], Mar Abril-Gil[3], Thomas Hopf[4], Leonie Reichart[4], Lin Chen[1], Fynn M. Hansen[1]‡, Severin Lechner[1], Patroklos Samaras[1], Stephan Eckert[1,2], Ludwig Lautenbacher[1], Maria Reinecke[1], Firas Hamood[1], Polina Prokofeva[1], Larsen Vornholz[3], Chiara Falcomatà[2,5], Madeleine Dorsch[6,7], Ayla Schröder[4], Anton Venhuizen[1], Stephanie Wilhelm[1], Guillaume Médard[1], Gabriele Stoehr[4], Jürgen Ruland[2,3,8,9], Barbara M. Grüner[6,7], Dieter Saur[2,5], Maike Buchner[3], Benjamin Ruprecht[1], Hannes Hahne[4], Matthew The[1], Mathias Wilhelm[1], Bernhard Kuster[1,2]*

Although most cancer drugs modulate the activities of cellular pathways by changing posttranslational modifications (PTMs), little is known regarding the extent and the time- and dose-response characteristics of drug-regulated PTMs. In this work, we introduce a proteomic assay called decryptM that quantifies drug-PTM modulation for thousands of PTMs in cells to shed light on target engagement and drug mechanism of action. Examples range from detecting DNA damage by chemotherapeutics, to identifying drug-specific PTM signatures of kinase inhibitors, to demonstrating that rituximab kills CD20-positive B cells by overactivating B cell receptor signaling. DecryptM profiling of 31 cancer drugs in 13 cell lines demonstrates the broad applicability of the approach. The resulting 1.8 million dose-response curves are provided as an interactive molecular resource in ProteomicsDB.

Most drugs act on proteins, are proteins themselves, lead to the production or degradation of proteins, or otherwise use the protein machinery of a cell to exert their therapeutic effects. Drug-regulated protein posttranslational modifications (PTMs) can constitute molecular target engagement markers, can identify drug-modulated pathways, and can illuminate downstream phenotypic responses of the cell. PTM-specific antibodies are most frequently used for this purpose. However, only a few exist, and those few yield semiquantitative information only, which biases the investigation of drug mechanism of action (MOA) to well-characterized proteins and pathways. Because desired or undesired polypharmacology is common and because drug responses often differ between cell types, it is important to characterize drugs on a proteome-wide scale to understand their MOAs. Consequently, proteomics has become an important tool in drug discovery and chemical biology (*1*–*4*). Yet, little systematic information is available about drug action at the level of PTMs, although many drugs modulate the activity of enzymes that regulate PTMs, such as kinases or lysine deacetylases (KDACs). Even more surprising is the lack of literature characterizing drugs at the level of proteins and PTMs in a dose- and time-dependent fashion, arguably among the most important characteristics of drug action in any biological context (*5*).

[1]Proteomics and Bioanalytics, Department of Molecular Life Sciences, School of Life Sciences, Technical University of Munich, 85354 Freising, Germany. [2]German Cancer Consortium, Partner Site Munich, 80336 Munich, Germany. [3]Institute of Clinical Chemistry and Pathobiochemistry, Klinikum rechts der Isar, School of Medicine, Technical University of Munich, 81675 Munich, Germany. [4]OmicScouts GmbH, 85354 Freising, Germany. [5]Institute of Experimental Cancer Therapy, Klinikum rechts der Isar, School of Medicine, Technical University of Munich, 80336 Munich, Germany. [6]Department of Medical Oncology, West German Cancer Center, University Hospital Essen, 45147 Essen, Germany. [7]German Cancer Consortium (DKTK), Partner Site University Hospital Essen, 45147 Essen, Germany. [8]German Center for Infection Research (DZIF), Partner Site Munich, 81675 Munich, Germany. [9]Center for Translational Cancer Research (TranslaTUM), 81675 Munich, Germany.
***Corresponding author. Email: kuster@tum.de**
†These authors contributed equally to this work.
‡Present address: Department of Proteomics and Signal Transduction, Max Planck Institute of Biochemistry, 82152 Martinsried, Germany.

DecryptM: Proteome-wide drug dose–response profiling of PTMs

In this work, we present a quantitative proteomic approach called decryptM, which is able to assess target and pathway engagement as well as the MOA of diverse cancer drugs by systematically measuring their dose- (and time-) resolved modulation of PTMs in cells (Fig. 1, A and B). Briefly, cells are treated with increasing concentrations of a drug and multiplexed using stable isotopes [tandem mass tags (TMTs); except for ubiquitinylation] (*6*). Tryptic peptides are fractionated by off-line chromatography for proteome expression profiling, and peptides bearing PTMs are enriched by immunoprecipitation (IP) (acetylation, ubiquitinylation) or immobilized metal affinity chromatography (IMAC) (phosphorylation). After liquid chromatography tandem mass spectrometry (LC-MS/MS) analysis, we derived dose-response characteristics for each peptide from the TMT reporter ion intensities by fitting and filtering sigmoidal curves using a four-parameter logistic regression (fig. S1A) (see materials and methods for details). Data collected for 31 drugs representing six drug classes in 13 human cancer cell line models (Fig. 1A) demonstrate that the decryptM approach is broadly applicable. The body of data represents 1.8 million quantitative cellular drug assays (dose-response curves) including 47,502 regulated phosphopeptides (124,660 detected on 11,982 proteins), 7316 regulated ubiquitinylated peptides (9173 detected on 3006 proteins), and 546 regulated acetylated peptides (2478 detected on 1377 proteins) (fig. S1, B and C). Most PTMs were not regulated by most drugs, which is valuable for understanding which pathways are addressed (or not) by each drug in cells. Only few examples can be highlighted in this study, but all primary mass spectrometry, peptide and protein identification, and quantification data as well as dose-response curves are available from PRIDE (PXD037285). Additionally, the decryptM data have been incorporated into ProteomicsDB (www.proteomicsdb.org/decryptm; Fig. 1C) (*7*), where it can be interactively explored using a web browser or mobile device (fig. S2A). Among the new functionalities is a drug-centric view that allows searching and filtering dose-response curves for EC_{50} values (half-maximal effective concentration), curve quality metrics, sequence motifs, and other parameters and cross-references to UniProt and PhosphoSitePlus (*8*, *9*). Multiple PTM peptides or a range of EC_{50} values can be compared to discover similarities that may place functionally unknown sites into the same pathway. In a protein-centric visualization, the position of drug-regulated PTM sites can be shown within the protein sequence and its three-dimensional (3D) structure (fig. S2, B and C).

Decrypting drugs and PTMs

DecryptM drug profiles are more informative than the conventional, differential approach of measuring drug effect sizes in replicates at one (typically high) drug concentration. This is because dose-response curves yield EC_{50} values, effect sizes, and additional curve fit parameters (Fig. 1B). These advantages of decryptM are illustrated by analyzing the phosphoproteome of A431 epidermoid carcinoma cells [dependent on epidermal growth factor receptor (EGFR) expression] in response to the EGFR inhibitor afatinib (Fig. 1D and fig. S3). Although replicates of single-dose treatments identified a large number of statistically significantly regulated phosphopeptides, only the dose-response data discriminate effects by potency (Fig. 1E and table S1). For afatinib, most phosphopeptides produced a coherent drug response at a pEC_{50} of ~8 (10 nM; $pEC_{50} = -\log EC_{50}$). Further phosphopeptides were regulated with weaker potency and smaller effect sizes, rendering these less interesting for primary MOA elucidation. Neither fold changes nor *P* values of single-dose replicates are indicative of such differences in afatinib potency

(fig. S4). DecryptM assays are reproducible with 70 and 90% of all determined EC_{50} values within half a log or one log of drug concentration, respectively (Fig. 1F).

The ability to assign potency to each regulated phosphopeptide has important implications for the interpretation of drug perturbation experiments. To illustrate this, we extended the experiment to include the lesser potent EGFR inhibitor gefitinib and the multikinase inhibitor dasatinib, which has a weak affinity for EGFR. Target deconvolution using Kinobeads (a proteome-wide quantitative drug-binding assay using immobilized kinase inhibitors) (*2*) showed that none of the three drugs interacts with extracellular signal–regulated kinase (ERK) [mitogen-activated protein kinase 1 and 3 (MAPK1/3)] or AKT, that dasatinib interacts with members of the SRC and EPH families with high potency, and that dasatinib and afatinib only weakly bind p38 mitogen-activated protein kinase (MAPK) (Fig. 1G). DecryptM profiling revealed that most regulated phosphopeptides, and the pathways that they are involved in, closely mirrored the potency for their targets (Fig. 1G and table S2). This close coherence between drug-target affinity (pK_D = $-\log K_D$, where K_D is the dissociation constant) and in-cell drug-PTM potency (pEC_{50}) raises the possibility that functionally uncharacterized PTM sites may be placed into known pathways and thus be decrypted on the grounds of guilt by association. In the following sections, examples representing six drug classes are discussed to highlight how decryptM profiling may be used to characterize the MOA of drugs in cells and to assign functional context to PTMs.

Chemotherapeutic drugs

DecryptM profiles were generated for the microtubule stabilizer paclitaxel and the antimetabolites cytarabine and methotrexate in K562 chronic myelogenous leukemia cells. Only two phosphopeptides showed regulation by methotrexate within the time frame (30-min drug treatment) of the experiment, and these could not be linked to antifolate-related biology. For paclitaxel, 7 of 7438 measured phosphopeptides were up-regulated with EC_{50} values of ~1 μM. The corresponding proteins, MAP7, MAP7D3, and ARHGEF2, all function in microtubule stabilization. This result demonstrates the extreme specificity with which drug regulation can be called by the dose-dependent measurements and shows that the molecular MOA of paclitaxel is detectable already after 30 min (fig. S5A). For cytarabine, 23 phosphopeptides were potently regulated (EC_{50} < 100 nM), and many of the underlying proteins are involved in the DNA damage response (e.g., NBM, NIPBL, and TIPIN) (fig. S5B). Most of these phosphopeptides are annotated to respond to ionizing radiation or ultraviolet (UV) light in PhosphoSitePlus (e.g., HMGA1, PSMD4,

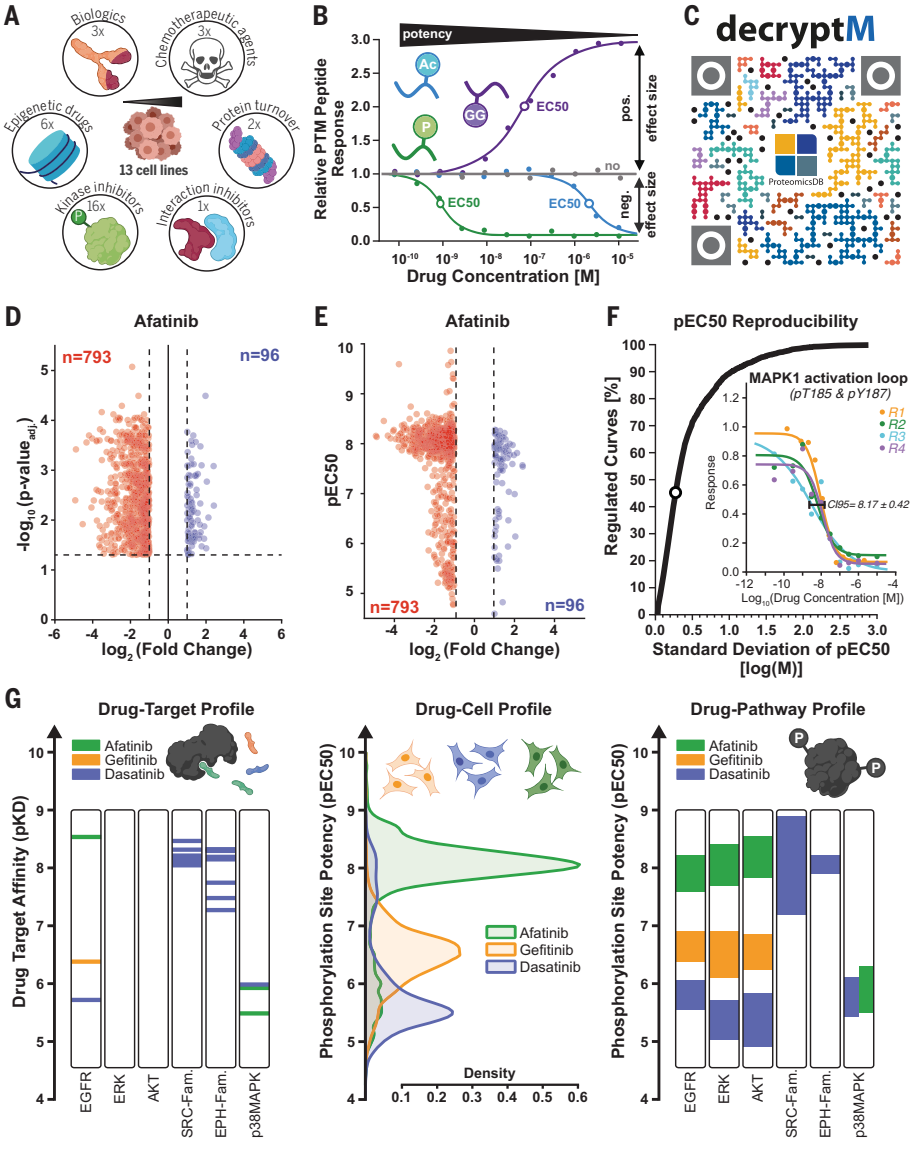

Fig. 1. DecryptM profiling of therapeutic drugs reveals essential details of their molecular MOAs. (**A**) Schematic representation of the dataset comprising 31 drugs from six different classes and 14 cellular models. (**B**) Schematic representation of the 1.8 million drug dose–response curves obtained for proteins or posttranslationally modified peptides by LC-MS/MS. P, phosphorylation; GG, ubiquitinylation; Ac, acetylation. For each peptide, PTM site, or protein, the EC_{50} and the cellular effect size were determined. (**C**) QR code linking to ProteomicsDB, where all dose-response curves can be interactively explored. (**D**) Volcano plot summarizing replicate (n = 4) single-dose afatinib treatments of A-431 cells [10-μM drug concentration, t test P value multiple testing corrected at 1% false discovery rate (FDR), fold change cut-off of 2]. Each dot is one phosphopeptide (blue, up-regulated by drug; red, down-regulated). Volcano plots for dasatinib and gefitinib can be found in fig. S4A. (**E**) Same as (D), but providing potency information for each regulated phosphopeptide (pEC_{50} = $-\log EC_{50}$). Not-regulated phosphopeptides were omitted for clarity. Potency plots for dasatinib and gefitinib can be found in fig. S4B. (**F**) Cumulative distribution plot shows the reproducibility of pEC50 estimations from replicate dose-response analysis (n = 4) of afatinib, gefitinib, and dasatinib. Seventy-two percent of all pEC_{50} estimates were reproducible within ½ log step of drug concentration. The inset shows replicate dose-response curves (along with the confidence interval at 95%) for the activation loop peptide of MAPK1 as a representative example, indicated by the dot in the cumulative distribution. (**G**) (Left) In vitro drug-target affinities of afatinib, gefitinib, and dasatinib measured by Kinobeads assays (pK_D = $-\log K_D$) (*2*) for selected kinases. (Middle) In cellulo potency (pEC_{50}) distributions of phosphorylation sites regulated by the same drugs in A-431 cells. (Right) Same as middle, but grouping regulated phosphopeptides by kinase substrate sites in annotated pathways (PhosphoSitePlus; table S1).

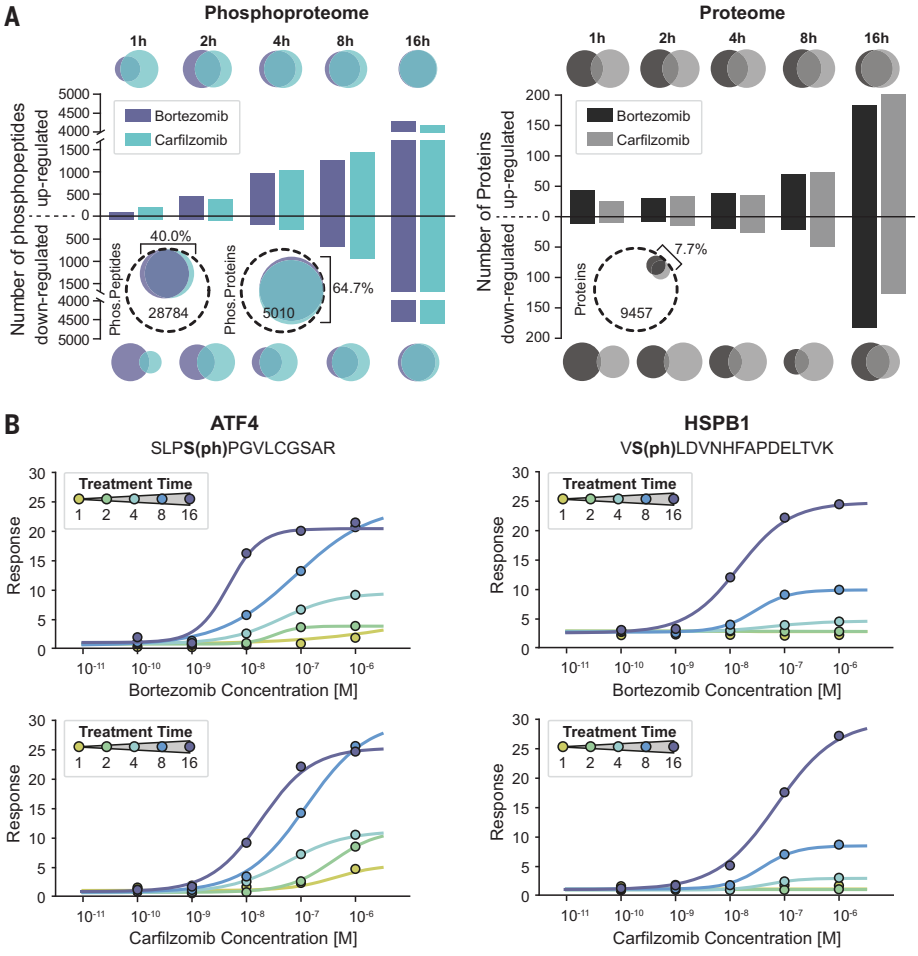

Fig. 2. 2D decryptM analysis of covalent proteasome inhibitors highlighting how cells mount a massive stress response. (**A**) (Left) Bar plot showing the number of dose-dependently up- or down-regulated phosphopeptides at a given time of treatment with BTZ and CFZ in RPMI8226 cells. The Venn diagrams at the top and bottom illustrate the number (size) and overlap of phosphopeptides between the two drugs at a given time point. The circled Venn diagrams illustrate the total (dashed line) and regulated fraction (colored circles) of phosphopeptides and proteins detected for the two drugs. (Right) Same as left, but for protein expression. (**B**) Examples for 2D decryptM profiles for BTZ (top row) and CFZ (bottom row) for two exemplary phosphopeptides on proteins involved in cellular stress responses (AFT4, HSPB1).

ZMYM4, and RFC1). Eight are phosphorylated at SQ sites, the substrate motif of the DNA damage response kinases ATM and ATR, and several have been shown to be substrates of these kinases. These data show that decryptM profiling can detect the cellular response to DNA damage after as little as 30 min—long before any phenotypic changes can be observed.

Protein interaction inhibitors

SHP099 is an allosteric inhibitor of the non-receptor tyrosine phosphatase SHP-2 (PTPN11). It inhibits the growth of cancer cells by stabilizing the inactive form of SHP-2, thereby blocking the activation of the MAPK pathway by receptor tyrosine kinases (RTKs) (*10*). This MOA is reflected in the 30-min decryptM profile of SHP099 in the EGFR overexpressing esophageal squamous cell carcinoma cell line KYSE-520 (fig. S5C). Although SHP099 does not inhibit phosphorylation sites indicating EGFR activity, phosphorylation of the EGFR substrate GAB1 is diminished in a dose-dependent fashion. This is because GAB1 can no longer associate with EGFR via SHP2, and this uncoupling prevents MAPK1/3 activation. Phosphorylation sites on proteins downstream of MAPK1/3 were inhibited with similar potencies (~700 nM; e.g., the kinases STK10 and RPS6KA1, the adaptor GAB2, the phosphatase DUSP16, and the transcription factor ELK1). About 30 further proteins, including many transcriptional regulators, also showed EC_{50} values between 100 and 500 nM. The current analysis places these proteins and phosphopeptides into the functional context of the RTK-MAPK axis and illustrates how pharmacological SHP-2 inactivation leads to a rapid breakdown of oncogenic signaling and transcriptional activity.

Proteasome inhibitors

The proteasome processes proteins that are marked for degradation by phosphorylation and ubiquitinylation. Bortezomib (BTZ) and carfilzomib (CFZ) have become the therapeutic backbone for treating multiple myeloma. Both drugs inhibit the proteasome by reversible covalent (BTZ) or irreversible (CFZ) binding to the protease PSMB5. 2D decryptM profiling (i.e., dose-response data collected at five different time points) in the multiple myeloma cell line RPMI 8226 showed broadly similar effects for both drugs (Fig. 2A and fig. S6). The number of regulated phosphorylation sites markedly increased over time and included very strong activation of cellular stress (table S6). Among these changes is the potent (EC_{50} < 100 nM) and strong (20-fold) up-regulation of phosphorylation at S248 of ATF4, the master transcription factor of the integrated stress response (*11*), and at S98 of the small heat shock protein HSPB1, both an activator of the proteasome and an inhibitor of apoptosis (Fig. 2B) (*12*, *13*). The 2D decryptM data also revealed that drug effects became more potent over time (Fig. 2B and fig. S6, A and B). This may be explained by the drugs' slow binding mode (*14*) or their covalent nature, which may reduce the number of functional proteasomes over time.

In stark contrast to the phosphorylation data, very few proteins showed expression changes (Fig. 2A). Most of these are stress response–related transcription factors and chaperones (fig. S6C), which can be rationalized as follows: Upon inhibition of the proteasome, misfolded proteins accumulate in the cell, reflected in a strong increase in ubiquitin levels (fig. S6D) and the detection of numerous known phosphodegrons (table S3). Consequently, the cell increases the production of stress-resolving proteins. At the same time, the decryptM data showed reduction in phosphorylation on many members of the transcription and translation machineries of the cell, indicating the shutdown of these processes in response to the drugs. This way, the cell may be able to sustain proteostasis for some time before eventually succumbing to the loss of the ability to degrade proteins.

Epigenetic drugs

Cancer cell proliferation requires frequent chromatin remodeling. Therefore, lysine acetyltransferases (KATs) and KDACs have become drug targets. To learn more about their cellular MOAs, we extended the decryptM approach to protein acetylation in HeLa cells. CUDC-101, a dual multikinase and histone deacetylases 1, 2, and 3 (HDAC1/2/3) inhibitor, up-regulated 139 of the 1133 measured acetylated peptides with nanomolar potency (Fig. 3A). The potency for

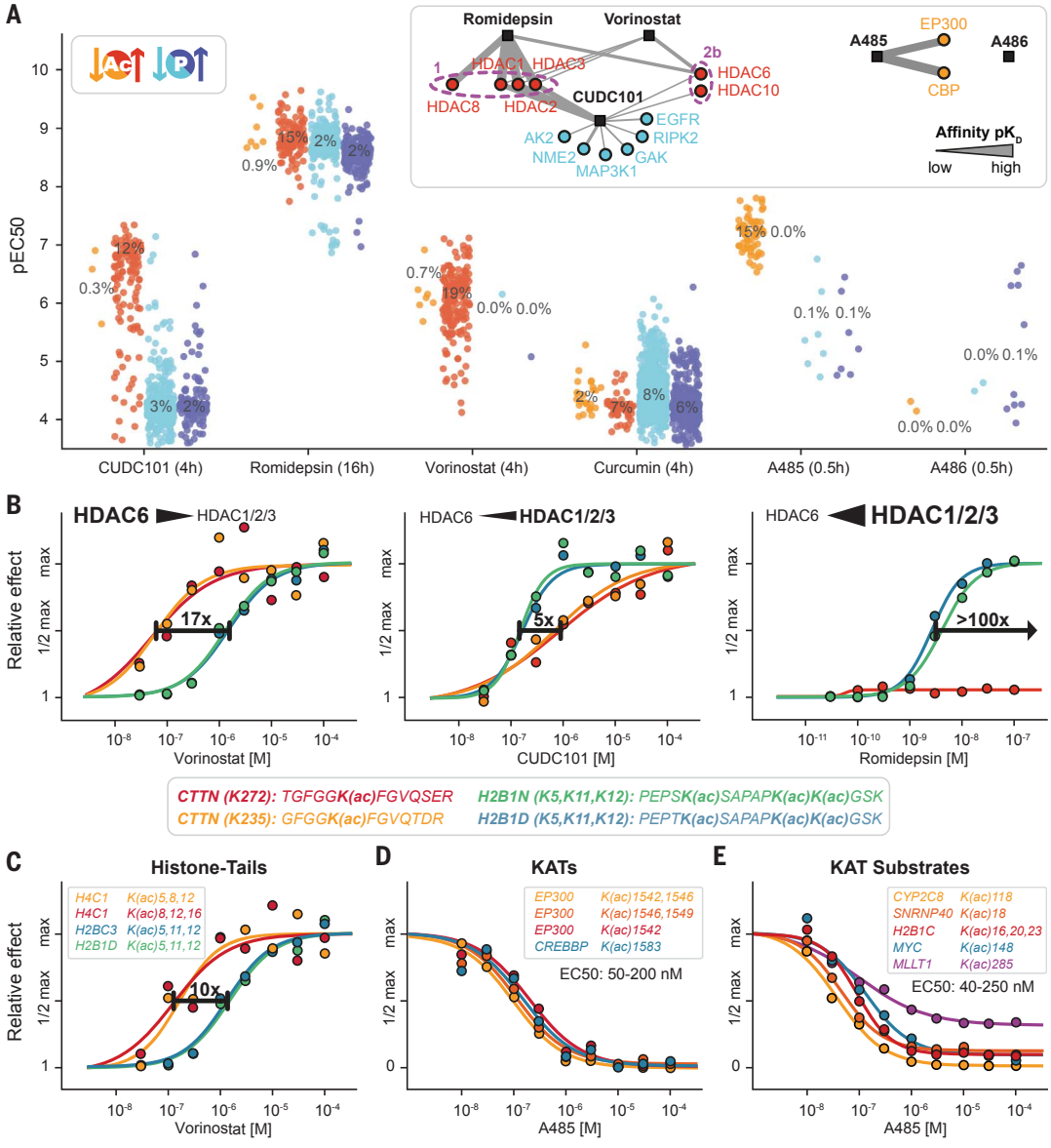

Fig. 3. Phosphorylation and acetylation decryptM signatures of epigenetic drugs delineate substrate preferences of KDACs and KATs. (**A**) Strip plots of the cellular potency (pEC_{50}) of drug-regulated acetylated (red) and phosphorylated peptides (blue). The insets show the affinity networks of targets engaged by the drugs determined by Kinobeads, KDAC beads, or recombinant KAT assays. The strength of the line indicates the potency of drug-target interactions (apparent dissociation constant, K_d^{app}; table S2) (*2*, *16*, *21*). The treatment time is indicated in parentheses next to the drug names, and percentages indicate the proportion of regulated PTM peptides versus all PTM peptides measured in the assay. (**B**) Examples of cellular dose-response curves for three HDAC inhibitors illustrating the different potencies by which these drugs regulate cellular acetylation levels on CTTN or histones. (**C**) Same as (B), but for several acetylation sites on histone tails. (**D**) Same as (B), but for autoacetylation sites on KATs after KAT inhibitor A485 treatment. (**E**) Same as (B), but for known and putative KAT substrate acetylation sites.

phosphopeptides was much weaker, which indicates that CUDC-101 engages its HDAC targets with 100-fold higher affinity than its kinase targets in cells. This questions the pharmacological relevance of kinase inhibition at least in this model system. The HDAC inhibitor vorinostat also had no noticeable effect on protein phosphorylation within 4 hours. By contrast, the natural compound romidepsin triggered a broad and potent response of the phosphoproteome after 16 hours, which may be related to HDAC inhibition but may also result from the extended incubation time, which was chosen because of the slow on rate of this peptidic drug (*15*).

DecryptM profiles of KDAC inhibitors mirrored their target selectivity (Fig. 3A). For instance, vorinostat binds much more potently to HDAC6 than HDAC1/2/3 (*15*, *16*). Consequently, the drug potently enhanced acetylation of the HDAC6 substrate cortactin (CTTN) (EC_{50} of 50 to 90 nM) (*17*) but not of the HDAC1/2/3 substrates H2B1N and H2B1D (EC_{50} of 1.0 to 1.5 μM). The weak HDAC6 inhibitor CUDC-101 increased CTTN acetylation only at substantially higher concentrations, and romidepsin had no effect on CTTN acetylation within the tested dose range (Fig. 3B). This confirms that CTTN acetylation at K235 and K272 are markers for HDAC6 engagement in cells. Other acetylated peptides with the same characteristics may thus be considered potential HDAC6 substrates. Examples include the cytoskeletal proteins PARVA and DBNL or proteins that play a regulatory role in autophagy, including DAP and PLAA (fig. S7A). These processes are regulated by HDAC6 (*18*), and a previous study had in fact shown increased acetylation of DBNL, PARVA, and PLAA in response to the HDAC6-selective inhibitor tubacin (*19*).

The decryptM data also uncovered details regarding the acetylation of histone tails. For instance, the N-terminal triacetylated peptide of H4C1 showed a 10-fold more-potent effect compared with the corresponding peptide of H2BC3 in response to vorinostat (Fig. 3C) and romidepsin (fig. S7B). We propose that this reflects different drug-target affinities for different HDAC1/2/3 isoforms and their complexes with defined substrate preferences. These drugs may have a distinct affinity for HDAC2 compared with HDAC1/3 because HDAC2 has recently been shown to deacetylate these sites on H2B, whereas HDAC1/3 primarily act on H4 (*20*).

The development of the KATs inhibitor A485 marked a breakthrough because it was the first compound that selectively and potently inhibited transcriptional coactivators CREB-binding protein (CBP) and p300 (*21*). In a

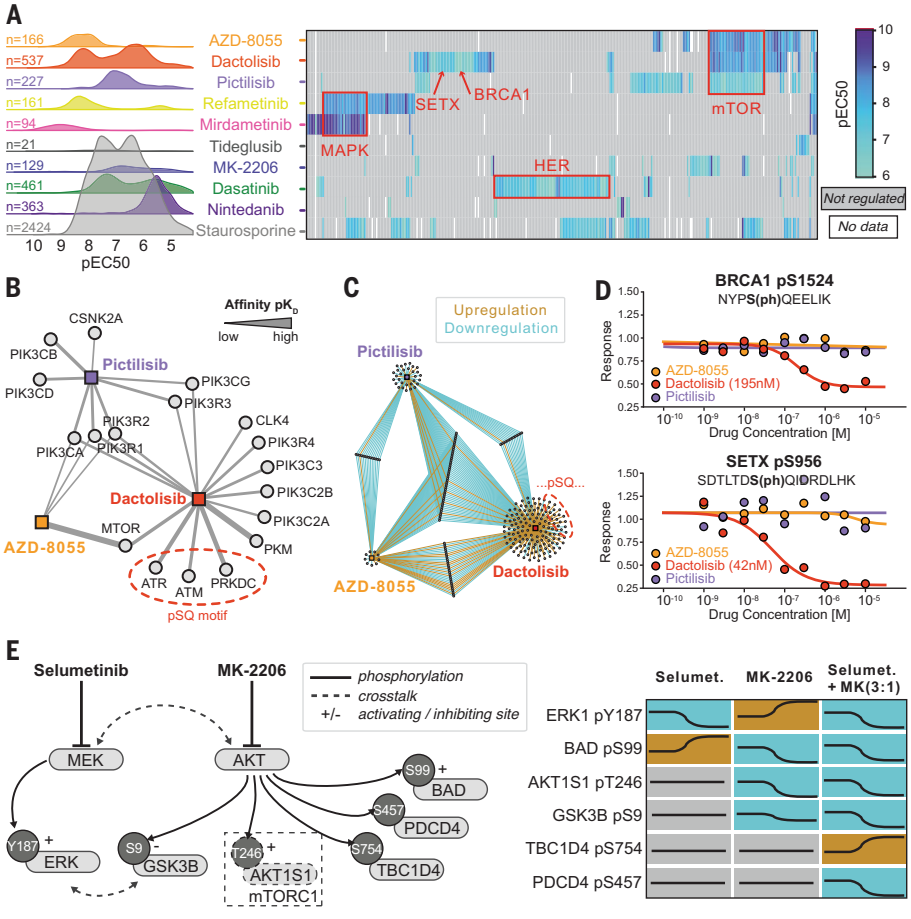

Fig. 4. DecryptM analysis of KIs identifies drug-specific signatures and places phosphorylation sites into functional contexts. (**A**) (Left) DecryptM-derived potency distribution plots of the number of phosphopeptides regulated by 10 KIs in A549 cells. (Right) pEC_{50} heatmap summarizing drug effects on annotated substrates of kinases or pathway members (red boxes). Not-regulated or missing values are shown in gray or white, respectively. (**B**) Affinity network (based on Kinobeads assays in pK_D) of kinases inhibited by the three designated PI3K and mTOR inhibitors pictilisib, AZD8055, and dactolisib. The strength of the line indicates the affinity of drug-target interactions. (**C**) Network of phosphopeptides regulated by the same three drugs as in (B). (**D**) Example dose-response curves for pSQ sites on BRCA1 and SETX that were specifically regulated by dactolisib. (**E**) Schematic representation of cross-talk between the MAPK and AKT pathways and dose-dependent phosphorylation changes by selumetinib and MK-2206 alone or in combination (concentration ratio of 3:1).

seminal study, Weinert *et al.* used proteomics and a single dose of A485 to identify a large number of potential CBP and/or p300 substrates and their temporal dynamics (*22*). DecryptM profiles of A485 in HeLa cells showed that A485 down-regulated relatively few ($n = 59$) acetylated peptides and did not have much effect on the phosphoproteome (Fig. 3A). Several (auto-) acetylation sites on CBP and p300 were inhibited with 50 to 200 nM EC_{50}, demonstrating target engagement in cells (Fig. 3D). Numerous histones and other nuclear proteins showed effects in the same dose range, including MYC K185, which confirms their specificity as substrates (Fig. 3E). Additionally, many previously unknown drug-responsive acetylation sites on functionally very diverse proteins were identified. Among these were MLLT1 (EC_{50} of 100 nM), a chromatin reader that recognizes protein acetylation; SNRNP40 (EC_{50} of 50 nM), a spliceosomal protein; and the P450 enzyme CYP2C8 (EC_{50} of 38 nM). CYP2C8 typically resides in the endoplasmic reticulum (ER) and detoxifies xenobiotics, such as the cancer drug paclitaxel (*23*). Because the protein is likely a CBP and/or p300 substrate, CYP2C8 may have additional functions in the nucleus akin to those of other oxygenases (*24*). The structurally similar but inactive analog A486 was ~350-fold less potent for CBP acetylation, which illustrates the potential value of decryptM profiles for understanding structure-activity relationships (fig. S7C). The natural compound curcumin has been proposed to inhibit KDACs and KATs (*25*). Because it is chemically reactive and among the strongest pan-assay interference compounds (PAINS) (*26*), the large number of regulated PTM peptides observed in the decryptM analysis (Fig. 3A) likely reflects unselective polypharmacology rather than any particular molecular mechanism.

Kinase inhibitors

Kinase inhibitors (KIs) have become important medicines, particularly in oncology. Although their target profiles and selectivities have been extensively studied, far less is known about which PTMs these drugs affect in cells. To begin to address this systematically, we performed decryptM for 10 KIs with a diverse target spectrum in A549 lung cancer cells. This survey uncovered drug-regulated phosphopeptides (Fig. 4A) in structured domains as well as disordered regions of proteins (fig. S8, A and B). The pan-kinase inhibitor staurosporine regulated nearly 2500 phosphopeptides over a broad range of potencies. All other drugs showed fewer regulated phosphopeptides (typically 10 to 100 s) and had narrower pEC_{50} distributions because of fewer targeted kinases. However, many KIs showed bimodal pEC_{50} distributions (fig. S9), implying engagement of different targets and pathways with distinct potencies or unspecific cellular toxicity at very high concentrations (fig. S10).

We next investigated to what extent KIs regulate the same phosphopeptides and signaling pathways. Each drug appeared to leave a particular decryptM signature that may constitute a pharmacodynamic marker for target and pathway engagement, identify points of conversion of several pathways, or distinguish closely related compounds. Evidence for these aspects could be delineated from clustering proteins with drug-regulated phosphorylation sites (Fig. 4A). For instance, the two MAPK kinase (MEK) inhibitors refametinib and mirdametinib shared regulated phosphopeptides in the MAPK pathway. Similarly, the designated mTOR inhibitor AZD-8055, the dual mTOR-PI3K inhibitor dactolisib, and the PI3K inhibitor pictilisib shared regulated phosphopeptides of mTOR pathway members. Extending the pathway analysis to all drugs portrayed a similar picture that can be rationalized by shared targets between drugs, but drug-pathway networks also highlighted connections beyond linear signal propagation that are the result of pathway cross-talk or feedback loops (fig. S11).

Other parts of the decryptM signatures appeared compound specific. Dactolisib is the only drug among the three mentioned above that potently targets the DNA damage sensor kinase PRKDC (K_D of 42 nM) as well as the DNA damage–activated kinases ATR (K_D of 91 nM) and ATM (K_D of 477 nM), as determined by the Kinobeads assay (Fig. 4B and table S2). These three kinases phosphorylate substrates with SQ/TQ motifs. The decryptM

profile of dactolisib contained 17 regulated SQ/TQ phosphorylation sites with EC_{50} values of 25 to 190 nM on 15 proteins not shared with the other two drugs, ruling them out as mTOR substrates (Fig. 4C). Among them is the BRCA1 oncogene, a known ATM and ATR substrate (Fig. 4D). The kinases for the other phosphorylation sites have not yet been delineated, but four respond to ionizing radiation (PhosphoSitePlus). It may, therefore, be reasoned that some of these sites could be targets of ATM, ATR, or PRKDC. Among these is the functionally orphan site pS956 of SETX (47 nM), a protein that has been reported to be involved in the cellular response to DNA damage (Fig. 4D; PhosphoSitePlus).

In an attempt to functionalize phosphorylation sites more systematically, we adopted a published machine learning approach that assigns functional scores to phosphorylation sites (*27*). The analysis revealed a small but statistically significant difference between drug-regulated and not-regulated phosphorylation sites for all 13 KIs tested (fig. S12). Most of the top-scoring cases were already functionally annotated in PhosphositePlus but also contained sites without an ascribed function. Distinctive cases identified from decryptM data may therefore be prioritized for functional follow-up studies on the basis of their computed functional scores. The data generated in this work may also aid in further developing such machine learning tools.

Cancer cells often develop resistance to single KIs, unfortunately. For instance, resistance to MEK or AKT inhibitors can be conveyed by cross-talk of the two pathways (*28*). DecryptM profiling in A549 lung cancer cells (Fig. 4E) confirmed that the AKT inhibitor MK-2206 reduced phosphorylation of the AKT substrates AKT1S1 (T2469) and GSK3B (S9) but induced ERK1 activity through phosphorylation at Y187. Conversely, the MEK inhibitor selumetinib abrogated ERK phosphorylation but induced phosphorylation of the AKT substrate BAD at S99. Drug combinations have proven effective in tackling such resistance mechanisms, and combining MK-2206 and selumetinib led to the desired inhibition of both pathways as well as to synergistic cell killing (fig. S13, A and B). The decryptM profiles also uncovered unexpected changes in protein phosphorylation. For instance, phosphorylation of the Rab guanosine triphosphatase (GTPase) activating protein TBC1D4 at S754 only increased, and phosphorylation of the tumor suppressor PDCD4 at S457 only decreased when combining both drugs (Fig. 4E and fig. S13C). These differing outcomes imply the presence of further players in the pathway cross-talk that have yet to be discovered.

The molecular wiring of signaling pathways in different cancer cells can diverge strongly, and decryptM profiling can uncover such cell line–specific signatures for a given drug. We chose the exquisitely selective EGFR and HER2 inhibitor lapatinib as an example and profiled three common cell line models that recapitulate important aspects of breast cancer biology: BT-474 (HR-positive, HER2-positive), SK-BR-3 (HR-negative, HER2-positive), and MDA-MB-175 (HR-negative, HER2-negative, HER3-positive) (*29*). Full proteome measurements confirmed that BT-474 cells express high levels of EGFR and HER2 (both inhibited by lapatinib), that SK-BR-3 cells express EGFR and HER2 at lower levels, and that MDA-MB-175 cells only express traces of EGFR and HER2 but high levels of HER3 (no functional kinase domain; fig. S14, A and B, and table S4). Lapatinib reduced growth in all cell lines (158 nM, 234 nM, and 695 nM, respectively; fig. S14C and table S5). The drug regulated hundreds of phosphopeptides in BT-474 and MDA-MB-175 cells but merely five in SK-BR-3 cells (fig. S14D). Notably, these five included potent inhibition of pY427 on SHC1 (18 nM) and pT246 on AKT1S1 (11 nM), verifying drug engagement of the RTK-SHC1-PI3K-AKT axis. In contrast to the other cell lines, SK-BR-3 cells showed no changes in SOS1, RAF, MEK, and ERK phosphorylation. This indicates that the

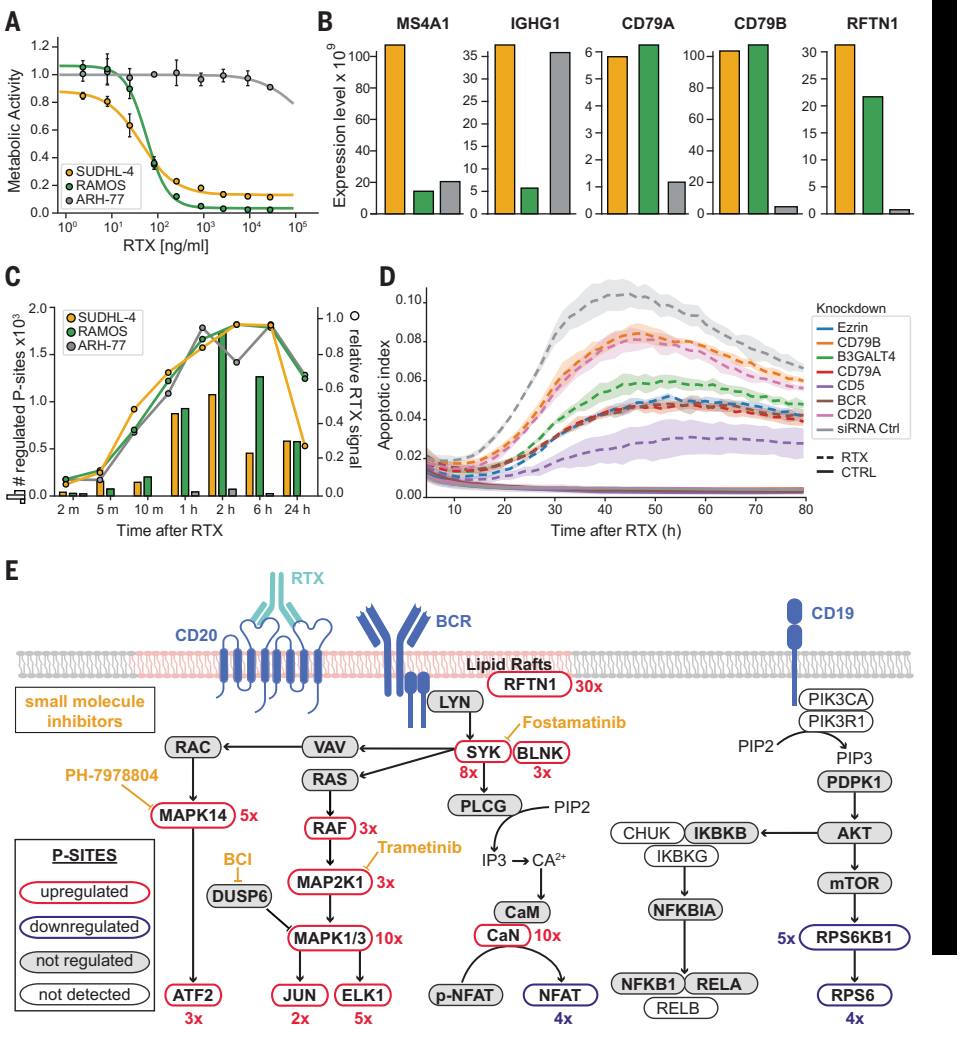

Fig. 5. DecryptM analysis of RTX reveals antibody-based killing of B cells through activation of the BCR-MAPK signaling axis. (**A**) Viability assays of RTX-sensitive and RTX-resistant cell lines. (**B**) Protein expression of BCR and lipid raft components in the same cell lines. (**C**) Number of dose-response regulated phosphopeptides at different times of RTX treatment for the same cell lines (left axis, bars) and the kinetics of RTX binding to these cells (right axis, lines). (**D**) Temporal dynamics of apoptosis induction upon addition of RTX to SUDHL-4 cells with and without prior siRNA-mediated knockdown of BCR and lipid raft components. Induction of apoptosis was monitored by annexin V labeling using live-cell imaging. Shaded areas indicate the standard deviation of replicate experiments (n = 3). (**E**) Summary representation of the major five pathways involved in BCR signaling and working model based on time- and dose-resolved decryptM profiles as well as pharmacological inhibition of certain proteins (yellow) of how engagement of these pathways (or lack thereof) leads to RTX-mediated cell death. Figures in red indicate the fold change of RTX-induced phosphorylation regulation.

MAPK pathway is decoupled from EGFR and HER2 signaling in SK-BR-3 cells and may explain why stronger phosphorylation changes were observed in BT-474 and MDA-MB-175 cells (fig. S14E). Their response to lapatinib resembled each other but differed in extent and detail. BT-474 cells showed a more prominent gene ontology (GO) signature for ERBB and MAPK than MDA-MB-175 cells. The opposite was observed for mTOR signaling (table S6). Both cells scored high for the spliceosome, which indicates cell stress. This is in line with live-cell imaging data of BT-474 spheroids, which detected cytotoxicity within 12 to 24 hours of lapatinib treatment (movie S1).

Antibodies

Therapeutic antibodies mark cells for recognition by the immune system, block receptor-ligand interactions, abrogate intracellular survival signaling, or promote death-inducing pathways. Notably, the intracellular MOAs of some of even the most established therapeutic antibodies are still rather unclear. As an example, we applied decryptM analysis to the breast cancer therapeutics trastuzumab (presumed to block signaling by preventing HER2 dimerization) and pertuzumab (blocking signaling by preventing HER2-HER3 dimerization) (*30*, *31*) in the same three breast cancer cell lines used for lapatinib above (fig. S15A). In stark contrast to lapatinib, trastuzumab had no potent effect on the cellular phosphoproteomes of any of the three cell lines (fig. S15B). Live-cell imaging of BT-474 spheroids showed that lapatinib led to their rapid disintegration, but spheroids continued to grow over the course of 7 days under trastuzumab treatment (fig. S15C and movie S1). The decryptM data concur with other studies in that the MOA of trastuzumab does not include a clear element of blocking mitogenic signaling (*30*, *31*). DecryptM analysis of pertuzumab resulted in ~30 regulated phosphopeptides in SK-BR-3 cells (no HER3 expression) and ~150 in BT-474 cells (low HER3 expression), but there was virtually no overlap with phosphopeptides regulated by lapatinib. By contrast, pertuzumab also regulated ~150 phosphopeptides in MDA-MB-175 cells (high HER3 expression), including down-regulated phosphopeptides shared with lapatinib, such as on SHC1, MAPK1/3, and AKT1S1 (fig. S15D). This result shows that pertuzumab cuts off the HER3-MAPK and HER3-PI3K/AKT signaling axis and explains how pertuzumab can retard cell cycle progression in breast cancer (*32*). We note that, in this context, among many other sites, pertuzumab reduced UCK2 phosphorylation at S254. This site is annotated to respond to EGF and nocodazole (PhosphoSitePlus). The former connects it to HER3, and the latter points to arresting cells in G2/M of the cell cycle. Similarly, the antibody led to the down-regulation of pS202 on OXR1. This site also responds to EGF (PhosphoSitePlus), and depletion of OXR1 in cells has been shown to lead to G2/M cell cycle arrest (*33*). Both sites are also regulated by lapatinib. This makes a case for placing UCK2 and OXR1 into a functional context with HER2 and HER3 signaling and cell cycle arrest in MDA-MB-175 cells.

Rituximab (RTX) is used for the treatment of B cell malignancies by way of targeting MS4A1 (CD20). Despite decades of research, many molecular aspects of how RTX leads to B cell depletion have remained elusive, and the relevance of the different response mechanisms in patients is still largely undetermined (*34*, *35*). To investigate to what extent phosphorylation-dependent signaling pathways are involved in the MOA of RTX, we chose the RTX-sensitive cell lines SU-DHL-4 (B cell lymphoma) and Ramos (Burkitt's lymphoma) as well as the RTX-insensitive plasma leukemia line ARH-77 (Fig. 5A and table S5) for decryptM analysis. Time-resolved full proteome analysis showed that all cell lines express MS4A1 and components of the B cell receptor (BCR) (Fig. 5B), that all cell lines rapidly bind RTX (Fig. 5C), and that all cells do not undergo substantial proteome expression changes over the course of the experiment. By contrast, 2D decryptM analysis of the phosphoproteome (RTX dose-response at eight time points between 0 min and 24 hours) showed massive responses in RTX-sensitive SU-DHL-4 and Ramos cells, whereas RTX-insensitive ARH-77 cells remained silent (Fig. 5C). Within 1 to 10 min of RTX treatment, GO analysis revealed a dominant signature for activation of BCR signaling ($P = 3.2 \times 10^{-6}$ in SU-DHL-4 cells; $P = 2.0 \times 10^{-9}$ in Ramos cells; table S6). In addition, a number of proteins involved in cytoskeleton remodeling and lipid raft formation were also strongly regulated. The response of SU-DHL-4 cells to RTX could be attenuated by small interfering RNA (siRNA)–mediated knockdown (2 days) of its target MS4A1 or CD20; components of the BCR (IGHG1, CD79A, CD79B, CD5); the lipid raft regulator EZR (*36*); and B3GT4, an enzyme involved in the biosynthesis of the ganglioside GM1, which is a major component of lipid rafts (Fig. 5D). At later time points (2 to 24 hours), the BCR signaling signature persisted ($P = 1.4 \times 10^{-8}$) and was accompanied by a strong signal for the spliceosome ($P = 1.0 \times 10^{-8}$), cellular senescence ($P = 1.2 \times 10^{-3}$), and apoptosis ($P = 1.3 \times 10^{-2}$; table S6), reflective of increasing cellular stress responses and shifting cells toward apoptotic cell death (fig. S16). This interpretation is backed by multiple lines of evidence, including a >10× down-regulation of phosphorylation on the proliferation marker MKI67, live-cell imagining data of SU-DHL-4 cells showing rapid aggregation of cells akin to other B cell stimuli (*37*), rapid annexin V staining indicating apoptosis induction, and cell death as measured by cytotox green (fig. S17A). Similar GO signatures were also observed in Ramos cells (table S6).

Regulating the survival (immune response) or death (tolerance induction) of B cells is essential to maintain the integrity of the immune system. The right balance is achieved by a concert of activated signaling networks, the details of which are not fully understood, are cell type specific, and are highly dynamic. Depending on the antigen bound by the BCR and other costimulating factors, MAPK, JNK, and PI3K-AKT-mTOR signaling—as well as translocation of the transcription factors nuclear factor κB (NF-κB) and nuclear factor of activated T cells (NFAT)—are induced upon BCR engagement. All four pathways are covered by the decryptM data of SU-DHL-4 cells, but very different levels of engagement after RTX treatment were detected (Fig. 5E). For instance, phosphorylation of the SYK (a BCR-proximal kinase of key importance in BCR signaling into the MAPK and p38 pathways) was up >10-fold. An even stronger up-regulation of the activation loop phosphorylation sites on MAPK1/3 and on many of their substrates was observed within minutes of RTX treatment. Robust induction of phosphorylation of calcineurin (PPP3CB/C) and, consequently, rapid and potent dephosphorylation of several sites on NFAT proteins was also observed (e.g., NFATC2-S110; fig. S17B). By contrast, engagement of the survival-promoting PI3K-AKT and NF-κB pathways could not be detected. Down-regulated phosphorylation sites on the mTORC1 substrate RPS6KB1 and its substrate RPS6 may even hint toward reduced mTORC1 activity upon RTX treatment (fig. S17B). Comparing protein expression across the three cell lines showed that ARH-77 cells express very low levels of the BCR complex partners CD79A and CD79B, which are necessary for the initiation of BCR signaling, and RFTN1 (raftlin), a major component of lipid rafts responsible for their integrity and required for BCR signaling (Fig. 5B) (*38*). This suggests that ARH-77 cells failed to respond to RTX because they are unable to form stable rafts and a functional BCR signalosome. We note that RFTN1 phosphorylation at S467 increased 10-fold within 2 min of RTX treatment, 30-fold within 5 min, and remained high for at least 2 hours in SU-DHL-4 cells (fig. S17C). Although the upstream kinase is not yet known, the decryptM data place this phosphorylation site (as well as many others not discussed here) into the functional context of BCR signaling. A recent study has also linked RTX to B cell death via engaging BCR signaling in SU-DHL-4 cells (*39*), and our study concurs with many of their observations. The time- and dose-dependent data provided here enabled a more fine-grained analysis of the events eventually leading to cell death.

Adding to the siRNA experiments presented above, we performed time-resolved live-cell

imaging experiments to measure cytotoxicity in SU-DHL-4 cells treated with RTX alone or pretreated with small molecule inhibitors directed against targets involved in BCR signaling and the MAPK pathway (fig. S18, A and B). Inhibition of SYK by fostamatinib and of MAP2K1 (the kinase upstream of MAPK1/3) by trametinib led to a clear reduction of RTX-mediated cytotoxicity. The same was observed, to a lesser extent, for inhibition of MAPK1/3 by ulixertinib and of p38 MAPK by PH-7978804. We then used fluorescence-activated cell sorting (FACS) to analyze SU-DHL-4 cells treated with RTX alone or in combination with the SYK inhibitor fostamatinib or the DUSP1/6 inhibitor BCI (fig. S18, C and D). Also in this assay, SYK inhibition diminished the cytotoxic effect of RTX. BCI alone was effective in killing cells (by indirectly activating MAPK1/3 through DUSP1/6 inhibition) and has been shown to induce cell death in patient-derived pre-B ALL cells through MAPK1/3 activation (*40*). Notably, the combination of BCI with RTX was even more effective in inducing cytotoxicity in SU-DHL-4 cells.

The collective evidence supports the following model of RTX-mediated killing of CD20-positive B cells: RTX binds to CD20 located in lipid rafts alongside the BCR complex leading to a strong activation of the MAPK pathway and the calcineurin-NFAT axis. Unlike in physiological BCR activation, the balancing activity of PI3K-AKT and NF-κB signaling appears to be missing in SU-DHL-4 cells. Consequently, RTX likely tips the balance toward tolerance or apoptotic cell death (Fig. 5E) (*41*–*44*). Our data may even suggest that the detection of MS4A1 in B cell cancer patients alone is insufficient to stratify them for RTX treatment (*35*) and that components such as BCR and RFTN1 should be considered in addition. To what extent the above preliminary model may be generalized remains to be investigated by extending the analysis to further cell lines and patient-derived models.

Conclusions

The examples above were meant to illustrate the substantial potential of decryptM to characterize the MOA of drugs, generate drug-specific PTM signatures, study resistance mechanisms, and place drug-regulated PTM sites of unclear significance into a functional context. Given the streamlined workflow developed in this study, decryptM can now be performed at scale. The method should be extendable to any molecule that modulates cellular activity by affecting PTMs or protein expression, including G protein–coupled receptor (GPCR) ligands, cytokines, chemokines, cofactors, metabolites, biologics, peptides, or hormones—to name a few.

There are also limitations of the approach in its current form. For instance, if a drug hits multiple targets with similar potency, it will still be difficult to attribute the decryptM data to one or the other target. This highlights the continuing need for more-selective chemical probes to study PTM biology. At present, only bulk material has been analyzed. Hence, effects specific to certain cellular states (or even single cells) are likely missed. The analysis is not fully comprehensive because standard MS-based PTM proteomics still misses PTM sites for which specific antibodies are available today. Another technical limitation is that the analysis of acetylation and ubiquitinylation requires rather large quantities of starting material. As with other profiling technologies, decryptM profiles are powerful starting points but may not fully stand alone. In other words, the profiles generate many hypotheses that will have to be followed up by further orthogonal experimentation.

In the future, decryptM profiles may serve to monitor and perhaps eventually predict drug responses in vivo once sufficient drugs and cell systems have been analyzed. Looking further, we envision that matching decryptM profiles of cancer drugs with cancer patient PTM profiles indicative of oncogenic signaling will become an important tool in molecular tumor boards for personalized and evidence-based treatment recommendations.

Materials and methods summary

Full details of the decryptM methodology are described in the supplementary materials and are summarized here as follows: Cell lines were treated with increasing concentrations of a drug (dose-dependent) or for increasing times at a fixed drug concentration (time-dependent). Cells were then lysed, proteins extracted, and peptides generated by trypsin digestion. The peptides were stable isotope–labeled using TMTs (*45*). Posttranslationally modified peptides were enriched by IP (acetylation, ubiquitinylation) or IMAC (phosphorylation) (*46*). Full proteome or PTM samples were analyzed by LC-MS/MS, and peptides and proteins identified and quantified using MaxQuant/Andromeda (*47*). Dose-response curves for each PTM peptide were fitted to a four-parameter sigmoidal curve on the basis of TMT reporter ion intensities, yielding drug EC_{50} values for each protein or PTM peptide, the size of each effect, as well as curve-fitting quality metrics. A set of filters was applied to extract regulated dose-response curves from each experiment. The dose- or time-dependent regulated PTMs (or protein expression values) were further analyzed to explore the mode of action of the respective drugs and the specific responses of different cell lines. Regulated curves were functionally annotated based on the PhosphoSitePlus database (*8*). Drug-target affinities were obtained from competition pull-down experiments using Kinobeads (*2*) and HDAC beads as described (*16*).

REFERENCES AND NOTES

1. H. J. Benns, C. J. Wincott, E. W. Tate, M. A. Child, *Curr. Opin. Chem. Biol.* **60**, 20–29 (2021).
2. S. Klaeger *et al.*, *Science* **358**, eaan4368 (2017).
3. J. R. Lill, W. R. Mathews, C. M. Rose, M. Schirle, *Expert Rev. Proteomics* **18**, 503–526 (2021).
4. M. M. Savitski *et al.*, *Science* **346**, 1255784 (2014).
5. H. G. Budayeva *et al.*, *Mol. Cell. Proteomics* **21**, 100221 (2022).
6. A. Thompson *et al.*, *Anal. Chem.* **75**, 1895–1904 (2003).
7. L. Lautenbacher *et al.*, *Nucleic Acids Res.* **50**, D1541–D1552 (2022).
8. P. V. Hornbeck *et al.*, *Nucleic Acids Res.* **43**, D512–D520 (2015).
9. UniProt Consortium, *Nucleic Acids Res.* **49**, D480–D489 (2021).
10. Y. N. Chen *et al.*, *Nature* **535**, 148–152 (2016).
11. K. Pakos-Zebrucka *et al.*, *EMBO Rep.* **17**, 1374–1395 (2016).
12. D. Kennedy *et al.*, *Cell Death Dis.* **8**, e3026 (2017).
13. A. Parcellier *et al.*, *Mol. Cell. Biol.* **23**, 5790–5802 (2003).
14. B. B. Hasinoff, *Arch. Biochem. Biophys.* **639**, 52–58 (2018).
15. M. B. Robers *et al.*, *Nat. Commun.* **6**, 10091 (2015).
16. S. Lechner *et al.*, *Nat. Chem. Biol.* **18**, 812–820 (2022).
17. X. Zhang *et al.*, *Mol. Cell* **27**, 197–213 (2007).
18. J. Y. Lee *et al.*, *EMBO J.* **29**, 969–980 (2010).
19. C. Schölz *et al.*, *Nat. Biotechnol.* **33**, 415–423 (2015).
20. C. Moreno-Yruela *et al.*, *Nat. Commun.* **12**, 62 (2021).
21. L. M. Lasko *et al.*, *Nature* **550**, 128–132 (2017).
22. B. T. Weinert *et al.*, *Cell* **174**, 231–244.e12 (2018).
23. C. Tsukada *et al.*, *Drug Metab. Pharmacokinet.* **30**, 366–373 (2015).
24. J. Wu *et al.*, *Redox Biol.* **47**, 102170 (2021).
25. F. U. Hassan *et al.*, *Front. Genet.* **10**, 514 (2019).
26. J. B. Baell, G. A. Holloway, *J. Med. Chem.* **53**, 2719–2740 (2010).
27. D. Ochoa *et al.*, *Nat. Biotechnol.* **38**, 365–373 (2020).
28. E. Kun, Y. T. M. Tsang, C. W. Ng, D. M. Gershenson, K. K. Wong, *Cancer Treat. Rev.* **92**, 102137 (2021).
29. X. Dai, H. Cheng, Z. Bai, J. Li, *J. Cancer* **8**, 3131–3141 (2017).
30. C. A. Hudis, *N. Engl. J. Med.* **357**, 39–51 (2007).
31. B. Nami, H. Maadi, Z. Wang, *Cancers* **10**, 342 (2018).
32. G. Brockhoff *et al.*, *Cell Prolif.* **40**, 488–507 (2007).
33. M. Yang *et al.*, *Sci. Rep.* **5**, 17409 (2015).
34. A. Felberg *et al.*, *Front. Immunol.* **11**, 584509 (2020).
35. T. M. Pierpont, C. B. Limper, K. L. Richards, *Front. Oncol.* **8**, 163 (2018).
36. N. Gupta *et al.*, *Nat. Immunol.* **7**, 625–633 (2006).
37. J. Zhou *et al.*, *PLOS ONE* **13**, e0191634 (2018).
38. K. Saeki, Y. Miura, D. Aki, T. Kurosaki, A. Yoshimura, *EMBO J.* **22**, 3015–3026 (2003).
39. J. Edelmann *et al.*, *iScience* **24**, 102089 (2021).
40. S. Shojaee *et al.*, *Cancer Cell* **28**, 114–128 (2015).
41. L. Barnabei, E. Laplantine, W. Mbongo, F. Rieux-Laucat, R. Weil, *Front. Immunol.* **12**, 716469 (2021).
42. A. M. Buhl, C. M. Pleiman, R. C. Rickert, J. C. Cambier, *J. Exp. Med.* **186**, 1897–1910 (1997).
43. J. I. Healy *et al.*, *Immunity* **6**, 419–428 (1997).
44. J. Schulze-Luehrmann, S. Ghosh, *Immunity* **25**, 701–715 (2006).
45. J. Zecha *et al.*, *Mol. Cell. Proteomics* **18**, 1468–1478 (2019).
46. B. Ruprecht *et al.*, *Mol. Cell. Proteomics* **14**, 205–215 (2015).
47. J. Cox, M. Mann, *Nat. Biotechnol.* **26**, 1367–1372 (2008).
48. F. P. Bayer, F. Hamood, kusterlab/decryptM: 2023 – Science, v0.1.0, Zenodo (2023).

ACKNOWLEDGMENTS

The authors are grateful to A. Hubauer, M. Krötz-Fahning, N. Goldbach, M. Lorenz, W. Gabriel, and E. Kahl for technical assistance. Some aspects of the figures were created with BioRender.com. **Funding:** This work was partly funded by the Federal Ministry of Education and Research (CLINSPECT-M, FKZ161L0214A; DIAS, FKZ 031L0168), the Deutsche Forschungsgemeinschaft (DFG, German Research Foundation; SFB1309 – 325871075; SFB 1335 – 360372040; GR 4575/1-1; SA 1374/4-2), the European Research Council (ERC; AdG grant nos. 833710 and 834154), the European Union's Horizon 2020 Program (grant agreement 823839 - H2020-INFRAIA-2018-1, EPIC-XS), the Wilhelm Sander-Foundation (2020.174.1), and the German Cancer Aid (Deutsche Krebshilfe, Max Eder Grant, project ID 70114720). **Author contributions:** J.Z., B.R., and B.K. conceived the decryptM approach. J.Z., F.P.B., S.Wie., J.W., N.B., A.Schn., M.A.-G., K.K., L.C., F.M.H., S.L., S.E., M.R., F.M.H., P.P., L.V., C.F., M.D., L.R., A.Schr., and A.V. performed laboratory experiments. F.P.B., J.M., T.H., P.S., L.L., G.S., M.T., J.Z., S.Wie., J.W., N.B., A.Schn., K.K., L.C., F.M.H., S.L., S.E., M.R., P.P., L.V., C.F., M.D., L.R., A.Schr., A.V., and B.K. performed data analysis. J.R., J.Z., S.Wil., B.M.G., D.S., G.M., M.B., H.H., M.T., M.W., and B.K. directed and supervised experiments and data analysis. F.P.B., A.Schn., M.T., and B.K. wrote the manuscript with

input from all authors. **Competing interests:** B.K. and M.W. are founders and shareholders of OmicScouts and MSAID. They have no operational role in either company. H.H. is cofounder, shareholder, and CEO of OmicScouts. T.H., L.R., A.Schr., and G.S. are present or past employees of OmicScouts. J.Z. is currently an employee of AstraZeneca, S.Wie. is an employee of Novartis, and F.M.H. is an employee of OmicEra Diagnostics GmbH, but all of the work in this study has been performed while at TUM. All other authors declare no competing interests. **Data and materials availability:** The data supporting the findings of this study are available within the paper, the supplementary materials, and public repositories. The raw mass spectrometry proteomics data, protein identification and quantification results (table S7), as well as time- and dose-response curves have been deposited with the ProteomeXchange Consortium via the PRIDE partner repository with the dataset identifier PXD037285. From these data, all analysis presented in this study can be reproduced. In addition, dose-response data are also available in ProteomicsDB (https://www.proteomicsdb.org/decryptm). The code of the decryptM data processing pipeline can be found at Github (https://github.com/kusterlab/decryptm) and is also archived at Zenodo (*48*). There are no restrictions on materials other than those imposed by the commercial availability of cell lines, antibodies, drugs, and other reagents used in this study. **License information:** Copyright © 2023 the authors, some rights reserved; exclusive licensee American Association for the Advancement of Science. No claim to original US government works. https://www.science.org/about/science-licenses-journal-article-reuse

SUPPLEMENTARY MATERIALS

science.org/doi/10.1126/science.ade3925
Materials and Methods
Figs. S1 to S18
Tables S1 to S7
References (*49*–*60*)
MDAR Reproducibility Checklist
Movie S1

View/request a protocol for this paper from *Bio-protocol*.

Submitted 12 August 2022; accepted 21 February 2023
Published online 16 March 2023
10.1126/science.ade3925

By **Cat Collins**

Rejection as redirection

Sitting in the bar for my friend's 21st birthday, I feel a buzz in my pocket. Glancing at the email's sender, my heart races. It starts off as you would expect: "Thank you for your interest" and "the deliberation process took longer than expected as we received many highly qualified applicants." It ends with "We are sorry to inform you" and my vision blurs. The position—measuring soil respiration in the Namib Desert as part of an undergraduate research program through my university—had felt like the answer I had spent years looking for. I had put so much time and emotional energy into applying, and I thought the rejection meant the end of the road for my science career. Only later would I see that instead, it provided an exciting new direction to follow.

I always wanted to be a scientist. I started off as a biology student but quickly felt unwelcome among the premeds. I tried out physics and spent a semester uninspired and lonely, lectures on a laptop screen as my only company. With each discipline switch I felt increasingly anxious I wouldn't find the right fit before my scholarship ran out—until, thanks to a random suggestion from my mom, I ended up in geology and fell in love. When I found that summer research program, I thought I had found the perfect topic for my honors thesis and a stepping stone to my dream academic career. This was the one program I wanted. I wasn't going to consider other options.

"I reminded myself that rejection would not be the end of the road."

Then came that rejection email. I replied graciously, but I felt myself spiraling. Once again, I felt lost and hopeless. It seemed clear I'd never get to work in a lab or become a scientist.

So I was shocked when, not long after the rejection email, the professor running the research program invited me to observe the work being done in her lab. I jumped at the chance, and a few weeks later I was equally shocked—and thrilled—when she invited me to talk with her about potential thesis projects I could pursue in her lab. What she proposed didn't seem as exciting as the original project I had applied to, but I felt I wasn't in a position to be picky; this was a great opportunity and I was going to give it my all.

I found myself collaborating with a robotics professor on techniques for collecting data from the desert remotely, and the work introduced me to a whole new way to think about geoscience. That project, which I could complete from my couch instead of in the searing heat of the desert, not only survived the pandemic lockdown but was innovative and fresh and worked where traditional methods didn't. In the end, I had a thesis and a new scientific interest to pursue.

When I applied to grad school, the earlier rejection and the good that came out of it centered me. I decided I would still be selective about the options I pursued rather than casting a broad net, but at the same time I reminded myself that rejection would not be the end of the road; being proactive and diligent can open doors when others close.

I found three programs that promised to allow me to follow my desired research direction and threw myself into the applications with the same anxious excitement as before. When I was rejected from one that had seemed like a perfect fit, it was undoubtedly difficult. But this time I had the perspective to keep it from sending me into a tailspin. It helped that in the end I was accepted into one of the other programs I was also excited about.

Despite my best intentions when applying, I ended up tackling yet another new research direction: using medical imaging techniques to characterize sediment samples from beneath the Greenland Ice Sheet. It's nothing like what I envisioned when I started grad school. But just as before, remaining open to unanticipated challenges and evolving interests has led me to new personal and intellectual horizons.

Rather than setting plans in stone, I've learned that sometimes I need to take the opportunities that are offered, even if they don't sound exactly perfect at the time, and make the most of them. And I've learned to look at each rejection as a redirection instead. ■

Cat Collins is a graduate student at the University of Vermont.
Send your career story to SciCareerEditor@aaas.org.

ILLUSTRATION: ROBERT NEUBECKER

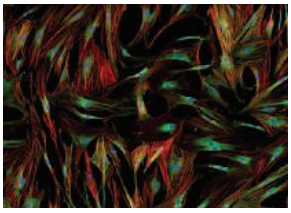

Cryopreserved Primary Human Cells
AMSBIO is a leading supplier of cryopreserved primary human cells for research from multiple organs including the lung, liver, intestine, and kidney. Every batch of cells is validated for cell viability, morphology, plating efficiency, and cell marker data. Cells are cultured for 5-7 days before being released and delivered with donor demographics and serology data demonstrating viral and mycoplasma negative status. The range of cryopreserved primary human cells from AMSBIO includes lung products (bronchial, tracheal, and small airway epithelial cells and fibroblasts); kidney products (cortical cells, podocytes, proximal tubules, mesangial cells, and glomerular endothelial cells); intestinal products (epithelial cells and myofibroblasts from the ascending, transverse, and descending colon, and from the duodenum, jejunum, and ilium); and liver products (Kupffer cells, stellate cells, sinusoidal endothelial cells, biliary epithelial cells, and hepatocytes).
AMS Biotechnology
For info: +1-617-945-5033
www.amsbio.com/human-normal-primary-cells

HEK293-Specific Viral Feed Medium
FUJIFILM Irvine Scientific announced the launch of its BalanCD HEK293 Viral Feed. The chemically defined, nutrient-based feed medium is designed to boost adeno-associated viral vector (AAV) production for gene therapy applications and viral vector-based vaccines. It is chemically defined and formulated to deliver consistent performance while increasing viral vector production in HEK293 cells grown in suspension and at scale. BalanCD HEK293 Viral Feed is GMP manufactured using raw materials sourced using a strict raw material and supply chain program to ensure continuity of supply and lot-to-lot reliability for HEK293-specific applications. It is available in a 500 mL liquid format (catalog) and made-to-order powder format (or other configuration), and may be used with a wide range of basal growth media.
FUJIFILM Irvine Scientific
For info: +1-800-577-6097
www.irvinesci.com

iPSC-Derived Ventricular Cardiomyocytes
Axol Bioscience (Axol) announced that its human induced pluripotent stem cell (iPSC)–derived ventricular cardiomyocytes have undergone comprehensive in vitro pro-arrhythmia assay (CiPA) validation. The human iPSC-derived ventricular cardiomyocytes are manufactured at scale according to strict quality control standards using ISO 9001–accredited quality management systems, providing a continuous source of cells from the same genetic background for use in multiple experiments. This offers a physiologically relevant in vitro research model of human heart cells to reliably and repeatably test drug candidates for cardiotoxicity at scale.
Axol Bioscience
For info: +1-800-678-2965
axolbio.com/cells/cardiovascular-system

NASH in Vitro Models
In conjunction with CN Bio's PhysioMimix microphysiological system (MPS), its NASH-in-a-box (NIAB) kit provides researchers with in-house capabilities to gain physiologically relevant insights into the mechanism of disease, human drug efficacy, and safety toxicology. The assay addresses the human-relevance limitations of existing approaches, bridging the gap between human 2D cell culture and expensive animal models, which are ineffective in mimicking the full disease spectrum. Within the NIAB kit, new users are guided through a simple-to-follow, software-based protocol for successfully co-culturing internally validated primary human hepatocytes, stellate, and Kupffer cells. By introducing fatty acids, researchers can recapitulate key NAFLD/NASH disease states: intracellular fat accumulation, inflammation, and fibrosis. Once created, the model enables the investigation of the precise mechanistic effects of drugs (of any modality) and disease via high-content, clinically translatable end-point measurements.
CN Bio
For info: +1-415-523-4005
cn-bio.com/nash-in-a-box

3D Cell Culture Reagents
Cell Guidance Systems and Manchester BIOGEL partnered to launch PODS-PeptiGels. The kit combines the benefits of two existing innovative cell culture technologies—synthetic peptide hydrogels (PeptiGels) and a range of sustained release growth factors (PODS)—to provide a reproducible and highly adaptable environment for 3D cell culture. The ready-to-use kit allows researchers to mix and match to suit the aims of their research by selecting from more than 70 growth factors and combining them with an assortment of hundreds of hydrogels, each with mechanical and biomimetic tuneability. Providing researchers with an all-in-one, animal-free solution for 3D cell culture applications, the PeptiGel hydrogel—available in a variety of gel stiffnesses and cell adhesion motifs—is produced using synthetic peptides, reducing batch variations and enabling reproducible results. The PODS crystal protects the growth factor cargo, allowing sustained release over a longer period, thereby reducing the frequency of media changes required and minimizing growth factor concentration cycles.
Cell Guidance Systems and Manchester BIOGEL
For info: 760 450 4304 and +44-(0)-1625-238800
www.cellgs.com and manchesterbiogel.com

Whole Tissue Sample Picker
Ziath announces the launch of the Mohawk 48 tube selector and picker. Designed to select and pick wide, heavy, or tall tubes, this new system is perfect for retrieving individual whole tissue samples from storage. The Mohawk 48 uses 48 solenoid pins to raise and select a specific frozen or thawed sample tube when a 48-position tube rack is presented according to a picklist from Excel or a LIMS system. Alternatively, specific individual tubes can be manually selected and picked via the user interface. Individual sample tubes can be picked from a single rack, or users can create a picklist to select tubes across multiple racks. Picklists can be created by connecting the Mohawk to a Ziath whole-rack reader, such as the Mirage. The advantage in this case is that destination racks of picked tubes can also be verified for accuracy on the same reader.
Ziath
For info: +1-858-880-6920
ziath.com/newmohawk48

Electronically submit your new product description or product literature information! Go to www.science.org/about/new-products-section for more information.

Newly offered instrumentation, apparatus, and laboratory materials of interest to researchers in all disciplines in academic, industrial, and governmental organizations are featured in this space. Emphasis is given to purpose, chief characteristics, and availability of products and materials. Endorsement by *Science* or AAAS of any products or materials mentioned is not implied. Additional information may be obtained from the manufacturer or supplier.